

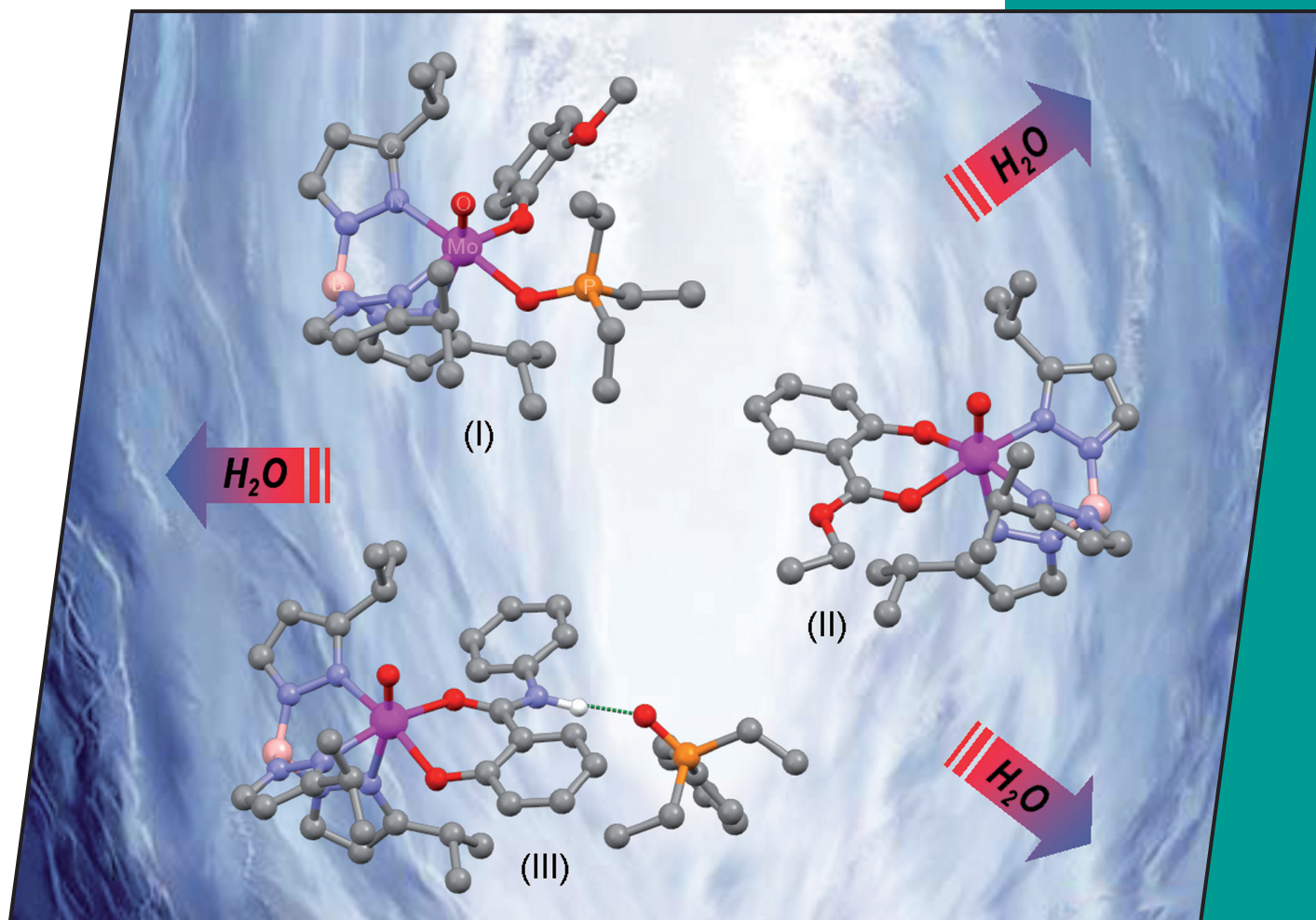
21/2010

3rd July Issue

[21]

EurJIC
European Journal of
Inorganic Chemistry

Eur. J. Inorg. Chem. 2010, 3233–3388

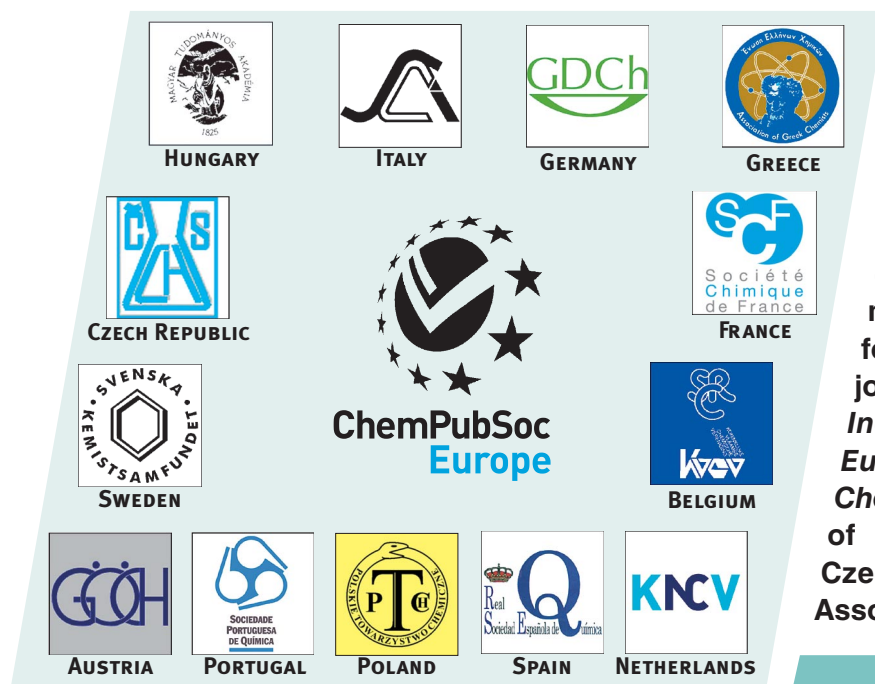
**Cover Picture**Charles G. Young *et al.*Novel O,O'-Donor Oxo-Mo^{IV} Complexes

A Journal of

ChemPubSoc
Europe

WILEY-VCH

www.eurjic.org

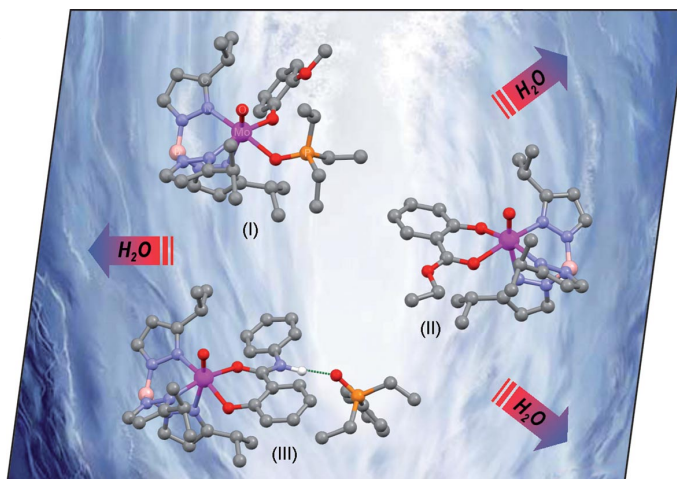


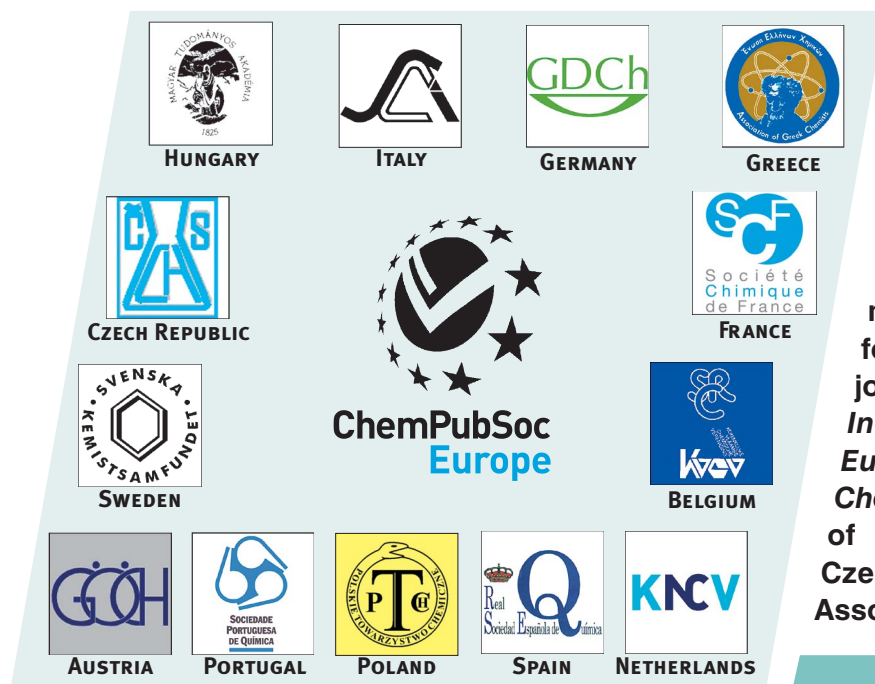
EurJIC is co-owned by 11 societies of ChemPubSoc Europe, a union of European chemical societies for the purpose of publishing high-quality science. All owners merged their national journals to form two leading chemistry journals, the *European Journal of Inorganic Chemistry* and the *European Journal of Organic Chemistry*. Three further members of ChemPubSoc Europe (Austria, Czech Republic and Sweden) are Associates of the two journals.

Other ChemPubSoc Europe journals are *Chemistry – A European Journal*, *ChemBioChem*, *ChemPhysChem*, *ChemMedChem*, *ChemSusChem* and *ChemCatChem*.

COVER PICTURE

The cover picture shows water being repelled by oxo-Mo^{IV} complexes of types I–III. The picture, inspired by the Bible story of Moses parting the Red Sea, is a visual metaphor for the inability of water to enter the coordination sphere and to generate H-bond-stabilized *cis*-oxo(aqua)-Mo^{IV} complexes when *cis*-Tp^{iPr}MoO₂(OAr-R) (R = H-bond donor/acceptor) complexes react with phosphanes. Instead, partial or complete oxygen-atom transfer results with the generation of oxo(phosphoryl)-Mo^{IV} species (I) or novel oxo-Mo^{IV} complexes containing tightly bound, bidentate *O,O'*-donor chelates (II, III), some of which retain the phosphane oxide by-product (III). The synthesis and characterization of complexes of types I–III are reported in the article by C. G. Young et al. on p. 3261ff.



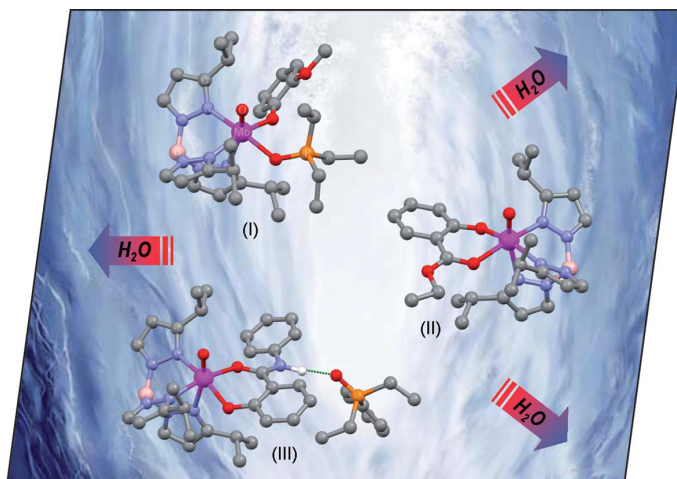


EurJIC is co-owned by 11 societies of ChemPubSoc Europe, a union of European chemical societies for the purpose of publishing high-quality science. All owners merged their national journals to form two leading chemistry journals, the *European Journal of Inorganic Chemistry* and the *European Journal of Organic Chemistry*. Three further members of ChemPubSoc Europe (Austria, Czech Republic and Sweden) are Associates of the two journals.

Other ChemPubSoc Europe journals are *Chemistry – A European Journal*, *ChemBioChem*, *ChemPhysChem*, *ChemMedChem*, *ChemSusChem* and *ChemCatChem*.

COVER PICTURE

The cover picture shows water being repelled by oxo-Mo^{IV} complexes of types I–III. The picture, inspired by the Bible story of Moses parting the Red Sea, is a visual metaphor for the inability of water to enter the coordination sphere and to generate H-bond-stabilized *cis*-oxo(aqua)-Mo^{IV} complexes when *cis*-Tp^{iPr}MoO₂(OAr-R) (R = H-bond donor/acceptor) complexes react with phosphanes. Instead, partial or complete oxygen-atom transfer results with the generation of oxo(phosphoryl)-Mo^{IV} species (I) or novel oxo-Mo^{IV} complexes containing tightly bound, bidentate *O,O'*-donor chelates (II, III), some of which retain the phosphane oxide by-product (III). The synthesis and characterization of complexes of types I–III are reported in the article by C. G. Young et al. on p. 3261ff.



SHORT COMMUNICATIONS

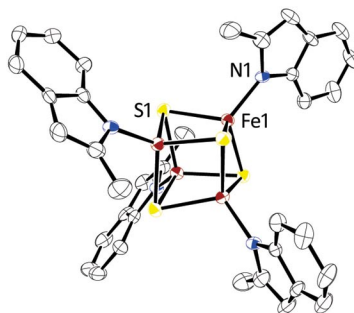
Bioinorganic Chemistry

M. G. G. Fuchs, S. Dechert, S. Demeshko,
F. Meyer* 3247–3251



N-Coordinated [2Fe–2S] and [4Fe–4S]
Clusters: Synthesis, Structures and Spectro-
scopic Characterisation

Keywords: Bioinorganic chemistry / Iron–
sulfur clusters / Moessbauer spectroscopy /
N ligands / Magnetic properties



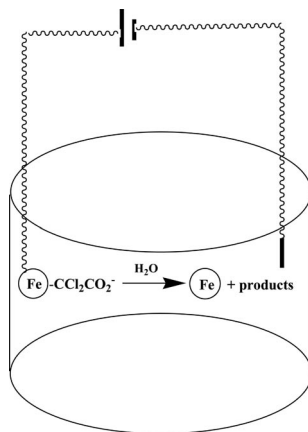
An all-N-ligated [4Fe–4S] cluster in the biomimetic mixed-valent state as well as the corresponding all-N-ligated [2Fe–2S] cluster could be isolated and characterised both crystallographically and spectroscopically, despite their rather low stability in solution.

Transient Decomposition

I. Rusonik, H. Cohen, A. Lugowskoy,
A. Krasnopolski, M. Zinigrad,
D. Meyerstein* 3252–3255

The Effect of an Electrical Bias on the
Mechanism of Decomposition of Transi-
ents with Metal–Carbon σ Bonds

Keywords: Dehalogenation / Iron / Electro-
chemistry / Radicals / Metal–carbon bonds



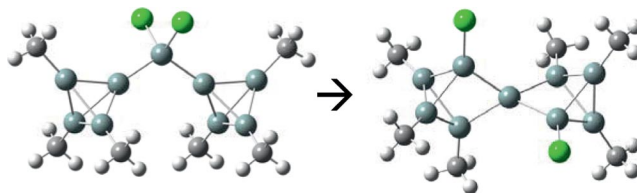
The effect of an electrical bias on the mech-
anism of decomposition of transient
 $\text{Fe}^0_{(s)}\text{--CCl}_2\text{COO}^-$ is reported.

Spirocyclic Silicon Clusters

T. M. Klapötke,* S. K. Vasisht,*
P. Mayer 3256–3260

Spirocycle $(\text{Si}t\text{Bu}_3)_6\text{Si}_9\text{Cl}_2$: The First of Its
Kind among Group 14 Elements

Keywords: Spiro compounds / Cluster com-
pounds / Silanes / Structure elucidation

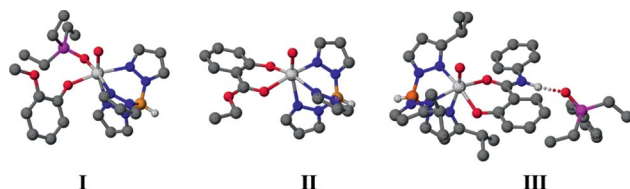


An Si_4 cage stabilizes itself in a heavily
loaded environment in tetrasilatetrahed-
ranide KR^*_3Si_4 ($\text{R}^* = \text{Si}t\text{Bu}_3$), but steric
congestion in $(\text{R}^*_3\text{Si}_4)_2\text{SiCl}_2$ results in re-

arrangement leading to cage opening into
less strained tricyclopentasilane rings in
 $(\text{R}^*_3\text{Si}_4\text{Cl})_2\text{Si}$, and the molecule acquires a
spiro[4.4]nonasilane structure.

FULL PAPERS

Oxo-Mo(IV) Chelates



A variety of oxo-Mo^{IV} complexes are formed in the reactions of Tp^{Pr}MoO₂-(OAr-R) (⁻OAr-R = potential H-bonding phenolate) with tertiary phosphanes. These include oxo(phosphoryl)-Mo^{IV} complexes (I), *O,O'*-donor chelate oxo-Mo^{IV} com-

plexes (II) and NH...O=PR'₃ H-bonded chelate/phosphane oxide adducts (III). Chelation of the phenolate ligand precludes the hydrogen bond stabilization of *cis*-(aqua)oxo-Mo^{IV} complexes as models for reduced molybdoenzyme states.

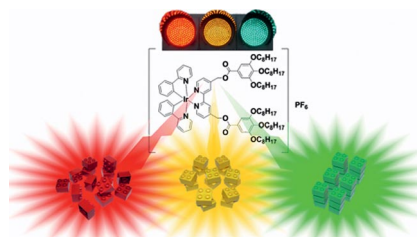
V. W. L. Ng, M. K. Taylor, L. M. R. Hill, J. M. White, C. G. Young* 3261–3269

Novel *O,O'*-Donor Oxo-Mo^{IV} Hydrotris(3-isopropylpyrazolyl)borate Complexes Formed by Chelation of Potentially Hydrogen-Bonding Phenolate Ligands on Reduction of Dioxo-Mo^{VI} Complexes

Keywords: Molybdenum / Chelates / Hydrogen bonds / O-donors

Order-Driven Switching

Order Matters and Matter Orders! What do you think of a single material that can perform in different ways? Liquid crystallinity, high luminescence efficiency and ease of processing are all properties displayed by a new cationic Ir^{III} derivative. Modulation of the molecular order/disorder, tuned by external stimuli, is accomplished by a traffic-light-like switching in the emission properties.



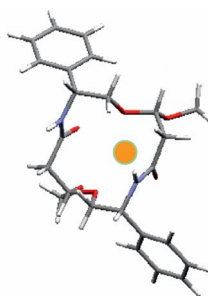
E. I. Szerb, A. M. Talarico, I. Aiello, A. Crispini, N. Godbert, D. Pucci, T. Pugliese, M. Ghedini* 3270–3277

Red to Green Switch Driven by Order in an Ionic Ir^{III} Liquid-Crystalline Complex

Keywords: Iridium / Metallomesogens / Luminescence / Supramolecular order / Multifunctional materials

Macrocyclic Ligands

The complexation of four new 14-membered-ring diketal dilactam macrocycles with divalent cation perchlorates has been investigated. The macrocycles formed complexes of essentially 1:1 stoichiometry with the coordination of all six oxygen atoms of the ligands or of five of them, depending on the *cis/trans* orientation of the OMe groups, and probably two oxygen atoms from the ClO₄⁻ counter-anion.

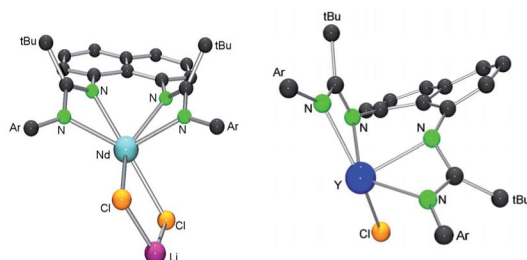


A.-G. Valade, D. Harakat, J. Guyot, O. Lapr  vote, D. Dugat* 3278–3289

Macrocyclic 14-Membered-Ring Diketal Dilactams: Spectroscopic Studies and Conformational Analysis of Their Complexes with Divalent Cations

Keywords: Lactams / Macrocyclic ligands / Divalent cations / Conformation analysis

Ln Bis(amidinate) Complexes



A new dianionic bis(amidinate) ligand framework with a conformationally rigid naphthalene linker was developed and

shown to form a suitable coordination environment for lanthanide ions.

M. V. Yakovenko, A. V. Cherkasov, G. K. Fukin, D. Cui, A. A. Trifonov* 3290–3298

Lanthanide Complexes Coordinated by a Dianionic Bis(amidinate) Ligand with a Rigid Naphthalene Linker

Keywords: Lanthanides / Amidinates / Coordination modes / Ligand design

CONTENTS

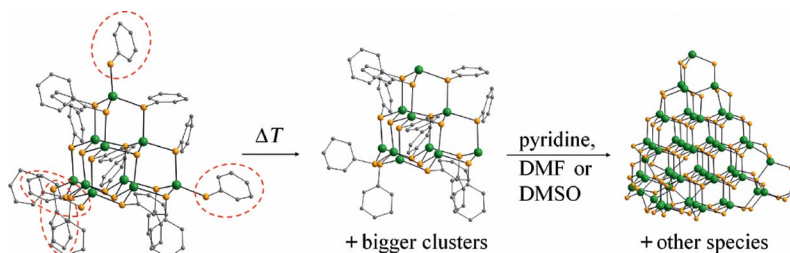
Cadmium Sulfide Clusters

M. Bendova, M. Puchberger,
U. Schubert* 3299–3306



Characterization of “ $\text{Cd}_{10}\text{S}_4(\text{SPh})_{12}$ ”, the Thermal Decomposition Product of $(\text{NMe}_4)_4[\text{Cd}_{10}\text{S}_4(\text{SPh})_{16}]$: Synthesis of a Neutral Cd_{54} Sulfide Cluster and of a Polymeric Chain of Thiolate-Bridged Cd_{17} Sulfide Clusters

Keywords: Cadmium / Nanoparticles / Cluster compounds / S ligands / Rearrangement



The cluster $[\text{Cd}_{10}\text{S}_4(\text{SPh})_{16}]^{4-}$ does not completely retain its core structure during heating and a mixture of $\text{Cd}_{10}\text{S}_4(\text{SPh})_{12}$ and bigger clusters is formed.

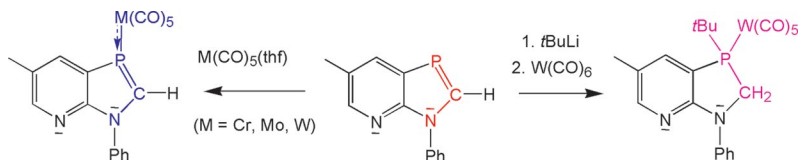
Pyrido-Annulated Azaphospholes

M. S. S. Adam, P. G. Jones,
J. W. Heinicke* 3307–3316



Pyrido-Annulated 1,3-Azaphospholes: Synthesis of 1,3-Azaphospholo[5,4-*b*]pyridines and Preliminary Reactivity Studies

Keywords: Phosphanes / Phosphaalkenes / P ligands / P,N heterocycles / Pyridine annulation



Pyrido-annulated 1,3-azaphospholes were synthesized by reduction of 2-aminopyridine-3-phosphonates and cyclocondensation with dimethylformamide or dimethylacetamide dimethyl acetal. The $\text{P}=\text{C}$ bond is resistant to diluted aqueous acids

and bases but adds *t*BuLi. $\text{M}(\text{CO})_5(\text{thf})$ form preferably $\eta^1\text{-P}$ -coordinated (azaphospholo[5,4-*b*]pyridine) $\text{M}(\text{CO})_5$ complexes ($\text{M} = \text{Cr}, \text{Mo}, \text{W}$) and exhibits π -acceptor properties.

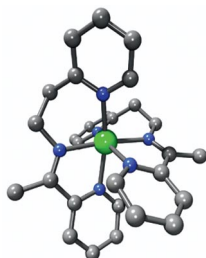
Schiff Base Complexes

R. W. Handel, H. Willms, G. B. Jameson,
K. J. Berry, B. Moubaraki, K. S. Murray,
S. Brooker* 3317–3327



Factors Influencing the Structural and Magnetic Properties of Octahedral Cobalt(II) and Iron(II) Complexes of Terdentate N_3 Schiff Base Ligands

Keywords: Cobalt / Iron / Electrochemistry / Magnetochemistry / Magnetic properties / Schiff base ligands



Four terpy-like Schiff base ligands were coordinated to iron(II) and cobalt(II). The resulting complexes were subjected to magnetic and electrochemical studies and three of them were structurally characterised.

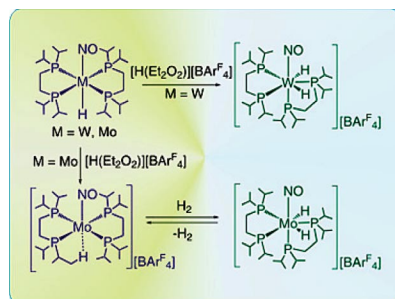
Mo and W Hydrides

A. Dybov, O. Blacque,
H. Berke* 3328–3337



Molybdenum and Tungsten Nitrosyl Complexes in Hydrogen Activation

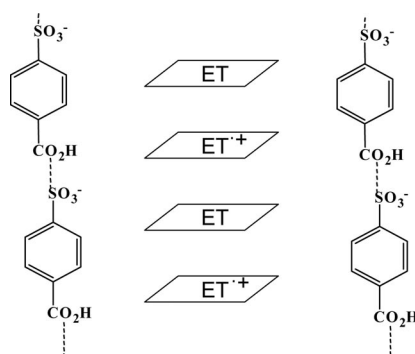
Keywords: Homogeneous catalysis / Hydrogenation / Hydrogen activation / Tungsten / Molybdenum / Hydrides



$[\text{H}(\text{Et}_2\text{O})_2][\text{BAR}^{\text{F}}_4]$ interacts with tungsten hydride to form stable dihydride species. The $[\text{Mo}(\text{dippe})_2\text{NO}][\text{BAR}^{\text{F}}_4]$ complex was isolated after reaction with the molybdenum hydride. $[\text{Mo}(\text{dippe})_2\text{NO}][\text{BAR}^{\text{F}}_4]$ reacts with hydrogen gas to form a dihydride complex, which is unstable in the absence of H_2 needed for equilibration. The dihydride is structurally similar to the tungsten complex.

Noncentrosymmetric Conductors

Noncentrosymmetric electroconducting salts such as BEDT-TTF₂[O₃S-C₆H₄-CO₂H] [BEDT-TTF = bis(ethylenedithio)-tetrathiafulvalene] can be obtained by electro-oxidation of tetrathiafulvalene derivatives in the presence of the dissymmetrical hydrogen-bonding *para*-carboxybenzenesulfonate anion.



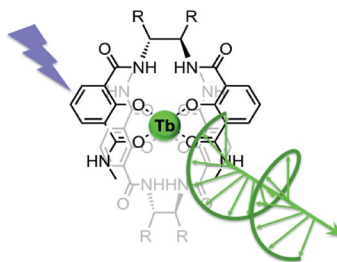
Y. Lakhdar, A. El-Ghayoury, L. Zorina, N. Mercier, M. Allain, C. Mézière, P. Auban-Senzier, P. Batail, M. Giffard* 3338–3342

Acentric Polymeric Chains in Radical Cation Salts of Tetrathiafulvalene Derivatives with the *p*-Carboxybenzenesulfonate Anion

Keywords: Tetrathiafulvalenes / Conducting materials / Mixed-valent compounds / Noncentrosymmetry / Self-assembly

Chiral Terbium Complexes

Chiral tetradentate 2-hydroxyisophthalamide (IAM)-based sensitizing ligands form terbium(III) complexes that possess both extremely large quantum yields (up to 60%) and high circularly polarized luminescence (CPL) activities in aqueous solution at neutral pH. The large CPL activity may be attributed to the conformational rigidity afforded by the ligand scaffold



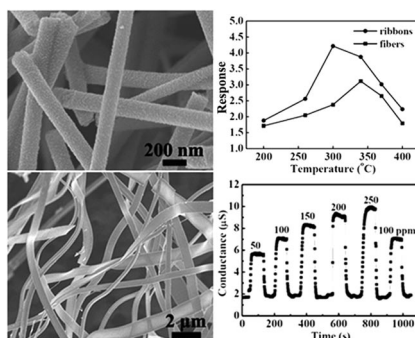
A. P. S. Samuel, J. L. Lunkley, G. Muller, K. N. Raymond* 3343–3347

Strong Circularly Polarized Luminescence from Highly Emissive Terbium Complexes in Aqueous Solution

Keywords: Lanthanides / Terbium / Luminescence / Circularly polarized luminescence (CPL) / Chirality

Electrospun Indium Oxide

In₂O₃ nanofibers and nanoribbons were prepared by using an electrospinning technique. The formation of nanoribbon structures with smaller size grains than the fibers can be ascribed to the rapid gelation on the surface of the electrospun jet at a higher concentration of the sol–gel precursor. Due to their size-dependent sensing property, In₂O₃ nanoribbons show a better gas sensing performance toward HCHO vapor.



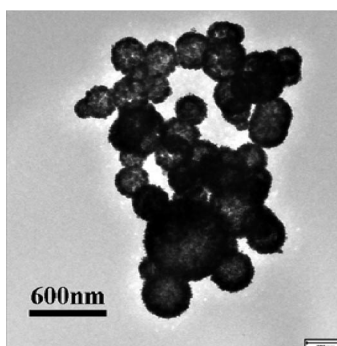
Z. Li, Y. Fan, J. Zhan* 3348–3353

In₂O₃ Nanofibers and Nanoribbons: Preparation by Electrospinning and Their Formaldehyde Gas-Sensing Properties

Keywords: Indium oxide / Formaldehyde / Nanostructures / Electrospinning / Sensors

Mesoporous Hollow Spheres

We present a simple one-pot, template-free route for the fabrication of CeO₂ hollow spheres with mesoporous shells. The combination of a hollow structure and a porous shell endows the materials with excellent properties: an outstanding adsorption capacity for organic pollutants from waste water and a catalytic activity towards CO oxidation higher than that of commercial CeO₂ powders.



Z. Yang, J. Wei, H. Yang, L. Liu, H. Liang, Y. Yang* 3354–3359

Mesoporous CeO₂ Hollow Spheres Prepared by Ostwald Ripening and Their Environmental Applications

Keywords: Hydrothermal synthesis / Template-free synthesis / Water treatment / Heterogeneous catalysis / Adsorption

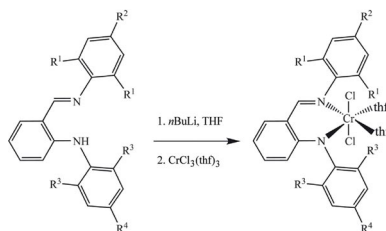
CONTENTS

Chromium Complexes

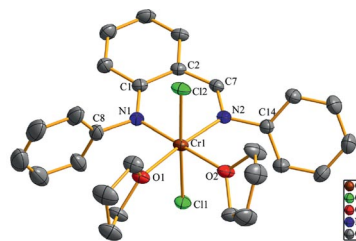
T. Xu,* H. An, W. Gao,
Y. Mu* 3360–3364

Chromium(III) Complexes with Chelating Anilido–Imine Ligands: Synthesis, Structures, and Catalytic Properties for Ethylene Polymerization

Keywords: Chromium / Polymerization / Homogeneous catalysis / Ligand effects



A series of chromium complexes that bear anilido–imine ligands were synthesized and characterized. Upon activation with meth-



ylaluminoxane, these complexes exhibit high activity for ethylene polymerization.

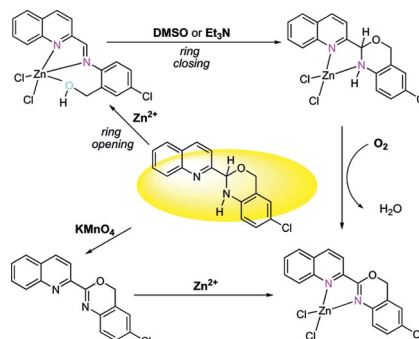
Heteropolydentate Ligands

G. A. Ardizzoia, S. Brenna,*
B. Therrien 3365–3371



The Adaptable Coordination Chemistry of 6-Chloro-2-(quinolin-2-yl)-2,4-dihydro-1*H*-benzo[*d*][1,3]oxazine Towards Zinc(II) and Mercury(II)

Keywords: Polydentate ligands / Coordination modes / N ligands / N,O ligands / Zinc / Mercury



Ligand 6-chloro-2-(quinolin-2-yl)-2,4-dihydro-1*H*-benzo[*d*][1,3]oxazine (LH₂) showed versatile coordination modes towards zinc and mercury. An “open” iminic form was found in complex [Zn(L^{OH})Cl₂], whereas the reaction with HgCl₂ afforded a trinuclear compound that contained the original form LH₂. An oxidized form **L** was also encountered.

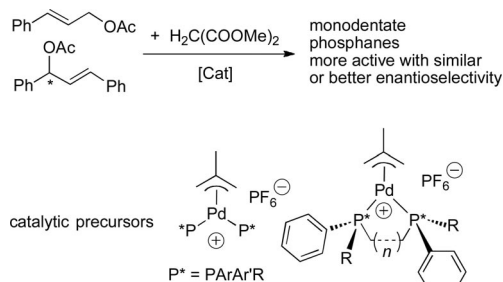
P-Stereogenic Ligands

A. Grabulosa, G. Muller,* R. Ceder,
M. Á. Maestro 3372–3383



Better Performance of Monodentate *P*-Stereogenic Phosphanes Compared to Bidentate Analogues in Pd-Catalyzed Asymmetric Allylic Alkylations

Keywords: Palladium / Allylic compounds / Asymmetric catalysis / Nucleophilic substitution



Novel cationic palladium allylic complexes with mono- and bidentate *P*-stereogenic phosphanes with similar electronic properties have been synthesized and tested in al-

lylic alkylation reactions. The monodentate phosphanes performed better in terms of activity and enantioselectivity.

* Author to whom correspondence should be addressed.

Supporting information on the WWW (see article for access details).



On these pages, we feature a selection of the excellent work that has recently been published in our sister journals. If you are reading these pages on a

computer, click on any of the items to read the full article. Otherwise please see the DOIs for easy online access through Wiley InterScience.

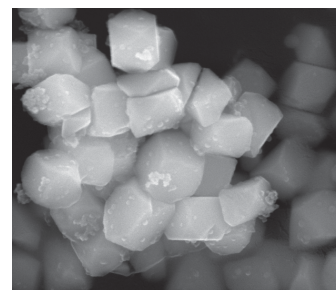


Organometallic Chemistry

S. Schulz*

Low-Valent Organometallics—Synthesis, Reactivity, and Potential Applications

Far beyond lab curiosities: The synthesis of kinetically stabilized (sterically demanding substituents) and electronically stabilized (base stabilization) low-valent complexes of Groups 2, 12, 13, and 15 is summarized as well as their potential application as selective reductants, unusual ligands in coordination chemistry, and as novel precursors in material sciences (see graphic).



Chem. Eur. J.
DOI: 10.1002/chem.201000580

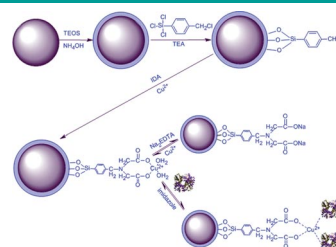


Microspheres

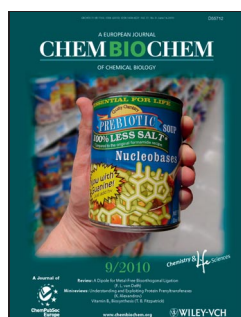
M. Zhang, D. Cheng, X. He, L. Chen,* Y. Zhang*

Magnetic Silica-Coated Sub-Microspheres with Immobilized Metal Ions for the Selective Removal of Bovine Hemoglobin from Bovine Blood

Vampire microspheres: Superparamagnetic silica-coated magnetite (Fe_3O_4) sub-microspheres with an immobilized metal-affinity ligand are prepared largely through a novel route (see scheme). Protein adsorption results show that the sub-microspheres have a high selective adsorption for bovine hemoglobin (BHb), low non-specific adsorption, and are capable of efficient removal of BHb from bovine blood.



Chem. Asian J.
DOI: 10.1002/asia.200900463

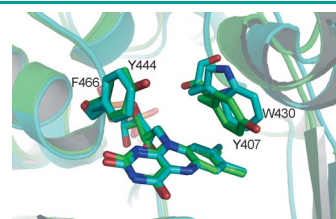


Enzyme Catalysis

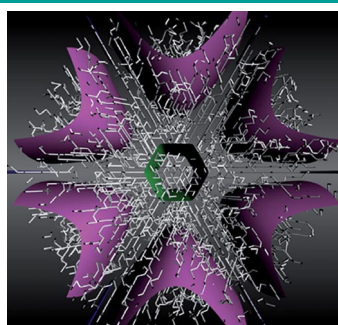
R. V. Dunn, A. W. Munro, N. J. Turner, S. E. J. Rigby, N. S. Scrutton*

Tyrosyl Radical Formation and Propagation in Flavin Dependent Monoamine Oxidases

MAO enzymes: Demonstration of the presence of tyrosyl radicals in partially reduced monoamine oxidases (MAO) was achieved by a combination of specific isotopic labelling and pulsed ENDOR techniques. Comparative studies between human MAO A and MAO N indicate that the equilibrium distribution of the radical species is not localised to the active site residues near the flavin cofactor.



ChemBioChem
DOI: 10.1002/cbic.201000184



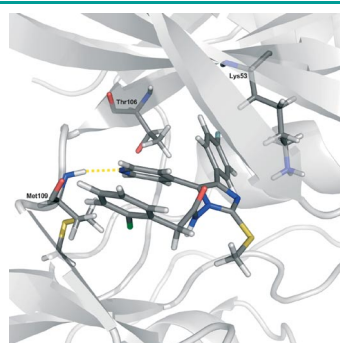
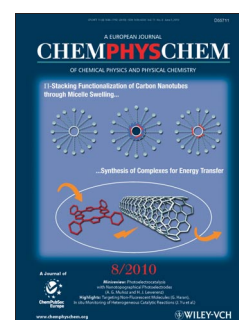
ChemPhysChem
DOI: 10.1002/cphc.201000232

Nanocomposites

J. Brickmann,* R. Paparcone, S. Kokolakis, D. Zahn,
P. Duchstein, W. Carrillo-Cabrera, P. Simon, R. Kniep*

Fluorapatite–Gelatin Nanocomposite Superstructures: New Insights into a Biomimetic System of High Complexity

The beauty of complexity is reflected by the formation of hierarchical patterns on various length scales (see picture). The simulation of the fibril pattern inside a fluorapatite-gelatin nanocomposite superstructure reveals excellent agreement with TEM data and seems to be a key scenario for the development of biogenic composite shapes and architectures.



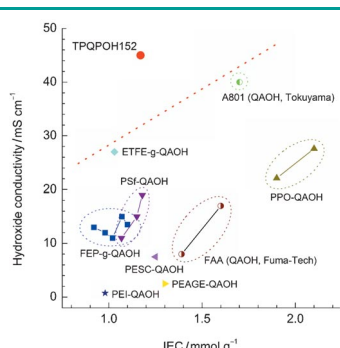
ChemMedChem
DOI: 10.1002/cmdc.201000114

Drug Discovery

C. Bracht, D. R. J. Hauser, V. Schattel, W. Albrecht,
S. A. Laufer*

Synthesis and Biological Testing of *N*-Aminoimidazole-Based p38 α MAP Kinase Inhibitors

We developed novel tetrasubstituted pyridinylimidazoles with acyl residues at the imidazole N1 position that interact with specific regions of p38 mitogen-activated protein (MAP) kinase α to improve both selectivity and activity. The substitution pattern was optimized by variation of the acyl group at the N1 position of the *N*-aminoimidazole core.



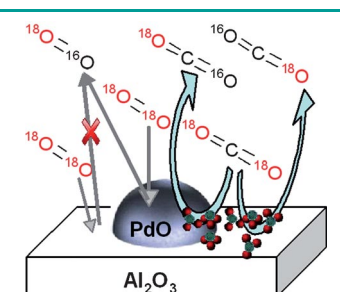
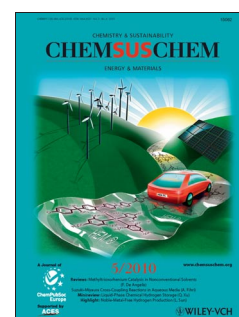
ChemSusChem
DOI: 10.1002/cssc.201000074

Fuel Cells

S. Gu, R. Cai, T. Luo, K. Jensen, C. Contreras, Y. S. Yan*

Quaternary Phosphonium-Based Polymers as Hydroxide Exchange Membranes

A new class of hydroxide exchange membranes (HEMs) is prepared by using a quaternary phosphonium-based polymer. The membranes display desirable properties, most notably a high conductivity. A corresponding fuel cell exhibits the highest HEM fuel cell performance to date and shows a better intrinsic catalyst-activity compared with state-of-the-art proton exchange membrane fuel cells.



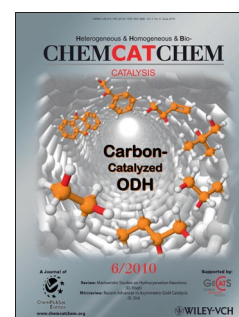
ChemCatChem
DOI: 10.1002/cctc.201000033

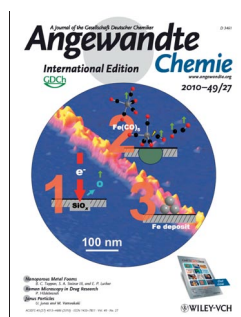
Supported Catalysts

S. Ojala, N. Bion,* S. Rijo Gomes, R. L. Keiski, D. Duprez

Isotopic Oxygen Exchange over Pd/Al₂O₃ Catalyst: Study on C¹⁸O₂ and ¹⁸O₂ Exchange

Exchange would do you good: Labeled C¹⁸O₂ was used to study oxygen isotopic exchange over Pd/Al₂O₃ catalyst. The improvement in exchange rate compared with the exchange from ¹⁸O₂ is at least a factor of ten. The roles of PdO and carbonates are essential in enhancing the oxygen exchange from C¹⁸O₂. C¹⁸O₂ exchange can be applied instead of ¹⁸O₂, when oxygen activation on Pd/Al₂O₃ catalysts is studied at low temperatures.



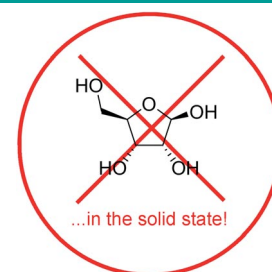


Structure Determination

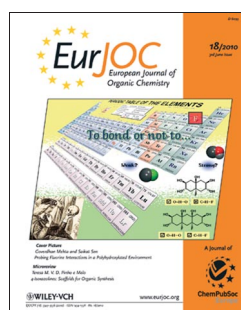
D. Šišak, L. B. McCusker,* G. Zandomenighi, B. H. Meier,*
D. Bläser, R. Boese,* W. B. Schweizer, R. Gilmour, J. D. Dunitz*

The Crystal Structure of D-Ribose—At Last!

Better late than never! The β -furanose form of D-ribose, present in countless biomolecules, does not occur in the crystalline compound. X-ray diffraction and NMR experiments show that D-ribose occurs in two crystal forms that contain β - and α -pyranose forms in various ratios.



Angew. Chem. Int. Ed.
DOI: 10.1002/anie.201001266

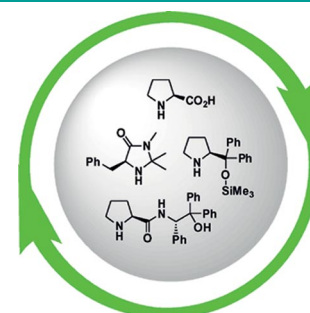


Polymer-Supported Organocatalysts

T. E. Kristensen, T. Hansen*

Polymer-Supported Chiral Organocatalysts: Synthetic Strategies for the Road Towards Affordable Polymeric Immobilization

The preparation and utilization of enamine and iminium organocatalysts have seen a tremendous growth during the last decade. In this microreview, we highlight the polymer-supported versions of these catalysts, with a special focus on the synthetic strategies that have been undertaken to prepare them and analyze these strategies in a historical context.



Eur. J. Org. Chem.
DOI: 10.1002/ejoc.201000319

New Journal

Heterogeneous, Homogeneous and BioCatalysis

www.chemcatchem.org

FREE ONLINE ACCESS

In 2010 for all users from institutions that have registered

Ask your librarian to register for complimentary online access TODAY

www.interscience.wiley.com/newjournals

Founding Societies:

GDCh

GESELLSCHAFT DEUTSCHER CHEMIKER

WILEY-VCH

N-Coordinated [2Fe–2S] and [4Fe–4S] Clusters: Synthesis, Structures and Spectroscopic Characterisation

Michael G. G. Fuchs,^[a] Sebastian Dechert,^[a] Serhiy Demeshko,^[a] and Franc Meyer*^[a]

Keywords: Bioinorganic chemistry / Iron–sulfur clusters / Moessbauer spectroscopy / N ligands / Magnetic properties

Examples for [2Fe–2S] clusters with non-chelating N-coordinating ligands are still relatively rare, and no mixed-valent [4Fe–4S] cluster with pure N-donor ligation has hitherto been reported. In the course of synthetic efforts to isolate a bio-relevant [2Fe–2S] cluster **2** with 2-methylindolato capping ligands, the respective [4Fe–4S] cluster **3** was isolated as a by-product and characterised by X-ray diffraction. Since **3** rep-

resents the first all-N-ligated mixed-valent [4Fe–4S] complex, rational syntheses for **3** as well as for **2** were then developed. Both complexes are quite unstable in solution, but have been characterised as far as possible by a variety of spectroscopic methods including ¹H NMR, UV/Vis and Mößbauer.

Introduction

Although cysteines are by far the most common ligands of biological Fe/S clusters, the importance of non-sulfur coordination is more and more recognised. This applies in particular to some [2Fe–2S] and [4Fe–4S] clusters with unusual properties such as the Rieske centers, or with biological functions other than electron-transfer.^[1] A prominent example is the [2Fe–2S] cluster in biotin synthase, which features unique arginine coordination at one of the metal ions.^[2] Besides oxygen, being the lower homologue of sulfur, it is mainly nitrogen that plays an important role as donor to biological Fe/S clusters. Some biomimetic [2Fe–2S] clusters with pure N-donor ligation, both monodentate^[3,4] and bidentate,^[5,6] have been reported to date. Yet this has not been the case for [4Fe–4S] clusters^[7,8] with the exception of the recent characterisation of an all-ferric [4Fe–4S]⁴⁺ cluster bearing amide ligands.^[9] Its oxidation state, however, is different from biological [4Fe–4S] clusters, and the amide ligands have very different properties as compared to biological N-donors in Fe/S proteins such as histidine or arginine. A synthetic N-coordinated [4Fe–4S]²⁺ cluster with prolinato ligands has been characterised by ¹H NMR spectroscopy, but has not been isolated.^[10] In addition there have been several approaches to site-differentiated clusters with one exchangeable ligand including imidazoles and other N-donor ligands,^[11,12] yet no other fully N-coordinated [4Fe–4S] cluster has been reported so far, to the best of the authors' knowledge. Furthermore, there is only one other example of a bioinspired [4Fe–4S] cluster

with non-S coordination that has been structurally characterised, namely (NEt₄)₂[Fe₄S₄(OPh)₄].^[13] All other known examples have to be considered as rather abiological clusters, since they have non-biomimetic terminal ligands like NO, CO, cyanide or Cp.^[14] Although there is no natural [4Fe–4S] cluster known to date with coordination by more than one histidine, an all-N-ligated model system would further extend biomimetic Fe/S chemistry and might help to identify new unusual biological [4Fe–4S] clusters in the future.

Results and Discussion

Initial Observations

Among the few examples of purely N-ligated synthetic [2Fe–2S] clusters that have been structurally characterised,^[3,6,9,15–17] there is only one with monodentate ligands, namely pyrrole.^[3] Complexes of two other ligands, indole and carbazole,^[4] have been characterised spectroscopically, but could not be obtained in crystalline form. Since the use of suitably substituted heterocycles was expected to favour crystallisation, 2-methylindole was chosen as a ligand for [2Fe–2S] cluster synthesis. Standard salt metathesis using 2-methylindole, *n*BuLi and (NEt₄)₂[Fe₂S₂Cl₄] (**1**)^[18] led to the formation of a cluster product as indicated by typical resonances in the ¹H NMR spectrum, but (NEt₄)₂[Fe₂S₂(2-methylindolate)₄] (**2**) could not be isolated by crystallisation. Instead, colour changes and gradual precipitation of amorphous sticky material suggested gradual decomposition of the initial product in MeCN or dmf solution. However, small black crystals suitable for X-ray diffraction were obtained from one experiment when a dilute solution of the reaction mixture in MeCN/Et₂O, which exhibited the red colour typical for [2Fe–2S] clusters, was left standing under

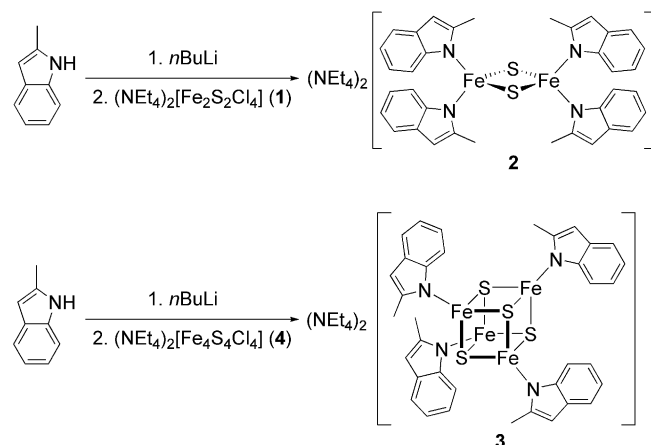
[a] Institut für Anorganische Chemie, Georg-August-Universität, Tammannstrasse 4, 37077 Göttingen, Germany
Fax: +49-551-39-3063

E-mail: franc.meyer@chemie.uni-goettingen.de

Supporting information for this article is available on the WWW under <http://dx.doi.org/10.1002/ejic.201000418>.

inert conditions. This crystalline material could then be identified as $(\text{NEt}_4)_2[\text{Fe}_4\text{S}_4(2\text{-methylindolate})_4]$ (**3**), which itself turned out to be insoluble in MeCN and soluble in dmf or dmsO only with rapid decomposition.

Based on these observations – viz. initial formation of a $[2\text{Fe}–2\text{S}]$ cluster that decomposes in MeCN solution to give the $[4\text{Fe}–4\text{S}]$ cluster, which in turn is rather unstable – a rational approach to both clusters was sought (Scheme 1).



Scheme 1. Synthesis of clusters **2** and **3**.

Synthesis and Characterisation of the $[2\text{Fe}–2\text{S}]$ Cluster

The synthesis of the $[2\text{Fe}–2\text{S}]$ cluster with 2-methylindolato capping ligands was first attempted in pure thf to avoid the more polar MeCN, yet product formation was not observed due to the insolubility of the starting complex **1** in thf. Thus, the reaction was performed with addition of a small amount of MeCN to enable complete dissolution of **1**. The precipitate that formed within few minutes was filtered off after 1 h and washed with Et_2O to remove remaining MeCN (Scheme 1). A ^1H NMR spectrum of the crude material in CD_2Cl_2 showed characteristic signals for a $[2\text{Fe}–2\text{S}]$ cluster, which is quite unusual as most of the known $[2\text{Fe}–2\text{S}]$ clusters are insoluble in dichloromethane. Upon repeated extraction with dichloromethane, an intensely red complex was obtained from the residue and then precipitated by slow diffusion of Et_2O and then pentane into the solution. Few crystals suitable for X-ray diffraction were also obtained, although the quality of these crystals was insufficient for complete refinement. Yet the diffraction data were of sufficient quality to clearly identify the cluster $(\text{NEt}_4)_2[\text{Fe}_2\text{S}_2(2\text{-methylindolate})_4]$ (**2**) (Figure 1).

Because of the short reaction time (which is important to prevent cluster decomposition) and the relatively poor solubility of **2** in dichloromethane, **2** could only be isolated in a low yield of 17%. In order to circumvent the difficulties with solubility and crystallisation, the counteranions were varied, and cluster syntheses were also performed by using $(\text{NMe}_4)_2[\text{Fe}_2\text{S}_2\text{Cl}_4]$ and $[\text{N}(\text{PPh}_3)_2][\text{Fe}_2\text{S}_2\text{Cl}_4]$. However, NEt_4^+ gave the best results.

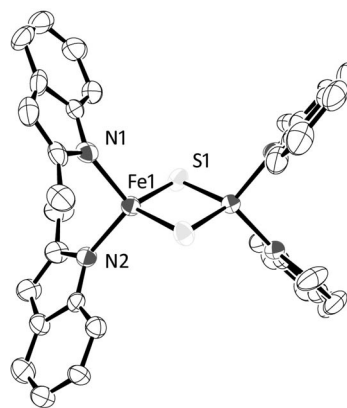


Figure 1. Molecular structure of **2**. ORTEP plot, 50% probability thermal ellipsoids; counterions, solvent molecules and hydrogen atoms omitted for clarity. Note: Crystallographic data was insufficient for complete refinement due to minor crystal quality; therefore the structure should be regarded as an educated guess only.

ESI mass spectrometry confirmed cluster formation. The ^1H NMR spectrum of **2** features broad singlets typical for $[2\text{Fe}–2\text{S}]$ clusters. The UV/Vis spectrum shows a high-energy band at 288 nm as well as two broad ligand-to-metal charge-transfer (LMCT) bands in the visible region at 457 and 540 nm (Figure 2). Compared to the parent indole-coordinated cluster (410 and 520 nm),^[4] these latter bands are redshifted since the +I effect of the methyl groups in **2** imparts higher electron density to the indolato ligand. Owing to its lability in solution, no electrochemical study was performed for **2**.

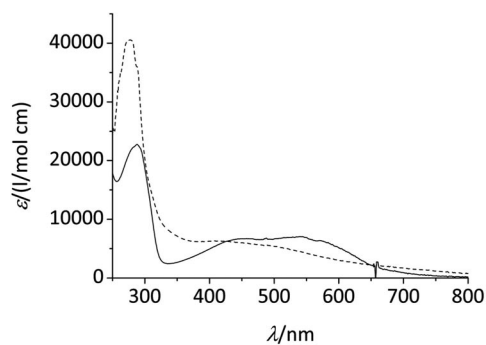


Figure 2. UV/Vis spectra of clusters **2** in MeCN (solid line) and **3** in dmf (dashed line).

The Mößbauer spectrum of **2** shows a quadrupole doublet with an isomer shift typical for diferric $[2\text{Fe}–2\text{S}]$ clusters and a relatively small quadrupole splitting ($\delta = 0.29$ mm/s, $\Delta E_Q = 0.53$ mm/s; Figure 3, Table 2). These values are in good agreement with those obtained for the parent indolato-coordinated complex ($\delta = 0.27$ mm/s, $\Delta E_Q = 0.61$ mm/s).^[4] In the case of chelating N-donor ligand caps such as dipyrromethanes, significantly larger quadrupole splittings $\Delta E_Q = 0.89–0.99$ mm/s have been observed, both in homoleptic complexes^[6] and in a Rieske model system.^[15] In contrast, for a cluster with N-ligation but five-coordinate iron atoms, the quadrupole splitting is even smaller (0.43 mm/s^[17]) than in **2**.

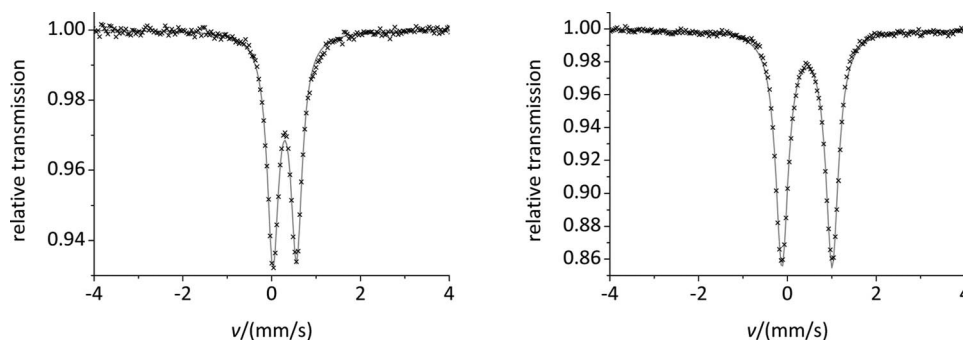


Figure 3. Mößbauer spectra of **2** (left) and **3** (right) at 80 K.

Magnetic susceptibility measurements were performed at 2 T in the temperature range from 295 to 2 K. The magnetic moment μ_{eff} decreases upon cooling, confirming the expected diamagnetic ground state ($S_T = 0$) with strongly antiferromagnetically coupled ferric ions (Figure S2). The coupling constant J was calculated by using a fitting procedure to the appropriate Heisenberg spin Hamiltonian for isotropic exchange coupling and Zeeman interaction according to

$$\hat{H} = -2J\hat{S}_1 \cdot \hat{S}_2 + g\mu_B(\hat{S}_1 + \hat{S}_2)B$$

The coupling constant $J = -180 \text{ cm}^{-1}$ reveals the strong antiferromagnetic coupling that is common to most [2Fe–2S] clusters. Its value lies between those for the related indolato- and carbazolato-coordinated complexes (-159 and -199 cm^{-1} , respectively).^[4]

Synthesis and Characterisation of the [4Fe–4S] Cluster

Initial attempts to synthesise the 2-methylindolato-ligated [4Fe–4S] cluster in pure thf by using 2-methylindole, $n\text{BuLi}$ and $(\text{NEt}_4)_2[\text{Fe}_4\text{S}_4\text{Cl}_4]$ (**4**)^[19] were unsuccessful. When the experiment was repeated in the presence of a sufficient amount of MeCN to allow complete dissolution of **4**, however, an immediate colour change from greenish brown to deep red occurred, accompanied by the precipitation of a black powder (Scheme 1). This was filtered off and washed with thf and Et₂O. As already observed for the

few crystals obtained from the gradual decomposition of **2** mentioned above, the product **4** is soluble only in dmf and dmsO, but unstable in these solvents. Recrystallisation was therefore impossible, yet the product was sufficiently pure according to ¹H NMR and Mößbauer spectroscopy. Therefore, the structure that is discussed is the one obtained from the exploratory synthesis of the [2Fe–2S] cluster (see above), whereas spectroscopic characterisation was performed on the bulk material produced according to the rational approach. As for the corresponding [2Fe–2S] cluster, the synthesis of derivatives with other counterions (NMe_4^+ , NnBu_4^+) was tested. Although the solubility of the NnBu_4^+ salt is better than that of the NEt_4^+ compound, isolation of a pure complex by crystallisation from acetonitrile, acetone or dichloromethane failed. In addition, the synthesis of the corresponding [4Fe–4S] cluster with parent indolato ligands was investigated. Although cluster formation was detected by ¹H NMR spectroscopy in several experiments, product precipitation did not yield a pure compound. No well-defined decomposition product could be identified either.

The [4Fe–4S] cluster **3** crystallises as an S_4 -symmetric complex with crystallographically identical iron atoms, sulfide ions and 2-methylindolato ligands, with the symmetry axis going through two of the cluster core plains (Figure 4). Selected interatomic distances and angles are listed in Table 1. To the best of the authors' knowledge, the N-coordinated cluster $[\text{Fe}_4\text{S}_4(\text{N}(\text{SiMe}_3)_2)_4]$ (**A**)^[9] and the O-coordinated cluster $(\text{NEt}_4)_2[\text{Fe}_4\text{S}_4(\text{OPh})_4]$ (**B**)^[13] are the only other examples of non-S-coordinated synthetic [4Fe–4S] clusters

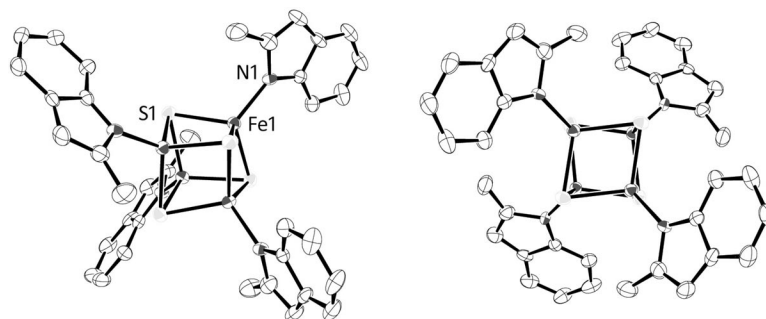


Figure 4. Molecular structure of **3** in two different orientations; in the right-hand side, the symmetry axis is perpendicular to the paper plane. ORTEP plot, 50% probability thermal ellipsoids; counterions and hydrogen atoms omitted for clarity; only crystallographically independent heteroatoms labelled.

that have been structurally characterised, with the exception of several abiological clusters that bear ligands such as NO, CO or Cp.^[14]

Table 1. Selected interatomic distances d [Å] and angles α [°] of complex **3**.

$d(\text{Fe}\cdots\text{Fe})$	$d(\text{Fe}-\text{S})$	$d(\text{Fe}-\text{N})$	$\alpha(\text{Fe}-\text{S}-\text{Fe})$	$\alpha(\text{N}-\text{Fe}-\text{S})$
2.768(2)	2.273(2)		74.74(7)	115.4(2)
2.792(2)	2.288(3)	1.957(6)	74.99(6)	114.2(2)
	2.314(2)		74.71(7)	115.6(2)

Distances between the iron atoms in **3** range from 2.76 to 2.79 Å, which is slightly longer than what is usually found for biological and biomimetic S-coordinated $[\text{4Fe}-4\text{S}]^{2+}$ clusters (2.72–2.74 Å) or for the O-coordinated cluster **B** (2.73–2.76 Å). The N-coordinated all-ferric $[\text{4Fe}-4\text{S}]^{4+}$ cluster **A** has even larger $\text{Fe}\cdots\text{Fe}$ distances of 2.87 to 3.00 Å but is not really comparable due to its different oxidation state. Fe–S distances in **3** range from 2.27 to 2.31 Å, which is in accordance with the distances found in the two complexes **A** and **B**, as are the angles Fe–S–Fe (74.7–75.0°). In general, the cluster-core geometry does not change much upon formal exchange of a thiolato by an indolato ligand, an observation that was already mentioned for the O-coordinated cluster.^[13]

Despite fast decomposition in dmf, a ^1H NMR spectrum could be recorded that shows broad signals at $\delta = 2.2$ (methyl group), 5.6, 6.1, 7.0 and 8.1 ppm (one signal is either hidden beneath a solvent signal or too broad and thus not detectable). Likewise, ESI mass spectrometry confirmed cluster formation (see Supporting Information, Figure S1). Like for the $[\text{2Fe}-2\text{S}]$ cluster, no electrochemical experiments were performed because of the compound's instability in solution. The UV/Vis spectrum of **3** shows absorptions at 277 and 414 nm (Figure 2, Table 2), which are similar to those of the O-coordinated cluster $(\text{NEt}_4)_2[\text{Fe}_4\text{S}_4(\text{OPh})_4]$ (270 and 410 nm).^[13]

Table 2. Selected spectroscopic data of complexes **2** and **3**.

	λ_{max} [nm]	ϵ [$\text{L mol}^{-1}\text{cm}^{-1}$]	δ [mm/s]	ΔE_{Q} [mm/s]
2	288/457/540	23000/6700/7100	0.29	0.53
3	277/287/414	41000/36000 (sh)/6300	0.44	1.13

The Mößbauer spectrum of **3** features a single doublet with $\delta = 0.44$ mm/s and $\Delta E_{\text{Q}} = 1.13$ mm/s (Figure 3, Table 2). Compared to the $[\text{2Fe}-2\text{S}]$ analogue **2**, the isomer shift is more positive, which is as expected for the lower oxidation number (2.5) of **3**; similar values have also been observed for related complexes.^[7,13] The quadrupole splitting of 1.13 mm/s is relatively small compared to the O-coordinated cluster **B** ($\Delta E_{\text{Q}} = 1.21$ mm/s)^[13] and various S-coordinated clusters;^[20] unfortunately, no Mößbauer data are available for the amido-coordinated cluster **A**.

Conclusions

Two new 2-methylindolato-coordinated Fe/S clusters have been synthesised and characterised by X-ray diffrac-

tion, mass spectrometry, ^1H NMR, UV/Vis, and Mößbauer spectroscopy. Spectroscopic signatures of the $[\text{2Fe}-2\text{S}]$ cluster **2** are comparable to those of related complexes bearing monodentate nitrogen ligands, but the stability of **2** is relatively low. The $[\text{4Fe}-4\text{S}]$ cluster **3** is the first example of an all-N-ligated mixed-valent $[\text{4Fe}-4\text{S}]^{2+}$ complex that has been isolated and structurally characterised. Its cluster core is only slightly distorted as compared to related O- and S-ligated $[\text{4Fe}-4\text{S}]$ clusters. Mößbauer isomer shifts for both **2** and **3** are in typical ranges. Notably though, quadrupole splittings are rather low for both $[\text{2Fe}-2\text{S}]$ and $[\text{4Fe}-4\text{S}]$ clusters as compared to systems with monodentate S- and O-ligation. Both clusters **2** and **3** undergo rapid decomposition in solution. Yet they may be valuable for complementing the range of biorelevant Fe/S model systems since N-ligation is increasingly recognised in biological Fe/S sites.

Experimental Section

General Considerations: All manipulations were performed under anaerobic and anhydrous dinitrogen by using standard Schlenk techniques or in a glovebox unless otherwise mentioned. Glassware was dried at 120 °C overnight; thf was dried with potassium benzophenone ketyl; Et_2O and pentane were dried with sodium benzophenone ketyl; MeCN and dmf were dried with CaH_2 ; CH_2Cl_2 was dried with P_4O_{10} . All solvents were distilled prior to use. Deuterated solvents were similarly dried and distilled. Alternatively, CH_2Cl_2 was dried with molecular sieves by using an MBraun SPS. $(\text{NEt}_4)_2[\text{Fe}_2\text{S}_2\text{Cl}_4]$ ^[18] (**1**) and $(\text{NEt}_4)_2[\text{Fe}_4\text{S}_4\text{Cl}_4]$ ^[19] (**4**) were synthesised according to literature procedures. ^1H NMR spectra were recorded with a Bruker Avance 500 MHz spectrometer. UV/Vis spectra were recorded with a Specord S 100 spectrometer by using quartz cuvettes. ESI mass spectra were recorded with a Thermo Finnigan Trace LCQ spectrometer, ESI-HRMS spectra with a Bruker FTICR APEX IV instrument. Temperature-dependent magnetic susceptibilities of a powdered sample were measured by using a Quantum Design MPMS-5S SQUID magnetometer. Simulation of the experimental data with a full-matrix diagonalisation of exchange coupling and Zeeman splitting was performed with the julX program (E. Bill, Max Planck Institute for Bioinorganic Chemistry, Mülheim/Ruhr, Germany). Before simulation, the experimental data were corrected for the underlying diamagnetism and for temperature-independent paramagnetism (TIP). A Curie–Weiss-behaved paramagnetic impurity (PI) with spin $S = 5/2$ was included according to

$$\chi_{\text{calcd}} = (1 - PI)\chi + PI\chi_{\text{mono}}$$

Mößbauer spectra were recorded at 80 K with a WissEl alternating constant acceleration spectrometer. Isomer shifts are given relative to α -iron metal at room temperature. The experimental data were fitted with Lorentzian line shapes by using the MFit program (E. Bill, Max Planck Institute for Bioinorganic Chemistry, Mülheim/Ruhr, Germany).

Bis(tetraethylammonium) Bis[bis(2-methylindolato)(μ -sulfido)ferrate(III)] (2**):** A solution of 2-methylindole (520 mg, 4.0 mmol) in thf (20 mL) was treated with $n\text{BuLi}$ (1.6 mol/L in hexane, 2.5 mL, 4.0 mmol). After stirring for 1 h, $(\text{NEt}_4)_2[\text{Fe}_2\text{S}_2\text{Cl}_4]$ ^[18] (**1**, 580 mg, 1.0 mmol) was added followed by a small amount of MeCN (10 mL). After stirring for a further 1 h, a brown solid was filtered off and washed with Et_2O (20 mL). The precipitate was then extracted with CH_2Cl_2 (300 mL) under vigorous stirring. After fil-

tration, the filtrate was layered with Et₂O (300 mL) in portions over several days to allow slow diffusion. After diffusion was complete, pentane (150 mL) was added to ensure complete product precipitation. The resulting black microcrystalline solid was separated by filtration, washed with Et₂O and dried in vacuo to yield the target compound **2** in moderate yield (160 mg, 0.17 mmol, 17%) and reasonable purity. ¹H NMR (500 MHz, [D₃]MeCN): δ = 0.99 (br. s, 24 H, NEt₄), 1.75 (br. s, 12 H, Me), 2.80 (br. s, 16 H, NEt₄), 4.70 (br. s, 4 H, Ar-H), 4.80 (br. s, 4 H, Ar-H), 6.66 (br. s, 4 H, Ar-H), 7.10 (br. s, 4 H, Ar-H), 10.06 (br. s, 4 H, Ar-H) ppm. UV/Vis (MeCN): λ_{max} (ε) = 288 (23000), 457 (6700), 540 (7100 L mol⁻¹ cm⁻¹) nm. MS [ESI(+), MeCN]: m/z (%) = 1087 (100) [M + NEt₄]⁺. MS [ESI(-), MeCN]: m/z (%) = 826 (10) [M – NEt₄]⁻, 436 (100) [M – 2 NEt₄ – 2 methylindolate]⁻. HRMS [ESI(-), MeCN]: calcd. for C₄₄H₅₂Fe₂N₅S₂ [M – NEt₄]⁻ 826.2370; found 826.2374. Due to the instability of the complex, no satisfactory elemental analysis could be obtained.

Bis(tetraethylammonium) Tetrakis[(2-methylindolato)(μ₃-sulfido)ferate(II,III)] (3): A solution of 2-methylindole (240 mg, 1.8 mmol) in thf (10 mL) was treated with *n*BuLi (1.6 mol/L in hexane, 1.15 mL, 1.8 mmol). After stirring for 1 h, a brown solution of (NEt₄)₂[Fe₄S₄Cl₄]^[9] (**4**, 350 mg, 0.46 mmol) in MeCN (60 mL) was added. The reaction mixture turned red, and, after 3 h, a black precipitate had formed. The precipitate was separated by filtration, washed with thf (20 mL) and Et₂O (20 mL) and dried in vacuo. ¹H NMR (500 MHz, [D₇]dmf): δ = 1.39 (br. s, 24 H, NEt₄), 2.22 (br. s, 12 H, Me), 3.40 (br. s, 16 H, NEt₄), 5.61 (br. s, 4 H, Ar-H), 6.05 (br. s, 4 H, Ar-H), 6.96 (br. s, 4 H, Ar-H), 8.1 (br. s, 4 H, Ar-H) ppm; rapid decomposition in solution; one proton could not be assigned. UV/Vis (dmf): λ_{max} (ε) = 277 (41000), 287 (sh, 36000), 414 (6300 L mol⁻¹ cm⁻¹) nm. MS [ESI(+), MeCN + dmf]: m/z (%) = 1262 (100) [M + NEt₄]⁺. MS [ESI(-), MeCN + dmf]: m/z (%) = 1002 (5) [M – NEt₄]⁻, 742 (15) [M – 2 NEt₄ – methylindolate]⁻, 612 (10) [M – 2 NEt₄ – 2 methylindolate]⁻, 437 (100) [M – 2 NEt₄]²⁻. C₅₂H₇₂Fe₄N₆S₄ (1132.81): calcd. C 55.13, H 6.41, N 7.42, S 11.32; found C 51.90, H 6.32, N 6.96, S 11.23; due to the instability of the complex, no satisfactory elemental analysis could be obtained.

Supporting Information (see footnote on the first page of this article): ESI mass spectrum of **3**, SQUID data for **2**, ORTEP plot and crystallographic data for **3**.

Acknowledgments

We sincerely thank Benjamin Schneider for additional Mößbauer measurements. Financial support by the Fonds der Chemischen Industrie (Kekulé fellowship for M. G. G. F.), the Deutsche For-

schungsgemeinschaft and the Swedish research council (International Research Training Group GRK 1422 “Metal Sites in Biomolecules: Structures, Regulation and Mechanisms”; see www.biometals.eu) is gratefully acknowledged.

- [1] a) D. H. Flint, R. M. Allen, *Chem. Rev.* **1996**, *96*, 2315–2334; b) H. Beinert, *J. Biol. Inorg. Chem.* **2000**, *5*, 2–15; c) R. Lill, *Nature* **2009**, *460*, 831–838.
- [2] a) F. Berkovitch, Y. Nicolet, J. T. Wan, J. T. Jarrett, C. L. Drennan, *Science* **2004**, *303*, 76–79; b) A. Marquet, B. T. S. Bui, A. G. Smith, M. J. Warren, *Nat. Prod. Rep.* **2007**, *24*, 1027–1040.
- [3] D. Coucouvanis, A. Salifoglou, M. G. Kanatzidis, A. Simopoulos, G. C. Papaefthymiou, *J. Am. Chem. Soc.* **1984**, *106*, 6081–6082.
- [4] J. Ballmann, X. Sun, S. Dechert, B. Schneider, F. Meyer, *Dalton Trans.* **2009**, 4908–4917.
- [5] P. Beardwood, J. F. Gibson, *J. Chem. Soc., Chem. Commun.* **1986**, 490–492.
- [6] J. Ballmann, X. Sun, S. Dechert, E. Bill, F. Meyer, *J. Inorg. Biochem.* **2007**, *101*, 305–312.
- [7] P. V. Rao, R. H. Holm, *Chem. Rev.* **2004**, *104*, 527–559.
- [8] S. Groysman, R. H. Holm, *Biochemistry* **2009**, *48*, 2310–2320.
- [9] Y. Ohki, Y. Sunada, K. Tatsumi, *Chem. Lett.* **2005**, *34*, 172–173.
- [10] D. J. Evans, G. J. Leigh, *J. Chem. Soc., Chem. Commun.* **1988**, 395–396.
- [11] G. P. F. van Strijdonck, P. T. J. H. ten Have, M. C. Feiters, J. G. M. van der Linden, J. J. Steggerda, R. J. M. Nolte, *Chem. Ber./Recueil* **1997**, *130*, 1151–1157.
- [12] C. Zhou, R. H. Holm, *Inorg. Chem.* **1997**, *36*, 4066–4077.
- [13] W. E. Cleland, D. A. Holtman, M. Sabat, J. A. Ibers, G. C. DeFotis, B. A. Averill, *J. Am. Chem. Soc.* **1983**, *105*, 6021–6031.
- [14] H. Ogino, S. Inomata, H. Tobita, *Chem. Rev.* **1998**, *98*, 2093–2121.
- [15] J. Ballmann, A. Albers, S. Demeshko, S. Dechert, E. Bill, E. Bothe, U. Ryde, F. Meyer, *Angew. Chem. Int. Ed.* **2008**, *47*, 9537–9541; *Angew. Chem.* **2008**, *120*, 9680–9684.
- [16] H. J. Ballmann, Dissertation Thesis, Georg-August-Universität Göttingen, Göttingen, Germany, **2008**.
- [17] M. G. G. Fuchs, S. Dechert, S. Demeshko, U. Ryde, F. Meyer, *Inorg. Chem.*, DOI: 10.1021/ic902559n.
- [18] Y. Do, E. D. Simhon, R. H. Holm, *Inorg. Chem.* **1983**, *22*, 3809–3812.
- [19] G. B. Wong, M. A. Bobrik, R. H. Holm, *Inorg. Chem.* **1978**, *17*, 578–584.
- [20] T. Herskovitz, B. A. Averill, R. H. Holm, J. A. Ibers, W. D. Phillips, J. F. Weiher, *Proc. Natl. Acad. Sci. USA* **1972**, *69*, 2437–2441.

Received: April 15, 2010
Published Online: June 23, 2010

The Effect of an Electrical Bias on the Mechanism of Decomposition of Transients with Metal–Carbon σ Bonds

Irena Rusonik,^[a] Haim Cohen,^[b] Alex Lugowskoy,^[b] Alexander Krasnopol'ski,^[b] Michael Zinigrad,^[b] and Dan Meyerstein^{*[a,b]}

Keywords: Dehalogenation / Iron / Electrochemistry / Radicals / Metal–carbon bonds

When $\text{CCl}_3\text{CO}_2^-$ reacts thermally with porous iron electrodes, the radical $\cdot\text{CCl}_2\text{CO}_2^-$ is formed. This radical reacts with the surface of the electrode to form a transient with a Fe–C σ bond, $\text{Fe}^0_{(\text{s})}\text{--CCl}_2\text{COO}^-$. The mechanism of decompo-

sition of this transient depends on the electrical bias applied to the electrode: at a low bias of $E > -0.9$ V vs. SCE, $\text{HCCl}_2\text{COO}^-$ is the major final product, whereas at a higher bias of $E < -1.2$ V vs. SCE, HC(O)CO_2^- is the major product.

Introduction

Radicals or radical ions are formed as primary intermediates in a large variety of organic electrochemical processes including oxidations (e.g. the Kolbe Reaction) and reductions (e.g. reduction of alkyl halides and diazonium salts). When the radical is formed at the electrode surface, for example, by reduction of a diazonium salt at the open circuit potential, then the radical is expected to react with the electrode to form an intermediate or a stable product with a covalently bound organic molecule to the electrode.^[1] Thus the reduction of aryl diazonium salts, mainly in aprotic media, is used to prepare covalently bound organic layers to conductive or semiconductive surfaces.^[2] For metals forming stable organometallic compounds, for example, Hg, Cd, and Pb, results point out that “in a few electrochemical reactions, the initial electron-transfer step does generate a σ radical at the electrode surface, and organometallic compounds are formed.”^[3a] The binding of radicals to other metals, semiconductors, and metal oxides was also recently reported.^[3b–3d] However, it was suggested that “In the majority of electroorganic reactions, the working electrode is an inert material. Electron transfer generates a radical-ion species with sufficient lifetime to migrate away from the electrode surface. Further reactions then generate more reactive free radical species, and these undergo terminal reactions before they are able to react with the electrode surface.”^[3a] Recent results^[4–7] suggest that the latter assumption has to be reconsidered, as radicals formed at the surface of metals react with them to form short-lived

intermediates with metal–carbon σ bonds; this is of special importance in the dehalogenation of halo-organic pollutants by Fe^0 .^[4–7]

Furthermore, for the Kolbe-type oxidations of RCO_2^- , it was pointed out^[8] that “the reaction is controlled by a variety of factors including anode material, anode potential, current density, solvent, supporting electrolyte, structure of R, and temperature.” Similarly, the reduction of acetone in 6 N H_2SO_4 was shown to yield 2-propanol on Hg cathodes (95%), propane on Zn and Cd electrodes, and mixture of 2-propanol (68%), propane (25%), and the corresponding pinacol (7%) on Pb electrodes.^[9] The observation that the nature of the electrode affects the composition of the products clearly points out that the intermediate, the radical, formed in these processes interacts with the electrode. It was also shown that the mechanism of reduction of dihaloalkanes greatly depends on the cathode potential, that is, the yield of cyclic products increases as the potential of the cathode becomes more negative.^[10] Thus, for example, the reduction of 1,4-dibromobutane in DMF yields 90% cyclobutane and 10% butane at -2.3 V vs. SCE, but 26% cyclobutane and 74% butane at -1.75 V vs. SCE.^[10] Again, this effect is difficult to explain if no bond is formed between the electrode and the initially formed radical.

The electrolytic reduction of CCl_4 on Fe^0 electrodes was reported to yield directly CH_4 without the formation of CHCl_3 , CH_2Cl_2 , and CH_3Cl as intermediates,^[11] though the latter compounds are reduced slower than CCl_4 by Fe^0 .^[5,12–15] It should be noted that other authors reported the formation of CHCl_3 when CCl_4 is treated with iron powder.^[5,12–15]

Results and Discussion

It seemed of interest to study the effect of an electrical bias on the dehalogenation of polychlorinated compounds.

[a] Department of Chemistry, Ben-Gurion University of the Negev, Beer-Sheva, Israel

[b] Department of Biological Chemistry, Ariel University Center of Samaria, Ariel, Israel
Fax: +972-3-9067440
E-mail: danmeyer@bgumail.bgu.ac.il

As an example, trichloroacetate was chosen. A porous iron electrode with a large surface area was used as cathode. Potentials at which the substrate is not reduced by a Faraday current were applied (Figure 1). Dehalogenation of CCl_3COO^- at constant potential was monitored within 4 h. Experiments were performed at four different potentials (open circuit, -0.9 V, -1.2 V, -1.5 V vs. SCE). The progress of the reaction was monitored by measuring the yield of Cl^- , one of the reaction products, determined by a specific color reaction^[16] (Figure 2). The results point out that:

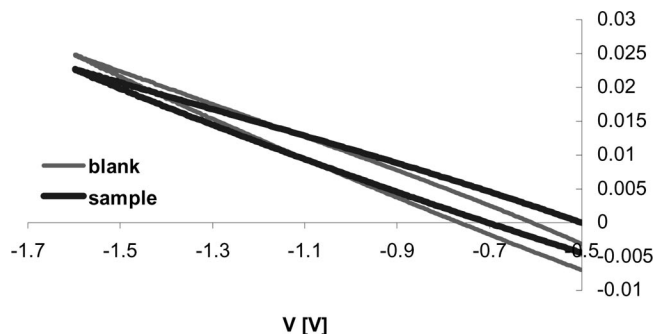


Figure 1. Cyclic voltammetry of CCl_3COOH on a porous iron electrode. Blank: NaClO_4 (0.1 M, pH 7.0, argon-saturated). Sample: CCl_3COOH (0.01 M), NaClO_4 (0.1 M), pH 7.0, argon-saturated. Note: The potential was measured vs. SCE electrode. (The oxidation current observed near 0 V vs. calomel is due to Fe^0 oxidation).

(1) A bias of -1.2 or -1.5 V vs. SCE increases the chloride yield, measured after 100 min from the start of the experiment, relative to that at an open circuit, by a factor of approximately three. The observation that the rate of chloride formation is not much higher at these potentials supports the suggestion that the substrate is not reduced by a Faraday process. The results point out that at these negative potentials three Cl^- ions can be removed in the dehalogenation process of CCl_3COOH instead of one Cl^- ion for the dehalogenation with iron powder.^[5]

(2) The ratio $[\text{Cl}^-]/[\text{H}^+]$ is 300 in the absence of or in the presence of a small electrical bias, $E > -0.9$ V, and the ratio is approximately 3 in its presence. These results prove that the electrical bias affects the dehalogenation mechanism.

(3) At small negative potentials and at open circuit experiments, the kinetic curve reaches saturation because of the precipitation of iron hydroxide/oxide on the electrode surfaces, which slows down the dehalogenation process. But at more negative potentials, the kinetic curve is almost linear, which means that the electrical bias inhibits electrode passivation as expected at potentials at which Fe^0 is deposited from solutions containing Fe^{2+} . Thus, the electrical bias prevents the corrosion of the iron electrode by keeping the surface area clean from oxide precipitation. This finding might be of importance in the dehalogenation of pollutants.

(4) At the more negative potentials, the pH_{final} value is considerably lower.

(5) The short initiation period observed for the dehalogenation process is attributed to reduction of the oxides adsorbed initially on the electrode surface. Alternatively, it could be argued that during the initiation period the solution near the electrode is acidified, which accelerates the dehalogenation process. Therefore, it was decided to perform the experiment in the presence of a buffer.

The effect of phosphate buffer on the dehalogenation process of CCl_3COOH at the surface of porous iron electrodes was examined (Figure 3). The results point out that under open circuit conditions the phosphate decreases the Cl^- yield to negligible values. On the other hand, at a negative electrical bias, the Cl^- yield remains linear with time, after a short induction period, though the yield is somewhat lower than that in the absence of the buffer. These results suggest that: (1) The induction period is not due to the decrease in the pH. (2) The phosphate buffer decreases somewhat the Cl^- yield. This result is attributed to the precipitation of iron(II) phosphate on the electrode surfaces (white precipitation was observed) that decreases the active surface area of the electrode and slows down the dehalogenation process.^[5]

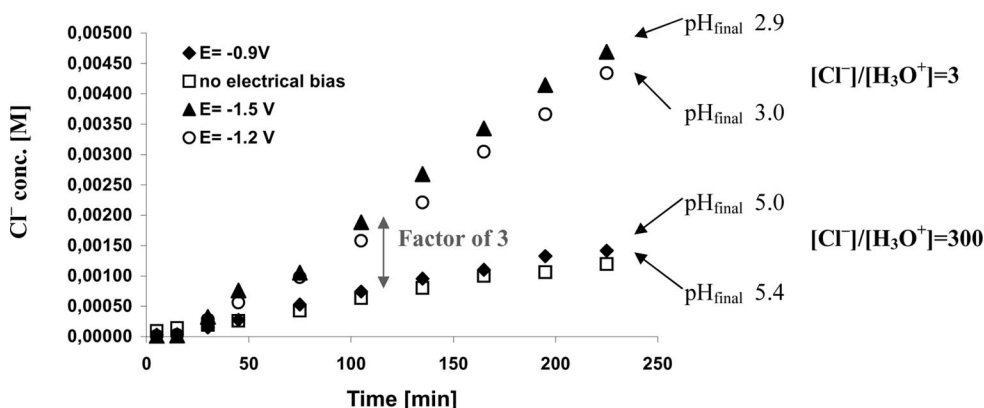


Figure 2. Kinetic study of the dehalogenation of CCl_3COOH on porous iron electrodes at different potentials. Fe^0 porous electrode, CCl_3COOH (0.01 M), NaClO_4 (0.1 M), $\text{pH}_{\text{initial}}$ 7.0, argon-saturated. Note: The potential was measured vs. SCE electrode.

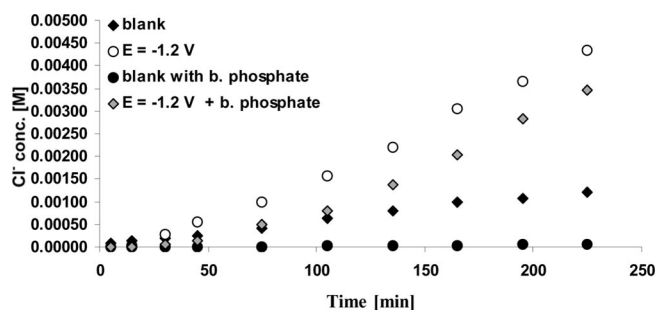


Figure 3. Effect of phosphate buffer on the kinetics of the reaction. Fe⁰ porous electrode, CCl₃COOH (0.01 M), NaClO₄ (0.1 M), phosphate buffer (0.02 M only for the systems that contained the buffer), pH_{initial} 7.0, argon-saturated. Note: The potential was measured vs. SCE electrode. Blank: Open circuit experiment.

The dependence of the Cl[−] yield on the CCl₃COOH concentration was examined (Figure 4). The results point out that increasing the initial CCl₃COOH concentration increases the Cl[−] yield. However, the increase in the yield is considerably smaller than that of the substrate. This result indicates that the diffusion of the substrate to the electrode surface is not the only rate-determining step. It is suggested that the rate of decomposition of the intermediate,



formed in the process contributes to the rate of the overall dehalogenation process.

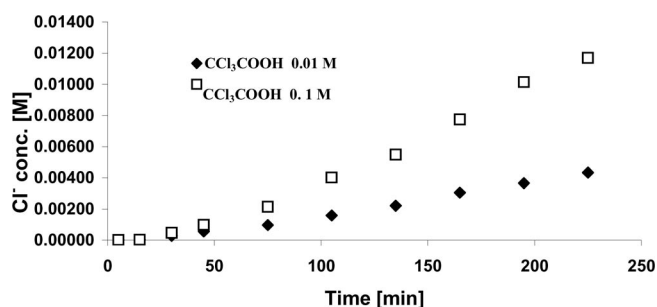
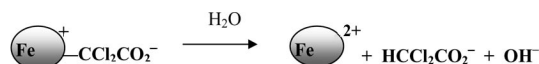


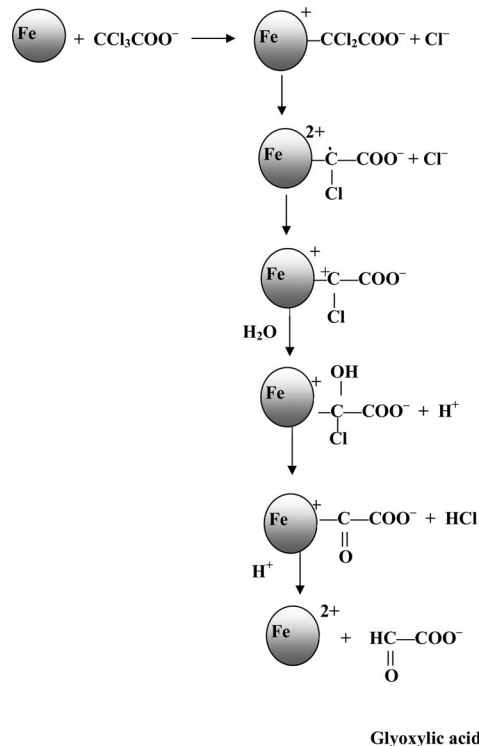
Figure 4. Dependence of the Cl[−] yield on the initial CCl₃COOH concentration. Fe⁰ porous electrode, CCl₃COOH, 0.1 M NaClO₄, pH_{initial} 7.0, Ar sat.

HPLC analysis of the final products points out that glyoxylic acid is formed quantitatively, based on the Cl[−] yield, at potentials < −1.2 V vs. SCE, whereas no glyoxylic acid is formed at potentials > −0.9 V vs. SCE. The observation of glyoxylic acid as one of the final products of the CCl₃COOH dehalogenation process suggests the following mechanism for the dehalogenation of CCl₃COOH on porous iron electrodes. In the first step, CCl₃COO[−] is reduced by the iron surface and 'CCl₂COO[−] radicals are formed. This radical then reacts with metal surface, forming a transient with a metal–carbon σ bond. This transient then decomposes by mechanisms depending on the electrical bias: (a) At potentials > −0.9 V vs. SCE the transient decomposes via:



HCCL₂COO[−] was not determined experimentally, as the substrate contained traces of it. The small change in pH during this process is due to precipitation of Fe(OH)₂, which lowers the pH.

(b) At potentials less than −1.2 V vs. SCE, glyoxylic acid is the sole organic product. It is proposed that the mechanism of this process is that outlined in Scheme 1. This mechanism is also in accord with the observation that the [Cl[−]]/[H⁺] yield is 3, as was experimentally observed.



Scheme 1. Mechanism of dehalogenation of CCl₃COOH on negatively biased iron porous electrodes.

The results thus prove that the electrical bias might change the mechanism of decomposition of transients with a metal–carbon σ bond formed in the initial step. This finding might be of general significance in electrochemical organic processes. Furthermore, this finding might be of interest to heterogeneous catalytic processes involving radicals and to the dehalogenation of halo-organic pollutants.^[4–7]

Experimental Section

Porous iron electrodes were prepared by thermal baking. Iron powder (10 μm) was mixed with boric acid powder and water. An iron rod was coated with the resulting thick mixture and put in an oven under an argon atmosphere. The rod was heated in steps in order to maintain slow and mild evaporation of volatile components, and it was finally heated up to 550 °C. The obtained electrodes were tested by resistance measurement between the rod and the coating and handled with diluted hydrochloric acid until the average resistance became less than 200 mOhm/cm.

Electrochemical measurements were performed with an EG&G Potentiostat/Galvanostat 263A. Working electrode: porous iron electrode, the potential was measured vs. an SCE electrode, Pt was used as counter electrode.

The determination of glyoxylic acid was performed by applying an HPLC system (SP Thermo, Spectraphysics Analytical Inc) with a UV/Vis detector. The separation was performed on a Beckman HPLC column, Ultrasphere ODS $5\ \mu\text{m} \times 4.6\ \text{mm} \times 25\ \text{cm}$. The eluent: MeOH/H₂O buffer phosphate 10 mM, flow 0.6 mL/min, UV detection.

- [1] M. P. Stewart, F. Maya, D. V. Kosynkin, S. M. Dirk, J. J. Stapleton, C. L. McGuinness, D. L. Allara, J. Mtour, *J. Am. Chem. Soc.* **2004**, *126*, 370.
- [2] J. Pinson, F. Podvorica, *Chem. Soc. Rev.* **2005**, *34*, 429.
- [3] a) J. Grishaw, *Electrochemical Reactions and Mechanisms in Organic Chemistry*, Elsevier, Amsterdam, **2000**, p. 9; b) M. M. Chehimi, G. Hallais, T. Matrab, J. Pinson, F. L. Podvorica, *J. Phys. Chem. C* **2008**, *112*, 18559; c) V. Jouikov, J. Simonet, *Electrochem. Commun.* **2010**, *12*, 331; d) V. Jouikov, J. Simonet, *Electrochem. Commun.* **2010**, DOI:10.1016/j.elecom.2010.03.032.
- [4] I. Rusonik, H. Polat, H. Cohen, D. Meyerstein, *Eur. J. Inorg. Chem.* **2003**, *23*, 4227.
- [5] I. Rusonik, H. Cohen, D. Meyerstein, *Eur. J. Inorg. Chem.* **2005**, 1227.
- [6] I. Rusonik, T. Zidky, H. Cohen, D. Meyerstein, *Glass Phys. Chem.* **2005**, *31*, 115.
- [7] I. Rusonik, H. Cohen, D. Meyerstein, *Inorg. Chem.* **2006**, *45*, 7389.
- [8] T. Shono, *Electroorganic Chemistry as a New Tool in Organic Chemistry*, Springer-Verlag, Berlin **1984**, p. 82.
- [9] A. Talec, *Electrochimie Organique*, Masson, Paris, **1985**, p. 24.
- [10] T. Shono, *Electroorganic Chemistry as a New Tool in Organic Chemistry*, Springer-Verlag, Berlin **1984**, p. 148.
- [11] T. Li, J. Farrell, *Environ. Sci. Technol.* **2000**, *34*, 173.
- [12] L. J. Matheson, P. G. Tratnyek, *Environ. Sci. Technol.* **1994**, *28*, 2045.
- [13] R. Muftikian, Q. Fernando, N. Korte, *Wat. Res.* **1995**, *29*, 2434.
- [14] B. R. Helland, P. J. J. Alvarez, J. L. Schnoor, *J. Hazard. Mater.* **1995**, *41*, 205.
- [15] K. D. Warren, R. G. Arnold, T. L. Bishop, L. C. Lindholm, E. A. Betterton, *J. Hazard. Mater.* **1995**, *41*, 217.
- [16] T. M. Florence, Y. J. Farrar, *Anal. Chim. Acta* **1971**, *54*, 373.

Received: April 11, 2010
Published Online: June 17, 2010

Spirocycle (Si*t*Bu₃)₆Si₉Cl₂: The First of Its Kind among Group 14 Elements

Thomas M Klapötke,^{*,[a]} Sham Kumar Vasisht,^{*,[a]} and Peter Mayer^[a]

Dedicated to the memory of Prof. Dr. Nils Wiberg

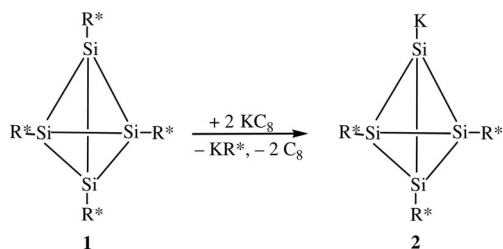
Keywords: Spiro compounds / Cluster compounds / Silanes / Structure elucidation

Structural studies on (R^{*}₃Si₄)₂SiCl₂, prepared by the reaction of tetrasilatetrahedranide KR^{*}₃Si₄ with SiCl₄, show that the tetrahedral moieties R^{*}₃Si₄ undergo structural transformation. The molecule exhibits a spiro[4.4]nonasilane network that comprises two homonuclear tricyclo[2.1.0.0^{2,5}]pentasilane rings with a common “naked” silicon bridge. The compound shows structural similarities with R^{*}₆Si₈, which con-

sists of similar rings fused together along an Si–Si bridge. Comparison of valence angles, interplanar angles and bridgehead distances with respect to tricyclo[2.1.0.0^{2,5}]pentanes or similar ring systems with heteronuclear group homologues are reported to highlight the influence of bulky supersilyl R^{*} groups in the structure.

Introduction

Fused polyhedral polysilanes (SiR)_{*n*} with *n* = 8, 6 or 4 are known,^[1,2] but a tetrahedron (*n* = 4) with four three-membered rings has been a challenge because of its highest strain energy, which leads to its collapse, almost without a barrier.^[3] The target molecule was first realized by Wiberg et al. in 1993 with the isolation of tetrasupersilyl-*tetrahedro*-tetrasilane, R^{*}₄Si₄ (**1**) (R^{*} = Si*t*Bu₃ = supersilyl).^[2] This highly strained Si₄ cage compound is stabilized by a symmetrical surrounding of large exocyclic supersilyl R^{*} groups, which provide higher thermal stability but are also responsible for its lowered reactivity under normal reaction conditions towards water, alcohols (MeOH, EtOH), acids (HBr, CF₃COOH), quaternary ammonium halides (Bu₄NBr, Me₄NF), Me₄PF and activated KF or CsF. However, it is susceptible to oxidation in solution by O₂ to R^{*}₄Si₄O₂^[4] and by I₂ to R^{*}₄Si₄I₂.^[5a] It undergoes addition-cum-substitution reaction with Br₂ or I₂ to form



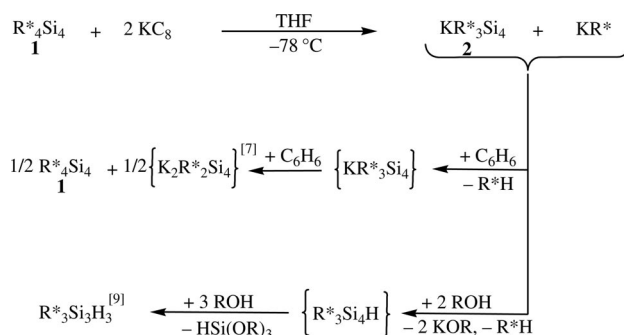
Scheme 1. Formation of **2**.

[a] Dept. Chemie, Ludwig-Maximilian Universität München, Butenandt-Str. 5-13, Haus D, 81377 München, Germany
Fax: +49-89-2180-77492
E-mail: tmk@cup.uni-muenchen.de

R^{*}₃Si₄X₅.^[5b,6] It is reduced, without structural transformation, by KC₈ at low temperatures to KR^{*}₃Si₄ (**2**) (Scheme 1).^[7] Sekiguchi et al. were the first to report a similar anion R₃Si₄[−] where R = SiMe[CH(SiMe₃)₂]₂, formed by the reaction of R₄Si₄ with KC₈, but its chemistry is unknown.^[8]

Results and Discussion

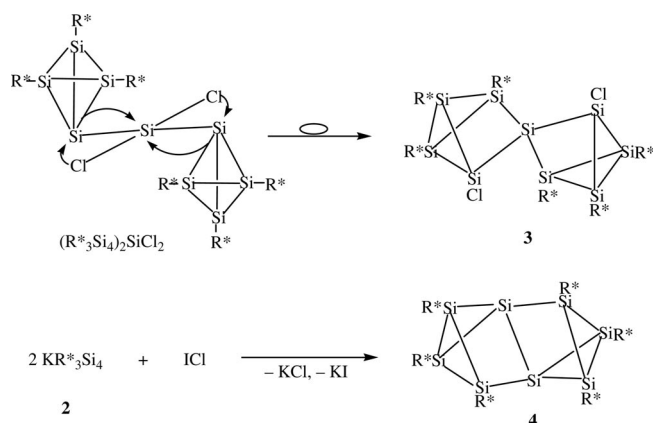
Reaction of **1** with 2 equiv. of KC₈ provided a 1:1 mixture of KR^{*}₃Si₄ and KR^{*}. Because of their nonvolatility, similar solubility, easier decomposition on warming and exposure to air and almost similar chemical reactivity, their separation turned out to be tedious. The mixture in benzene as solvent at room temperature indicated reasonably fast proton abstraction by KR^{*} to form R^{*}H, but KR^{*}₃Si₄ was also found to undergo partial disproportionation (Scheme 2). It was almost impossible to remove the latter impurity from KR^{*}₃Si₄.



Scheme 2. Separation of a mixture of **2** and KR^{*}.

Protolysis with alcohols was carried out in order to obtain a mixture of R^{*}H and R^{*}₃Si₄H, so that the former could be removed in vacuo at 10^{−3} Torr/r.t. to leave behind pure R^{*}₃Si₄H (which could then be transformed into R^{*}₃Si₄Br followed by R^{*}₃Si₄K); but this was not successful, because R^{*}₃Si₄H turned out to be unstable. It decomposed due to destabilization of the tetrahedron by an insufficient surrounding with the small proton, which facilitated further reaction towards cyclotrisilane, R^{*}₃Si₃H₃^[7,9] (Scheme 2). There was hardly any other practical chemical approach left that could improve the situation, and hence KR^{*}₃Si₄ (**2**) had to be separated from KR^{*} by repeated crystallization of the former from concentrated solutions in thf at −78 °C to isolate red crystals of KR^{*}₃Si₄·2thf, which turned into an orange-red solid of **2** by loss of thf in vacuo.^[7]

Compound **2** reacted with SiCl₄ to form R^{*}₃Si₄–SiCl₃ along with impurities of R^{*}₃Si₄–Si₂Cl₅ and (R^{*}₃Si₄)₂SiCl₂ (**3**).^[10] However, a reaction of **2** with SiCl₄ (2:1) provided higher yields of the latter compound, (R^{*}₃Si₄)₂SiCl₂ (**3**). It is a pink-red solid with low solubility in organic solvents like *n*-heptane, benzene or toluene. It crystallizes from warm toluene or benzene solutions to provide pink-red crystals suitable for X-ray analysis. Its ²⁹Si NMR spectrum in [D₈]toluene shows three equally intense singlets at δ = 52.16, 49.41 and 43.74 ppm for the six exocyclic R^{*} groups. Similarly, the ¹H NMR spectrum shows three signals at δ = 1.471, 1.448 and 1.372 ppm with relative integrals of 1:1:1. A tetrahedral geometry of the R^{*}₃Si₄ groups is unlikely to justify three NMR signals for (R^{*}₃Si₄)₂SiCl₂. This indicates that the molecule may not have the structural arrangement visualized for (R^{*}₃Si₄)₂SiCl₂ (Scheme 3). Steric impossibility of accommodating two heavily substituted R^{*}₃Si₄ groups on the SiCl₂ moiety is responsible for the collapse of the tetrahedra, which releases its inherent strain by opening up with reduction in the number of three-membered strained rings from four to two in each polyhedron, thus imparting a higher stability to the system.^[3] A less strained tricyclo[2.1.0.0^{2,5}]pentasilane arrangement arises from the migration of chloro groups to unsubstituted Si positions to form R^{*}₆Si₉Cl₂ (**3**) as shown in Scheme 3.

Scheme 3. Formation of **3**, **4**.

The energy difference between (R^{*}₃Si₄)₂SiCl₂ (*C*_{2v} symmetry) and *spiro*-R^{*}₆Cl₂Si₉ (**3**, *C*₂ symmetry) was estimated by using the corresponding methyl derivatives (R^{*} = CH₃) as model compounds. At the B3LYP/SDD level of theory the isomerization of (R^{*}₃Si₄)₂SiCl₂ (*C*_{2v} symmetry) to *spiro*-R^{*}₆Cl₂Si₉ (**3**, *C*₂ symmetry), according to Scheme 3, is strongly favored {*E*[(R^{*}₃Si₄)₂SiCl₂] = −3765.029737 a.u., *E*(*spiro*-R^{*}₆Cl₂Si₉) = −3765.147242 a.u.; Δ*E*^{cal} = −73.7 kcal mol^{−1}}. This is in agreement with the experimental findings and the isolation of **3**. The optimized molecular structure of (R^{*}₃Si₄)₂SiCl₂ is shown in Figure 1 and the optimized molecular structure of *spiro*-R^{*}₆Cl₂Si₉ corresponds essentially to the solid state (X-ray) structure (Figure 2).

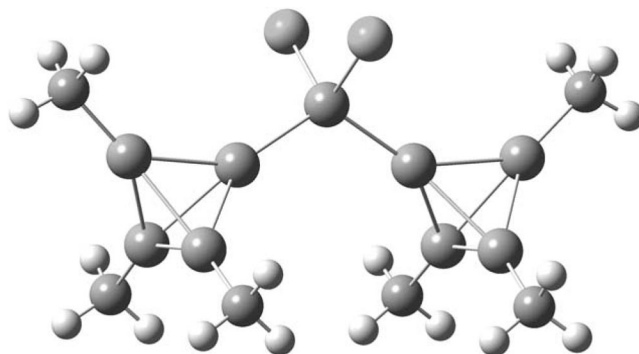
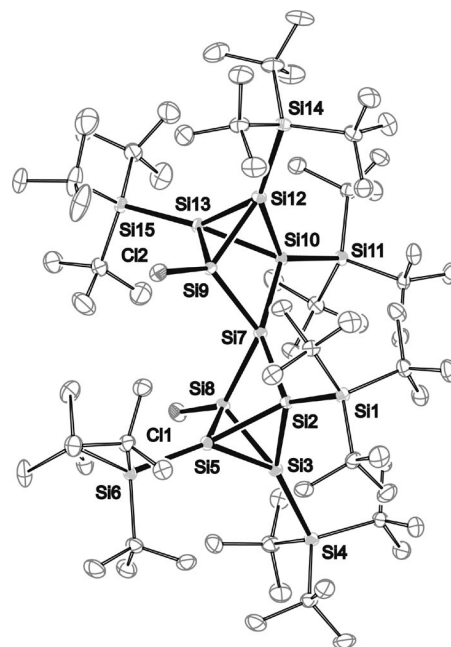
Figure 1. Optimized molecular structure (B3LYP/SDD) of (R^{*}₃Si₄)₂SiCl₂ (R^{*} = CH₃).

Figure 2. Molecular structure of **3** (50% ellipsoid probability level; arbitrary radii for H). Selected bond lengths [Å] and bond angles [°]: Si8–Cl1 2.083(8), Si9–Cl2 2.084(9), Si8–Si7 2.323(9), Si8–Si3 2.333(10), Si8–Si5 2.340(9), Si9–Si7 2.319(9), Si9–Si13 2.339(9), Si9–Si12 2.335(10), Si7–Si2 2.470(10), Si7–Si10 2.464(10); Si2–Si7–Si8 73.20(3), Si9–Si7–Si10 73.53(3), Si2–Si7–Si9 121.30(4), Si8–Si7–Si10 124.95(4) (angle sum at Si7 392.98 indicates non-planar environment).

The Si_9 cluster $\text{R}^*_6\text{Si}_9\text{Cl}_2$, with spiro[4.4]nonasilane network is the first compound of its kind among Group 14 elements. Its two strained homonuclear tricyclo[2.1.0.0^{2,5}]-pentasilane moieties are bridged by unsubstituted “naked” Si as shown in **3**. A violet Si_8 cluster R^*_6Si_8 (**4**) reported earlier,^[7,11] has an almost similar arrangement of two fused tricyclo[2.1.0.0^{2,5}]-pentasilane moieties. Here the rings are not capped by a lone Si atom but are fused along an Si–Si edge as shown in **4** (Scheme 3). The atoms comprising the fused edge are “naked” silicon atoms. Both these Si atoms have an inverted “umbrella”-type tetrahedral structure (X-ray) shown in Figure 3.^[11]

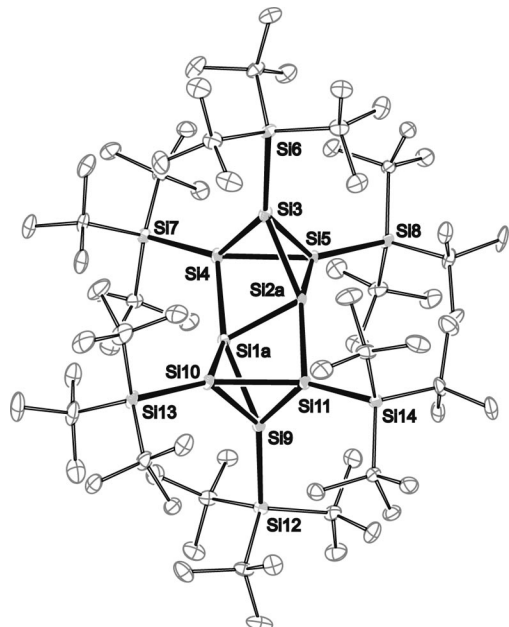
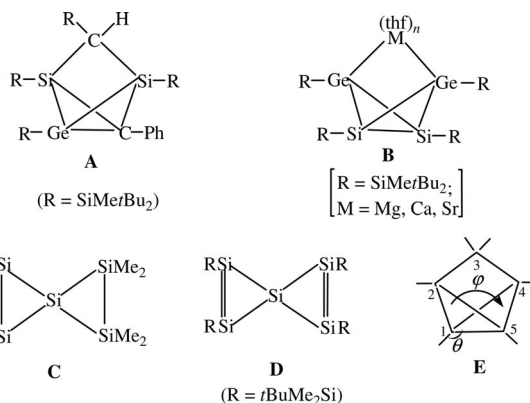


Figure 3. Molecular structure of **4**.

Tricyclo[2.1.0.0^{2,5}]-pentanes with heteronuclear tetrel atoms as shown in **A**^[12] and **B**^[13] are known but the homonuclear derivatives with skeletal atoms other than carbon^[14a] are not reported in any of the higher homologues Si, Ge, Sn or Pb. Although homonuclear trisilacycles such as five-vertex cluster R_6Si_5 ^[15] and an aromatic isomer of hexasilabenzene R_6Si_6 ,^[16] ($\text{R} = 2,4,6$ -triisopropylphenyl) are known, yet homonuclear spiroasilacycles other than octamethylspiro[2.2]pentasilane Me_8Si_5 (**C**)^[17] and spiro[2.2]pentasiladiene (**D**)^[18] have not been reported.



Tricyclo[2.1.0.0^{2,5}]-pentanes (**E**) are assigned the following characteristics:^[14] (i) large valence angle θ as shown in **E**, (ii) small interplanar angle ϕ with average value 97° , (iii) short bridgehead bond C1–C5 with bulky substituents. These structural parameters for **3** and **4** are listed in Table 1.

Steric hindrance due to bulky substituents R^* at bridgehead locations force an increase of the valence angle θ , which has an average value of 144° in **3** and 139° in **4** (Table 1). This value for tricyclo[2.1.0.0^{2,5}]-pentanes falls in the range 120 – 145° (highest)^[14] but ranges between 132 and 135° in **B**.^[13] A large θ value lowers the interplanar angle ϕ in **3** to an average value of 89° . The value for **4** is the smallest known so far with an average of 79° (Table 1). The reported range for carbon derivatives lies between 94 and 99° ^[14] and for hetero-atom-incorporated higher homologues **B** between 99 and 105° .^[13] Small angles ϕ force the hybrid orbitals on the bridgehead vertices to form short bonds between 1.41 and 1.51 Å (calcd. single bond length 1.54 Å) in tricyclo[2.1.0.0^{2,5}]-pentanes.^[14] The bridging Si–Si distance in **B** is also short and reported to be between 2.32 and 2.33 Å.^[13] However, this is neither reflected in **3** and **4** nor reported in $\text{R}^*_4\text{Si}_4\text{O}$.^[5a] With the smallest interplanar angle ϕ of 79° , the bridgehead bond in **4** is not the shortest but among the longest ones with an Si–Si distance of 2.39 Å (the same for $\text{R}^*_4\text{Si}_4\text{O}$ is 2.40 Å).^[5a] Similarly, the bridgehead bond in compound **3** (with the next higher ϕ value of 89°), instead of being longer than that in **4**, is in fact shorter with an average distance of 2.36 Å. The concept of small interplanar angles forcing the hybrid orbitals on positions 1 and 5 in **E** to form extraordinary short bent bridgehead bonds is not valid for **3** or **4** because of the overriding influence of the bulky supersilyl R^* groups, which create a larger outer cage to stabilize the skeleton and to let the inner core

Table 1. Structural parameters of **3** and **4**.

Compound	Bridgehead bond lengths [Å]	Interplanar angle ϕ [°]	Angle θ [°]
$\text{R}^*_6\text{Si}_9\text{Cl}_2$ (3)	Si3–Si5 2.362(9)	88.85(5)	142.99(4) Si3–Si5–Si6
	Si12–Si13 2.357(10)	88.94(5)	144.65(4) Si4–Si3–Si5
			141.70(4) Si13–Si12–Si14
			145.21(4) Si12–Si13–Si15
R^*_6Si_8 (4)	Si3–Si5 2.393(2)	79.00(14)	139.36(8) Si3–Si5–Si8
			139.16(8) Si5–Si3–Si6
	Si9–Si10 2.392(2)	78.53(14)	140.09(8) Si10–Si9–Si12
			139.06(9) Si9–Si10–Si13

structure of silicon atoms expand and stabilize with release of strain. This is further supported by other features in the structure of **3**. (i) All the six exocyclic Si–Si bonds (2.41–2.42 Å) are longer than a regular single bond (2.34 Å); this agrees with the range of 2.41–2.43 Å observed in **4**. (ii) All Si–Si skeletal bonds between silicon atoms bearing R* substituents are also longer with a range of 2.37–2.39 Å (regular single bond 2.34 Å); this is also true for **4** with distances 2.37–2.40 Å. (iii) All the six Si–Si skeletal bonds emanating from silicon atoms Si8 or Si9 (bearing less bulky Cl ligands) fall in the normal single-bond range of 2.32–2.34 Å. This is not due to the electron-withdrawing effect of the Cl substituent (which will do the opposite)^[3] but more so due to the shrinkage of the ligand surrounding.

With release of strain in going from a tetrahedral geometry to a tricyclopentasilane, the skeletal distances increase, and the short-bond isomers with somewhat elongated bridgehead bonds assume a higher stability^[3] as observed in **3** as well as **4**.^[19]

Conclusions

Reduced covering of the Si₄ cage by exocyclic groups leads to decreased thermal stability: R*₄Si₄ (350 °C) > KR*₃Si₄ (r.t.) > HR*₃Si₄ (unstable). On the other hand, increased congestion in (R*₃Si₄)₂SiCl₂ results in collapse of the tetrahedral moieties R*₃Si₄ into tricyclo[2.1.0.0^{2,5}]-pentasilane rings in *spiro*-R*₆Si₉Cl₂, which has structural similarities with R*₆Si₈. The unique *spiro*[4.4]nonasilane, R*₆Si₉Cl₂, and R*₆Si₈ are thermally stable due to overriding influence of bulky supersilyl groups R* in allowing the inner core to expand and stabilize.

Experimental Section

General: All reactions were carried out in vacuum-line vessels by using purified reagents and solvents under an inert gas with rigorously dried equipment. NMR spectra were recorded with Jeol Eclipse-270 or -400 and Jeol EX-400 instruments. The NMR spectra were recorded conventionally or with the INEPT and DEPT pulse sequences by using empirically optimized parameters for various groups for finer assignments. MS measurements were performed with a Jeol Mstation JMS700.

3: A KR*₃Si₄ (**2**) (0.690 g, 0.92 mmol) solution in thf (20 mL) was treated with SiCl₄ (0.95 mL, 0.5 M in thf, 0.47 mmol) in thf (20 mL) at –78 °C. The pink-red solution (after removal of KCl) was concentrated at room temp. and the residue dissolved in warm toluene or benzene to obtain crystals for X-ray crystallography and other analyses (yield ca. 60%). ¹H NMR ([D₈]toluene, 400 MHz, 25 °C): δ = 1.471 (s, 54 H, 2 R*), 1.448 (s, 54 H, 2 R*), 1.372 (s, 54 H, 2 R*) ppm. ²⁹Si NMR: δ = 52.165 (s, 2 R*), 49.414 (s, 2 R*), 43.740 (s, 2 R*) ppm. ¹³C NMR: δ = 33.161 (s, 6 Me₃C), 32.627 (s, 6 Me₃C), 32.217 (s, 6 Me₃C), 25.228 (s, 6 CMe₃), 24.885 (s, 6 CMe₃), 24.580 (s, 6 CMe₃) ppm. MS (FAB⁺, Xe, NBA): *m/z* (%) = 1519 (17) [M⁺], 1462 (3) [M – Bu]⁺, 1320 (5) [M – R*]⁺, 1264 (5) [M – R* – C₄H₈]⁺, 1206 (4) [M – R* – 2 Bu]⁺, 1120 (3) [M – 2 R*]⁺, 1086 (5) [M – 2 R* – Cl]⁺, 1058 (3) [M – R*₂SiCl]⁺, 738 (45) [R*₃Si₃]⁺, 710 (100) [R*₃Si₄]⁺, 682 (40) [R*₃Si₃]⁺. HR-MS: calcd. for C₇₂K₁₆₂Cl₂Si₁₅ [M⁺] 1519.8595; found 1519.8607.

Crystal Structure of 3: A Nonius Kappa CCD with a rotating anode was employed for data collection at 200 K by using Mo-*K*_α radiation. The structure was solved by direct methods with SIR97^[20] and refined by means of the full-matrix least-squares procedures with SHELXL97.^[21] Anisotropic displacement parameters were used to refine all non-hydrogen atoms. The hydrogen atoms were placed in ideal geometries and refined in a riding model. For further details, see Table 2. Graphical representations of the molecular structures were generated with ORTEP.^[22] CCDC-773139 contains the supplementary crystallographic data for this paper. These data can be obtained free of charge from The Cambridge Crystallographic Data Centre via www.ccdc.cam.ac.uk/data_request/cif.

Table 2. Crystallographic data for **3**·2C₆H₆.

Empirical formula	C ₈₄ H ₁₇₄ Cl ₂ Si ₁₅
<i>M_r</i> [g mol ^{–1}]	1676.468
Crystal size [mm]	0.28 × 0.26 × 0.18
Crystal system	monoclinic
Space group	<i>P</i> 2 ₁ / <i>c</i>
<i>a</i> [Å]	17.3014(2)
<i>b</i> [Å]	21.5745(2)
<i>c</i> [Å]	27.7419(3)
<i>α</i> [°]	90
<i>β</i> [°]	96.6375(6)
<i>γ</i> [°]	90
<i>V</i> [Å ³]	10285.78(19)
<i>Z</i>	4
<i>ρ</i> _{calcd.} [g cm ^{–3}]	1.082613(20)
<i>μ</i> [mm ^{–1}]	0.275
Refls. measured	60936
<i>R</i> _{int}	0.0430
Mean <i>σ</i> (<i>I</i>)/ <i>I</i>	0.0411
<i>θ</i> range [°]	3.18–24.00
Observed refls.	12471
<i>x</i> , <i>y</i> (weighting scheme)	0.0667, 3.7274
Refls. in refinement	16099
Parameters	964
Restraints	0
<i>R</i> (<i>F</i> _{obsd.})	0.0435
<i>R</i> _w (<i>F</i> ²)	0.1250
<i>S</i>	1.068
Shift/error _{max}	0.001
Max. electron density [e Å ^{–3}]	0.987
Min. electron density [e Å ^{–3}]	–0.415

Acknowledgments

S. K. V. is thankful to the Deutsche Forschungsgemeinschaft for financial support.

- [1] a) S. Kyushin, H. Matsumoto, *Adv. Organomet. Chem.* **2003**, 49, 133; b) H. Matsumoto, K. Higuchi, Y. Hoshino, Y. Naoi, Y. Nagai, *J. Chem. Soc., Chem. Commun.* **1988**, 27, 1725; c) K. Furukawa, M. Fujino, N. Matsumoto, *Appl. Phys. Lett.* **1992**, 60, 2744; d) A. Sekiguchi, T. Yatabe, H. Kamatani, C. Kabuto, H. Sakurai, *J. Am. Chem. Soc.* **1992**, 114, 6260; e) H. Matsumoto, K. Higuchi, S. Kyushin, M. Goto, *Angew. Chem. Int. Ed. Engl.* **1992**, 31, 1354; f) A. Sekiguchi, T. Yatabe, C. Kabuto, H. Sakurai, *J. Am. Chem. Soc.* **1993**, 115, 5853.
- [2] N. Wiberg, C. M. M. Finger, K. Polborn, *Angew. Chem.* **1993**, 105, 1140; *Angew. Chem. Int. Ed. Engl.* **1993**, 32, 1055.
- [3] a) S. Nagase, M. Nakano, *Angew. Chem. Int. Ed. Engl.* **1988**, 27, 1081; b) S. Nagase, *Acc. Chem. Res.* **1995**, 28, 469.
- [4] N. Wiberg, H. Auer, H. Nöth, S. Wagner, K. Polborn, G. Kramer, *J. Organomet. Chem.* **2001**, 619, 110.

- [5] a) N. Wiberg, H. Auer, H. Nöth, J. Krizeck, K. Polborn, *Angew. Chem.* **1998**, *110*, 3030; *Angew. Chem. Int. Ed.* **1998**, *37*, 2869; b) N. Wiberg, H. Auer, K. Polborn, M. Veith, V. Huch, *Organosilicon Chemistry IV – From Molecules to Materials*, Wiley-VCH, Weinheim, **2000**, p. 124.
- [6] N. Wiberg, S. K. Vasisht, G. Fischer, P. Mayer, V. Huch, M. Veith, *Z. Anorg. Allg. Chem.* **2007**, *633*, 2425.
- [7] T. M. Klapötke, S. K. Vasisht, G. Fischer, P. Mayer, *J. Organomet. Chem.* **2010**, *695*, 667.
- [8] M. Ichinohe, M. Toyoshima, R. Kinja, A. Sekiguchi, *J. Am. Chem. Soc.* **2003**, *125*, 13328.
- [9] N. Wiberg, C. M. M. Finger, H. Auer, K. Polborn, *J. Organomet. Chem.* **1996**, *521*, 377.
- [10] Compound $R^*_3Si_4-SiCl_3$ is formed as a primary product in the reaction of $KR^*_3Si_4$ with about 1.2 equiv. of $SiCl_4$. This light yellow solid along with other similar derivatives will be published separately.
- [11] G. Fischer, V. Huch, P. Mayer, S. K. Vasisht, M. Veith, N. Wiberg, *Angew. Chem. Int. Ed.* **2005**, *44*, 7884.
- [12] V. Ya. Lee, M. Ichinohe, A. Sekiguchi, *J. Am. Chem. Soc.* **2002**, *124*, 9962.
- [13] V. Ya. Lee, K. Takanashi, M. Ichinohe, A. Sekiguchi, *Angew. Chem. Int. Ed.* **2004**, *43*, 6703.
- [14] a) M. D. Levin, P. Kaszynski, J. Michl, *Chem. Rev.* **2000**, *100*, 169; b) P. Dowd, R. Irnghartinger, *Chem. Rev.* **1989**, *89*, 985.
- [15] D. Scheschkewitz, *Angew. Chem. Int. Ed.* **2005**, *44*, 2954.
- [16] K. Abersfelder, A. J. P. White, H. S. Rzepa, D. Scheschkewitz, *Science* **2010**, *327*, 564.
- [17] P. Boudjouk, R. Sooriyakumaran, *J. Chem. Soc., Chem. Commun.* **1984**, 777.
- [18] M. Kira, *Pure Appl. Chem.* **2000**, *72*, 2333.
- [19] Compounds **3** and **4** cannot be classified as long-bond (LB) isomers because of a slight elongation of the bridgehead bonds. Long-bond isomers are usually 0.4 Å longer (ca. 2.7 Å) than the short-bond isomers. R. Koch, T. Bruhn, M. Weidenbruch, *J. Mol. Struct.* **2004**, *680*, 91.
- [20] *SIR97, a New Tool for Crystal Structure Determination and Refinement*: A. Altomare, M. C. Burla, M. Camalli, G. L. Cascarano, C. Giacovazzo, A. Guagliardi, A. G. G. Moliterni, G. Polidori, R. Spagna, *J. Appl. Crystallogr.* **1999**, *32*, 115–119.
- [21] G. M. Sheldrick, *Acta Crystallogr., Sect. A* **2008**, *64*, 112.
- [22] M. N. Burnett, C. K. Johnson, *ORTEP-III, Oak Ridge Thermal Ellipsoid Plot Program for Crystal Structure Illustrations*, Oak Ridge National Laboratory Report ORNL-6895, **1996**, Windows version (L. J. Farrugia, Univ. Glasgow).

Received: May 4, 2010

Published Online: June 23, 2010

Novel *O,O'*-Donor Oxo-Mo^{IV} Hydrotris(3-isopropylpyrazolyl)borate Complexes Formed by Chelation of Potentially Hydrogen-Bonding Phenolate Ligands on Reduction of Dioxo-Mo^{VI} Complexes

Victor W. L. Ng,^[a] Michelle K. Taylor,^[a,b] Lyndal M. R. Hill,^[a] Jonathan M. White,^[a,b] and Charles G. Young*^[a]

Keywords: Molybdenum / Chelates / Hydrogen bonds / O-donors

The oxo-Mo^{IV} complexes formed in the reactions of *cis*-Tp^{IPr}Mo^{VI}O₂(OAr-R) [Tp^{IPr} = hydrotris(3-isopropylpyrazol-1-yl)borate, [−]OAr-R = phenolate derivative] complexes with PEt₃ or PEt₂Ph in acetonitrile depend on the nature of the potential hydrogen-bonding group (R) incorporated into the phenolate ligand. Green, diamagnetic, oxo(phosphoryl)-Mo^{IV} complexes, Tp^{IPr}Mo^{IV}O(OAr-R)(OPR'₃), are produced when R is absent or is a non-coordinating group such as 2-OMe and 3-NEt₂; six-coordinate Tp^{IPr}MoO(OC₆H₄OMe-2)-(OPEt₃) was structurally characterized and exhibits a distorted octahedral geometry typical of such species. When R is a carbonyl functionality, complete oxygen atom transfer leads to green or purple, diamagnetic, chelate complexes of

the type, Tp^{IPr}Mo^{IV}O(OAr-R-κ²O,O'). The R = 2-COEt, 2-CO₂Me and 2-CO₂Ph derivatives exhibit six-coordinate, distorted-octahedral structures possessing *fac* Tp^{IPr}, terminal oxo and bidentate *O,O'*-donor [−]OAr-R ligands. Where R is an amido functionality, CONHPh, the complexes, Tp^{IPr}Mo^{IV}O-(OC₆H₄CONHPh-2-κ²O,O')·OPR'₃ (R'₃ = Et₃, Et₂Ph), are isolated. Here, the six-coordinate, distorted-octahedral complex forms an intermolecular NH...OPR'₃ hydrogen bond to the lattice OPR'₃ molecule. Thus, facile chelation of potential hydrogen-bonding phenolate ligands suppresses hydrogen-bond-stabilized aquation or hydroxylation *cis* to the oxo group in these Mo^{IV} complexes.

Introduction

Oxygen atom transfer (OAT) and coupled electron-proton transfer (CEPT) are key processes in the catalytic cycles of pterin-containing molybdenum enzymes.^[1–4] These enzymes are responsible for the oxidation or reduction of a wide variety of biological substrates using water as the source or sink of the oxygen atom transferred to or from the substrate.^[1–4] Most mechanisms written for molybdenum enzymes involve *cis*-oxo(aqua)- or *cis*-oxo(hydroxo)-Mo(IV–VI) species but model complexes of these types are extremely rare.

We have reported model systems containing hydrotrispyrazolylborate ligands that exhibit forward and reverse OAT reactions involving mononuclear *cis*-dioxo-Mo^{VI} and oxo-Mo^{IV} complexes, and CEPT reactions leading to EPR-active *cis*-oxo(hydroxo)-Mo^V complexes; importantly, reactions that catalyze the transfer of water oxygen to substrates

have been realized.^[5–7] The formation of Mo^V species and the incorporation of water oxygen into substrates logically involves intermediate *cis*-oxo(aqua)-Mo^{IV} or *cis*-oxo(hydroxo)-Mo(IV/V) complexes.^[5–7] At the Mo^V level, *cis*-dioxo-Mo^V complexes have been isolated and thoroughly characterized but oxo(hydroxo)-Mo^V species have only been observed in solution or in combination with their conjugate base.^[8] To date, *cis*-oxo(aqua)-Mo^{IV} complexes have not been isolated from this system although a related *cis*-oxo(aqua)-W^{IV} complex, viz., [Tp*WO(OH₂)(MeCCMe)]-(O₃SCF₃) {Tp* = hydrotris(3,5-dimethylpyrazol-1-yl)borate}, has been reported by Crane et al.^[9] Other known oxo(aqua)-Mo^{IV} complexes adopt a *trans* geometry, e.g., [MoO(OH₂)(CN)₄]^{2−} and [MoO(OH₂)(dppe)₂]²⁺ {dppe = 1,2-bis(diphenylphosphanyl)ethane}.^[10]

Most of the compounds reported herein contain salicylaldehyde- or salicylic acid-based ligands; surprisingly, given their extensive coordination chemistry, few Mo complexes containing these ligands have been reported; all structurally characterized examples contain bidentate O₂-donor ligands. Thus, the reaction of aqueous molybdate solutions with salicylaldehyde yields the *cis*-dioxo-Mo^{VI} complex, MoO₂(OC₆H₄CHO)₂.^[11,12] This complex and a number of its ring-substituted derivatives react with amines to yield Schiff base complexes of varying nuclearity.^[11,13] The reactions of [MoO₂(CN)₄]^{4−} and salicylaldehyde at pH 7.8–12 are postulated to form [MoO(CN)₃(OC₆H₄CHO)]^{2−},^[14]

[a] School of Chemistry, University of Melbourne, Parkville, Victoria 3010, Australia
Fax: +613-349-5180
E-mail: cgyoung@unimelb.edu.au

[b] Bio21 Molecular Science and Biotechnology Institute, University of Melbourne, Parkville, Victoria 3010, Australia
Fax: +613-349-5180

Supporting information for this article is available on the WWW under <http://dx.doi.org/10.1002/ejic.201000214>.

while the reaction of $(\text{NH}_4)_2[\text{MoS}_4]$ with salicylaldehyde in water is claimed to produce the *cis*-bis(sulfido)- Mo^{VI} complex, $\text{MoS}_2(\text{OC}_6\text{H}_4\text{CHO})_2$.^[15]

cis-Dioxo- Mo^{VI} salicylate and salicylate ester complexes, $\text{MoO}_2(\text{OC}_6\text{H}_4\text{CO}_2\text{H})_2$ and $\text{MoO}_2(\text{OC}_6\text{H}_4\text{CO}_2\text{R})(\text{OR}')$ ($\text{R} = \text{Me}, \text{Et}$), have been known for more than a century,^[16] although no crystal structures for these compounds have been reported. More recently, two *cis*-dioxo- Mo^{VI} complexes containing bidentate salicylate ligands were isolated and structurally characterized by Edwards et al.^[17,18] The first, six-coordinate $(\text{pyH})[\text{MoO}_2(\text{OC}_6\text{H}_4\text{CO}_2)(\text{OC}_6\text{H}_4\text{CO}_2\text{H})]$, contained bidentate mono- and dianionic forms of the ligand and was isolated from the reaction of molybdenic and salicylic acids in aqueous pyridine (py).^[17] The second, $(\text{NMe}_4)_2[\text{MoO}_2(\text{OC}_6\text{H}_4\text{CO}_2)_2] \cdot 2\text{H}_2\text{O}$, containing bidentate dianionic ligands, was prepared by refluxing MoO_3 , salicylic acid and NEt_4OH in water.^[18] Both complexes exhibit the anticipated distorted octahedral structures. Related complexes are formed with, e.g., 2,3-, 2,6- or 3,4-dihydroxybenzoate; six-coordinate, octahedral $(\text{NMe}_4)_2[\text{MoO}_2(2,3\text{-O}_2\text{C}_6\text{H}_3\text{CO}_2\text{H})_2]$ contains bidentate 2,3-dihydroxybenzoate ligands coordinated in a catecholate(2-) fashion, with an uncoordinated carboxylic acid group.^[19]

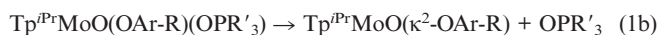
Recently, we reported *cis*-dioxo- Mo^{VI} complexes of hydrotris(3-isopropylpyrazol-1-yl)borate (Tp^{IPr}) bearing phenolate co-ligands containing potential hydrogen-bond donor/acceptor groups ($-\text{OAr-R}$), viz., $\text{Tp}^{\text{IPr}}\text{MoO}_2(\text{OAr-R})$.^[20] We anticipated that these hydrogen-bonding functionalities would stabilize *cis*-oxo(aqua/hydroxo)- Mo^{IV} complexes formed via OAT in the presence of water. Herein, we report that these reactions generally produce *O,O'*-donor, chelate complexes in preference to *cis*-oxo(aqua/hydroxo)- Mo^{IV} species, although the outcomes of specific reactions depend on the nature of the R group. Oxo(phosphoryl)- Mo^{IV} complexes, $\text{Tp}^{\text{IPr}}\text{MoO}(\text{OAr-R})(\text{OPR}'_3)$, are formed when R is

absent or incapable of coordinating to the metal center. However, when R is a potential donor to Mo, oxo- Mo^{IV} chelate complexes, $\text{Tp}^{\text{IPr}}\text{MoO}(\text{OAr-R-}\kappa^2\text{O,O'})$, are produced. Finally, when $\text{R} = \text{CONHPh}$, the resultant chelate complex co-crystallizes with a H-bonded OPR'_3 molecule to yield $\text{Tp}^{\text{IPr}}\text{MoO}(\text{OC}_6\text{H}_4\text{CONHPh-}\kappa^2\text{O,O'}) \cdot \text{OPR}'_3$. Oxo-(phosphoryl)- Mo^{IV} complexes of Tp^{IPr} ^[21–25] and Tp^{IPr} ^[26–28] have been reported but the chelate complexes and phosphane oxide adducts are new classes of Mo complex. Unfortunately, we have been unable to identify or isolate any oxo(aqua/hydroxo)- Mo^{IV} species in this system; thus, it appears that the phosphane oxide or chelate ligands are better *cis*-ligands than water in these oxo- Mo^{IV} complexes. The structures of the phenolate co-ligands included in this study and the numbering scheme for their oxo- Mo^{IV} complexes are given in Scheme 1.

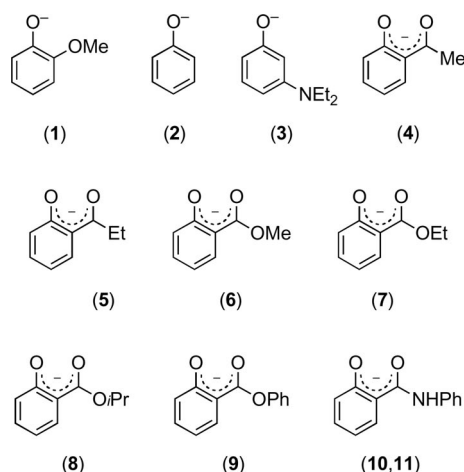
Results and Discussion

Syntheses

The syntheses of the various oxo- Mo^{IV} complexes were based on the reactions shown in Equations (1a) and (1b). The procedures reported in the Exp. Sect. employed dried, deoxygenated solvents in order to optimize the yields and purity. The same compounds are formed in reactions in wet solvents, although a number of by-products, e.g., $[\text{Tp}^{\text{IPr}}\text{MoO}(\mu\text{-O})_2\text{MoO}](\mu\text{-OMe})_2$, are formed under these conditions; these reactions/products will be described in a separate paper.



Incomplete OAT leads to the formation of green, oxo-(phosphoryl)- Mo^{IV} complexes, $\text{Tp}^{\text{IPr}}\text{MoO}(\text{OAr-R})(\text{OPR}'_3)$, according to Equation (1a). Complexes of this type are formed from dioxo- Mo^{VI} complexes bearing unsubstituted and methoxy- or amine-substituted phenolate co-ligands. Complete OAT, leading to green or purple, oxo- Mo^{IV} chelate complexes, $\text{Tp}^{\text{IPr}}\text{MoO}(\text{OAr-R-}\kappa^2\text{O,O'})$ [Equations (1a) and (1b)], was observed for phenolate co-ligands bearing ketone, ester and amido substituents. Certain complexes (**10** and **11**) co-crystallized with the phosphane oxide by-product, as the result of a strong, intermolecular $\text{NH} \cdots \text{OPR}'_3$ hydrogen-bond interaction. All the compounds are soluble in toluene and tetrahydrofuran and sparingly soluble in hexane, acetonitrile and (cold) diethyl ether. They are moderately air-stable in the solid state and can be handled in air for short periods; however, a nitrogen atmosphere is required for storage. In solution, the complexes rapidly decompose when exposed to air. Microanalytical and mass spectrometric data (Supporting Information) were consistent with the formulations given. Selected spectroscopic data are presented in Table 1. Selected bond lengths and angles for all structurally characterized compounds are given in Table 2 (see Exp. Sect. for crystallographic data).



Scheme 1. The phenolate ligands (L) used and the corresponding numbering code for $\text{Tp}^{\text{IPr}}\text{MoO}(\text{OC}_6\text{H}_4\text{OMe-2})(\text{OPEt}_3)$ (**1**), $\text{Tp}^{\text{IPr}}\text{MoOL}(\text{OPEt}_2\text{Ph})$ (**2**, **3**), $\text{Tp}^{\text{IPr}}\text{MoOL}$ (**4–9**), and $\text{Tp}^{\text{IPr}}\text{MoO}(\text{OC}_6\text{H}_4\text{CONHPh}) \cdot \text{OPR}'_3$ ($\text{R}'_3 = \text{Et}_3$ (**10**) and Et_2Ph (**11**)).

Table 1. Selected spectroscopic data.^[a]

R (OPR') ₃	IR Spectrum, $\tilde{\nu}$ [cm ⁻¹]			¹ H NMR spectrum, δ (multiplicity, number of H), solvent: C ₆ D ₆			
	$\nu(\text{CN})$	$\nu(\text{MoO})$	$\nu(\text{CO})$ ^[b]	CH_3 ^[c,d]	$\text{CH}(\text{CH}_3)_2$ ^[c,e]	4/5- CH ^[c,f]	-OAr and OPR' ₃
OMe-2 (OPET ₃) (1)	1508	949	–	0.90, 1.10, 1.18, 1.21, 1.37, 1.56	2.80, 3.65, 4.04	5.74, 5.90, 6.13, 7.24, 7.55, 7.57	0.86 (dt, 9 H), 1.1–1.2 (m, 6 H), 3.69 (s, 3 H), 6.59 (t, 1 H), 6.65 (d, 1 H), 7.02 (t, 1 H), 7.26 (dd, 1 H)
None (OPET ₂ Ph) (2)	1507	952	–	0.63, 0.85, 1.03, 1.10, 1.22, 1.64	2.74, 4.18, 4.34	5.87, 5.98, 6.03, 7.37, 7.46, 7.74	0.91 (m, 3 H), 1.12 (m, 3 H), 2.07 & 2.27 (m, 2 H), 2.27 & 2.51 (m, 2 H), 6.42 (d, 2 H), 6.73 (t, 1 H), 7.08 (m), 7.12 (t), 7.70 (m, 2 H)
NEt ₂ -3 (OPET ₂ Ph) (3)	1508	950	–	0.77, 0.8–1.1 (9 H), 1.25, 1.63	2.79, 4.25, 4.36	5.71, 5.89, 6.02, 7.37, 7.48, 7.73	0.8–1.1 (m, 12 H), 2.08 & 2.35 (m, 2 H), 2.68 & 2.35 (m, 2 H), 2.91 (m, 4 H), 6.02 (m, 1 H), 6.2 (m, 2 H), 7.09 (s, 3 H), 7.62 (t, 1 H), 7.60 (m, 1 H), 7.73 (m, 1 H)
COMe-2 (4)	1508	948	1607 (1663)	0.88, 0.93, 1.25, 1.32, 1.34, 1.45	3.05, 3.72, 3.97	5.65, 5.99, 6.01, 7.19, 7.50, 7.58	2.43 (s, 3 H), 6.54 (t, 1 H), 7.04 (d, 1 H), 7.18 (m, 1 H), 7.26 (dd, 1 H)
COEt-2 (5)	1509	956	1603 (1668)	0.90, 0.92, 1.26, 1.34, 1.35, 1.53	3.04, 3.70, 3.97	5.66, 6.01, 6.02, 7.20, 7.51, 7.59	1.09 (t, 3 H), 2.66 & 2.95 (m, 2 H), 6.53 (t, 1 H), 7.07 (d, 1 H), 7.17 (m, 1 H), 7.34 (d, 1 H)
CO ₂ Me-2 (6)	1509	951	1609 (1701)	0.92, 0.98, 1.18, 1.25, 1.34, 1.58	3.35, 3.64, 3.98	5.68, 6.01, 6.08, 7.20, 7.57, 7.64	3.44 (s, 3 H), 6.54 (m, 1 H), 7.19 (m, 1 H), 7.28 (m, 1 H), 7.93 (dd, 1 H)
CO ₂ Et-2 (7)	1508	954	1611 (1697)	0.94, 1.00, 1.20, 1.25, 1.35, 1.60	3.36, 3.64, 4.00	5.69, 6.01, 6.09, 7.21, 7.57, 7.65	0.92 (t, 3 H), 4.18 & 4.01 (m, 2 H), 6.55 (t, 1 H), 7.20 (m, 1 H), 7.29 (m, 1 H), 7.99 (dd, 1 H)
CO ₂ iPr-2 (8)	1508	960	1610 (1694)	0.96, 1.02, 1.23, 1.24, 1.36, 1.63	3.33, 3.63, 4.00	5.69, 6.01, 6.10, 7.21, 7.58, 7.64	1.01 (d, 3 H), 1.03 (d, 3 H), 5.31 (sept, 1 H), 6.54 (m, 1 H), 7.20 (m, 1 H), 7.29 (m, 1 H), 8.01 (dd, 1 H)
CO ₂ Ph-2 (9)	1508	956	1616 (1774)	0.65, 1.07, 1.08, 1.22, 1.36, 1.56	3.32, 3.44, 3.54	5.71, 5.95, 6.00, 7.19, 7.46, 7.62	6.54 (t, 1 H), 6.80 (m, 5 H), 7.20 (m, 1 H), 7.30 (m, 1 H), 8.13 (dd, 1 H)
CONHPh (OPET ₃) (10)	1505	952	1608 (1659)	1.07, 1.19, 1.26, 1.34, 1.46 (6 H)	3.69, 3.94, 3.94	5.79, 6.02, 6.15, 7.24, 7.62, 7.67	0.7 (dt, 9 H), 1.02 (dq, 6 H), 6.53 (t, 1 H), 6.8–6.9 (m, 3 H), 7.2–7.4 (m, 2 H), 7.91 (m, 3 H), 11.28 (br. s, 1 H)
CONHPh (OPET ₂ Ph) (11)	1507	949	1608 (1659)	1.08, 1.14, 1.22, 1.33, 1.46 (6 H)	3.71, 3.92, 3.94	5.77, 6.02, 6.15, 7.23, 7.61, 7.67	0.77 (dt, 6 H), 1.2–1.3 (m, 4 H), 6.45 (m, 1 H), 6.8–6.9 (m, 3 H), 7.0–7.1 (m, 3 H), 7.2–7.4 (m, 2 H), 7.3–7.4 (m, 2 H), 7.79 (dd, 1 H), 7.85 (d, 2 H), 10.76 (br. s, 1 H)

[a] Complete data and assignments are included as Supporting Information. [b] Values in parentheses are for the corresponding dioxo-Mo^{VI} complexes (containing uncoordinated carbonyl groups). [c] Specified protons of the Tp^{iPr} ligand. [d] Each resonance is a doublet ($J = 6.8$ Hz) integrating for 3 protons. [e] Each resonance is a septet ($J = 6.8$ Hz) integrating for 1 proton. [f] Each resonance is a doublet ($J = 2.4$ Hz) integrating for 1 proton.

Characterization of Oxo(phosphoryl) Complexes

The oxo(phosphoryl) complexes **1–3** exhibited IR absorptions or fingerprint patterns indicative of the presence of oxo [$\nu(\text{Mo}=\text{O})$ ca. 950 cm⁻¹], phosphoryl [$\nu(\text{P}=\text{O})$ ca. 1080 cm⁻¹], Tp^{iPr} [$\nu(\text{BH})$ 2480–2440 cm⁻¹, $\nu(\text{CN})$ ca. 1508 cm⁻¹] and phenolate ligands. The $\nu(\text{Mo}=\text{O})$ bands are around the middle of the region established for complexes of this type.^[26–28] Definitive assignment of the $\nu(\text{P}=\text{O})$ band was prevented by overlapping ligand bands in the 1100 cm⁻¹ region.

NMR spectra were consistent with molecular C₁ symmetry, all protonic groups in the molecules being inequivalent. Thus, the Tp^{iPr} ligand was characterized by six doublet isopropyl methyl resonances, three septet isopropyl methine resonances and six doublet 4-/5-CH ring proton resonances. As observed for related complexes, the septet isopropyl methine resonances have quite different chemical shifts ($\Delta\delta > 1.2$ ppm). For **1**, the diastereotopic methylene protons of the OPET₃ group were observed as overlapping multiplets

obscured by the isopropyl methyl resonances. Complete assignment of the spectrum of **2** was assisted by 2D NMR experiments (see Supporting Information). The ³¹P resonances of the OPET₂Ph complexes lie in the range 67–69 ppm, considerably deshielded relative to the free ligand ($\delta = 44.2$ ppm).^[29]

Six-coordinate **1** (Figure 1) exhibits a distorted octahedral geometry, the molybdenum centre being coordinated by a tridentate *fac*-Tp^{iPr} ligand and mutually *cis* terminal oxo, phenolate and triethylphosphane oxide ligands. The bond lengths and angles involving the molybdenum center (see Table 2) closely approximate those reported for related complexes, e.g., Tp^{iPr}MoO(OPh)(OPET₃),^[26] Tp^{iPr}MoO(OC₆H₄sBu-2)(OPET₃)^[27] and Tp^{iPr}MoO(SnBu)(OPET₃),^[27] the Mo=O and Mo–O distances being typical of oxo-Mo^{IV} complexes [Mo=O 1.674(2) Å, Mo–O_{phenoxo} 2.026(2) Å and Mo–O_{OPET₃} 2.146(2) Å].^[30] The Mo–N distances range from 2.155(3) to 2.426(3) Å and reflect the *trans* influence of the various O-donor ligands, viz., oxo > phenoxo > OPET₃. Apart from the angles subtended by the N-donors

Table 2. Selected bond lengths [Å] and angles [°].

Parameter	1	5	7 (1) ^[a]	7 (2) ^[a]	9	11 (1) ^[a]	11 (2) ^[a]
Mo(1)–O(1)	1.674(2)	1.671(6)	1.679(4)	1.679(4)	1.672(3)	1.672(4)	1.686(5)
Mo(1)–O(2)	2.146(2)	2.044(4)	2.047(4)	2.064(4)	2.044(2)	2.050(5)	2.043(5)
Mo(1)–O(3)	2.026(2)	2.131(4)	2.142(4)	2.148(4)	2.174(2)	2.102(4)	2.131(5)
Mo(1)–N(11)	2.426(3)	2.417(7)	2.435(4)	2.412(4)	2.413(3)	2.428(6)	2.403(6)
Mo(1)–N(21)	2.156(3)	2.186(5)	2.174(4)	2.184(5)	2.189(3)	2.151(6)	2.197(6)
Mo(1)–N(31)	2.199(3)	2.155(5)	2.138(5)	2.131(4)	2.139(3)	2.150(5)	2.113(7)
O(2)–C/P(1)	1.526(2)	1.317(7)	1.330(6)	1.328(7)	1.325(4)	1.317(8)	1.328(9)
O(3)–C(7/41)	1.333(4)	1.263(8)	1.256(6)	1.307(6)	1.236(4)	1.260(8)	1.267(8)
Mo(1)–O(2)–C/P(1)	130.78(13)	128.2(4)	127.1(3)	129.2(4)	127.9(2)	123.3(4)	122.1(5)
Mo(1)–O(3)–C(7/41)	137.2(2)	127.9(4)	126.6(4)	127.1(4)	127.0(2)	129.6(5)	126.5(5)
O(1)–Mo(1)–O(2)	98.09(9)	107.4(2)	106.97(17)	107.28(17)	106.69(11)	105.1(2)	106.2(2)
O(1)–Mo(1)–O(3)	107.52(10)	98.0(2)	100.50(16)	98.75(17)	99.27(11)	103.9(2)	102.1(2)
O(1)–Mo(1)–N(11)	163.81(10)	168.4(2)	169.02(17)	168.84(17)	168.80(11)	167.7(2)	168.8(2)
O(1)–Mo(1)–N(21)	91.80(10)	92.9(2)	92.27(17)	92.59(18)	91.09(12)	93.1(2)	91.7(2)
O(1)–Mo(1)–N(31)	90.12(10)	93.3(2)	94.83(17)	94.58(17)	94.07(12)	93.1(2)	94.2(2)
O(2)–Mo(1)–O(3)	79.59(8)	83.48(17)	84.22(14)	83.20(16)	83.83(9)	84.5(2)	83.80(19)
O(2)–Mo(1)–N(11)	90.04(8)	82.49(19)	83.12(15)	82.69(15)	83.31(10)	83.3(2)	82.9(2)
O(2)–Mo(1)–N(21)	169.99(9)	159.7(2)	160.76(15)	160.10(17)	162.20(11)	161.8(2)	162.0(2)
O(2)–Mo(1)–N(31)	92.97(9)	90.51(19)	89.22(16)	88.58(16)	90.01(10)	89.3(2)	88.7(2)
O(3)–Mo(1)–N(11)	87.65(9)	89.06(19)	84.69(13)	87.23(15)	86.61(9)	85.65(19)	85.19(19)
O(3)–Mo(1)–N(21)	96.00(9)	93.36(18)	92.37(15)	95.05(17)	94.23(10)	90.7(2)	94.3(2)
O(3)–Mo(1)–N(31)	161.57(9)	168.4(2)	164.54(15)	165.93(15)	166.44(10)	162.9(2)	163.4(2)
N(11)–Mo(1)–N(21)	80.75(9)	77.4(2)	77.71(15)	77.43(16)	78.91(11)	78.8(2)	79.1(2)
N(11)–Mo(1)–N(31)	75.43(9)	80.3(2)	80.63(15)	80.39(15)	80.67(10)	77.7(2)	79.2(2)
N(21)–Mo(1)–N(31)	88.54(10)	88.85(19)	89.22(17)	88.80(17)	87.94(11)	90.2(2)	88.3(2)
Mo–O ₃ ^[b]	0.9691(13)	0.9515(32)	0.9375(22)	0.9558(23)	0.9515(16)	0.9204(30)	0.9351(30)
Mo–N ₃ ^[c]	1.0621(13)	1.4462(31)	1.4338(26)	1.4383(27)	1.4396(18)	1.4315(37)	1.4374(37)
Mo–equatorial ^[d]	0.2493(12)	0.2867(30)	0.3155(20)	0.3016(21)	0.2847(16)	0.3196(27)	0.3111(28)

[a] Parameters for crystallographically unique molecules 1 and 2. [b] The distance of the Mo atom from the plane defined by O(1)–O(3). [c] The distance of the Mo atom from the plane defined by N(11), N(21) and N(31). [d] The displacement of the Mo atom from the equatorial plane defined by N(21), N(31), O(2) and O(3).

at Mo [75.44(9)–88.55(10)°], the greatest angular deviations from an ideal octahedral geometry are observed for O(1)–Mo–O(3) and O(3)–Mo–N(31) [107.5(1)° and 169.99(9)°, respectively].

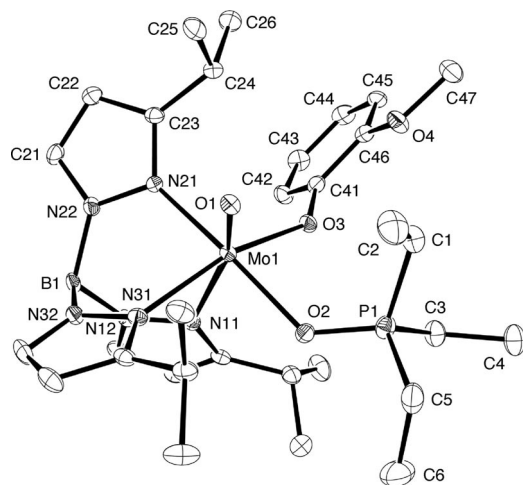


Figure 1. ORTEP projection of **1**. The labeling of the pyrazole groups containing N(11) and N(31) follow that shown for the group containing N(21).

Characterization of κ^2 -*O,O'* Chelate Complexes

The infrared spectra of complexes **4–9** (Table 1) exhibited a band at ca. 950 cm^{−1}, which was assigned to the $\nu(\text{Mo}=\text{O})$

mode of the oxo-Mo^{IV} moiety; the position and intensity of the band was consistent with literature values for related complexes. Bands characteristic of the Tp^{iPr} [$\nu(\text{BH})$ 2440–2480 cm^{−1}, $\nu(\text{CN})$ ca. 1509 cm^{−1}] and phenolate ligands were also present.^[31] Coordination of the carbonyl groups was indicated by a shift of the $\nu(\text{C}=\text{O})$ band to lower energy ($\Delta\nu$ 50–160 cm^{−1}), compared to the free ligand or its dioxo-Mo^{VI} complex.^[20]

The ¹H NMR spectra of the complexes (Table 1) were indicative of molecular C₁ symmetry. This is most clearly evident in the Tp^{iPr} ligand resonances, comprised of six doublet resonances from the isopropyl methyl groups, three septet resonances from the isopropyl methine protons and two sets of three doublet resonances assignable to the 4- and 5-CH (ring) protons, i.e., all protonic groups are inequivalent as expected for C₁ symmetric molecules. Full assignments of the NMR spectra are given in the Supporting Information.

X-ray Crystallography

The *O,O'*-chelate complexes, **5**, **7** and **9** (see Figure 2, Figure 3, and Figure 4, respectively), crystallize in non-chiral space groups with both enantiomers present in the crystal lattice. There are two independent molecules in the asymmetric unit of **7** (average parameters or those of molecules 1 and 2, respectively, are quoted below). The complexes themselves display distorted octahedral geometries

defined by tridentate *fac*-Tp^{iPr} and mutually *cis* oxo and bidentate *O,O'*-donor ligands. The most significant distortions from octahedral geometries involve the displacement of the Mo atom from the equatorial plane defined by N(21), N(31), O(2) and O(3) and O(2)–Mo–N(21) angles that deviate from 180°. For all three complexes, the Mo atoms lie an av. of 0.30 Å out of the equatorial plane, toward the terminal oxo ligand, and the O(2)–Mo–N(21) angles average 161°. The Mo atoms are ca. 0.95 and 1.44 Å from the O₃- and the N₃-donor faces of the complexes, respectively.

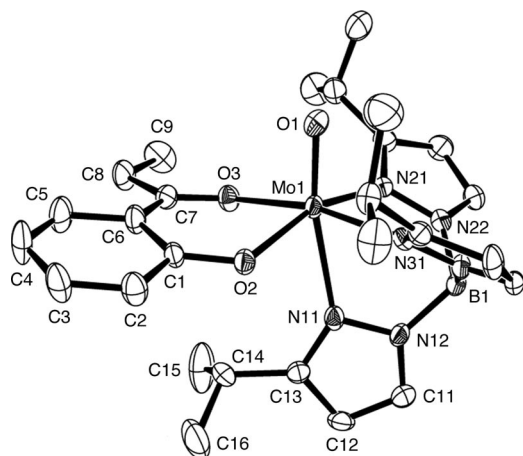


Figure 2. ORTEP projection of **5**. The labeling of the pyrazole groups containing N(21) and N(31) follow that shown for the group containing N(11).

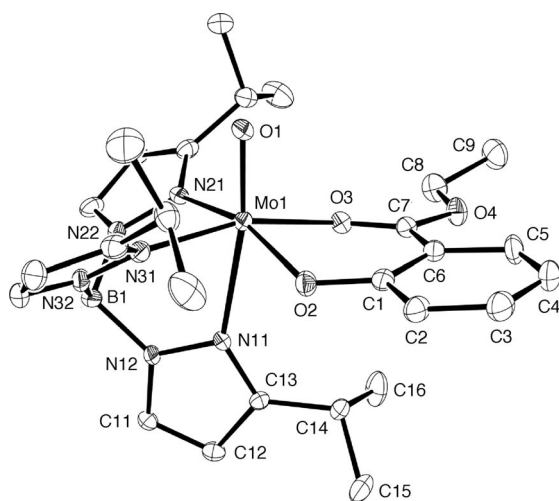


Figure 3. ORTEP projection of molecule 1 of **7**. The labeling of the pyrazole groups containing N(21) and N(31) follow that shown for the group containing N(11).

The Mo=O distances range from 1.671(6) to 1.680(4) Å, the short distances being typical of oxo-Mo^{IV} complexes in general and oxo-Mo^{IV} scorpionate complexes in particular.^[10] The Mo–O(2) distances range from 2.044(4)–2.064(4) Å, with an average of 2.05 Å, a little longer than corresponding distances for the monodentate phenolates in dioxo-Mo^{VI} precursors.^[20] The C(1)–O(2) (phenolate) distances of ca. 1.32 Å are typical of those observed in similar

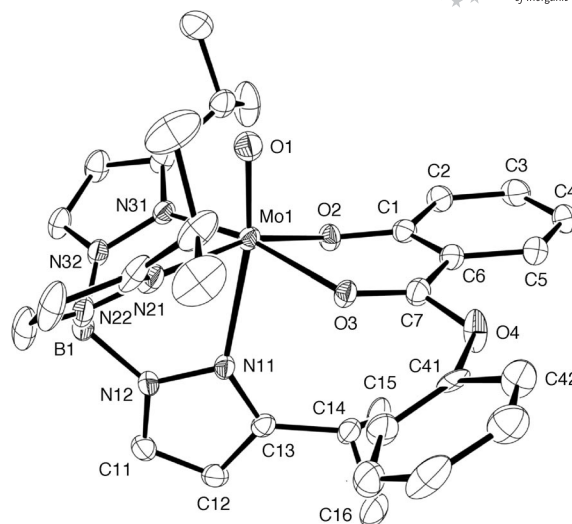


Figure 4. ORTEP projection of conformer 1 (48%) of **9**. The labeling of the pyrazole groups containing N(21) and N(31) follow that shown for the group containing N(11).

complexes. Coordination of the carbonyl oxygen results in a lengthening of the C=O bond compared to that found in analogous dioxo-Mo^{VI} complexes, e.g., the C=O distances in **5** and its dioxo-Mo^{VI} analogue are 1.263(8) Å and 1.184 Å, respectively. The C=O distance of the carbonyl group is shorter than that of the C–O (phenolate) bond [1.317(7) Å for **5**] consistent with partial double bond character in the coordinated C=O moiety. The carbonyl Mo–O(3) bonds are also longer than the phenolate Mo–O(2) bonds, suggesting that the former are weaker than the latter.

The phenolate moieties are planar, with mean atom displacements for the OC₆ planes of 0.0240, 0.017 (av.) and 0.021 Å for **5**, **7** and **9**, respectively. There is a slight twisting of the 4-atom OC_{ipso}CC_R plane relative to the phenolate arene plane in all complexes; these twists are defined by dihedral angles of 5.5(3), 2.3 (av.) and 4.9(2)° for **5**, **7** and **9**, respectively. The chelating moieties are nearly planar, with mean atom displacements of 0.026 Å, 0.015/0.025 and 0.048 Å for the C₃O₂ chelate rings of **5**, **7** and **9**, respectively. The fold angles of the six-membered chelate rings, viz., the dihedral angles between the C₃O₂ and MoO₂ planes, are 23.9(3)°, 23.7(2)/22.9(2)° and 19.9(1)°, respectively. The chelate ligand is folded toward the terminal oxo ligand and away from the proximal isopropyl group of the Tp^{iPr} ligand. The phenolate moiety is also tilted with respect to the plane containing O(1), Mo(1) and B(1), both the C₃O₂ and OC_{6(arene)} planes making dihedral angles of ca. 83° and 85° with this plane. In all compounds, the *trans* influence of the terminal oxo ligand is manifest by a significant lengthening of the Mo–N(11) bonds compared to the other Mo–N bonds (>0.22 Å). The phenyl group in **9** adopts two conformations with roughly equal populations (48 and 52%).

Finally, a number of other complexes, including **4**, **6** and **8**, were examined by X-ray diffraction. All complexes displayed the same general structure described above for complexes **5**, **7** and **9**, viz., they were monomeric, distorted octa-

hedral species with the same ligand types and connectivities. However, serious unresolved disorder in the chelate ligand or poor crystal quality prevented publishable structures from being obtained.

Characterization of OPR'₃ Adducts

The complex $\text{Tp}^{\text{iPr}}\text{MoO}(\text{OC}_6\text{H}_4\text{CONHPh-2})$ co-crystallized with a molecule of by-product OPR'₃. This was revealed by elemental analysis, mass spectrometry, IR and NMR spectroscopy (Table 1), and X-ray crystallography (vide infra). IR spectra showed bands typical of the ligands present, as well as a broadening of the amido NH group [$\nu(\text{N-H}) \approx 3183 \text{ cm}^{-1}$]; the latter is indicative of the presence of H-bonding. NMR spectra showed resonances assignable to the complex and free OPR'₃, the integration indicating a 1:1 ratio of complex:phosphane oxide.

The crystal structure of **11** was determined by X-ray crystallography, two independent molecules (H-bonded units) being observed (mean parameters are cited below). The Mo complex (see Figure 5) displays a distorted octahedral geometry defined by tridentate *fac*- Tp^{iPr} and mutually *cis* oxo and bidentate *O,O'*-donor ligands. As observed for the bidentate complexes discussed above, the Mo atom lies 0.315 Å out of the equatorial plane, toward the apical oxo ligand, and the O(1)–Mo–N(11) angle is less than 180° (av. 168°). The Mo=O distance of 1.68 Å is within the range observed for oxo-Mo^{IV} scorpionate complexes, while the Mo–O(2) distance of 2.05 Å, is close to values reported for Mo phenolate complexes.^[10] The phenolate ring is planar, with mean and maximum atom displacements for the OC₆ planes of 0.028 and 0.043 Å (for C4 and C4'), respectively. There is a slight twisting of the 4-atom C(6),C(7),O(3),N(1) plane relative to the phenolate OC₆ unit in both molecules, as defined by the dihedral angles of 24.7(4)° and 30.2(3)°, respectively. The atoms of the O₂C₃ chelate rings are nearly coplanar, with mean atom displacements of 0.144(5) (C7) and 0.164(5) (C7') Å for molecules 1 and 2, respectively. The fold angles of the six-membered chelate rings, viz., the dihedral angles between the C₃O₂ and MoO₂ planes, are 26.6(3)° and 32.9(3)° for molecules 1 and 2, respectively. Again, the chelate ligand is folded toward the terminal oxo ligand and away from the proximal isopropyl group of the Tp^{iPr} ligand. The *trans* influence of the terminal oxo ligand is manifest by a significant lengthening of the Mo–N(11) bonds, compared to the other Mo–N bonds. The isopropyl substituents of the Tp^{iPr} ligand adopt the same conformation as in the other structures.

The lattice OPEt₂Ph molecule is hydrogen bonded to the NH groups of the amido group in **11** (see Figure 5). The N(1)···O(4) distances average 2.81 Å while their H···O distances average 1.85 Å; these interactions are considered to be rather strong since the N(1)···O(4) distances fall just outside the criterion suggested for very strong N···O hydrogen bonds (ca. 2.75 Å).^[32] The N(1)–H···O(4) angles for these complexes are ca. 168°, a slight deviation from the ideal angle of 180°. These bond lengths and angles are comparable to those found in simple organic amide–phosphane ox-

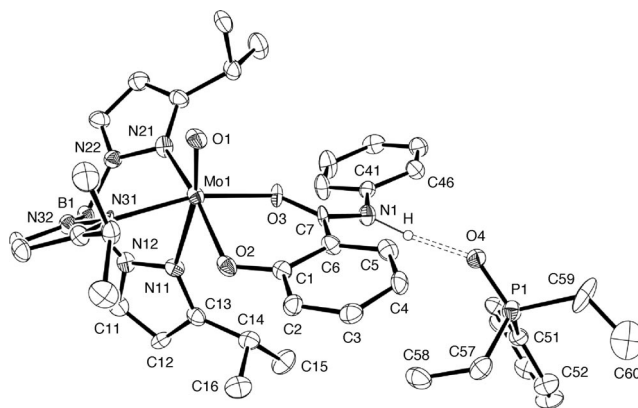


Figure 5. ORTEP projection of molecule 1 of **11**. The labeling of the pyrazole groups containing N(21) and N(31) follow that shown for the group containing N(11). The N(1)–H···O(4) H-bond is shown as dashed lines.

ide adducts, e.g., 2-aminobenzothiazole–HMPA (HMPA = hexamethylphosphoramide) [$\text{N} \cdots \text{O} = 2.783(5) \text{ Å}$, $\text{H} \cdots \text{O} = 1.94(4) \text{ Å}$, $\text{N-H} \cdots \text{O} = 169.9(11)^\circ$]^[33] and PSA–HMPA (PSA = phenylsulfonylacetamide) ($\text{N} \cdots \text{O} = 2.823 \text{ Å}$, $\text{H} \cdots \text{O} = 2.182 \text{ Å}$).^[34] More recently, Burke and co-workers^[35] have employed such interaction in their crystal engineering investigations of phosphane oxides and guanidinium sulfonates.

A similar structure was established for $\text{Tp}^{\text{iPr}}\text{MoO}(\text{OC}_6\text{H}_4\text{CONHPh-2})\cdot\text{OPEt}_3$ (**10**) but poor crystal quality prevented a publishable structure from being determined. However, the connectivity around the Mo^{IV} center and the presence of a lattice OPEt₃ molecule hydrogen-bonded to the amido moiety was clearly revealed.

Cyclic Voltammetry

The electrochemical properties of selected Mo^{IV} complexes in acetonitrile were investigated by cyclic voltammetry and the results are summarized in Table 3. Most complexes exhibited a single, reversible, one-electron oxidation in the potential range +0.045 to +0.117 V vs. SCE [Equation (2)].

Table 3. Electrochemical data for $\text{Tp}^{\text{iPr}}\text{MoO}(\text{OAr-R-2})$ vs. SCE.

R	$E_{1/2}$ [V]	ΔE_{pp} [mV]	$I_{\text{pc}}/I_{\text{pa}}$
COMe (4)	+0.045	76	1.05
COEt (5) ^[a]	+0.046	67	1.40
CO ₂ iPr (8)	+0.060	79	1.05
CONHPh (10/11) ^[b]	+0.072	74	0.83
CO ₂ Me (6)	+0.074	85	1.11
CO ₂ Et (7)	+0.074	74	1.03
CO ₂ Ph (9) ^[a]	+0.117	89	1.62

[a] Quasi-reversible. [b] A second irreversible oxidation occurs at +0.245 V affecting accuracy of the $I_{\text{pc}}/I_{\text{pa}}$ value.



The oxidation potentials span a narrow range of ca. 72 mV, reflecting their insensitivity to the substituent on the phenolate co-ligand. The ligand field splitting of the d-or-

bital manifold is dominated by the strong field oxo ligand, with the Mo-based d_{z^2} , d_{xz} and d_{yz} orbitals strongly destabilized by the σ - and π -antibonding interactions. The $d_{x^2-y^2}$ orbital is destabilized by σ -antibonding interactions with the equatorial donor ligands, while the d_{xy} orbital, oriented orthogonal to the Mo=O bond, lies lowest in energy and is non-bonding in character. Dramatic changes in the reduction potentials of related oxo-Mo^V Tp* complexes result from changes in orbital energies induced by the nature of the co-ligand, e.g., in donor atom, denticity, chelate ring size, and the identity and position of substituents.^[36–41] However, this co-ligand effect is quite marginal across the series of Tp^{Pr}Mo^{IV}O(OAr-R-2) complexes reported here.

The cyclic voltammograms of **10** and **11** are identical, indicating that their reduction potentials are independent of the loosely bound phosphane oxide; an additional oxidation peak was observed for both these complexes at +0.245 V, which is likely to be due to oxidation of the amido ligand.

An interesting feature was observed for the oxidation of the 2-methoxy derivative **1**; the number of oxidized species in solution is dependent on the scan rate of the cyclic voltammetric study. With scan rates slower than 50 mV s^{−1}, only one oxidation process was observed, while at higher scan rates two oxidations were evident. A series of simulated voltammograms were produced, based on a proposed square scheme electrochemical mechanism, and these were found to closely match the experimental observations (see Supporting Information).^[42] A similar observation was reported by Sengar and co-workers for the oxidation of Tp*MoO(SPh)(OPMe₃).^[24] although the two peaks were not found to be affected by scan-rate.

Conclusions

Reactions of *cis*-dioxo-Mo^{VI} complexes containing phenolate co-ligands possessing potential H-bond acceptor or donor substituents (R) with tertiary phosphanes produce oxo-Mo^{IV} species. Three types of complex, viz., oxo(phosphoryl), *O,O'*-chelate, and H-bonded phosphane oxide adducts, are observed to form depending on the R group involved. Oxo(phosphoryl) complexes are formed when the R group is unable to coordinate in a bidentate fashion, while *O,O'*-chelate complexes are formed when the R group contains a coordinating carbonyl group. Chelate complexes containing amido functions co-crystallize with the by-product phosphane oxide due to the formation of strong NH \cdots OPR'₃ H-bonds. The stability of the chelate complexes has to date thwarted attempts to stabilize (through H-bonding) and isolate *cis*-oxo(aqua)-Mo^{IV} species that model reduced molybdoenzyme states.

Experimental Section

Materials and Methods: All reactions were performed under an atmosphere of dinitrogen using dried, deoxygenated solvents but work-ups were performed in air. Samples of Tp^{Pr}MoO₂(OAr-R)

were prepared as described previously.^[20] Other chemicals were obtained from Aldrich Chemical Co. and used without further purification.

Infrared spectra were recorded on a Bio-Rad FTS 165 FTIR spectrophotometer as pressed KBr disks. Electrospray ionization mass spectrometric (ESI-MS) experiments were carried out in positive-ion mode using a Micromass Quattro II mass spectrometer using samples dissolved in MeCN. NMR spectra were recorded at room temperature on Varian Unity-Plus 400 MHz or Inova 500 MHz spectrometers. Spectra were referenced to residual solvent peaks (for C₆D₆, $\delta_H = 7.16$, $\delta_C = 128.39$). ³¹P NMR spectra were referenced to external D₃PO₄ (85% v/v solution in D₂O) at $\delta_P = 0.00$. Cyclic voltammograms were recorded using a 2 mm glassy carbon working electrode, platinum counter electrode and a freshly prepared double-jacketed Ag/AgNO₃ reference electrode (10 mm AgNO₃ in MeCN with 0.1 M *n*Bu₄PF₆ and clean silver wire), connected to an Autolab Potentiostat operated by the General Purpose Electrochemical System software (version 4.9). Samples were prepared as 1–2 mM solutions in MeCN with 0.1 M *n*Bu₄PF₆ as supporting electrolyte and scan rates over the range 20–400 mV s^{−1}. Potentials were referenced against the ferrocene couple, Fc⁺/Fc, and are reported relative to SCE. The Fc⁺/Fc couple was set to the reported value of +0.400 V vs. SCE for acetonitrile/0.1 M *n*(*n*Bu)₄PF₆ solutions.^[43] Microanalyses were performed by Atlantic Micro-lab Inc., Norcross, Georgia, U.S.A.

As mentioned previously, spectroscopic data are summarized in Table 1 while full characterization data are included as Supporting Information.

Syntheses and Characterization Data

Tp^{Pr}MoO(OC₆H₄OMe-2)(OPEt₃) (1**):** A suspension of Tp^{Pr}MoO₂(OC₆H₄OMe-2) (1 g, 1.69 mmol) in acetonitrile (15 mL) was treated with PET₃ (270 μ L, 1.85 mmol) whereupon the solution turned deep green. The solution was stirred at room temperature for 17 h. The solvent was removed to leave a deep green residue that was triturated with hexane (5 mL) to yield crystals of the product. The compound was collected by filtration, washed with 3–5 mL of hexane and dried under vacuum. The complex was recrystallized from tetrahydrofuran/hexane; yield 0.97 g (81%).

Diethylphenylphosphane Oxide Complexes: Diethylphenylphosphane (130 μ L, 0.75 mmol) was added to a stirred solution of Tp^{Pr}MoO₂(OAr-R) (0.5 mmol) in toluene (10 mL). After stirring at room temperature for 48 h, the solvent volume was reduced to ca. 3 mL and hexane (6–8 mL) was added. Precipitation of the product was induced by storage in a freezer or enrichment of the solvent in hexane. The green powders were collected by filtration and washed with a minimum volume of hexane (ca. 2–3 mL) and dried under high vacuum; yields ca. 60%.

Chelate Tp^{Pr}MoO(OAr-R- κ^2) Complexes: The following general procedure was adopted for all the Tp^{Pr}MoO(OAr-R) complexes. A suspension of Tp^{Pr}MoO₂(OAr-R) (1 g, \approx 1.6 mmol) in acetonitrile (15 mL) was treated with excess tertiary phosphane (PET₃ or PET₂Ph) (1.1 molar equivalents) whereupon the solution turned deep green or purple. After approximately one hour, the yellow solid dissolved to give a clear green or purple solution. The solution was stirred at room temperature for 4 h (**6–8**), 5 h (**9**) or 17 h (**4** and **5**). The solvent was removed to leave a deep green or purple residue. Following trituration with hexane (5 mL) a solid precipitated which was collected by filtration, washed with 3–5 mL of hexane and dried under vacuum. The complexes were recrystallized from tetrahydrofuran/hexane or hot acetonitrile; yields for **4**: 0.86 g (90%), **5**: 0.90 g (93%), **6**: 0.88 g (90%), **7**: 0.88 g (90%), **8**: 0.39 g (40%), **9**: 0.34 g (35%).

Table 4. Crystallographic data.

Parameter	1	5	7	9	11·1/2OEt₂
Formula	C ₃₁ H ₅₀ BMoN ₆ O ₄ P	C ₂₇ H ₃₇ BMoN ₆ O ₃	C ₅₄ H ₇₃ B ₂ Mo ₂ N ₁₂ O ₈	C ₆₂ H ₄₇ B ₂ Mo ₂ N ₁₂ O ₈	C ₈₆ H ₁₁₆ B ₂ Mo ₂ N ₁₄ O ₉ P ₂
Fw	708.49	600.38	616.38	1328.83	1765.37
Crystal system	monoclinic	monoclinic	orthorhombic	triclinic	triclinic
Space group	<i>P</i> 2 ₁ / <i>c</i>	<i>P</i> 2 ₁ / <i>n</i>	<i>Pbca</i>	<i>P</i> $\bar{1}$	<i>P</i> $\bar{1}$
<i>a</i> /Å	10.6156(11)	9.3292(15)	18.1075(18)	8.9817(7)	10.5180(5)
<i>b</i> /Å	17.4143(18)	17.037(3)	18.1158(18)	9.9661(8)	20.4198(13)
<i>c</i> /Å	19.2539(19)	18.655(4)	35.678(4)	18.3129(15)	21.7129(14)
<i>a</i> /deg	90	90	90	94.590(2)	97.384(5)
<i>β</i> /deg	100.169(2)	104.434(3)	90	92.5370(10)	92.184(4)
<i>γ</i> /deg	90	90	90	102.9130(10)	101.969(4)
<i>V</i> /Å ³	3503.4(7)	2871.5(9)	11703(2)	1589.4(2)	4514.1(5)
<i>Z</i>	4	4	8	1	2
<i>T</i> /K	130(2)	293(2)	130(2)	130(2)	130(2)
<i>ρ</i> /g cm ^{−3}	1.343	1.389	1.399	1.388	1.299
<i>μ</i> /cm ^{−1}	4.63	4.95	4.90	4.57	3.102
Data	21919	35724	34527	8384	15970
Unique data	8189	4687	13324	5532	6247
<i>R</i> ₁ [<i>I</i> > 2σ(<i>I</i>)] ^[a]	0.0498	0.0614	0.0746	0.0471	0.0585
<i>wR</i> ₂ (<i>F</i> ² , all data) ^[b]	0.0775	0.1602	0.1597	0.1119	0.1043
GOF	0.849	0.996	1.052	1.035	0.828

[a] $R_1 = \sum ||F_o| - |F_c|| / \sum |F_o|$. [b] $wR_2 = \{[\sum w(F_o^2 - F_c^2)^2 / \sum w(F_o^2)^2]\}^{1/2}$.

Tp^{Pr}MoO(OC₆H₄CONHPh-κ²)-OPR'₃ Compounds: The procedure employed for chelate complexes **4–9** (vide supra) was adopted for complexes **10** [reaction time 4 h, yield 0.96 g (82%)] and **11** [reaction time 6 h, yield 1.00 g (80%)].

X-ray Crystallography

Crystals of **1** were grown by a slow diffusion of hexane into a THF solution of the complex while crystals of **9** and **11** were grown by slow diffusion of hexane into toluene solutions of the complexes. Crystals of **5** and **7** were grown by slowly cooling concentrated THF and acetonitrile solutions of the complexes, respectively, to −30 °C.

Crystal data are summarized in Table 4. X-ray diffraction data were collected on a Bruker CCD area detector at 130 K (except for **5** at 293 K) using Mo-*K*_α radiation (0.71073 Å) for complexes **1**, **5**, **7** and **9** and an Oxford XCalibur diffractometer at 130 K using Cu-*K*_α radiation (1.54184 Å) for complex **11**. Cell parameters for complexes **1**, **5**, **7** and **9** were acquired by the SMART software package and data reduction was performed using SAINT;^[44] the cell parameters and data reduction for complex **11** was performed on the CrysAlis software. Structures were solved by direct methods (SHELXS-97^[45]) and refined using full-matrix least-squares on *F*² (SHELXL-97^[46]). Molecular diagrams were generated using ORTEP-3^[47] and the Mercury^[48,49] software from CCDC. All non-hydrogen atoms were included in difference maps and anisotropic parameters were employed. Hydrogen atoms were included in calculated positions. All ORTEP projections were drawn at the 30% probability level.

CCDC-744598 (for **1**) through -744602 (for **11·1/2OEt₂**) (in numerical order) contain the supplementary crystallographic data for this paper. These data can be obtained free of charge from The Cambridge Crystallographic Data Centre via www.ccdc.cam.ac.uk/data_request/cif.

Supporting Information (see also the footnote on the first page of this article): Full listings of analytical, mass spectrometric and spectroscopic data for all compounds.

Acknowledgments

We thank Assoc. Prof. Brendan F. Abrahams for assistance with crystallographic studies and Dr. Stephen P. Best for assistance with cyclic voltammetric simulations. We gratefully acknowledge the financial support from the Australian Research Council and the Donors of the Petroleum Research Fund (administered by the American Chemical Society).

- [1] R. Hille, *Chem. Rev.* **1996**, *96*, 2757–2816.
- [2] R. S. Pilato, E. I. Stiefel, in: *Bioinorganic Catalysis*, 2nd ed. (Eds.: J. Reedijk, E. Bouwman), Marcel Dekker, New York, **1999**, p. 81–152.
- [3] J. M. Tunney, J. McMaster, C. D. Garner, in: *Comprehensive Coordination Chemistry II* (Eds.: J. A. McCleverty, T. J. Meyer), Elsevier Pergamon, Amsterdam, **2004**, vol. 8, chapter 8.18, p. 459–477.
- [4] C. G. Young, in: *Encyclopedia of Inorganic Chemistry 2* (Ed.: R. B. King), Wiley, Chichester, UK, **2005**, vol. V, p. 3321–3340.
- [5] C. G. Young, in: *Biomimetic Oxidations Catalyzed by Transition Metal Complexes* (Ed.: B. Meunier), Imperial College Press, London, **2000**, p. 415–459.
- [6] Z. Xiao, M. A. Bruck, J. H. Enemark, C. G. Young, A. G. Wedd, *Inorg. Chem.* **1996**, *35*, 7508–7515.
- [7] L. J. Laughlin, C. G. Young, *Inorg. Chem.* **1996**, *35*, 1050–1058.
- [8] Z. Xiao, R. W. Gable, A. G. Wedd, C. G. Young, *J. Am. Chem. Soc.* **1996**, *118*, 2912–2921.
- [9] T. W. Crane, P. S. White, J. L. Templeton, *Inorg. Chem.* **2000**, *39*, 1081–1091.
- [10] C. G. Young, in: *Comprehensive Coordination Chemistry II* (Eds.: J. A. McCleverty, T. J. Meyer), Elsevier Pergamon, Amsterdam, **2004**, vol. 4, chapter 4.7, p. 415–527.
- [11] K. Yamanouchi, S. Yamada, *Inorg. Chim. Acta* **1974**, *9*, 83–86.
- [12] P. Nag, R. C. Bohra, R. C. Mehrotra, R. Ratnani, *Trans. Met. Chem.* **2002**, *27*, 321–325.
- [13] B. Kamenar, B. Korpar-Colig, M. Penavic, M. Cindric, *J. Chem. Soc., Dalton Trans.* **1990**, 1125–1130.
- [14] J. Szklarzewicz, A. Samotus, *Trans. Met. Chem.* **1998**, *23*, 807–811.
- [15] K. S. Nagaraja, M. R. Udupa, *Trans. Met. Chem.* **1986**, *11*, 217–220.

- [16] A. Rosenheim, A. Bertheim, *Z. Anorg. Chem.* **1903**, 34, 427–447.
- [17] C. F. Edwards, W. P. Griffith, A. J. P. White, D. J. Williams, *Polyhedron* **1992**, 11, 2711–2712.
- [18] C. F. Edwards, W. P. Griffith, A. J. P. White, D. J. Williams, *J. Chem. Soc., Dalton Trans.* **1993**, 3813–3819.
- [19] W. P. Griffith, H. I. S. Nogueira, B. C. Parkin, R. N. Sheppard, A. J. P. White, D. J. Williams, *J. Chem. Soc., Dalton Trans.* **1995**, 1775–1781.
- [20] L. M. R. Hill, M. K. Taylor, V. W. L. Ng, C. G. Young, *Inorg. Chem.* **2008**, 47, 1044–1052.
- [21] V. N. Nemykin, J. Laskin, P. Basu, *J. Am. Chem. Soc.* **2004**, 126, 8604–8605.
- [22] V. N. Nemykin, P. Basu, *Inorg. Chem.* **2005**, 44, 7494–7502.
- [23] R. S. Sengar, P. Basu, *Inorg. Chim. Acta* **2007**, 360, 2092–2099.
- [24] R. S. Sengar, V. N. Nemykin, P. Basu, *J. Inorg. Biochem.* **2008**, 102, 748–756.
- [25] P. Basu, V. N. Nemykin, R. S. Sengar, *Inorg. Chem.* **2009**, 48, 6303–6313.
- [26] P. D. Smith, A. J. Millar, C. G. Young, A. Ghosh, P. Basu, *J. Am. Chem. Soc.* **2000**, 122, 9298–9299.
- [27] A. J. Millar, C. J. Doonan, P. D. Smith, V. N. Nemykin, P. Basu, C. G. Young, *Chem. Eur. J.* **2005**, 11, 3255–3267.
- [28] C. J. Doonan, A. J. Millar, D. J. Nielsen, C. G. Young, *Inorg. Chem.* **2005**, 44, 4506–4514.
- [29] A. I. Rezvukhin, G. N. Dolenko, S. A. Krupoder, *Magn. Res. Chem.* **1985**, 23, 221–224.
- [30] A. G. Orpen, L. Brammer, F. H. Allen, O. Kennard, D. G. Watson, R. Taylor, *J. Chem. Soc., Dalton Trans.* **1989**, S1–S83.
- [31] R. M. Silverstein, C. G. Bassler, T. C. Morrill, *Spectrophotometric Identification of Organic Compounds*, 4th ed., Wiley, New York, **1981**.
- [32] J. Emsley, *Chem. Soc. Rev.* **1980**, 9, 91–124.
- [33] D. R. Armstrong, S. Bennett, M. G. Davidson, R. Snaith, D. Stalke, D. S. Wright, *J. Chem. Soc., Chem. Commun.* **1992**, 262–264.
- [34] I. Cragg-Hine, M. G. Davidson, A. J. Edwards, E. Lamb, P. R. Raithby, R. Snaith, *Chem. Commun.* **1999**, 153–154.
- [35] N. J. Burke, A. D. Burrows, M. F. Mahon, J. E. Warren, *Inorg. Chim. Acta* **2006**, 359, 3497–3506.
- [36] W. E. Cleland Jr., K. M. Barnhart, K. Yamanouchi, D. Collison, F. E. Mabbs, R. B. Ortega, J. H. Enemark, *Inorg. Chem.* **1987**, 26, 1017–1025.
- [37] C.-S. J. Chang, D. Collison, F. E. Mabbs, J. H. Enemark, *Inorg. Chem.* **1990**, 29, 2261–2267.
- [38] A. M. McDonagh, M. D. Ward, J. A. McCleverty, *New J. Chem.* **2001**, 25, 1236–1243.
- [39] C.-S. J. Chang, J. H. Enemark, *Inorg. Chem.* **1991**, 30, 683–688.
- [40] A. E. McElhaney, F. E. Inscore, J. T. Schirlin, J. H. Enemark, *Inorg. Chim. Acta* **2002**, 341, 85–90.
- [41] J. N. Graff, A. E. McElhaney, P. Basu, N. E. Gruhn, C.-S. Chang, J. H. Enemark, *Inorg. Chem.* **2002**, 41, 2642–2647.
- [42] D. K. Gosser Jr., *Cyclic Voltammetry: Simulation and Analysis of Reaction Mechanisms*, VCH, New York, **1993**.
- [43] N. G. Connelly, W. E. Gieger, *Chem. Rev.* **1996**, 96, 877–910.
- [44] SMART, SAINT and SADABS Software Programs, Siemens Analytical X-ray Instruments Inc., Madison, Wisconsin, USA, **1999**.
- [45] G. M. Sheldrick, *SHELXS-97 Program for Crystal Structure Solution*, University of Göttingen, Göttingen, Germany, **1997**.
- [46] G. M. Sheldrick, *SHELXL-97 Program for Crystal Structure Refinement*, University of Göttingen, Göttingen, Germany, **1997**.
- [47] L. J. Farrugia, *J. Appl. Crystallogr.* **1997**, 30, 565.
- [48] I. J. Bruno, J. C. Cole, P. R. Edgington, M. Kessler, C. F. Macrae, P. McCabe, J. Pearson, R. Taylor, *Acta Crystallogr., Sect. B* **2002**, 58, 389–397.
- [49] C. F. Macrae, P. R. Edgington, P. McCabe, E. Pidcock, G. P. Shields, R. Taylor, M. Towler, J. van de Streek, *J. Appl. Crystallogr.* **2006**, 39, 453–457.

Received: February 23, 2010
Published Online: May 19, 2010

Red to Green Switch Driven by Order in an Ionic Ir^{III} Liquid-Crystalline Complex

Elisabeta I. Szerb,^[a] Anna M. Talarico,^[a] Iolinda Aiello,^[a] Alessandra Crispini,^[b] Nicolas Godbert,^[a] Daniela Pucci,^[a] Teresa Pugliese,^[a] and Mauro Ghedini*^[a]

Keywords: Iridium / Metallomesogens / Luminescence / Supramolecular order / Multifunctional materials

New cationic Ir^{III} materials of general formula [Ir(ppy)₂(C_n-bpy)]PF₆ {H(ppy) = 2-phenylpyridine; C_n-bpy = 3,4,5-R-4,4'-benzoyloxymethyl-2,2'-bipyridine; *n* = 8, R = OC₈H₁₇; *n* = 0, R = H} were synthesised and fully characterised. Both complexes show high phosphorescence quantum yields in their condensed phases. Moreover, the introduction of long alkoxy chains on the bipyridine ligand in [Ir(ppy)₂(C₈-bpy)]PF₆ (**1**) has induced mesomorphism, and consequently a dynamic functional material with properties modulated by external stimuli has been obtained. Starting from the isotropic phase, on slow cooling a crystalline phase characterised by a bright green emission is obtained. However, on fast cooling a kinet-

ically favoured columnar hexagonal mesophase is preferentially formed, which is stable down to room temperature. In this phase, the high luminescence is still maintained, even if a switch to yellow emission colour is observed. Moreover, through spin coating of solutions of **1**, it has been possible to obtain its amorphous thin film to accomplish a further shift of the emission wavelength in the orange-red spectral range. A fully reversible colour tuning process by surface stress and heating from the orange-red film to the green crystalline phase, indicative of a mechanochromic behaviour, is also achieved.

Introduction

Most of the best performing phosphorescent emitters in electroluminescent devices are based on neutral heteroleptic octahedral cyclometallated Ir^{III} complexes for which suitable changes in the nature of the ligands enable high tunability in the emission energy and phosphorescence quantum efficiency.^[1] However, the recent use of ionic transition metal complexes as materials for electroluminescent devices (light-emitting electrochemical cell, LEC) with novel architectures and improved processing features promoted the use of various neutral polypyridine ligands to complete the coordination sphere of the Ir^{III} centre in bis-cyclometallated species. The ionic nature of these materials facilitates electronic charge injection from electrodes into the organic molecular semiconductor, eliminating the need for extra layers.^[2] Redox and photophysical properties of such cationic Ir^{III} complexes have been fine-modulated by selective functionalisation on both the cyclometallated and the diimine

ancillary ligands, extending their potentiality beyond usual light emitting applications.^[1,2]

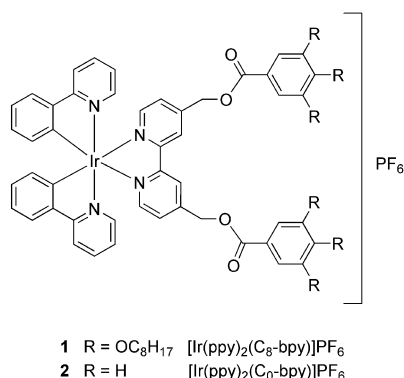
In particular, the family of complexes derived from [Ir(ppy)₂(bpy)]PF₆, where H(ppy) is 2-phenylpyridine and bpy is 2,2'-bipyridine,^[3] is attracting much interest in the design of efficient Ir^{III} phosphors.^[4] In order to improve both the processability of these materials and the performance of the final device, current developments are based on embedding the Ir^{III} emitters within polymeric or dendritic assemblies, but these approaches require a massive synthetic effort.^[1a,1b,5] In this context, the incorporation of promesogenic units at the periphery of phosphorescent Ir^{III} complexes can represent an alternative appealing strategy for adding the advantages of 2D ordered soft materials to the properties of phosphorescent, heteroligand, *ortho*-metallated, charged Ir^{III} complexes. Indeed, liquid-crystalline systems, due to their multifunctionality consisting of high charge mobility, ease of processing, responsiveness to stimuli and capability of self-organisation through intermolecular interactions, are becoming more and more advanced technological materials, and their role is increasingly expanding towards highly interesting applications in different nanotechnology fields.^[6] In particular, among the metal-containing liquid crystals (metallomesogens),^[7] the design of room-temperature luminescent complexes is a current challenge for new effective applications.^[8] Thus, taking advantage of the experience in the synthesis of functionalised 2,2'-bipyridines as organic synthons for the formation of octahedral mesogenic transition metal complexes,^[9] we syn-

[a] Centro di Eccellenza CEMIF.CAL, LASCAMM – CR INSTM, Unità INSTM della Calabria and LiCryl, CNR-INFM Dipartimento di Chimica, Università della Calabria, 87036 Arcavacata di Rende (CS), Italy
Fax: +39-0984-492066
E-mail: m.ghedini@unical.it

[b] Centro di Eccellenza CEMIF.CAL, LASCAMM – CR INSTM, Unità INSTM della Calabria and LiCryl, CNR-INFM, Dipartimento di Scienze Farmaceutiche, Università della Calabria, 87036 Arcavacata di Rende (CS), Italy

Supporting information for this article is available on the WWW under <http://dx.doi.org/10.1002/ejic.201000462>.

thesised a new Ir^{III} complex of general formula [Ir(ppy)₂-(C_n-bpy)]PF₆ (**1**), where C_n-bpy is the ancillary 2,2'-bipyridinic ligand functionalised in the 4,4'-position with [3,4,5-(triethoxy)benzoyloxymethyl] units (Scheme 1). Moreover, in order to gain more insight into the molecular organisation in the 3D space of this new Ir^{III} complex, model compound **2** of formula [Ir(ppy)₂(C₀-bpy)]PF₆, where C₀-bpy is the 2,2'-bipyridinic ligand lacking the six alkoxy chains grafted on the peripheral phenyl rings, has been synthesised and then structurally characterised (Scheme 1).



Scheme 1. Structure of the [Ir(ppy)₂(C_n-bpy)]PF₆ complexes, **1** and **2**.

Results and Discussion

Synthesis and Characterisation

Heteroligand complexes **1** and **2** have been prepared through a bridge-splitting reaction of the dinuclear precursor [Ir(ppy)₂Cl]₂ with two equivalents of the appropriate 2,2'-bipyridinic ligand (C_n-bpy), by following the method reported for the synthesis of similar derivatives.^[4a] The ¹H NMR spectra showed that both complexes are in pure isomeric form (one set of proton signals). A comparison with a related structure previously reported of a similar ionic Ir^{III} complex^[4a] confirmed the coordination of the 2,2'-bipyridine core at the metal centre with *cis* carbon and *trans* nitrogen atoms in the ppy cyclometallated fragments. Finally, the conductivity values of both complexes in acetone solution in the range 100–160 ohm⁻¹cm²mmol⁻¹ are in agreement with a 1:1 univalent electrolyte type.^[10] The thermogravimetric analysis (TGA) confirmed that both complexes are highly thermally stable until approximately 300 °C in a reproducible manner. Single crystals of complex **2** suitable for X-ray structural analysis (SXRD) were isolated from the reaction as yellow plates. A perspective view of the cations (two independent molecules are found in the asymmetric unit of the monoclinic unit cell) is shown in Figure 1. The coordination of the Ir^{III} centre is distorted octahedral with the metallated C atoms of the ppy ligands in a mutually *cis* arrangement. Their high *trans* influence leads to Ir–N(bpy) distances [2.127(6)–2.149(5) Å] longer than the corresponding distances [2.010(7)–2.055(6) Å] in the cyclometallated ligands.

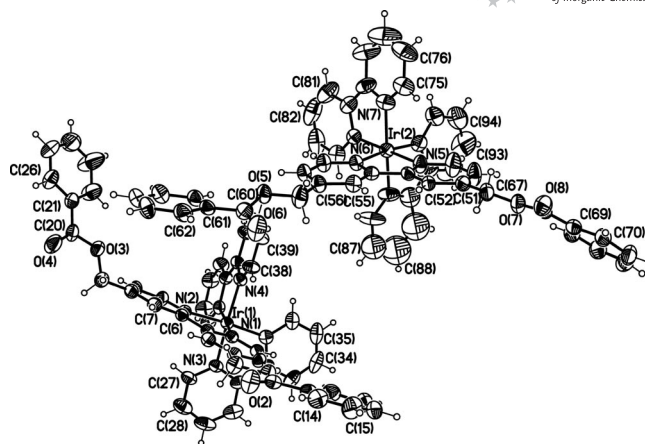


Figure 1. Molecular structure of the cation of complex **2** with atomic numbering scheme; ellipsoids at the 30% level.

The two substituents on the 2,2'-bipyridinic ligand run in opposite directions, and the conformation around the rotationally free “CH₂–O” bonds varies according to the different intermolecular interactions of the carboxylic oxygen atoms (Figure 2).

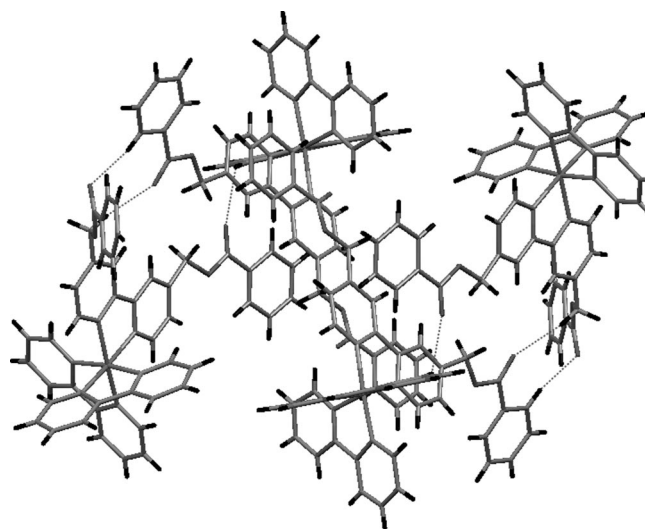


Figure 2. Crystal packing view of complex **2** showing C–H...O intermolecular interactions.

The crystal packing is dominated by C–H...O hydrogen-bonding interactions between the bulky substituents of the 2,2'-bipyridinic ligands, preventing the aromatic rings of the ppy ligands to interact through π–π stacking interactions.

Mesomorphism

Thermal studies have been performed on both Ir^{III} derivatives **1** and **2**. Polycatenar complex **1** shows liquid-crystalline behaviour, while **2** simply decomposes at just above 300 °C. The mesomorphism of **1** has been studied by a combination of polarised optical microscopy (POM), differential scanning calorimetry (DSC) and powder X-ray diffraction (PXRD). At room temperature, **1** is a yellow solid that,

on the first heating, shows only the transition between the solid and the isotropic liquid, as confirmed by the presence of only an endothermic broad peak in the DSC thermogram (Supporting Information), which occurs at 184 °C. However, in the second cycle, the thermal behaviour of complex **1** differs depending on the cooling process from the isotropic phase. A rapid cooling from the isotropic state to room temperature leads to the formation of the liquid-crystalline state, whereas a crystalline phase is obtained by cooling the sample at a rate less than 10 °C/min. In particular, the polarised optical texture of **1** upon rapid cooling from the isotropic state displays, at about 130 °C, a fan-shaped texture with large homeotropic domains, which suggests that the mesophase is a columnar phase (Supporting Information). The mesophase persists down to room temperature, and no DSC transition peaks are observed in this first cooling cycle. On reheating the bulk sample, even if a change in colour from yellow-orange to green is detected at about 120 °C, the texture remains unmodified up to the isotropisation. The DSC trace of this second heating cycle (Supporting Information) provides evidence that the columnar mesophase leads to crystallisation (one exothermic peak at 94 °C) before melting to the isotropic state. This crystalline phase has been triggered also on the first cooling cycle either by POM upon thermal annealing performed at 120 °C and by DSC by slow cooling (2 °C/min instead of 10 °C/min). In this way, the crystalline state remains stable down to room temperature, and the mesophase does not form any more. In order to determine the symmetry and check the stability of both the monotropic columnar mesophase and the crystalline phase, the thermal behaviour of **1** has been deeply investigated by PXRD measurements. The stability of the mesophase, which is dependent on the thermal procedure, has been confirmed. The presence of the thermodynamically favoured crystalline phase is detected already in the first cooling cycle, by fixing the temperature at 130 °C (Supporting Information) so that the molecules have time to organise in their lowest energy configuration. On the other hand, the kinetically favoured mesophase is preferentially formed under fast cooling from the isotropic phase and can be characterised at room temperature. The PXRD pattern of the mesophase (Supporting Information)

consists of three small-angle reflections with spacing ratios of 1, $\sqrt{3}$ and $\sqrt{9}$ and corresponding to indices (hk) = (10), (11) and (30), characteristic of a two-dimensional hexagonal columnar phase (Col_h). In the wide-angle region, the broad halo centred at 4.6 Å derives from the molten alkyl chains (h_{ch}). The absence of any reflections (or even a broad halo) around 3.0–3.5 Å is indicative of a lack of any kind of long-range order between molecules due to π – π intermolecular interactions within the columns. Moreover, synchrotron X-ray diffraction measurements (SR-PXRD), performed in order to improve the resolution and the powder pattern recorded at room temperature on cooling from the melt, have confirmed the formation of the Col_h mesophase (Figure 3).

Even if more reflections are present in the middle-angle part of the diffraction pattern, leading to indices (hk) = (20), (21), (22) and (51), in the wide-angle region only the broad halo centred at 4.7 Å (h_{ch}) and corresponding to the liquid-like order of the molten chains is observed. The lattice parameter of 36.5 Å has been calculated by indexing the SR-PXRD pattern as reported in Table 1.

Table 1. SR-PXRD data for complex **1**.

	Phase and cell parameters	d_{exp} / Å	Miller indices	$d_{\text{theor.}}$ / Å
1	Col _h , room temp. $a = 36.5$ Å	32.0	10	32.0
		18.5	11	18.5
		15.0	20	16.0
		12.1	21	12.1
		9.9	30	10.7
		9.5	22	9.2
		5.9	51	5.7
		4.7	h_{ch}	

The formation of the crystalline phase has never been detected during the SR-PXRD measurements, even when fixing the temperature at 130 °C on cooling. A possible explanation of this finding could be related to the use of a high rotation of the sample around the capillary axis. For this material, a mechanical stress is able, as well as the fast cooling, to induce the transition into the liquid-crystalline organisation, preventing the molecules to organise in a crystalline solid phase.

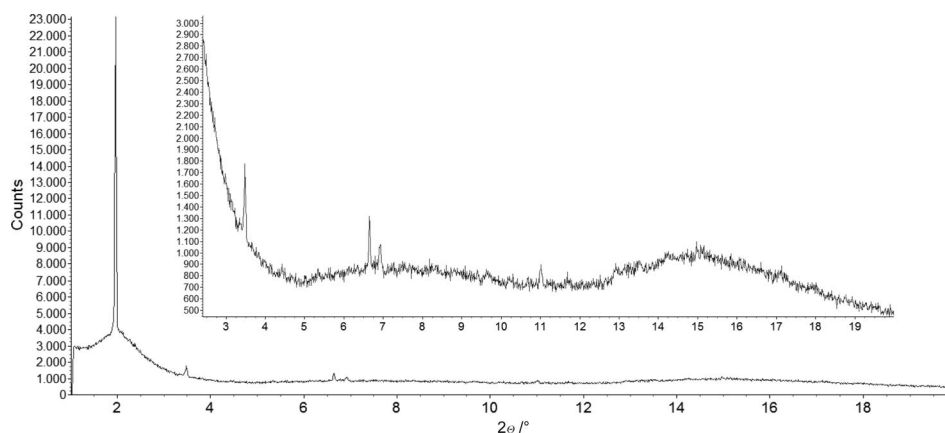


Figure 3. SR-PXRD of complex **1**, with enlargement of the middle- and wide-angle region of the spectra in the inset.

Photophysics

A full photophysical investigation has been conducted on complexes **1** and **2**, both in dichloromethane solution and in their condensed phases (Supporting Information). Complexes **1** and **2** are both luminescent in solution. In particular, in deoxygenated dichloromethane solutions they show a structureless orange-red emission with a maximum centred at 600 nm, a luminescence quantum yield of 0.12 and an emission lifetime of about 320 ns, corresponding to the triplet metal-to-ligand charge transfer (³MLCT) transition in agreement with the behaviour of the family of complexes derived from [Ir(ppy)₂(bpy)]PF₆.^[11] The thermal features exhibited by complex **1** enabled us to measure its photophysical properties in both crystalline and liquid-crystalline phases. In particular, the photophysical properties of complex **1** were studied in films prepared by pressing the sample between two quartz plates. The films were heated in order to induce the formation of the selected phases (checked by PXRD analysis) and cooled down rapidly to room temperature to freeze the supramolecular order into a glassy state. The photophysical data are summarised in Table 2.

Table 2. Emission properties of complexes **1** and **2** in condensed phases.

Film	λ_{max} /nm	ϕ
1-Crystalline	520	0.48
1-Mesophase	560	0.39
1-Amorphous	580	0.27
1-PMMA	528	0.59
2-Crystalline	528	0.48

Unlike the modest luminescence efficiency in solution, strong luminescence was detected in the two condensed phases. In both liquid-crystalline and crystalline phases the photoluminescence spectrum exhibits a structureless emission band, the maximum moving from 560 to 520 nm as the aggregation state changes (Figure 4a, b). Moreover, a difference in the phosphorescence quantum yield is also observed, which was 0.39 and 0.48 in the liquid-crystalline and crystalline phases, respectively. Therefore, a progressive blueshift of the emission maximum, accompanied by a strong enhancement of the emission efficiency, is observed

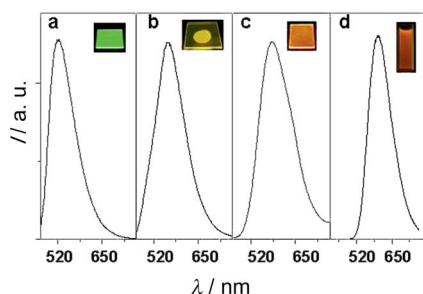


Figure 4. Emission spectra of complex **1**: (a) crystalline film (green), (b) mesophase film (yellow), (c) amorphous film (orange-red), (d) dichloromethane solution; insets: real samples under UV illumination.

on moving from solution to the liquid-crystalline organisation and finally to the crystalline solid.

This change in emission energy can be associated, at least on a spectroscopic basis, to a progressive shift toward higher energy of the ³MLCT state owing to a progressive change of the molecular environment and medium rigidity in the different molecular organisations. Regarding luminescence, for Ir^{III} complexes containing a combination of *ortho*-metallated and neutral ligands, both ³MLCT and ligand-centred (³LC) transitions are feasible.^[12] In particular, in the case of the parent [Ir(ppy)₂(bipy)]PF₆ complex, it has been shown that, depending on the molecular environment, the ³MLCT state can be found at any energy within an energy range, the upper limit being the energy of the ³LC state and the lower limit the energy of the ³MLCT state found in solution at room temperature. In the crystalline organisation, the ³MLCT state shifts so high in energy that the ³LC state becomes the effective emissive state.^[11b] Nevertheless, in the case of complex **1**, the featureless emission spectral shape observed in the crystalline phase differently suggests that the effective emissive state remains MLCT in nature also in the crystals.^[12b] Since the formation of MLCT excited states involves substantial charge redistribution, these transitions typically display solvatochromic and rigidochromic effects, and consequently the emission energy strongly depends on the environment.^[13] In order to evaluate the effect of medium rigidity on the photophysical properties of complex **1**, a very low-doped poly(methylmethacrylate) (PMMA) film (2 wt.-%) was prepared and photophysically characterised (Supporting Information). The 1-PMMA film showed a bright green emission with a maximum at 528 nm, indicating a significant rigidochromic behaviour, similar to that observed for the parent compound [Ir(ppy)₂(bipy)]PF₆, and a phosphorescence quantum yield of 0.59.^[11b]

Whereas the luminescence behaviour of molecules is normally investigated in solution, most of the luminescent materials are practically used in their solid state. It is well known that phosphorescence in Ir^{III} complexes in their condensed phases is governed by different phenomena. In some cases aggregation phenomena can produce significant photoluminescence quenching. The excited states of the aggregates often decay by nonradiative pathways as a result of exciton migration quenching phenomena favoured by the presence of closely packed Ir^{III} chromophores in the condensed phase. This phenomenon, known as the concentration quenching effect, has been reported both for monomeric and dendrimeric phosphorescent materials.^[14] However, a different phenomenon, which causes an opposite effect with respect to concentration quenching, is aggregation-induced phosphorescence emission (AIPE), which essentially comes from π – π stacks of ligands and/or restriction of rotational motion due to aggregation.^[15] In the case of complex **1**, the observed increase in phosphorescence quantum yield on going from solution to the crystalline solid state, passing through the intermediate mesophase, could depend on both the absence of the effects of aggregation quenching phenomena and the progressive molecular

rigidity in condensed phases. Photophysical measurements performed on the crystals obtained from complex **2** showed the analogous photophysical properties observed for the crystalline film of complex **1**, that is, a high blueshifted emission band ($\lambda_{\text{max}} = 528$ nm) and a high phosphorescence quantum yield (0.48). Therefore, it is reasonable to assume an analogous molecular organisation in the two solids. Moreover, the photophysical properties obtained from crystals of complex **2** are in agreement with those observed for the highly dispersed PMMA-**1** film usually corresponding to the photophysical properties of the rigid isolated molecule. The SXRD measurement of **2** revealed the absence, in the crystal, of strong interchromophoric interactions, such as π - π stacking, pointing out that the Ir^{III} cations behave similarly to isolated molecules. This structural feature is kept in the mesophase of complex **1**, as proved by the absence of reflections around 3.0–3.5 Å in the PXRD pattern, associated to π - π intermolecular interactions between cations. However, the photophysical differences between the two condensed phases of **1** are in line with the intrinsically different surroundings experienced by molecules in the frozen liquid-crystalline and in the crystalline organisations and directly correlated to the degree of order/disorder in the two states. Change in the photoluminescence on the basis of a dynamic change in the liquid-crystalline assembled structure has been observed in few examples including both organic liquid crystals and metallomesogens.^[16] Nevertheless, in all the reported cases, the change in emission colour was associated with a switch between monomeric and excimeric molecular emission, active in the different liquid-crystalline organisation. The high phosphorescence quantum yield (ϕ_p) observed for complexes **1** and **2** in the different solid organisations with respect to that in solution seems to be correlated with the emission energy and, in particular, it increases as the emission energy increases. Assuming a unitary intersystem crossing efficiency, ϕ_p is determined in relation to the radiative rate constant (k_r) and the nonradiative rate constant (k_{nr}) according to the equation $\phi_p = k_r/(k_r + k_{nr})$. Thus, high ϕ_p can be attainable either by reducing k_{nr} or increasing k_r . It is known that k_{nr} decreases exponentially with the increase in the emission energy in line with the energy gap law, while k_r should increase roughly as the cube of the emission energy in line with the Einstein law for spontaneous emission.^[11d] As a consequence, both a reduction of k_{nr} and an increase in k_r could contribute to the significant enhancement of the phosphorescence quantum yield observed for our complexes upon moving from solution to solid state.

Thin Films

Considering the great attention that is currently devoted to the production of thin films of materials that are easy to process, thin films of complex **1** have been prepared by spin coating and characterised by UV/Vis spectroscopy. Moreover, DSC and PXRD measurements were performed by inserting scratched film powder into the sample holder or

glass capillaries, respectively. By spin coating dichloromethane solutions of complex **1**, an amorphous thin film was obtained. The amorphous film shows a structureless emission spectrum with a maximum centred at 580 nm and a phosphorescence quantum yield of 0.27 (Figure 4c and Table 2). DSC and PXRD analyses performed on the scratched sample confirm its amorphous nature (Supporting Information). The colour emission of thin films of complex **1** is also dependent on the temperature of the annealing process. As seen on the DSC trace and confirmed by PXRD analysis, at 100 °C thin films of complex **1** undergo a microcrystallisation process and consequently the emission is highly blueshifted ($\lambda_{\text{max}} = 520$ nm). On the other hand, by rubbing the microcrystalline film surface with a velvet cloth or by exerting slight surface friction, the red-orange emission returns, suggesting that mechanical stress causes such a disorder of the film structure that an “amorphous-like” state is obtained. This process of colour tuning by surface stress and heating, fully reversible and cyclically repeatable, is typical of mechanochromic luminescent materials.^[16a–16b,17]

Conclusions

In summary, new cationic Ir^{III}-based materials showing high luminescence in their condensed phases were synthesised and characterised. Both complexes **1** and **2** proved to be good examples of new inorganic materials with enhanced emitting properties as a result of aggregation-induced effects only due to restricted intramolecular motion in their crystalline solid states. Indeed, the SXRD measurement of **2** revealed the absence, in the crystal packing, of strong interchromophoric interactions, such as π - π stacking, pointing out that the Ir^{III} cations behave similarly to isolated molecules. The presence of long alkoxy chains on the bipyridine ligand in complex **1** causes the formation of a liquid-crystalline state induced by temperature and therefore a further aggregation state with respect to complex **2**. Moreover, this structural difference introduces a peculiar fluidity at the molecular level, implying an ease of supramolecular reorganisation as a function of temperature. The kinetically favoured mesophase of **1** is preferentially formed under fast cooling from the isotropic phase and characterised at room temperature as a columnar hexagonal phase (Col_h). The 2D columnar hexagonal organisation of the molecules of **1** is kept at room temperature, generating a frozen liquid-crystalline phase that still maintains the high emissive properties of the solid crystalline aggregation. The decrease of order on going from the crystalline to the frozen liquid-crystalline state in **1** is followed by a shift of the luminescence wavelength from green to yellow and only a slight decrease in the luminescence quantum yield, even in absence of detectable strong interchromophoric π - π interactions in the Col_h phase. Moreover, by spin coating of solutions of **1**, it has been possible to obtain an amorphous thin film, whose photophysical properties show that the high

molecular disorder achieved in this condensed phase results in a further shift in the emission colour, turning it into orange-red (Figure 4). By heating the thin films, it is possible to switch to green emission, returning to the solid crystalline phase of **1**, and go back again to orange-red by just rubbing the cooled material with a velvet cloth or by exerting slight surface friction. This colour tuning process by surface heating and stress is fully reversible and is indicative of a mechanochromic luminescent material. Therefore, the changes from order to disorder, going from the crystalline to the amorphous phase, passing through the liquid-crystalline state, are associated with switches in emission colours from green to orange-red, passing through yellow. The overall properties exhibited by complex **1**, including the ease of processing as a thin film, are key features for its application in light-emitting devices taking advantage of LCD technologies.

Experimental Section

Materials and Measurements: All commercially available starting materials were used as received without further purification while the C₀-bpy ligand and the Ir^{III} dichlorido-bridged dimer precursor [Ir(ppy)₂Cl]₂ were synthesised according to the procedure previously described.^[18,19] ¹H NMR spectra were acquired with a Bruker Advance DRX-300 spectrometer in CDCl₃ solution, with TMS as internal standard. Infrared spectra were recorded with a Spectrum One FTIR Perkin–Elmer spectrometer. Elemental analyses were performed with a Perkin–Elmer 2400 microanalyser by the Microanalytical Laboratory at the University of Calabria. Conductivity measurements were performed in acetone, with an InoLab Cond Level 1–720 conductometer equipped with an LR 325/001 immersion cell. Thermogravimetry (TGA) measurements were performed with a PyrisTGA6 Perkin–Elmer Thermogravimetric Analyser, and differential scanning calorimetry (DSC) measurements were made with a Perkin–Elmer Pyris1 Differential Scanning Calorimeter. The TGA traces were obtained while heating the samples at 2 °C/min from 25 to 350 °C. The DSC traces were obtained for complex **1** while heating the sample from 25 to 200 °C for DSC with two different heating-cooling rates: 10 °C/min for the fast heating-cooling rate and 2 °C/min for the slow rate.

Powder X-ray Diffraction (PXRD): The powder X-ray diffraction patterns of **1** were obtained by using a Bruker AXS General Area Detector Diffraction System (D8 Discover with GADDS) with Cu-K_α radiation ($\lambda = 1.54056$ Å). Measurements taken at variable temperature were performed by placing samples in Lindemann capillary tubes with an inner diameter of 0.5 mm.

The highly sensitive area detector was placed at a distance of 20 cm from the sample (2 θ detector placed at 14°) and equipped with a CalCTec (Italy) heating stage. The samples were heated at a rate of 5.0 °C/min to the appropriate temperature. High-resolution synchrotron X-ray diffraction measurements on **1** (SR-PXRD) were performed at the MCX Elettra Synchrotron Light Laboratory beamline (Trieste, Italy). The diffraction patterns were acquired at $\lambda = 1.1260$ Å. All SR-PXRD experiments were performed in Debye–Scherrer (transmission) geometry. Powders were loaded in 0.5 mm capillaries and spun at approximately 10 Hz for improved statistics.

Single-Crystal X-ray Diffraction (SXRD): Suitable crystals for the X-ray diffraction analysis of complex **2** were obtained by concen-

tration of a dichloromethane solution. The intensity data were collected at room temperature with a Bruker-Nonius X8 Apex CCD area detector single-crystal diffractometer equipped with a graphite monochromator and Mo-K_α radiation ($\lambda = 0.71073$ Å). Data were processed with the SAINT^[20] reduction and SADABS^[21] absorption software. The structure was solved by direct methods with the SHELXTL-NT^[22] structure determination package and refined by full-matrix least-squares based on F^2 . Although several data collections on different crystals (obtained from different crystallisation batches) were performed, varying the acquisition time for the data frame, the very weak diffracting power of all of them has permitted to acquire reflections in the best measurements up to a resolution of 24.11° of θ . Generally, all non-hydrogen atoms were refined anisotropically and hydrogen atoms were included as idealised atoms riding on the respective carbon atoms with C–H bond lengths appropriate to carbon atom hybridisation. The heavy disorder found in one pyridine ring of one ppy ligand [N(8)–C(86)/C(90)] required an initial refinement as a rigid phenyl group, which was removed in the final stages of the refinement. However, C(87)/C(90) atoms were left with isotropic displacement parameters. Fluorine atoms of the PF₆ anions are disordered in two sets, A and B, with group occupancies of about 0.6 and 0.4, respectively, and therefore they were introduced in the refinement isotropically.

CCDC-765554 (**1**) contains the supplementary crystallographic data for this paper. These data can be obtained free of charge from The Cambridge Crystallographic Data Centre via www.ccdc.cam.ac.uk/data_request/cif.

Photophysics: Spectrofluorometric grade dichloromethane (Acros Organics) was used for the photophysical investigations in solution, at room temperature. Absorption spectra were recorded with an UV/Vis Perkin–Elmer Lambda 900 spectrophotometer. The experimental uncertainty in the band maximum for absorption spectra is 2 nm. Steady-state emission spectra were recorded with a Horiba Jobin Yvon Fluorolog 3 spectrofluorometer, equipped with a Hamamatsu R-928 photomultiplier tube. Emission quantum yields of samples in solution were determined by using the optical dilution method on deaerated solutions whose absorbance at excitation wavelengths was <0.1; Ru(bpy)₃Cl₂ (bpy = 2,2′-bipyridine) in H₂O was used as standard ($\phi = 0.028$).^[23] The experimental uncertainty in the emission quantum yields is 10%. The emission quantum yields of solid samples were obtained by means of an integrating sphere 102 mm in diameter coated with Spectralon® and mounted in the optical path of the spectrofluorometer by using, as excitation source, a 450 W Xenon lamp coupled with a double-grating monochromator for selecting wavelengths. The experimental uncertainty in the emission quantum yields is 5%.

Time-resolved measurements were performed by using the time-correlated single-photon counting (TCSPC) option on the Fluorolog 3. NanoLED at 370 nm, fwhm < 200 ps, was used to excite the sample. Excitation sources were mounted directly on the sample chamber at 90° to a single-grating emission monochromator (2.1 nm mm^{−1} dispersion; 1200 grooves mm^{−1}) and collected with a TBX-04-D single-photon-counting detector. The photons collected at the detector were correlated by a time-to-amplitude converter (TAC) to the excitation pulse. Signals were collected by using an IBH Data Station Hub photon counting module, and data analysis was performed by using the commercially available DAS6 software (HORIBA Jobin Yvon IBH). Goodness of fit was assessed by minimising the reduced chi squared function (χ^2) and visual inspection of the weighted residuals.

C₈-bpy: For the synthesis of the hexacatenar ancillary 2,2′-bipyridinic ligand (C₈-bpy), the synthetic route reported for the C₀-bpy

ligand was followed.^[18] In particular, 4,4'-bis(hydroxymethyl)-2,2'-bipyridine (0.050 g, 0.2312 mmol) was treated with the appropriate 3,4,5-trioctyloxybenzoic acid (0.234 g, 0.4625 mmol) by using a DCC-PPy esterification. The reaction mixture was stirred at room temperature and under N₂ for eight days. The ligand was isolated as a pure product after recrystallisation from chloroform/methanol as a white solid in 75% yield (0.207 g). C₇₄H₁₁₆N₂O₁₀ (1193.72): calcd. C 74.46, H 9.79, N 2.35; found C 74.40, H 9.70, N 2.49. ¹H NMR (300 MHz, CDCl₃): δ = 8.68 (d, ³J = 4.8 Hz, 2 H, bpyH); 7.50 (s, 2 H, bpyH); 7.37 (dd, ³J = 5.4, ⁴J = 1.8 Hz, 2 H, bpyH); 7.33 (s, 4 H, bpyH); 5.45 (s, 4 H, bpyCH₂); 4.03 (m, 12 H, OCH₂); 1.79 (m, 12 H, OCH₂CH₂); 1.48–1.21 (overlapped peaks, 60 H); 0.88 (t, ³J = 8.4 Hz, 18 H, CH₃) ppm. IR (KBr): ν_{C=O} = 1710.3 cm⁻¹.

[Ir(ppy)₂(C₈-bpy)]PF₆ (1): A stirred suspension of (ppy)₂Ir(μ-Cl)(ppy)₂ (0.090 g, 0.0838 mmol) and C₈-bpy (0.200 g, 0.1675 mmol) in CH₂Cl₂/MeOH (60 mL, 2:1 v/v) was heated to reflux. After 2 h, the resulting orange solution was cooled to room temperature, and NH₄PF₆ (5 equiv., 0.068 g, 0.4189 mmol) dissolved in MeOH (5 mL) was added. The resulting mixture was stirred for 4 h. After evaporating the solvents, dichloromethane was added, and the inorganic salts were removed by filtration through Celite. The pure product was obtained after recrystallisation with acetone/*n*-hexane as a greenish waxy solid in 75% yield (0.231 g). C₉₆H₁₃₂F₆IrN₄O₁₀P (1839.28): calcd. C 62.69, H 7.23, N 3.0; found C 62.52, H 7.17, N 2.90. ¹H NMR (300 MHz, CDCl₃): δ = 8.65 (s, 2 H, bpyH); 7.87 (m, 4 H, bpyH, ppyH); 7.74 (t, ³J = 7.7 Hz, 2 H, ppyH); 7.64 (d, ³J = 7.9 Hz, 2 H, ppyH); 7.54 (d, ³J = 5.2 Hz, 2 H, ppyH); 7.36 (d, ³J = 5.9 Hz, 2 H, bpyH); 7.29 (s, 2 H, bpyH); 7.04 (m, 4 H, ppyH); 6.88 (t, ³J = 7.5 Hz, 2 H, ppyH); 6.26 (d, ³J = 7.1 Hz, 2 H, ppyH); 5.62 (s, 4 H, bpyCH₂); 4.02 (m, 12 H, OCH₂); 1.77 (m, 12 H, OCH₂CH₂); 1.43 (m, 60 H); 0.88 (t, ³J = 6.5 Hz, 18 H, CH₃) ppm. IR (KBr): ν_{C=O} = 1727.6 cm⁻¹; ν_{PF₆} = 844.0 cm⁻¹; A_M (c = 0.99 × 10⁻⁵ mol/L in acetone) = 133 Ω⁻¹ cm² mmol⁻¹.

[Ir(ppy)₂(C₀-bpy)]PF₆ (2): A stirred suspension of (ppy)₂Ir(μ-Cl)(ppy)₂ (0.1263 g, 0.1178 mmol) and C₀-bpy (0.100 g, 0.2356 mmol) in CH₂Cl₂/MeOH (40 mL, 2:1 v/v) was heated to reflux. After 2 h, the resulting orange solution was cooled to room temperature, and NH₄PF₆ (5 equiv., 0.1029 g, 0.6315 mmol) dissolved in MeOH (10 mL) was added. The resulting mixture was stirred for 4 h. After evaporating the solvents, dichloromethane was added, and the inorganic salts were removed by filtration through Celite. The pure product was obtained by recrystallisation from acetone/methanol as a yellow microcrystalline powder in 79% yield (0.199 g). C₄₈H₃₆F₆IrN₄O₄P (1070.01): calcd. C 53.88, H 3.39, N 5.24; found C 53.80, H 3.40, N 5.14. M.p. 300 °C with decomposition. ¹H NMR (300 MHz, CDCl₃): δ = 8.62 (s, 2 H, bpyH); 8.08 (dd, ³J = 7.8, ⁴J = 1.5 Hz, 4 H, bpyH); 7.80 (m, 4 H, bpyH, ppyH); 7.74 (td, ³J = 7.8, ⁴J = 1.5 Hz, 2 H, ppyH); 7.61 (m, 6 H, ppyH, bpyH); 7.48 (m, 4 H, bpyH); 7.15 (m, 4 H, ppyH); 6.89 (td, ³J = 7.2, ⁴J = 1.4 Hz, 2 H, ppyH); 6.26 (d, ³J = 7.2 Hz, 2 H ppyH); 5.63 (s, 4 H, bpyCH₂) ppm. IR (KBr): ν_{C=O} = 1730.0 cm⁻¹; ν_{PF₆} = 840.4 cm⁻¹; A_M (c = 0.99 × 10⁻⁵ mol/L in acetone) = 133 Ω⁻¹ cm² mmol⁻¹.

Supporting Information (see footnote on the first page of this article): DSC traces of complex **1**, POM micrograph of complex **1**, PXRD patterns of complex **1**, PXRD pattern of a film of complex **1**, photophysical properties of complexes **1** and **2** in solution, emission spectra of complex **1** in PMMA film, emission spectra of complex **2** crystalline powder.

Acknowledgments

This work has been supported by Ministero dell'Istruzione, dell'Università e della Ricerca (MiUR) through the Progetti di Ricerca di Interesse Nazionale (PRIN 2007–2007WJMF2W) project and by Consorzio Interuniversitario Nazionale per la Scienza e la Tecnologia dei Materiali (INSTM) through a PRISMA 2007 (PC26/2007) grant.

- [1] a) E. Holder, B. M. W. Langeveld, U. Schubert, *Adv. Mater.* **2005**, *17*, 1109–1121; b) L. Flamigni, A. Barbieri, C. Sabatini, B. Ventura, F. Barigelletti, *Top. Curr. Chem.* **2007**, *281*, 143–203; c) C. Ulbricht, B. Beyer, C. Friebe, A. Winter, U. S. Schubert, *Adv. Mater.* **2009**, *21*, 4418–4441; d) Y. You, S. Y. Park, *Dalton Trans.* **2009**, 1267–1282.
- [2] J. D. Slinker, J. Rivnay, J. S. Moskowitz, J. B. Parker, S. Bernhard, H. D. Abruna, G. G. Malliaras, *J. Mater. Chem.* **2007**, *17*, 2976–2988.
- [3] a) Y. Ohsawa, S. Sprouse, K. A. King, M. K. DeArmond, K. W. Hanck, R. J. Watts, *J. Phys. Chem.* **1987**, *91*, 1047–1054; b) M. G. Colombo, A. Hauser, H. U. Güdel, *Inorg. Chem.* **1993**, *32*, 3088–3092; c) F. O. Garces, K. A. King, R. J. Watts, *Inorg. Chem.* **1998**, *37*, 3464–3471.
- [4] a) F. Neve, M. La Deda, A. Crispini, A. Bellusci, F. Puntoriero, S. Campagna, *Organometallics* **2004**, *23*, 5856–5863; b) Md. K. Nazeeruddin, R. T. Wegh, Z. Zhou, C. Klein, Q. Wang, F. De Angelis, S. Fantacci, M. Grätzel, *Inorg. Chem.* **2006**, *45*, 9245–9250; c) F. De Angelis, S. Fantacci, N. Evans, C. Klein, S. M. Zakeeruddin, J. E. Moser, K. Kalyanasundaram, H. J. Bolink, M. Grätzel, M. K. Nazeeruddin, *Inorg. Chem.* **2007**, *46*, 5989–6001; d) H.-C. Su, F.-C. Fang, T.-Y. Hwu, H.-H. Hsieh, H.-F. Chen, G.-S. Lee, S.-M. Peng, K.-T. Wong, C.-C. Wu, *Adv. Funct. Mater.* **2007**, *17*, 1019–1027; e) H. J. Bolink, E. Coronado, R. D. Costa, N. Lardis, E. Ort, *Inorg. Chem.* **2008**, *47*, 9149–9151; f) H. J. Bolink, E. Coronado, R. D. Costa, E. Orti, M. Sessolo, S. Graber, K. Doyle, M. Neuburger, C. E. Housecroft, E. C. Constable, *Adv. Mater.* **2008**, *20*, 3910–3913; g) M. Yu, Q. Zhao, L. Shi, F. Li, Z. Zhou, H. Yang, T. Yia, C. Huang, *Chem. Commun.* **2008**, 2115–2117; h) H.-C. Su, H.-F. Chen, F.-C. Fang, C.-C. Liu, C.-C. Wu, K.-T. Wong, Y.-H. Liu, S.-M. Peng, *J. Am. Chem. Soc.* **2008**, *130*, 3413–3419; i) K. K.-W. Lo, K. Y. Zhang, S.-K. Leung, M.-C. Tang, *Angew. Chem. Int. Ed.* **2008**, *47*, 2213–2216.
- [5] V. Marin, E. Holder, R. Hoogenboom, U. S. Schubert, *Chem. Soc. Rev.* **2007**, *36*, 618–635.
- [6] a) M. O'Neill, S. M. Kelly, *Adv. Mater.* **2003**, *15*, 1135–1145; b) J. W. Goodby, I. M. Saez, S. J. Cowling, V. Götz, M. Draper, A. W. Hall, S. Sia, G. Cosquer, S.-E. Lee, E. P. Raynes, *Angew. Chem. Int. Ed.* **2008**, *47*, 27542–2787.
- [7] a) L. Serrano (Ed.), *Metallomesogens*, VCH, Weinheim, **1996**; b) B. Donnio, D. W. Bruce in *Structure and Bonding*, Vol. 95, *Liquid Crystals II. Metallomesogens* (Ed.: D. M. P. Mingos), Springer, Berlin, **1999**; c) B. Donnio, D. Guillon, R. Deschenaux, D. W. Bruce in *Comprehensive Coordination Chemistry II*, Vol. 6, *Metallomesogens* (Eds: J. A. McCleverty, T. J. Meyer), Elsevier, Oxford, **2003**; d) J. L. Sessler, W. B. Callaway, S. P. Dudek, R. W. Date, D. W. Bruce, *Inorg. Chem.* **2004**, *43*, 6650–6653.
- [8] K. Binnemans, *J. Mater. Chem.* **2009**, *19*, 448–453.
- [9] a) K. E. Amos, N. J. Brooks, N. C. King, S. Xie, J. Canales-Vázquez, M. J. Danks, H. B. Jervis, W. Zhou, J. M. Seddon, D. W. Bruce, *J. Mater. Chem.* **2008**, *18*, 5282–5292 and references cited therein; b) D. Pucci, A. Bellusci, A. Crispini, M. Ghedini, N. Godbert, E. I. Szerb, A. M. Talarico, *J. Mater. Chem.* **2009**, *19*, 7643–7649.
- [10] W. J. Geary, *Coord. Chem. Rev.* **1971**, *7*, 81–122.
- [11] a) F. O. Garces, K. A. King, R. J. Watts, *Inorg. Chem.* **1988**, *27*, 3464–3471; b) M. G. Colombo, A. Hauser, A. U. Güdel, *Top. Curr. Chem.* **1994**, *171*, 144–171; c) F. Neve, M. La Deda, A.

- Crispini, A. Bellusci, F. Puntoriero, S. Campagna, *Organometallics* **2004**, *23*, 5856–5863; d) F. De Angelis, S. Fantacci, N. Evans, C. Klein, S. M. Zakeeruddin, J.-E. Moser, K. Kalyanasundaram, H. J. Bolink, M. Gratzel, M. K. Nazeeruddin, *Inorg. Chem.* **2007**, *46*, 5989–6001.
- [12] a) L. Flamigni, A. Barbieri, C. Sabatini, B. Ventura, F. Barigelli, *Top. Curr. Chem.* **2007**, *281*, 143–203; b) Y. You, S. Young Park, *Dalton Trans.* **2009**, 1267–1282.
- [13] a) A. Tsuboyama, H. Iwawaki, M. Furugori, T. Mukaide, J. Kamatani, S. Igawa, T. Moriyama, S. Miura, T. Takiguchi, S. Okada, M. Hoshino, K. Ueno, *J. Am. Chem. Soc.* **2003**, *125*, 12971–12979; b) T. Sajoto, P. I. Djurovich, A. Tamayo, M. Yousufuddin, R. Bau, M. E. Thompson, *Inorg. Chem.* **2005**, *44*, 7992–8003.
- [14] a) Y. Kawamura, K. Goushi, J. Brooks, J. J. Brown, H. Sasabe, C. Adachi, *Appl. Phys. Lett.* **2005**, *86*, 071104–071104; b) E. B. Namdas, A. Ruseckas, I. D. W. Samuel, S.-C. Lo, P. L. Burn, *J. Phys. Chem. B* **2004**, *108*, 1570–1577.
- [15] C. H. Shin, J. O. Huh, M. H. Lee, Y. Do, *Dalton Trans.* **2009**, 6476–6479 and reference therein.
- [16] a) Y. Sagara, T. Kato, *Angew. Chem. Int. Ed.* **2008**, *47*, 5175–5178; b) V. N. Kozhevnikov, B. Donnio, D. W. Bruce, *Angew. Chem. Int. Ed.* **2008**, *47*, 6286–6289; c) J. Kunzelman, M. Kinami, B. R. Crenshaw, J. D. Protasiewicz, C. Weder, *Adv. Mater.* **2008**, *20*, 119–122; d) Y. Sagara, S. Yamane, T. Mutai, K. Araki, T. Kato, *Adv. Funct. Mater.* **2009**, *19*, 1869–1875.
- [17] G. Zhang, J. Lu, M. Sabat, C. L. Fraser, *J. Am. Chem. Soc.* **2010**, *132*, 2160–2162.
- [18] G. Barberio, A. Bellusci, A. Crispini, M. Ghedini, A. Golemme, P. Prus, D. Pucci, *Eur. J. Inorg. Chem.* **2005**, 181–188.
- [19] M. Nonoyama, *Bull. Chem. Soc. Jpn.* **1974**, *47*, 767–768.
- [20] SAINT, Version 6.45 Copyright © **2003**, Bruker Analytical X-ray Systems Inc.
- [21] G. M. Sheldrick, *SADABS*. Version 2.10, Bruker AXS Inc., Madison, WI, USA, **2003**.
- [22] *SHELXTL-NT*, Version 5.1 Copyright **1999**, Bruker Analytical X-ray Systems Inc.
- [23] a) J. N. Demas, G. A. Crosby, *J. Phys. Chem.* **1971**, *75*, 991–1024; b) K. Nakamaru, *Bull. Chem. Soc. Jpn.* **1982**, *55*, 2697–2705.

Received: April 26, 2010
Published Online: June 8, 2010

Macrocyclic 14-Membered-Ring Diketal Dilactams: Spectroscopic Studies and Conformational Analysis of Their Complexes with Divalent Cations

Anne-Gaëlle Valade,^[a,b] Dominique Harakat,^[a,b] Jacques Guyot,^[a,b] Olivier Lapr v te,^[c] and Denise Dugat^{*[a,b]}

Keywords: Lactams / Macrocyclic ligands / Divalent cations / Conformation analysis

The complexation behaviour of four new 14-membered-ring diketal dilactam macrocycles towards some divalent cation perchlorates has been investigated. Stoichiometries and binding constants were determined by ¹H NMR titration experiments. The structures of the complexes were studied by IR, NMR (¹H and ¹³C) and electrospray mass spectrometry. ¹³C longitudinal relaxation time data allowed identification of the donor atoms involved in the complexation and provided information on the intramolecular mobility of the complexed ligands. Molecular modelling was also used to gain further insights into the conformational changes undergone

by these molecules as a result of metal ligation. It was found that i. the macrocycles formed complexes of essentially 1:1 stoichiometry in the binding order $\text{Sr}^{2+} \geq \text{Ca}^{2+} > \text{Mg}^{2+} > \text{Ba}^{2+}$, ii. the coordination process caused conformational changes that resulted in cleavage of the hydrogen bonds in the ligand structure and a new orientation of the NH–CO bonds and iii. the coordination of the cations involved either all six oxygen atoms of the ligands or five of them, depending on whether the OMe groups were *cis* or *trans*, and probably two oxygen atoms from the ClO_4^- counter-anion.

Introduction

Over the last three decades, molecular recognition between metal ions and diversely functionalized macrocycles has been an important topic in supramolecular chemistry.^[1–7] The host–guest complexing process can be characterized by several methods^[2b] among which UV,^[3c,3d,3f,4,5,6k] NMR,^[3d–3h,4,5c–5e,6] IR^[3d–3g,4,5d] and mass^[3f,5c,6e,6f,6n,7] spectroscopic techniques are widely used as well as X-ray diffraction^[3g,6f,6j,6m,6n] and molecular modelling^[3d,3e,4,5d] techniques.

We have already published a first evaluation of the binding abilities of new substituted 14-membered-ring diketal dilactam macrocycles,^[8] the synthesis of which has been described elsewhere.^[9a] The study, which was performed by UV/Vis spectrophotometry using picrate anion absorbance, showed appreciable complexation with some divalent cations, particularly strontium and calcium ($\text{Sr}^{2+} \geq \text{Ca}^{2+} > \text{Zn}^{2+} \geq \text{Mg}^{2+} > \text{Ba}^{2+}$), both of which have important applications in pharmacology, radiotherapy and biology,^[10,11] whereas no association was observed with

monovalent cations, revealed a marked predominance ($\geq 90\%$) of complexes with a 1:1 stoichiometry and allowed the determination of stability constants in mono- and bi-phasic systems.

To explore the complexation properties of our ligands with the above cations, we undertook a further study using other spectroscopic techniques with four main aims: i. corroboration of the stoichiometry, the stability constant size scale and the cation selectivity order by ¹H NMR spectrometry, ii. identification of the coordination sites by IR and ¹³C NMR spectroscopy (chemical shifts and longitudinal relaxation time measurements), iii. determination of the conformational structures of the complexes by ¹H NMR spectroscopy and molecular modelling and iv. additional characterization of the complexes by mass spectrometry. An inability to obtain single crystals of these complexes precluded an X-ray study, but valuable information was obtained from the IR, ¹³C NMR, MS and computation data.

The study was performed on four previously synthesized macrocycles: **1c**, **2c**, **3c** and **3b**, the last two compounds differing in the stereochemistry of the OMe groups (Figure 1).^[9b] Complexation with a perchlorate counter-anion was explored for **1c** with Mg^{2+} , Ca^{2+} , Sr^{2+} , Ba^{2+} and Zn^{2+} , for **2c** with Ca^{2+} , Sr^{2+} and Zn^{2+} and for **3c** and **3b** with Ca^{2+} , that is, for complexes **1c**– $\text{Mg}(\text{ClO}_4)_2$, **1c**– $\text{Ca}(\text{ClO}_4)_2$, **1c**– $\text{Sr}(\text{ClO}_4)_2$, **1c**– $\text{Ba}(\text{ClO}_4)_2$, **1c**– $\text{Zn}(\text{ClO}_4)_2$, **2c**– $\text{Ca}(\text{ClO}_4)_2$, **2c**– $\text{Sr}(\text{ClO}_4)_2$, **2c**– $\text{Zn}(\text{ClO}_4)_2$, **3c**– $\text{Ca}(\text{ClO}_4)_2$ and **3b**– $\text{Ca}(\text{ClO}_4)_2$. The choice of these complexes was guided by the availability of ligands and by the best results obtained in the UV/Vis study.^[8]

[a] CNRS, UMR 6504, SEESIB, 63177 Aubi re, France

[b] Clermont Universit , Universit  Blaise Pascal, SEESIB, B. P. 10448, 63000 Clermont-Ferrand, France
Fax: +33-4-73407717
E-mail: denise.dugat@univ-bpclermont.fr

[c] CNRS, UPR, UPR 2301, Institut de Chimie des Substances Naturelles, 91198 Gif-sur-Yvette, France

Supporting information for this article is available on the WWW under <http://dx.doi.org/10.1002/ejic.201000060>.

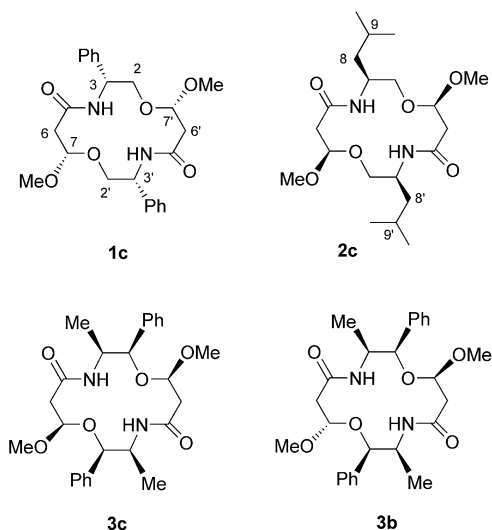
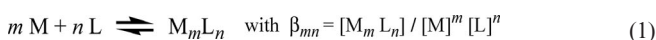


Figure 1. Structure and stereochemistry of the diketetal dilactam macrocycles **1c**, **2c**, **3c** and **3b**.

Results and Discussion

Determination of Stoichiometries and Stability Constants

Host–guest equilibria [Equation (1)] between the ligand **L** and the metal cation **M** are given by the following general equation in which β_{mn} is the corresponding association constant.



The complexation of each metal perchlorate with a macrocycle was monitored by ^1H NMR spectroscopy by measuring the change in the dilactam proton chemical shifts upon mixing the two components in CD_3CN , a solvent in which the perchlorate salts are appreciably soluble. The study was carried out on the macrocyclic ring hydrogen atoms (2-H^A, 2-H^B, 6-H^A, 6-H^B, 3-H and 7-H) and on the OMe groups, common to the four ligands.

The stoichiometries of the host–guest complexes were obtained from ^1H NMR spectroscopic data by the mole ratio method.^[12] In this method, the differences in the chemical shifts $\Delta\delta$ for each proton in the complex and the ligand was correlated with the ratio $[\text{M}]/[\text{L}]$ in which $[\text{L}]$ (ligand concentration) was maintained constant and $[\text{M}]$ (cation concentration) progressively increased. The intersection of the straight lines of the $\Delta\delta$ versus $[\text{M}]/[\text{L}]$ plots indicated the stoichiometry of the complexes. Owing to the rapid interconversion between the free and complexed ligands in solution, only time-averaged values of the proton chemical shifts were observed, as are usually reported.^[6d] All the NMR signals were sharp and well-resolved irrespective of the amplitude of the changes in the chemical shifts and the guest/host ratios studied.

The titration curves $\Delta\delta$ versus $[\text{M}]/[\text{L}]$ obtained for **1c**– $\text{Mg}(\text{ClO}_4)_2$, **1c**– $\text{Ca}(\text{ClO}_4)_2$, **1c**– $\text{Sr}(\text{ClO}_4)_2$, **1c**– $\text{Ba}(\text{ClO}_4)_2$ and **2c**– $\text{Zn}(\text{ClO}_4)_2$ were similar: they all exhibited a plateau with

1 equiv. of added cation, which indicates the formation of 1:1 complexes. The δ changes corresponding to the complex **1c**– $\text{Sr}(\text{ClO}_4)_2$ are shown as an example in Figure 2(a). The other complex curves are given in Figure SI-1(a–c,f) of the Supporting Information. With regard to the **2c**– $\text{Ca}(\text{ClO}_4)_2$, **2c**– $\text{Sr}(\text{ClO}_4)_2$, **3c**– $\text{Ca}(\text{ClO}_4)_2$ and **3b**– $\text{Ca}(\text{ClO}_4)_2$ complexes, the plateau was reached at $[\text{M}]/[\text{L}] \approx 0.75$ [see Figure 2 (b) for **2c**– $\text{Sr}(\text{ClO}_4)_2$ and Figure SI-1(e,g,h) for other couples]. These observations indicate the partial presence of ML_2 species in addition to the ML complexes. Finally, for **1c**– $\text{Zn}(\text{ClO}_4)_2$, the variations in $\Delta\delta$ were weak (± 0.03 – 0.09) and so the change in slope was not very marked [Figure SI-1(d)].

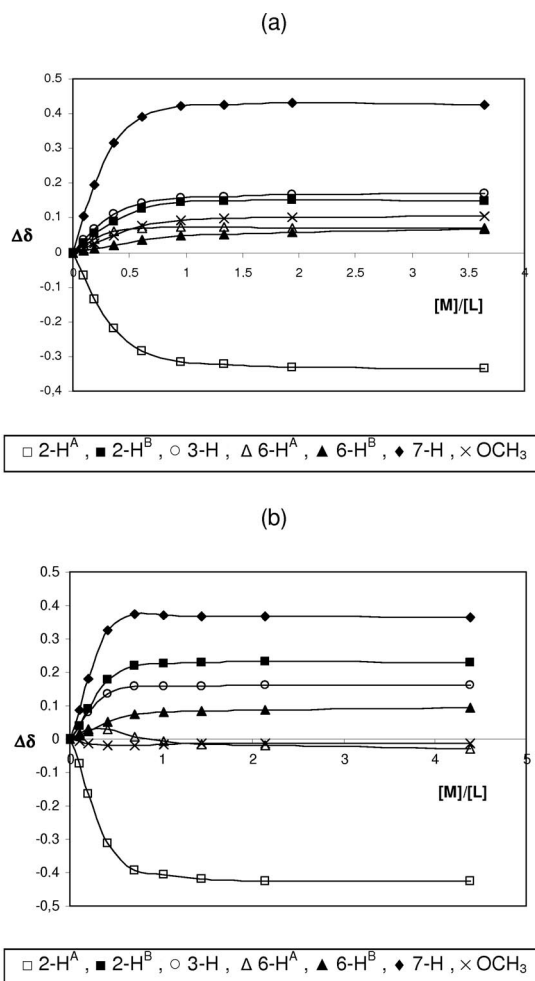


Figure 2. Variations in the ^1H NMR chemical shift ($\Delta\delta = \delta_{\text{complex}} - \delta_{\text{ligand}}$) of macrocyclic protons in CD_3CN by progressive addition of metal perchlorate: (a) **1c** + $\text{Sr}(\text{ClO}_4)_2$ and (b) **2c** + $\text{Sr}(\text{ClO}_4)_2$.

These results are in agreement with those obtained by UV spectrometry. They underline the exclusive presence of ML complexes for **1c** with Mg^{2+} , Ca^{2+} , Sr^{2+} and Ba^{2+} and for **2c**– Zn^{2+} , and a marked predominance of ML species accompanied by a small percentage of ML_2 for **2c**– Sr^{2+} and **3c**– Ca^{2+} , as previously reported,^[8] and also for **2c**– Ca^{2+} and **3b**– Ca^{2+} .

The equilibrium constants were determined using the EQNMR program^[13] from the variation of the ¹H NMR chemical shifts of the ligands upon complexation (Table SI-2). All of the hydrogen atoms were shifted downfield except for the 2-H^A protons, which exhibited upfield shifts. The association constants of each complex studied were calculated for the ML model and also for the ML/ML₂ model for the second series of complexes (**2c**–Ca, **2c**–Sr, **3c**–Ca and **3b**–Ca; Table 1).

Table 1. Association constants of ligands **1c**, **2c**, **3b** and **3c** with metal perchlorates in CD₃CN and in italics the corresponding ligand–metal picrate association constants previously determined in the UV study conducted in THF.^[8]

Complex	log	EQNMR (NMR)		STAR (UV)
		ML model	ML/ML ₂ model	
1c –Mg ²⁺	β ₁₁ ^[a]	3.50 ± 0.34	–	2.90
	β ₁₂ ^[b]	–	–	–
1c –Ca ²⁺	β ₁₁	4.37 ± 1.05	–	3.10
	β ₁₂	–	–	–
1c –Sr ²⁺	β ₁₁	4.42 ± 1.26	–	3.67
	β ₁₂	–	–	–
1c –Ba ²⁺	β ₁₁	3.37 ± 0.40	–	2.12
	β ₁₂	–	–	–
1c –Zn ²⁺	β ₁₁	2.42 ± 0.16	–	3.20
	β ₁₂	–	–	–
2c –Ca ²⁺	β ₁₁	4.80 ± 1.70	1.34 ± 0.74	3.31
	β ₁₂	–	4.44 ± 1.88	–
2c –Sr ²⁺	β ₁₁	4.43 ± 1.88	1.84 ± 0.73	3.61
	β ₁₂	–	4.54 ± 1.86	5.85
2c –Zn ²⁺	β ₁₁	4.08 ± 1.06	–	3.33
	β ₁₂	–	–	–
3c –Ca ²⁺	β ₁₁	4.82 ± 2.20	4.04 ± 2.07	3.92
	β ₁₂	–	5.02 ± 2.43	5.14
3b –Ca ²⁺	β ₁₁	4.25 ± 1.79	2.37 ± 1.28	3.83
	β ₁₂	–	3.77 ± 1.51	–

[a] β₁₁ given in L mol^{−1}. [b] β₁₂ given in L² mol^{−2}.

In fact, in these four last cases, the δ_{obs} values were in much better agreement with the data calculated for the ML model by the computational treatment than with the data obtained with the ML/ML₂ model, which indicates that the ML₂ species were formed in relatively low amounts. Comparison of the log β₁₁ values determined for both models with those previously obtained from the UV study leads to the same conclusion (Table 1), except for **3c**–Ca for which the two constants determined with the ML/ML₂ model are similar to those determined from the UV data.

Besides, for all the couples apart from **1c**–Zn²⁺, the constants log β₁₁ calculated by the EQNMR program are higher than those determined in the UV study. These variations (0.12 to 1.49) can be explained by differences in the counter-anions and solvents, that is, perchlorates/CD₃CN in the present case and picrates/THF in the UV study. Identical or even much greater variation with solvent has been reported in the literature,^[1e,14] for example, for ether 18-crown-6/K⁺ (log K_s = 6.10 in MeOH, 5.70 in CH₃CN, 4.31 in DMF, 3.21 in DMSO).^[14c]

The cation selectivity order disclosed here (Sr²⁺ ≥ Ca²⁺ > Mg²⁺ > Ba²⁺) corresponds exactly to that established in the UV study.^[8] The constants obtained are in

the range of those reported for several Ca²⁺–macrocylic lactam complexes, for example, log β₁₁ = 3.96 (18-membered ring tetralactam),^[3c] 4.60 (dioxazaphosphocane macrocycle).^[3f]

Identification of the Complexation Sites

The complexation sites were identified by IR spectroscopy in the solid state, as usually reported,^[3d–3g,5d] and by ¹³C NMR spectroscopy in solution (chemical shifts and T₁ measurements).

IR Analysis

The spectra of the free ligands **1c**, **2c**, **3c**, **3b** and their complexes were recorded in KBr pellets. We focused on two absorption bands: the lactam carbonyl stretching vibration (ν_{C=O}) and the perchlorate anion vibration (ν_{Cl–O}). Other vibrations and ν(NH) bands were either difficult to locate because their frequencies were similar to that of the perchlorate anion band (e.g., ν_{C–O–C–O}) or difficult to observe owing to the presence of water in the complexes from the slightly deliquescent initial perchlorate salts (e.g., ν_{NH}).

CO Stretching Vibration: Complexation shifted the carbonyl band to lower wavenumbers with appreciable differences in the frequency (Δν = −5 to −30 cm^{−1}) for all of the complexes except **1c**–Ba(ClO₄)₂ and **2c**–Sr(ClO₄)₂ (Δν = −1 cm^{−1}) (Table 2). These results, which correspond to a weakening of the C=O double bond character, are known to be due to a coordination of the oxygen donor atoms with the cations.^[3d–3g,15] The same variations (Δν = −13 to −37 cm^{−1}) have already been reported for alkaline-earth complexes with linear amides,^[15] tetralactams,^[3d,3e] polyoxadilactams^[3g] and dioxazaphosphocane macrocycles.^[3f]

Table 2. IR CO lactam frequencies of the free ligands and their metal perchlorate complexes.

Host–guest	ν _{CO} lactam		Δν ^[a] [cm ^{−1}]
	Ligand	Complex	
1c –Mg ²⁺	1645	1639	−6
1c –Ca ²⁺	1645	1640	−5
1c –Sr ²⁺	1645	1640	−5
1c –Ba ²⁺	1645	1644	−1
1c –Zn ²⁺	1645	1615	−30
2c –Ca ²⁺	1643	1637	−6
2c –Sr ²⁺	1643	1642	−1
2c –Zn ²⁺	1643	1615	−28
3c –Ca ²⁺	1651	1636	−15
3b –Ca ²⁺	1651	1638	−13

[a] Δν = ν_{complex} − ν_{ligand}.

Perchlorate Vibrations: Three bands (1144–1147, 1113–1119 and 1086–1089 cm^{−1}) were invariably observed for the Cl–O bonds of our complexes. In theory, the “isolated” perchlorate anion, which has T_d symmetry, shows a ν_{Cl–O} (ν₃) single band at 1100 cm^{−1}.^[16] Coordination with a cation in-

duces changes in the infrared spectrum: a double (unidentate C_{3v} , perchlorate) or triple (bidentate C_{2v} , perchlorate) band appears related to the loss of tetrahedral symmetry. In the case of our complexes, the presence of three ν_3 bands indicates the probable participation of two of the ClO_4^- oxygen atoms in the complexation, as concluded in previous reports,^[3d,3e,5d] with very few exceptions.^[3g]

In summary, the IR spectroscopic analysis identified four coordination sites in most of the complexes: the two oxygen atoms of the ligand carbonyl groups and two oxygen atoms of the ClO_4^- counter-anion, which evidently remains bound to the cation.

^{13}C NMR Chemical Shifts

A comparative analysis of the ^{13}C NMR spectra of the free and bound ligands, which present a simpler picture than the 1H NMR spectra, is informative in several respects regarding the participation of donor atoms in the complex. The study was conducted on seven complexes: **1c**– $Mg(ClO_4)_2$, **1c**– $Ca(ClO_4)_2$, **1c**– $Sr(ClO_4)_2$, **2c**– $Ca(ClO_4)_2$, **2c**– $Zn(ClO_4)_2$, **3c**– $Ca(ClO_4)_2$ and **3b**– $Ca(ClO_4)_2$. The ^{13}C NMR spectra were recorded in CD_3CN and the carbon assignments made on the basis of their chemical shifts with reference to the data already reported in $CDCl_3$.^[9a]

The addition of perchlorate salts of alkaline-earth and Zn cations to the ligands studied induced NMR chemical shifts (Table SI-3). Thus, the significant downfield shift observed for the carbonyl resonance of the four complexing macrocycles ($\Delta\delta = +0.6$ to $+4.2$ ppm) suggests a simultaneous coordination of the two lactam oxygen atoms,^[3d,3e,3g] consistent with the IR data.

Also, for the first six complexes named above, the C-2, C-7 and OCH_3 carbon resonances were shifted upfield (C-2: $\Delta\delta = -0.1$ to -5.1 ppm; C-7: -0.3 to -5.0 ppm; OCH_3 : -0.3 to -2.6 ppm). These values, which are comparable to those observed for carbon atoms α to the ether oxygen atoms in the ETH 129/ $Ca(ClO_4)_2$ complex ($\Delta\delta = -1.5$ ppm)^[3d] and in the benzo-18-crown-6/ $KSCN$ couple ($\Delta\delta = -0.1$ to -2.3 ppm),^[6a] indicate that the four ketal oxygen atoms of macrocycles **1c**, **2c** and **3c** participate in the complexation. Consequently all six oxygen atoms of these ligands are involved in the binding process. Concerning the variation in shifts observed for C-3 ($\Delta\delta = +0.2$ to -3.5 ppm), identical $\Delta\delta$ values, fluctuating between positive and negative values, were reported for the carbon atoms α to the nitrogen atoms in the diamide ETH 1001/ $Ca(SCN)_2$ complex ($\Delta\delta = +0.2$ to -0.6 ppm).^[17] These variations are probably due to the coordination of the γ CO oxygen atoms and also, in the present case, of the β -O-1 atoms, participation of the nitrogen atoms being excluded. Indeed, the nitrogen and oxygen atoms of the $NH-CO$ links, because of their opposite orientation within the amide bond, cannot both be involved in the process, as confirmed by molecular modelling (see below) and various studies of Ca -lactam and -amide complexes,^[3d–3h,15,18] some of them including X-ray diffraction analyses.^[3g,18] The corresponding complexes, for which only one signal was observed for the two

chains of the ring, present a C_2 symmetry axis perpendicular to the median plane of the ring, like the ligands, that dissects the cation.

In the unsymmetrical compound **3b**, binding with Ca^{2+} induced i. almost identical effects on both carbonyls, ii. a greater upfield shift on C-7' than on carbon C-7 and iii. upfield shifts for C-2' and 7- OCH_3 (-1.8 and -2.7 ppm, respectively) and downfield shifts for C-2 and 7'- OCH_3 ($+1.1$ and $+2.5$ ppm, respectively). For these two last carbon atoms, the magnetic effect caused by the adjacent cationic centre seems to play a minor role compared with the conformational contribution.^[3d] All these results indicate an unequal participation of the analogous ketal oxygen atoms in the complexation, 7-OMe being more involved than 7'-OMe, and, to a lesser degree, O-1' being more involved than O-1.

^{13}C NMR Longitudinal Relaxation Times T_1

This technique provides further insight into the complexation process. It offers a convenient means of detecting specific binding interactions in different portions of a ligand and in turn gives accurate information on spatial structural changes in the complexes.^[6b,6d] The T_1 values reflect the inter- and intramolecular mobility of a system, longer T_1 times implying greater flexibility.^[6b,6g,6i]

The ^{13}C relaxation time measurements were made at 75 MHz in a $CD_3CN/MeOD/CDCl_3$ (80:10:10) solution for compound **1c** and its complexes **1c**– Mg^{2+} , **1c**– Ca^{2+} and **1c**– Sr^{2+} , and in CD_3CN for the free molecules **2c**, **3c**, **3b** and their complexes **2c**– Ca^{2+} , **2c**– Zn^{2+} , **3c**– Ca^{2+} and **3b**– Ca^{2+} . The differences between the T_1 values before and after interaction with the designated cation are expressed as the percentage by which the relaxation time is shortened [sign (–)] or lengthened [sign (+)] (Table 3).

Table 3. Variation in the ^{13}C NMR relaxation times [$\Delta T_1 = T_1$ (complex) – T_1 (ligand) (%)] for the ring carbon atoms of macrocycles **1c**, **2c**, **3c** and **3b** under complexation.

Complex	Chain	ΔT_1 [%]					
		C-2	C-3	OC-5	C-6	C-7	OCH_3
	1'	C-2'	C-3'	OC-5'	C-6'	C-7'	O'CH ₃
1c – Mg^{2+}	1/1'	–7	–8	–43	–23	–3	+12
1c – Ca^{2+}	1/1'	–47	–19	–76	–53	–56	–69
1c – Sr^{2+}	1/1'	–53	–69	–78	–24	–62	–44
2c – Ca^{2+}	1/1'	–72	–69	–67	–62	–75	–53
2c – Zn^{2+}	1/1'	–62	–72	–49	–70	–68	–54
3c – Ca^{2+}	1/1'	–47	–62	–61	–54	–58	–37
3b – Ca^{2+}	1	–68	–70	–76	–64	–68	–62
	1'	–51	–72	–66	–63	–68	–60

When a cation is bound to a ligand, a decrease in the longitudinal relaxation times of the carbon atoms and therefore in their mobility is generally observed.^[6b,6d] Thus, the complexation of **1c** by calcium and strontium led to decreased T_1 values for all carbon atoms compared with the free ligand. For each macro-ring carbon (except for C-3), these values are roughly equivalent in the two complexes. The ionic radii of calcium and strontium are almost identical (Ca : 0.99 Å; Sr : 1.10 Å) and so the conformational rearrangement occurring during the complexation was proba-

bly similar. The extent of the decrease in T_1 for the ring carbon atoms is in the order $\text{CO} > \text{C-7} > \text{C-2}$. This result indicates that the complexation occurred around the six oxygen atoms of the macrocycle: two CO, two OMe and two O-1 α to the cited carbon atoms.

For **1c**–Mg(ClO₄)₂, the increase in the longitudinal relaxation times for the OMe carbon atoms (12%) and the weak decrease in the C-2 and C-7 T_1 values (7 and 3%, respectively) reflects the probable non-involvement of the O-1 and OMe oxygen atoms in the binding. For this complex, only the T_1 of the CO carbon atom fell significantly (43%). Interactions between Mg²⁺ and the macrocycle **1c** thus seem to be different to those occurring during the Ca²⁺ and Sr²⁺ complexation of **1c**, probably because of the difference in their ionic radii (Table 3).

On complexation of **2c** by calcium and zinc, the T_1 values of all the carbon atoms were found to decrease. For the same carbon atom, these variations were similar, however, despite the difference in ionic radii of the two metals (Ca: 0.99 Å; Zn: 0.77 Å). Hence, the same oxygen atoms of the macrocycle were probably involved in the complexation.

For the **3c**–Ca²⁺ and **3b**–Ca²⁺ complexes, comparison of the ¹³C NMR longitudinal relaxation times revealed some differences between the two complexes, in contrast to their association constants, which were found to be in the same range (see above). As seen for other macrocycles, the T_1 values of the ring carbons fell significantly in both cases, but the decrease was greater for all the carbon atoms of the asymmetric isomer **3b**. In addition, concerning this last ligand, significant differences in the change in T_1 values were observed for some carbon atoms between the two chains: CO-5/CO-5' (76/66%) and C-2/C-2' (68/51%). This result again reflects a slightly weaker participation of one of the two parts of the molecule in the complexation, which underlines in the present case an additional slight difference between the two carbonyl bindings.

Conclusions

The IR and ¹³C NMR analyses of the studied complexes have given appreciable information on the coordination sites. It reveals the participation of the six oxygen atoms of the macrocycles in the complexation for five of the C₂-symmetrical complexes [**1c**–Ca(ClO₄)₂, **1c**–Sr(ClO₄)₂, **2c**–Ca(ClO₄)₂, **2c**–Zn(ClO₄)₂ and **3c**–Ca(ClO₄)₂]. In contrast, the binding process seems to involve essentially the carbonyl oxygen atoms in **1c**–Mg(ClO₄)₂, and preferentially one oxygen of each double function in the unsymmetrical **3b**–Ca(ClO₄)₂ complex. Also, in all the complexes, two of the oxygen atoms of the perchlorate anion apparently remain bound to the cation.

Conformational Analysis

¹H NMR Spectroscopic Data

An analysis of the splitting of 6-H^A and 6-H^B due to the coupling with 7-H proton showed that these hydrogen atoms exhibited identical patterns in the spectra of the com-

plexes and the free ligands,^[19] that is, i. as an ABX system in all the **1c**, **2c**, **3c** complexes and in **3b**–Ca (chain 1') with a downfield shift of the three protons under complexation (Table SI-2) and ii. as two doublets of doublets in **3b**–Ca (chain 1). Identical analysis of the 2-H^A and 2-H^B splittings in the complexes of the 3-monosubstituted compounds **1c** and **2c** also revealed a deshielding of hydrogen atoms 2-H^B and 3-H upon binding, in contrast with a shielding of 2-H^A. In addition, an inversion of the chemical shifts of the two methylene protons 2-H^A and 2-H^B was observed as the ratio [M]/[L] progressively increased. The corresponding patterns thus switched from two doublets of doublets with $\delta_{\text{H2A}} > \delta_{\text{H2B}}$ to two doublets of doublets with $\delta_{\text{H2B}} > \delta_{\text{H2A}}$ via ABX systems and a single doublet corresponding to the equivalence of the two protons for a specific [M]/[L] ratio that depends on the complex, for example, [M]/[L] \approx 1 for **1c**–Mg (see the Exp. Section). Such variations in the ring proton chemical shifts reflect a modification of the ring shape to favour the binding of the oxygen atoms with the cation.

Molecular Modelling

The molecular modelling study was performed on three couples: **1c**–Ca²⁺, **3c**–Ca²⁺ and **3b**–Ca²⁺. The Monte–Carlo calculations indicated some flexibility of the complexes. For **1c**–Ca²⁺ and **3c**–Ca²⁺, this flexibility was less than that of the corresponding free ligands, as expected in the case of appreciable complexation. The first 15 conformations were observed within 35–45 kJ mol^{–1} of the global minimum for **1c**–Ca²⁺ and **3c**–Ca²⁺, whereas they were in the range of around 11 kJ mol^{–1} for **1c** and **3c**. In contrast, the corresponding values for the complex **3b**–Ca²⁺ and its ligand **3b** were 4 and 6 kJ mol^{–1}, respectively, that is, relatively close, which reflects a weaker coordination (Table SI-4). As previously reported for the macrocycles,^[19] a greater energy difference was observed between the first two conformers than between the second and third ($\Delta E_{2-1} > \Delta E_{3-2}$). Hence, for the three complexes, the modelling study was initially conducted on the two first lowest-energy conformers and then exclusively on the first, because of the results obtained (see below).

A comparison of the conformations of the macrocycles **1c**, **3c** and **3b** and of their Ca complexes shows (Figure 3) i. the disappearance in the complexes of the N–H \cdots O hydrogen bonds present in the free ligands,^[19] ii. a rotation of one (**3b**–Ca) or both (**1c**–Ca, **3c**–Ca) NH–CO links, which adopt a position roughly perpendicular to the average macrocyclic plane in contrast to their previous parallel position in the ligands with, in the present cases, a slight orientation of the two carbonyl double bonds into the cavity whereas they are directed outwards in the macrocycles and iii. the orientation also inwards of all the ketal oxygen atoms, that is, not only of the endocyclic oxygen atoms O-1, O-1', which already occupy this position in the ligands, but also of the methoxy oxygen atoms, one in **3b**–Ca and both in **1c**–Ca and **3c**–Ca (Figures 3 and 4). These arrangements allow the binding of the six oxygen atoms of the symmetrical macrocycles **1c** and **3c** and of five of them in **3b**

with distances $d_{\text{Ca-O}}$ in the range 2.42–2.90 Å, the 7'-OMe oxygen of **3b** with $d_{\text{Ca-OMe}} \geq 4.88$ Å being excluded from the complexation process (Table SI-5). In addition, the distances $d_{\text{N-Ca}}$ (3.95–4.55 Å) confirm the impossibility of coordination between the metal and the nitrogen atoms of the lactam link, as mentioned above. The cation thus appeared to be located on the same side of the average macrocyclic plane as the two OMe groups in **1c**-Ca and **3c**-Ca and on the same side as the 7 α -OMe substituent in **3b**-Ca, the 7' β -OMe oxygen being almost in the ring plane in this last complex (Figure 4). The additional participation of the two anions in the complexes, as seen above, again gives Ca^{2+} eight (**1c**-Ca and **3c**-Ca) or seven (**3b**-Ca) coordination sites. These results agree closely with those obtained by the molecular modelling of macrocyclic polyether tetralactams/ $\text{Ca}(\text{ClO}_4)_2$ ^[3d] and by X-ray diffraction of diacetamide/ $\text{Ca}(\text{ClO}_4)_2$,^[3d,18a] 18-crown-6/ $\text{Ca}(\text{SCN})_2$,^[3d,20] trioxadilactam/ $\text{Ca}(\text{ClO}_4)_2$ ^[3g] and ETH 129/ $\text{Ca}(\text{SCN})_2$.^[3d,18b]

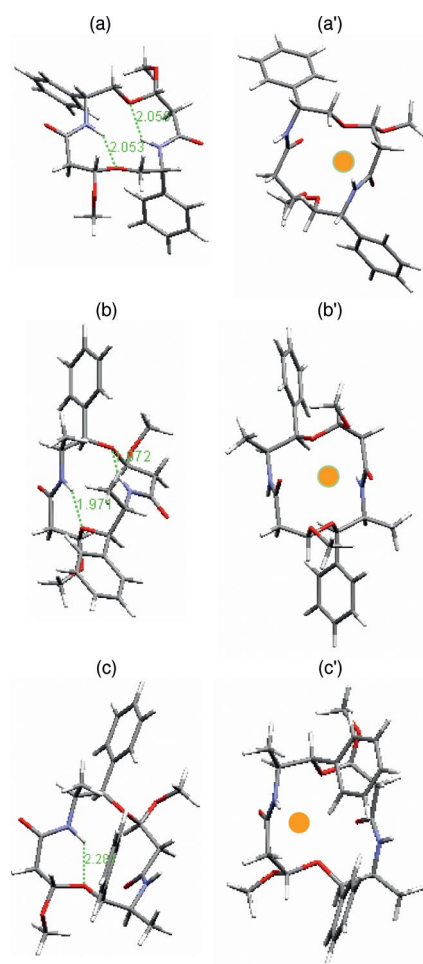


Figure 3. Top view representations of ligands **1c**, **3c** and **3b** (conformer 1) and of their Ca complexes (conformer 1) by molecular modelling: (a) **1c**, (a') **1c**- Ca^{2+} , (b) **3c**, (b') **3c**- Ca^{2+} , (c) **3b** and (c') **3b**- Ca^{2+} . In ligands **1c**, **3c** and **3b**, interatomic hydrogen bonds are indicated by green dashed lines with the corresponding interatomic distances.

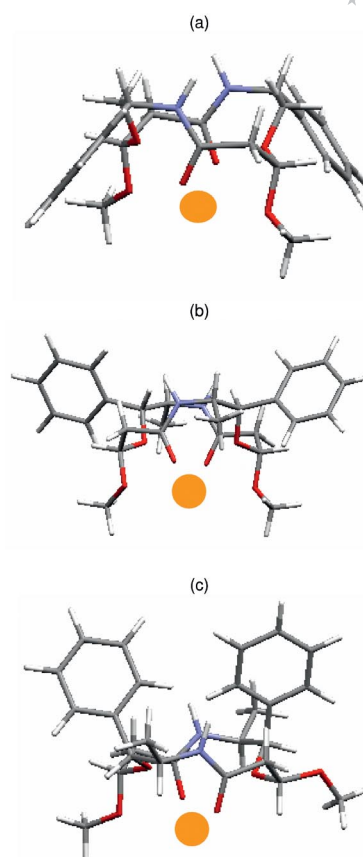


Figure 4. Representation of the complexes with a horizontal $\text{C}7\text{--C}7'$ axis by molecular modelling: (a) **1c**-Ca (conformer 1), (b) **3c**-Ca (conformer 1) and (c) **3b**-Ca (conformer 1).

Calculations, made on the basis of the measured distances $\text{Ca--C}5$, $\text{Ca--C}5'$ and $\text{C}5\text{--C}5'$, positioned the cation about 2.1–2.2 Å below the $\text{C}5\text{--C}5'$ axis in the three complexes **1c**-Ca, **3c**-Ca and **3b**-Ca (Table SI-6). Also, the identical values of the distances $\text{O}1\text{--Ca}$, $\text{C}5\text{O--Ca}$, MeO--Ca and $\text{N}4\text{--Ca}$ for chains 1 and 1' of **1c**-Ca and **3c**-Ca (Table SI-5) testified to the total symmetry of their conformers 1, in agreement with the above NMR spectroscopic data. This symmetry was not exhibited by conformers 2, which were therefore no longer taken into consideration.

The torsion angles of the complexes are reported in Table 4 along with those previously measured for the macrocycles.^[19] First, these angles confirm the C_2 symmetry of **1c**-Ca and **3c**-Ca, as previously observed for the free ligands. Secondly, all the complexes exhibit, like the free ligands, i. *trans* conformations *t* along the two bonds $\text{C}3\text{--N}4\text{--CO--C}6$ corresponding to the amide functions (torsion angle range: 171–179°) and the two bonds $\text{C}7'\text{--O}1\text{--C}2\text{--C}3$ (torsion angle range: 121–178°) and ii. *gauche* conformations *g* (positive value) or *g'* (negative value) along the bonds $\text{O}1\text{--C}2\text{--C}3\text{--N}4$ (torsion angle range: 40–62°) and $\text{C}5\text{--C}6\text{--C}7\text{--O}1'$ (torsion angle range: 52–73°). In contrast, the values of the $\text{C}2\text{--C}3\text{--N}4\text{--C}5$, $\text{N}4\text{--C}5\text{--C}6\text{--C}7$ and $\text{C}6\text{--C}7\text{--O}1'\text{--C}2'$ angles, which range from 41 to 177°, are different for the free and complexed molecules, reflecting a

Table 4. Torsion angles τ for diketal dilactam macrocycles **1c**, **3c**, **3b** and their Ca complexes (conformer 1; $+40^\circ < g < +98^\circ$, $-40^\circ < g' < -98^\circ$, $\pm 121^\circ < t < \pm 180^\circ$).

Complex	Chain	τ [$^\circ$]							Nomenclature	Structure
	1	C7'-O1-	O1-C2-	C2-C3-	C3-N4-	N4-C5-	C5-C6-	C6-C7-		
		C2-C3	C3-N4	N4-C5	C5-C6	C6-C7	C7-O8	O1'-C2'		
	1'	C7-O1'-	O1'-C2'-	C2'-C3'-	C3'-N4'-	N4'-C5'-	C5'-C6'-	C6'-C7'-		
		C2'-C3'	C3'-N4'	N4'-C5'	C5'-C6'	C6'-C7'	C7'-O1	O1-C2		
1c cf. 1	1	+176	+51	+155	+178	+47	-71	+175	tggtgg'-t-gtggg't	En Ic ^[a]
	1'	+176	+51	+155	+178	+47	-71	+175		
1c -Ca cf. 1	1	+169	+60	-80	+175	-126	+52	+80	tggttgg-tgg'ttgg	En IIIc ^[a]
	1'	+169	+60	-80	+175	-126	+52	+80		
3c cf. 1	1	+121	-60	-78	-177	-41	+68	-176	tg'g'tg'-gt-tg'g'tg'gt	IIc
	1'	+121	-60	-78	-177	-41	+68	-176		
3c -Ca cf. 1	1	-178	-62	+79	-179	+123	-53	-68	tg'gttg'g'-tg'gttg'g'	IIIc
	1'	-178	-62	+79	-179	+123	-53	-68		
3b cf. 1	1	+143	-52	-151	+175	+62	-73	+177	tg'ttgg'-t-tgg'ttgg	Ib
	1'	+158	+59	-93	+179	-122	+70	-171		
3b -Ca cf. 1	1	+170	+62	-90	+171	-129	+57	+131	tggttgg-tgg'ttgg	IIb
	1'	+164	+40	-91	+177	-141	+59	+98		

[a] En: enantiomer with the (3*R*,10*R*) configuration for phenyl macrocycle **1c** and its complex **1c**-Ca. To make a comparison with the (2*R*,3*S*,10*S*) series **3c** and **3b**, we have to consider the (3*S*,10*S*) enantiomers of **1c** and **1c**-Ca, the designations of which are tg'ttgg'-tg'gttg'g' and tg'gttg'g'-tg'gttg'g', respectively.

rotation of the C3-N4, C5-C6 and C7-O1' bonds during the binding process, that is, of the ring bonds α to the CO-NH moieties and the OMe groups.

A conformation apparently close to the [3434] or tgggtg'g'tg'g'ttgg strain-free "rectangular" diamond lattice structure of the 14-membered-ring compounds^[19,21,22] was observed for the *cis*-OMe complexes **1c**-Ca and **3c**-Ca (structure IIIc). Instead of the four corners that characterize the above ideal structure and that are defined by a gg or g'g' sequence, the two complexes present two corners at C-7, C-7' and two "pseudo-corners" defined by a gg' or g'g sequence at C-3, C-3'. In addition, the presence of hybrid angles (126 and 123 $^\circ$) somewhat distant from the theoretical value for pure *trans* conformations (ca. 180 $^\circ$) reveals a distortion from the potential rectangular shape. Moreover, both complexes present a C_2 symmetry axis and not the symmetry center required for a true [3434] conformation. In both couples, the O-1, O-1' atoms are located on "three-bond" sides and the amide links on the "four-bond" sides (Figure 3). In contrast, in **3b**-Ca, the two chains of the molecule, which are involved in the complexation differently, adopt two different conformations but both present a "pseudo-corner" at C3.

Characterization of the Complexes by Mass Spectrometry

In addition to the IR and NMR spectroscopic data (^1H and ^{13}C) reported above, we performed a complementary characterization of our complexes by mass spectrometry.

The identification of the different species present in the coordinated compounds by MS requires the use of soft ionization/desorption techniques such as FAB-MS,^[7a,7b,7f] LSIMS^[6e,6f,7c,7d] and ESI-MS in the positive mode.^[3f,7b,7e]

The study was conducted using the electrospray process with a mass resolution of ≈ 1000 (solvent: CH_3OH , $c \approx 10^{-4}$ M, $t = 30^\circ\text{C}$) on the following ligand-cation pairs: **1c**-

Mg^{2+} , **1c**- Ca^{2+} , **1c**- Sr^{2+} , **1c**- Ba^{2+} , **1c**- Zn^{2+} , **2c**- Ca^{2+} , **2c**- Sr^{2+} , **2c**- Zn^{2+} , **3c**- Ca^{2+} and **3b**- Ca^{2+} . The results show the presence of essentially three doubly charged species $[\text{ML}]^{2+}$, $[\text{ML}_2]^{2+}$ and $[\text{ML}_3]^{2+}$ in various ratios with, as the major peak, in six cases the $[\text{ML}]^{2+}$ ion corresponding to a M/L stoichiometry of 1:1 (Table SI-7). However, none of the species detected here can be considered as representative of the initial complex composition. Indeed, the amounts of the different ions were observed to vary with the injection conditions: a stronger concentration increased the percentage of the $[\text{ML}_2]^{2+}$ and $[\text{ML}_3]^{2+}$ ions, which, in large part, were probably formed in the source during the ionization process, whereas a higher temperature (50 $^\circ\text{C}$) or a weaker concentration ($c = 10^{-5}$ M) favoured the formation of $[\text{L} + \text{Na}^+]$ species due to cationization of the ligand by the sodium present in the solvent system.

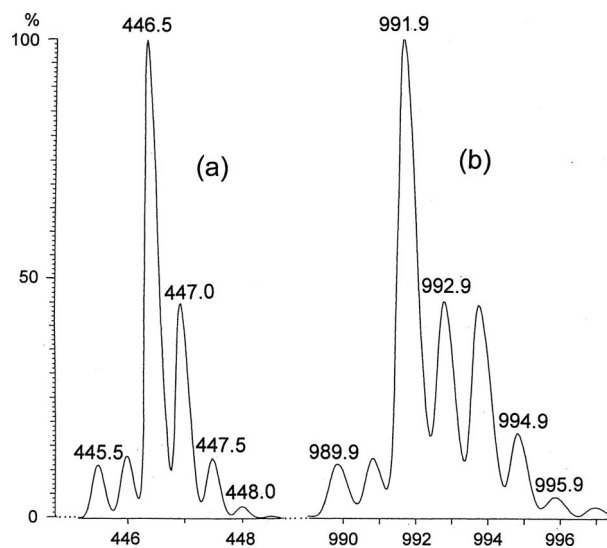


Figure 5. ESI mass spectrum of **2c**-Sr: isotopic profiles for (a) $[\text{ML}_2]^{2+}$ and (b) $[\text{ML}_2, \text{ClO}_4]^+$.

To ascertain the charge z of the ions obtained and then identify them without ambiguity, an additional study was performed with a mass resolution of about 5000 for the two complexes **2c**-Ca²⁺ and **2c**-Sr²⁺ taken as examples. Under the conditions used (solvent: CH₃CN, $c = 10^{-5}$ M, $t = 25$ °C), four main peaks characterizing the complexes were detected in both cases: [ML₂]²⁺, [ML₂·2HClO₄]²⁺, [ML₃]²⁺ and [ML₂·ClO₄]⁺. The isotopic patterns for [ML₂]²⁺ and [ML₂·ClO₄]⁺ are reproduced in Figure 5 (complex **2c**-Sr) and the data are presented in Table SI-8. For each ion, the charge state z could be deduced from the mass difference Δm between two successive isotopic peaks by $z = 1/\Delta m$. Thus, even if mass spectrometry does not lead to the exact complex composition, it contributes to a more complete characterization.

Conclusions

We have described the complexing behaviour towards divalent cations of a new class of 14-membered-ring ligands bearing two acetal and secondary amide functions. The stoichiometries and binding constants of the complexes were determined by ¹H NMR spectrometry. The results obtained indicate, in agreement with a previous UV/Vis study,^[8] that i. the complexes formed were essentially of the ML type sometimes accompanied by a small percentage of ML₂ species and ii. the best complexation occurred with Sr²⁺ and Ca²⁺, the ionic radii of which are close to 1 Å.

The coordination sites were identified by IR and ¹³C NMR spectroscopy using, in particular, the ¹³C longitudinal relaxation times, whereas a conformational study was undertaken by using ¹H NMR and molecular modelling methods. All the data obtained from these studies revealed a complete reorganization of the molecules during the binding process through the breaking of the hydrogen bonds in the free ligands and a rotation of the NH-CO moieties. They also underlined the participation in the complexation of i. all six oxygen atoms of the molecules in most of the *cis*-OMe complexes of C₂ symmetry or five of them in the unsymmetrical *trans*-OMe complex **3b**-Ca, and ii. probably two oxygen atoms of the perchlorate anion. Consequently, the calcium binding sites in all the complexes consist of seven or eight metal-bound oxygen atoms.

Finally, in addition to the IR and NMR spectroscopic data, a complementary characterization of the complexes was carried out by ESI mass spectrometry in the positive ion mode.

Experimental Section

General: Metal perchlorates Mg(ClO₄)₂, [Ca(ClO₄)₂·6H₂O], [Sr(ClO₄)₂·6H₂O], [Ba(ClO₄)₂·3H₂O] and [Zn(ClO₄)₂·6H₂O] were purchased from STREM and dried under vacuum in the presence of P₂O₅ at room temperature for 48 h prior to use. ¹H and ¹³C NMR spectra were recorded with Bruker Avance 400 and DSX 300 spectrometers, respectively. The solvent CD₃CN was used as the internal reference (¹H: $\delta = 1.94$ ppm; ¹³C: $\delta = 118.26$ ppm).^[23] Values of δ are given in ppm and J in Hz. Proton and carbon reso-

nances were assigned on the basis of the numbering indicated in Figure 1. Splitting patterns were designated as follows: s, singlet; d, doublet; t, triplet; q, quartet; m, multiplet. The IR analyses were conducted in 16 scans on a FT-IR Nicolet 55XC spectrophotometer with OMNIC software with samples in KBr pellets previously dried under vacuum. ES⁺ mass spectra were recorded with a Hewlett-Packard 5989B mass spectrometer (solvent: CH₃OH, $c \approx 10^{-4}$ M, $t = 30$ °C, flow rate: 10 μ L min⁻¹, cone voltage: 20 V) and for two complexes (**2c**-Ca²⁺ and **2c**-Sr²⁺) with a ZabSpec Micro-mass spectrometer (solvent: CH₃CN, $c \approx 10^{-5}$ M, $t = 25$ °C, flow rate: 5 μ L min⁻¹, cone voltage: 15 V) with nitrogen as nebulizing and desolvation gas. HRMS (ES⁺) of complexes **3c**-Ca²⁺ and **3b**-Ca²⁺ were recorded with a micro Q-TOF Waters spectrometer (solvent: CH₃CN, $c \approx 5 \times 10^{-5}$ M, $t = 50$ °C, flow rate: 50 μ L min⁻¹, cone voltage: 30 V).

Synthesis of Macrocycles 1c, 2c, 3c and 3b: The 14-membered-ring diketal dilactams were synthesized and recrystallized as described previously.^[9a] Their IR and NMR (¹H, ¹³C) data, already reported in CHCl₃ and CDCl₃, respectively,^[9a] are given here in KBr pellets and in CD₃CN.

Macrocycle 1c: IR (KBr): $\tilde{\nu} = 3325$ (NH), 1645 (C=O) cm⁻¹. ¹H NMR (400 MHz, CD₃CN, 22 °C): $\delta = 2.52$ (ABX, AB part, ² $J = 14.1$, ³ $J = 7.2$, 2.2, $\Delta\nu = 28.3$ Hz, 4 H, 6-H^B, 6-H^A, 6'-H^B, 6'-H^A), 3.18 (s, 6 H, 2 OCH₃), 3.71 (dd, ² $J = 9.8$, ³ $J = 3.4$ Hz, 2 H, 2-H^B, 2'-H^B), 3.98 (dd, ² $J = 9.8$, ³ $J = 6.5$ Hz, 2 H, 2-H^A, 2'-H^A), 4.76 (ABX, X part, ³ $J = 7.2$, 2.2 Hz, 2 H, 7-H, 7'-H), 5.15 (ddd, ³ $J = 8.0$, 6.5, 3.4 Hz, 2 H, 3-H, 3'-H), 7.26–7.44 (m, 10 H, 10 Ar-H), 7.49 (d, ³ $J = 8.0$ Hz, 2 H, NH, NH') ppm. ¹³C NMR (75 MHz, CD₃CN, 30 °C): $\delta = 42.0$ (C-6, C-6'), 53.8 (C-3, C-3'), 54.3 (2 OCH₃), 72.2 (C-2, C-2'), 102.9 (C-7, C-7'), 127.8 (4 Ar-CH), 128.3 (2 Ar-CH), 129.3 (4 Ar-CH), 140.9 (2 Ar-C), 170.1 (2 CO) ppm.

Macrocycle 2c: IR (KBr): $\tilde{\nu} = 3335$ (NH lactam), 1643 (C=O) cm⁻¹. ¹H NMR (400 MHz, CD₃CN, 22 °C): $\delta = 0.90$ (d, ³ $J = 6.7$ Hz, 6 H, CH₃, CH₃'), 0.91 (d, ³ $J = 6.8$ Hz, 6 H, CH₃, CH₃'), 1.31 (ddd, ² $J = 13.7$, ³ $J = 8.1$, 5.9 Hz, 2 H, 8-H^B, 8'-H^B), 1.50 (ddd, ² $J = 13.7$, ³ $J = 9.2$, 6.0 Hz, 2 H, 8-H^A, 8'-H^A), 1.62 (m, 2 H, 9-H, 9'-H), 2.42 (ABX, AB part, ² $J = 14.0$, ³ $J = 8.0$, 1.8, $\Delta\nu = 55.6$ Hz, 4 H, 6-H^B, 6'-H^B, 6-H^A, 6'-H^A), 3.28 (s, 6 H, 2 OCH₃), 3.43 (dd, ² $J = 9.4$, ³ $J = 2.9$ Hz, 2 H, 2-H^B, 2'-H^B), 3.63 (dd, ² $J = 9.4$, ³ $J = 3.8$ Hz, 2 H, 2-H^A, 2'-H^A), 4.07 (m, 2 H, 3-H, 3'-H), 4.63 (ABX, X part, ³ $J = 8.0$, 1.8 Hz, 2 H, 7-H, 7'-H), 6.66 (d, ³ $J = 8.4$ Hz, 2 H, NH, NH') ppm. ¹³C NMR (75 MHz, CD₃CN, 30 °C): $\delta = 22.5$ (2 CH₃), 23.2 (2 CH₃), 25.5 (C-9, C-9'), 41.4 (C-8, C-8'), 42.3 (C-6, C-6'), 47.7 (C-3, C-3'), 53.2 (2 OCH₃), 70.7 (C-2, C-2'), 102.3 (C-7, C-7'), 169.2 (2 CO) ppm.

Macrocycle 3c: IR (KBr): $\tilde{\nu} = 3390$, 3300 (NH lactam), 1651 (C=O) cm⁻¹. ¹H NMR (400 MHz, CD₃CN, 22 °C): $\delta = 0.96$ (d, ³ $J = 6.9$ Hz, 6 H, CH₃, CH₃'), 2.50 (dd, ² $J = 14.8$, ³ $J = 5.7$ Hz, 2 H, 6-H^B, 6'-H^B), 2.69 (dd, ² $J = 14.8$, ³ $J = 2.5$ Hz, 2 H, 6-H^A, 6'-H^A), 3.12 (s, 6 H, 2 OCH₃), 4.30 (m, 2 H, 3-H, 3'-H), 4.76 (d, ³ $J = 3.0$ Hz, 2 H, 2-H, 2'-H), 4.96 (dd, ³ $J = 5.7$, 2.5 Hz, 2 H, 7-H, 7'-H), 6.87 (d, ³ $J = 8.8$ Hz, 2 H, NH, NH'), 7.30–7.46 (m, 10 H, 10 Ar-H) ppm. ¹³C NMR (75 MHz, CD₃CN, 30 °C): $\delta = 15.4$ (CH₃, CH₃'), 42.5 (C-6, C-6'), 49.6 (C-3, C-3'), 55.0 (2 OCH₃), 84.1 (C-2, C-2'), 103.7 (C-7, C-7'), 128.3 (4 Ar-CH), 128.7 (2 Ar-CH), 129.0 (4 Ar-CH), 139.8 (2 Ar-C), 169.4 (2 CO) ppm.

Macrocycle 3b: IR (KBr): $\tilde{\nu} = 3395$, 3305 (NH lactam), 1651 (C=O) cm⁻¹. ¹H NMR (400 MHz, CD₃CN, 25 °C): $\delta = 0.92$ (d, ³ $J = 6.9$ Hz, 3 H, CH₃'), 1.05 (d, ³ $J = 6.9$ Hz, 3 H, CH₃), 2.45 (dd, ² $J = 14.7$, ³ $J = 1.6$ Hz, 1 H, 6-H^B), 2.57 (ABX, AB part, ² $J = 14.9$, ³ $J = 7.8$, 1.9, $\Delta\nu = 63.1$ Hz, 2 H, 6'-H^B, 6'-H^A), 2.68 (dd, ² $J = 14.7$, ³ $J = 7.2$ Hz, 1 H, 6-H^A), 3.06 (s, 3 H, O'CH₃), 3.28 (s, 3 H, OCH₃),

3.96 (m, 1 H, 3-H), 4.40 (dd, $^3J = 7.2$, 1.6 Hz, 1 H, 7-H), 4.45 (m, 1 H, 3'-H), 4.79 (d, $^3J = 2.4$ Hz, 1 H, 2-H), 4.90 (ABX, X part, $^3J = 7.8$, 1.9 Hz, 1 H, 7'-H), 4.98 (d, $^3J = 3.3$ Hz, 1 H, 2'-H), 6.54 (d, $^3J = 8.4$ Hz, 1 H, NH'), 7.30–7.45 (m, 11 H, NH, 10 Ar-H) ppm. ^{13}C NMR (75 MHz, CD_3CN , 30 °C): $\delta = 13.4$ (CH_3), 15.9 (CH_3'), 42.1 (C-6), 42.5 (C-6'), 49.5 (C-3'), 51.9 (C-3), 54.4 (OCH_3), 55.1 ($\text{O}'\text{CH}_3$), 78.9 (C-2'), 83.5 (C-2), 98.4 (C-7), 104.8 (C-7'), 127.7 (2 C), 128.3 (2 C'), 128.8 (1 C'), 129.0 (2 C'), 129.1 (1 C), 129.3 (2 C, 10 Ar-CH), 137.4 (Ar-C'), 141.4 (Ar-C), 168.8 (CO), 169.4 (CO') ppm.

Synthesis of the Complexes: The complexes were prepared by mixing equimolar 0.02 M solutions of macrocycles **1**, **2**, **3a** and **3b** in acetonitrile and metal perchlorates $\text{M}(\text{ClO}_4)_2$ in acetonitrile. Most of the solvent was evaporated under reduced pressure and the complexes were precipitated by addition of diethyl ether. The solids were filtered, washed with diethyl ether and vacuum dried.

Complex [1c–Mg(ClO₄)₂]: This complex was prepared from macrocycle **1c** (35.4 mg, 0.08 mmol) and $\text{Mg}(\text{ClO}_4)_2$ (17.8 mg, 0.08 mmol) in acetonitrile (8 mL) according to the general procedure (evaporation of the solvent to about $1/3$ of the initial volume). The complex was isolated as a pale-yellow solid (41.9 mg, 71 %); m.p. 223–226 °C (dec.). IR (KBr): $\tilde{\nu} = 1639$ (C=O), 1145, 1114, 1089 (Cl–O) cm^{-1} . ^1H NMR (400 MHz, CD_3CN , 22 °C): $\delta = 2.61$ (dd, $^2J = 14.4$, $^3J = 2.4$ Hz, 2 H, 6-H^B, 6'-H^B), 2.66 (ABX, AB part, $^2J = 14.4$, $^3J = 8.1$, 2.2, $\Delta\nu = 42.2$ Hz, 4 H, 6-H^B, 6'-H^B, 6-H^A, 6'-H^A), 3.26 (s, 6 H, 2 OCH_3), 3.83 (d, $^3J = 6.5$ Hz, 4 H, 2-H^B, 2'-H^B, 2-H^A, 2'-H^A), 5.08 (ABX, X part, $^2J = 8.1$, 2.2 Hz, 2 H, 7-H, 7'-H), 5.31 (dt, $^3J = 9.0$, 6.5 Hz, 2 H, 3-H, 3'-H), 7.29–7.43 (m, 10 H, 10 Ar-H), 7.80 (d, $^3J = 9.0$ Hz, 2 H, NH, NH') ppm. ^{13}C NMR (75 MHz, CD_3CN , 30 °C): $\delta = 41.7$ (C-6, C-6'), 53.9 (C-3, C-3'), 54.0 (2 OCH_3), 72.1 (C-2, C-2'), 102.6 (C-7, C-7'), 127.7 (4 Ar-CH), 128.3 (2 Ar-CH), 129.3 (4 Ar-CH), 140.5 (2 Ar-C), 170.7 (2 CO) ppm. MS (ES^+): m/z (%) = 233 (81) [$\text{L} + \text{Mg}^{2+}$], 259 (72), 265 (75), 271 (93), 285 (44), 333 (47) [$\text{L} + \text{Mg} + 2\text{HClO}_4^{2+}$], 429 (62), 454 (100) [$2\text{L} + \text{Mg}^{2+}$], 675 (10) [$3\text{L} + \text{Mg}^{2+}$]. $\text{MgC}_{24}\text{H}_{30}\text{N}_2\text{O}_{14}\text{Cl}_2\cdot 4\text{H}_2\text{O} = \text{C}_{24}\text{H}_{38}\text{Cl}_2\text{MgN}_2\text{O}_{18}$ (737.79): calcd. C 39.07, H 5.19, N 3.80; found C 38.60, H 5.11, N 3.53.

Complex [1c–Ca(ClO₄)₂]: This complex was prepared from macrocycle **1c** (35.4 mg, 0.08 mmol) and $[\text{Ca}(\text{ClO}_4)_2\cdot 6\text{H}_2\text{O}]$ (27.8 mg, 0.08 mmol) in acetonitrile (8 mL) according to the general procedure (evaporation of the solvent to about $1/3$ of the initial volume). The complex was isolated as a white solid (45.9 mg, 82 %); m.p. 174–180 °C. IR (KBr): $\tilde{\nu} = 1640$ (C=O), 1145, 1115, 1088 (Cl–O) cm^{-1} . ^1H NMR (400 MHz, CD_3CN , 22 °C): $\delta = 2.66$ (ABX, AB part, $^2J = 14.1$, $^3J = 8.8$, 2.3, $\Delta\nu = 37.2$ Hz, 4 H, 6-H^B, 6'-H^B, 6-H^A, 6'-H^A), 3.27 (s, 6 H, 2 OCH_3), 3.77 (ABX, AB part, $^2J = 12.5$, $^3J = 11.0$, 3.1, $\Delta\nu = 51.9$ Hz, 4 H, 2-H^B, 2'-H^B, 2-H^A, 2'-H^A), 5.21 (ABX, X part, $^3J = 8.8$, 2.3 Hz, 2 H, 7-H, 7'-H), 5.30 (m, 2 H, 3-H, 3'-H), 7.25–7.38 (m, 10 H, 10 Ar-H), 7.79 (d, $^3J = 9.8$ Hz, 2 H, NH, NH') ppm. ^{13}C NMR (75 MHz, CD_3CN , 30 °C): $\delta = 41.3$ (C-6, C-6'), 52.9 (C-3, C-3', 2 OCH_3), 70.7 (C-2, C-2'), 100.5 (C-7, C-7'), 127.6 (4 Ar-CH), 128.6 (2 Ar-CH), 129.5 (4 Ar-CH), 139.4 (2 Ar-C), 171.0 (2 CO) ppm. MS (ES^+): m/z (%) = 241 (100) [$\text{L} + \text{Ca}^{2+}$], 290 (25), 330 (24), 341 (20) [$\text{L} + \text{Ca} + 2\text{HClO}_4^{2+}$], 351 (9) [$3\text{L} + 2\text{Ca}^{2+}$], 362 (22), 388 (23), 454 (33), 462 (26) [$2\text{L} + \text{Ca}^{2+}$], 465 (16) [$\text{L} + \text{Na}^+$], 562 (19) [$2\text{L} + \text{Ca} + 2\text{HClO}_4^{2+}$], 573 (11) [$5\text{L} + 2\text{Ca}^{2+}$], 581 (14) [$\text{L} + \text{CaClO}_4^+$], 683 (17) [$3\text{L} + \text{Ca}^{2+}$]. $\text{CaC}_{24}\text{H}_{30}\text{N}_2\text{O}_{14}\text{Cl}_2\cdot \text{H}_2\text{O} = \text{C}_{24}\text{H}_{32}\text{CaCl}_2\text{N}_2\text{O}_{15}$ (699.51): calcd. C 41.21, H 4.61, N 4.01; found C 41.67, H 5.06, N 4.16.

Complex [1c–Sr(ClO₄)₂]: This complex was prepared from macrocycle **1c** (35.4 mg, 0.08 mmol) and $[\text{Sr}(\text{ClO}_4)_2\cdot 6\text{H}_2\text{O}]$ (31.6 mg, 0.08 mmol) in acetonitrile (8 mL) according to the general pro-

cedure (evaporation of the solvent to about $1/3$ of the initial volume). The complex was isolated as a white solid (52.6 mg, 84 %); m.p. 208–211 °C (dec.). IR (KBr): $\tilde{\nu} = 1640$ (C=O), 1146, 1115, 1088 (Cl–O) cm^{-1} . ^1H NMR (400 MHz, CD_3CN , 22 °C): $\delta = 2.58$ (ABX, AB part, $^2J = 14.1$, $^3J = 8.9$, 2.2, $\Delta\nu = 37.6$ Hz, 4 H, 6-H^B, 6'-H^B, 6-H^A, 6'-H^A), 3.28 (s, 6 H, 2 OCH_3), 3.67 (dd, $^2J = 12.4$, $^3J = 10.9$ Hz, 2 H, 2-H^A, 2'-H^A), 3.86 (dd, $^2J = 12.4$, $^3J = 3.1$ Hz, 2 H, 2-H^B, 2'-H^B), 5.18 (ABX, X part, $^3J = 8.9$, 2.2 Hz, 2 H, 7-H, 7'-H), 5.31 (ddd, $^3J = 10.9$, 9.9, 3.1 Hz, 2 H, 3-H, 3'-H), 7.31–7.41 (m, 10 H, 10 Ar-H), 7.55 (d, $^3J = 9.9$ Hz, 2 H, NH, NH') ppm. ^{13}C NMR (75 MHz, CD_3CN , 30 °C): $\delta = 41.1$ (C-6, C-6'), 52.0 (C-3, C-3'), 52.5 (2 OCH_3), 69.8 (C-2, C-2'), 99.5 (C-7, C-7'), 127.6 (4 Ar-CH), 128.6 (2 Ar-CH), 129.5 (4 Ar-CH), 139.1 (2 Ar-C), 170.8 (2 CO) ppm. MS (ES^+): m/z (%) = 265 (100) [$\text{L} + \text{Sr}^{2+}$], 274 (44), 285 (33), 314 (54), 458 (61), 465 (64) [$\text{L} + \text{Na}^+$], 486 (64) [$2\text{L} + \text{Sr}^{2+}$], 504 (36), 523 (27), 552 (69), 610 (60), 707 (52) [$3\text{L} + \text{Sr}^{2+}$]. $\text{SrC}_{24}\text{H}_{30}\text{N}_2\text{O}_{14}\text{Cl}_2\cdot 3\text{H}_2\text{O} = \text{C}_{24}\text{H}_{36}\text{Cl}_2\text{N}_2\text{O}_{17}\text{Sr}$ (783.08): calcd. C 36.81, H 4.63, N 3.58; found C 36.63, H 4.32, N 3.49.

Complex [1c–Ba(ClO₄)₂]: This complex was prepared from macrocycle **1c** (35.4 mg, 0.08 mmol) and $[\text{Ba}(\text{ClO}_4)_2\cdot 3\text{H}_2\text{O}]$ (31.2 mg, 0.08 mmol) in acetonitrile (8 mL) according to the general procedure (evaporation of the solvent to about $1/3$ of the initial volume). The complex was isolated as a white solid (44.0 mg, 69 %); m.p. 164–170 °C. IR (KBr): $\tilde{\nu} = 1644$ (C=O), 1144, 1114, 1089 (Cl–O) cm^{-1} . ^1H NMR (400 MHz, CD_3CN , 22 °C): $\delta = 2.55$ (ABX, AB part, $^2J = 14.0$, $^3J = 8.6$, 2.2, $\Delta\nu = 41.4$ Hz, 4 H, 6-H^B, 6'-H^B, 6-H^A, 6'-H^A), 3.26 (s, 6 H, 2 OCH_3), 3.77 (ABX, AB part, $^2J = 12.0$, $^3J = 9.8$, 3.0, $\Delta\nu = 47.4$ Hz, 4 H, 2-H^B, 2'-H^B, 2-H^A, 2'-H^A), 5.13 (ABX, X part, $^3J = 8.6$, 2.2, 2 H, 7-H, 7'-H), 5.29 (m, 2 H, 3-H, 3'-H), 7.30–7.40 (m, 10 H, 10 Ar-H), 7.48 (d, $^3J = 9.4$ Hz, 2 H, NH, NH') ppm. MS (ES^+): m/z (%) = 290 (100) [$\text{L} + \text{Ba}^{2+}$], 322 (61), 351 (49), 600 (52), 640 (41), 653 (54), 662 (29), 732 (67) [$3\text{L} + \text{Ba}^{2+}$]. $\text{BaC}_{24}\text{H}_{30}\text{N}_2\text{O}_{14}\text{Cl}_2\cdot \text{H}_2\text{O} = \text{C}_{24}\text{H}_{32}\text{BaCl}_2\text{N}_2\text{O}_{15}$ (796.77): calcd. C 36.18, H 4.05, N 3.52; found C 36.04, H 4.44, N 3.20.

Complex [1c–Zn(ClO₄)₂]: This complex was prepared from macrocycle **1c** (35.4 mg, 0.08 mmol) and $[\text{Zn}(\text{ClO}_4)_2\cdot 6\text{H}_2\text{O}]$ (29.8 mg, 0.08 mmol) in acetonitrile (8 mL) according to the general procedure (evaporation of the solvent to about $1/3$ of the initial volume). The complex was isolated as a brownish solid (35.6 mg, 63 %); m.p. 200–205 °C. IR (KBr): $\tilde{\nu} = 1615$ (C=O), 1146, 1115, 1088 (Cl–O) cm^{-1} . ^1H NMR (400 MHz, CD_3CN , 22 °C): $\delta = 2.55$ (ABX, AB part, $^2J = 14.2$, $^3J = 7.3$, 2.0, $\Delta\nu = 29.4$ Hz, 4 H, 6-H^B, 6'-H^B, 6-H^A, 6'-H^A), 3.20 (s, 6 H, 2 OCH_3), 3.74 (dd, $^2J = 10.1$, $^3J = 3.2$ Hz, 2 H, 2-H^B, 2'-H^B), 3.97 (dd, $^2J = 10.1$, $^3J = 6.9$ Hz, 2 H, 2-H^A, 2'-H^A), 4.82 (ABX, X part, $^3J = 7.3$, 2.0 Hz, 2 H, 7-H, 7'-H), 5.17 (ddd, $^3J = 8.1$, 6.9, 3.2 Hz, 2 H, 3-H, 3'-H), 7.27–7.42 (m, 10 H, 10 Ar-H), 7.57 (d, $^3J = 8.1$ Hz, 2 H, NH, NH') ppm. MS (ES^+): m/z (%) = 253 (100) [$\text{L} + \text{Zn}^{2+}$], 293 (89), 407 (77), 591 (49), 695 (71) [$3\text{L} + \text{Zn}^{2+}$]. $\text{C}_{24}\text{H}_{30}\text{Cl}_2\text{N}_2\text{O}_{14}\text{Zn}$ (706.79): calcd. C 40.79, H 4.28, N 3.96; found C 41.28, H 4.73, N 4.31.

Complex [2c–Ca(ClO₄)₂]: This complex was prepared from macrocycle **2c** (32.2 mg, 0.08 mmol) and $[\text{Ca}(\text{ClO}_4)_2\cdot 6\text{H}_2\text{O}]$ (27.8 mg, 0.08 mmol) in acetonitrile (8 mL) according to the general procedure (evaporation of the solvent to about $1/4$ of the initial volume). The complex was isolated as a white solid (42.1 mg, 82 %); m.p. 155–156 °C. IR (KBr): $\tilde{\nu} = 1637$ (C=O), 1147, 1119, 1087 (Cl–O) cm^{-1} . ^1H NMR (400 MHz, CD_3CN , 22 °C): $\delta = 0.87$ (d, $^3J = 6.9$ Hz, 6 H, CH_3 , CH_3'), 0.90 (d, $^3J = 6.9$ Hz, 6 H, CH_3 , CH_3'), 1.16 (ddd, $^2J = 13.9$, $^3J = 8.9$, 4.6 Hz, 2 H, 8-H^B, 8'-H^B), 1.26 (ddd, $^2J = 13.9$, $^3J = 9.8$, 5.2 Hz, 2 H, 8-H^A, 8'-H^A), 1.59 (m, 2 H, 9-H, 9'-H), 2.51 (ABX, AB part, $^2J = 13.7$, $^3J = 8.3$, 1.8, $\Delta\nu = 25.1$ Hz,

4 H, 6-H^B, 6'-H^B, 6-H^A, 6'-H^A), 3.25 (dd, $^2J = 12.2$, $^3J = 10.7$ Hz, 2 H, 2-H^A, 2'-H^A), 3.27 (s, 6 H, 2 OCH₃), 3.66 (dd, $^2J = 12.2$, $^3J = 2.5$ Hz, 2 H, 2-H^B, 2'-H^B), 4.20 (m, 2 H, 3-H, 3'-H), 4.99 (ABX, X part, $^2J = 8.3$, 1.8 Hz, 2 H, 7-H, 7'-H), 7.00 (d, $^3J = 9.6$ Hz, 2 H, NH, NH') ppm. ¹³C NMR (75 MHz, CD₃CN, 30 °C): $\delta = 22.3$ (2 CH₃), 23.3 (2 CH₃), 25.4 (C-9, C-9'), 39.9 (C-8, C-8'), 41.0 (C-6, C-6'), 46.7 (C-3, C-3'), 52.3 (2 OCH₃), 68.4 (C-2, C-2'), 98.2 (C-7, C-7'), 171.7 (2 CO) ppm. MS (ES⁺, $R = 1000$): m/z (%) = 221 (59) [L + Ca]²⁺, 403 (15) [L + H]⁺, 422 (100) [2L + Ca]²⁺, 425 (20) [L + Na]⁺, 523 (15) [2L + Ca + 2HClO₄]²⁺, 623 (20) [3L + Ca]²⁺, 944 (13) [2L + CaClO₄]⁺. MS (ES⁺, $R = 5000$): m/z (%) = 321 (4) [L + Ca + 2HClO₄]²⁺, 403 (17) [L + H]⁺, 422 (100) [2L + Ca]²⁺, 425 (18) [L + Na]⁺, 523 (70) [2L + Ca + 2HClO₄]²⁺, 623 (15) [3L + Ca]²⁺, 805 (12) [2L + H]⁺, 827 (21) [2L + Na]⁺, 944 (16) [2L + CaClO₄]⁺, 1145 (5) [2L + CaClO₄ + 2HClO₄]⁺, 1346 (1) [3L + CaClO₄]⁺. C₂₀H₃₈CaCl₂N₂O₁₄ (641.51): calcd. C 37.45, H 5.97, N 4.37; found C 37.61, H 6.46, N 4.53.

Complex [2c-Sr(ClO₄)₂]: This complex was prepared from macrocycle **2c** (32.2 mg, 0.08 mmol) and [Sr(ClO₄)₂·6H₂O] (31.6 mg, 0.08 mmol) in acetonitrile (8 mL) according to the general procedure (evaporation of the solvent to about 1/4 of the initial volume). The complex was isolated as a white solid (43.5 mg, 79%); m.p. 150–155 °C. IR (KBr): $\tilde{\nu} = 1642$ (C=O), 1147, 1117, 1087 (Cl–O) cm⁻¹. ¹H NMR (400 MHz, CD₃CN, 22 °C): $\delta = 0.89$ (d, $^3J = 7.4$ Hz, 6 H, CH₃, CH₃'), 0.91 (d, $^3J = 7.1$ Hz, 6 H, CH₃, CH₃'), 1.14 (ddd, $^2J = 13.9$, $^3J = 9.1$, 4.3 Hz, 2 H, 8-H^B, 8'-H^B), 1.26 (ddd, $^2J = 13.9$, $^3J = 10.2$, 5.1 Hz, 2 H, 8-H^A, 8'-H^A), 1.60 (m, 2 H, 9-H, 9'-H), 2.46 (ABX, AB part, $^2J = 13.7$, $^3J = 8.7$, 2.2, $\Delta\nu = 21.3$ Hz, 4 H, 6-H^B, 6'-H^B, 6-H^A, 6'-H^A), 3.22 (dd, $^2J = 12.3$, $^3J = 10.7$ Hz, 2 H, 2-H^A, 2'-H^A), 3.27 (s, 6 H, 2 OCH₃), 3.65 (dd, $^2J = 12.3$, $^3J = 2.9$ Hz, 2 H, 2-H^B, 2'-H^B), 4.23 (m, 2 H, 3-H, 3'-H), 5.00 (ABX, X part, $^2J = 8.7$, 2.2 Hz, 2 H, 7-H, 7'-H), 6.79 (d, $^3J = 9.7$ Hz, 2 H, NH, NH') ppm. MS (ES⁺, $R = 1000$): m/z (%) = 245 (10) [L + Sr]²⁺, 414 (29) [2L + Sr – CH₃OH]⁺, 425 (41) [L + Na]⁺, 446 (100) [2L + Sr]²⁺, 547 (5) [2L + Sr + 2HClO₄]⁺, 647 (56) [3L + Sr]²⁺, 991 (1) [2L + SrClO₄]⁺. MS (ES⁺, $R = 5000$): m/z (%) = 345 (5) [L + Sr + 2HClO₄]²⁺, 403 (12) [L + H]⁺, 425 (37) [L + Na]⁺, 446 (100) [2L + Sr]²⁺, 547 (40) [2L + Sr + 2HClO₄]²⁺, 647 (5) [3L + Sr]²⁺, 806 (5) [2L + H]⁺, 828 (9) [2L + Na]⁺, 992 (9) [2L + SrClO₄]⁺, 1193 (2) [2L + SrClO₄ + 2HClO₄]⁺, 1394 (1) [3L + SrClO₄]⁺. C₂₀H₃₈Cl₂N₂O₁₄Sr (689.06): calcd. C 34.86, H 5.60, N 4.06; found C 35.36, H 6.07, N 3.93.

Complex [2c-Zn(ClO₄)₂]: This complex was prepared from macrocycle **2c** (32.2 mg, 0.08 mmol) and [Zn(ClO₄)₂·6H₂O] (29.8 mg, 0.08 mmol) in acetonitrile (8 mL) according to the general procedure (evaporation of the solvent to about 1/4 of the initial volume). The complex was isolated as a dark-yellow solid (43.2 mg, 73%); m.p. 110–112 °C. IR (KBr): $\tilde{\nu} = 1615$ (C=O), 1146, 1113, 1089 (Cl–O) cm⁻¹. ¹H NMR (400 MHz, CD₃CN, 22 °C): $\delta = 0.86$ (d, $^3J = 6.6$ Hz, 6 H, CH₃, CH₃'), 0.91 (d, $^3J = 6.7$ Hz, 6 H, CH₃, CH₃'), 1.23 (ddd, $^2J = 13.9$, $^3J = 9.0$, 4.6 Hz, 2 H, 8-H^B, 8'-H^B), 1.39 (ddd, $^2J = 13.9$, $^3J = 9.8$, 5.2 Hz, 2 H, 8-H^A, 8'-H^A), 1.63 (m, 2 H, 9-H, 9'-H), 2.61 (ABX, AB part, $^3J = 14.7$, $^3J = 7.4$, 1.9, $\Delta\nu = 21.2$ Hz, 4 H, 6-H^B, 6'-H^B, 6-H^A, 6'-H^A), 3.33 (s, 6 H, 2 OCH₃), 3.44 (dd, $^2J = 11.0$, $^3J = 9.7$ Hz, 2 H, 2-H^A, 2'-H^A), 3.68 (dd, 2 H, 2-H^B, 2'-H^B, $^2J = 11.0$, $^3J = 3.0$ Hz), 4.26 (m, 2 H, 3-H, 3'-H), 4.93 (ABX, X part, $^3J = 7.4$, 1.9 Hz, 2 H, 7-H, 7'-H), 7.32 (d, $^3J = 8.8$ Hz, 2 H, NH, NH') ppm. ¹³C NMR (75 MHz, CD₃CN, 30 °C): $\delta = 22.0$ (2 CH₃), 23.1 (2 CH₃), 25.4 (C-9, C-9'), 39.5 (C-8, C-8'), 40.4 (C-6, C-6'), 47.9 (C-3, C-3'), 54.0 (2 OCH₃), 69.4 (C-2, C-2'), 100.0 (C-7, C-7'), 173.4 (2 CO) ppm. MS (ES⁺): m/z (%) = 233 (100) [L + Zn]²⁺, 270 (75), 274 (51), 359 (76), 434 (52) [2L + Zn]²⁺, 635 (30) [3L + Zn]²⁺. ZnC₂₀H₃₈N₂O₁₄Cl₂·4H₂O =

C₂₀H₄₆Cl₂N₂O₁₈Zn (738.87): calcd. C 32.51, H 6.27, N 3.79; found C 31.96, H 5.85, N 4.08.

Complex [3b-Ca(ClO₄)₂]: This complex was prepared from macrocycle **3b** (37.6 mg, 0.08 mmol) and [Ca(ClO₄)₂·6H₂O] (27.8 mg, 0.08 mmol) in acetonitrile (8 mL) according to the general procedure (evaporation of the solvent to about 1/8 of the initial volume). The complex was isolated as a yellow solid (47.8 mg, 78%); m.p. 210–212 °C (dec.). IR (KBr): $\tilde{\nu} = 1638$ (C=O), 1147, 1115, 1086 (Cl–O) cm⁻¹. ¹H NMR (400 MHz, CD₃CN, 22 °C): $\delta = 0.83$ (d, $^3J = 7.1$ Hz, 3 H, CH₃'), 0.95 (d, $^3J = 6.9$ Hz, 3 H, CH₃), 2.23 (dd, $^2J = 15.9$, $^3J = 3.8$ Hz, 1 H, 6-H^B), 2.60 (ABX, AB part, $^2J = 13.4$, $^3J = 8.8$, 1.6, $\Delta\nu = 40.4$ Hz, 2 H, 6'-H^B, 6'-H^A), 2.66 (dd, $^2J = 15.9$, $^3J = 0.5$ Hz, 1 H, 6-H^A), 3.16 (s, 3 H, OCH₃), 3.54 (s, 3 H, OCH₃), 4.67 (m, 1 H, 3-H), 4.68 (dd, $^3J = 3.8$, ≤ 0.5 Hz, 1 H, 7-H), 4.84 (m, 1 H, 3'-H), 4.90 (d, $^3J = 4.6$ Hz, 1 H, 2'-H), 4.91 (d, $^3J = 3.9$ Hz, 1 H, 2-H), 5.35 (ABX, X part, $^3J = 8.8$, 1.6 Hz, 1 H, 7'-H), 6.80 (d, $^3J = 10.3$ Hz, 1 H, NH'), 7.20 (d, $^3J = 9.0$ Hz, 1 H, NH), 7.30–7.55 (m, 10 H, 10 Ar-H) ppm. ¹³C NMR (75 MHz, CD₃CN, 30 °C): $\delta = 16.3$ (CH₃), 17.6 (CH₃'), 39.1 (C-6), 41.7 (C-6'), 44.9 (C-3'), 49.3 (C-3), 51.7 (OCH₃), 57.6 (O'CH₃), 77.1 (C-2'), 84.6 (C-2), 98.0 (C-7), 103.1 (C-7'), 127.0 (2 C), 128.9 (2 C'), 129.1 (1 C'), 129.2 (2 C'), 129.4 (1 C), 129.8 (2 C, 10 Ar-CH), 136.6 (Ar-C'), 137.9 (Ar-C), 171.7 (CO), 172.5 (CO') ppm. MS (ES⁺): m/z (%) = 255 (10) [L + Ca]²⁺, 490 (100) [2L + Ca]²⁺, 494 (50) [L + Na]²⁺, 725 (10) [3L + Ca]²⁺. HRMS (ESI): calcd. for CaC₂₆H₃₄N₂O₆ [L + Ca]²⁺ 255.1021; found 221.1006.

Complex [3c-Ca(ClO₄)₂]: This complex was prepared from macrocycle **3c** (37.6 mg, 0.08 mmol) and [Ca(ClO₄)₂·6H₂O] (27.8 mg, 0.08 mmol) in acetonitrile (8 mL) according to the general procedure (evaporation of the solvent to about 1/8 of the initial volume). The complex was isolated as a yellow solid (46.1 mg, 79%); m.p. 223–228 °C (dec.). IR (KBr): $\tilde{\nu} = 1636$ (C=O), 1146, 1116, 1087 (Cl–O) cm⁻¹. ¹H NMR (400 MHz, CD₃CN, 22 °C): $\delta = 0.94$ (d, $^2J = 6.9$ Hz, 6 H, CH₃, CH₃'), 2.52 (ABX, AB part, $^2J = 14.2$, $^3J = 8.1$, 3.0, $\Delta\nu = 20.1$ Hz, 4 H, 6-H^B, 6'-H^B, 6-H^A, 6'-H^A), 3.13 (s, 6 H, 2 OCH₃), 4.66 (m, 2 H, 3-H, 3'-H), 4.78 (d, $^3J = 3.4$ Hz, 2 H, 2-H, 2'-H), 5.25 (ABX, X part, $^3J = 8.1$, 3.0 Hz, 2 H, 7-H, 7'-H), 6.74 (d, $^3J = 10.3$ Hz, 2 H, NH, NH'), 7.30–7.55 (m, 10 H, 10 Ar-H) ppm. ¹³C NMR (75 MHz, CD₃CN, 30 °C): $\delta = 17.6$ (CH₃, CH₃'), 41.4 (C-6, C-6'), 46.1 (C-3, C-3'), 52.4 (2 OCH₃), 79.0 (C-2, C-2'), 98.7 (C-7, C-7'), 129.0 (4 Ar-CH), 129.1 (2 Ar-CH), 129.2 (4 Ar-CH), 137.8 (2 Ar-C), 171.0 (2 CO) ppm. MS (ES⁺): m/z (%) = 255 (100) [L + Ca]²⁺, 426 (62), 490 (7) [2L + Ca]²⁺, 494 (12) [L + Na]²⁺, 553 (51), 593 (90), 633 (44), 682 (50), 725 (60) [3L + Ca]²⁺. HRMS (ESI): calcd. for CaC₂₆H₃₄N₂O₆ [L + Ca]²⁺ 255.1021; found 221.1001.

¹H NMR Titration Experiments: First, a 5–8 × 10⁻² M stock solution of metal perchlorate in CD₃CN was prepared. Nine tubes containing identical quantities of ligand (2 mg, 4.2–5.0 μmol) and increasing aliquots of the stock metal solution were then prepared. [D₃]Acetonitrile was added to each tube to reach a total sample volume of 520 μL. This procedure thus gave nine metal concentrations corresponding to an [M]/[L] ratio ranging from 0 to approx. 4, whereas the ligand concentration was kept constant. Metal and ligand concentrations were calculated exactly for each tube and the ¹H NMR spectra were recorded with a Bruker AC 400 spectrometer equipped with a DUAL ¹H/¹³C NMR probe at 30 °C. For each stoichiometry considered (ML and ML/ML₂), titration curves were analyzed by computer least-squares curve fitting (EQNMR) using Equation (2) to determine the optimum values of δ_{mn} (chemical shift of each species present) and β_{mn} .^[13] Reported constants were calculated from the average of at least three independent chemical shifts.

$$\delta_{\text{calc}} = \sum_{m=1}^{m=i} \sum_{n=0}^{n=j} \delta_{mn} \beta_{mn} m[M]^m [L]^n / [L]_{\text{total}} \quad (2)$$

The choice of stoichiometry model was validated by examination of several parameters, that is, the standard deviation (σ), the sum of residual squares (Σr^2), the error in the constant and the “merit function” (R) expressed by Equation (3) in which W_i is the weight attributed to observation i .

$$R = 100 [\sum W_i (\delta_{\text{obs}} - \delta_{\text{calc}})^2 / \sum W_i (\delta_{\text{obs}})^2]^{1/2} \quad (3)$$

Not all the relevant protons (see above) could always be taken into consideration as some of them showed inconsistent program data: either a high error on the constant or a “merit function” $R > 1$.

¹³C Relaxation Time Measurements: The solutions were prepared by mixing equimolar quantities of macrocycle and perchlorate salt in 500 μL ($c \approx 0.13 \text{ M}$) of either CD_3CN for macrocycles **2c**, **3c** and **3b** or $\text{CD}_3\text{CN}/\text{MeOD}/\text{CDCl}_3$ (80:10:10) for **1c**. Dry argon was carefully bubbled for 30 min through all the solutions in the NMR tubes to remove atmospheric paramagnetic oxygen. The ¹³C longitudinal relaxation time measurements were conducted with a Bruker DSX 300 spectrometer at 75 MHz using the inversion-recovery pulse sequence (delay– π –pulse–pulse interval– $\pi/2$ –pulse–FID) under ¹H broad-band decoupling conditions. All the spectra were recorded at 35 $^\circ\text{C}$ using a standard temperature-control unit. The relaxation time values T_1 were determined by exponential fitting of the peak intensities I from a direct equation implemented in the spectrometer software and derived from Equation (4)^[24] in which t is the pulse interval and I_∞ the peak intensity relative to t_{max} (35 s; see below). Here T_1^{obs} could be taken as the relaxation time T_1^{DD} corresponding to the dipole–dipole (DD) interaction between directly bonded ¹³C and ¹H nuclei, this interaction being the strongest one in small organic molecules.^[6g,6i] Nuclear Overhauser enhancement (NOE) factors, which were measured in each case, attested that the interactions were roughly dipolar.

$$I = I_\infty \left(1 - 2 e^{-t/T_1^{\text{obs}}} \right) \quad (4)$$

A pulse delay time of 35 s, that is, a time longer than the theoretically required minimum of $5T_1$, was used for all the carbon atoms studied. Fifteen different pulse intervals t , ranging between 35 s and 5 ms, were successively utilized for each individual measurement. Usually 256 scans were necessary for each t value to obtain a reasonable signal-to-noise ratio.

Molecular Modelling: The MACROMODEL molecular modelling program (version 7.0) developed by Still and co-workers^[25] was used to determine the global minimum conformations of the complexes. The AMBER force-field^[26] implemented in the program and well-suited to the study of compounds incorporating amide functions was chosen. The method known as the Monte–Carlo Multiple Minimum Search (MCOMM) was applied. The structures were written from the minimum energy conformation of the corresponding macrocycles.^[19] At least 5000 conformations were minimized in each case.

Supporting Information (see also the footnote on the first page of this article): SI-1: Variations in the ¹H NMR chemical shifts of the macrocyclic protons in CD_3CN by progressive addition of metal perchlorate for **1c**–Mg, **1c**–Ca, **1c**–Ba, **1c**–Zn, **2c**–Ca, **2c**–Zn, **3c**–

Ca, **3b**–Ca. SI-2: Differences in the ¹H NMR chemical shifts between the metal perchlorate complexes and the corresponding ligands in CD_3CN . SI-3: Differences in the ¹³C NMR chemical shifts between the metal perchlorate complexes and the corresponding ligands in CD_3CN . SI-4: Relative energies of the first 15 conformers of macrocycles **1c**, **3c** and **3b** and their Ca complexes with respect to the lowest-energy conformer **1** of each system. SI-5: Interatomic distances between the heteroatoms and the metal in the Ca complexes of **1c**, **3c** and **3b**. SI-6: Interatomic distances in the Ca complexes of **1c**, **3c** and **3b**. SI-7: Main characteristic peaks for the complexes observed in positive ion mode ESI mass spectrometry. SI-8: Isotopic profiles of the main peaks observed in positive ion mode ESI mass spectrometry for complexes **2c**–Ca and **2c**–Sr.

Acknowledgments

The authors wish to thank Prof. M. J. Hynes, University of Galway, for providing the EQNMR program, Dr B. Combourieu for valuable discussions and apposite advice on the ¹³C NMR relaxation time measurements and B. L  geret for recording the exact mass by ESI–HR–MS.

- [1] a) C. J. Pedersen, *Angew. Chem. Int. Ed. Engl.* **1988**, 27, 1021–1027; b) D. J. Cram, *Angew. Chem. Int. Ed. Engl.* **1988**, 27, 1009–1020; c) J.-M. Lehn, *Angew. Chem. Int. Ed. Engl.* **1988**, 27, 89–112; d) G. W. Gokel, H. D. Durst, *Synthesis* **1976**, 168–184; e) R. M. Izatt, J. S. Bradshaw, S. A. Nielsen, J. D. Lamb, J. J. Christensen, *Chem. Rev.* **1985**, 85, 271–339; f) R. M. Izatt, K. Pawlak, J. S. Bradshaw, R. L. Bruening, *Chem. Rev.* **1991**, 91, 1721–2085; R. M. Izatt, K. Pawlak, J. S. Bradshaw, R. L. Bruening, *Chem. Rev.* **1995**, 95, 2529–2586; g) G. W. Gokel, W. M. Leevy, M. E. Weber, *Chem. Rev.* **2004**, 104, 2723–2750, and references cited therein.
- [2] a) G. W. Gokel, *Comprehensive Supramolecular Chemistry*, vol. 1, *Molecular Recognition: Receptors for Cationic Guests* (Eds.: J.-M. Lehn, J. L. Atwood, J. E. D. Davies, D. D. MacNicol, F. V  gtle), Elsevier, Oxford, **1996**; b) J. A. Ripmeester, *Comprehensive Supramolecular Chemistry*, vol. 8, *Physical Methods in Supramolecular Chemistry* (Eds.: J.-M. Lehn, J. L. Atwood, J. E. D. Davies, D. D. MacNicol, F. V  gtle), Elsevier, Oxford, **1996**.
- [3] a) J. Petranek, O. Ryba, *Coll. Czechoslov. Chem. Commun.* **1980**, 45, 1567–1574; b) Y. Nakatsuji, H. Kobayashi, M. Okahara, K. Matsushima, *Chem. Lett.* **1982**, 1571–1574; c) T. Pigot, M.-C. Duriez, C. Picard, L. Cazaux, P. Tisn  s, *Tetrahedron* **1992**, 48, 4359–4368; d) T. Pigot, M.-C. Duriez, C. Picard, L. Cazaux, P. Tisn  s, *J. Chem. Soc. Perkin Trans. 2* **1993**, 221–227, and references cited therein; e) B. Cathala, C. Picard, L. Cazaux, P. Tisn  s, *J. Molecular Struct.* **1996**, 385, 167–174; f) A. Pujo-Bouteill  , L. Lamand  , L. Lopez, L. Cazaux, J. Bellan, *Tetrahedron* **1998**, 54, 3817–3826; g) A. Szumna, D. T. Gryko, J. Jurczak, *J. Chem. Soc. Perkin Trans. 2* **2000**, 1553–1558; h) D. T. Gryko, A. Pecak, W. Kozminski, P. Piatek, J. Jurczak, *Supramol. Chem.* **2000**, 15, 229–235.
- [4] I. Dayan, J. Libman, A. Shanzer, C. E. Felder, S. Lifson, *J. Am. Chem. Soc.* **1991**, 113, 3431–3439.
- [5] a) M. Bourgoin, K. H. Wong, J. Y. Hui, J. Smid, *J. Am. Chem. Soc.* **1975**, 97, 3462–3467; b) R. T. Bronson, J. S. Bradshaw, P. B. Savage, S. Fuangwasdi, S. C. Lee, K. E. Krakowiak, R. M. Izatt, *J. Org. Chem.* **2001**, 66, 4752–4758; c) F. Le Derf, M. Mazari, N. Mercier, E. Levillain, G. Tripp  , A. Riou, P. Richomme, J. Becher, J. Garin, J. Ordu  , N. Gallego-Planas, A. Gorgues, M. Sall  , *Chem. Eur. J.* **2001**, 7, 447–455; d) I. Stanculescu, C. Mandravel, D. Landy, P. Woisel, G. Surpateanu, *J. Mol. Struct.* **2003**, 655, 81–87; e) J.-Y. Balandier, A. Belyasmine, M. Sall  , *Eur. J. Org. Chem.* **2008**, 269–276.

- [6] a) D. Live, S. I. Chan, *J. Am. Chem. Soc.* **1976**, *98*, 3769–3778; b) L. Echegoyen, A. Kaifer, H. Durst, R. A. Schultz, D. M. Dishong, D. M. Goli, G. W. Gokek, *J. Am. Chem. Soc.* **1984**, *106*, 5100–5103; c) S. Sasaki, H. Naito, K. Maruta, E. Kawahara, M. Maeda, *Tetrahedron Lett.* **1994**, *35*, 3337–3340; d) J.-F. Peyrat, J. Mahuteau, B. Figadère, A. Cavé, *J. Org. Chem.* **1997**, *62*, 4811–4815; e) F. Le Derf, M. Mazari, N. Mercier, E. Levillain, P. Richomme, J. Becher, J. Garin, J. Orduna, A. Gorgues, M. Sallé, *Chem. Commun.* **1999**, 1417–1418; f) F. Le Derf, M. Mazari, N. Mercier, E. Levillain, P. Richomme, J. Becher, J. Garin, J. Orduna, A. Gorgues, M. Sallé, *Inorg. Chem.* **1999**, *38*, 6096–6100; g) C. Erk, M. D. Zeidler, *J. Mol. Liquids* **1999**, *79*, 17–26; h) L. Fielding, *Tetrahedron* **2000**, *56*, 6151–6170; i) C. Erk, M. D. Zeidler, *Chem. Phys.* **2004**, *303*, 115–120, and references cited therein; j) M.-J. Blesa, B.-T. Zhao, M. Allain, F. Le Derf, M. Sallé, *Chem. Eur. J.* **2006**, *12*, 1906–1914; k) J. Lyskawa, F. Le Derf, E. Levillain, M. Mazari, M. Sallé, *Eur. J. Org. Chem.* **2006**, 2322–2328; l) S. Dolder, S.-X. Liu, F. Le Derf, M. Sallé, A. Neels, S. Decurtins, *Organic. Lett.* **2007**, *9*, 3753–3756; m) C. Benhaoua, M. Mazari, F. Le Derf, M. Sallé, *New J. Chem.* **2008**, *32*, 913–916; n) M. Martinez Belmonte, E. C. Escudero-Adan, J. Benet-Buchholz, A. W. Kleij, *Eur. J. Org. Chem.* **2009**, 5307–5318.
- [7] a) T. Takahashi, A. Uchiyama, K. Yamada, B. C. Lynn, G. W. Gokel, *Supramol. Chem.* **1993**, *2*, 177–182; b) K. Wang, G. W. Gokel, *Pure Appl. Chem.* **1996**, *68*, 1267–1272, and references cited therein; c) D. Giraud, O. Laprèvote, B. C. Das, *Org. Mass Spectrom.* **1994**, *29*, 169–175; d) D. Giraud, I. Scherrens, M.-L. Lever, O. Laprèvote, B. C. Das, *J. Chem. Soc. Perkin Trans. 2* **1996**, 901–905; e) E. Leize, A. Van Dorsselaer, R. Krämer, J.-M. Lehn, *J. Chem. Soc., Chem. Commun.* **1993**, 990–993, and references cited therein; f) F. Le Derf, M. Sallé, N. Mercier, J. Becher, P. Richomme, A. Gorgues, J. Orduna, J. Garin, *Eur. J. Org. Chem.* **1998**, 1861–1865.
- [8] Y. Pointud, A.-G. Valade, C. Pointon, D. Dugat, G. Jeminet, J.-L. Beltran, *Supramol. Chem.* **2003**, *15*, 261–269.
- [9] a) A.-G. Valade, D. Dugat, G. Jeminet, J. Royer, H.-P. Husson, *Eur. J. Org. Chem.* **2001**, 2041–2053; b) diketetal dilactams, which were prepared in two steps from chiral β -amino alcohols, were isolated in three diastereoisomeric forms: an unsymmetrical *trans*-OMe isomer **b** and two *cis*-OMe isomers **a** and **c** of C_2 symmetry, **a** (minor isomer) and **c** (major isomer) differing in the *trans* or *cis* relationship of the OMe and 3-R groups (see ref.^[9a]).
- [10] a) P. J. Marie, *Curr. Opin. Pharmacol.* **2005**, *5*, 633–636; b) I. G. Finlay, M. D. Mason, M. Shelley, *Lancet Oncol.* **2005**, *6*, 392–400; c) A. Lin, M. E. Ray, *Cancer Metastasis Rev.* **2006**, *25*, 669–675.
- [11] a) N. Chattopadhyay, E. M. Brown, *Cell Signal* **2000**, *12*, 361–366; b) A. M. Hofer, E. M. Brown, *Nat. Rev. Mol. Cell Biol.* **2003**, *4*, 530–538.
- [12] A. S. Meyer Jr., G. H. Ayres, *J. Am. Chem. Soc.* **1957**, *79*, 49–53.
- [13] M. J. Hynes, *J. Chem. Soc., Dalton Trans.* **1993**, 311–312.
- [14] a) J.-M. Lehn, J.-P. Sauvage, *J. Am. Chem. Soc.* **1975**, *97*, 6700–6707; b) H. K. Frensdorff, *J. Am. Chem. Soc.* **1971**, *93*, 600–606; c) J. Y. Takeda, Y. Ohayagi, S. Akabori, *Bull. Chem. Soc. Jpn.* **1984**, *57*, 3381–3385.
- [15] N. L. Kirsch, W. Simon, *Helv. Chim. Acta* **1976**, *59*, 357–363.
- [16] a) M. R. Rosenthal, *J. Chem. Educ.* **1973**, *50*, 331–335; b) K. Nakamoto, *Infrared Spectra of Inorganic and Coordination Compounds*, 2nd ed., Wiley-Interscience, New York, **1970**, pp. 175–176.
- [17] D. Amman, E. Pretsch, W. Simon, *Tetrahedron Lett.* **1972**, *13*, 2473–2476.
- [18] a) J. P. Roux, G. J. Kruger, *Acta Crystallogr., Sect. B* **1976**, *32*, 1171–1174; b) K. Neupert-Laves, M. Dobler, *J. Cryst. Spectrosc. Res.* **1982**, *12*, 287–290.
- [19] D. Dugat, A.-G. Valade, B. Combourieu, J. Guyot, *Tetrahedron* **2005**, *61*, 5641–5653.
- [20] J. D. Dunitz, P. Seiler, *Acta Crystallogr., Sect. B* **1974**, *30*, 2750.
- [21] a) J. Dale, *Acta Chem. Scand.* **1973**, *27*, 1115–1129; J. Dale, *Acta Chem. Scand.* **1973**, *27*, 1130–1148; b) in Dale's convention, the numbers in brackets indicate the number of C–C bonds between corner carbon atoms corresponding to gg or g'g' sequences; thus the [3434] conformer has two “three-bond” sides and two “four-bond” sides.
- [22] a) V. L. Shannon, H. L. Strauss, R. G. Snyder, C. A. Elliger, W. L. Mattice, *J. Am. Chem. Soc.* **1989**, *111*, 1948–1958; b) in Snyder's designation, the letters g, g' and t, which correspond to *gauche* and *trans* bonds, refer to dihedral angles that vary significantly from +60, –60 and 180°.
- [23] H. E. Gottlieb, V. Kotlyar, A. Nudelman, *J. Org. Chem.* **1997**, *62*, 7512–7515.
- [24] J. K. M. Sanders, B. K. Hunter, *Modern NMR Spectroscopy, A Guide for Chemists*, 2nd ed., Oxford University Press, New York, **1993**, pp. 177–188.
- [25] F. Mohamadi, N. G. J. Richards, W. C. Guida, R. Liskamp, M. Lipton, C. Caufield, G. Chang, T. Hendrickson, W. C. Still, *J. Comput. Chem.* **1990**, *11*, 440–467.
- [26] S. J. Weiner, P. A. Kollman, D. T. Nguyen, D. A. Case, *J. Comput. Chem.* **1986**, *7*, 230–252.

Received: February 2, 2010
Published Online: June 1, 2010

Lanthanide Complexes Coordinated by a Dianionic Bis(amidinate) Ligand with a Rigid Naphthalene Linker

Marina V. Yakovenko,^[a] Anton V. Cherkasov,^[a] Georgy K. Fukin,^[a] Dongmei Cui,^[b] and Alexander A. Trifonov^{*[a]}

Keywords: Lanthanides / Amidinates / Coordination modes / Ligand design

The synthetic pathway to a new bis(amidinate) ligand with a conformationally rigid naphthalene linker, 1,8- $\text{C}_{10}\text{H}_6[\text{NHC}(\text{tBu})=\text{N}(2,6\text{-Me}_2\text{-C}_6\text{H}_3)][\text{N}=\text{C}(\text{tBu})\text{NH}(2,6\text{-Me}_2\text{-C}_6\text{H}_3)]$ (**3**) was elaborated. Deprotonation of this bis(amidinate) ligand with two equivalents of $n\text{BuLi}$ and subsequent reaction with anhydrous LnCl_3 ($\text{Ln} = \text{Y}, \text{Nd}, \text{Sm}$) allowed the synthesis of the chlorido complexes $[\text{1,8-}\text{C}_{10}\text{H}_6\{\text{NC}(\text{tBu})\text{N-2,6-Me}_2\text{-C}_6\text{H}_3\}_2]\text{YCl}(\text{dme})$ (**4**), $[\text{1,8-}\text{C}_{10}\text{H}_6\{\text{NC}(\text{tBu})\text{N-2,6-Me}_2\text{-C}_6\text{H}_3\}_2]\text{Nd}(\text{dme})(\mu\text{-Cl})_2\text{Li}(\text{dme})$ (**5**), and $[\text{1,8-}\text{C}_{10}\text{H}_6\{\text{NC}(\text{tBu})\text{N-2,6-Me}_2\text{-C}_6\text{H}_3\}_2]\text{Sm}(\text{thf})(\mu\text{-Cl})_2\text{Li}(\text{thf})_2$ (**6**), which are coordinated by the linked dianionic bis(amidinate) ligand. The

structures of complexes **4–6** were established by X-ray diffraction studies, which reveal that the new ligand framework can coordinate to the lanthanide atoms in different fashions depending on the central atom ion size. Alkylation of complex **6** with equimolar amounts of $\text{LiCH}_2\text{SiMe}_3$ afforded the unexpected amido–amidinate complex $[\text{1,8-}\text{C}_{10}\text{H}_6\{\text{NC}(\text{tBu})\text{N-2,6-Me}_2\text{-C}_6\text{H}_3\}_2]\{\text{1,8-}\text{C}_{10}\text{H}_6\{\text{NC}(\text{tBu})\text{N-2,6-Me}_2\text{-C}_6\text{H}_3\}(\text{NH})\}\text{Sm}][\text{Li}(\text{dme})_3]$ (**7**), which obviously results from the cleavage of one amidinate group during decomposition of the transient alkyl species and ligand redistribution.

Introduction

The amidinate ligands $[\text{RC}(\text{NR}')_2]^-$ belong to the group of four-electron chelating monoanionic ligands in which the negative charge is delocalized in the NCN fragment. Amidinates have proven to be versatile ligands because of the fact that their steric and electronic properties can easily be modified through variations of the organic substituents on the nitrogen atoms. The combination of flexibility and variety of coordination modes of amidinate ligands with donor properties results in their compatibility with a wide number of metal ions across the periodic table^[1] and their suitability as a supporting ligand framework, which allows control over the metal atom coordination sphere and metal-mediated chemical processes. Application of amidinate ligands, which were introduced in the organometallic chemistry of rare-earth metals by Edelmann^[2] and Teuben,^[3] greatly influenced the development of this area and allowed the synthesis and characterization of a new series of isolable, highly reactive species. Monoalkyl, bis(alkyl), cationic alkyl, and hydrido rare-earth complexes supported by amidinate ligands have been described, and some of them demonstrated

catalytic potential in reactions of transformation of unsaturated substrates (olefin polymerization,^[3d,e;4] isoprene polymerization,^[5] acetylene dimerization,^[3c] olefin hydroboration,^[6] hydrosilylation,^[7] and hydroamination^[8]). The stability and reactivity of rare-earth organometallic compounds are known to be largely determined by the degree of saturation of the coordination sphere of metal atom; therefore in recent years, the trend was toward the development of new ancillary ligands, which would allow greater flexibility in the design of the metal coordination environment.^[9] Greater stability of rare-earth complexes can be achieved by use of more sterically hindered ligands or ligands that can give additional electronic stabilization to highly electronically unsaturated metal centers. Thus, employment of bulky amidinate ligands^[3d,e;5;7] and amidinates containing an additional donor group^[10] in the side chain allows to overcome the limitations inherent to the initially used N,N' -bis(trimethylsilyl)benzamidinate ligand and to synthesize the formerly inaccessible bis(alkyl) rare-earth species. Dianionic linked bis(amidinate) ligands^[11] are highly interesting from the point of view of design and control of the geometry of the metal coordination sphere, and their use can stimulate progress in lanthanide chemistry similar to that observed by the transposition from metallocene to ansa-metallocene-type structures. Several examples of lanthanide complexes coordinated by linked bis(amidinate) ligands with flexible backbones have been reported.^[12] In order to provide control of the geometry of the metal coordination sphere and control of the selectivity of the catalytic reactions mediated by metal complexes, we focused

[a] G. A. Razuvaev Institute of Organometallic Chemistry of Russian Academy of Sciences, Tropinina 49, 603600 Nizhny Novgorod GSP-445, Russian Federation
Fax: +7-831-462-74-97
E-mail: trif@iomc.ras.ru

[b] State Key Laboratory of Polymer Physics and Chemistry, Changchun Institute of Applied Chemistry, Chinese Academy of Sciences, Changchun 130022, People's Republic of China

on elaboration of a new bulky bis(amidinate) ligand framework containing a rigid 1,8-disubstituted naphthalene linker. Herein, we report on the synthesis of a new linked bis(amidine) ligand, 1,8- $\text{C}_{10}\text{H}_6[\text{NHC}(t\text{Bu})=\text{N}(2,6\text{-Me}_2\text{-C}_6\text{H}_3)]\text{[N}=\text{C}(t\text{Bu})\text{NH}(2,6\text{-Me}_2\text{-C}_6\text{H}_3)]$, and its application for the preparation of lanthanide bis(amidinate) complexes.

Results and Discussion

Synthesis of 1,8- $\text{C}_{10}\text{H}_6[\text{NHC}(t\text{Bu})=\text{N}(2,6\text{-Me}_2\text{-C}_6\text{H}_3)]\text{[N}=\text{C}(t\text{Bu})\text{NH}(2,6\text{-Me}_2\text{-C}_6\text{H}_3)]$ (**3**)

1,8-Diaminonaphthalene was used as a platform for the synthesis of bis(amidine) ligand containing a conformationally rigid planar linker between two functional groups. The general procedure was based on those previously reported by Arnold^[11a] and Hill^[11c] that use pivaloyl chloride to give a tertiary butyl group at the amidine C functionality. The synthetic route is shown in Scheme 1. Synthesis of bis(amide) **1** proceeded easily by reacting 1,8-diaminonaphthalene with pivaloyl chloride in the presence of triethylamine in CH_2Cl_2 ; compound **1** was obtained in a 77% yield. Conversion of bis(amide) **1** to bis(imidoylchloride) **2** was achieved by addition of PCl_5 to a solution of **1** in chlorobenzene. In contrast to previously published synthetic procedures,^[11a,11c] at this step, chlorobenzene was used instead of toluene in order to solubilize **1**. By heating the reaction mixture at 65 °C for 3 d, a yield of 42% was achieved. Extension of the reaction time to up to 5 d does not result in an increase in the product yield. The bis(amidine) **3** was synthesized by reaction of 2,6-dimethylaniline with **2** in chlorobenzene (65 °C, 3 d). Recrystallization of **3** from a CH_2Cl_2 /hexane mixture allowed its isolation in a 70% yield as a pale-yellow crystalline solid, while when acetonitrile was used as the solvent, the solvate **3**·(MeCN) was obtained (63% yield). Products **1**–**3** returned acceptable microanalytical results.

Pale-yellow crystals of the bis(amidine) **3** suitable for X-ray diffraction studies were obtained by slow concentration of its solutions in CH_2Cl_2 /hexane mixture (**3**) or in acetonitrile [**3**·(MeCN)] at room temperature. The molecular structure of **3** is shown in Figure 1, and the structure refinement data are listed in Table 1 [for the structure of **3**·(MeCN), see Supporting Information].

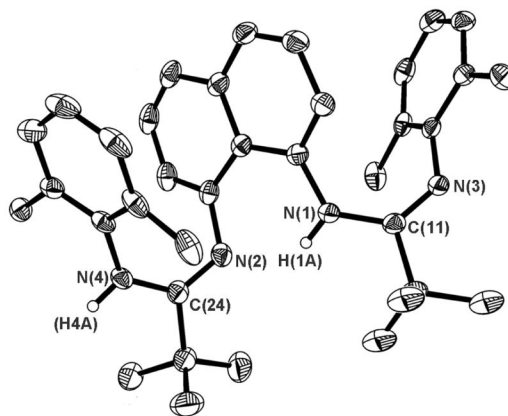
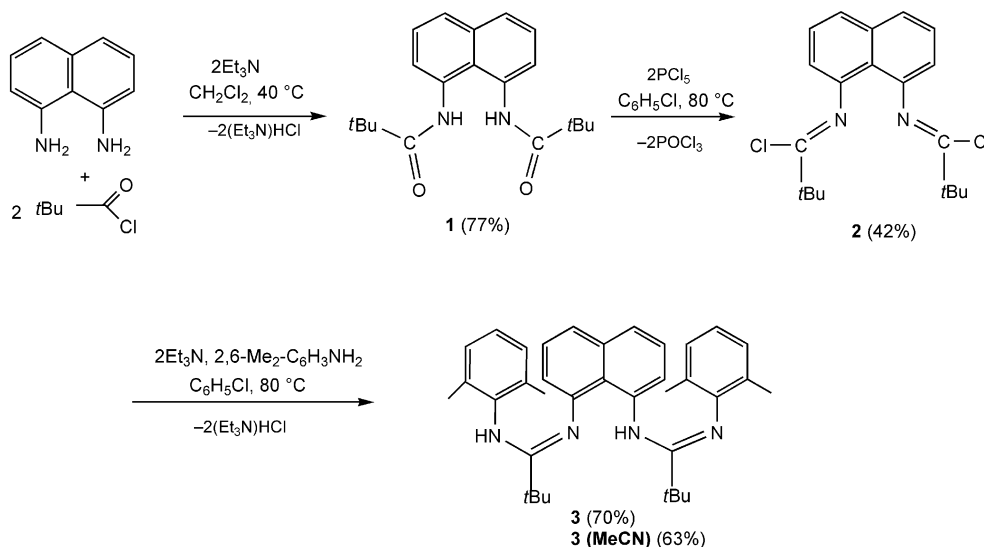


Figure 1. ORTEP diagram (30% probability thermal ellipsoids) of **3**. Hydrogen atoms (except those of the amidine fragments) are omitted for clarity. Selected bond lengths [Å] and angles [°]: N(1)–C(1) 1.404(3), N(1)–C(11) 1.390(3), N(2)–C(3) 1.416(3), N(2)–C(24) 1.295(3), N(3)–C(11) 1.280(3), N(3)–C(16) 1.402(3), N(4)–C(24) 1.369(3), N(4)–C(29) 1.425(3), N(1)–C(11)–N(3) 128.3(2), C(11)–N(3)–C(16) 127.3(2), N(2)–C(24)–N(4) 126.7(2), C(24)–N(4)–C(29) 128.5(2).

The X-ray diffraction study reveals that bis(amidine) **3** can adopt conformations with different mutual arrangements of the amidine groups relative to the naphthalene fragment. Thus, in **3**, the amidine groups are situated in an *anti* position, while in **3**·(MeCN), they are in a *syn* position with respect to the naphthalene ring. The C(29–34) and C(2–7) rings in **3** are located in a “face to face” fashion, with a value of 22.2° for the dihedral angle between their



Scheme 1.

Table 1. Crystallographic data and structure refinement details for **3**–**7**.

	3	4	5	6	7
Empirical formula	C ₃₆ H ₄₄ N ₄	C ₄₀ H ₅₂ ClN ₄ O ₂ Y	C ₅₂ H ₈₂ Cl ₂ LiN ₄ NdO ₆	C ₄₈ H ₆₆ Cl ₂ LiN ₄ O ₃ Sm	C ₇₁ H ₉₇ LiN ₇ O ₆ Sm
Formula weight	532.75	745.22	1081.30	975.24	1301.85
Crystal size [mm]	0.50 × 0.50 × 0.48	0.40 × 0.40 × 0.27	0.26 × 0.15 × 0.07	0.28 × 0.15 × 0.09	0.40 × 0.12 × 0.10
Space group	<i>Pbca</i>	<i>P2₁/c</i>	<i>P2₁/c</i>	<i>P1</i>	<i>P2₁/c</i>
<i>a</i> [Å]	15.715(2)	14.3924(4)	28.2427(14)	13.1746(3)	15.7262(3)
<i>b</i> [Å]	13.885(2)	13.7686(4)	17.7600(9)	14.6174(3)	19.3451(4)
<i>c</i> [Å]	28.972(4)	20.4216(6)	22.1877(11)	24.3385(6)	22.3292(5)
α [°]	90	90	90	93.4900(10)	90
β [°]	90	107.6570(10)	96.0580(10)	92.0370(10)	97.1330(10)
γ [°]	90	90	90	93.2970(10)	90
<i>V</i> [Å ³]	6322.1(16)	3856.16(19)	11067.0(10)	4667.05(18)	6740.5(2)
<i>Z</i>	8	4	8	4	4
Calculated density [mg/m ³]	1.119	1.284	1.298	1.388	1.283
μ [mm ^{−1}]	0.066	1.620	1.083	1.417	0.926
<i>T</i> _{min} / <i>T</i> _{max}	0.9679/0.9710	0.5635/0.6689	0.7660/0.9280	0.6925/0.8831	0.7082/0.9131
<i>F</i> (000)	2304	1568	4536	2020	2740
2 θ [°]	52	52	53	55	52
Unique reflections collected (<i>R</i> _{int})	6202 (0.0448)	7541 (0.0281)	22872 (0.0536)	21191 (0.0175)	57778 (0.0436)
<i>R</i> ₁ [<i>I</i> > 2 σ (<i>I</i>)]	0.0649	0.0331	0.0650	0.0331	0.0377
<i>wR</i> ₂ (all data)	0.1801	0.0861	0.1692	0.0875	0.0980
Parameters	380	445	1111	1063	800
Goodness-of-fit on <i>F</i> ₂	1.031	1.046	1.046	1.060	1.050
Largest diff. hole and peak [e/Å ³]	−0.612/0.685	−0.240/1.078	−1.286/2.472	−0.825/1.940	−0.544/1.676

planes. The short distance between the centers of these rings (3.473 Å) allows for the realization of π – π interactions^[13] in **3**.

Unlike in previously reported linked bis(amidine) groups,^[11a,11c] in both **3** and **3**·(MeCN), the hydrogen atoms in the amidine groups are attached to different nitrogen atoms. This fact becomes evident from analysis of the geometric parameters of the amidine groups. Within one of the two NCN fragments, the bond length N(C₁₀H₆)–C [1.292(2) Å] is comparable to that of a normal double C=N bond,^[14] while the bond between central carbon atom and the nitrogen atom of the 2,6-dimethylaniline moiety is substantially longer [1.371(2) Å] and corresponds better to a single N–C bond. In the second NCN fragment, the bonding situation is reverse: the bond N(C₁₀H₆)–C is long [1.414(2) Å] and the C–N(2,6-Me₂-C₆H₃) is short [1.272(2) Å]. It should be noted that intramolecular N···H hydrogen bonds are realized in **3** and **3**·(MeCN). The N(2)···H(1A) and N(1)···H(2A) distances in **3** and **3**·(MeCN) are 2.10(2) and 2.02(2) Å, respectively. The NHN bond angles at the hydrogen atoms are 138.9(3)° in **3** and 135.1(4)° in **3**·(MeCN). The different locations of the hydrogen atoms within the two amidine fragments is proved also by the solid-state IR spectrum of **3**: the NH groups give rise to two different absorption bands at 3400 and 3278 cm^{−1}. Obviously, the same situation is retained in solution since the protons attached to the nitrogen atoms in the ¹H NMR spectrum of **3** give rise to a set of two singlets of equal intensity at δ = 6.07 and 8.98 ppm.

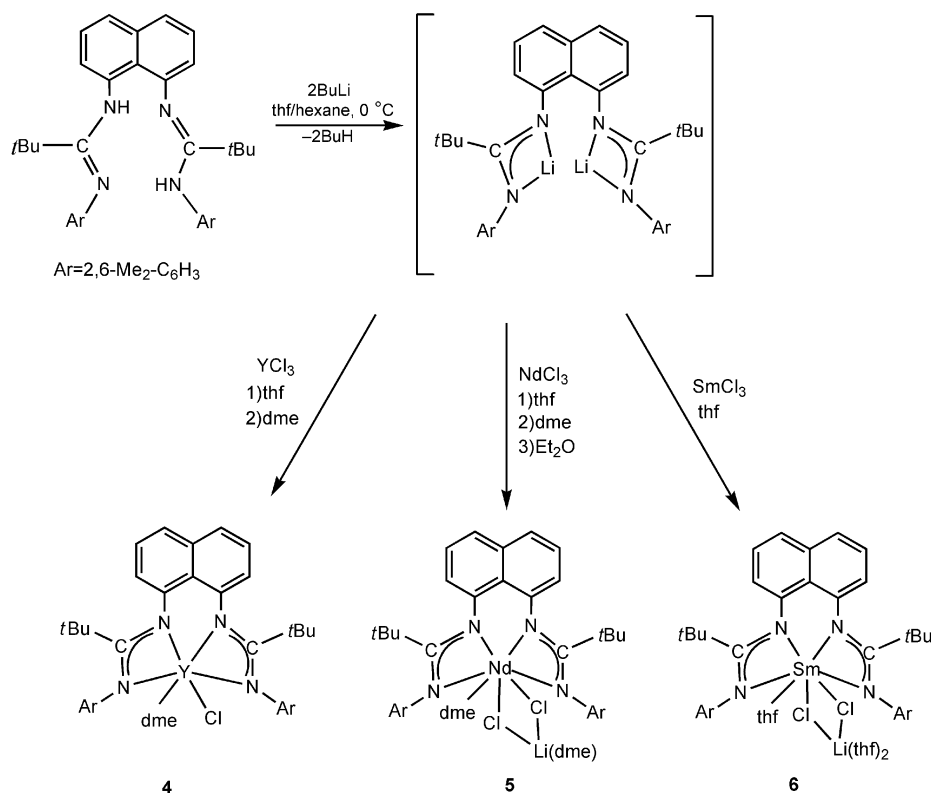
In order to evaluate the difference in the energies of the conformers and the energy of the intramolecular N···H hydrogen bonds, density functional theory (DZVP basis set) calculations on the isolated molecules **3** and **3**·(MeCN) were carried out with the program Firefly 71c.^[15] According to

these calculations, the conformation that is realized in complex **3** is energetically preferable (1.18 kcal/mol) relative to that of **3**·(MeCN). Probably stabilization of the conformation of **3**·(MeCN) is reached because of the presence of solvate molecules of MeCN in the crystal. In order to evaluate the energy of the intramolecular N···H hydrogen bonds, the Bader theory^[16] and the correlation equation of Espinosa^[17] were used. The calculations have shown that the energy of the bonds N(2)···H(1A) and N(1)···H(2A) in **3** and **3**·(MeCN) are 9.68 and 9.93 kcal/mol, respectively.

Synthesis of Bis(amidinate)Chlorido Lanthanide Complexes

Bis(amidine) **3** can easily be deprotonated by treatment with 2 equiv. of *n*BuLi in a thf/hexane mixture at 0 °C. The dilithium derivative of **3** obtained after metallation with *n*BuLi was used in situ in the reaction with anhydrous LnCl₃ (Ln = Y, Nd, Sm; 1:1 molar ratio) in thf at ambient temperature (Scheme 2).

Evaporation of thf, extraction of the solid residue with toluene, and subsequent recrystallization of the reaction product from dme/hexane (**4**), diethyl ether (**5**), or thf/hexane (**6**) mixtures led to the isolation of bis(amidinate)-chlorido lanthanide complexes [1,8-C₁₀H₆{NC(*t*Bu)N-2,6-Me₂-C₆H₃}₂]YCl(dme) (**4**), [1,8-C₁₀H₆{NC(*t*Bu)N-2,6-Me₂-C₆H₃}₂]Nd(dme)(μ -Cl)₂Li(dme) (**5**), and [1,8-C₁₀H₆{NC(*t*Bu)N-2,6-Me₂-C₆H₃}₂]Sm(thf)(μ -Cl)₂Li(thf)₂ (**6**) in reasonable yields (45–61%). Complexes **4**–**6** were obtained as pale-yellow crystalline moisture- and air-sensitive solids. They are soluble in thf, dme, Et₂O, and toluene and are slightly soluble in hexane. The ¹H and ¹³C{¹H}NMR spectra of the diamagnetic yttrium derivative **4** in C₆D₆ at 20 °C show the expected set of signals corresponding to the bis-



Scheme 2.

(amidinate) ligand and the dme molecule. The protons of the *t*Bu groups give rise to a single singlet at $\delta = 0.88$ ppm, and the protons of the xyllyl fragments appear as a singlet at $\delta = 2.46$ ppm. Two broad singlets at $\delta = 2.67$ and 2.99 ppm correspond to the methyl and methylene protons of the dme molecules. The variable-temperature ^1H and $^{13}\text{C}\{^1\text{H}\}$ NMR spectroscopic data for **4** is indicative of complex dynamic behavior over the temperature range +60 to -60°C (in C_7D_8), which results in an apparent mirror plane within the molecule. Clear pale-yellow crystals of complexes **4–6** suitable for X-ray diffraction studies were obtained by slow concentration of their solutions (**4**: dme/hexane mixture, **5**: diethyl ether, **6**: thf/hexane mixture) at ambient temperature. Complex **5** was isolated as a solvate $5 \cdot (2\text{Et}_2\text{O})$, while the crystals of **4** and **6** do not contain solvent molecules. Crystals of complexes **5** and **6** contain two crystallographically independent molecules. The molecular structures of **4–6** are shown in Figures 2, 3, and 4, respectively; the structure refinement data are listed in Table 1. X-ray diffraction studies reveal that compound **4** is a monomeric salt-free complex, while **5** and **6** are heterobimetallic complexes. The coordination sphere of the yttrium atom in **4** is made up of four nitrogen atoms of two amidinate fragments, two oxygen atoms of the dme molecule, and one terminal chlorido ligand. In complexes **5** and **6**, the coordination spheres of the metal atoms contain two chlorine atoms that μ -bridge the lanthanide and lithium atoms, in addition to four nitrogen atoms of the bis(amidinate) ligand and the oxygen atoms of coordinated Lewis bases (**5**: two oxygen

atoms of the dme molecule, **6**: one oxygen atom of the thf molecule). The lithium atom in **5** is coordinated by one dme molecule and in complex **6** by two thf molecules. The four Ln–N distances in compounds **4–6** have rather similar values [**4**: 2.331(1)–2.369(1); **5**: 2.454(3)–2.573(3); **6**: 2.404(2)–2.481(2) Å], and the average bond lengths are comparable to those reported for related bis(amidinate) complexes ($\text{Y}^{[3a,12a]}$ $\text{Nd}^{[2c]}$ $\text{Sm}^{[18]}$).

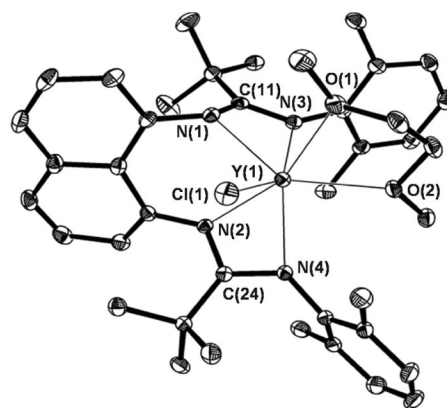


Figure 2. ORTEP diagram (30% probability thermal ellipsoids) of **4**. Hydrogen atoms are omitted for clarity. Selected bond lengths [Å] and angles [°]: Y(1)–N(1) 2.331(1), Y(1)–N(4) 2.348(1), Y(1)–N(3) 2.354(1), Y(1)–N(2) 2.369(1), Y(1)–O(1) 2.409(1), Y(1)–O(2) 2.421(1), Y(1)–Cl(1) 2.596(4), N(1)–C(11) 1.348(2), N(2)–C(24) 1.341(2), N(3)–C(11) 1.328(2), N(4)–C(24) 1.354(2), N(1)–Y(1)–N(3) 56.17(5), N(4)–Y(1)–N(2) 55.88(4).

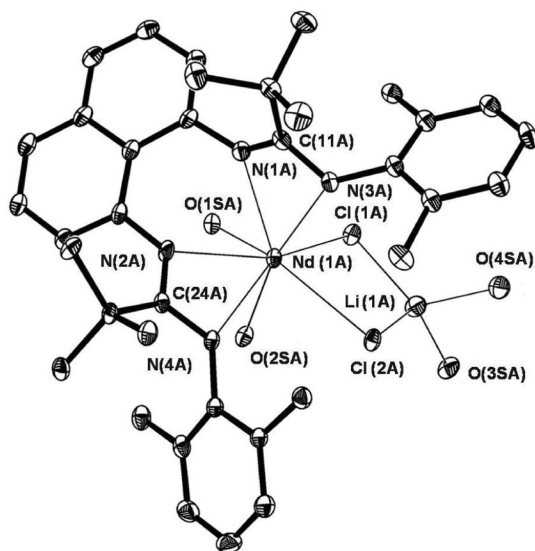


Figure 3. ORTEP diagram (30% probability thermal ellipsoids) of **5**. Hydrogen atoms and methyl and methylene groups of the dme molecules are omitted for clarity. Selected bond lengths [Å] and angles [°]: Nd(1A)–N(2A) 2.454(3), Nd(1A)–N(1A) 2.479(3), Nd(1A)–N(3A) 2.496(3), Nd(1A)–O(1SA) 2.555(2), Nd(1A)–N(4A) 2.573(3), Nd(1A)–O(2SA) 2.602(2), Nd(1A)–Cl(2A) 2.8056(9), Nd(1A)–Cl(1A) 2.8869(9), N(1A)–C(11A) 1.320(5), N(2A)–C(24A) 1.334(5), N(3A)–C(11A) 1.339(5), N(4A)–C(24A) 1.330(4), Cl(1A)–Li(1A) 2.287(7), Cl(2A)–Li(1A) 2.318(7), Li(1A)–O(4SA) 1.947(8), Li(1A)–O(3SA) 2.015(8), N(1A)–Nd(1A)–N(3A) 52.7(1), N(2A)–Nd(1A)–N(4A) 51.8(1).

The bonding situation within the NCN fragments of complexes **4–6** indicates a negative charge delocalization. Comparison of the structures of complexes **4–6** reveals versatility of the coordination modes of the new bis(amidinate) ligand framework to the lanthanide atoms, which is dependent on ion size of the central atom. Thus, in complexes of yttrium and samarium, the amidinate groups are located in a *trans* position with respect to the naphthalene fragment, while in the neodymium derivative with a larger ion,^[19] they adopt a *cis* configuration (Figure 5). At the same time, the values of the dihedral angles in these cases differ substantially: in complexes **4** and **6** they are in the region 77.6–79.7°, while in complex **5** this value is much larger – 109.4

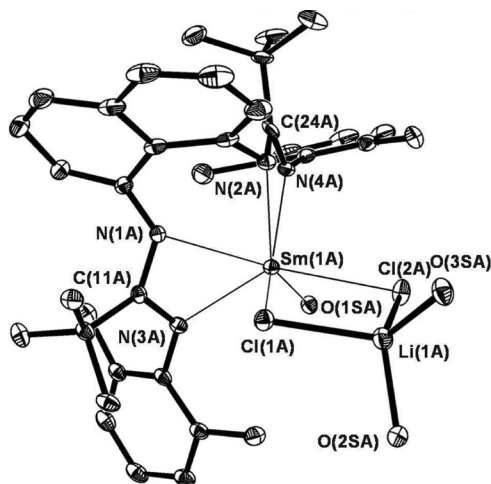


Figure 4. ORTEP diagram (30% probability thermal ellipsoids) of **6**. Hydrogen atoms and the methylene groups of the thf molecules are omitted for clarity. Selected bond lengths [Å] and angles [°]: Sm(1A)–N(2A) 2.404(2), Sm(1A)–N(4A) 2.415(2), Sm(1A)–N(3A) 2.419(2), Sm(1A)–N(1A) 2.481(2), Sm(1A)–O(1SA) 2.576(2), Sm(1A)–Cl(2A) 2.7611(7), Sm(1A)–Cl(1A) 2.7675(6), Cl(1A)–Li(1A) 2.328(5), Cl(2A)–Li(1A) 2.326(5), N(1A)–C(11A) 1.327(3), N(2A)–C(24A) 1.358(3), N(3A)–C(11A) 1.359(3), N(4A)–C(24A) 1.338(3), N(2A)–Sm(1A)–N(4A) 54.52(7), N(3A)–Sm(1A)–N(1A) 53.62(7).

and 109.6°. Moreover, the coordination of bis(amidine) **3** to lanthanide atoms of different sizes provokes distortions of different magnitudes in the naphthalene linker. In parent bis(amidine) **3**, the mean deviation of the carbon atoms of the naphthalene ring from the plane is 0.0483 Å [0.0505 Å for **3**·(MeCN)]. However, the same parameter in complexes **4** and **6**, which display a *trans* disposition of the amidinate groups, has values of 0.1119 Å and 0.1069, 0.1016 Å respectively. In complex **5**, where the amidinate groups are located on the same side of the naphthalene ring the value of mean deviation (0.0461, 0.0459 Å) is noticeably lower and is similar to that observed for starting bis(amidine) **3**. The attempt to alkylate complex **6** with an equimolar amount of LiCH₂SiMe₃ was carried out in toluene at 0 °C. Separation of the precipitate of LiCl, evaporation of toluene in vacuo, and subsequent recrystallization of the solid residue from a

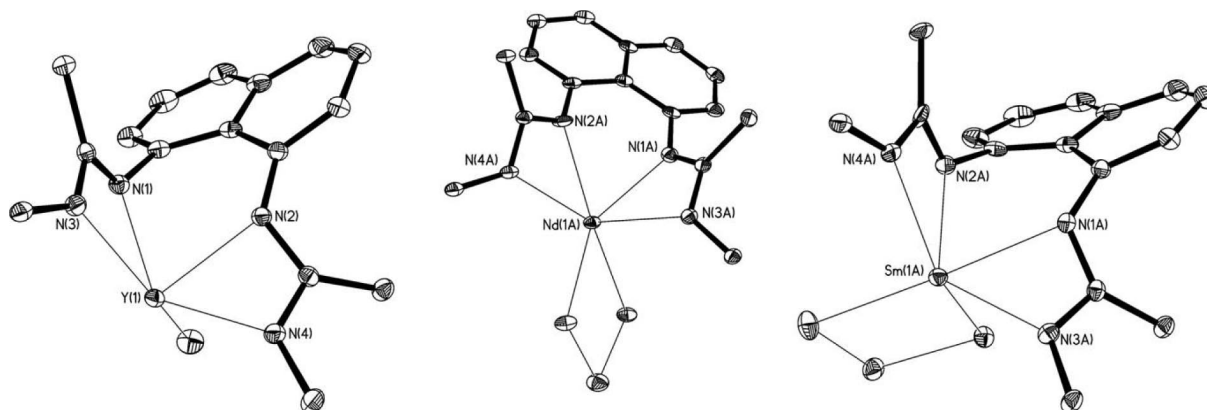
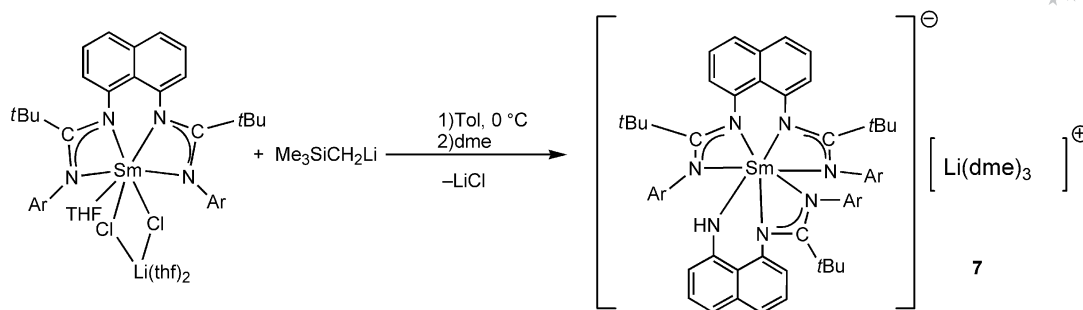


Figure 5. Dihedral angles between planes N(3)LnN(1) and N(2)LnN(4) in complexes **4–6** (**4**: 77.6°; **5**: 109.4, 109.6°; **6**: 78.5, 79.7°).



Scheme 3.

dme/hexane mixture led to the isolation of an unexpected product $[\{1,8\text{-C}_{10}\text{H}_6(\text{NC}(\text{tBu})\text{N-2,6-Me}_2\text{-C}_6\text{H}_3)_2\}\{1,8\text{-C}_{10}\text{H}_6(\text{NC}(\text{tBu})\text{N-2,6-Me}_2\text{-C}_6\text{H}_3)(\text{NH})\}\text{Sm}][\text{Li}(\text{dme})_3]$ (**7**) (Scheme 3). All attempts to isolate other samarium-containing products failed. Complex **7** was obtained as a yellow crystalline moisture- and air-sensitive solid in 24% yield. Complex **7** is soluble in thf, dme, Et_2O , and toluene and insoluble in hexane. Transparent yellow crystals of **7** suitable for X-ray single-crystal structure investigation were obtained by slow concentration of the solution in a dme/hexane mixture at ambient temperature. The X-ray diffraction study reveals that complex **7** is an ionic compound (Figure 6) consisting of the complex anion formed by the Sm^{3+} cation coordinated to one dianionic bis(amidinate) ligand and one dianionic amido-amidinate ligand $\{1,8\text{-C}_{10}\text{H}_6(\text{NC}(\text{tBu})\text{N-2,6-Me}_2\text{-C}_6\text{H}_3)(\text{NH})\}^{2-}$. The coordination sphere of the samarium atom in **7** is made up of seven nitrogen atoms, thus providing a formal coordination number of

seven. The formation of **7** obviously results from the cleavage of one amidinate fragment during decomposition of the transient alkyl complex and ligand redistribution. The cationic part consists of the Li cation coordinated to three dme molecules. The average $\text{Sm-N}(\text{amidinate})$ bond length in **7** [2.470(2) Å] is somewhat longer than those in the parent complex of the seven-coordinate samarium **6** [2.429(2) Å] and ionic bis(guanidinate) complexes $[(\text{Me}_3\text{Si})_2\text{NC}(\text{N-R})_2]_2\text{-Sm}-(\mu\text{-BH}_4)_2\text{Li}(\text{thf})_2$ ($\text{R} = \text{Cy}$, 2.424 Å;^[20] $\text{R} = i\text{Pr}$, 2.455 Å^[21]). The $\text{Sm-N}(\text{amido})$ bond length [2.350(2) Å] in **7** is similar to that formerly reported for a related ionic amido complex $\{\text{Li}(\text{thf})_4\}\{\text{Sm}[(\text{R})\text{-C}_{20}\text{H}_{12}\text{N}_2(\text{C}_{10}\text{H}_{22})]_2\}$ [2.348(3) Å].^[22]

Further studies on the synthesis of alkyl, hydrido, borohydride, alkoxide, and amido species supported by new linked bis(amidinate) ligand systems are currently in progress.

Conclusions

A new dianionic bis(amidinate) ligand framework with a conformationally rigid naphthalene linker was developed and shown to form a suitable coordination environment for lanthanide ions. The salt metathesis reactions of dilithium derivatives of **3** with LnCl_3 ($\text{Ln} = \text{Y}, \text{Nd}, \text{Sm}$) for the metals with a small ion size (Y) results in the synthesis of monomeric salt-free bis(amidinate)chlorido complexes, while for the metals possessing larger ion sizes (Nd, Sm), the formation of heterobimetallic complexes was observed. The structures of complexes **4–6** were established by X-ray diffraction studies, which reveal that a new ligand framework can coordinate to lanthanide atoms in different fashions depending on the central atom ion size. The attempt to synthesize a samarium alkyl species that is supported by the linked bis(amidinate) ligand by reaction of complex **6** with an equimolar amount of $\text{LiCH}_2\text{SiMe}_3$ afforded the unexpected amido-amidinate complex **7**, which obviously was formed by cleavage of one amidinate group during decomposition of the transient alkyl species and ligand redistribution.

Experimental Section

All experiments were performed in evacuated tubes by using standard Schlenk techniques, with the rigorous exclusion of traces of

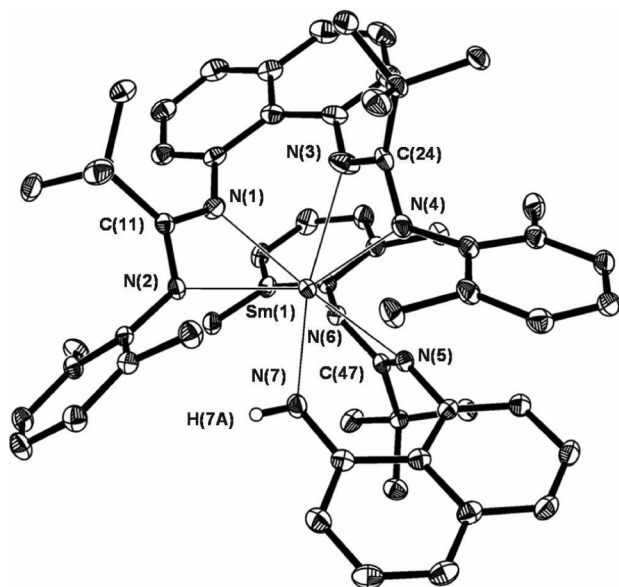


Figure 6. ORTEP diagram (30% probability thermal ellipsoids) of the anionic part of **7**. Hydrogen atoms (except that of the amido group) are omitted for clarity. Selected bond lengths [Å] and angles [°]: $\text{Sm}(1)\text{-N}(7)$ 2.350(2), $\text{Sm}(1)\text{-N}(6)$ 2.420(2), $\text{Sm}(1)\text{-N}(5)$ 2.434(2), $\text{Sm}(1)\text{-N}(3)$ 2.473(2), $\text{Sm}(1)\text{-N}(1)$ 2.476(2), $\text{Sm}(1)\text{-N}(4)$ 2.483(2), $\text{Sm}(1)\text{-N}(2)$ 2.538(2), $\text{N}(7)\text{-Sm}(1)\text{-N}(6)$ 100.72(7), $\text{N}(7)\text{-Sm}(1)\text{-N}(5)$ 69.49(7), $\text{N}(6)\text{-Sm}(1)\text{-N}(5)$ 54.50(6), $\text{N}(1)\text{-Sm}(1)\text{-N}(2)$ 52.17(6), $\text{N}(3)\text{-Sm}(1)\text{-N}(4)$ 52.56(7).

moisture and air. After drying over KOH, thf was purified by distillation from sodium/benzophenone ketyl and hexane and toluene by distillation from sodium/triglyme benzophenone ketyl prior to use. C₆D₆ was dried with sodium/benzophenone ketyl and condensed in vacuo prior to use. CH₂Cl₂ and C₆H₅Cl were dried with P₂O₅, distilled twice, and degassed by freeze-vacuum-thaw cycles prior to use. 1,8-diaminonaphthalene and pivaloyl chloride were purchased from Acros. Anhydrous YCl₃, SmCl₃, NdCl₃,^[23] and Me₃SiCH₂Li^[24] were prepared according to literature procedures. All other commercially available chemicals were used after appropriate purification. NMR spectra were recorded on Bruker Avance DRX-400 and DPX-200 spectrometers in C₆D₆ or CDCl₃ at 20 °C, unless otherwise stated. Chemical shifts for ¹H and ¹³C spectra were referenced internally by using the residual solvent resonances and are reported relative to tms in parts per million (ppm). IR spectra were recorded as Nujol mulls on a "Bruker-Vertex 70" instrument. Lanthanide metal analyses were carried out by complexometric titration. Mass spectra were recorded on a Polaris Q/Trace GC Ultra (Ion Trap analyser) chromatography mass spectrometer. The C, H, N elemental analysis was performed in the microanalytical laboratory of the G. A. Razuvaev Institute of Organometallic Chemistry.

1,8-C₁₀H₆{NHC(O)*r*Bu}₂ (1): Pivaloyl chloride (3.15 g, 26.20 mmol) was added slowly to a solution of 1,8-diaminonaphthalene (2.00 g, 12.65 mmol) and Et₃N (2.65 g, 26.23 mmol) in CH₂Cl₂ (30 mL) at room temperature to give an exothermic reaction. The reaction mixture was stirred at 35 °C for 16 h, and the volatiles were removed in vacuo at room temperature. After trituration with water (3 × 50 mL), the grey solid was washed with hexane (3 × 50 mL) and dried in vacuo at room temperature for 2 h. Yield: 3.16 g (77%). C₂₀H₂₆N₂O₂ (326.4): calcd. C 73.69, H 8.03, N 8.58; found C 73.25, H 8.29, N 8.15. ¹H NMR (200 MHz, C₅D₅N, 20 °C): δ = 1.46 (s, 18 H, CMe₃), 7.36–8.71 (m, 6 H, aryl), 10.34 (br. s, 2 H, NH) ppm. ¹³C{¹H} NMR (50 MHz, C₅D₅N, 20 °C): δ = 27.6 [s, C(CH₃)₃], 40.0 [s, C(CH₃)₃], 123.5, 123.6, 124.6, 124.7, 126.7, 136.2 (s, C aryl), 179.263 (C=O) ppm. IR (Nujol, KBr): ν̄ = 3374 (s, NH), 3065 (w, aryl), 1655 (s, C=O), 1580 (m), 1498 (s), 1278 (m), 1252 (w), 1231 (m), 1192 (m), 1169 (m), 1034 (m), 940 (m), 833 (m), 808 (m) cm⁻¹. MS (EI): *m/z* = 326.2 [M⁺].

1,8-C₁₀H₆{N=C(Cl)*r*Bu}₂ (2): PCl₅ (3.30 g, 15.80 mmol) was added in portions to a solution of **1** (2.60 g, 7.90 mmol) in chlorobenzene (30 mL) in vacuo to give a cloudy, green solution, which was stirred at 65 °C for 3 d. The solution was filtered, the volatiles were removed in vacuo at room temperature, and the solid residual was extracted with hexane (2 × 20 mL). The hexane extracts were filtered, slowly concentrated in vacuo at room temperature to half of the initial volume, and left overnight at 0 °C. The mother liquor was separated by decantation and the pale-yellow crystalline solid was washed with cold hexane (15 mL) and dried in vacuo at room temperature for 40 min to yield 1.20 g (42%) of **2**. C₂₀H₂₄Cl₂N₂ (363.4): calcd. C 66.12, H 6.66, Cl 19.52, N 7.71; found C 66.01, H 6.35, Cl 19.05, N 7.43. ¹H NMR (200 MHz, CDCl₃, 20 °C): δ = 1.46 (s, 18 H, CMe₃), 6.62–7.69 (m, 6 H, aryl) ppm. ¹³C{¹H} NMR (200 MHz, CDCl₃, 20 °C): δ = 27.1 [C(CH₃)₃], 27.6 [C(CH₃)₃], 39.9 [C(CH₃)₃], 124.1, 124.4, 125.6, 127.4, 132.9, 136.1 (s, C aryl), 179.2 (N=C) ppm. IR (Nujol, KBr): ν̄ = 3050 (w), 1673 (s, N=C), 1611 (w), 1569 (s), 1477 (m), 1327 (m), 1263 (m), 1210 (s), 1033.9 (m), 934 (s), 835 (s), 808 (s), 791 (m), 760 (s) cm⁻¹.

1,8-C₁₀H₆[NHC(*r*Bu)=N(2,6-Me₂-C₆H₃)]N=C(*r*Bu)NH(2,6-Me₂-C₆H₃) (3): 2,6-Dimethylaniline (1.53 g, 12.70 mmol) was added in portions to a solution of **2** (2.00 g, 5.52 mmol) in chlorobenzene (30 mL) in vacuo to give a yellow solution. The reaction mixture

was stirred at 65 °C for 3 d, and the volatiles were removed in vacuo to yield a pale-yellow solid. Et₂O (50 mL) and an aqueous solution of Na₂CO₃ (50 mL, 0.5 M) were added to the residual solid, and the mixture was stirred for 30 min. The organic layer was separated, washed with water (3 × 20 mL) and dried with MgSO₄. The solvent was removed in vacuo at room temperature to give a yellow solid. Recrystallization of the residue from a mixture of hexane/CH₂Cl₂ (2:1) afforded **3** as pale-yellow crystals (2.94 g, 70%). If **3** was recrystallized from acetonitrile, pale-yellow crystals of **3**·(MeCN) were obtained (2.65 g, 63%). C₃₆H₄₄N₄ (532.8): calcd. C 81.16, H 8.32, N 10.52; found C 81.42, H 8.00, N 10.31. ¹H NMR (200 MHz, CDCl₃, 20 °C): δ = 1.45 [s, 9 H, C(CH₃)₃], 1.55 [s, 9 H, C(CH₃)₃], 2.01 (s, 3 H, CH₃), 2.05 (s, 9 H, CH₃), 6.07 (s, 1 H, NH), 6.24–6.81 (m, 12 H, aryl), 8.99 (s, 1 H, NH) ppm. ¹³C{¹H} NMR (50 MHz, C₆D₆, 20 °C): δ = 18.5 (CH₃), 29.4 [C(CH₃)₃], 39.6 [C(CH₃)₃], 40.4 [C(CH₃)₃], 113.3, 115.7, 120.0, 121.1, 122.5, 123.7, 124.1, 125.6, 127.6 (aryl, CH), 117.6, 127.4, 135.1, 135.8, 137.8, 147.0 (aryl, C), 159.3 (NCN), 162.4 (NCN) ppm. IR (Nujol, KBr): ν̄ = 3400 (m), 3278 (m, N–H), 3043 (w), 1638 (m, C=N), 1608 (w), 1570 (w), 1369 (w), 1288 (m), 1209 (w), 1135 (m), 1034 (w), 925 (w), 894 (m), 884 (m), 831 (m), 820 (m), 806 (m), 760 (s) cm⁻¹. MS (EI): *m/z* = 532.3 [M⁺].

Synthesis of [1,8-C₁₀H₆{NC(*r*Bu)N-2,6-Me₂-C₆H₃}₂]YCl(dme) (4): A solution of *n*BuLi in hexane (2.18 mL, 0.95 N, 2.07 mmol) was added to a solution of **3** (0.55 g, 1.03 mmol) in thf (30 mL) at 0 °C; the reaction mixture was stirred for 40 min and was then slowly warmed up to 20 °C. YCl₃ (0.20 g, 1.03 mmol) was added, and the reaction mixture was stirred overnight. The solvent was evaporated in vacuo, and the solid residue was extracted with toluene (2 × 20 mL). The toluene extracts were filtered, and the solvent was evaporated in vacuo. After recrystallization of the residue from a mixture of hexane/dme, pale-yellow crystals of **4** were obtained in a yield of 0.45 g (45%). C₄₀H₅₂ClN₄O₂Y (745.3): calcd. C 64.47, H 7.03, Y 11.93; found C 64.21, H 6.85, Y 11.86. ¹H NMR (200 MHz, C₆D₆, 20 °C): δ = 0.88 [s, 18 H, C(CH₃)₃], 2.46 (s, 12 H, CH₃), 2.67 (br. s, 4 H, OCH₂, dme), 2.99 (br. s, 6 H, OCH₃, dme), 6.79–7.49 (m, 12 H, C–H aryl) ppm. ¹³C{¹H} NMR (50 MHz, C₆D₆, 20 °C): δ = 20.1 (CH₃), 30.3 [C(CH₃)₃], 42.9 [C(CH₃)₃], 61.2 (s, OCH₃, dme), 69.9 (s, OCH₂, dme), 120.5, 121.7, 122.1, 124.8, 128.0, 130.7, 135.7, 145.6, 148.7 (s, aryl), 179.9 (d, ¹J_{Y-C} = 2.4 Hz, NCN) ppm. IR (Nujol, KBr): ν̄ = 3054 (w), 1673 (m), 1569 (m), 1503 (w), 1261 (w), 1218 (m), 1172 (m), 1091 (s), 1046 (s), 934 (w), 860 (s), 764 (s) cm⁻¹.

[1,8-C₁₀H₆{NC(*r*Bu)N-2,6-Me₂-C₆H₃}₂]Nd(dme)(μ-Cl)₂Li(dme) (5): A solution of *n*BuLi in hexane (6.13 mL, 0.79 N, 4.84 mmol) was added to a solution of **3** (1.29 g, 2.42 mmol) in thf (30 mL) at 0 °C; the reaction mixture was stirred for 40 min and was then slowly warmed up to 20 °C. NdCl₃ (0.61 g, 2.42 mmol) was added to the solution, and the reaction mixture was stirred overnight. Volatiles were removed in vacuo, and the remaining solid was extracted with toluene (2 × 20 mL). The extracts were filtered, and toluene was removed in vacuo. The solid residue was treated with dme and recrystallized from diethyl ether. Pale-yellow crystals of **5** were obtained in a yield of 0.98 g (47%). C₅₂H₈₂Cl₂LiN₄NdO₈ (1113.4): calcd. C 56.10, H 7.42, Nd 5.03; found C 56.03, H 7.01, Nd 4.95. IR (Nujol, KBr): ν̄ = 1590 (s), 1258 (m), 1122 (w), 1122 (w), 1047 (s), 931 (s), 861 (m), 890 (m), 806 (m), 759 (s) cm⁻¹.

[1,8-C₁₀H₆{NC(*r*Bu)N-2,6-Me₂-C₆H₃}₂]Sm(thf)(μ-Cl)₂Li(thf)₂ (6): A solution of *n*BuLi in hexane (1.56 mL, 1.08 N, 1.68 mmol) was added to a solution of **3** (0.45 g, 0.84 mmol) in thf (30 mL) at 0 °C; the reaction mixture was stirred for 40 min and was then slowly warmed up to 20 °C. SmCl₃ (0.22 g, 0.84 mmol) was added, and the

reaction mixture was stirred overnight. The solvent was removed in vacuo, and the solid residue was extracted with toluene (2 × 20 mL). The toluene extracts were filtered, and the solvent was removed in vacuo. Recrystallization of the residue from a hexane/thf mixture afforded pale-yellow crystals of **6** (0.50 g, 61%). $C_{48}H_{66}Cl_2LiN_4O_3Sm$ (975.4): calcd. C 59.11, H 6.82, Sm 15.42; found C 58.83, H 6.91, Sm 14.98. 1H NMR (200 MHz, C_5D_5N , 20 °C): δ = 1.54 [s, 9 H, $C(CH_3)_3$], 1.55 (br. s, 12 H, thf β - CH_2), 1.66 [s, 9 H, $C(CH_3)_3$], 2.16 (s, 12 H, CH_3), 3.60 (br. s, 12 H, thf α - CH_2), 6.49–8.56 (m, 12 H, C-H aryl) ppm. $^{13}C\{^1H\}$ NMR (50 MHz, C_5D_5N , 20 °C): δ = 19.0 (CH_3), 26.0 (thf, β - CH_2), 29.5 [$C(CH_3)_3$], 29.8 [$C(CH_3)_3$], 40.2 [$C(CH_3)_3$], 41.0 [$C(CH_3)_3$], 67.9 (thf, α - CH_2), 113.4, 116.9, 118.2, 120.6, 121.6, 122.5, 124.6, 125.9, 127.9, 128.8, 129.5, 134.4, 137.3, 138.8, 146.7, 148.0 (s, aryl), 154.5 (s, NCN), 164.9 (s, NCN) ppm. 7Li NMR (78 MHz, C_5D_5N , 20 °C): δ = 5.4 ppm. IR (Nujol, KBr): $\tilde{\nu}$ = 3041 (w), 1638 (s), 1565 (m), 1566 (m), 1257 (m), 1223 (m), 1180 (m), 1113 (w), 1095 (s), 1053 (s), 1050 (m), 1030 (m), 929 (w), 775 (s), 764 (m) cm^{-1} .

Reaction of [1,8- $C_{10}H_6\{NC(tBu)N$ -2,6- $Me_2-C_6H_3\}_2]Sm(thf)(\mu-Cl)_2Li(thf)_2$ with $LiCH_2SiMe_3$. Synthesis of **7:** To a solution of **6** (0.38 g, 0.39 mmol) in toluene (20 mL) was slowly added a solution of Me_3SiCH_2Li (0.04 g, 0.47 mmol) in toluene (10 mL) at 0 °C, and the reaction mixture was stirred for 1 h. The yellow solution was filtered, the solvent was removed in vacuo, and the solid residue was recrystallized from a mixture of hexane/dme to give yellow crystals of **7** (0.12 g, 24%). $C_{72}H_{100}LiN_7O_6Sm$ (1316.1): calcd. C 65.67, H 7.65, Sm 11.42; found C 65.19, H 7.32, Sm 11.38. 1H NMR (400 MHz, C_6D_6 , 20 °C): δ = 0.15 [br. s, 18 H, $C(CH_3)_3$], 0.42 [br. s, 9 H, $C(CH_3)_3$], 1.24 (br. s, 6 H, CH_3), 1.54 (br. s, 12 H, CH_3), 3.11 (br. s, 18 H, OCH_3 , dme), 3.32 (br. s, 12 H, OCH_2 , dme), 6.17–7.71 (m, 21 H, C-H aryl) ppm. $^{13}C\{^1H\}$ NMR (50 MHz, C_6D_6 , 20 °C): δ = –0.2 [$C(CH_3)_3$], 1.0 [$C(CH_3)_3$], 28.9 (CH_3), 29.7 (CH_3), 39.1 [$C(CH_3)_3$], 40.4 [$C(CH_3)_3$], 58.3 (s, OCH_3 , dme), 71.9 (s, OCH_2 , dme), 113.6, 114.7, 115.9, 116.7, 119.2, 120.4, 121.4, 122.1, 122.9, 123.7, 124.1, 124.3, 126.1, 127.0, 127.2, 128.5, 129.7, 133.4, 135.4, 137.4 (s, CH aryl), 157.1, 158.7, 162.2 (NCN) ppm. 7Li NMR (156 MHz, C_6D_6 , 20 °C): δ = 6.0 ppm. IR (Nujol, KBr): $\tilde{\nu}$ = 3289 (w), 3038 (w), 1638 (s), 1608 (m), 1570 (w), 1291 (m), 1262 (m), 1156 (w), 1035 (m), 963 (m), 820 (s) cm^{-1} .

X-ray Crystallography: The data were collected on a SMART APEX diffractometer (graphite-monochromated, Mo- K_α radiation, ω - and θ -scan technique, λ = 0.71073 Å) at 100 K. The structures were solved by direct methods and were refined on F^2 by using the SHELXTL^[25] package. All non-hydrogen atoms were refined anisotropically. The NH hydrogen atoms in **3**, **3**·(MeCN) and **7** were found from Fourier syntheses of electron density and were refined isotropically, whereas the other H atoms in **3**–**7** were placed in calculated positions and were refined in the riding model. SADABS^[26] was used to perform the area-detector scaling and absorption corrections. CCDC-753381 (**3**), -753382 [**3**·(MeCN)], -753383 (**4**), -753384 (**5**), -753385 (**6**), and -753386 (**7**) contain the supplementary crystallographic data for this paper. These data can be obtained free of charge from The Cambridge Crystallographic Data Centre via www.ccdc.cam.ac.uk/data_request/cif.

DFT Calculations: The theoretical study of **3** and **3**·(MeCN) was performed at the density functional theory (DFT) level with the hybrid B3LYP functional by using the DZVP basis set and the program PC-Gamess (Firefly 71c).^[15] The absence of imaginary frequencies shows that the molecules are in a minimum for the potential energy. The AIMALL^[27] program was used to search for critical points and for the calculation of the hydrogen bond energy.

Acknowledgments

This work was supported by the Russian Foundation for Basic Research (Grant No 08-03-00391-a), the Program of the Presidium of the Russian Academy of Science (RAS), and the RAS Chemistry and Material Science Division.

- a) F. T. Edelmann, *Coord. Chem. Rev.* **1994**, *137*, 403–481; b) J. Barker, M. Kilner, *Coord. Chem. Rev.* **1994**, *133*, 219–300; c) M. P. Coles, *Dalton Trans.* **2006**, 985–1001; d) P. C. Junk, M. L. Cole, *Chem. Commun.* **2007**, 1579–1590; e) M. L. Cole, G. B. Deacon, P. C. Junk, K. Konstas, *Chem. Commun.* **2005**, 1581–1583; f) M. L. Cole, P. C. Junk, *Chem. Commun.* **2005**, 2695–2697.
- a) C. Hagen, H. Reddmann, H.-D. Amberger, F. T. Edelmann, U. Pegelow, G. V. Shalimoff, N. M. Edelstein, *J. Organomet. Chem.* **1993**, *462*, 69–78; b) M. Wedler, F. Knosel, U. Pieper, D. Stalke, F. T. Edelmann, H.-D. Amberger, *Chem. Ber.* **1992**, *125*, 2171–2181; c) A. Recknagel, F. Knosel, H. Gornitzka, M. Noltemeyer, F. T. Edelmann, U. Behrens, *J. Organomet. Chem.* **1991**, *417*, 363–375; d) M. Wedler, M. Noltemeyer, U. Pieper, D. Schmidt, H.-G. Stalke, F. T. Edelmann, *Angew. Chem. Int. Ed. Engl.* **1990**, *29*, 894–896; e) M. Wedler, A. Recknagel, J. W. Gilje, M. Noltemeyer, F. T. Edelmann, *J. Organomet. Chem.* **1992**, *426*, 295–306; f) F. T. Edelmann, *J. Alloys Compd.* **1994**, *207/208*, 182–188. For review see: g) F. T. Edelmann, *Angew. Chem. Int. Ed. Engl.* **1995**, *34*, 2466–2488; h) F. T. Edelmann, *Adv. Organomet. Chem.* **2008**, *57*, 183–352; i) F. T. Edelmann, *Chem. Soc. Rev.* **2009**, *38*, 2253–2268.
- a) R. Duchateau, C. T. Van Wee, A. Meetsma, P. T. Van Duijnen, J. H. Teuben, *Organometallics* **1996**, *15*, 2279–2290; b) R. Duchateau, C. T. Van Wee, A. Meetsma, J. H. Teuben, *J. Am. Chem. Soc.* **1993**, *115*, 4931–4932; c) R. Duchateau, C. T. Van Wee, J. H. Teuben, *Organometallics* **1996**, *15*, 2291–2302; d) S. Bambirra, D. van Leusen, A. Meetsma, B. Hessen, J. H. Teuben, *Chem. Commun.* **2003**, 522–523; e) S. Bambirra, M. W. Bouwkamp, A. Meetsma, B. Hessen, *J. Am. Chem. Soc.* **2004**, *126*, 9182–9183; f) S. Bambirra, F. Perazzolo, S. J. Boot, T. J. J. Sciarone, A. Meetsma, B. Hessen, *Organometallics* **2008**, *27*, 704–712.
- J. R. Hagardon, J. Arnold, *Organometallics* **1996**, *15*, 984–991.
- L. Zhang, M. Nishiura, M. Yuki, Y. Luo, Z. Hou, *Angew. Chem. Int. Ed.* **2008**, *47*, 2642–2645.
- E. A. Bijpost, R. Duchateau, J. H. Teuben, *J. Mol. Catal.* **1995**, *95*, 121–128.
- S. Ge, A. Meetsma, B. Hessen, *Organometallics* **2008**, *27*, 3131–3135.
- S. Bambirra, H. Tsurugi, D. van Leusen, B. Hessen, *Dalton Trans.* **2006**, 1157–1161.
- a) W. E. Piers, D. J. H. Emslie, *Coord. Chem. Rev.* **2002**, *233*–234, 131–155; b) A. A. Trifonov, *Russ. Chem. Rev.* **2007**, *76*, 1051–1072.
- a) S. Bambirra, M. J. R. Brandsma, E. A. C. Brussee, A. Meetsma, B. Hessen, J. H. Teuben, *Organometallics* **2000**, *19*, 3197–3204; b) D. Doyle, Yu. Gun'ko, P. B. Hitchcock, M. F. Lappert, *J. Chem. Soc., Dalton Trans.* **2000**, 4093–4097.
- a) G. D. Whitener, J. R. Hagadorn, J. Arnold, *J. Chem. Soc., Dalton Trans.* **1999**, 1249–1255; b) J.-F. Li, L.-H. Weng, X.-H. Wei, D.-S. Liu, *J. Chem. Soc., Dalton Trans.* **2002**, 1401–1405; c) M. S. Hill, P. B. Hitchcock, S. M. Mansell, *Dalton Trans.* **2006**, 1544–1553; d) S.-D. Bai, J.-P. Guo, D.-S. Liu, *Dalton Trans.* **2006**, 2244–2250.
- a) S. Bambirra, A. Meetsma, B. Hessen, J. H. Teuben, *Organometallics* **2001**, *20*, 782–785; b) J. Wang, Y. Yao, Y. Zhang, Q. Shen, *Inorg. Chem.* **2009**, *48*, 744–751; c) J. Wang, F. Xu, T. Cai, Q. Shen, *Org. Lett.* **2008**, *10*, 445–448.
- C. Janiak, *J. Chem. Soc., Dalton Trans.* **2000**, 3885–3896.
- F. A. Allen, O. Kennard, D. G. Watson, L. Brammer, G. Orpen, R. Taylor, *J. Chem. Soc. Perkin Trans. 1* **1987**, 1–19.

- [15] A. A. Granovsky, *PC GAMESS/Firefly version 7.1.C*, <http://classic.chem.msu.su/gran/gamess/index.html>.
- [16] R. F. W. Bader, *Atoms in Molecules – A Quantum Theory*, Oxford University Press, Oxford, **1990**.
- [17] E. Espinosa, E. Molins, C. Lecomte, *Chem. Phys. Lett.* **1998**, 285, 170–173.
- [18] M. L. Cole, P. C. Junk, *Chem. Commun.* **2005**, 2695–2697.
- [19] R. D. Shannon, *Acta Crystallogr.* **1976**, A32, 751–767.
- [20] G. G. Skvortsov, M. V. Yakovenko, P. M. Castro, G. K. Fukin, A. V. Cherkasov, J.-F. Carpentier, A. A. Trifonov, *Eur. J. Inorg. Chem.* **2007**, 3260–3267.
- [21] G. G. Skvortsov, M. V. Yakovenko, G. K. Fukin, A. V. Cherkasov, A. A. Trifonov, *Russ. Chem. Bull.* **2007**, 56, 1742–1748.
- [22] J. Collin, J.-C. Daran, E. Shulz, A. Trifonov, *Chem. Commun.* **2003**, 3048–3049.
- [23] M. D. Taylor, C. P. Carter, *J. Inorg. Nucl. Chem.* **1962**, 24, 387–393.
- [24] L. H. Sommer, R. M. Murch, F. A. Miton, *J. Am. Chem. Soc.* **1954**, 76, 1619–1626.
- [25] G. M. Sheldrick, *SHELXTL v. 6.12, Structure Determination Software Suite*, Bruker AXS, Madison, Wisconsin, USA, **2000**.
- [26] G. M. Sheldrick, *SADABS v. 2.01, Bruker/Siemens Area Detector Absorption Correction Program*, Bruker AXS, Madison, Wisconsin, USA, **1998a**.
- [27] T. A. Keith, *AIMAll*, **2008**.

Received: March 25, 2010
Published Online: June 2, 2010

Characterization of “Cd₁₀S₄(SPh)₁₂”, the Thermal Decomposition Product of (NMe₄)₄[Cd₁₀S₄(SPh)₁₆]: Synthesis of a Neutral Cd₅₄ Sulfide Cluster and of a Polymeric Chain of Thiolate-Bridged Cd₁₇ Sulfide Clusters

Maria Bendova,^[a] Michael Puchberger,^[a] and Ulrich Schubert*^[a]

Keywords: Cadmium / Nanoparticles / Cluster compounds / S ligands / Rearrangement

Contrary to claims in the literature that a cluster of the composition of “Cd₁₀S₄(SPh)₁₂” was formed by thermal treatment of (NMe₄)₄[Cd₁₀S₄(SPh)₁₆], experimental evidence was gathered that the core structure of the cluster is not exclusively retained and other CdS species are also formed. When “Cd₁₀S₄(SPh)₁₂” was treated with PhSH/NEt₃ only a part of

the material was converted into (NHET₃)₄[Cd₁₀S₄(SPh)₁₆]. From solutions of “Cd₁₀S₄(SPh)₁₂” in strongly coordinating solvents the new neutral CdS clusters Cd₅₄S₂₈(SPh)₅₂L_x (L = pyridine, DMSO or DMF) and [Cd₁₇S₄(SPh)₂₆py]_∞ were crystallized. The latter forms polymeric chains of phenylthiolate-bridged Cd₁₇ units.

Introduction

The cluster (NMe₄)₄[Cd₁₀S₄(SPh)₁₆]^[1] (**1**, Figure 1, left) decomposes upon heating in vacuo, and a compound with the postulated composition Cd₁₀S₄(SPh)₁₂ (**2**, Figure 1, right) is formed. Loss of four NMe₃ and MeSPh equivalents was proven by TGA-MS;^[2] see Equation (1). The postulated structure of **2** is derived from that of **1** by removal of four terminal SPh[−] ligands and counter-cations.^[2]

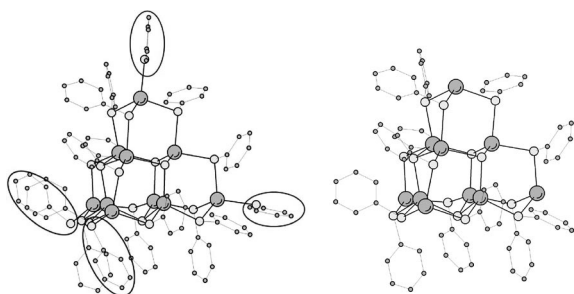
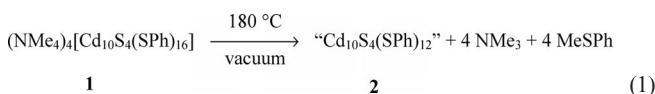


Figure 1. Schematic drawing of the experimentally determined structure of the anion of **1** (left) and the postulated structure of **2** (right). The latter is obtained from **1** by removal of four terminal SPh[−] ligands (circles).



Farneth et al.^[2] concluded from various characterization methods that **2** is a neutral Cd₁₀S₄(SPh)₁₂ cluster that tends

to aggregate to different degrees in the solid state and in solution. Herron et al.^[3] synthesized Cd₃₂S₁₄(SPh)₃₆-(DMF)₄ by addition of dimethylformamide (DMF) to a pyridine solution of **2**. They postulated that both **2** and Cd₃₂S₁₄(SPh)₃₆(DMF)₄ undergo rearrangement processes caused by fracture of the cluster cores which led to a dynamic mixture of species with lower nuclearities. The Cd₃₂ cluster apparently assembled from these smaller species and was probably the least soluble species in the system resulting in its preferred crystallization.^[2] In other studies,^[4] the thiophenolate ligands of **2** were exchanged by HSC₆H₅(OCH₂CH₂)_nOMe or dendritic thiols, and it was claimed that a Cd₁₀ cluster capped by these thiolate ligands was formed. A few experiments indicate the possibility that neutral or anionic ligands can be coordinated to the empty coordination sites of **2** generated by loss of the four SPh[−] ligands. It was thus postulated that [Cd₁₀Br₄S₄(SPh)₁₂]^{4−} was formed when **2** was treated with tetraalkylammonium bromides.^[5]

We became interested in **2** because we wanted to use its vacant Cd coordination sites for reactions with functional thiols, i.e. to use the back reaction of Equation (1) to introduce four functional ligands. In this paper, we summarize our results on the structural characterization of “Cd₁₀S₄(SPh)₁₂” (**2**) and on experiments indicating that the cluster core of **2** rearranges, especially in solutions of strongly coordinating solvents, and bigger clusters can be crystallized.

There are several reports on the rearrangement of various CdS or CdSe clusters in coordinating solvents (e.g., ref.^[3,6,7]). We showed recently that bigger clusters, and eventually CdS nanoparticles (NP) are formed in dimethyl sulfoxide (DMSO), DMF or acetonitrile solutions of **1**.^[8] According to our and other investigations, strongly coordi-

[a] Institute of Materials Chemistry, Vienna University of Technology, Getreidemarkt 9, 1060 Wien, Austria

Supporting information for this article is available on the WWW under <http://dx.doi.org/10.1002/ejic.201000454>.

nating solvents (such as pyridine, DMF or DMSO) cause fracture and rearrangement of diverse CdS or CdSe clusters, whereas in weakly coordinating solvents (such as acetonitrile or tetrahydrofuran) the rearrangement is slow, even at higher temperatures.

Eichhöfer et al.^[9] investigated a related cluster, viz. $\text{Cd}_{10}\text{Se}_4(\text{SPh})_{12}(\text{PR}_3)_4$, and concluded that this cluster grows upon thermal treatment in the solid state and forms larger clusters. This growth was not totally specific. They were also able to crystallize larger CdSe clusters (Cd_{17} and Cd_{32}) from THF solutions. DeGroot et al.^[10] investigated solid-state thermolysis of mixed metal clusters $\text{M}_{10}\text{E}_4(\text{EPh})_{12}(\text{PnPr}_3)_4$ ($\text{M} = \text{Zn} + \text{Cd}$; $\text{E} = \text{Se}, \text{Te}$) and also showed that the M_{10} clusters grow during the treatment.

Results and Discussion

" $\text{Cd}_{10}\text{S}_4(\text{SPh})_{12}$ " (**2**) was synthesized by solid-state thermolysis of **1** as reported in the literature^[2,5] and a yellow solid was obtained. We first characterized **2** in the *solid state* (in the remainder of this article, we refer to "**2**" as the thermolysis product of **1**. We will show that this is not a single compound).

There is a clear connection between the cluster or nanoparticle (NP) size and its lowest excited electronic state due to quantum size effects. The absorption maximum with lowest energy shifts to higher wavelengths with increasing size, until the characteristics of bulk CdS are reached at a diameter of about 6 nm.^[11,12] The absorption maxima of the Cd_{17} , Cd_{32} and Cd_{54} clusters are at around 290 nm, 325 nm and 350 nm, respectively (Table 1).^[11,13,14] The UV/Vis absorption spectrum of solid **2** in mineral oil (Figure 2) revealed a shift of the absorption edge from 323 nm in solid **1** to about 390 nm. We define an absorption edge as an inflection point of the absorption curve, i.e. a minimum of the first derivative curve;^[15] this allowed a better comparison of the solid state spectra of **1** and **2**, since there is no clearly visible maximum in the spectrum of **2**. Thus, the UV spectra clearly indicate that **2** also contains CdS clusters or NPs which are bigger than the core of **1**.

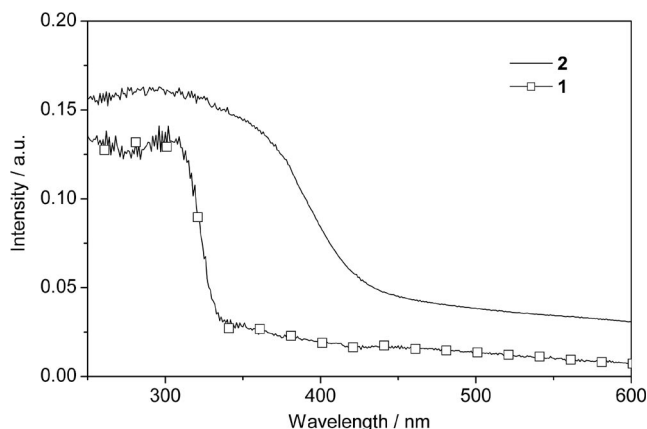


Figure 2. UV/Vis absorption spectra of **1** and **2** (suspension in mineral oil).

Powder XRD of **2** (Figure 3) revealed a pattern very similar to that reported in ref.^[2] The fact that a (weak) diffraction pattern is obtained is evidence for the presence of CdS NPs in addition to other, non-crystalline Cd/S species formed upon thermolysis of **1**. Because of the small size of the NPs, a distinction between wurtzite or sphalerite is not unequivocally possible.

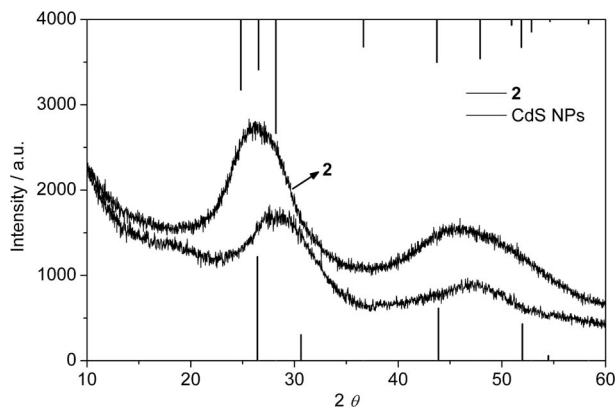


Figure 3. X-ray powder patterns of **2** and CdS NPs.^[8] The XRD patterns of wurtzite (top) and sphalerite (bottom) are shown for comparison.

Table 1. Summary of UV/Vis absorption of single-sized CdS clusters.

Cluster size	Cluster	Solvent	Absorption maximum [nm]	Ref.
Cd_{17}	$\text{Cd}_{17}\text{S}_4(\text{SPh})_{26}(\text{H}_2\text{NCSNH}_2)_2$	THF	291	[11]
	$\text{Cd}_{17}\text{S}_4(\text{SCH}_2\text{CH}_2\text{OH})_{26}$	H_2O , DMF, DMSO	ca. 290	[13]
Cd_{20}	probably $[\text{Cd}_{20}\text{S}_{13}(\text{SPh})_{22}]^{8-}$ [a]	DMF	351	[29][b]
Cd_{32}	$(\text{PPh}_4)_4[\text{Cd}_{32}\text{S}_{14}(\text{SPh})_{40}]$	DMF	327	[11]
	$\text{Cd}_{32}\text{S}_{14}(\text{SCH}_2\text{CH}(\text{OH})\text{CH}_3)_{36}(\text{H}_2\text{O})_4$	DMF	ca. 325	[14]
Cd_{54}	$\text{Cd}_{32}\text{S}_{14}(\text{SPh})_{36}(\text{DMF})_4$	THF	358	[3][b]
	$(\text{PPh}_4)_4[\text{Cd}_{54}\text{S}_{32}(\text{SPh})_{48}(\text{H}_2\text{O})_4]$	DMF	353	[11]
	$\text{Cd}_{54}\text{S}_{28}(\text{SPh})_{52}\text{L}_x$ ($\text{L} = \text{solvent}$) 4 , 5 , 6	THF, DMF, DMSO	345–359	

[a] No crystal structure. [b] Absorption does not match with cluster size. We assume that the UV/Vis absorptions are due to other clusters in both cases. We crystallized a Cd_{54} cluster ($F\bar{4}3c$, $a = 4753$ pm) at similar conditions as described in ref. [3].

The solid-state ^{113}Cd NMR spectrum of **2** (Figure 4) showed four broad, overlapping resonances at 494, 589, 660 and 736 ppm. For comparison, crystalline **1** shows sharp resonances at 598, 668 and 705 ppm in agreement with values from the literature.^[16] The broad signals of **2** also indicate that it does not consist of a single compound.

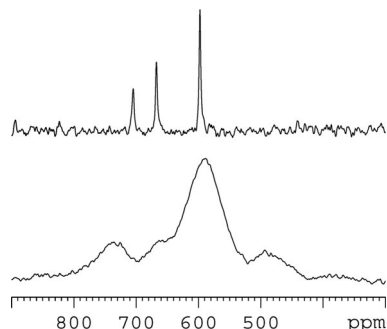


Figure 4. ^{113}Cd -CP MAS spectrum of **1** (crystallized in space group $I\bar{4}$) at 15 kHz (top) and of **2** at 6 kHz (bottom).

Compound **2** is insoluble in acetonitrile (and in other non or weakly coordinating solvents), while the starting cluster **1** is soluble in acetonitrile. For NMR investigations, four equivalents of PhSH/NEt_3 , $\text{NaSPh}/(\text{NMe}_4)\text{Cl}$ or $(\text{NMe}_4)\text{SPh}$ were added to suspension of **2** in $[\text{D}_3]\text{acetonitrile}$. If **2** would have the postulated composition $\text{Cd}_{10}\text{S}_4(\text{SPh})_{12}$ (Figure 1), the cluster anion of **1** should be re-formed upon addition of thiolate anions to the vacant coordination sites. The obtained spectra of the acetonitrile reaction suspensions were not identical with the spectrum of **1**. The most similar ^1H NMR spectrum was obtained for the reaction of **2** with NaSPh in $[\text{D}_3]\text{acetonitrile}$ (Figure 5), although there was a noticeable lowfield shift of one PhS group and a high, unresolved background. Interestingly, when four molar equivalents of PhSH and NEt_3 were added to the suspension of **2** in $[\text{D}_3]\text{acetonitrile}$ at high concentration of **2** (40 mg/mL), crystals of the known derivative $(\text{NEt}_3)_4[\text{Cd}_{10}\text{S}_4(\text{SPh})_{16}]$ ^[16] were obtained at room temperature. No resonances of the Cd_{10} cluster were observed in the solution NMR spectrum, probably because most of it was crystallized and the concentration in solution was too low ($(\text{NEt}_3)_4[\text{Cd}_{10}\text{S}_4(\text{SPh})_{16}]$ has a 10-times lower solubility in acetonitrile than **1**). The ^1H - ^{113}Cd HMBC correlation pattern with the most intense ^{113}Cd signals at 581, 601 and 655 ppm (Figure S1), as well as HSQC and HMBC spectra can be assigned to a bigger cluster, probably Cd_{32} .

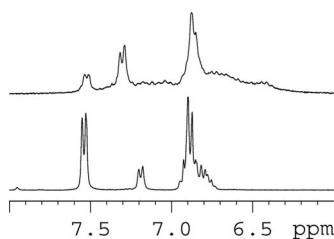


Figure 5. ^1H NMR spectra of the reaction of **2** with NaSPh (top) and of the starting cluster **1** (bottom) in $[\text{D}_3]\text{acetonitrile}$.

This was confirmed by the UV/Vis spectrum of the reaction solution (which was formed at concentration of **2** < 4.6 mg/mL). A shoulder at 325 nm was observed, which was previously assigned to a Cd_{32} cluster (see Table 1). Besides this, features below 300 nm also confirmed the presence of $(\text{NEt}_3)_4[\text{Cd}_{10}\text{S}_4(\text{SPh})_{16}]$ (Figure 6).

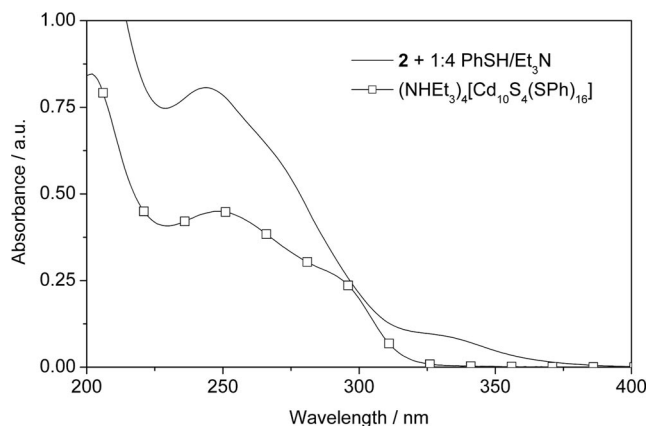


Figure 6. UV/Vis spectra of **2** (0.01 mg/mL) after addition of four equivalents of PhSH/NEt_3 and of $(\text{NEt}_3)_4[\text{Cd}_{10}\text{S}_4(\text{SPh})_{16}]$ (0.005 mg/mL) in acetonitrile.

In summary, characterization of **2** in the solid state and in solutions of weakly coordinating solvents indicate that the solid obtained upon thermolysis of **1** is not pure $\text{Cd}_{10}\text{S}_4(\text{SPh})_{12}$, as shown in Equation (1). Bigger CdS clusters and/or NPs are also formed. To gain more insight into the transformation of the cluster(s), we also investigated solutions of **2** in solvents with different coordination capability.

In the following, the solubility of **2** in *strongly coordinating solvents* (pyridine [py], DMF, DMSO) was investigated. Solubility varied from up to 100 mg/mL in pyridine and 40 mg/mL in DMSO to at least 3 mg/mL in DMF.

Pyridine Solutions: UV/Vis and dynamic light scattering (DLS) measurements showed that bigger particles than **1** were present in pyridine solution of **2**. According to DLS, particle radii were mainly between 0.55 and 4 nm (concentration 0.1 g/mL). In the UV/Vis spectra, only an indistinctive absorption edge at ca. 370 nm was observed (Figure S2). NMR investigation in $[\text{D}_5]\text{pyridine}$ revealed the presence of one PhS group [7.95 (d, 2 H), 7.06 (t, 2 H), 6.95 (t, 1 H) ppm] which would be in good agreement with the supposed structure of “ $\text{Cd}_{10}\text{S}_4(\text{SPh})_{12}$ ” (**2**). A similar ^1H NMR spectrum had been obtained previously.^[2] However, the ^{113}Cd resonances differed to the reported values. We obtained only one sharp signal at $\delta = 443$ ppm, whereas two signals at 647 and 440 ppm had been reported,^[2] the second being very broad. Since the concentration of the sample was not reported, a comparison with our results is not possible. The resonance at $\delta = 443$ ppm is upfield shifted compared with ca. 600 and 680 ppm for **1**,^[8,17] due to coordination of pyridine to Cd.^[18] The reason for only one ^{113}Cd signal instead of two could be fast intramolecular exchange of the PhS ligands.

In order to suppress the exchange in pyridine solution of **2**, we evaporated non-coordinated pyridine and dissolved the residue ("pyridine adduct of **2**") in CH_2Cl_2 . The UV/Vis spectrum directly after the preparation of the solution had an absorption edge at 351 nm (Figure S2). This might be due to the presence of Cd_{32} clusters (see above). Two sets of PhS groups and one ^{113}Cd signal at $\delta = 615$ ppm were observed in the NMR spectra in CD_2Cl_2 . After two weeks at room temperature, one PhS group disappeared and many small crystals were formed, which were bright in polarized light. Two weeks later, cubic crystals were also present in the sample, which were dark in polarized light. None of them was suitable for single-crystal X-ray diffraction measurement (SC-XRD). After about one month, many bigger crystals, bright in polarized light, were obtained. A single-crystal X-ray structure determination revealed that the crystals have the composition $[\text{Cd}_{17}\text{S}_4(\text{SPh})_{26}\text{py}]_\infty$ (**3**) where $\text{Cd}_{17}\text{S}_4(\text{SPh})_{25}\text{py}$ units are connected by bridging SPh groups. This crystallization sequence was repeated at concentrations 20–50 mg/mL of **2** in CH_2Cl_2 several times, but the first two crystalline compounds could not be characterized by SC-XRD. Another crystalline cluster, viz. neutral $\text{Cd}_{54}\text{S}_{28}(\text{SPh})_{52}(\text{py})_{7.5}$ (**4**) was obtained directly from the pyridine solution of **2** by addition of toluene. Similarly, Herron et al.^[3] obtained crystalline $\text{Cd}_{32}\text{S}_{14}(\text{SPh})_{36}(\text{DMF})_4$ by addition of DMF to the pyridine solution of **2**. The crystal structures of **3** and **4** are discussed below.

DMF and DMSO Solutions: The UV/Vis spectra of **2** in DMF and DMSO showed that clusters bigger than Cd_{10} were present (Figure S3). Additionally, the spectra changed upon heating at 80 °C for 14 h. A pronounced maximum developed at 325 nm in DMF, and at 350 nm in DMSO. The first derivative curves showed that several species were present in the solutions after heating. The UV spectra thus indicate that the DMF solution could contain Cd_{32} and Cd_{54} clusters, and the DMSO solution a Cd_{54} cluster and bigger NPs.

NMR spectra of **2** in $[\text{D}_6]\text{DMSO}$ directly after dissolution were complex. In the ^1H - ^{113}Cd HMBC correlation spectrum, intense ^{113}Cd resonances were found at 578, 589, 591 and 651 ppm and less intense at 576, 584, 586, 595, 599 and 602 ppm. After heating the solution to 80 °C for 4 h, the spectra simplified substantially as only three intense ^{113}Cd signals at 579, 599.5 and 652 ppm, one less intense at $\delta = 621.5$ ppm, and four different PhS groups were observed. In the ^1H - ^{113}Cd HMBC correlation (Figure 7), the first PhS group (T^1) [7.36 (d, 2 H), 6.61 (t, 2 H), 6.87 (m, 1 H) ppm] correlated to the ^{113}Cd resonances at 579 and 599.5 ppm, the second (T^2) [6.97 (d, 2 H), 6.30 (t, 2 H), 6.61 (t, 1 H) ppm] to those at 599.5 and 652 ppm and the third (T^3) [6.94 (d, 2 H)] to that at $\delta = 621.5$ ppm. The fourth group (T^4) [7.25 (m, 2 H), 6.90 (m, 2 H), 6.83 (m, 1 H) ppm] did not show any correlation. Detailed analysis of molecular symmetry and possible solution NMR behavior of a neutral Cd_{54} cluster (**4** or **5**)^[19] indicated that T^1 , T^2 and T^3 could originate from a Cd_{54} cluster formed during heating, which would be in line with the UV/Vis spectra.

The observed ^1H - ^{113}Cd correlations and intensities of ^1H and ^{113}Cd signals were also in good agreement with those supposed for a Cd_{54} cluster. The ^{113}Cd resonance at $\delta = 579$ ppm would then belong to a Cd site with a $[\text{Cd}(\text{SPh})_3(\text{DMSO})_1]$ environment, those at $\delta = 599.5$ and 621.5 ppm to a $[\text{CdS}_1(\text{SPh})_3]$ and the one at $\delta = 652$ ppm to a $[\text{CdS}_2(\text{SPh})_2]$ coordination. These resonances are slightly upfield shifted compared to about 600 ppm for a $[\text{Cd}(\text{SPh})_4]$ environment in **1** or $[\text{Cd}(\text{SPh})_4]^{2-}$, 680 ppm for $[\text{CdS}_2(\text{SPh})_2]$ in **1**, and ca. 725 ppm for a $[\text{CdS}_4]$ environment.^[8,17,20] The fourth observed PhS group (T^4), which did not show a ^1H - ^{113}Cd HMBC correlation, could originate from byproducts formed during the heat treatment, similar to previous observations.^[8]

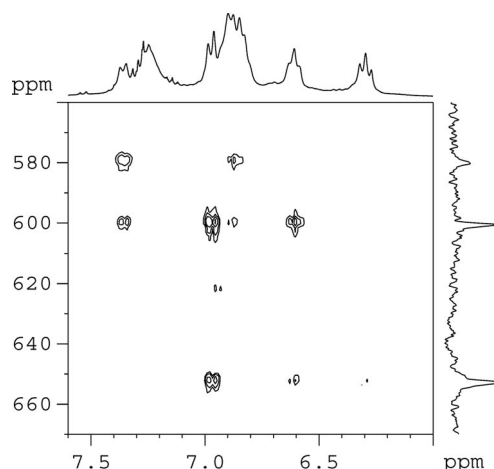


Figure 7. ^1H - ^{113}Cd HMBC correlation of **2** in $[\text{D}_6]\text{DMSO}$ after heating to 80 °C for 4 h.

We were able to crystallize $\text{Cd}_{54}\text{S}_{28}(\text{SPh})_{52}(\text{DMF})_4$ (**5**) and possibly $\text{Cd}_{54}\text{S}_{28}(\text{SPh})_{52}(\text{DMSO})_4$ (**6**) from solutions of **2** in DMF or DMSO heated to 80 °C for 14 h by addition of acetone or toluene, respectively. Crystals were only obtained when the solutions were heated. The structure of **5** was determined by SC-XRD (see below), but crystals **6** were too small and were characterized only by UV/Vis. Their absorption maximum in THF was at 359 nm, which is similar but slightly red-shifted compared to the maxima of other Cd_{54} clusters (Table 1). Maybe cluster **6** has a Cd_{54} core, but a larger core cannot be excluded.

The $\text{Cd}_{54}\text{S}_{28}(\text{SPh})_{52}\text{L}_x$ clusters **4**, **5** and **6** were characterized in THF, DMF or DMSO solution by UV/Vis absorption (Table 1, Figure S4). Their maxima were in the range 345–359. The range of the absorption maxima is rather broad; this may be due to the different solvents. For example, the absorption maxima of molecular CdSe clusters also vary in the range 360–375 nm.^[9,21] Thus, comparing the absorption maxima of our Cd_{54} clusters with CdS clusters of the same and smaller sizes (Table 1), their dependence on the cluster size is obvious. The fact that the spectra of **4** are similar in weakly and strongly coordinating solvents (THF and DMF, DMSO) leads to the conclusion that

its core structure present in solid-state is temporally preserved in the solutions. However, exchange of ligands *L* by excess solvent molecules is very probable.

Crystal Structures

The cluster core of $[\text{Cd}_{17}\text{S}_4(\text{SPh})_{26}(\text{py})]_{\infty}$ (**3**) (Figure 8) is the same as that of the anionic cluster $(\text{NMe}_4)_2[\text{Cd}_{17}\text{S}_4(\text{SPh})_{28}]$.^[6] In the latter cluster, each corner of the Cd_{17} -capped “super-tetrahedron”^[22] is coordinated by terminal SPh groups. In the related neutral cluster $\text{Cd}_{17}\text{S}_4(\text{SCH}_2\text{CH}_2\text{OH})_{26}$, the same tetrahedral coordination of the corner Cd atoms is achieved by SR bridging.^[13] A 3D network is thus formed where each Cd_{17} tetrahedron is sharing corners with four neighboring Cd_{17} tetrahedra through μ_2 - $\text{SCH}_2\text{CH}_2\text{OH}$ bridges. Similar 3D arrangements of clusters owing to bridging SPh groups was also found for Cd_{17} ^[23] and Cd_{32} ^[24] clusters. The structure of **3** is in between. Since one corner Cd atom is coordinated by pyridine, only two SPh groups per cluster must be bridging to render all corner Cd atoms tetrahedrally coordinated (the fourth corner Cd atom is coordinated by a terminal SPh group). This results in an uncharged 1D polymeric chain of connected clusters. To the best of our knowledge, this is the first 1D polymer of CdS clusters connected through SR bridges.

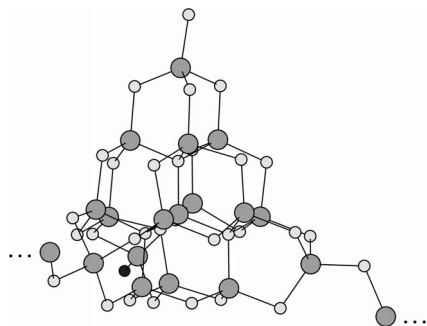


Figure 8. Molecular structure of $[\text{Cd}_{17}\text{S}_4(\text{SPh})_{26}\text{py}]_{\infty}$ (**3**). The phenyl groups and pyridine ring (the black sphere indicates the nitrogen atom) were omitted for clarity. The dotted lines indicate the inter-cluster bridges.

The clusters **4** and **5** have the same tetrahedral $\text{Cd}_{54}\text{S}_{28}(\text{SPh})_{52}\text{L}_x$ structure (Figure 9) with probably 7.5 pyridine ligands (**4**) (see below) and 4 DMF ligands (**5**) in the apical positions. Their core structure is the same as that of anionic Cd_{54} clusters such as $[\text{Cd}_{54}\text{S}_{32}(\text{SPh})_{48}(\text{H}_2\text{O})_4]^{4-}$ ^[11] which can be described as a hybrid between a cubic zincblende-type core (16 adamantane CdS cages) and hexagonal wurtzite-type corners (4 barrelene CdS cages at each of the corners). To get a neutral cluster with the same core structure, four μ_3 -bridging sulfide ions in the structure of $[\text{Cd}_{54}\text{S}_{32}(\text{SPh})_{48}\text{L}_4]^{4-}$ must be replaced by μ_3 -SPh groups, probably one on each face of the super-tetrahedral cluster core. As a matter of fact, we found residual electron density in **4** and **5** which was assigned to phenyl rings attached to the μ_3 -S atoms located at the faces of the Cd_{54} super-tetrahedron. However, the phenyl groups were disordered in a sense that each of the three μ_3 -S atoms at the faces can be

substituted by a thiophenolate group. Each phenyl group position was thus refined with 33% occupancy and reasonable thermal parameters were obtained. μ_3 -Coordination of thiolate ligands in CdS clusters or Cd complexes is unusual and was found in the CSD database only in six complexes. Examples are $[\text{Cd}_{10}(\text{SCH}_2\text{CH}_2\text{OH})_{16}]^{4+}$ ^[25] or $\text{Cd}_{10}(\text{SCH}_2\text{CH}_2\text{OH})_{16}\text{Cl}_4$ ^[26] with four μ_3 -coordinating ligands.

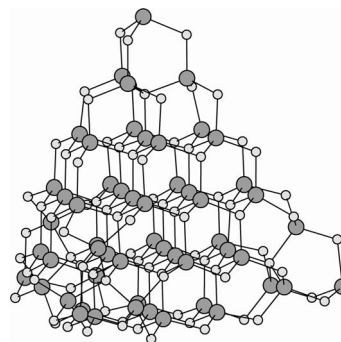


Figure 9. Molecular structure of $\text{Cd}_{54}\text{S}_{28}(\text{SPh})_{52}\text{L}_x$ (**4**: *L* = pyridine, **5**: *L* = DMF). The phenyl groups and neutral ligands *L* were omitted for clarity.

The assignment of the ligands *L* in the structures **4** and **5** was problematic. In **5**, the DMF ligands could not be assigned unequivocally from the residual electron density. The situation was complicated also by the threefold axis passing through the vertices. We thus placed only an oxygen atom in tetrahedral position to each vertex Cd atom of the Cd_{54} tetrahedron, which could be refined satisfactorily.

In **4**, three pyridine positions were found at each vertex Cd atom (Figure 10). This renders these Cd atoms octahedrally coordinated. However, the occupancy of these pyridine sites could not be determined with sufficient accuracy. One of the pyridine positions at three of the four vertices overlapped with a pyridine position of neighboring Cd_{54} clusters. Therefore, the three non-overlapping pyridine rings were refined with 100% occupancy, all the others with 50% occupancy. This leads to a total of 7.5 pyridine ligands for one cluster. However, this number of pyridine ligands is only approximate and probably overestimated. The average Cd–N distance in **4** is 263(3) pm. For comparison, the Cd–N distances in CdS clusters with pyridine ligands in tetrahedral Cd coordination are in the range 225–233 pm (**3**, ref.^[11,27]), which supports the octahedral coordination of the vertex Cd atoms in **4**.

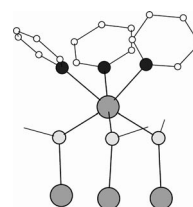


Figure 10. Arrangement of three pyridine ligands on one vertex of the Cd_{54} tetrahedron in the crystal structure of **4**.

Conclusions

The structure of compound **2** formed by thermolysis of $[\text{Cd}_{10}\text{S}_4(\text{SPh})_{16}]^{4-}$ (**1**), postulated to have the composition $\text{Cd}_{10}\text{S}_4(\text{SPh})_{12}$,^[2] was investigated in solid state and various solvents. Analysis in solid state revealed that part of the Cd_{10} clusters grew unspecifically during the heat treatment. Other CdS clusters and/or nanoparticles were formed, as indicated by the solid state ^{113}Cd NMR spectra. On the other hand it was shown that a part of **1** retained its Cd_{10} core structure since crystals of $(\text{NHET}_3)_4[\text{Cd}_{10}\text{S}_4(\text{SPh})_{16}]$ could be crystallized after addition of four equivalents of PhSH/NET_3 to a suspension of **2**. Our conclusions are in disagreement with the investigation of Farneth et al.^[2] claiming that **2** is a neutral $\text{Cd}_{10}\text{S}_4(\text{SPh})_{12}$ cluster that tends to aggregate to different degrees in the solid state and in solution. This difference should not be caused by modification of the thermal treatment of **1**, but instead our interpretation of the data is different.

Additional information was obtained in strongly coordinating solvents (pyridine, DMF, DMSO). From pyridine solutions of **2**, we were able to crystallize a Cd_{17} (**3**) and Cd_{54} (**4**) clusters. DMF and DMSO solutions showed appreciable changes in the UV/Vis and NMR spectra when heated to 80 °C. Neutral Cd_{54} (**5**, **6**) clusters crystallized from these solutions. These structural changes of **2** can be attributed to rearrangement processes in strongly coordinating solvents, as has been observed previously for other CdS clusters.^[3,7,8]

The obtained Cd_{54} clusters **4**, **5** are unusual because they are not charged owing to μ_3 -PhS groups. Syntheses of **5** and **6** were relatively easy and no solid by-product was obtained. This renders **5** and **6** suitable for applications which require usage of neutral CdS clusters.

Experimental Section

Syntheses: Standard Schlenk techniques were employed for all syntheses using a double-manifold vacuum line with high-purity dry argon. Oxygen was removed from the solvents using Schlenk and cannula techniques, and sparging of argon. $\text{Cd}(\text{NO}_3)_2$, PhSH , NET_3 and NMe_4Cl were purchased from Aldrich and used as received. Pyridine, dimethylformamide (DMF) and dimethyl sulfoxide (DMSO) as well as all other solvents were distilled, dried and deoxygenated by standard techniques.

$(\text{NMe}_4)_4[\text{Cd}_{10}\text{S}_4(\text{SPh})_{16}]$ (1**):** The synthesis was performed according to published procedures.^[1] The product was recrystallized from boiling acetonitrile.

$\text{Cd}_{10}\text{S}_4(\text{SPh})_{12}$ (2**):** The compound was synthesized by slight modification of the published procedure.^[2,5] Cluster **1** was heated under vacuum at 180 °C for 6 h and a yellow solid was obtained. Thermogravimetric analysis (TGA) and elemental analysis show that composition of **2** is equivalent to that reported in ref.^[2] The corresponding TGA is shown in Figure S5; it was obtained by using a stream of N_2 instead of vacuum. The measured weight decrease of 21.7% corresponds well with the theoretical value: 22.3%. The elemental analysis of **2** was also in good agreement with the expected formula: $\text{Cd}_{10}\text{S}_4(\text{SPh})_{12} = \text{C}_{72}\text{H}_{60}\text{S}_{16}\text{Cd}_{10}$ (2562.4); calcd. C 33.75, H 2.36, N 0.00, S 20.02; found C 34.3, H 2.3, N 0.07, S 20.8.

$[\text{Cd}_{17}\text{S}_4(\text{SPh})_{26}\text{py}]_\infty$ (3**):** 139 mg (0.054 mmol) of **2** was dissolved in 1.5 mL of pyridine. After evaporation of all volatile compounds at room temperature at $p < 2$ mbar, the residue was dissolved in 6 mL of CH_2Cl_2 . After 4 d at room temperature, many small crystals were present in the sample which were bright in polarized light. After another 3 weeks, other cubic crystals formed, which were dark in polarized light. None of them had sufficient diffraction quality to be measured by single-crystal XRD. After one additional month, few big block pale-yellow crystals of **3** crystallized which were bright in polarized light. The total solid yield was 98 mg, from which around 10% were crystals of **3**.

$\text{Cd}_{54}\text{S}_{28}(\text{SPh})_{52}(\text{py})_{7.5}$ (4**):** 116 mg (0.045 mmol) of **2** was dissolved in 1.1 mL of pyridine, and 2.3 mL of toluene was added. From the formed suspension, few big cubic, pale-yellow crystals of **4** (dark in polarized light) crystallized after one month at room temperature. Solid yield was 10 mg from which around 70% were crystalline **4**.

$\text{Cd}_{54}\text{S}_{28}(\text{SPh})_{52}(\text{DMF})_4$ (5**):** 60 mg (0.023 mmol) of **2** was heated in 10 mL of DMF at 80 °C for 14 h. The suspension was then filtered through a Nylon syringe filter (0.2 μm), then 7.5 mL of acetone was added. The solution was left undisturbed at room temperature, clear cubic crystals of **5** (dark in polarized light) crystallized within a few days. No other solid species was formed, even not after few weeks; yield 6 mg of **5**.

$\text{Cd}_{54}\text{S}_{28}(\text{SPh})_{52}(\text{DMSO})_4$ (6**):** 6 mg (0.0023 mmol) of **2** was heated in 1 mL of DMSO at 80 °C for 14 h. Then 3 mL of toluene was added. The resulting solution was allowed to stand undisturbed at room temperature. After one month, small yellow cubic crystals were present as the only solid phase. They were too small for single-crystal XRD characterization. They were characterized by UV/Vis absorption; yield 0.5 mg of **6**.

Physical Measurements: Solution UV/Vis absorption spectra were recorded on a Perkin–Elmer Lambda 35 UV/Vis spectrophotometer in 1 cm quartz cuvettes against air. Spectra of the pure solvents were subtracted. Solid-state spectra were measured for the micron-sized powders in mineral oil between quartz plates with a Labsphere integrating sphere.

Dynamic light scattering (DLS) experiments were performed with an ALV/CGS-3 Compact Goniometer system equipped with an ALV/LSE-5003 Multiple τ Digital Correlator (ALV-GmbH, Germany) at a scattering angle of 90° and a 632.8 nm JDSU laser 1145P. All measurements were carried out at a temperature 25 ± 0.1 °C in glass containers. Measured intensity correlation functions were regularized fitted by $g_2(t)$ function with radius distribution limits 0.5 and 2500 nm. The obtained mass weight linear distribution functions are summarized in Figure S6 of the Supporting Information.

Powder X-ray diffraction measurements were performed on a Philips X'Pert Pro diffractometer system [Cu-K_α radiation ($\lambda = 1.542$ Å) equipped with an X'Celerator multi-channel detector; Bragg–Brentano geometry]. The samples were placed on a single-crystal Si wafer sample holder and measured with a rate of 3°/min.

Solution NMR spectra were recorded on a Bruker DPX 300 (^1H at 300.13 MHz, ^{13}C at 75.47 MHz, ^{113}Cd at 66.61 MHz) equipped with a 5 mm inverse-broadband probe head with a z -gradient unit. 2D-Experiments were measured with Bruker standard pulse sequences (COSY (Correlated Spectroscopy), HSQC (Heteronuclear Single Quantum Correlation), HMBC (Heteronuclear Multi Bond Correlation), ^1H - ^{113}Cd HMBC). Shifts for solution ^{113}Cd NMR were referenced against 1 M $\text{Cd}(\text{NO}_3)_2$ (aq) ($\delta = 0$); for comparison, literature data were re-calculated to 1 M $\text{Cd}(\text{NO}_3)_2$ (aq) as reference.

Table 2. Summary of crystallographic parameters for [Cd₁₇S₄(SPh)₂₆py]_∞ (**3**), Cd₅₄S₂₈(SPh)₅₂(py)_{7.5} (**4**), Cd₅₄S₂₈(SPh)₅₂(DMF)₄ (**5**).

	3	4	5
Formula	C ₁₆₁ H ₁₃₅ Cd ₁₇ N ₁ S ₃₀	C _{349.5} H _{297.5} Cd ₅₄ N _{7.5} S ₈₀	C ₃₂₄ H ₂₈₈ Cd ₅₄ N ₄ O ₄ S ₈₀
Formula weight	4956.3	13236.9	12936.0
Crystal size [mm]	0.20 × 0.15 × 0.15	0.25 × 0.20 × 0.12	0.32 × 0.24 × 0.15
Crystal system	monoclinic	cubic	cubic
Space group	<i>P</i> 2 ₁ / <i>c</i>	<i>P</i> 4̄3 <i>n</i>	<i>F</i> 4̄3 <i>c</i>
<i>a</i> [pm]	2439.1(3)	4731.6(1)	4768.0(4)
<i>b</i> [pm]	2617.3(3)		
<i>c</i> [pm]	3069.8(4)		
β [°]	92.539(2)		
<i>V</i> · 10 ⁶ [pm ³]	19578(4)	105928(4)	108395(14)
<i>Z</i>	4	8	8
$\rho_{\text{calcd.}}$ [g cm ⁻³]	1.681	1.660	1.585
μ [mm ⁻¹] (Mo- <i>K</i> _α)	2.165	2.467	2.409
θ_{max} [°]	25.00	22.50	24.99
Reflections measured	103074	849271	101570
Unique reflections	34425	23086	7969
Reflections <i>I</i> > 2σ(<i>I</i>)	11732	15999	2932
parameters	1069	1411	471
<i>R</i> ₁ [<i>I</i> > 2σ(<i>I</i>)]	0.0972	0.1161	0.1120
<i>wR</i> ₂ [<i>I</i> > 2σ(<i>I</i>)]	0.2287	0.2789	0.3251
GOF for <i>I</i> ²	0.866	1.092	1.060
Min./max. electron density [e Å ⁻³]	2.525/−1.304	1.612/−1.075	1.363/−0.846
<i>V</i> (solvent accessible voids) [Å ³] / unit cell	3197.3	26457.1	35806.1
<i>e</i> [−] in solvent accessible voids / unit cell	218.0	1629.1	1318.4

0.1 M Cd(NO₃)₂ (aq) resonates at δ = 17 ppm while the chemical shift difference is 65 ppm for Cd(NO₃)₂ (aq) from 4 M to infinite dilution.^[28] NMR solvents were purchased from euriso-top in high purity grade. **2** in [D₅]pyridine solution was measured at concentration 100 mg/mL, resonance at δ = 443 ppm had FWHM = 2.1 ppm. **2** in [D₆]DMSO was measured at concentration 50 mg/mL before and after heating to 80 °C for 4 h.

Solid State NMR spectra were recorded on a Bruker Avance 300 (¹³C at 75.47 MHz, ¹¹³Cd at 66.54 MHz) equipped with a 4 mm broadband MAS probe head. ¹³C and ¹¹³Cd NMR spectra were recorded with ramped CP/MAS (Cross Polarization and Magic Angle Spinning). Rotor spinning speed was 6 and 8 kHz. Shifts were referenced against 1 M Cd(NO₃)₂ (aq) (δ = 0).

Thermogravimetric analysis (TGA) of **1** was carried out on a Netzsch TG209C instrument, with a heating program equivalent to the synthesis of **2** (a heating phase with a rate of 4 K/min to 180 °C followed by holding at 180 °C for 6 h) in N₂ atmosphere at a flow rate of 25 mL/min. Temperature calibration was performed using standard Netzsch calibration sets.

X-ray Structure Analyses: Crystals suitable for single-crystal X-ray diffraction were taken directly from the reaction solutions, selected in perfluoropolyether oil, mounted on a Bruker AXS SMART diffractometer with an APEX CCD area detector and measured in a nitrogen stream at 100 K. Graphite-monochromated Mo-*K*_α radiation (λ = 71.073 pm) was used for all measurements. The data collection covered at least a hemisphere of the reciprocal space using 0.3° ω -scan frames. The crystal-to-detector distance was 5 cm. The data were corrected for polarization and Lorentz effects, and corrections for absorption and $\lambda/2$ effects were applied.

The structures were solved with direct methods and were then refined by the full-matrix least-squares method based on *F*² using the program package SHELXTL (Bruker AXS Inc.).

The data for all structures were of poor quality because of high degree of cluster and ligand disorder, which resulted in a resolution of about 1 Å. Also the CdS overstructure influenced the appear-

ance of diffraction patterns and quality of the data. Residual electron density was high in all structures and could not be exactly assigned to disordered solvent molecules, so it was removed by the program package PLATON (Squeeze).^[29] Calculated densities and absorption coefficients are consequently lower than the experimental values. Important parameters for all structures are summarized in Table 2. Site occupancies of the μ_3 -PhS groups in **4** and **5** were set to 0.33. Their anisotropic parameters are reasonable, but they have slightly higher standard deviations than μ_2 -PhS groups. Phenyl rings in the vicinity of the μ_3 -PhS groups were disordered.

3: All Cd and S atoms were refined with anisotropic displacement parameters. All C and N atoms were treated isotropically to get a sufficient data-to-parameter ratio. Hydrogen atoms were inserted only to phenyl groups with relatively small *U*_{iso}. The highest peaks in residual electron density map are located ca. 1 Å off the Cd atoms.

4: All Cd, S, C and N atoms were refined with anisotropic displacement parameters. All phenyl and pyridine rings were treated as rigid hexagons. The occupancy factor for pyridine ligands was not refined but set to 1.0 at one corner and 0.5 at the remaining three corners of the tetrahedron, resulting in overall 7.5 pyridine ligands per cluster. Hydrogen atoms were not inserted. The highest peaks in residual electron density map are located about 10 pm from Cd atoms.

5: All Cd, S, C and O atoms were refined with anisotropic displacement parameters, but hydrogen atoms were not added to the phenyl rings. The apex DMF ligands could not be distinguished in the residual electron density, except the Cd-bonded oxygen atom.

CCDC-767707 (for **3**), -767708 (for **4**) and -767709 (for **5**) contain the supplementary crystallographic data for this paper. These data can be obtained free of charge from The Cambridge Crystallographic Data Center via www.ccdc.cam.ac.uk/data_request/cif.

Supporting Information (see also the footnote on the first page of this article) Supporting Information contains additional data on NMR measurement of **2** in [D₃]acetonitrile, UV/Vis spectra of **2**

and Cd₅₄ cluster compounds, TGA analysis equivalent to the syntheses of **2**, and various DLS measurements.

Acknowledgments

This work was financially supported by the Austrian Science Funds (FWF), Wien (project P19199). The authors thank K. Mereiter for help with the single-crystal X-ray analyses, and B. Stöger and G. Wieser for powder XRD analyses.

- [1] I. G. Dance, A. Choy, M. L. Scudder, *J. Am. Chem. Soc.* **1984**, *106*, 6285–6295.
- [2] W. E. Farneth, N. Herron, Y. Wang, *Chem. Mater.* **1992**, *4*, 916–922.
- [3] N. Herron, J. C. Calabrese, W. E. Farneth, Y. Wang, *Science* **1993**, *259*, 1426–1428.
- [4] K. Konishi, T. Hiratani, *Angew. Chem. Int. Ed.* **2006**, *45*, 5191–5194; T. Tsuboi, Y. Takaguchi, S. Tsuboi, *Chem. Commun.* **2008**, *1*, 76–78.
- [5] T. Hiratani, K. Konishi, *Angew. Chem. Int. Ed.* **2004**, *43*, 5943–5946.
- [6] G. S. H. Lee, D. C. Craig, I. Ma, M. L. Scudder, T. D. Bailey, I. G. Dance, *J. Am. Chem. Soc.* **1988**, *110*, 4863–4864.
- [7] S. L. Cumberland, K. M. Hanif, A. Javier, G. A. Khitrov, G. F. Strouse, S. M. Woessner, C. S. Yun, *Chem. Mater.* **2002**, *14*, 1576–1584; M. W. DeGroot, H. Rosner, J. F. Corrigan, *Chem. Eur. J.* **2006**, *12*, 1547–1554; D. D. Lovingood, R. E. Oyler, G. F. Strouse, *J. Am. Chem. Soc.* **2008**, *130*, 17004–17011.
- [8] M. Bendova, M. Puchberger, S. Pabisch, H. Peterlik, U. Schubert, *Eur. J. Inorg. Chem.* **2010**, 2266–2275.
- [9] A. Eichhoefer, *Eur. J. Inorg. Chem.* **2005**, 1245–1253; A. Eichhoefer, O. Hampe, *J. Cluster Sci.* **2007**, *18*, 494–504.
- [10] M. W. DeGroot, N. J. Taylor, J. F. Corrigan, *Inorg. Chem.* **2005**, *44*, 5447–5458.
- [11] N. Zheng, X. Bu, H. Lu, Q. Zhang, P. Feng, *J. Am. Chem. Soc.* **2005**, *127*, 11963–11965.
- [12] L. E. Brus, *J. Chem. Phys.* **1984**, *80*, 4403–4409; A. P. Alivisatos, *J. Phys. Chem.* **1996**, *100*, 13226–13239; R. Rossetti, J. L. Ellison, J. M. Gibson, L. E. Brus, *J. Chem. Phys.* **1984**, *80*, 4464–4469.
- [13] T. Vossmeier, G. Reck, L. Katsikas, E. T. K. Haupt, B. Schulz, H. Weller, *Science* **1995**, *267*, 1476–1479.
- [14] T. Vossmeier, G. Reck, L. Katsikas, E. T. K. Haupt, B. Schulz, H. Weller, *J. Am. Chem. Soc.* **1995**, *117*, 12881–12882.
- [15] O. Alvarez-Fregoso, J. G. Mendoza-Alvarez, O. Zelaya-Angel, *J. Appl. Phys.* **1997**, *82*, 708–711.
- [16] G. S. H. Lee, K. J. Fisher, A. M. Vassallo, J. V. Hanna, I. G. Dance, *Inorg. Chem.* **1993**, *32*, 66–72.
- [17] I. G. Dance, *Aust. J. Chem.* **1985**, *38*, 1745–1755; I. G. Dance, J. K. Saunders, *Inorg. Chim. Acta* **1985**, *96*, L71–L73.
- [18] R. A. Haberkorn, L. Que Jr., W. O. Gillum, R. H. Holm, C. S. Liu, R. C. Lord, *Inorg. Chem.* **1976**, *15*, 2408–2414.
- [19] For a neutral Cd₅₄S₂₈(SPh)₅₂L_x cluster (**4** or **5**) with an approximate T_d symmetry in solution, one would expect following NMR pattern. The cluster contains 7 nonequivalent Cd sites with coordination 2 × [CdS₄], 1 × [CdS₃(SPh)₁], 1 × [CdS₂(SPh)₂], 2 × [CdS₁(SPh)₃], and 1 × [Cd(SPh)₃(DMSO)₁] in a 6:4:4:16:12:8:4 ratio. Only those would be visible in ¹H-¹¹³Cd HMBC correlation, which are directly bonded to a PhS group and which have enough intensity depending on the number of Cd atoms and PhS ligands. Thus, at least the last four Cd sites should be observable, possibly also the [CdS₃(SPh)₁] site. Similarly, there are 4 chemically nonequivalent PhS groups: 3 × μ₂-PhS and 1 × μ₃-PhS in a 12:12:24:4 ratio. One μ₂-PhS (T¹) is bonded to the apical Cd atom, two others (T²) are located on the edges between the tetrahedral corners and are probably chemically very similar and different to T¹.^[17] T¹ would show ¹H-¹¹³Cd HMBC correlation to [Cd(SPh)₃(DMSO)₁] and [CdS₁(SPh)₃], T² to [CdS₁(SPh)₃] and [CdS₂(SPh)₂] and μ₃-PhS (T³) to [CdS₁(SPh)₃] and [CdS₃(SPh)₁]. The observed correlations are in good agreement, except for the last one related to T³, which is not observed probably due to low proportion of [CdS₃(SPh)₁] sites.
- [20] N. Herron, Y. Wang, H. Eckert, *J. Am. Chem. Soc.* **1990**, *112*, 1322–1326.
- [21] V. N. Soloviev, A. Eichhoefer, D. Fenske, U. Banin, *J. Am. Chem. Soc.* **2000**, *122*, 2673–2674; S. Kudera, M. Zanella, C. Giannini, A. Rizzo, Y. Li, G. Gigli, R. Cingolani, G. Ciccarella, W. Spahl, W. J. Parak, L. Manna, *Adv. Mater.* **2007**, *19*, 548–552.
- [22] P. Feng, X. Bu, N. Zheng, *Acc. Chem. Res.* **2005**, *38*, 293–303.
- [23] Q. Zhang, Y. Liu, X. Bu, T. Wu, P. Feng, *Angew. Chem. Int. Ed.* **2008**, *47*, 113–116.
- [24] N. Zheng, H. Lu, X. Bu, P. Feng, *J. Am. Chem. Soc.* **2006**, *128*, 4528–4529.
- [25] S. Lacelle, W. C. Stevens, D. M. Kurtz Jr., J. W. Richardson Jr., R. A. Jacobson, *Inorg. Chem.* **1984**, *23*, 930–935.
- [26] I. G. Dance, R. G. Garbutt, D. C. Craig, *Aust. J. Chem.* **1986**, *39*, 1449–1463.
- [27] N. Zheng, X. Bu, H. Lu, L. Chen, P. Feng, *J. Am. Chem. Soc.* **2005**, *127*, 11490–11491.
- [28] R. J. Kostelnik, A. A. Bothner-By, *J. Magn. Reson.* **1974**, *14*, 141–151.
- [29] A. L. Spek, *J. Appl. Crystallogr.* **2003**, *36*, 7–13.

Received: April 23, 2010
Published Online: June 2, 2010

Pyrido-Annulated 1,3-Azaphospholes: Synthesis of 1,3-Azaphospholo[5,4-*b*]pyridines and Preliminary Reactivity Studies

Mohamed Shaker S. Adam,^[a] Peter G. Jones,^[b] and Joachim W. Heinicke^{*[a]}

Dedicated to Professor Gerd Becker on the occasion of his 70th birthday

Keywords: Phosphanes / Phosphaalkenes / P ligands / P,N heterocycles / Pyridine annulation

Pyrido-annulated σ^2 -phosphorus heterocycles, 1,3-azaphospholo[5,4-*b*]pyridines **4** and **5**, were synthesized by reduction of diethyl 2-aminopyridine-3-phosphonates **1** with LiAlH_4 and cyclocondensation of the resulting 2-amino-3-phosphanylpiperidines **2** with dimethylformamide and dimethylacetamide dimethyl acetal, respectively, via intermediate phosphalkenes **3**. The P=C–N heterocycles are stable in the presence of OH and NH compounds but add *t*BuLi at the P=C bond. Reaction with one equivalent of $\text{M}(\text{CO})_5(\text{thf})$ leads

to η^1 -P-coordinated (azaphospholo[5,4-*b*]pyridine) $\text{M}(\text{CO})_5$ complexes ($\text{M} = \text{Cr}, \text{Mo}, \text{W}$). Spectroscopic data are in accordance with the dominance of π -acceptor properties. X-ray crystal structure analyses reveal “base-pairing” of 2-amino-3-phosphanylpiperidine (**2a**) and NH-functional azaphospholo-pyridine **5a** by N–H...N hydrogen bonds, and the competing formation of 1,3-diphosphetane **6c** from the phosphaalkene intermediate.

Introduction

Trivalent phosphorus ligands are widely tunable in their stereoelectronic properties and play a key role in many late-transition-metal-catalyzed reactions.^[1] Highly basic and bulky phosphane ligands^[2] represent an important focus of current research in this field, but the range of less basic and even π -acidic phosphorus ligands is also being extended by increasing research activities on the catalytic use of phosphite ligands^[3] and phosphabenzene^[4] and phosphaalkene^[5] derivatives with neutral σ^2 -phosphorus. Our interest is directed at another type of dicoordinated phosphorus compounds with a P=C–N substructure. This is stabilized by σ -electron withdrawal towards nitrogen, which in turn favors π -backbonding within the P=C–N unit or stronger stabilization within π -cyclodelocalized 1,3-azaphospholes^[6] or annulated heterocycles thereof.^[7] The π -donation of nitrogen changes the reactivity of the P=C group, studied so far mainly for 1,3-benzazaphospholes. The NH and CH lithiation of P=CR–NH or P=CH–NR by *t*BuLi and introduction of functional groups, alkylation at phosphorus, and also modification of the coordination properties have been

reported.^[8,9] Coordination of Rh^{I} , Pd^{II} , or Ni^{II} at the σ^2 -phosphorus atom of these P=C–N heterocycles is disfavored, and preliminary attempts to generate in situ (benzazaphosphole)Pd catalysts for amination of 2-bromopyridine or benzazaphosphol-2-carboxylate Ni^{II} catalysts for ethylene oligomerization both failed.^[9] This inspired us to explore whether electron-withdrawing annulation changes the reactivity and coordination properties of azaphospholes towards those of phosphabenzene. Phosphaindolizines and related N-bridgehead annulated 1,3-azaphospholes indeed show much stronger deshielding of the phosphorus atom in ^{31}P NMR spectroscopy, are less stable towards addition at the P=C bond,^[10] and display π -acidic properties in $\text{LM}(\text{CO})_5$ complexes ($\text{L} = \text{annulated azaphosphole}$).^[11] The first pyridine-annulated 1,3-azaphospholes with a C–C bridge, 1,3-azaphospholo[4,5-*b*]pyridines, were recently described, but their purification proved difficult.^[12] Here we report on the more easily accessible 1,3-azaphospholo[5,4-*b*]pyridines, their positional isomers with both nitrogen atoms bonded to the same carbon atom, and preliminary reactivity studies.

Results and Discussion

Synthesis

Annulated 1,3-azaphospholes are accessible by four synthetic routes: generation and orthoformate cyclization of the corresponding 2-phosphanyllarylamines,^[7,9,12] reductive cyclization of 2-phosphonoarylamines,^[13] flash-vacuum py-

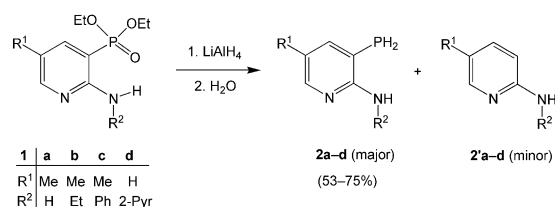
[a] Institut für Biochemie – Anorganische Chemie, Ernst-Moritz-Arndt-Universität Greifswald, Felix-Hausdorff-Str. 4, 17487 Greifswald, Germany
Fax: +49-3834-864377
E-mail: heinicke@uni-greifswald.de

[b] Institut für Anorganische und Analytische Chemie, Technische Universität Braunschweig, Hagenring 30, 38106 Braunschweig, Germany

Supporting information for this article is available on the WWW under <http://dx.doi.org/10.1002/ejic.201000253>.

rolysis of P-alkyldihydroazaphospholes,^[14] or cyclocondensation of suitable N-ylides with PCl_3 in the presence of base.^[10] However, the latter route is applicable only for N-bridgehead annulated systems, and the pyrolysis functions only for compounds of sufficient thermal stability. Therefore, the synthesis according to the first two routes was studied. The starting materials, primary and secondary 2-amino- and 2-acylamido-3-diethylphosphonopyridines, respectively, were obtained by Pd-catalyzed phosphonylation of the corresponding 2-amino- and 2-acylamido-3-bromo-pyridines with triethyl phosphite.^[15]

For the first route, 2-amino-3-phosphonopyridines **1a–d** were reduced with LiAlH_4 to provide the corresponding 2-amino-3-phosphanylpyridines **2a–d** in reasonable yields. Small amounts of 2-aminopyridines were formed as side products by P–C bond cleavage (Scheme 1).

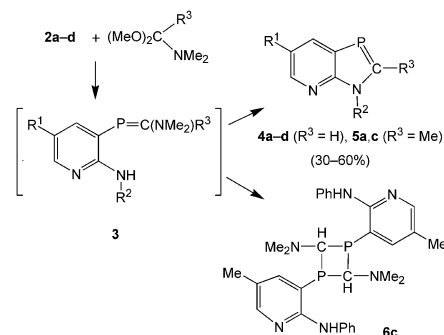


Scheme 1. Reduction of 2-amino-3-phosphonopyridines.

Relative to the rather smooth reduction of 2-phosphonoanilines to 2-phosphanylanilines,^[9] the competing reductive P–C bond cleavage is only slightly faster for 2-amino-3-phosphonopyridines **1a–d**, whereas introduction of a further N atom into the heterocycle strongly enhances this side reaction. Attempts to reduce 2-amino-3-phosphonoquinoxalines^[15] to 2-amino-3-phosphanyl-quinoxalines resulted in quantitative dephosphanylation. This prevented the extension of our studies to quinoxaline-annulated azaphospholes. Similar P–C bond cleavage reactions by LiAlH_4 were observed for sterically hindered *o*-phosphonophenols and quantitatively for 1-phosphono- and 1-(phenylphosphinoyl)naphth-2-ols.^[16] In combination with the detection of a bicyclic oxadiphosphole, these findings imply the facilitation of phosphanylidene extrusion if PHR-groups are sited in the *o*-position to NHR or OH groups and subjected to electron withdrawal or to the sterically enforced proximity of the PHR and OH groups (in 6-*tert*-butyl-2-phosphanylphenols^[16a]).

The envisaged pyrido-annulated P=C–N heterocycles were synthesized by cyclocondensation of 2-amino-3-phosphanylpyridines with dimethylformamide dimethyl acetal (DMFA) or dimethylacetamide dimethyl acetal (DMAA), respectively. The reactions proceed slowly and need heating at 50 °C for approximately 5 d. The cyclocondensation reaction proceeds via phosphalkene intermediates **3**, which undergo cyclization to 1,3-azaphospholo[5,4-*b*]pyridines **4a–d** and **5a,c**, respectively. This was detected by NMR spectroscopic monitoring of the conversion of **2a** with DMAA, initially revealing signals characteristic for **3a** ($\text{R}^3 = \text{Me}$) that disappear with the progress of the reaction, in a similar manner to that observed in the synthesis of bulky *N*-substi-

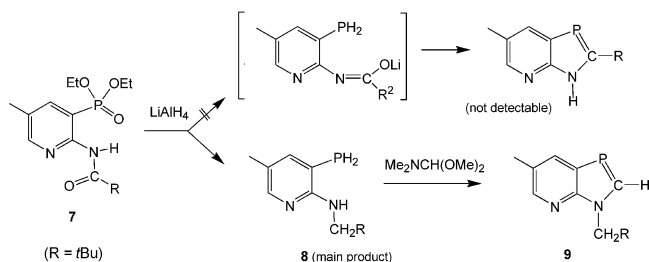
tuted benzazaphospholes^[9b] and azaphospholo[4,5-*b*]pyridines.^[12] For purification, the volatile byproducts (MeOH and dimethylamine) and excess starting material were removed in vacuo, and the residues were distilled in high vacuum to give oils that rapidly crystallized. In an attempt to crystallize crude **5c** by overlaying the concentrated thf solution with *n*-hexane, the single-crystalline phosphalkene dimer **6c** with 1,3-diphosphetane structure was obtained. The dimerization of **3c** to **6c** represents an alternative reaction of the intermediates **3** known for acyclic phosphalkenes^[17] but detected here for the first time for 1,3-azaphosphole precursors (Scheme 2).



Scheme 2. Cyclization of 2-amino-3-phosphanylpyridines with dimethylformamide dimethyl acetal or dimethylacetamide dimethyl acetal.

To test the applicability of the reductive cyclization of 2-acylamidopyridine-3-phosphonates to access 1,3-azaphospholo[5,4-*b*]pyridines, in a manner corresponding to the above-mentioned second route to benzazaphospholes, 2-acylamidopyridine 3-phosphonate **7**^[15,18] was reduced in diethyl ether with excess LiAlH_4 . However, the reaction took a different course from that in the case of phosphonoanilides. Instead of the pyrido-annulated azaphospholes, which should form by primary reduction of the phosphono group and subsequent cyclocondensation with the imide group, *N*-secondary 2-amino-3-phosphanylpyridine **8** was formed as the main product (Scheme 3) contaminated by unidentified products. The main product was formed by reduction of the amide group prior to the phosphono group, controlled by the electron-withdrawing influence of the pyridine ring (cf. ref.^[12]). Variation of R did not change the reaction course. For benzoyl, naphthoyl, 2-furoyl, and 2-thenoyl derivatives, the results are analogous. The crude aminophosphanylpyridine **8** was converted into the corresponding pyrido[*b*]azaphosphole **9** by heating with excess dimethylformamide dimethyl acetal. The heterocycle could not be obtained in pure form by high-vacuum distillation but was unambiguously identified by spectroscopic methods.

The structure elucidation of compounds **2–9** is based on conclusive HRMS and fully assigned NMR spectroscopic data, together with X-ray structure investigations of **2a**, **5a**, and **6c**. Typical features of primary phosphanes **2** and **8** are the proton doublets of the PH_2 group with $^1J_{\text{PH}} = 201\text{--}222\text{ Hz}$ at $\delta = 3.2\text{--}3.7\text{ ppm}$ and upfield phosphorus signals



Scheme 3. Attempts at reductive cyclization of 2-acylamido-3-phosphonopyridines and cyclocondensation of the reduction products.

($\delta = -147$ to -151 ppm). Further information was obtained by the X-ray structure analysis of single crystals of **2a** grown by slow evaporation of the solvent from a concentrated solution of **2a** in diethyl ether. As depicted in Figure 1, inversion-symmetric pairs of molecules are formed by intermolecular hydrogen bonds between the N–H group and pyridine nitrogen atom of a neighboring molecule. The phosphorus lone electron pair is directed away from the amino group and thus cannot interact with the second proton at nitrogen. There are no other short intermolecular contacts. Bond lengths and bond angles of **2a** exhibit usual values.

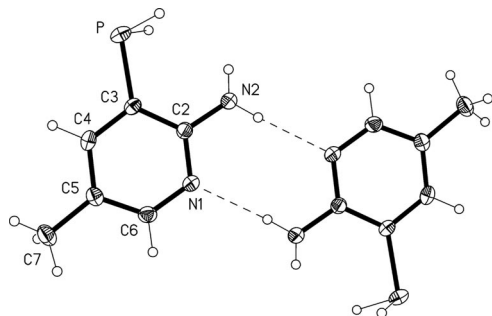


Figure 1. Dimeric aggregate of **2a** in the crystal (ellipsoids with 50% probability). Selected bond lengths [Å] and angles [°]: P–C3 1.8223(19), N1–C2 1.338(2), N1–C6 1.342(3), N2–C2 1.359(2); N2–C2–C3 121.70(17), C4–C3–P 118.52(14), C2–C3–P 123.95(14); N2–H04 0.85(2), H04...N1#1 2.19(2), N2...N1#1 3.029(2), N2–H04...N1#1 172(2), (symmetry transformation: #1 $-x, -y, -z + 1$).

Phosphaalkene intermediate **3a** was detected in the reaction of **2a** with DMAA by the upfield phosphorus signal relative to that of **5a** ($\delta = 49.5$ vs. 66.6 ppm) and a slightly larger $^2J_{PC}$ coupling (27.2 vs. 24.9 Hz) of the 2-methyl ^{13}C resonance, indicative of the Me–C=P structural unit. The strongly upfield position of the signal of **3a** relative to the typical phosphaalkene range ($\delta = 200$ – 350 ppm)^[19] is attributable to the +M effect of the amino group and is slightly diminished in pyrido-azaphospholes **4** and **5** ($\delta = 65$ – 78 ppm) by cyclodelocalization. The nature of **6c**, formed in competition with **4c** from the corresponding phosphaalkene intermediate as a byproduct, was proved by X-crystal structure analysis (Figure 2). The molecule possesses no crystallographic symmetry. In the four-membered ring, the substituents at the carbon atoms are mutually *cis*, as are the substituents at the phosphorus atoms. The transannular dis-

tances are C1...C5 2.485(2) and P1...P2 2.6859(6) Å, with fold angles about these axes of 38.6(1) and 41.5(1)°, respectively. Two intramolecular hydrogen bonds of the form N–H...N are observed.

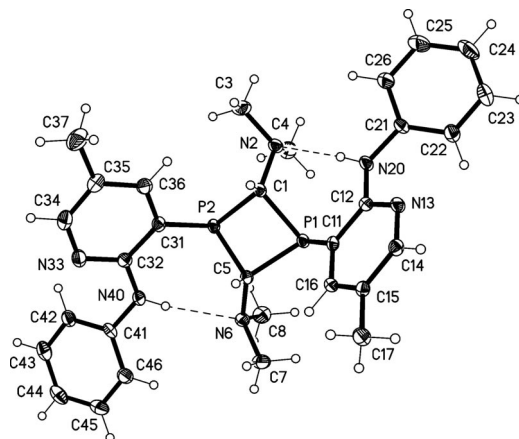


Figure 2. Molecular structure of **6c** in the crystal (ellipsoids with 50% probability). Two disordered CDCl₃ molecules were omitted for clarity. Selected bond lengths [Å] and angles [°]: P1–C1 1.8868(17), P1–C5 1.8995(17), P1–C11 1.8220(16), P2–C1 1.8862(17), P2–C5 1.8838(16), P2–C31 1.8207(18), P1...P2 2.6859(6), H20...N2 2.20(3), H40...N6 2.25(3), N20...N2 3.003(2), N40...N6 3.043(2); C1–P1–C5 82.03(7), C5–P2–C1 82.46(7), P2–C1–P1 90.77(7), P2–C5–P1 90.46(7), N2–C1–P2 121.30(11), N2–C1–P1 115.32(12), N6–C5–P1 122.32(12), N6–C5–P2 114.01(11), N20–H20...N2 173(2), N40–H40...N6 173(2).

The structures of all the 1,3-azaphospholo[4,5-*b*]pyridines are proved by unambiguous NMR spectroscopic data. Characteristic are the aforementioned phosphorus chemical shifts, although they vary with substituents at the nitrogen atom and C-2. For 1,3-azaphospholo[5,4-*b*]pyridines without substituent at C-2, a marked upfield shift is observed in the series **4a** ($R^2 = H$), **4d** ($R^2 = 2\text{-Pyr}$), **4c** ($R^2 = Ph$), **4b** ($R^2 = Et$) ($\delta = 78.3, 76.0, 71.5, 65.9$ ppm, respectively), which reflects the influence of the *N*-substituents on the conjugative shift of π -density from the N lone electron pair to phosphorus. Compared to 1,3-benzazaphospholes and the *N*-position-isomeric 1,3-azaphospholo[4,5-*b*]pyridines, the phosphorus chemical shifts are changed only slightly, whereas pyrido[*a*]-annulated 1,3-azaphospholes with an N-bridgehead experience strong downfield shifts.^[10] This shows that the electron-withdrawing effect of the pyridine nitrogen atom in annulated pyrido-azaphospholes is strong only if this atom also acts as the N-donor site in the azaphosphole ring. The chemical shifts of C-2 and the P–C coupling constants within the five-membered ring are only marginally influenced by the *N*-substituent. In the proton NMR spectra, the most characteristic features are the large downfield shifts ($\delta = 8.8$ – 9.6 ppm) and $^2J_{PH}$ coupling constants (37–39 Hz) of the hydrogen atom in the 2-position. The 2-methyl signals of **5a,c** appear in the region of aromatic methyl compounds. Detailed structural information on **5a** is given by its crystal structure analysis (Figure 3). The heterocycles are planar, and the two distinct σ^2 -P–C bond lengths display similar values to those of the

1,3-benzazaphospholes, as do the other bond lengths and angles within the azaphosphole ring. The molecules are connected to inversion-symmetric pairs via N...H–N hydrogen bonds in the crystal, as found for **2a**. This facilitates crystallization and purification relative to the *N*-substituted derivatives **9** or to the 1,3-azaphospholo[4,5-*b*]pyridines with the pyridine N atom on the P side.^[12]

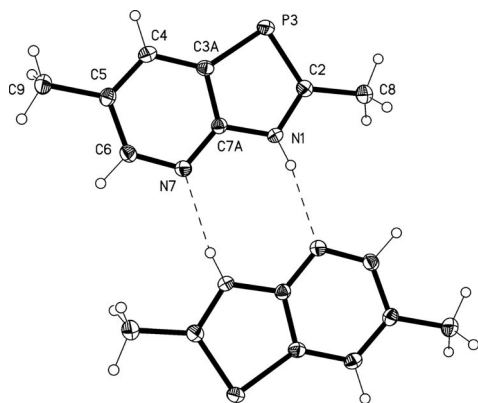
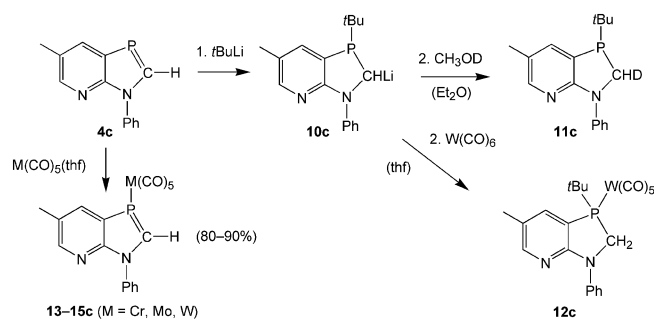


Figure 3. Dimeric aggregate of **5a** in the crystal (ellipsoids with 50% probability). Selected bond lengths [Å] and angles [°]: C2–P3 1.7321(15), P3–C3A 1.7878(15), N1–C2 1.3608(19), N1–C7A 1.3735(19), C6–N7 1.3378(19), N7–C7A 1.3411(19); C2–N1–C7A 113.81(13), C2–P3–C3A 88.86(7), C4–C3A–P3 133.37(11), C7A–C3A–P3 110.75(11), C6–N7–C7A 115.33(12); N1–H01 0.81(2), H01...N7#1 2.09(2), N1...N7#1 2.8934(18), N1–H01...N7#1 171(2) (symmetry transformation: #1 = $-x, -y + 1, -z + 1$).

Reactivity

The pyrido[*b*]-annulated 1,3-azaphospholes **4** and **5** are slowly attacked by air in the solid state, but rapidly in solution. They are basic because of the pyridine nitrogen atom and are stable towards cold water, dilute aqueous sulfuric acid, or sodium hydroxide solution; in this respect they resemble the 1,3-benzazaphospholes more than the hydrolytically sensitive N-bridgehead pyrido[*a*]-annulated 1,3-azaphospholes. Treatment of **4c** with *tert*-butyllithium in diethyl ether at low temperature (−80 °C) resulted, however, in addition at the P=C bond, as known for phosphabenzene^[20] or benzoxaphospholes,^[21] even in the presence of KO^{*t*}Bu, which favors CH-lithiation in the case of benzazaphospholes.^[9] Quenching of the addition product **10c** with CH₃OD afforded the pyridine-annulated 3-*tert*-butyl-2-deuterio-azaphospholine **11c** (Scheme 4), whereas treatment of **10c** with chlorotrimethylsilane led to a mixture of the expected 2-trimethylsilyl-3-*tert*-butylbenzazaphospholine with unidentified byproducts. If the reaction with *t*BuLi is carried out in thf (−80 °C), which is more easily deprotonated by strong metalating agents,^[22] the primarily formed **10c** is rapidly protonated by the solvent. Subsequent addition of W(CO)₆ did not afford the heterocyclic Fischer carbene W(CO)₅CROLi but the η¹-P-(pyrido-azaphospholine)W(CO)₅ complex **12c**, characterized by conclusive spectroscopic data. With the *N*-ethyl-pyridoazaphosphole **4b**, minor CH lithiation (<20%) by *t*BuLi was detected, af-

ter quenching with CH₃OD, by the phosphorus triplet slightly upfield from the singlet of **4b** ($\delta^{31}\text{P} = 64.7$ ppm, $^2J_{\text{PD}} = 5.5$ Hz), but the major reaction remains addition with formation of **11b** after deuteriolysis ($\delta^{31}\text{P} = -20.1$ ppm).



Scheme 4. Reactivity of **4c**.

Reaction of **4c** with a slight excess to one equivalent of W(CO)₅(thf) or the analogous molybdenum and chromium compounds provided the corresponding η¹-P-(pyrido-azaphosphole)M(CO)₅ complexes **13c** (M = Cr), **14c** (M = Mo), and **15c** (M = W). These complexes are yellow solids, air-stable in the solid state, sparingly soluble in hydrocarbons such as *n*-hexane or benzene but soluble in thf or CHCl₃. As shown by the NMR spectroscopic data, coordination through the σ²-phosphorus is preferred to coordination via the pyridine nitrogen [pyridine M(CO)₅ derivatives]^[23], as observed for 2-pyridylphosphorines.^[24] The upfield phosphorus chemical shift of tungsten complex **15c** relative to ligand **4c** ($\Delta\delta = -26.3$ ppm) is comparable to the upfield coordination shift of (triphenylphosphorine)W(CO)₅ ($\Delta\delta = -21.9$ ppm)^[25] but forms a strong contrast to the downfield shift of tungsten complex **12c** vs. pyridoazaphospholine complex **11c** ($\Delta\delta = 37.9$ ppm) and illustrates the different coordination properties of σ²- vs. σ³-phosphorus ligands. For *N*-ethyl derivative **15b**, synthesized analogously to **15c**, the upfield coordination shift from **4b** is even larger ($\Delta\delta = -34.4$ ppm) and similar to the value observed for the W(CO)₅ complex of 2-methyl-1,3-benzazaphosphole ($\Delta\delta = -36.3$ ppm).^[8c,8d] It can be attributed to π-backbonding from tungsten to phosphorus, which is involved in the cyclodelocalized π-system.^[26] For the analogous Mo(CO)₅ and Cr(CO)₅ complexes with 2-methylbenzazaphosphole and **4c** as ligands, the upfield coordination shifts are reduced or changed to small downfield shifts ($\Delta\delta = -8.3, 6.8$;^[8b] 1.5, 21.0 ppm) but are far away from the strong downfield shifts of phosphane M(CO)₅ complexes (Mo $\Delta\delta \approx 40$ –44, Cr $\Delta\delta \approx 55$ –63 ppm)^[27] so that the results can be interpreted in the same way and the σ²-P atoms of pyridoazaphospholes can be classified as weak donors but rather strong π-acceptors. The larger upfield shifts for *N*-ethyl derivative **15b** and benzazaphosphole complexes can be attributed to the π-donor properties of the tricoordinate nitrogen atom in the 1,3-azaphosphole ring resulting in increased π density at phosphorus. The carbon chemical shifts of **13c** and **14c** vs. those of **4c** show a strong upfield coordination shift for C-2 and a rather weak effect for C3a ($\Delta\delta = -19.8, -2.6$ ppm) while both $^1J_{\text{PC}}$ coupling constants are

strongly reduced ($\Delta^1J = -31.9, -28.6$ Hz). For (2-methylbenzazaphosphole)Cr(CO)₅ the coordination chemical shifts for C-2 and C3a are more similar ($\Delta\delta = -4.8, -5.3$ ppm) and indicate thus, in addition to the stronger ³¹P coordination shift, a clear difference from pyridoazaphosphole ligands. The effects on the ¹J_{PC} coupling constants ($\Delta^1J = -29.9, -28.3$ Hz) are comparable with those in **13c** and indicative for the common σ^2 -P nature of the two P ligands. The coordination chemical shift for C-5 and C-6 ($\Delta\delta = 0.0, 2.0$ ppm) is low and indicates absence of *N*-coordinated Cr(CO)₅, which should cause downfield shifts of $\Delta\delta = 4-6$ ppm.^[23b] Coordination at the nitrogen atom allows a further modification of the character of pyrido-annulated 1,3-azaphosphole ligands, which has still to be investigated.

Conclusions

2-Amino-3-phosphanyl-pyridines are accessible by LiAlH₄ reduction of 2-amino-3-phosphonopyridines. P–C bond cleavage may occur as a minor side reaction. [4+1]-Cyclocondensation with dimethylformamide dimethyl acetal or dimethylacetamide dimethyl acetal provides pyrido-[*b*]-annulated 1,3-azaphospholes with both nitrogen atoms on the same side, that is, 1,3-azaphospholo[5,4-*b*]pyridines. 2-Amino-3-phosphanyl-pyridines and the heterocycles with NH functions tend to form dimers by intermolecular N...H–N bridges, which favors crystallization and raises the question whether pairing with other types of 2-amino or 2-amidopyridines is possible. The stability of the P=C bond towards usual nucleophiles such as water, alcohols, or amines facilitates work with these compounds. Addition of *t*-BuLi at the P=C bond prevents access to functionally substituted derivatives at the 2-position. However, the addition will allow access to functionally substituted dihydropyrido-azaphospholes if solvents such as hexane are used, which are not deprotonated by the strongly basic heterocyclic Li adducts. With respect to the easier addition of RLi at the P=C bond, the heterocycles are somewhat closer to phosphabenzenes, but the coordination behavior remains more similar to that of 1,3-benzazaphospholes. In contrast to the latter, the 1,3-azaphospholo[5,4-*b*]pyridines are ambidentate σ^2 P,N ligands. Electron-rich, zero-valent group 6 metal carbonyls coordinate preferably at the σ^2 phosphorus atom. The NMR spectra indicate dominant π -acceptor properties. Coordination at both coordination sites, P and N, the influence of *N*-coordination on the coordination properties at phosphorus, and the potential use in catalysis or for synthesis of new ligands by addition reactions at the P=C bond are challenges for further investigations of the new heterocycles.

Experimental Section

General: All preparations were carried out in dried and deoxygenated solvents. Reactions with air- or moisture-sensitive compounds were conducted under an argon atmosphere by using Schlenk techniques. All reagents were used as received from com-

mercial suppliers. Compounds **1a–d** were prepared as reported recently.^[15] NMR spectra were measured with a multinuclear FTNMR spectrometer (Bruker ARX300). The ¹H, ¹³C, and ³¹P chemical shifts are δ values and are given in ppm relative to Me₄Si and H₃PO₄ (85%), respectively. Coupling constants refer to *J*_{HH} in ¹H and to *J*_{PC} in ¹³C NMR spectra unless indicated otherwise. HRMS measurements were carried out at the Institut für Organische und Biomolekulare Chemie, University of Göttingen with a double focusing sector-field Finnigan MAT 95 instrument with EI (70 eV, PFK as reference substances) or with ESI in MeOH, MeOH/NH₄OAc or MeCN with a 7T Fourier transform ion APEX IV (Bruker Daltonics) cyclotron resonance mass spectrometer. LR Mass spectra were measured with a single focusing AMD40 sector-field mass spectrometer. Elemental analyses were carried out with a CHNS-932 analyzer from LECO under standard conditions. IR spectra were recorded as KBr pellets or capillaries or in Nujol with a Nicolet® Magna550 instrument. Absorption bands are given as wavenumbers in cm^{−1}.

General Procedure for the Reduction of 3a–d with LiAlH₄: A solution of **3a–d** in diethyl ether (10–20 mL) was added dropwise at 0 °C to a solution of LiAlH₄ pellets in diethyl ether (10–20 mL). The reaction mixture was stirred for 2 d at room temperature. Then, on cooling with ice-water, degassed water was added dropwise until the evolution of hydrogen ceased. Solids were filtered off and washed with diethyl ether. The combined filtrates were dried with Na₂SO₄. Compounds **4a–d** were worked up by concentration and crystallization or by vacuum distillation or used directly in cyclocondensations.

2-Amino-5-methyl-3-phosphanylpyridine (2a): Reduction of **1a** (0.59 g, 2.40 mmol) by LiAlH₄ pellets (0.30 g, 7.30 mmol) provided 0.20 g (59%) of **2a** as white crystals from the concentrated solution in diethyl ether. The X-ray crystal data are compiled in Table 1, the molecular structure is shown in Figure 1. ¹H NMR (CDCl₃): δ = 2.17 (s, 3 H, 5-CH₃), 3.61 (d, ¹J_{PH} = 202.2 Hz, 2 H, PH₂), 4.71 (vbr. s, 2 H, NH), 7.52 (ddd, ³J_{PH} = 10.8, ⁴J = 2.2 Hz, 1 H, 4-H), 7.91 (s, 1 H, 6-H) ppm. ¹³C{¹H} NMR (CDCl₃): δ = 17.21 (CH₃-5), 105.41 (d, ¹J = 12.8 Hz, C_q-3), 123.28 (d, ³J = 8.6, C_q-5), 147.00 (d, ²J = 28.5 Hz, CH-4), 149.43 (CH-6), 158.49 (d, ²J = 1.3 Hz, C_q-2) ppm. ³¹P{¹H} NMR (CDCl₃): δ = −147.0 ppm. MS (EI 70 eV, 25 °C): *m/z* (%) = 141 (5), 140 (100) [M]⁺, 139 (8), 123 (26), 107 (35), 106 (11), 93 (17), 80 (11). HRMS (EI): calcd. for C₆H₉N₂P⁺ 140.0503; found 140.0504.

2-(Ethylamino)-5-methyl-3-phosphanylpyridine (2b): Reduction of **1b** (2.07 g, 7.60 mmol) by LiAlH₄ pellets (0.87 g, 22.8 mmol) yielded 0.96 g (75%) of colorless oily **2b**, slightly contaminated with the P–C cleavage product **2b'**. For **2b**: ¹H NMR (CDCl₃): δ = 1.25 (t, ³J = 7.2 Hz, 3 H, CH₃), 2.13 (s, 3 H, 5-CH₃), 3.48 (qd, ³J = 7.2, 5.3 Hz, 2 H, NCH₂), 3.51 (d, ¹J_{PH} = 201.5 Hz, 2 H, PH₂), 4.52 (br. s, 1 H, NH), 7.48 (dd, ³J_{PH} = 11.9, ⁴J = 2.1 Hz, 1 H, 4-H), 7.98 (br. s, 1 H, 6-H) ppm. ¹³C{¹H} NMR (CDCl₃): δ = 14.97 (CH₃), 17.16 (CH₃-5), 36.71 (CH₂), 105.18 (d, ¹J = 13.4 Hz, C_q-3), 120.80 (d, ³J = 9.8 Hz, C_q-5), 146.77 (d, ²J = 31.8 Hz, CH-4), 148.99 (CH-6), 157.92 (C_q-2) ppm. ³¹P{¹H} NMR (CDCl₃): δ = −150.4 ppm. MS (EI 70 eV, 150 °C): *m/z* (%) = 168 (76) [M]⁺, 167 (81), 108 (100). HRMS (ESI in MeOH, NH₄OAc): calcd. for C₈H₁₄N₂P⁺ [M + H]⁺ 169.08892; found 169.08891. 2-Ethylamino-5-methylpyridine (**2b'**): ¹H NMR (CDCl₃): δ = 1.22 (t, ³J = 7.2 Hz, CH₃), 2.16 (s, 5-CH₃), 3.26 (qd, ³J = 7.2 Hz, CH₂), 4.87 (s br, NH), 6.32 (d, ³J = 8.3 Hz, 3-H), 7.24 (dd, ³J = 8.2, ⁴J = 2–3 Hz, 4-H), 7.83 (d br, 6-H) ppm. ¹³C{¹H} NMR (CDCl₃): δ = 14.63 (CH₃), 16.98 (5-CH₃), 36.96 (NCH₂), 106.32 (CH-3), 124.17 (C_q-5), 138.97 (CH-4), 140.79 (CH-6), 153.40 (C_q-2) ppm.

5-Methyl-2-(phenylamino)-3-phosphanylpuridine (2c): Reduction of **1c** (5.0 g, 15.6 mmol) by LiAlH_4 pellets (1.8 g, 47.4 mmol) provided 1.8 g (53%) of colorless crude viscous oily **2c**, which was used without further purification for cyclocondensations. ^1H NMR (C_6D_6): δ = 1.82 (s, 3 H, 5- CH_3), 3.24 (d, $^1J_{\text{PH}}$ = 222.0 Hz, 2 H, PH_2), 6.52 (br. s, 1 H, NH), 6.98 (t, 3J = 7.3 Hz, 1 H, *p*-H), 7.24–7.32 (m, 3 H, 4-H, *m*-H), 7.74 (d br, 3J = 7.9 Hz, 2 H, *o*-H), 8.08 (br. s, 1 H, 6-H) ppm. $^{13}\text{C}\{^1\text{H}\}$ NMR (C_6D_6): δ = 17.72 (CH_3 -5), 108.30 (d, 1J = 15.2 Hz, C_q -3), 120.45 (2 CH-*o*), 122.81 (CH-*p*), 124.53 (d, 3J = 9.2 Hz, C_q -5), 129.70 (2 CH-*m*), 142.19 (C_q -*i*), 147.84 (d, 2J = 32.0 Hz, CH-4), 150.01 (CH-6), 156.40 (C_q -2) ppm. $^{31}\text{P}\{^1\text{H}\}$ NMR (C_6D_6): δ = –150.6 ppm. MS (EI 70 eV, 340 °C): m/z (%) = 217 (11), 216 (100) [$\text{M}]^+$, 215 (41), 182 (40), 138 (24), 93 (32). HRMS (EI): calcd. for $\text{C}_{12}\text{H}_{13}\text{N}_2\text{P}^+$ 216.0816; found 216.0812.

3-Phosphanyl-2-[(2'-pyridyl)amino]pyridine (2d): Reduction of **1d** (0.69 g, 2.25 mmol) by LiAlH_4 pellets (0.26 g, 6.85 mmol) furnished 0.25 g (55%) of pale yellow oily **2d**, contaminated by ca. 8 mol-% of the P–C cleavage product **2d'**. The crude product was used without further purification. **2d**: ^1H NMR (CDCl_3): δ = 3.73 (d, $^1J_{\text{PH}}$ = 203.3 Hz, 2 H, PH_2), 6.72 (dd, 3J = 7.3, 4.8 Hz, 1 H, 5'-H), 6.83 (ddd, 3J = 7.3, 5.0, 4J = 0.9 Hz, 1 H, 5-H), 7.50 (br. s, 1 H, NH), 7.59 (td, 3J = 8.5, 3J = 7.3, 4J = 1.9 Hz, 1 H, 4'-H), 7.75 (ddd, $^3J_{\text{PH}}$ = 10.8, 3J = 7.4, 4J = 1.9 Hz, 1 H, 4-H), 8.18 (ddd, 3J = 5.0, 4J = 1.9, 5J = 0.8 Hz, 1 H, 6-H), 8.21 (d br, superimposed, 3J = 4–5 Hz, 1 H, 6'-H), 8.30 (d br, 3J = 8.5 Hz, 1 H, 3'-H) ppm. $^{13}\text{C}\{^1\text{H}\}$ NMR (CDCl_3): δ = 109.38 (d, 1J = 16.5 Hz, C_q -3), 112.45 (CH-3'), 116.01 (d, 3J = 9.0 Hz, CH-5), 117.43 (CH-5'), 137.79 (CH-4'), 146.51 (d, 2J = 30.2 Hz, CH-4), 147.81 (CH-6'), 148.83 (CH-6), 153.20 (C_q -2'), 155.85 (noise level, C_q -2) ppm. $^{31}\text{P}\{^1\text{H}\}$ NMR (CDCl_3): δ = –147.5 ppm. MS (EI 70 eV, 50 °C): m/z (%) = 204 (12), 203 (100) [$\text{M}]^+$, 202 (81), 187 (21), 171 (24) [$\text{M} - \text{PH}]^+$, 170 (80), 123 (36), 109 (61), 78 (84). HRMS (ESI in MeOH, NH_4OAc): calcd. for: $\text{C}_{10}\text{H}_{11}\text{N}_3\text{P}^+$ [$\text{M} + \text{H}]^+$ 204.06851; found 204.06862. **2d'**: ^{13}C NMR: δ = 111.53 (CH-3), 116.31 (CH-5), 137.66 (CH-4), 147.69 (CH-6), ca. 154 (C_q -2) ppm.

General Procedure for the Synthesis of 4 and 5: A mixture of *N,N*-dimethylformamide or *N,N*-dimethylacetamide dimethyl acetal and **1a–d** was heated with stirring for about 5 d at 40–50 °C. The product mixture was separated by distillation at ca. 10^{-5} mbar.

5-Methyl-1*H*-1,3-azaphospholo[5,4-*b*]pyridine (4a): Compound **2a** (0.20 g, 1.43 mmol) and *N,N*-dimethylformamide dimethyl acetal (0.20 mL, 1.50 mmol) gave 0.12 g (56%) **4a**, which crystallized after distillation at 10^{-5} mbar/48–50 °C (bath temperature). ^1H NMR (CDCl_3): δ = 2.48 (s, 3 H, 5- CH_3), 8.26 (t br, $^3J_{\text{PH}}$ \approx 4J = 2–3 Hz, 1 H, 4-H), 8.36 (s br, 1 H, 6-H), 8.82 (d br, $^2J_{\text{PH}}$ = 37.8 Hz, 1 H, 2-H), 11.22 (br. s, 1 H, NH) ppm. $^{13}\text{C}\{^1\text{H}\}$ NMR (CDCl_3): δ = 18.26 (CH_3 -5), 125.29 (d, 3J = 10.4 Hz, C_q -5), 133.29 (d, 1J = 42.7 Hz, C_q -3a), 139.12 (d, 2J = 18.0 Hz, CH-4), 145.94 (CH-6), 151.63 (d, 2J = 5.5 Hz, C_q -7a), 160.01 (d, $^1J_{\text{PC}}$ = 55.4 Hz, C_q -2) ppm. $^{31}\text{P}\{^1\text{H}\}$ NMR (CDCl_3): δ = 78.3 ppm. MS (EI 70 eV, 260 °C): m/z (%) = 150 (6) [$\text{M}]^+$, 149 (100), 148 (7), 98 (16), 85 (15), 84 (14), 43 (29). HRMS (EI): calcd. for $\text{C}_7\text{H}_7\text{N}_2\text{P}^+$ 150.0347; found 150.0349.

1-Ethyl-5-methyl-1,3-azaphospholo[5,4-*b*]pyridine (4b): Compound **2b** (0.36 g, 2.14 mmol) and *N,N*-dimethylformamide dimethyl acetal (0.30 mL, 2.26 mmol) gave 0.23 g (60%) of **4b**, forming a white powder after distillation at 10^{-5} mbar/40 °C (bath temperature). ^1H NMR (CDCl_3): δ = 1.51 (t, 3J = 7.2 Hz, 3 H, CH_3), 2.45 (s, 3 H, 5- CH_3), 4.51 (t, 3J = 7.2 Hz, 2 H, CH_2), 8.19 (unresolved. m, 1 H, 4-H), 8.34 (br. s, 1 H, 6-H), 8.67 (d br, $^2J_{\text{PH}}$ = 37.7 Hz, 1 H, 2-H) ppm. $^{13}\text{C}\{^1\text{H}\}$ NMR (CDCl_3): δ = 15.32 (CH_3), 18.22 (CH_3 -5), 43.67 (NCH₂), 124.93 (d, 3J = 10.4 Hz, C_q -5), ca. 134.0 (d, 1J =

43 Hz, C_q -3a), 137.97 (d, 2J = 19.0 Hz, CH-4), 146.78 (d, 2J = 6.6 Hz, C_q -7a), 146.81 (d, 4J = 3.0 Hz, CH-6), 161.11 (d, 1J = 54.5 Hz, C_q -2) ppm. $^{31}\text{P}\{^1\text{H}\}$ NMR (CDCl_3): δ = 65.9 ppm. MS (EI 70 eV, 285 °C): m/z (%) = 179 (10), 178 (86) [$\text{M}]^+$, 163 (48), 150 (100), 149 (22), 122 (18), 92 (17), 69 (18). HRMS (ESI in MeOH, NH_4OAc): calcd. for $\text{C}_9\text{H}_{12}\text{N}_2\text{P}^+$ [$\text{M} + \text{H}]^+$ 179.07329; found 179.07326.

5-Methyl-1-phenyl-1,3-azaphospholo[5,4-*b*]pyridine (4c): Compound **2c** (1.50 g, 6.94 mmol) and *N,N*-dimethylformamide dimethyl acetal (0.95 mL, 7.14 mmol) gave 0.48 g (31%) **4c**, which, after high vacuum distillation at 10^{-5} mbar/56–60 °C (bath temperature), formed white crystals, m.p. 78 °C. ^1H NMR (CDCl_3 , ref. 7.25): δ = 2.45 (d, $^5J_{\text{PH}}$ = 0.6 Hz, 3 H, 5- CH_3), 7.43 (tt, 1 H, *p*-H), 7.50–7.63 (m, 4 H, 2 *m*-H, 2 *o*-H), 8.23 (ddd, $^3J_{\text{PH}}$ = 3.0, 4J = 2.2, 5J = 0.8 Hz, 1 H, 4-H), 8.34 (s br, 1 H, 6-H), 8.79 (d, $^2J_{\text{PH}}$ = 37.6 Hz, 1 H, 2-H) ppm. $^{13}\text{C}\{^1\text{H}\}$ NMR (CDCl_3): δ = 18.20 (CH_3 -5), 125.62 (superimposed, C_q -5), 125.76 (2 CH-*o*), 127.86 (CH-*p*), 129.28 (2 CH-*m*), 133.72 (d, 1J = 43.2 Hz, C_q -3a), 138.07 (d, 2J = 19.1 Hz, CH-4), 140.21 (d, 3J = 2.4 Hz, C_q -*i*), 147.56 (d, 4J = 2.8 Hz, CH-6), 151.67 (d, 2J = 6.5 Hz, C_q -7a), 162.69 (d, 1J = 54.3 Hz, CH-2) ppm. $^{31}\text{P}\{^1\text{H}\}$ NMR (CDCl_3): δ = 71.5 ppm. MS (EI 70 eV, 25 °C): m/z (%) = 227 (13), 226 (100) [$\text{M}]^+$, 225 (61), 184 (30), 183 (64), 84 (14), 77 (18), 51 (14). HRMS (EI): calcd. for $\text{C}_{13}\text{H}_{11}\text{N}_2\text{P}^+$ 226.0660; found 226.0656.

The attempt to isolate **4c** before distillation by overlaying of a saturated solution of the crude product in thf by *n*-hexane led to single crystals of **6c**, the dimer of the phosphalkene precursor. The structure of **6c** is depicted in Figure 3, and the crystal data are given in Table 1. Crude **4c** also contains 20 mol-% of 5-methyl-2-phenylaminopyridine (**2d'**) as impurity. ^1H NMR (CDCl_3): δ = 2.20 (s, 3 H, 5- CH_3), 6.82 (br. d, 3J = 8.5 Hz, 3-H), 7.00 (m, *p*-CH), 7.27–7.32 (m, 4 H, *o*-H, *m*-H), 7.32 (dd, superimposed, 1 H, 4-H), 8.03 (dd, 4J = 1.5, 5J = 0.7 Hz, 1 H, 6-H) ppm. $^{13}\text{C}\{^1\text{H}\}$ NMR (CDCl_3): δ = 17.50 (CH_3 -5), 108.23 (CH-3), 119.56 (2 CH-*o*), 122.20 (CH-*p*), 124.08 (C_q -5), 129.21 (2 CH-*m*), 138.54 (CH-4), 140.93 (C_q -*i*), 147.91 (CH-6), 153.77 (s, C_q -2) ppm.

1-(2'-Pyridyl)-1,3-azaphospholo[5,4-*b*]pyridine (4d): Compound **2d** (0.43 g, 2.12 mmol) and *N,N*-dimethylformamide dimethyl acetal (0.32 mL, 2.41 mmol) gave oily **4d**, which crystallized after distillation at 10^{-5} mbar/58–62 °C (bath temperature), yield 0.21 g (47%), m.p. 79 °C. ^1H NMR (CDCl_3 ref. solv. 7.25): δ = 7.23 (ddd, 3J = 7.8, $^4J_{\text{PH}}$ \approx 4J \approx 1.9 Hz, 1 H, 5-H), 7.33 (ddd, 3J = 7.3, 4.9, 4J = 1.0 Hz, 1 H, 5'-H), 7.93 (ddd, 3J = 8.3, 7.3, 4J = 1.9 Hz, 1 H, 4'-H), 8.46 (ddd, 3J = 7.8, $^3J_{\text{PH}}$ = 3.2, 4J = 1.8 Hz, 1 H, 4-H), 8.51 (dt, 3J = 8.3, 4J \approx $^5J_{\text{PH}}$ \approx 1 Hz, 1 H, 3'-H), 8.55 (dt, 3J = 4.6, 4J \approx $^5J_{\text{PH}}$ = 1.5 Hz, 1 H, 6-H), 8.61 (ddd, 3J = 4.9, 4J = 1.9, 5J = 1 Hz, 1 H, 6'-H), 9.62 (d br, $^2J_{\text{PH}}$ = 38.4 Hz, 1 H, CH-2) ppm. $^{13}\text{C}\{^1\text{H}\}$ NMR (CDCl_3): δ = 117.09 (d, 3J = 9.9 Hz, CH-5), 118.57 (CH-5'), 122.25 (CH-3'), 134.77 (d, 1J = 43.1 Hz, C_q -3a), 138.19 (CH-4'), 138.78 (d, 2J = 19.6 Hz, CH-4), 145.95 (d, 4J = 2.9 Hz, CH-6), 148.86 (CH-6'), 158.92 (low intensity d, 2J = 7 Hz, C_q -7a), 161.95 (d, 1J = 52.2 Hz, CH-2) ppm, C_q -2' at noise level. $^{31}\text{P}\{^1\text{H}\}$ NMR (CDCl_3): δ = 76.0 ppm. MS (EI 70 eV, 250 °C): m/z (%) = 213 (8) [$\text{M}]^+$, 186 (21), 178 (93), 177 (24), 163 (53), 150 (100), 149 (24). HRMS (ESI in MeOH, NH_4OAc): calcd. for $\text{C}_{11}\text{H}_9\text{N}_3\text{P}^+$ [$\text{M} + \text{H}]^+$ 214.05286; found 214.05299.

2,5-Dimethyl-1*H*-1,3-azaphospholo[5,4-*b*]pyridine (5a): Compound **1a** (0.34 g, 2.43 mmol) and *N,N*-dimethylacetamide dimethyl acetal (0.39 mL, 2.67 mmol) were heated for 1 d at 50 °C. ^{31}P NMR spectroscopic monitoring showed formation of a mixture of an intermediate phosphalkene **3a** (R^3 = Me) and product **5a** (in CDCl_3 δ = 49.5, 66.6 ppm; intensity ca. 1:1). Heating was continued for 4 d

to complete the reaction. Distillation at 10^{-5} mbar/54–56 °C (bath temperature) furnished 0.22 g oil, rapidly crystallizing to a white solid. The main component was **5a** (60 mol-%, corrected yield 35%), contaminated by 2-amino-5-methylpyridine. Crystallization by slow evaporation of CDCl_3 provided pure single crystalline **5a**, m.p. 74 °C. ^1H NMR (CDCl_3). The crystal data are compiled in Table 1, selected bond lengths and angles are given in Figure 2. ^1H NMR (CDCl_3): δ = 2.38 (s, 3 H, 5- CH_3), 2.79 (d, $^3J_{\text{PH}}$ = 12.3 Hz, 3 H, 2- CH_3), 8.05 (br. s, 1 H, 4-H), 8.16 (br. s, 1 H, 6-H), 11.87 (br. s, 1 H, NH) ppm. $^{13}\text{C}\{^1\text{H}\}$ NMR (CDCl_3): δ = 18.30 (d, 2J = 22.7 Hz, 2- CH_3), 18.32 (5- CH_3), 125.21 (d, 3J = 9.2 Hz, C_q -5), 134.15 (d, 1J = 45.0 Hz, C_q -3a), 137.60 (d, 2J = 18.2 Hz, CH-4), 145.25 (d, 4J = 2.4 Hz, CH-6), 152.64 (d, 2J = 5.0 Hz, C_q -7a), 175.84 (d, $^1J_{\text{PC}}$ = 52.8 Hz, C_q -2) ppm. $^{31}\text{P}\{^1\text{H}\}$ NMR (CDCl_3): δ = 67.6 ppm. MS (EI 70 eV, 125 °C): m/z (%) = 165 (9), 164 (100) $[\text{M}]^+$, 163 (75), 149 (6), 136 (10), 69 (14). HRMS (EI): calcd. for $\text{C}_8\text{H}_9\text{N}_2\text{P}^+$ 164.0503; found 164.0497.

Characteristic NMR spectroscopic data of intermediate **3a** (R^3 = Me) in a mixture with **5a**. ^1H NMR (CDCl_3): δ = 2.05 (d, $^3J_{\text{PH}}$ = 5.3 Hz, 3 H, 2- CH_3), 2.38 (s, 3 H, 5- CH_3), 3.10 (d, $^4J_{\text{PH}}$ = 4.0 Hz, 6 H, NMe_2), 4.87 (br. s, 2 H, NH_2), 7.30 (dd, $^3J_{\text{PH}}$ = 6.4, 4J = 2.4 Hz, 1 H, 4-H), 7.76 (dd, 4J = 2.4, $^5J_{\text{PH}}$ = 0.6 Hz, 1 H, 6-H) ppm. $^{13}\text{C}\{^1\text{H}\}$ NMR (CDCl_3): δ = 15.06 (d, 2J = 27.2 Hz, $\text{P}=\text{CCH}_3$), 18.13 (CH_3 -5), 37.15 (NMe_2), 105.40 (C_q -3a), 121.39 (C_q -5), 138.60 (d, 2J = 21.1 Hz, CH-4), 147.65 (CH-6), 148.37 (C_q -7a), 157.17 (C_q -2) ppm. $^{31}\text{P}\{^1\text{H}\}$ NMR (CDCl_3): δ = 49.5 ppm.

2,5-Dimethyl-1-phenyl-1,3-azaphospholo[5,4-*b*]pyridine (5c): Compound **2c** (0.50 g, 2.31 mmol) and *N,N*-dimethylacetamide dimethyl acetal (0.38 mL, 2.60 mmol) gave oily **5c**, which crystallized after distillation at 10^{-5} mbar/65–68 °C (bath temperature), yield 0.31 g (56%), m.p. 84 °C. ^1H NMR (C_6D_6): δ = 1.96 (s, 3 H, 5- CH_3), 2.28 (d, $^3J_{\text{PH}}$ = 13.6 Hz, 3 H, 2- CH_3), 6.90 (m, 3J = 7.8 Hz, 2 H, *o*-H), 7.00–7.10 (m, 3 H, *p*-H, *m*-H), 7.82 (unresolved t, 1 H, 4-H), 8.20 (s br, 1 H, 6-H) ppm. $^{13}\text{C}\{^1\text{H}\}$ (DEPT) NMR (C_6D_6): δ = 18.56 (CH_3 -5), 18.91 (d, 2J = 24.9 Hz, CH_3 -2), 126.63 (d, 3J = 9.8 Hz, C_q -5), 129.02 (2 CH-*o*), 129.52 (CH-*p*), 129.88 (2 CH-*m*), 133.94 (d, 1J = 42.4 Hz, C_q -3a), 137.66 (d, 2J = 18.7 Hz, CH-4), 139.35 (C_q -*i*), 147.39 (d, 4J = 2.8 Hz, CH-6), 155.4 (unresolved d, C_q -7a), 177.17 (d, 1J = 52.1 Hz, C_q -2) ppm. $^{31}\text{P}\{^1\text{H}\}$ NMR (CDCl_3): δ = 66.8 ppm. MS (EI 70 eV, 100 °C): m/z (%) = 241 (21), 240 (100) $[\text{M}]^+$, 239 (88), 198 (33), 183 (78), 170 (44), 152 (47), 138 (90), 136 (69), 84 (73), 57 (86). HRMS (ESI in MeOH, NH_4OAc): calcd. for $\text{C}_{14}\text{H}_{14}\text{N}_2\text{P}^+$ [M + H] $^+$ 240.08891; found 240.08896.

Attempts to Synthesize Benzazaphospholes by Reductive Cyclization

5-Methyl-2-(neopentylamino)-3-phosphanylpyridine (8a): A solution of **7a** (0.40 g, 1.22 mmol) in diethyl ether (20 mL) was added dropwise at 0 °C to LiAlH_4 pellets (0.14 g, 3.69 mmol) stirred in diethyl ether (10 mL) for almost 1 h. The reaction mixture was stirred for 2 d at room temperature. Then, on cooling with ice-water, degassed water was added dropwise until the evolution of hydrogen ceased. Solids were filtered off and washed with diethyl ether. The filtrate was dried with Na_2SO_4 , and the solvent was removed in vacuo. Vacuum distillation at 10^{-5} mbar/40–44 °C (bath temperature) gave 0.19 g of viscous liquid **8a** (yield 55%), contaminated by ca. 15 mol-% 5-methyl-2-(neopentylamino)-pyridine (**8a'**), based on ^1H NMR integration, and three unidentified phosphanes (each 5 mol-%). Compound **8a**: ^1H NMR (CDCl_3): δ = 0.90 (s, 9 H, CMe_3), 1.83 (s, 3 H, 5- CH_3), 3.29 (d, $^1J_{\text{PH}}$ = 199.0 Hz, 2 H, PH_2), 3.49 (d, 3J = 6.0 Hz, 2 H, NCH_2), 4.58 (br. s, 1 H, NH), 7.25 (dd, $^3J_{\text{PH}}$ = 12.3, 4J = 2.4 Hz, 1 H, 4-H), 8.07 (s, 1 H, 6-H) ppm. $^{13}\text{C}\{^1\text{H}\}$ NMR (CDCl_3): δ = 17.71 (s, 5- CH_3), 28.32 (s, CMe_3), 32.94 (s, CMe_3), 53.61 (NCH_2), 105.49 (d, 1J = 13.4 Hz, C-3), 121.57 (d, 3J

= 9.1 Hz, C-5), 147.65 (d, 2J = 33.1 Hz, C-4), 150.62 (d, 4J = 1.0 Hz, C-6), 159.71 (C-2) ppm. $^{31}\text{P}\{^1\text{H}\}$ NMR (CDCl_3): δ = –153.55 ppm. HRMS (EI): calcd. for $\text{C}_{11}\text{H}_{19}\text{N}_2\text{P}^+$ 210.1286; found 210.1284. **8a'**: ^1H NMR (C_6D_6): δ = 0.83 (CMe_3), 1.93 (5- CH_3), 3.06 (d, 3J = 6.5 Hz, NCH_2), 4.45 (s br, NH), 6.08 (d, 3J = 8.4 Hz, 1 H, 3-H), 6.68 (s br, 1 H, 6-H), 6.96 (dd, 3J = 8.4, 4J = 2.4 Hz, 1 H, 4-H) ppm; 6-H superimposed at δ = 8.07 ppm. $^{13}\text{C}\{^1\text{H}\}$ NMR (C_6D_6): δ = 18.02 (CH_3 -5), 28.41 (CMe_3), 32.51 (CMe_3), 54.33 (NCH_2), 107.11 (CH-3), 121.50 (C_q -5), 138.62 (CH-4), 149.00 (CH-6), 159.00 (C_q -2) ppm.

5-Methyl-1-neopentyl-1,3-azaphospholo[5,4-*b*]pyridine (9a): A mixture of *N,N*-dimethylformamide dimethyl acetal (0.13 mL, 0.95 mmol) and crude **8a** (200 mg, 0.95 mmol) was heated whilst stirring for almost 4 d at 50 °C. Volatiles were removed in vacuo, and 110 mg (<48%) of colorless oil was separated by distillation at 10^{-5} mbar/60–65 °C (bath temperature). NMR spectroscopic and HRMS data indicated impure **9a**. ^1H NMR (CDCl_3): δ = 1.00 (s, 9 H, CH_3), 2.44 (s, 3 H, 5- CH_3), 4.33 (s, 2 H, NCH_2), 8.17 (td, $^3J_{\text{PH}} \approx ^4J$ = 2–3, 5J = 0.8 Hz, 1 H, 4-H), 8.31 (s, 1 H, 6-H), 8.61 (d, $^2J_{\text{PH}}$ = 38.0 Hz, 1 H, 2-H) ppm. $^{13}\text{C}\{^1\text{H}\}$ NMR (CDCl_3): δ = 18.20 (CH_3 -5), 27.60 (CMe_3), 31.99 (CMe_3), 59.01 (d, 3J = 2.9 Hz, NCH_2), 124.78 (d, 3J = 10.4 Hz, C_q -5), 133.21 (d, 1J = 42.3 Hz, C_q -3a), 137.72 (d, 2J = 19.3 Hz, CH-4), 146.62 (d, 4J = 3.0 Hz, CH-6), 147.1 (br., C_q -7a), 163.46 (d, 1J = 54.0 Hz, CH-2) ppm. $^{31}\text{P}\{^1\text{H}\}$ NMR (CDCl_3): δ = 62.22 ppm. MS (EI 70 eV, 340 °C): m/z (%) = 220 (9) $[\text{M}]^+$, 121 (100). HRMS (EI): calcd. for $\text{C}_{12}\text{H}_{17}\text{N}_2\text{P}^+$ 220.1129; found 220.1126.

3-*tert*-Butyl-2-deutero-5-methyl-1-phenyl-1,3-azaphospholino-

[5,4-*b*]pyridine (11c): A solution of *t*BuLi in pentane (0.27 mL, 1.7 M in pentane, 0.46 mmol) was added to a solution of **4c** (100 mg, 0.44 mmol) in diethyl ether (15 mL), cooled to –80 °C. After warming up slowly to room temperature, the solution was cooled again to –80 °C, and CH_3OD (10 μL , 0.63 mmol) was added. The solvent was removed in vacuo, the residue was washed with degassed water, and the product was extracted with diethyl ether and dried with Na_2SO_4 . Removing of ether afforded 61 mg (48%) of white solid **11c**, slightly contaminated by **4c**. ^1H NMR (C_6D_6): δ = 0.80 (d, $^3J_{\text{PH}}$ = 12.4 Hz, 9 H, CMe_3), 1.86 (s, 3 H, 5- CH_3), 3.49 (d, $^2J_{\text{PH}}$ = 3.9 Hz, 0.7 H, 2- $\text{H}_{\text{anti to lp}}$), 3.65 (d, $^2J_{\text{PH}}$ = 23.9 Hz, 0.3 H, 2- $\text{H}_{\text{syn to lp}}$), 6.96 (tt, 3J = 7.3, 4J = 1 Hz, 1 H, *p*-H), 7.27 (tm, 3 H, 2 *m*-H, 4-H), 7.78 (tm, 3J = 7.9, 4J = 1 Hz, 2 H, *o*-H), 8.03 (dd, 4J , $^5J_{\text{PH}}$ = 1.6, 0.8 Hz, 1 H, 6-H) ppm. $^{13}\text{C}\{^1\text{H}\}$ (DEPT) NMR (C_6D_6): δ = 18.11 (CH_3 -5), 26.60 (d, 2J = 15.0 Hz, CMe_3), 30.80 (d, 1J = 18.4 Hz, CMe_3), 46.01 (q, $^1J_{\text{PC}} \approx ^1J_{\text{CD}}$ = 23 Hz, CH-2), 120.34 (d, 1J = 14.9 Hz, C_q -3a), 120.97 (d, 4J = 1.8 Hz, 2 CH-*o*), 123.07 (s, CH-*p*), 123.51 (d, 3J = 5.6 Hz, C_q -5), 129.41 (s, 2 CH-*m*), 141.74 (d, 2J = 20.9 Hz, CH-4), 144.33 (s, C_q -*i*), 149.69 (s, CH-6), 161.57 (s, C_q -7a) ppm. $^{31}\text{P}\{^1\text{H}\}$ NMR (C_6D_6): δ = –26.49 ppm. MS (EI 70 eV, 60 °C): m/z (%) = 286 (6), 285 (27) $[\text{M}]^+$, 229 (35), 228 (100), 227 (62), 226 (50), 183 (33), 77 (36), 51 (32). HRMS (ESI in MeOH, NH_4OAc): calcd. for $\text{C}_{17}\text{H}_{21}\text{N}_2\text{PD}^+$ [M + H] $^+$ 286.15779; found 286.15783.

3- η^1 -(3-*tert*-Butyl-5-methyl-1-phenyl-1,3-azaphospholino[5,4-*b*]pyr-

idine)pentacarbonyltungsten (12c): A solution of *t*BuLi in pentane (0.27 mL, 1.7 M, 0.46 mmol) was added to a solution of **4c** (102 mg, 0.45 mmol) in thf (10 mL), cooled to –80 °C. After warming up slowly to 0 °C, the solution was cooled again to –80 °C, and tungsten hexacarbonyl (159 mg, 0.45 mmol) in thf (5 mL) was added. The reaction mixture was stirred for 1 h at –80 °C and for 3 d at room temperature. The solvent and volatiles were removed in vacuo. The product was extracted with CDCl_3 , leaving 196 mg (72%) of pale brownish solid after evaporation of the solvent. ^1H

NMR (CDCl₃): δ = 1.15 (d, $^3J_{\text{PH}}$ = 15.6 Hz, 9 H, CH₃), 2.28 (s, 3 H, 5-CH₃), 4.33 (dd, 2J = 13.1, $^2J_{\text{PH}}$ = 7.1 Hz, 1 H, NCH_A), 4.44 (dd, 2J = 13.1, $^2J_{\text{PH}}$ = 5.9 Hz, 1 H, NCH_B), 7.14 (t, 3J = 7.4, 4J = 1–2 Hz, 1 H, *p*-H), 7.36–7.42 (m, 3 H, 2 *m*-H, 7-H), 7.51 (dd, 3J = 8.5, 4J = 1 Hz, 2 H, *o*-H), 7.61 (dd, 3J = 7.8, 4J = 2.1 Hz, 1 H, 6-H), 8.03 (br. s, 1 H, 4-H) ppm. $^{13}\text{C}\{^1\text{H}\}$ NMR (CDCl₃): δ = 17.81 (CH₃-5), 25.09 (d, $^2J_{\text{PC}}$ = 6.6 Hz, CMe₃), 34.78 (d, $^1J_{\text{PC}}$ = 15.9 Hz, CMe₃), 53.20 (d, 1J = 21.9 Hz, PCH₂), 121.39 (2 C, CH-*o*), 123.88 (d, 3J = 7.1 Hz, C_q-5), 124.21 (CH-*p*), 129.15 (2 C, CH-*m*), 140.80 (d, 2J = 10.6 Hz, CH-4), 151.19 (br., CH-6), 196.46 (d, 2J = 7.0 Hz, 4 CO_{cis}) ppm; C_q-3a, C_q-7a, C_q-*i* and CO_{trans} at noise level. $^{31}\text{P}\{^1\text{H}\}$ NMR (CDCl₃): δ = 11.4 ppm (satellites, $^1J_{\text{PW}}$ = 239.5 Hz). IR (KBr): $\tilde{\nu}_{\text{CO}}$ = 2071 (w), 1980 (sh), 1934 (vst) cm⁻¹. HRMS (ESI in CH₃CN): calcd. for the three most intensive isotopic peaks of C₂₂H₂₁N₂O₅PW⁺ 607.07422, 609.07743, 611.08054; found 607.07445, 609.07761, 611.08073.

η^1 -(5-Methyl-1-phenyl-1,3-azaphospholo[5,4-*b*]pyridine-*P*)pentacarbonylchromium (13c): A solution of Cr(CO)₅(thf), prepared by UV irradiation of Cr(CO)₆ (0.191 g, 0.868 mmol) in thf (30 mL), was added to a solution of **4c** (0.140 g, 0.619 mmol) in thf (5 mL) at –10 °C. The solution was stirred for two days at room temperature. Then thf was removed in vacuo. The residual dark yellow powder, which was sparingly soluble in C₆D₆, was separated from the solution, dried in vacuo and high vacuum, and extracted with CDCl₃ (yield 230 mg, 89%). ^1H NMR (CDCl₃): δ = 2.51 (s, 3 H, 5-CH₃),

7.42–7.65 (m, 5 H, phenyl), 8.21 (d br, $^3J_{\text{PH}}$ = 7.2 Hz, 1 H, 4-H), 8.42 (t, 4J = $^5J_{\text{PH}}$ = 1.9 Hz, 1 H, 6-H), 8.69 (d, $^2J_{\text{PH}}$ = 31.3 Hz, 1 H, 2-H) ppm. $^{13}\text{C}\{^1\text{H}\}$ NMR (CDCl₃): δ = 18.39 (CH₃-5), 125.85 (d, 4J = 0.9 Hz, 2 CH-*o*), 126.62 (d, 3J = 12.4 Hz, C_q-5), 128.46 (CH-*p*), 129.48 (2 CH-*m*), 131.31 (d, 1J = 13.8 Hz, C_q-3a), 135.73 (d, 2J = 11.4 Hz, CH-4), 139.58 (C_q-*i*), 149.35 (d, 4J = 4.3 Hz, CH-6), 151.57 (C_q-7a), 157.38 (d, 1J = 20.2 Hz, CH-2), 214.87 (d, 2J = 16.6 Hz, 4 *cis* CO), 221.13 (d, 2J = 4.5 Hz, *trans* CO) ppm. $^{31}\text{P}\{^1\text{H}\}$ NMR (CDCl₃): δ = 87.84 ppm. IR (KBr): $\tilde{\nu}_{\text{CO}}$ = 2068 (w), 1935 (vs) cm⁻¹. MS (EI 70 eV, 40 °C): *m/z* (%) = 419 (1) [M]⁺, 418 (5), 362 (4) [M⁺ – 2CO], 334 (1) [M⁺ – 3CO], 306 (6) [M⁺ – 4CO], 278 (63) [M⁺ – 5CO], 227 (4) [L]⁺, 226 (20). C₁₈H₁₁CrN₂O₅P (418.26): calcd. C 51.69, H 2.65, N 6.70; found C 51.35, H 2.83, N 6.53.

Detection of η^1 -(5-Methyl-1-phenyl-1,3-azaphospholo[5,4-*b*]pyridine-*P*)pentacarbonylmolybdenum (14c): Reaction of **4c** (0.107 g, 0.473 mmol) with Mo(CO)₅(thf), prepared by UV irradiation of Mo(CO)₆ (0.150 g, 0.568 mmol) in thf (with replacement of CO by N₂), and workup as described for **13c** gave 0.189 g of yellow solid containing residual Mo(CO)₆. ^1H NMR (CDCl₃): δ = 2.51 (s, 3 H, 5-CH₃), 7.42–7.63 (m, 5 H, phenyl), 8.16 (ddq, $^3J_{\text{PH}}$ = 7.4, 4J = 2.0, 4J = 0.9 Hz, 1 H, 4-H), 8.42 (t, 4J = $^5J_{\text{PH}}$ = 2.1 Hz, 1 H, 6-H), 8.68 (d, $^2J_{\text{PH}}$ = 31.8 Hz, 1 H, 2-H) ppm. $^{13}\text{C}\{^1\text{H}\}$ NMR (CDCl₃): δ = 18.38 (CH₃-5), 125.0 (d, 3J = 12 Hz, C_q-5), 125.83 (2 CH-*o*), 128.47 (CH-*p*), 129.47 (2 CH-*m*), ca. 130.8 (noise level, C_q-3a), 138.4 (C_q-*i*), 136.0 (d, 2J = 12 Hz, CH-4), 149.2 (br., CH-6), 151.2

Table 1. Crystal data and structure refinement of the X-ray crystallographic analyses.

Compound	2a	5a	6c ·2CDCl ₃
Empirical formula	C ₆ H ₉ N ₂ P	C ₈ H ₉ N ₂ P	C ₃₂ H ₃₆ D ₂ Cl ₆ N ₆ P ₂
Formula weight	140.12	164.14	783.33
Temperature [K]	133(2)	133(2)	133(2)
Wavelength [Å]	0.71073	0.71073	0.71073
Crystal system	triclinic	monoclinic	triclinic
Space group	<i>P</i> $\bar{1}$	<i>P</i> 2 ₁ / <i>n</i>	<i>P</i> $\bar{1}$
Unit cell dimensions			
<i>a</i> [Å]	3.9982(8)	6.0780(7)	11.2029(9)
<i>b</i> [Å]	8.5561(16)	11.6398(14)	12.8093(10)
<i>c</i> [Å]	10.800(2)	11.5946(16)	15.6194(12)
α [°]	77.041(4)	90	112.449(2)
β [°]	88.774(4)	105.058(4)	90.904(2)
γ [°]	82.332(4)	90	112.887(2)
Volume [Å ³]	356.83(12)	2792.11(17)	1872.6(3)
<i>Z</i>	2	4	2
Density (calculated) [Mg m ⁻³]	1.304	1.376	1.390
Absorption coefficient [mm ⁻¹]	0.29	0.28	0.58
<i>F</i> (000)	148	344	808
Crystal habit	colorless lath	colorless tablet	colorless tablet
Crystal size [mm ³]	0.35 × 0.20 × 0.10	0.23 × 0.20 × 0.10	0.4 × 0.3 × 0.2
θ range for data collection [°]	1.93 to 28.28	2.52 to 30.48	1.44 to 30.51
Index ranges	–5 ≤ <i>h</i> ≤ 5, –11 ≤ <i>k</i> ≤ 11, –14 ≤ <i>l</i> ≤ 14	–8 ≤ <i>h</i> ≤ 8, –16 ≤ <i>k</i> ≤ 16 –16 ≤ <i>l</i> ≤ 16	–16 ≤ <i>h</i> ≤ 16, –18 ≤ <i>k</i> ≤ 18, –22 ≤ <i>l</i> ≤ 22
Reflections collected	4048	8839	34749
Independent reflections	1726 [<i>R</i> (int) = 0.061]	2405 [<i>R</i> (int) = 0.062]	11306 [<i>R</i> (int) = 0.030]
Completeness	98.1% to θ = 28°	99.4% to θ = 30°	99.1% to θ = 30°
Absorption correction; transmissions	none	none	semi-empirical from equivalents; 0.738–0.893
Refinement method		full-matrix least-squares on <i>F</i> ²	
Data/restraints/parameters	1726/3/99	2405/0/106	11306/96/455
Goodness-of-fit on <i>F</i> ²	1.04	1.04	1.01
Final <i>R</i> indices	<i>R</i> 1 = 0.047, <i>wR</i> ₂ = 0.109	<i>R</i> 1 = 0.044, <i>wR</i> ₂ = 0.095	<i>R</i> 1 = 0.045, <i>wR</i> ₂ = 0.105
<i>R</i> indices (all data)	<i>R</i> 1 = 0.060, <i>wR</i> ₂ = 0.114	<i>R</i> 1 = 0.061, <i>wR</i> ₂ = 0.100	<i>R</i> 1 = 0.071, <i>wR</i> ₂ = 0.119
Largest diff. peak/hole [e Å ⁻³]	0.35/–0.33	0.38/–0.27	0.85/–0.86

(C_q-7a), ca. 157 (uncertain, CH-2), 203.7 (d, ²J = 11 Hz, 4 *cis*-CO) ppm; *trans*-CO at noise level. ³¹P{¹H} NMR (CDCl₃): δ = 68.33 ppm. IR (KBr): ν_(CO) = 2075 (w), 1943 (vs) cm⁻¹.

η¹-P-(1-Ethyl-5-methyl-1,3-azaphospholo[5,4-*b*]pyridine)pentacarbonyltungsten (15b): Reaction of **4b** (0.124 g, 0.697 mmol) with a solution of W(CO)₅(thf), prepared by UV irradiation of W(CO)₆ (0.368 g, 1.045 mmol) in thf (30 mL), and work up as described for **13c** afforded 0.288 g (ca. 80%) of orange solid, containing a small amount of residual W(CO)₆. ¹H NMR (CDCl₃): δ = 1.47 (t, ³J = 7.3 Hz, 3 H, CH₃), 2.43 (s, 3 H, 5-Me), 4.50 (qd, ³J = 7.3, ⁴J_{PH} = 1.9 Hz, 2 H, CH₂), 8.01 (ddq, ³J_{PH} = 7.4, ⁴J = 2.0, ⁴J = 0.8 Hz, 1 H, 4-H), 8.35 (t, ⁴J ≈ ⁵J_{PH} ≈ 2.1 Hz, 1 H, 6-H), 8.42 (d, ²J_{PH} = 31.3 Hz, 1 H, 2-H) ppm. ¹³C{¹H} NMR (CDCl₃): δ = 15.38 (CH₃), 18.38 (5-Me), 44.16 (CH₂), 126.26 (d, ³J = 12.4 Hz, C_q-5), 130.06 (d, ¹J = 22.7 Hz, C_q-3a), 135.82 (d, ²J = 11.8 Hz, CH-4), 148.75 (d, ³J = 4.3 Hz, CH-6), 150.52 (s, C_q-7a), 154.59 (d, ¹J = 27.4 Hz, CH-2), 194.44 (d, ²J = 9.1 Hz, 4 CO, *cis*-CO), 199.21 (d, ²J = 30.8 Hz, 1 CO, *trans*-CO) ppm. ³¹P{¹H} NMR (CDCl₃): δ = 31.5 (satellites, ¹J_{PW} = 247.6 Hz) ppm. C₁₄H₁₁N₂O₅PW (502.06): calcd. C 33.49, H 2.21, N 5.58; found C – (incomplete combustion), H 2.43, N 5.27.

Detection of η¹-P-(5-Methyl-1-phenyl-1,3-azaphospholo[5,4-*b*]pyridine)pentacarbonyltungsten (15c): Reaction of **4c** (0.111 g, 0.49 mmol) with a solution of W(CO)₅(thf), prepared by UV irradiation of W(CO)₆ (0.207 g, 0.59 mmol) in thf (30 mL), and work up as described for **13c** afforded 218 mg of a yellow solid containing residual W(CO)₆. ¹H NMR (CDCl₃): δ = 2.51 (s br, 3 H, 5-CH₃), 7.44–7.64 (m, 5 H, phenyl), 8.13 (dq, ³J_{PH} = 7.8, ⁴J = 2.0, ⁴J = 0.8 Hz, 1 H, 4-H), 8.42 (br. t, ⁴J ≈ ⁵J_{PH} ≈ 2.2 Hz, 1 H, 6-H), 8.62 (br. d, ²J_{PH} = 31.0 Hz, 1 H, 2-H) ppm. ¹³C{¹H} NMR (CDCl₃): δ = 18.39 (CH₃-5), 127.29 (C_q-5), 129.33 (2 CH-*o*), 129.49 (CH-*p*), 129.80 (2 CH-*m*), 135.92 (d, ²J = 11.3 Hz, CH-4), 139.5 (C_q-*i*), 149.50 (d, ⁴J = 3.8 Hz, CH-6), 194.55 (d, ²J = 8.8 Hz, 4 CO_{*cis*}) ppm; other signals in noise. ³¹P{¹H} NMR (CDCl₃): δ = 40.55 (satellites, ¹J_{PW} = 252.9 Hz) ppm. IR (KBr): ν_(CO) = 2075 (w), 1936 (vs) cm⁻¹.

Crystal Structure Analyses: X-ray diffraction data for **2a**, **5a**, and **6c** were recorded with a Bruker SMART CCD 1000 diffractometer by using monochromated Mo-K_α radiation. The structures were refined by full-matrix least-squares methods on *F*² for all unique reflections (SHELXL-97).^[28] Hydrogen atoms bonded to nitrogen or phosphorus were located directly in difference syntheses and refined freely, but with restraints to bond lengths; other H atoms were calculated by assuming idealized geometries and refined with a riding model or rigid methyl groups. *Special features:* Compound **6c** crystallizes as a deuteriochloroform disolvate; the solvent molecules are disordered by rotation about the C–D bond. Alternative chlorine positions were refined by using a system of similarity restraints. Crystallographic data are given in Table 1, and selected bond lengths and angles are presented in Figures 1, 2, and 3.

CCDC-767984 (for **2a**), -767985 (for **5a**), and -767986 (for **6c**) contain the crystallographic data for this article. These data can be obtained free of charge from The Cambridge Crystallographic Data Centre via www.ccdc.cam.ac.uk/data_request/cif.

Supporting Information (see also the footnote on the first page of this article): ³¹P and ¹³C NMR spectra of **4a–d**, **5a**, **5c**, and **11c**, **13c**, **15b**; ³¹P NMR spectra of **12c**, **14c**, **15c**, tables of positional parameters, bond lengths and bond angles, dihedral angles, hydrogen bonds for compounds **2a**, **5a**, and **6c**.

Acknowledgments

Financial support by the Deutsche Forschungsgemeinschaft (DFG) and a scholarship by the Deutsche Akademische Auslandsdienst (to M. S. S. A.) are gratefully acknowledged. Furthermore, we thank Dr. M. K. Kindermann and B. Witt for numerous NMR spectra and Dr. H. Frauendorf and G. Sommer-Udvarnoki (Georg-August-Universität Göttingen, Institut für Organische und Biomolekulare Chemie) for HRMS measurements.

- [1] For recent reviews, see, e.g.: a) L. A. Adrio, K.-K. Hii, *Organomet. Chem.* **2009**, *35*, 62–92 and references cited therein; b) M. L. Clarke, J. J. R. Frew, *Organomet. Chem.* **2009**, *35*, 19–46; c) *Phosphorus Ligands in Asymmetric Catalysis* (Ed.: A. Börner), Wiley-VCH, Weinheim, **2008**; d) M. Dieguez, C. Claver, O. Pamies, *Eur. J. Org. Chem.* **2007**, 4621–4634; e) O. Kühl, *Coord. Chem. Rev.* **2005**, *249*, 693–704.
- [2] Recent reviews e.g.: a) D. S. Surry, S. L. Buchwald, *Angew. Chem. Int. Ed.* **2008**, *47*, 6338–6361; b) R. Martin, S. L. Buchwald, *Acc. Chem. Res.* **2008**, *41*, 1461–1473; c) J. F. Hartwig, *Acc. Chem. Res.* **2008**, *41*, 1534–1544; d) G. C. Fu, *Acc. Chem. Res.* **2008**, *41*, 1555–1564; e) A. Zapf, M. Beller, *Chem. Commun.* **2005**, 431–440.
- [3] Recent work e.g.: a) C. K. Seubert, Y. Sun, W. R. Thiel, *Dalton Trans.* **2009**, 4971–4977; b) E. Raluy, O. Pamies, M. Dieguez, *Adv. Synth. Catal.* **2009**, *351*, 1648–1670; c) J. Velder, T. Robert, I. Weidner, J.-M. Neudoerfl, J. Lex, H.-G. Schmalz, *Adv. Synth. Catal.* **2008**, *350*, 1309–1315; d) J. Klosin, C. R. Landis, *Acc. Chem. Res.* **2007**, *40*, 1251–1259; e) A. J. Minnaard, B. L. Feringa, L. Lefort, J. G. de Vries, *Acc. Chem. Res.* **2007**, *40*, 1267–1277; f) K. N. Gavrilov, O. G. Bondarev, A. I. Polosukhin, *Russ. Chem. Rev.* **2004**, *73*, 671–699.
- [4] a) C. Müller, D. Vogt, *Dalton Trans.* **2007**, 5505–5523; b) L. Floch, *Coord. Chem. Rev.* **2006**, *250*, 627–681; c) F. Mathey, P. Le Floch in: *Science of Synthesis*, vol. 15, Thieme, Stuttgart, **2004**, pp. 1097–1156; d) *Phosphorus-Carbon Heterocyclic Chemistry: The Rise of a New Domain* (Ed.: F. Mathey), Pergamon, Amsterdam, **2001**; e) P. Le Floch, F. Mathey, *Coord. Chem. Rev.* **1998**, *179–180*, 771–791.
- [5] a) S. Ito, K. Nishide, M. Yoshifuji, *Organometallics* **2006**, *25*, 1424–1430; b) M. Freytag, S. Ito, M. Yoshifuji, *Chem. Asian J.* **2006**, *1*, 693–700; c) M. Van der Sluis, V. Beverwijk, A. Termaten, F. Bickelhaupt, H. Kooijman, A. L. Spek, *Organometallics* **1999**, *18*, 1402–1407.
- [6] a) L. Nyulászi, *Chem. Rev.* **2001**, *101*, 1229–1246; b) L. Nyulászi, T. Veszprémi, *J. Mol. Struct.* **1995**, *347*, 57–72; c) T. Veszprémi, L. Nyulászi, J. Refly, J. Heinicke, *J. Phys. Chem.* **1992**, *96*, 623–626; d) J. Heinicke, *Tetrahedron Lett.* **1986**, *27*, 5699–5702; e) G. Märkl, G. Dorfmeister, *Tetrahedron Lett.* **1986**, *27*, 4419–4422.
- [7] a) R. K. Bansal, J. Heinicke, *Chem. Rev.* **2001**, *101*, 3549–3578; b) J. Heinicke, A. Tzschach, *Tetrahedron Lett.* **1982**, *23*, 3643–3646; c) K. Issleib, R. Vollmer, *Z. Allg. Anorg. Chem.* **1981**, *481*, 22–32.
- [8] a) J. Heinicke, K. Steinhauser, N. Peulecke, A. Spannenberg, P. Mayer, K. Karaghiosoff, *Organometallics* **2002**, *21*, 912–919; b) A. Surana, S. Singh, R. K. Bansal, N. Peulecke, A. Spannenberg, J. Heinicke, *J. Organomet. Chem.* **2002**, *646*, 113–124; c) J. Heinicke, N. Gupta, S. Singh, A. Surana, O. Kühl, R. K. Bansal, K. Karaghiosoff, M. Vogt, *Z. Anorg. Allg. Chem.* **2002**, *628*, 2869–2876; d) J. Heinicke, A. Surana, N. Peulecke, R. K. Bansal, A. Murso, D. Stalke, *Eur. J. Inorg. Chem.* **2001**, 2563–2567.
- [9] a) B. R. Aluri, M. K. Kindermann, P. G. Jones, J. Heinicke, *Chem. Eur. J.* **2008**, *14*, 4328–4335; b) B. R. Aluri, M. K. Kindermann, P. G. Jones, I. Dix, J. Heinicke, *Inorg. Chem.* **2008**, *47*, 6900–6912.
- [10] a) R. K. Bansal, K. Karaghiosoff, A. Schmidpeter, *Tetrahedron* **1994**, *50*, 7675–7745; b) R. K. Bansal, K. Karaghiosoff, N.

- Gupta, A. Schmidpeter, C. Spindler, *Chem. Ber.* **1991**, *124*, 475–480.
- [11] a) N. Gupta, C. B. Jain, J. Heinicke, R. K. Bansal, P. G. Jones, *Eur. J. Inorg. Chem.* **1998**, 1079–1086; b) C. B. Jain, D. C. Sharma, N. Gupta, J. Heinicke, R. K. Bansal, *J. Organomet. Chem.* **1999**, *577*, 337–341.
- [12] M. S. S. Adam, O. Köhl, M. K. Kindermann, J. Heinicke, P. G. Jones, *Tetrahedron* **2008**, *64*, 7960–7967.
- [13] a) J. Heinicke, N. Gupta, A. Surana, N. Peulecke, B. Witt, K. Steinhäuser, R. K. Bansal, P. G. Jones, *Tetrahedron* **2001**, *57*, 9963–9972; b) R. K. Bansal, N. Gupta, J. Heinicke, G. N. Nikonov, F. Saguitova, D. C. Sharma, *Synthesis* **1999**, 264–269.
- [14] J. Heinicke, *J. Organomet. Chem.* **1989**, *364*, C17–C21.
- [15] M. S. S. Adam, M. K. Kindermann, M. Köckerling, J. W. Heinicke, *Eur. J. Org. Chem.* **2009**, 4655–4665.
- [16] a) J. Heinicke, M. He, R. Kadyrov, P. G. Jones, *Heteroat. Chem.* **1998**, *9*, 183–193; b) J. Heinicke, R. Kadyrov, M. Kindermann, M. Kloss, A. Fischer, P. G. Jones, *Chem. Ber.* **1996**, *129*, 1061–1071.
- [17] G. Becker, W. Becker, O. Mundt, *Phosphorus Sulfur Relat. Elem.* **1983**, *14*, 267–283.
- [18] For further examples, see: M. S. S. Adam, PhD Thesis, Greifswald, **1988**.
- [19] a) O. Köhl, *Concise Introduction to ³¹P-NMR Spectroscopy – A Guide for the Synthetic Organic and Organometallic Chemist*, Springer-Verlag, Heidelberg, **2008**; b) S. Berger, S. Braun, H. O. Kalinowski, *NMR-Spektroskopie von Nichtmetallen*, vol. 3, *³¹P-NMR-Spektroskopie*, Thieme, Stuttgart, **1993**, p. 173.
- [20] a) G. Märkl, C. Martin, W. Weber, *Tetrahedron Lett.* **1981**, *22*, 1207–1210; b) A. J. Ashe III, *Acc. Chem. Res.* **1978**, *11*, 153–157; c) H. G. DeGraaf, F. Bickelhaupt, *Tetrahedron* **1975**, *31*, 1097–1103.
- [21] J. Heinicke, A. Tzschach, *Phosphorus Sulfur Relat. Elem.* **1984**, *20*, 347–356.
- [22] M. Schlosser in *Organometallics in Synthesis*, 2nd ed. (Ed.: M. Schlosser), Wiley, Chichester, **2002**, p. 290.
- [23] a) W. Strohmeier, K. Gerlach, G. Matthias, *Z. Naturforsch., Teil B* **1960**, *15*, 621–622. ¹³C NMR spectroscopic data: b) H. Daamen, A. Oskam, *Inorg. Chim. Acta* **1978**, *26*, 81–89; c) W. Buchner, W. A. Schenk, *Inorg. Chem.* **1984**, *23*, 132–137.
- [24] A. Breque, C. C. Santini, F. Mathy, J. Fischer, A. Mitschler, *Inorg. Chem.* **1984**, *23*, 3463–3467.
- [25] J. Deberitz, H. Noeth, *J. Organomet. Chem.* **1973**, *49*, 453–467.
- [26] L. Nyulászi, G. Csonka, J. Réffy, T. Veszprémi, J. Heinicke, *J. Organomet. Chem.* **1989**, *373*, 49–56.
- [27] S. O. Grim, D. A. Wheatland, W. McFarlane, *J. Am. Chem. Soc.* **1967**, *89*, 5573–5577.
- [28] G. M. Sheldrick, *Acta Crystallogr., Sect. A* **2008**, *64*, 112–122.

Received: March 3, 2010

Published Online: May 31, 2010

After publication in Early View, a dedication has been added.

Factors Influencing the Structural and Magnetic Properties of Octahedral Cobalt(II) and Iron(II) Complexes of Terdentate N₃ Schiff Base Ligands

Robyn W. Handel,^[a] Holger Willms,^[a] Geoffrey B. Jameson,^[b] Kevin J. Berry,^[c] Boujemaa Moubaraki,^[d] Keith S. Murray,^[d] and Sally Brooker^{*,[a]}

Keywords: Cobalt / Iron / Electrochemistry / Magnetochemistry / Magnetic properties / Schiff base ligands

The influence of the length of the linking alkyl spacer and of the presence of either a proton or a methyl group, in four related terdentate N₃ Schiff base ligands, on the structures and properties of the resulting iron(II) and cobalt(II) complexes has been investigated. The four ligands were prepared in situ by condensation of 2-(2-aminoethyl)pyridine or 2-(aminomethyl)pyridine with 2-acetylpyridine (**L1** vs. **L3**) or 2-formylpyridine (**L2** vs. **L4**). Hence they comprised a mixture of a relatively rigid chelate with a 2-iminopyridyl moiety, comparable to bipyridine coordination, and a more flexible chelate containing the $-(CH_2)_n-$ spacer. Four iron(II) complexes, $[Fe(L1)_2](BF_4)_2$ (**1**), $[Fe(L2)_2](BF_4)_2$ (**2**), $[Fe(L3)_2](BF_4)_2$ (**3**), $[Fe(L4)_2](BF_4)_2$ (**4**), were obtained whereas only in the case of the two ethylene (i.e. not methylene) spaced ligands could pure cobalt(II) complexes, $[Co(L1)_2](BF_4)_2$ (**5**), $[Co(L2)_2](BF_4)_2$ (**6**), be obtained. The ¹H NMR spectra confirmed that

in MeCN **1–4** are diamagnetic whereas **5** and **6** are paramagnetic. X-ray structure determinations of the ethylene-linked complexes, **1**, **5** and **6**, revealed distorted octahedral geometries due to chelate ring restrictions. The M–N distances were typical for high-spin cobalt(II) (**5** and **6**) and for low-spin iron(II) (**1**). The magnetic data on **5** and **6** are typical of those expected for distorted octahedral high-spin d⁷ species; fitting attempts have yielded zero-field splitting and low symmetry ligand field parameters. A metal-centred M^{2+/3+} redox wave and ligand-based reduction processes were observed for **1–6** in MeCN. The metal-centred redox potential (Fe: **1** 0.59, **2** 0.68, **3** 0.58, **4** 0.70 V; Co: **5** 0.03, **6** 0.09 V vs. Fc/Fc⁺) was influenced much more strongly by the presence of the proton vs. methyl group (Fe: shift of 0.09–0.12 V, Co: shift of 0.06 V) than by the bridging methylene vs. ethylene group (Fe: shift of 0.01–0.02 V).

Introduction

Schiff base ligands are one of the most widely used ligand types as they are easily prepared and remarkably versatile.^[1] They readily form stable complexes with most transition metal ions and many of the resulting complexes are of potential interest in bioinorganic chemistry, metal extraction, catalysis, electrochemistry and magnetochemistry.^[2]

Relatively few references can be found in the literature concerning complexes with an N₆ Schiff base-containing coordination environment such as that provided by the family of terdentate N₃ ligands of interest to us, **L1–L4** (Figure 1), whereas numerous terpyridine (tpy) and bipyridine (bpy) ligands have been prepared.^[3] 2,2':6',2''-Tpy can be

considered a “parent imine” ligand for **L1–L4** and is of particular interest to coordination and magnetochemists as its coordination results in one of the major classes of spin-crossover systems for six-coordinate cobalt(II), $[Co(tpy)_2]^{2+}$, whereas all such iron(II) complexes are low-spin.^[4] This illustrates an important distinction between cobalt(II) and iron(II) spin-crossover chemistry, in that the intrinsic ligand-field strength required to effect spin-pairing in cobalt(II) is greater.^[5] Thus ligands that create spin-crossover situations in iron(II) tend to yield purely high-spin cobalt(II). Several investigations of the influence of substituent groups on cobalt(II) and iron(II) complexes of tpy have shown that the spin state of the complexes is tunable by the steric bulk of their ligands,^[6] whilst variation of the inductive influence of the ligands gave modifications of the spin state and facilitated tuning of the Co^{III/II} and Fe^{III/II} redox potentials.^[7]

Several cobalt and iron complexes of “terpyridine-like” N₃ tridentate ligands containing the motif $-N=C-C=N-C-C=N-$ (**I**, Figure 1) have been prepared and investigated with respect to their structural and chromophoric properties.^[8–11] In general, however, complexes of the N₃ amide analogues, $-N=C-C(O)-N-C-C=N-$, are more numerous than these imine compounds. Also, mixed donor sets (e.g., NNO) are often preferred over N₃.^[12]

[a] Department of Chemistry and MacDiarmid Institute for Advanced Materials and Nanotechnology, University of Otago, P. O. Box 56, Dunedin, New Zealand
Fax: +64-3-479 7906
E-mail: sbrooker@chemistry.otago.ac.nz

[b] Institute of Fundamental Sciences, Chemistry, Massey University,
P. O. Box 11222, Palmerston North, New Zealand

[c] 23 Seabreeze Street, Balnarring, Victoria 3926, Australia

[d] School of Chemistry, Building 23, Monash University,
Clayton, Victoria 3800, Australia

Supporting information for this article is available on the WWW under <http://dx.doi.org/10.1002/ejic.201000288>.

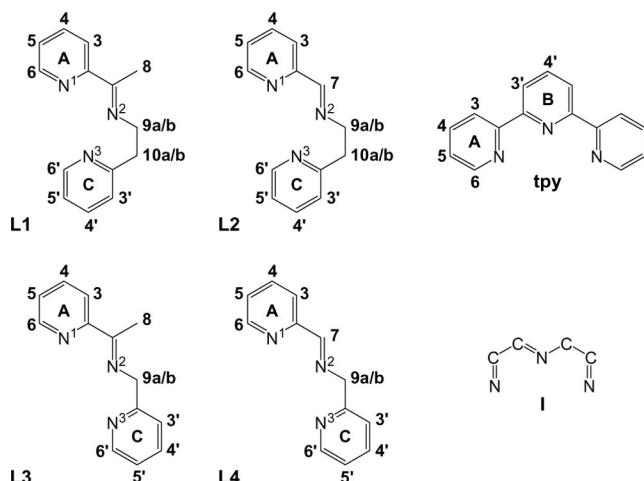


Figure 1. Schiff base ligands **L1**–**L4** with the numbering scheme used in the assignment of the NMR spectra (Note: two such ligands are bound per complex so in the NMR section the second ligand is indicated by underlining the number), 2,2':6',2''-terpyridine (tpy), and the “terpyridine-like” ligand motif (**I**).

Among the known compounds matching motif **I** are homoleptic Fe^{II} complexes of ligands **L1**–**L4**, obtained as perchlorate salts^[8,10] and [Co(**L4**)₂](ClO₄)₂·H₂O,^[10] the characterisations of which are incomplete, and, more recently, heteroleptic Co^{II} complexes of **L1** and **L2**.^[11] Earlier this year, access to a new class of ligands and complexes was established by Wolczanski and co-workers. They deprotonated the methylene linker in **L4** with LiHMDS to obtain an azaallyl ligand (smif[−]), which was then treated with Fe^{II} and Co^{II} precursors to yield homoleptic, *neutral* complexes.^[13]

In this paper we describe a systematic investigation into the coordination chemistry of the four closely related tridentate N₃ Schiff base ligands **L1**–**L4** in mononuclear octahedral complexes of cobalt(II) and iron(II) with BF₄[−] anions. Spectroscopic, magnetic and electrochemical properties of all of the compounds obtained, and crystal structures of three of them, are discussed. Variation of both the length of the alkyl linker (ethylene vs. methylene) and the nature of the reactive carbonyl group of the ligand precursors (aldehyde vs. methyl ketone) were expected to change the ligand bite angles as well as the stability, flexibility and redox behaviour of the resulting Schiff bases. These features of the ligand design can potentially play a role in the (de) stabilisation of particular spin states or oxidation states in the resulting complexes, providing valuable information for further developments, in particular for the design of larger Schiff base ligands capable of generating mixed-spin state or mixed-valent multinuclear compounds.

Results and Discussion

Synthesis

The preparation of the free ligands, **L1**–**L4**, was found to be non-trivial and as this was not necessary it was not pur-

sued further. Instead, the six racemic complexes [Fe(**L1**)₂](BF₄)₂ (**1**), [Fe(**L2**)₂](BF₄)₂ (**2**), [Fe(**L3**)₂](BF₄)₂ (**3**), [Fe(**L4**)₂](BF₄)₂ (**4**), [Co(**L1**)₂](BF₄)₂ (**5**), [Co(**L2**)₂](BF₄)₂ (**6**) were prepared in a one-pot reaction of the appropriate combination of 2-acetyl- or 2-formylpyridine with 2-(2-aminoethyl)- or 2-(aminomethyl)pyridine and M^{II}(BF₄)₂. Generally, stoichiometric amounts of the ligand components were refluxed in isopropyl alcohol or dry ethanol, with a trace of glacial acetic acid, for one or two hours before cooling to room temperature. The subsequent addition of 0.5 equiv. of the metal(II) salt resulted in an immediate colour change and the precipitation of the desired metal complex in pure form and good yield (51–99%). The reactions were tried in other solvents as well, such as methanol and acetonitrile, but isopropyl alcohol or dry ethanol were found to work best.

Although [Co(**L4**)₂](ClO₄)₂·H₂O was reported by Lions and Martin in 1957 to be a *blue* substance with $\mu_{\text{eff}} = 4.2$ BM at 296 K,^[10] and others have subsequently made it according to that method (and reported $\mu_{\text{eff}} = 3.64$ BM at 300 K, 3.31 BM at 100 K),^[14] we were not able to obtain clean Co^{II} complexes of the methylene-bridged ligands **L3** and **L4**, even when different solvents and anions were employed and the reactions were performed under a strict inert atmosphere. The *red* (**L3**) or *rose* (**L4**) products (not blue) we obtained were impure – this holds especially for **L4** – and paramagnetic according to ¹H NMR spectra. Decomposition to diamagnetic material (NMR) occurred too rapidly to allow for further characterisation. Our inability to prepare these two complexes was perplexing, especially given the relative ease with which we were able to prepare (a) the Co^{II} complexes (both high-spin and orange, see later) of the ethylene linked ligands **L1** and **L2** and (b) the Fe^{II} complexes of all four ligands **L1**–**L4** (all low-spin). The reasons for this failure are unknown. However, our experimental difficulties are likely to have been exacerbated by the instability of imine ligands (in contrast tpy is a very robust ligand), especially in strained coordination environments such as those found in the methylene-linked ligands **L3** and **L4**. Indeed the IR spectra of the Fe^{II} complexes of **L3** and **L4** provide an indication that a trace of ligand hydrolysis (or some oxidation of the methylene linker to C=O, increasing the conjugation^[15]) readily occurs on preparation of the KBr disk (trace C=O str. at 1721 or 1700 cm^{−1}). No IR data were reported for [Co(**L4**)₂](ClO₄)₂·H₂O, a monohydrate; only elemental analysis and magnetic moment data have been reported.^[10,14] However, it was noted that this *blue* complex, a colour we find unexpected and intriguing, turned to a *red* gum on exposure to air.^[10]

General Characterisation of 1–6

Mass spectra were recorded for **1**–**6** using the electrospray technique and peaks were observed that were consistent with the consecutive loss of counterions. Specifically, for compound **1** both [M – BF₄]⁺ and [M – 2BF₄]²⁺ signals

were detected, with the expected isotope pattern and charge-related line separation, whereas for **2–6** only the latter signal was observed.

IR spectra were recorded for **1–6** as KBr discs. In each case the formation of the Schiff base was confirmed by an intense $\nu(\text{C}=\text{N})$ band at $1605 \pm 5 \text{ cm}^{-1}$. Carbonyl stretches, for RCHO or $\text{R}_2\text{C}=\text{O}$, were completely absent for **1** & **2** and **5** & **6** whereas some weak bands at 1721 and 1700 cm^{-1} were observed in the spectra of the complexes of **L3** and **L4**. However, no carbonyl starting material was observed in the NMR spectra of the diamagnetic iron(II) complexes **3** & **4**, so it is thought that perhaps some ligand hydrolysis occurred in preparing these KBr discs from imperfectly dried KBr. The presence of BF_4^- anions was confirmed by absorptions at about 1060 and 525 cm^{-1} .

Conductivity measurements were recorded in acetonitrile for all of the complexes **1–6**. They have molar conductivities in or very near the literature range for 2:1 electrolytes (Exp. Section),^[16] which is consistent with the expected presence of two dissociated anions per dication in solution. The molar conductivities of complexes **2** and **6**, of the ligand **L2**, are slightly higher than expected.

¹H NMR Spectra of Fe^{II} Complexes **1–4**

¹H NMR spectra were recorded for all four of the iron(II) complexes **1–4** in deuterated acetonitrile. In all four spectra the signals were sharp and spanned a range of ppm consistent with low-spin (diamagnetic) iron(II).

The peaks obtained for $[\text{Fe}(\text{L2})_2](\text{BF}_4)_2$ (**2**) were assigned on the basis of peak-area integration and splitting pattern. COSY (see Supporting Information) and NOESY (Figure 2) spectra were recorded in order to differentiate between, and thereby identify, the two different pyridine ring systems present in each ligand. An NOE cross peak from the imine group proton H7 to pyridine proton H3 identified one pyridine ring and the COSY spectrum then allowed identification of all of the protons, H3–H4–H5–H6, on that

pyridine ring (numbering scheme as in Figure 1; note: two terdentate ligands are present per complex so the second ligand is indicated by underlining the number).

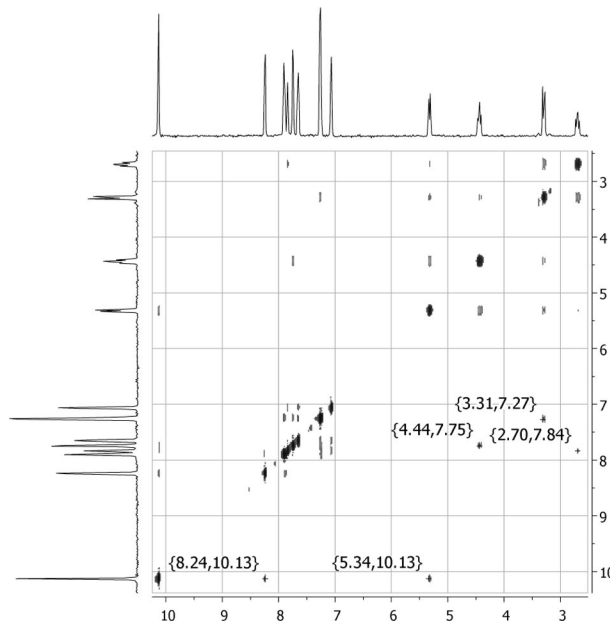


Figure 2. NOESY spectrum of $[\text{Fe}(\text{L2})_2](\text{BF}_4)_2$ (**2**) in CD_3CN . See text, Figures 1 and 3 and ¹H NMR assignments (Experimental Section).

Cross peaks from H7 to H9b and from H10b to H3' (which is a doublet overlapped with a doublet of triplets signal) were also observed. This, along with the COSY spectrum, facilitated the complete assignment of the second pyridine ring system, H3'–H4'–H5'–H6', and the pairing up of the four separate one-proton signals of the linker ethylene group into two sets, H9a & H9b and H10a & H10b, followed by their individual assignment. The assignment of the four ethylene protons was confirmed by the presence of a weak NOE interaction between H9a and H6 from a second ligand strand (the X-ray structure of **1** shows H9a in

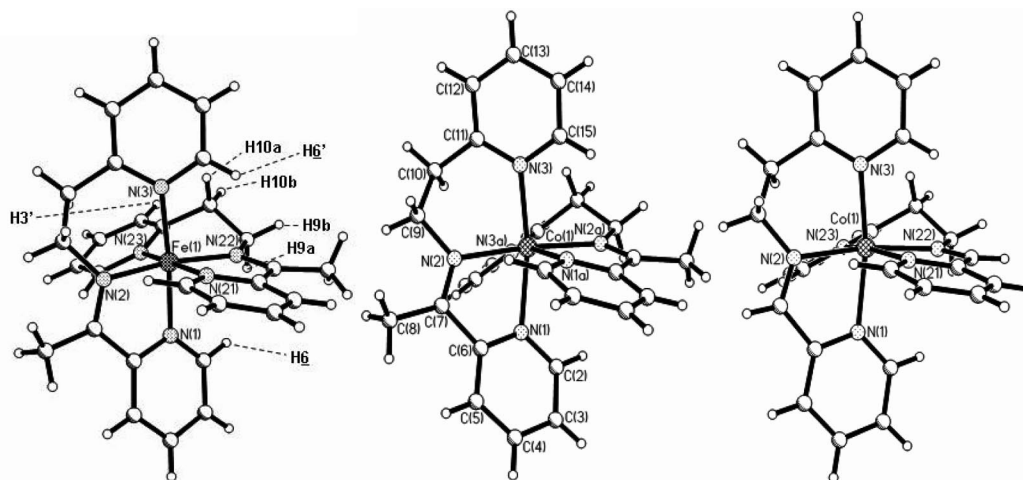


Figure 3. Perspective views of one of the three independent cations of $[\text{Fe}(\text{L1})_2](\text{BF}_4)_2$ (**1**), of the cation of $[\text{Co}(\text{L1})_2](\text{BF}_4)_2$ (**5**), and of one of the two independent cations of $[\text{Co}(\text{L2})_2](\text{BF}_4)_2$ (**6**).

close proximity to H6 of the pyridine A ring from the second ligand strand, see later, Figure 3) and the observation that, as might be expected, H10b shows a stronger cross coupling with H3' than H10a does with H6' (in **1** H10a is held in close proximity to H6' of the pyridine C ring from the second ligand strand; see later, Figure 3). In this way every individual signal was assigned.

The ^1H NMR spectra of the other three iron(II) complexes **1**, **3** and **4** were assigned by careful examination of the integration and splitting patterns, as well as by comparison to **2**.

^1H NMR Spectra of Co^{II} Complexes **5** & **6**

As expected, the ^1H NMR spectra of the two cobalt(II) complexes **5** and **6** are entirely consistent with them being paramagnetic. The ^1H NMR spectrum of a CD_3CN solution of $[\text{Co}(\text{L1})_2](\text{BF}_4)_2$ (**5**) exhibits eight broadened signals in the range 1.0 to 155.0 ppm and three signals in the range –4.0 to –34.8 ppm with no detectable coupling (Table 1). The signals in the ^1H NMR spectrum of $[\text{Co}(\text{L2})_2](\text{BF}_4)_2$ (**6**) are also broad and cover a very wide range of chemical shifts (almost 270 ppm, Table 1, Supporting Information). In comparison to the published data for $[\text{Co}(\text{tpy})_2](\text{PF}_6)_2$ in acetonitrile^[17] a similar pattern is observed for both pyridine rings, but with significantly different shifts. The most shifted and broadened peaks for **5**, at $\delta = 77.9$ ppm and 155.0 ppm, show no detectable cross peaks and are tentatively assigned to be the H6 protons since they are the closest (of the pyridine protons) to the paramagnetic centre. Two sets of three one-proton signals are observed in the COSY spectrum (Supporting Information), and are assigned to be H3–H4–H5 corresponding to the pyridine system A (which has comparable shifts to those observed for the tpy complex)^[17] and H3'–H4'–H5' of the pyridine ring

C, where H4 and H4' are at 1.0 ppm and 18.8 ppm, respectively. The individual proton signals within each of these two pyridine ring systems were assigned by comparing the shifts with those observed for $[\text{Co}(\text{tpy})_2](\text{PF}_6)_2$ in acetonitrile.^[17] The peak integration of the signal at $\delta = -4.0$ ppm indicates it may be the methyl group, H8. Similarly, the peak integration of the two peaks at $\delta = -29.4$ ppm and –34.8 ppm indicates that these are the ethylene linker signals. In contrast to the ^1H NMR spectrum of the diamagnetic complex $[\text{Fe}(\text{L1})_2](\text{BF}_4)_2$ (**1**), the broad signals observed in these two paramagnetic Co^{II} complexes show no splitting patterns.

UV/Vis Spectra of **1**–**6**

Absorption data for compounds **1**–**6** in acetonitrile are summarised in Table 2 (see Supporting Information for plots). The six spectra are characterised by two strong transitions in the UV and by somewhat weaker absorptions in the visible region of the spectrum. The two high-energy transitions are ligand centred (LC): in all six complexes the first appears at around 240 nm and the second occurs at around 275 nm. Both transitions are assigned to $\pi\text{--}\pi^*$ transitions in the pyridine rings. In the visible region, two allowed MLCT transitions are observed for $[\text{Fe}(\text{LX})_2]^{2+}$, at about 580 nm (ethylene bridged)/570 nm (methylene bridged) and 490 nm. These two transitions occur due to the lowering of the symmetry around the metal centre in $[\text{Fe}(\text{LX})_2]^{2+}$ relative to that in $[\text{Fe}(\text{tpy})_2]^{2+}$ complexes in which a single transition is observed at about 550 nm.^[18] In the case of the cobalt(II) complexes **5** and **6**, a weak band is observed at 467 and 478 nm, respectively. The extinction coefficients are higher than expected for a d–d transition but are similar to those reported, and assigned as d–d in origin, for $[\text{Co}(\text{tpy})_2](\text{ClO}_4)_2$.^[18] However, in the latter case

Table 1. ^1H NMR spectra assignments (COSY NMR) for the paramagnetic Co^{II} complexes in CD_3CN .

Compound		Pyridine systems						Other	CH_2	CH_2
$[\text{Co}(\text{tpy})_2](\text{PF}_6)_2$	ref. ^[17]		99.8	57.2	48.2	34.5	21.8	8.9		
		A	H6	H3/5		H3/5		H4		
		B			H3		H4			
$[\text{Co}(\text{L1})_2](\text{BF}_4)_2$	5	A	77.9	66.1		40.6		1.0	–4.0	–29.4
		C	155.0	85.0		49.8		18.8	H8	–34.8
$[\text{Co}(\text{L2})_2](\text{BF}_4)_2$	6	A	96.1	58.8		47.4		5.1	235.5	–25.3
		C	187.1	66.8		59.0		18.5	H7	–33.6

Table 2. UV/Vis data, λ_{max} [nm] (ϵ [$10^3 \text{ dm}^3 \text{ mol}^{-1} \text{ cm}^{-1}$]), of complexes in acetonitrile. Complexes **1**–**6** were studied at $c = 0.1 \text{ mmol L}^{-1}$.

		MLCT (Fe)/MLCT or dd-transitions (Co)		Intraligand	LC $\pi\text{--}\pi^*$ transitions	
$[\text{Fe}(\text{L1})_2](\text{BF}_4)_2$	1	580 (6.51)	490 (4.73)	392 (7.25)	278 (16.0)	253 (15.0)
$[\text{Fe}(\text{L2})_2](\text{BF}_4)_2$	2	576 (7.50)	492 (5.63)	377 (7.14)	279 (19.4)	247 (16.8)
$[\text{Fe}(\text{L3})_2](\text{BF}_4)_2$	3	569 (8.74)	488 (5.36)	375 (7.14)	276 (17.2)	243 (18.7)
$[\text{Fe}(\text{L4})_2](\text{BF}_4)_2$	4	568 (5.63)	483 (3.55)	362 (8.52)	278 (12.9)	245 (14.7)
$[\text{Fe}(\text{tpy})_2](\text{BF}_4)_2$	ref. ^[19]	551 (11.6)		318 (51.8)	280 (33.7)	272 (38.7)
$[\text{Co}(\text{L1})_2](\text{BF}_4)_2$	5		467 (0.12)	335 (2.08)	270 (15.6)	229 (18.0)
$[\text{Co}(\text{L2})_2](\text{BF}_4)_2$	6		478 (0.15)	336 (2.33)	279 (16.7)	232 (18.6)
$[\text{Co}(\text{tpy})_2](\text{PF}_6)_2$	ref. ^[20]	495 (0.6)	441 (0.7)	326 (25.8)	281 (27.8)	
				317 (29.6)	273 (26.9)	

the tail of a charge-transfer band overlaps the band, contributing to the higher than expected intensity; this is not the case in our complexes so the origin of these bands in **5** and **6** is less clearcut. Between the LC and MLCT/d-d transitions a band can be observed at 360–390 nm. This band is at a slightly longer wavelength and has significantly lower intensity than the band(s) observed in this area for [M(tpy)₂]²⁺ (Table 2, M = Fe or Co). It is tentatively assigned as an intraligand transition, associated with the Schiff base moiety. In the iron complexes, this band moves to shorter wavelengths on replacing Me by H, i.e., on going from **1** to **2**, and from **3** to **4**, by 15 and 13 nm, respectively.

Crystal Structures

Single crystals of **1**, **5** and **6** were grown by slow diffusion of diethyl ether vapour into acetonitrile solutions. All these racemic complexes crystallise in centric space groups so that each crystal structure contains both enantiomers. The molecular structures of the cations [Fe(**L1**)₂]²⁺, [Co(**L1**)₂]²⁺ and [Co(**L2**)₂]²⁺ are depicted in Figure 3. Selected bond

lengths and angles for these three complexes, and for the related complexes [Fe(tpy)₂](ClO₄)₂·H₂O and [Co(tpy)₂](ClO₄)₂·1.3H₂O, are provided in Table 3 and Table 4.

[Fe(**L1**)₂](BF₄)₂ (**1**)

There are three entire [Fe(**L1**)₂]²⁺ complexes in the asymmetric unit. These are very similar to one-another (Table 3) so for simplicity in the following discussion the complex centred on Fe(1) is taken as representative. The iron(II) atom has a distorted octahedral geometry. This is due to the steric requirements of the Fe²⁺ centre and is facilitated by the intrinsic flexibility that the ethylene linker part of the ligand provides. Both **L1** and tpy bind to iron(II) in a meridional fashion, but unlike the tpy complex, [Fe(tpy)₂](ClO₄)₂·H₂O,^[5] in which there are only two distinct sets of Fe–N bonds, with the central Fe–N bonds, on average, 0.097 Å shorter than the distal Fe–N bonds, there are three distinct sets of Fe–N bond lengths in [Fe(**L1**)₂](BF₄)₂, as the distal nitrogen atoms in **L1** are not equivalent to one-another. Specifically, the average Fe(1)–N(1) bond length (1.977 Å) in **1** is close to the average Fe–N(distal) distance

Table 3. Selected bond lengths [Å] and angles [°] for [Fe(**L1**)₂](BF₄)₂ (**1**), [Co(**L1**)₂](BF₄)₂ (**5**) and [Co(**L2**)₂](BF₄)₂ (**6**).

			M–N(1)	M–N(2)	M–N(3)	N(1)–M–N(2)	N(2)–M–N(3)	N(1)–M–N(3)
[Fe(L1) ₂](BF ₄) ₂ (1)	Fe(1)	N(1)	1.971(6)	1.921(6)	2.031(5)	80.9(2)	92.2(2)	172.1(2)
		N(21)	1.964(6)	1.941(6)	2.017(6)	80.8(2)	93.2(2)	173.1(2)
	Fe(2)	N(41)	1.980(6)	1.964(6)	2.034(6)	81.7(3)	92.3(3)	173.9(2)
		N(61)	1.973(6)	1.938(6)	2.032(6)	82.3(3)	92.1(3)	174.1(3)
	Fe(3)	N(81)	1.987(6)	1.932(6)	2.017(6)	80.8(3)	92.0(3)	172.5(3)
		N(101)	1.989(6)	1.944(6)	2.029(6)	80.6(2)	92.5(3)	172.7(3)
[Fe(tpy) ₂](ClO ₄) ₂ ·H ₂ O ^[5]			1.977(6)	1.890(5)	2.002(6)	80.5(3)	80.6(3)	161.0(3)
			1.984(6)	1.892(5)	1.988(6)	80.8(2)	80.4(2)	161.1(2)
[Co(L1) ₂](BF ₄) ₂ (5)			2.1736(16)	2.1151(15)	2.1220(15)	75.83(6)	89.25(6)	160.63(6)
[Co(L2) ₂](BF ₄) ₂ (6)	Co(1)		2.172(3)	2.105(3)	2.156(3)	76.11(10)	89.11(10)	162.30(11)
	Co(2)		2.162(3)	2.095(3)	2.178(3)	76.95(11)	89.85(11)	164.45(10)

Table 4. Selected structurally characterised [Co(4'-X-tpy)₂]^{x+} complexes and aspects of their coordination sphere geometries,^[a,b] as well as the oxidation state and the magnetic moment at the specified temperature (chosen to be close to room temperature).

	μ _{eff} (μ _B)/T(K)	X	Counter ion	Hydration ^[c]	Co–N (central)	Co–N _d (distal)	<N _d –Co–N _d	Ref.
Co ^{III}	1.0(2)	H	Cl [–]	11	1.863(7) 1.853(7)	1.930(7), 1.926(7) 1.937(7), 1.921(7)	164.2(3) 164.4(3)	[22,23]
Co ^{III} [d]	3.50/300	OH	BF ₄ [–]	1	1.909(6) 1.892(6)	2.027(7), 2.036(7) 2.007(7), 2.021(7)	161.0(3) 160.8(3)	[31]
Co ^{II}	3.58/300	OC ₈ H ₁₇	BF ₄ [–]	1	1.861(7) ^[b] 1.871(6) ^[b]	1.953(6), 1.940(6) ^[b] 1.940(7), 1.945(6) ^[b]	164.5(3) ^[b] 164.7(3) ^[b]	[30]
Co ^{II}	2.94/300	H	Br [–]	3	1.89(1) 1.88(1)	2.11(1), 2.11(1) 2.09(1), 2.08(1)	157.8(4) 158.8(4)	[18,24]
Co ^{II}	2.96/300 ^[e]	H	NO ₃ [–]	2	2.101(4) 2.075(5)	2.189(3) 2.180(3)	151.03(12) 150.03(10)	[18,25]
Co ^{II}	3.2(1)/295	H	I [–]	2	1.942(7)	2.104(5)	157.0(2)	[26]
Co ^{II}	3.67/288 ^[f]	H	SCN [–]	2	2.00(2) 1.96(2)	2.12(2), 2.12(2) 2.11(2), 2.12(2)	157.2(8) 159.3(8)	[27,28]
Co ^{II}	4.23(4)/295	H	ClO ₄ [–]	1.3	2.030(6) 2.026(6)	2.140(5) 2.133(5)	153.4(2) 153.7(2)	[22]
Co ^{II} [g]	4.97/295	H	–	0	2.09(2)	2.17(2), 2.13(2)	147(1)	[28,29]

[a] All but one set (see footnote b) of structural data was obtained near room temperature, so the structural parameters are indicative of high-spin/low-spin mixtures or high-spin compounds. [b] Only in one case was the single-crystal X-ray diffraction analysis performed at low temperatures, 123 K, and this led to the structural characterisation of the low-spin complex. [c] Number of water molecules of hydration. [d] One of two polymorphs the formation of which depends on the solvents used for synthesis. [e] Value quoted is for the anhydrous salt as it is not available for the structurally characterised dihydrate. [f] Value quoted is for the sesquihydrate salt. [g] [Co(tpy)Cl₂].

observed in the low-spin Fe^{II} compound $[\text{Fe}(\text{tpy})_2](\text{ClO}_4)_2 \cdot \text{H}_2\text{O}$ (1.988 Å),^[5] the average $\text{Fe}(1)\text{--N}(2)$ bond length (1.940 Å) is 0.049 Å longer than the average $\text{Fe}\text{--N}(\text{central})$ distance (1.891 Å)^[5] and the average $\text{Fe}(1)\text{--N}(3)$ bond length (2.027 Å) is 0.039 Å longer than the average $\text{Fe}\text{--N}(\text{distal})$ distance. This is because, on coordination to a metal ion, the terdentate ligand **L1** provides two quite different sets of *cis* chelate bite angles as it is composed of a rigid tpy-like part between N1 and N2 ($\text{N1}\text{--Fe1}\text{--N2}$ of 80.9° for **L1** vs. ca. 80.5° for tpy), and a more flexible part between N2 and N3 due to the ethylene linker ($\text{N2}\text{--Fe1}\text{--N3}$ of 92.1° for **L1**). The substantially larger bite angle provided by the more flexible portion of the **L1** ligand presumably allows the central $\text{Fe}\text{--N}$ bond length to be closer to normal whereas the tpy ligand with the two small, adjacent bite angles requires this bond to be shorter in order to open up the $\text{N}(\text{distal})\text{--Fe}\text{--N}(\text{central})$ bond angle to an acceptable extent. These $\text{Fe}\text{--N}$ distances are typical for low-spin Fe^{II} compounds.^[21]

Within the $\text{Fe}(1)$ molecule of $[\text{Fe}(\text{L1})_2](\text{BF}_4)_2$ (**1**), the mean planes of pyridine ring A (Figure 1, N1–C2–C3–C4–C5–C6; Figure 3, N1 ring) and pyridine ring A (Figure 3, N21 ring), of the two independent **L1** ligand strands, are not at right angles to one-another but instead are slightly tilted towards each other, making an angle of 68.8° [for $\text{Fe}(2)$ and $\text{Fe}(3)$ these angles are substantially larger, being 79.1° and 79.3°, respectively]. Within a given ligand strand the mean plane through pyridine ring A is tilted at a 43.7° angle with respect to the mean plane through pyridine ring C (Figure 1, N3–C2'–C3'–C4'–C5'–C6'; Figure 3, N3 ring). This gives the ligand strand a helical twist. The $\text{H}\cdots\text{H}$ distances associated with the key intra- and inter-strand interactions that were observed in the NOESY spectrum in CD_3CN solution of **1** (which is similar to that of **2** which is shown in Figure 2) were measured [for $\text{Fe}(1)$] and found to be 2.33 Å for the intra-strand interaction between H10b to H3', and 2.56 Å and 2.62 Å respectively, for the inter-strand interactions between H9a and H6 and between H10a and H6' (see Figures 1 and 3), in the crystal structure (solid state). Consistent with the absence of NOE interactions between H9b and either H6 or H6' are the long distances observed (> 3.0 Å). No significant intermolecular short contacts were observed.

$[\text{Co}(\text{L1})_2](\text{BF}_4)_2$ (**5**) and $[\text{Co}(\text{L2})_2](\text{BF}_4)_2$ (**6**)

Many X-ray crystal structures of $[\text{Co}(\text{tpy})_2]^{x+}$, with a wide variety of anions, degrees of hydration, oxidation state and spin state as well as with attachment of long $\text{C}_n\text{H}_{2n+1}$ tails to tpy, have been reported (Table 4).^[18,22–32] The $\text{Co}\text{--N}$ distances and tpy bite angles are largely dependent on the spin state. It predominantly affects the $\text{Co}\text{--N}(\text{central})$ distance, which contracts by about 0.20 Å on passing from the high-spin ($\mu_{\text{eff}} \approx 5.0 \mu_{\text{B}}$) to the low-spin ($\mu_{\text{eff}} \approx 2.5 \mu_{\text{B}}$) state, in the Co^{II} species included in Table 4. The restricted bite angle of the tpy ligand causes considerable distortion from octahedral symmetry in the cobalt(II) coordination sphere. The $\text{N1}\text{--Co}^{\text{II}}\text{--N3}$ angle is reduced from the ideal

180° to less than 160°, something which could be expected to be relieved to some extent in the complexes of the ethylene-linked ligands **L1** and **L2**.

In $[\text{Co}(\text{L1})_2](\text{BF}_4)_2$ (**5**) the cobalt atom is located on a twofold axis. The two, symmetry-related, terdentate ligands are arranged around the metal ion in a distorted octahedral geometry. The rigid tpy-like part in ligand **L1** has a similar coordination geometry ($\text{N1}\text{--Co}\text{--N2}$ of 75.8°, Table 3) to that normally seen for tpy ($\text{N}\text{--Co}\text{--N}$ of 76.7 and 76.8° for the perchlorate salt).^[22] As was seen in the iron compound **1**, **L1** also contains a more flexible part due to the ethylene linker and this is reflected in a substantially larger $\text{N2}\text{--Co}\text{--N3}$ chelate bite angle of 89.3°. It is noteworthy that in the tpy complex $[\text{Co}(\text{tpy})_2](\text{ClO}_4)_2$ the average $\text{Co}\text{--N}(\text{central})$ bond (2.028 Å, Table 4) is 0.109 Å shorter than the average $\text{Co}\text{--N}(\text{distal})$ bond (2.137 Å),^[22] whereas in the **L1** complex **5** the $\text{Co}\text{--N}(\text{central})$ distance is only 0.033 Å shorter than the average $\text{Co}\text{--N}(\text{distal})$ distance of 2.148 Å. It is important to note that, as in **1**, there are two different $\text{Co}\text{--N}(\text{distal})$ bond lengths in **5** and whilst both are longer than the $\text{Co}\text{--N}(\text{central})$ distance the differences are not nearly as marked as they are in $[\text{Co}(\text{tpy})_2](\text{ClO}_4)_2$. Specifically, in **5** the $\text{Co}\text{--N}(1)$ distance is 0.059 Å longer, whilst the $\text{Co}\text{--N}(3)$ distance is only 0.007 Å longer than the $\text{Co}\text{--N}(2)$ bond length. These observations are similar to those made on **1** and likely occur for the same reasons. The $\text{Co}\text{--N}$ distances are typical for high-spin Co^{II} compounds (compare Tables 3 and 4).

Within the ligand strand, the mean plane through pyridine ring A (Figure 1, N1–C2–C3–C4–C5–C6; Figure 3, N1 ring) is tilted at a 52.8° angle with respect to the mean plane through pyridine ring C (Figure 1, N3–C2'–C3'–C4'–C5'–C6'; Figure 3, N3 ring), once again giving the strand a helical twist. Within the molecule the mean planes of pyridine A (Figure 3, N1 ring) and pyridine A (Figure 3, N1a ring) are tilted substantially towards each other, making an angle of 46.3° (their centroids are separated by 3.88 Å). This contrasts with the situation observed for $[\text{Fe}(\text{L1})_2](\text{BF}_4)_2$ (**1**) where the rings are more nearly orthogonal, making angles of 68.8–79.3°, the variation showing the effects of crystal packing.

The iron(II) and cobalt(II) complexes of **L1** show similar characteristics to their respective tpy analogues. Specifically, for both metal ions, the $\text{N}(1)\text{--M}\text{--N}(2)$ chelate bite angles observed for **L1** (Fe: 80.6–82.3°; Co: 75.8°) are comparable to the $\text{N}(\text{distal})\text{--M}\text{--N}(\text{central})$ chelate bite angles observed for tpy (Fe: 80.5°; Co: 75.5°), whereas in every case the $\text{N}(2)\text{--M}\text{--N}(3)$ chelate bite angles of **L1** are significantly greater, by about 12° (Fe: 92.0–93.2°) to 14° (Co: 89.25°), and are much closer to 90°. Due to the shorter $\text{M}\text{--N}$ bond lengths in the low-spin Fe^{II} complex, the $\text{N}(2)\text{--M}\text{--N}(3)$ angles all slightly exceed 90°, whereas in the high-spin Co^{II} complexes, which have longer $\text{M}\text{--N}$ bond lengths, these angles closely approach but do not exceed 90°.

As ligand **L2** differs from **L1** by just the missing methyl group on the exocyclic imine nitrogen, one would expect similar structural features for their respective cobalt(II) complexes, and this is observed (Figure 3, Table 3). How-

ever, there are two minor points of difference between these two sets of crystals: unlike the cobalt(II) complex of **L1** (**5**), [Co(**L2**)₂](BF₄)₂ (**6**) crystallised as twinned crystals and there are two entire [Co(**L2**)₂]²⁺ complexes in the asymmetric unit. These are very similar to one-another (Table 3), so for simplicity in the following discussion the complex centred on Co(1) is taken as representative, except where noted.

The N1–Co–N2 and N2–Co–N3 bite angles in [Co(**L2**)₂](BF₄)₂ (76.1° & 77.0° vs. 89.1° & 89.9°) are very similar to those of the rigid and the more flexible parts, respectively, in [Co(**L1**)₂](BF₄)₂ (75.8° vs. 89.3°). The same holds for the Co–N distances (Table 3). However, for **5** the Co ion is substantially displaced from the plane of the imino-pyridyl moiety [Co1 is 0.612(3) Å out of the mean plane through ring A] compared to **6** [Co1 and Co2 are 0.122(5)–0.320(5) Å out of the mean planes through rings A and A', respectively] and to **1** [Fe1, Fe2 and Fe3 are 0.047(9)–0.322(9) Å out of the mean planes through rings A, A' and A'', respectively]. The metal ions are displaced far less from the mean planes through rings C than they are from the mean planes through rings A [distances out of mean planes C: for **5** 0.131(3) Å; for **6** 0.005(5)–0.234(5) Å; and for **1** 0.027(9)–0.123(9) Å]. As observed for **5** the two meridionally coordinated terdentate ligands in **6** are arranged around the metal ion in a distorted octahedral geometry. The non-planarity of the ligand forces the mean plane of pyridine A (N1 ring) to tilt with respect to the pyridine C mean plane (N3 ring) by an angle of 38.5° [N(1) to N(3) ligand strand] and 36.6° [N(21) to N(23) ligand strand], respectively. This twist angle is significantly less than it was in **L1** (52.8°) and highlights the steric influence of the methyl group.

Within the molecule of [Co(**L2**)₂](BF₄)₂ the mean planes of pyridine A and pyridine A are also tilted towards each other, with angles of 65.5° and 66.6° for Co(1) and Co(2) respectively; these tiltings are much less than the 46.3° observed for [Co(**L1**)₂](BF₄)₂ but are similar to the 68.8–79.3° observed for [Fe(**L1**)₂](BF₄)₂ (**1**). No intermolecular short contacts were observed.

Electrochemistry

All six complexes were electrochemically active in solution. Cyclic voltammetric data for complexes **1**–**6** were recorded in acetonitrile and results are provided in Table 5 (see Supporting Information for plots). Generally, a fully reversible predominantly metal-centred M^{2+/3+} redox wave is observed, along with some presumably ligand-based, mainly irreversible, reduction processes. In the Fe^{II} series **1**–**4**, there is a significant difference between the pair of compounds derived from the ketone (**1** and **3** with *E*_{1/2} = 0.59 and 0.58 V) and the pair derived from the aldehyde (**2** and **4** with *E*_{1/2} = 0.68 and 0.70 V). Specifically, for **1** and **3** the metal-centred Fe^{2+/3+} redox potentials are shifted to more negative potentials by at least 0.09 V, consistent with stabilisation of the higher oxidation state due to the stronger elec-

tron donation into the imine system expected for the methyl group over that for the hydrogen atom. This trend is also observed between Co^{II} complexes **5** and **6** with the *E*_{1/2} diminishing from 0.09 to –0.03 V. The length of the alkyl spacer causes just marginal changes to the redox potentials of the Fe complexes (0.01–0.02 V) and a clear trend is not evident.

Table 5. Cyclic voltammetric data in acetonitrile with 0.1 M [Bu₄N]PF₆ electrolyte, vs. Fc⁺/Fc^[a].

Compound		<i>E</i> _{1/2} /V (Δ <i>E</i> _p /V) or <i>E</i> _{pa} ^[b] /V			
[Fe(L1) ₂](BF ₄) ₂	1	–1.62 (0.08)	–1.46 ⁱ		0.59 (0.08)
[Fe(L2) ₂](BF ₄) ₂	2	–1.52 (0.08)			0.68 (0.09)
[Fe(L3) ₂](BF ₄) ₂	3	–1.62 ^{qr}		–1.24 ⁱ	0.58 (0.08)
[Fe(L4) ₂](BF ₄) ₂	4	–1.83 ^{qr}	–1.55 ⁱ	–1.20 ⁱ	0.70 (0.09)
[Fe(tpy) ₂](BF ₄) ₂	ref. ^[19]	–1.82	–1.64		
[Co(L1) ₂](BF ₄) ₂	5	–1.73 ⁱ	–1.50 ⁱ	–1.26 ⁱ	–0.03 (0.13) ^{qr}
[Co(L2) ₂](BF ₄) ₂	6	–1.77 (0.10) ^{qr}	–1.52 (0.07)	–1.20 ⁱ	0.09 (0.09)
[Co(tpy) ₂](ClO ₄) ₂	ref. ^{[33][c]}	–1.97	–1.62	–0.74	0.31
[Co(tpy) ₂](ClO ₄) ₂	ref. ^{[34][d]}			–1.04	–0.02

[a] i: irreversible, hence value quoted is *E*_{pa}; qr: quasi-reversible; all other processes are reversible. Δ*E* are quoted for reversible processes and for those qr processes in which *E*_{pa} and *E*_{pc} are well defined. The scan rates were 100 mV/s for the Fe and 200 mV/s for the Co compounds. However, in the case of the M^{2+/3+} oxidation potential of **4**, data from a scan at 200 mV/s were used. [b] For the irreversible process. [c] Referenced to Ag/AgCl satd. NaCl, acetonitrile, 0.1 M [Et₄N]BF₄. [d] Referenced to Ag/0.01 M AgNO₃, acetonitrile, 0.1 M [Bu₄N]BF₄.

Magnetochemistry

The Fe^{II} complexes are low-spin d⁶ compounds as evidenced by their “normal” (diamagnetic) NMR resonance positions. The magnetic moment data for the Co^{II} complexes [Co(**L1**)₂](BF₄)₂ (**5**) and [Co(**L2**)₂](BF₄)₂ (**6**) are shown in Figure 4. Between 300 and 50 K, the μ_{eff} value in **5** remains constant at 4.5 μ_B. This is indicative of high-spin behaviour but is smaller in value than for many high-spin octahedral Co^{II} complexes that have μ_{eff} ≈ 5 μ_B because of orbital degeneracy (⁴T_{1g} state), but similar (or slightly higher) than values for the distorted octahedral [Co-(tpy)₂]²⁺ complexes (Table 4). The moments decrease below 50 K to reach 3.65 μ_B at 2 K. The data are compatible with a distorted octahedral CoN₆ geometry which removes the orbital degeneracy by splitting the ⁴T_{1g} state concomitant with spin-orbit splitting. Perusal of plots of the Figgis-Kotani type shows that the axial splitting parameter Δ = νλ, where ν is a constant and λ is the spin-orbit coupling constant, is very large.^[35] The rapid decrease in μ_{eff}, below 50 K, will partly arise from zero field splitting (zfs) of the ⁴A₂ state derived from ⁴T_{1g}.

The μ_{eff} vs. temperature data for **6** were broadly similar, although the μ_{eff} value of 4.75 μ_B (300–100 K) starts to decrease more gradually than in **5**, below 100 K, reaching

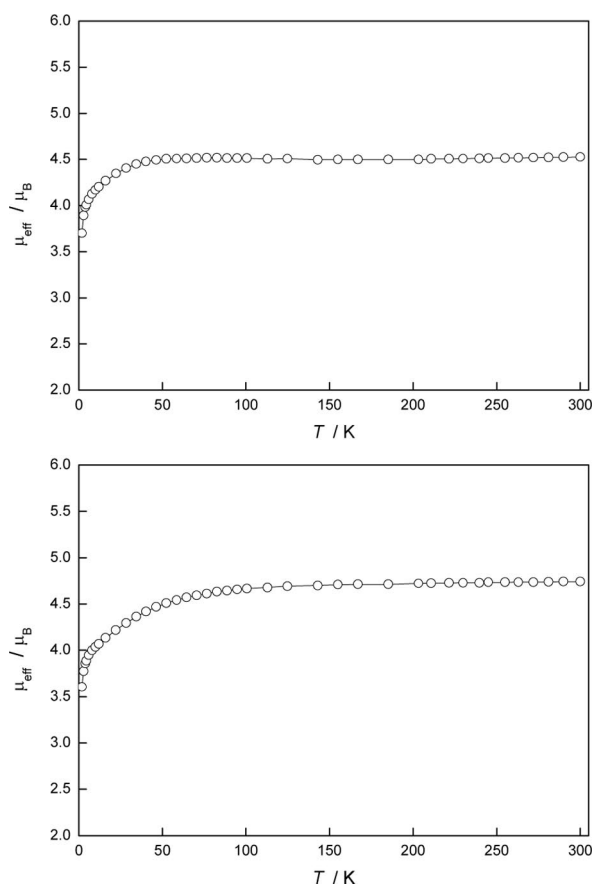


Figure 4. Magnetic moment data for $[\text{Co}(\text{L1})_2](\text{BF}_4)_2$ (**5**) (top) and $[\text{Co}(\text{L2})_2](\text{BF}_4)_2$ (**6**) (bottom) between 300 and 2 K. The solid lines are just guides to the eye. See text and Supporting Information for fitting attempts.

$3.6 \mu_{\text{B}}$ at 2 K. The $^4\text{T}_{1\text{g}}$ ground state of this high-spin example is split by the low-symmetry ligand-field, but less so than in **5**. To check the possibility of zfs, the magnetic moment plots in Figure 4 were fitted to a $DS_z^2 + g\beta H_z$ axial spin Hamiltonian, where $S = 3/2$. In the case of **6**, the moments start decreasing below ca. 100 K and this can not be reproduced by zfs alone. However, in the case of **5**, the data above ca. 50 K and below ca. 5 K are fitted reasonably well to the parameters $g = 2.34$ and $D = \pm 2.5 \text{ cm}^{-1}$ (see Supporting Information). The μ_{eff} data between 50 and 5 K were lower than the calculated data and this is probably due to remaining orbital degeneracy or to a rhombic component, E . Use of the axial model to a square-pyramidal high-spin complex, $[\text{Co}(\text{salophen})(2\text{-Me-imidazole})]$,^[36] {salophen = N,N' -phenylene-bis(salicylaldiminato) dianion} a geometry different to that of **5**, yielded parameters $g = 2.14$ and $D = \pm 22.6 \text{ cm}^{-1}$.

Use of the Van Vleck equation and the Figgis–Kotani $^4\text{T}_{1\text{g}}$ model^[35] gave a reasonable fit to the 170–300 K data for **6**, although a little higher than observed, when the ligand-field parameter, A , was ca. 1.5 and the spin-orbit coupling constant was -170 cm^{-1} . While these parameters also reproduced the ca. 2 K value for **6**, the 170 to 2 K region had the calculated data significantly lower than the ob-

served (see Supporting Information). It is likely that a Hamiltonian^[35] that incorporates λ , κ (orbital reduction factor), a tetragonal ligand-field term, $V_{\text{tetragonal}}$, and the orbital angular momentum operator, \mathbf{L}_z , used with the thermodynamic form of susceptibility and matrix diagonalization methods would improve the overall quality of the fit, but we do not have access to this model. It is clear from these fitting attempts that the low symmetry CoN_6 ligand field present in **5** and **6** splits the $^4\text{T}_{1\text{g}}$ state to a large degree. What is also clear is that the decrease in μ_{eff} at low temperatures is not due to population of a $S = 1/2$ state arising from spin crossover. A recent review article on the theory of orbital degeneracy and anisotropy in Co^{II} octahedral compounds, particularly dinuclear, exchange-coupled species, highlights the challenges faced in fully understanding the magnetism of cobalt(II) in molecular materials.^[37]

Finally, we note that the anionic ligand derivative of **L4**, smif^- , yields low-spin magnetic, Mössbauer spectral and structural features for $[\text{Fe}^{\text{II}}(\text{smif})_2]$ and apparently spin-crossover features for $[\text{Co}^{\text{II}}(\text{smif})_2]$, although these authors also note that is a possibility that the ligand is redox-active, a comment pertinent to our experiences with the ligands **L3** and **L4** in the presence of Co^{II} .^[13]

Conclusions

The preparation and properties of the iron(II) and cobalt(II) complexes of the terdentate pyridine-based imine ligands **L1–L4** have been thoroughly investigated. However, the coordination of the methylene-linked imine ligands **L3** and **L4** to Co^{II} was not successful in our hands. NMR spectra, X-ray structures and magnetic moments proved the low-spin character of all four of the Fe^{II} complexes and the high-spin state of the two Co^{II} complexes. No spin-crossovers were detected in either the Fe^{II} or the Co^{II} compounds. The crystal structures highlighted close intramolecular interactions between the pyridine rings in the cobalt(II) complex of **L1** (**5**), where the mean planes of pyridine A and pyridine A are tilted significantly more towards each other than is observed in either the iron(II) complex of **L1** or the cobalt(II) complex of **L2**. Moreover, the ethylene spacer group introduces a helical twist in the terdentate ligand strand, that is more distinct in the complex derived from the ketimine ligand **L1** than in the one obtained from the aldimine ligand **L2**. The better stabilisation of the higher oxidation state by the ketimines rather than the aldimines, revealed by the electrochemical data of the iron complexes, should be kept in mind as larger Schiff-base ligands designed to facilitate the formation of mixed-valent multimetallic compounds are developed.

Experimental Section

General Remarks: All reagents were used as received except CH_3CN which was dried with CaH_2 and ethanol which was dried with molecular sieves (4 Å).

Elemental analyses (C, H, N, Cl) were performed by the Campbell Microanalytical Laboratory, University of Otago. Infrared spectra

were recorded on a Perkin–Elmer FT-IR 1600 spectrometer and NMR spectra on Varian Inova 300 MHz and 500 MHz spectrometers. All electrochemical measurements were made using a EG&G Princeton Applied Research 273A potentiostat. Cyclic voltammograms were obtained in acetonitrile/0.1 M [Bu₄N]PF₆ solution containing 1 mmol/L complex. Solutions were degassed using a N₂ purge; a N₂ atmosphere was maintained throughout all experiments. The working electrode was a 1 mm diameter Pt disk electrode and the reference electrode was Ag/Ag⁺ (0.01 mol/L AgNO₃ in 0.1 mol/L [Bu₄N]PF₆–CH₃CN). Ferrocene was added at the conclusion of each experiment and the Fc⁺/Fc couple consistently occurred at 0.06 V ± 0.01 V with ΔE = 0.08 V.

The magnetic susceptibilities were measured using a Quantum Design Squid magnetometer, PPMS 5, at a dc field of 1 T, with the samples (ca. 20 mg) contained in gel capsules held at the centre of a drinking straw that was fixed to the end of the sample rod. Checks were made on the Co^{II} compounds for any crystallite orientation effects, by dispersing the powders in Vaseline mulls, and none were present. Ligand diamagnetic corrections were obtained using Pascal's constants. Note that converting μ_{eff} values to χ_MT, at any temperature, requires the equation (μ_{eff})² = 7.999(χ_MT).

The X-ray data were collected on a Bruker Kappa Apex II (1 at 83 K) or a Bruker SMART (5 at 93 K and 6 at 88 K) area-detector diffractometer using graphite-monochromated Mo-K_α radiation (λ = 0.71073 Å). All non-hydrogen atoms were refined anisotropically. All hydrogen atoms, except where noted below, were placed at calculated positions using a riding model with thermal parameters 1.2 times (1.5 times for methyl hydrogen atoms) the equivalent isotropic thermal parameter of the atom to which they were bonded. Selected details of the refinement of each of the structures (disorder in 5; twinning in 6) can be found below.

CCDC-294964 (for 5), -294965 (for 6), -294966 (for 1) contain the supplementary crystallographic data for this paper. These data can be obtained free of charge from The Cambridge Crystallographic Data Centre via www.ccdc.cam.ac.uk/data_request/cif.

[Fe(L1)₂](BF₄)₂ (1). Method A (IPA): 2-Acetylpyridine (0.121 g, 1.0 mmol) and 2-(2-aminoethyl)pyridine (0.122 g, 1.0 mmol) were dissolved in 20 mL of 2-propanol with 2 drops of glacial acetic acid. The solution was refluxed for 2 h to give a pale yellow solution. After cooling to room temperature Fe(BF₄)₂·6H₂O (0.168 g, 0.5 mmol) was added and a purple precipitate formed straight away. It was stirred at room temperature for another hour, before the precipitate was filtered off onto filter paper and dried under vacuum overnight. Purple solid, 0.233 g, 0.34 mmol, 69% yield.

Method B (dry EtOH): Same experiment, purple solid, 0.204 g, 0.3 mmol, 60% yield. C₂₈H₃₀B₂F₈FeN₆ (680.04) + 1.5H₂O: calcd. C 47.56, H 4.70, N 11.89; found C 47.54, H 4.54, N 11.75. ¹H NMR (CD₃CN, 300 MHz): δ = 8.17 (d, J = 8.3 Hz, 1 H, 3-H), 7.88 (t, J = 7.3 Hz, 1 H, 4-H), 7.69 (t, J = 7.3 Hz, 1 H, 4-H'), 7.65 (d, J = 5.9 Hz, 1 H, 6-H'), 7.61 (d, J = 4.9 Hz, 1 H, 6-H), 7.29 (d, J = 7.3 Hz, 1 H, 3-H'), 7.26 (t, J = 6.8 Hz, 1 H, 5-H), 7.04 (t, J = 5.9 Hz, 1 H, 5-H'), 5.06 (d, J = 16.1 Hz, 1 H, 9-Hb), 4.11 (t, J = 14.6 Hz, 1 H, 9-Ha), 3.26 (d, J = 16.6 Hz, 1 H, 10-Hb), 3.21 (s, 3 H, Me), 2.52 (t, J = 14.6 Hz, 1 H, 10-Ha) ppm. ES MS: m/z (calcd.): 253.1 (253.2 [M – 2BF₄]²⁺), 593.2 (593.2 [M – BF₄]⁺). IR (KBr): 3417, 3057, 2343, 1654, 1636, 1605, 1584, 1477, 1442, 1371, 1329, 1296, 1260, 1070, 1036, 862, 779, 659, 609, 533, 521, 460. UV λ_{max} (CH₃CN) [nm] (ε [dm³ mol^{–1} cm^{–1}]): 580 (6.51 × 10³), 490 (4.73 × 10³), 392 (7.25 × 10³), 278 (16.0 × 10³), 253 (15.0 × 10³). Λ_m (CH₃CN) = 290 mol^{–1} cm² Ω^{–1} (cf. 220–300 mol^{–1} cm² Ω^{–1} for a 2:1 electrolyte in CH₃CN).

Crystal Data for 1: C₂₈H₃₀B₂F₈FeN₆, purple rod, 0.36 × 0.08 × 0.04 mm³, triclinic, space group P1, a = 14.2709(10), b = 19.5539(14), c = 19.8201(14) Å, α = 64.954(4)°, β = 76.994(4)°, γ = 69.694(4)°, V = 4679.4(6) Å³, Z = 6, μ = 0.565 mm^{–1}. Of 81667 reflections collected, 19226 were independent and used in the structure analysis. The structure was solved by direct methods (SHELXS-97)^[38] and refined against F² data (SHELXL-97)^[38] to R1 = 0.0951 for the 10282 data with F > 4σ(F), and wR2 = 0.2798 and GOF = 1.045 for all 19226 F² data. There were three [Fe^{II}(L1)₂](BF₄)₂ complexes in the asymmetric unit, along with two full occupancy MeCN and a quarter occupancy H₂O. The hydrogen atoms of the partial-occupancy water molecule were placed in calculated/suggested (HTAB in SHELXL-97) positions and fixed in these positions.

[Fe(L2)₂](BF₄)₂ (2). Method A (IPA): 2-Formylpyridine (0.107 g, 1.0 mmol) and 2-(2-aminoethyl)pyridine (0.122 g, 1.0 mmol) were dissolved in 20 mL of 2-propanol with 2 drops of glacial acetic acid. The solution was refluxed for 2 h to result in a pale yellow solution. After cooling to room temperature Fe(BF₄)₂·6H₂O (0.168 g, 0.5 mmol) was added and a purple precipitate formed straight away. It was stirred at room temperature for another hour, before the precipitate was filtered off onto filter paper and dried under vacuum overnight. Purple solid, 0.246 g, 0.37 mmol, 75% yield. C₂₆H₂₆B₂F₈FeN₆ (651.99) + 0.5H₂O: calcd. C 47.24, H 4.12, N 12.71; found C 47.10, H 4.08, N 12.50. ¹H NMR (CD₃CN, 500 MHz, COSY, NOESY): δ = 10.13 (d, J = 2.0 Hz, 1 H, 7-H), 8.24 (d, J = 7.8 Hz, 1 H, 3-H), 7.90 (dt, J = 1.0, 7.5 Hz, 1 H, 4-H), 7.84 (d, J = 5.5 Hz, 1 H, 6-H'), 7.75 (d, J = 5.5 Hz, 1 H, 6-H), 7.65 (dt, J = 1.2, 7.6 Hz, 1 H, 4-H'), 7.27 (d, J = 7.9 Hz, 1 H, 3-H'), 7.25 (dt, J = 1.2, 7.2 Hz, 1 H, 5-H), 7.07 (t, J = 6.6 Hz, 1 H, 5-H'), 5.33 (dt, J = 2.9, 15.1 Hz, 1 H, 9-Hb), 4.44 (t, J = 14.2 Hz, 1 H, 9-Ha), 3.30 (d, J = 16.1 Hz, 1 H, 10-Hb), 2.70 (dt, J = 2.4, 14.7 Hz, 1 H, 10-Ha) ppm. ES MS: m/z (calcd.): 239.1 (239.1) [M – 2BF₄]²⁺. IR (KBr): 3416, 3030, 2374, 2343, 1655, 1636, 1607, 1587, 1549, 1469, 1442, 1379, 1297, 1262, 1230, 1060, 1036, 918, 773, 649, 602, 522, 462. UV λ_{max} [nm] (ε [dm³ mol^{–1} cm^{–1}]): 576 (7.50 × 10³), 492 (5.63 × 10³), 377 (7.14 × 10³), 279 (19.4 × 10³), 247 (16.8 × 10³). Λ_m (CH₃CN) = 313 mol^{–1} cm² Ω^{–1} (cf. 220–300 mol^{–1} cm² Ω^{–1} for a 2:1 electrolyte in CH₃CN).

[Fe(L3)₂](BF₄)₂ (3). Method B (dry EtOH): 2-Acetylpyridine (0.121 g, 1.0 mmol) and 2-(aminomethyl)pyridine (0.108 g, 1.0 mmol) were dissolved in 20 mL of dry ethanol with 2 drops of glacial acetic acid. The solution was refluxed for 1 h to result in a pale yellow solution. After cooling to room temperature Fe(BF₄)₂·6H₂O (0.168 g, 0.5 mmol) was added and a purple precipitate formed straight away. It was stirred at room temperature for another hour, before the precipitate was filtered off onto filter paper and dried under vacuum overnight. Dark purple solid, 0.167 g, 0.56 mmol, 51% yield. C₂₆H₂₆B₂F₈FeN₆ (651.99) + 2 H₂O: calcd. C 45.39, H 4.40, N 12.22; found C 45.19, H 4.06, N 12.32. ¹H NMR (CD₃CN, 300 MHz): δ = 8.17 (d, J = 7.8 Hz, 1 H, 3-H), 7.88 (dt, J = 1.0, 7.8 Hz, 1 H, 4-H), 7.78 (d, J = 4.9 Hz, 1 H, 6-H'), 7.68 (dt, J = 1.0, 7.3 Hz, 1 H, 4-H'), 7.65 (d, J = 4.9 Hz, 1 H, 6-H), 7.54 (d, J = 7.8 Hz, 1 H, 3-H'), 7.21 (dt, J = 1.0, 6.8 Hz, 1 H, 5-H), 7.03 (t, J = 7.3 Hz, 1 H, 5-H'), 6.27, 6.38 (2d, J = 22.7 Hz, 2 H, 9-Ha+b), 3.35 (s, 3 H, 8-H) ppm. ES MS: m/z (calcd.) 497.2 (497.3) [M – 2BF₄ + F]⁺, 239.1 (239.2) [M – 2BF₄]²⁺. IR (KBr): 3421, 2872, 1721, 1696, 1637, 1602, 1559, 1463, 1441, 1384, 1334, 1297, 1254, 1060, 770, 720, 618, 521, 475. UV λ_{max} [nm] (ε [dm³ mol^{–1} cm^{–1}]): 569 (8.74 × 10³), 488 (5.3 × 10³), 375 (7.14 × 10³), 276 (17.2 × 10³), 243 (18.7 × 10³). Λ_m (CH₃CN) = 267 mol^{–1} cm² Ω^{–1} (cf. 220–300 mol^{–1} cm² Ω^{–1} for a 2:1 electrolyte in CH₃CN).

[Fe(L4)₂](BF₄)₂ (4). Method A (IPA): 2-Formylpyridine (0.107 g, 1.0 mmol) and 2-(aminomethyl)pyridine (0.108 g, 1.0 mmol) were dissolved in 20 mL of 2-propanol with 2 drops of glacial acetic acid. The solution was refluxed for 2 h to result in a pale yellow solution. After cooling to room temperature Fe(BF₄)₂·6H₂O (0.168 g, 0.5 mmol) was added and a purple precipitate formed straight away. It was stirred at room temperature for another hour, before the precipitate was filtered off onto filter paper and dried under vacuum overnight. Purple solid, 0.245 g, 0.39 mmol, 78% yield. C₂₄H₂₂B₂F₈FeN₆ (623.93) + H₂O: calcd. C 44.90, H 3.77, N 13.09; found C 44.95, H 3.75, N 12.75. ¹H NMR (CD₃CN, 300 MHz): δ = 10.17 (s, 1 H, 7-H), 8.19 (d, *J* = 7.3 Hz, 1 H, 3-H), 7.86 (t, *J* = 7.3 Hz, 1 H, 4-H), 7.82 (d, *J* = 6.3 Hz, 1 H, 6-H'), 7.69 (t, *J* = 7.8 Hz, 1 H, 4-H'), 7.63 (d, *J* = 5.6 Hz, 1 H, 6-H), 7.55 (d, *J* = 8.3 Hz, 1 H, 3-H'), 7.20 (t, *J* = 6.8 Hz, 1 H, 5-H), 7.04 (t, *J* = 6.8 Hz, 1 H, 5-H'), 6.63, 6.51 (2d, *J* = 23.7 Hz, 2 H, 9-Ha+b) ppm. ES MS: *m/z* (calcd.) 225.0 (225.1) [M – 2BF₄]²⁺. IR (KBr): 3414, 2879, 2364, 2339, 1700, 1634, 1604, 1544, 1463, 1378, 1340, 1297, 1250, 1222, 1069, 1036, 870, 768, 657, 585, 520, 465. UV λ_{max} [nm] (ε [dm³mol^{−1}cm^{−1}]): 568 (5.63 × 10³), 483 (3.55 × 10³), 362 (8.52 × 10³), 278 (12.9 × 10³), 245 (14.7 × 10³). Λ_m (CH₃CN) = 247 mol^{−1}cm²Ω^{−1} (cf. 220–300 mol^{−1}cm²Ω^{−1} for a 2:1 electrolyte in CH₃CN).

[Co(L1)₂](BF₄)₂ (5). Method A (IPA): 2-Acetylpyridine (0.121 g, 1.0 mmol) and 2-(2-aminoethyl)pyridine (0.122 g, 1.0 mmol) were dissolved in 20 mL of 2-propanol with 2 drops of glacial acetic acid. The solution was refluxed for 2 h to result into a pale yellow solution. After cooling to room temperature Co(BF₄)₂·6H₂O (0.170 g, 0.5 mmol) was added and an orange precipitate formed straight away. It was stirred at room temperature for another hour, before the precipitate was filtered off onto filter paper and dried under vacuum overnight. Orange solid, 0.219 g, 0.32 mmol, 64% yield.

Method B (dry EtOH): Same experiment, orange solid, 0.197 g, 0.28 mmol, 57% yield. C₂₈H₃₀B₂CoF₈N₆ (683.13) + EtOH: calcd. C 49.41, H 4.98, N 11.53; found: C 49.61, H 4.89, N 11.48. ¹H NMR (CD₃CN, 300 MHz): paramagnetic, δ = 155.0 (1 H, pyC, 6-H'), 85.0 (1 H, pyC), 77.9 (1 H, pyA, 6-H), 66.1 (1 H, pyA), 49.8 (1 H, pyC), 40.6 (1 H, pyA), 18.8 (1 H, pyC, 4-H'), 1.0 (1 H, pyA, 4-H), −4.0 (3 H, Me), −29.4 (2 H, CH₂), −34.8 (2 H, CH₂) ppm. ES MS: *m/z* (calcd.): 254.6 (254.7 [M – 2BF₄]²⁺). IR (KBr): 3422, 2365, 1625, 1600, 1567, 1479, 1438, 1371, 1312, 1262, 1082, 1032, 791, 590, 452. UV λ_{max} [nm] (ε [dm³mol^{−1}cm^{−1}]): 335 (2.08 × 10³), 270 (15.6 × 10³), 229 (18.0 × 10³). Λ_m (CH₃CN) = 282 mol^{−1}cm²Ω^{−1} (cf. 220–300 mol^{−1}cm²Ω^{−1} for a 2:1 electrolyte in CH₃CN).

Crystal Data for 5: C₂₈H₃₀B₂CoF₈N₆, orange-red block, 0.65 × 0.60 × 0.33 mm³, orthorhombic, space group *Pbcn*, *a* = 15.6514(13), *b* = 13.8444(12), *c* = 14.9468(13) Å, *V* = 3238.7(5) Å³, *Z* = 4, μ = 0.610 mm^{−1}. Of 26197 reflections collected, 3309 were independent and used in the structure analysis. The structure was solved by direct methods (SHELXS-97)^[38] and refined against *F*² data (SHELXL-97)^[38] to *R*1 = 0.0315 for the 2722 data with *F* > 4σ(*F*), and *wR*2 = 0.1014 and GOF = 1.063 for all 3309 *F*². The 0.375 occupancy EtOH of solvation per asymmetric unit (half a complex cation and one BF₄[−] anion) is badly disordered, including across a twofold axis. No bond length or angle restraints/constraints were applied but EXYZ and EADP were used to make: a) O50' and C50 the same site and thermal motion as each other but different atom types (end-for-end disorder); and b) C51, C61 and O60' the same site and thermal motion as one-another but different atom types and/or parts of the disorder. The residual elec-

tron density (+1.14 vs. −0.31) is in this region of space. The hydrogen atoms on the two partial-occupancy EtOH oxygen atoms were treated as follows. H50C (on O50') was located from a difference map and its O–H distance improved (HIMP in SHELXTL) before being fixed in this position. H60C (on O60') was placed in a calculated/suggested (HTAB in SHELXL-97) position and fixed in this position.

[Co(L2)₂](BF₄)₂ (6). Method B (EtOH): 2-Formylpyridine (0.107 g, 1.0 mmol) and 2-(2-aminoethyl)pyridine (0.122 g, 1.0 mmol) were dissolved in 20 mL of dry ethanol with 2 drops of glacial acetic acid. The solution was refluxed for 1 h to result in a pale yellow solution. After cooling to room temperature Co(BF₄)₂·6H₂O (0.170 g, 0.5 mmol) was added and an orange precipitate formed straight away. It was stirred at room temperature for another hour, before the precipitate was filtered off onto filter paper and dried under vacuum overnight. Orange solid, 0.304 g, 0.46 mmol, 99% yield. C₂₆H₂₆B₂CoF₈N₆ (655.07): calcd. C 47.67, H 4.00, N 12.83; found C 47.62, H 4.07, N 12.55. ¹H NMR (CD₃CN, 300 MHz): δ = paramagnetic: 235.5 (1 H, 7-H), 187.1 (1 H, pyC, 6-H'), 96.1 (1 H, pyA, 6-H), 66.8 (1 H, pyC), 59.0 (1 H, pyC), 58.8 (1 H, pyA), 47.4 (1 H, pyA), 18.5 (1 H, pyC, 4-H'), 5.1 (1 H, pyA, 4-H), −25.3 (2 H, CH₂), −33.6 (2 H, CH₂) ppm. ES MS: *m/z* (calcd.): 240.1 (240.7) [M – 2BF₄]²⁺. IR (KBr): 3421, 2368, 2341, 1640, 1600, 1567, 1478, 1440, 1385, 1304, 1222, 1059, 882, 785, 639, 590, 521, 422. UV λ_{max} [nm] (ε [dm³mol^{−1}cm^{−1}]): 336 (2.3 × 10³), 279 (16.7 × 10³), 232 (18.6 × 10³). Λ_m (CH₃CN) = 305 mol^{−1}cm²Ω^{−1} (cf. 220–300 mol^{−1}cm²Ω^{−1} for a 2:1 electrolyte in CH₃CN).

Crystal Data for 6: C₂₆H₂₆B₂CoF₈N₆, orange block, 0.53 × 0.50 × 0.35 mm³, triclinic, space group *C*−1, *a* = 19.627(4), *b* = 19.586(4), *c* = 19.042(4) Å, β = 118.69(3)°, *V* = 6421(2) Å³, *Z* = 8, μ = 0.615 mm^{−1}. Of 20391 reflections collected, 11167 were independent and used in the structure analysis. The structure was solved by direct methods (SHELXS-97)^[38] and refined against *F*² data (SHELXL-97)^[38] to *R*1 = 0.0399 for the 9196 data with *F* > 4σ(*F*), and *wR*2 = 0.1075 and GOF = 1.062 for all 11167 *F*² data. Initial refinements in space group *C*2 resulted in disorder at one of the Co sites, and, even after inclusion of disorder, large peaks of residual electron density were still apparent near the Co sites. The structure was re-solved in space group *C*1, which produced a very clean E-map. Again refinement died at *R*1 (observed data) ca. 0.11. Analysis of the intensity distribution gave a value for <*E*² − 1> of 0.88, suggestive, but not conclusive, for the presence of twinning. However, the structure is noticeably hypercentric, distorting intensity statistics. Two-fold twinning (twin matrix: −1 0 0/0 1 0/0 0 −1) lowered *R*1 to 0.049, at which stage one of each pair of centrosymmetrically related cations, anions and solvate species was removed. Refinement of the remaining two cations, four anions and three acetonitrile molecules continued in space group *C*−1 (non-standard setting of *P*1̄, the better to show the twin relationship). *R*1 (observed data) dropped to 0.0399, commensurate with the intrinsic quality of the diffraction data. All hydrogen atoms, including those on the acetonitrile molecules, were clearly discernible in difference Fourier electron-density maps (but were still inserted, where calculable, at calculated positions as noted above).

Supporting Information (see also the footnote on the first page of this article): H,H-COSY NMR of complexes **2** and **6**, fits to magnetic data for **5** and **6**, electrochemical data and UV/Vis spectra of **1**–**6**.

Acknowledgments

This work was supported by postdoctoral fellowships from the Deutsche Akademie der Naturforscher Leopoldina (BMBF-LPD

9901/8-102, to R. W. H.) and the Postdoc-Programme of the German Academic Exchange Service (DAAD) (to H. W.), as well as grants from the Royal Society of New Zealand (Marsden Fund) and the Australian Research Council. We are grateful to Dr. J. Wikaira and Professor W. T. Robinson (University of Canterbury) for the X-ray data collections and to Mr B. M. Clark (University of Canterbury) for the ES mass spectra.

- [1] R. Hernandez-Molina, A. Mederos, in: *Comprehensive Coordination Chemistry II*, vol. 1 (Eds.: J. A. McCleverty, T. J. Meyer), Elsevier, Oxford, **2004**, pp. 411.
- [2] P. A. Tasker, P. G. Plieger, L. C. West, in: *Comprehensive Coordination Chemistry II*, vol. 9 (Eds.: J. A. McCleverty, T. J. Meyer), Elsevier, Oxford, **2004**, pp. 759; S. Brooker, *Eur. J. Inorg. Chem.* **2002**, 2535; H. Okawa, H. Furutachi, D. E. Fenton, *Coord. Chem. Rev.* **1998**, 174, 51; V. McKee, *Adv. Inorg. Chem.* **1993**, 40, 323; D. E. Fenton, P. A. Vigato, *Chem. Soc. Rev.* **1988**, 17, 69.
- [3] P. V. Bernhardt, G. A. Lawrance, in: *Comprehensive Coordination Chemistry II*, vol. 6 (Eds.: A. McCleverty, T. J. Meyer), Elsevier, Oxford, **2004**, pp. 1; M. V. Twigg, J. Burgess, in: *Comprehensive Coordination Chemistry II*, vol. 5 (Eds.: A. McCleverty, T. J. Meyer), Elsevier, Oxford, **2004**, pp. 403; A. P. Smith, C. L. Fraser, in: *Comprehensive Coordination Chemistry II*, vol. 1 (Eds.: A. McCleverty, T. J. Meyer), Elsevier, Oxford, **2004**, pp. 1; R. P. Thummel, in: *Comprehensive Coordination Chemistry II*, vol. 1 (Eds.: A. McCleverty, T. J. Meyer), Elsevier, Oxford, **2004**, pp. 41; M. B. Davies, *Coord. Chem. Rev.* **1998**, 169, 237; E. Nordlander, A. M. Whalen, *Coord. Chem. Rev.* **1995**, 142, 43.
- [4] H. A. Goodwin, *Top. Curr. Chem.* **2004**, 234, 23.
- [5] A. T. Baker, H. A. Goodwin, *Aust. J. Chem.* **1985**, 38, 207.
- [6] E. C. Constable, G. Baum, E. Bill, R. Dyson, R. van Eldik, D. Fenske, S. Kaderli, D. Morris, A. Neubrand, M. Neuburger, D. R. Smith, K. Wieghardt, M. Zehnder, A. D. Zuberbühler, *Chem. Eur. J.* **1999**, 5, 498.
- [7] J. Chambers, B. Eaves, D. Parker, R. Claxton, P. S. Ray, S. J. Slattery, *Inorg. Chim. Acta* **2006**, 359, 2400; D. J. Hathcock, K. Stone, J. Madden, S. J. Slattery, *Inorg. Chim. Acta* **1998**, 282, 131.
- [8] T. E. Chavez-Gil, M. Yasaka, T. Senokuchi, M. Sumimoto, H. Kurosaki, M. Goto, *Chem. Commun.* **2001**, 2388; K. Ramesh, R. N. Mukherjee, *Indian J. Chem. Ser. A* **1991**, 30, 1057; Y. Maeda, S. Shite, Y. Takashima, Y. Nishida, *Bull. Chem. Soc. Jpn.* **1977**, 50, 2902; P. Krumholz, *Inorg. Chem.* **1965**, 4, 757.
- [9] P. Krumholz, *Inorg. Chem.* **1965**, 4, 612; H. A. Goodwin, F. Lions, *J. Am. Chem. Soc.* **1959**, 81, 6415.
- [10] F. Lions, K. V. Martin, *J. Am. Chem. Soc.* **1957**, 79, 2733.
- [11] S. K. Padhi, V. Manivannan, *Polyhedron* **2007**, 26, 1619; S. K. Padhi, V. Manivannan, *Polyhedron* **2007**, 26, 3092.
- [12] P. V. Bernhardt, E. J. Hayes, *Inorg. Chem.* **2003**, 42, 1371.
- [13] B. A. Frazier, P. T. Wolczanski, E. B. Lobkovsky, T. R. Cundari, *J. Am. Chem. Soc.* **2009**, 131, 3428.
- [14] R. C. Stouffer, D. W. Smith, E. A. Clevenger, T. E. Norris, *Inorg. Chem.* **1966**, 5, 1167.
- [15] R. M. Hellyer, D. S. Larsen, S. Brooker, *Eur. J. Inorg. Chem.* **2009**, 1162–1171.
- [16] W. J. Geary, *Coord. Chem. Rev.* **1971**, 7, 81.
- [17] H. S. Chow, E. C. Constable, C. E. Housecroft, K. J. Kulicke, Y. Tao, *Dalton Trans.* **2005**, 236.
- [18] J. S. Judge, W. A. Baker, *Inorg. Chim. Acta* **1967**, 1, 68.
- [19] E. C. Constable, A. M. W. Cargill Thompson, *J. Chem. Soc., Dalton Trans.* **1994**, 1409.
- [20] U. S. Schubert, C. Eschbaumer, C. H. Weidl, *Des. Monomers Polym.* **1999**, 2, 185.
- [21] J. A. Kitchen, S. Brooker, *Coord. Chem. Rev.* **2008**, 252, 2072–2092.
- [22] B. N. Figgis, E. S. Kucharski, A. H. White, *Aust. J. Chem.* **1983**, 36, 1537.
- [23] B. N. Figgis, E. S. Kucharski, A. H. White, *Aust. J. Chem.* **1983**, 36, 1563.
- [24] E. N. Maslen, C. L. Raston, A. H. White, *J. Chem. Soc., Dalton Trans.* **1974**, 1803.
- [25] F. Takusagawa, P. G. Yohannes, K. B. Mertes, *Inorg. Chim. Acta* **1986**, 114, 165.
- [26] B. N. Figgis, E. S. Kucharski, A. H. White, *Aust. J. Chem.* **1983**, 36, 1527.
- [27] C. L. Raston, A. H. White, *J. Chem. Soc., Dalton Trans.* **1976**, 7.
- [28] C. M. Harris, T. N. Lockyer, R. L. Martin, H. R. H. Patil, E. Sinn, I. M. Stewart, *Aust. J. Chem.* **1969**, 22, 2105.
- [29] E. Goldschmied, N. C. Stephenson, *Acta Crystallogr., Sect. B* **1970**, 26, 1867.
- [30] P. Nielsen, H. Toftlund, A. D. Bond, J. F. Boas, J. R. Pilbrow, G. R. Hanson, C. Noble, M. J. Riley, S. M. Neville, B. Moubarak, K. S. Murray, *Inorg. Chem.* **2009**, 48, 7033.
- [31] A. Galet, A. B. Gaspar, M. C. Munoz, J. A. Real, *Inorg. Chem.* **2006**, 45, 4413.
- [32] S. Hayami, K. Murata, D. Urakami, Y. Kojima, M. Akita, K. Inoue, *Chem. Commun.* **2008**, 6510; S. Hayami, Y. Shigeyoshi, M. Akita, K. Inoue, K. Kato, K. Osaka, M. Takata, R. Kawajiri, T. Mitani, Y. Maeda, *Angew. Chem. Int. Ed.* **2005**, 44, 4899.
- [33] J. M. Rao, M. C. Hughes, D. J. Macero, *Inorg. Chim. Acta* **1976**, 16, 231.
- [34] R. Prasad, D. B. Scaife, *J. Electroanal. Chem.* **1977**, 84, 373.
- [35] B. N. Figgis, M. A. Hitchman, *Ligand Field Theory and Its Applications*, Wiley-VCH, Weinheim, **2000**.
- [36] B. J. Kennedy, G. D. Fallon, B. M. K. C. Gatehouse, K. S. Murray, *Inorg. Chem.* **1984**, 23, 580.
- [37] A. Pali, B. Tsukerblat, J. M. Clemente-Juan, E. Coronado, *Int. Rev. Phys. Chem.* **2010**, 29, 135.
- [38] G. M. Sheldrick, *Acta Crystallogr., Sect. A* **2008**, 64, 112.

Received: March 14, 2010

Published Online: June 10, 2010

Molybdenum and Tungsten Nitrosyl Complexes in Hydrogen Activation

Alexander Dybov,^[a] Olivier Blacque,^[a] and Heinz Berke^{*[a]}*Dedicated to Professor Uwe Rosenthal on the occasion of his 60th birthday***Keywords:** Homogeneous catalysis / Hydrogenation / Hydrogen activation / Tungsten / Molybdenum / Hydrides

Two transition-metal hydride complexes of the type $[M(\text{dippe})_2(\text{NO})(\text{H})]$ [$M = \text{W}$ (**2a**), Mo (**2b**); $\text{dippe} = 1,2\text{-bis}(\text{diisopropylphosphanyl})\text{ethane}$] have been prepared by the reaction of $[M(\text{dippe})_2(\text{NO})(\text{Cl})]$ [$M = \text{W}$ (**1a**), Mo (**1b**)] with LiBH_4 . The nitrosyl groups of the tungsten complexes **1a** and **2a** are capable to coordinate a LiBH_4 molecule to form the stable adducts $\text{W}(\text{dippe})_2(\text{Cl})(\text{NO}\cdots\text{LiBH}_4)$ (**1c**) and $\text{W}(\text{dippe})_2(\text{H})(\text{NO}\cdots\text{LiBH}_4)$ (**2c**). Addition of ethylenediamine to a toluene solution of **2c** led to rupture of the **2c** adduct and afforded **2a** in good yield. After the interaction of **2a** with $[\text{H}(\text{Et}_2\text{O})][\text{BF}_4]$, the stable seven-coordinated cationic dihydride $[\text{W}(\text{dippe})(\text{H})_2(\text{dippe})(\text{NO})][\text{BF}_4]$ (**6a**) was isolated. The reaction between **2b** and $[\text{H}(\text{Et}_2\text{O})][\text{BF}_4]$ led to the formation of $[\text{Mo}(\text{dippe})_2(\text{NO})(\text{FBF}_3)]$ (**6b**) in which BF_4^- was found to be coordinated to the metal centre. The $[\text{H}(\text{Et}_2\text{O})_2][\text{BAR}^{\text{F}}_4]$

acid interacted with **2a** to yield the seven-coordinated complex $[\text{W}(\text{dippe})(\text{H})_2(\text{dippe})(\text{NO})][\text{BAR}^{\text{F}}_4]$ (**5a**) similar to **6a**. In the reaction between **2b** and $[\text{H}(\text{Et}_2\text{O})_2][\text{BAR}^{\text{F}}_4]$, the $16e^-$ five-coordinated complex $[\text{Mo}(\text{dippe})_2(\text{NO})][\text{BAR}^{\text{F}}_4]$ (**4b**) was formed. X-ray diffraction revealed that **4a** has a weak agostic interaction *trans* to the NO ligand. Complex **4b** was found to react rapidly with hydrogen gas under ambient conditions to form the dihydride complex $[\text{Mo}(\text{dippe})(\text{H})_2(\text{dippe})(\text{NO})][\text{BAR}^{\text{F}}_4]$ (**5b**), which is unstable in the absence of a hydrogen atmosphere. The equilibrium constant for the reversible reaction of **4b** with hydrogen was found to be $K = 2.6 \text{ bar}^{-1}$ at 25°C . Complex **4b** was tested as a catalyst for acetone hydrogenation; a maximum TON of 7 was found.

Introduction

Homogeneous catalysis of ketone hydrogenation is mainly accomplished with ruthenium and rhodium complexes. A mechanism related to the Wilkinson hydrogenation of olefins is anticipated in which the initial binding of the ketone to the metal, subsequent insertion of the ketone into the $M\text{--H}$ bond and reductive elimination of the alcohol are the key steps.^[1] An alternative reaction mechanism for ketone hydrogenation proceeds via ions. This mechanism does not require primary insertion into the $M\text{--H}$ bond, rather heterolytic splitting of the H_2 molecule and transfer of H^+ and H^- to the ketone.^[2,3] Molybdenum and tungsten dihydride complexes are thought to bear both these functions in the same molecule acting as proton and hydride donors at the same time.^[4–6] In 1994 Bullock and co-workers showed that transition-metal monohydrides are capable of providing a H_2 equivalent in the presence of acids: $[\text{HW}(\text{CO})_3\text{Cp}]$ and other metal hydrides were used for

the stoichiometric ionic hydrogenation of alkenes,^[7] alkynes^[8] and ketones.^[9] These stoichiometric reactivity studies have led to the development of a series of Mo and W catalysts for the homogeneous hydrogenation of ketones.

Related to this chemistry, hydride transfer reactions between $[\text{HM}(\text{CO})_2\text{Cp}(\text{PR}_3)]$ ($M = \text{Mo}, \text{W}$; $R = \text{Me}, \text{Ph}, \text{Cy}$) and $[\text{H}(\text{Et}_2\text{O})_2][\text{BAR}^{\text{F}}_4]$ in the presence of $\text{Et}_2\text{C}=\text{O}$ gave ketone complexes $[\text{M}(\text{CO})_2\text{Cp}(\text{PR}_3)(\eta^1\text{-Et}_2\text{C}=\text{O})][\text{BAR}^{\text{F}}_4]$ [$\text{Ar}^{\text{F}} = 3,5\text{-bis}(\text{trifluoromethyl})\text{phenyl}$] and Et_2HCOH . The ketone complexes were shown to be catalyst precursors for the homogeneous hydrogenation of various ketones.^[10,11] Mechanistic experiments supported the proposed ionic hydrogenation mechanism that involves proton transfer from a cationic dihydride $[\text{M}(\text{H})_2]^+$. Neutral $16e^-$ complexes of the type $[\text{Mo}(\text{CO})(\text{R}_2\text{PCH}_2\text{CH}_2\text{PR}_2)_2]$ ($R = \text{Ph}, \text{Bz}, \text{Et}, i\text{Bu}$) stabilized by an agostic $\text{Mo}\cdots\text{H}\text{--C}$ interaction are known that can cleave the H_2 molecule to form molybdenum dihydride complexes.^[12–15] These can be considered as analogues of the dihydride intermediate complexes in the catalytic cycle proposed by Bullock and co-workers.^[16,17]

Our group was interested in the development of systems that can activate the hydrogen molecule in a heterolytic fashion. For this purpose we designed a system bearing two alkylendiphosphanes and a NO ligand oriented *trans* to a vacant complexation site of the metal centre. We supposed

[a] Anorganisch-Chemisches Institut, Universität Zürich, Winterthurerstrasse 190, 8057 Zürich, Switzerland
Fax: +41-44-6356803
E-mail: hberke@aci.uzh.ch

Supporting information for this article is available on the WWW under <http://dx.doi.org/10.1002/ejic.201000301>.

that the nitrosyl ligand might effect weakening of any *trans* M–H bond through its *trans* influence. In this paper we report the preparation and characterization of complexes of the type $[M(\text{dippe})_2(\text{NO})^+]$ ($M = \text{Mo}, \text{W}$; $\text{dippe} = i\text{Pr}_2\text{PCH}_2\text{CH}_2\text{P}i\text{Pr}_2$) and their hydrogen activation reactions.

Results and Discussion

Preparation of $[M(\text{dippe})_2(\text{NO})(\text{H})]$ [$M = \text{Mo}, \text{W}$; $\text{dippe} = 1,2\text{-bis}(\text{diisopropylphosphanyl})\text{ethane}$]

The chloride complexes $[\text{W}(\text{dippe})_2(\text{NO})\text{Cl}]$ (**1a**) and $[\text{Mo}(\text{dippe})_2(\text{NO})\text{Cl}]$ (**1b**) were prepared according to literature procedures starting from the $[M(\text{CH}_3\text{CN})_2(\text{NO})\text{Cl}_3]$ complexes ($M = \text{W}, \text{Mo}$).^[18]

The consecutive addition of 2.1 equiv. of the dippe ligand and excess of sodium amalgam (1%) to a THF solution of the $[M(\text{CH}_3\text{CN})_2(\text{NO})\text{Cl}_3]$ species led to the formation of the chloride compounds $[M(\text{dippe})_2(\text{NO})(\text{Cl})]$ **1a** ($M = \text{W}$) and **1b** ($M = \text{Mo}$) (see Scheme 1), which were isolated in 85 and 80% yields, respectively. The $^{31}\text{P}\{^1\text{H}\}$ NMR spectra exhibits single resonances at $\delta = 44.5$ ppm for **1a** and at $\delta = 59.9$ ppm for **1b**, which indicates the presence of four equivalent phosphorus atoms in each complex. The ^1H NMR spectra of **1a** and **1b** show two multiplets at $\delta = 2.62$ and 2.49 ppm and at $\delta = 2.69$ and 2.51 ppm, respectively, attributed to the CH protons of the isopropyl groups.

The bridging CH_2 protons display multiplets at $\delta = 1.63$ ppm for **1a** and at $\delta = 1.79$ ppm for **1b**. The IR spectra reveal strong bands attributed to NO vibrations at 1516 cm^{-1} for **1a** and at 1527 cm^{-1} for **1b**. X-ray diffraction studies of **1a** and **1b** confirmed the *trans* structures. An ORTEP drawing of **1a** is presented in Figure 1. The X-ray data and a description of the crystal structure of **1b** are given in the Supporting Information.

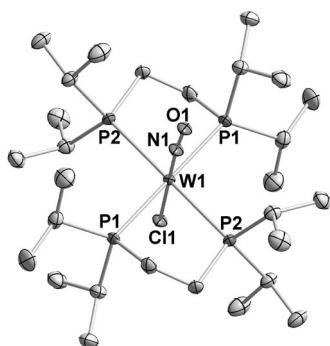


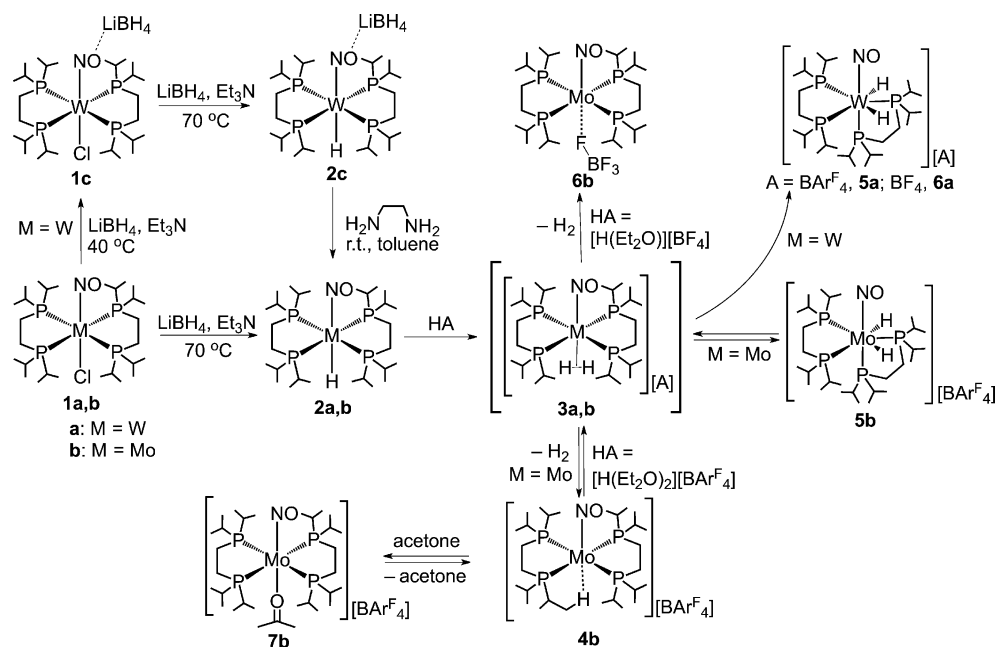
Figure 1. ORTEP drawing of one crystallographically independent molecule of $[\text{W}(\text{dippe})_2(\text{NO})(\text{Cl})]$ (**1a**). Displacement ellipsoids are drawn at the 50% probability level. The NO/Cl disorder and all hydrogen atoms have been omitted for clarity. Selected bond lengths [\AA] and angles [$^\circ$]: W1–N1 1.761(5), W2–N2 1.795(5), W1–P1 2.4971(8), W1–Cl1 2.5180(19), W1–P2 2.5403(8), W2–P3 2.5381(7), W2–Cl2 2.4842(16), W2–P4 2.4864(7), N1–O1 1.241(8), N2–O2 1.229(6), N1–W1–Cl1 178.48(17), N2–W2–Cl2 177.59(17).

The asymmetric units of **1a** and **1b** are composed of two independent halves of the $[M(\text{NO})(\text{dippe})_2\text{Cl}]$ molecules ($M = \text{Mo}, \text{W}$) with the metal centres lying on crystallographic centres of symmetry. In both structures the *trans* NO and Cl groups are disordered. The four phosphorus atoms are in-plane with the tungsten or molybdenum coordination centres. The average metal–phosphorus bond lengths are $2.515(2)\text{ \AA}$ for **1a** and $2.532(1)\text{ \AA}$ for **1b**, which are slightly longer than those of $[\text{W}(\text{dmpe})_2(\text{NO})\text{Br}]$ [$2.427(2)\text{ \AA}$],^[19] $[\text{W}(\text{dmpe})_2(\text{O})(\text{Cl})][\text{ClO}_4]$ ^[20] [$2.481(6)\text{ \AA}$], $[\text{Mo}(\text{dmpe})_2(\text{NO})\text{Cl}]$ ^[21] [$2.446(1)\text{ \AA}$] and $[\text{Mo}(\text{depe})_2(\text{N})(\text{Cl})]$ [$2.489(2)\text{ \AA}$],^[22] which can be explained in terms of the higher steric congestion of the dippe ligand. The average metal–chloride bond lengths are $2.501(2)\text{ \AA}$ for **1a** and $2.529(1)\text{ \AA}$ for **1b**, which are shorter than the metal–chloride bond lengths of related complexes, for example, $2.539(5)\text{ \AA}$ in $[\text{W}(\text{dmpe})_2(\text{O})(\text{Cl})][\text{ClO}_4]$,^[20] $2.556(1)\text{ \AA}$ in $[\text{W}(\text{dmpe})_2(\text{Cl})(\text{CH})][\text{B}(\text{C}_6\text{F}_5)_4]$ ^[23] and $2.772(2)\text{ \AA}$ in $[\text{Mo}(\text{depe})_2(\text{N})(\text{Cl})]$.^[22] Only in $[\text{Mo}(\text{dmpe})_2(\text{NO})\text{Cl}]$ ^[21] is the Mo–Cl bond [$2.488(1)\text{ \AA}$] shorter than in **1b**.

Treatment of $[\text{W}(\text{dippe})_2(\text{NO})\text{Cl}]$ (**1a**) with 5 equiv. of LiBH_4 in Et_3N at room temperature resulted in the formation of the $[\text{W}(\text{dippe})_2(\text{Cl})(\text{NO}\cdots\text{LiBH}_4)]$ complex (**1c**) (Scheme 1). The $^{31}\text{P}\{^1\text{H}\}$ NMR spectrum of **1c** exhibits a singlet at $\delta = 43.0$ ppm, which is in agreement with a planar arrangement of the phosphorus atoms. In addition to the signals of the dippe ligands, the ^1H NMR spectrum exhibits a quintet at $\delta = 0.20$ ppm ($^1J_{\text{BH}} = 79.8\text{ Hz}$), which is attributed to the protons of the BH_4 unit. The IR spectrum shows an intense absorption band at 1489 cm^{-1} assigned to the NO stretching vibration (Table 1). The difference of 27 cm^{-1} in the wavenumbers of the $\nu(\text{NO})$ band of **1a** and **1c** is due to the fact that the N–O bond order for the adduct **1c** is lowered by Li coordination in comparison with **1a**. A similar tendency has been observed in molybdenum nitrosyl complexes.^[24] For instance, a difference of 49 cm^{-1} in the stretching vibration frequency of the nitrosyl group was identified for the pair $[\text{Mo}(\text{dmpe})_2(\text{Cl})(\text{NO})]/[\text{Mo}(\text{dmpe})_2(\text{Cl})(\text{NO})][\text{LiHBEt}_3]$ [$\text{dmpe} = 1,2\text{-bis}(\text{dimethylphosphanyl})\text{-ethane}$].

Single crystals of **1c** suitable for X-ray diffraction study were obtained by slow diffusion of hexane into a benzene solution of **1c**. The crystal structure of **1c** can be seen to be a dimer of two molecules of **1a** bridged by a $(\text{LiBH}_4)_2$ unit (Figure 2) with a unique Li–O_{NO} interaction.^[24,25] The lithium ion is attached to the O_{NO} atom at an angle of $161.6(4)^\circ$. The average W–P and W–Cl distances were found to be approximately equal to the corresponding bond lengths in **1a**.

When the temperature of the reaction leading to **1c** was increased to 70°C , the LiBH_4 bound hydride complex $[\text{W}(\text{dippe})_2(\text{H})(\text{NO}\cdots\text{LiBH}_4)]$ (**2c**) was formed. The ^{31}P NMR spectrum of **2c** shows a singlet resonance at $\delta = 62.8$ ppm. In the ^1H NMR spectrum, in addition to a set of multiplets attributed to dippe ligands, a multiplet characteristic of a hydride ligand was observed at -2.91 ppm ($^2J_{\text{HP}} = 26.0\text{ Hz}$). A quadruplet corresponding to BH_4 was also detected at $\delta = 0.15$ ppm ($^1J_{\text{BH}} = 82.2\text{ Hz}$). The IR spec-



Scheme 1. The general scheme for all transformations. Complexes **5b** and **7b** were detected in solution by NMR spectroscopy and were not isolated. Complexes **3a** and **3b** are proposed short-lived intermediates. HA = [H(Et₂O)₂][BARF₄] [ArF₄ = 3,5-(CF₃)₂C₆H₃] or [H(Et₂O)][BF₄] acids; [A] = BARF₄[−] or BF₄[−] counter-ions.

Table 1. IR stretching vibrations of NO in **1a–c** and **2a–c** and M–H in **2a–c**.

	$\nu(\text{NO})$ [cm ^{−1}]	$\nu(\text{M–H})$ [cm ^{−1}]
1a	1516	
1b	1527	
1c	1489	
2a	1492	1671
2b	1500	1670
2c	1459	1672

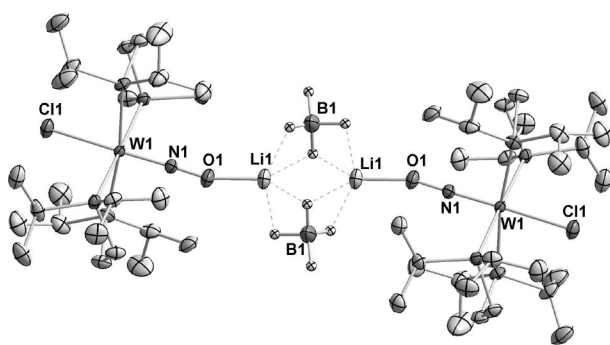


Figure 2. ORTEP drawing of [W(dippe)₂(Cl)(NO...LiBH₄)] (**1c**). Displacement ellipsoids are drawn at the 50% probability level. Selected hydrogen atoms have been omitted for clarity. Selected bond lengths [Å] and angles [°]: W1–N1 1.764(4), W1–P4 2.4949(13), W1–Cl1 2.5083(12), W1–P1 2.5176(12), W1–P3 2.5372(13), W1–P2 2.5501(13), O1–N1 1.256(5), Cl–W1–N1 178.79(13), N1–O1–Li1 161.6(4).

trum reveals an intense absorption band from a NO stretching vibration at 1460 cm^{−1} and a W–H stretching vibration band at 1673 cm^{−1}.

A single crystal of **2c** suitable for X-ray diffraction analysis was obtained by the slow diffusion of hexane through a concentrated benzene solution of complex **2c**. The crystal structure of **2c** exhibits similarities with that of **1c**. Identical to **1c**, two [W(dippe)₂(H)(NO)] species are bridged through (LiBH₄)₂; the hydride ligand is located *trans* to the NO group. An ORTEP drawing of **2c** and the experimental crystallographic data are presented in the Supporting Information.

To obtain the hydride complex **2a**, ethylenediamine was added to a toluene solution of **2c** at room temperature, which resulted in the quantitative precipitation of [Li(en)₂·BH₄].^[26] The ³¹P{¹H} NMR of **2a** spectrum reveals a sharp singlet at δ = 64.4 ppm, which demonstrates the presence of chemically identical phosphorus atoms. In addition to the multiplets at δ = 2.47 and 2.10 ppm attributed to the chemically different protons of the dippe methylene groups and sets of resonances from the diastereotopic isopropyl methyl groups, a characteristic W–H quintet was observed in the ¹H NMR spectrum at −3.38 ppm (²J_{PH} = 24.8 Hz). The IR spectrum of **2a** shows a weak band at 1671 cm^{−1} attributed to the $\nu(\text{W–H})$ vibration and a strong $\nu(\text{NO})$ band at 1492 cm^{−1} (Table 1). In analogy with the chloride complexes **1a** and **1c**, the $\nu(\text{NO})$ bands of **2a** and **2c** differ by 33 cm^{−1}, which again indicates a lower NO bond order for **2c** caused by Li coordination.^[25]

Compound **2a** crystallizes in the centrosymmetric space group *Pccn*. Similarly to the structure of **1a**, **2a** displays a pseudo-octahedral coordination geometry (Figure 3). The four phosphorus atoms of the dippe ligands are in-plane with the tungsten centre. The mean W–P distance is 2.4826(6) Å, which is slightly shorter than the correspond-

ing distances in **1a**. The hydride ligand is located in the Fourier difference map and its coordinates and isotropic thermal parameter could be freely refined. The W–H bond length was found to be 1.88(3) Å. Taking into account its high standard deviations, it is in the range of elongated hydride bonds, for example, [W(PMe)₃(NO)(H)]^[18] [1.93(3) Å] and [W(dmpe)₂(CMes)(H)] [2.00(4) Å].^[27]

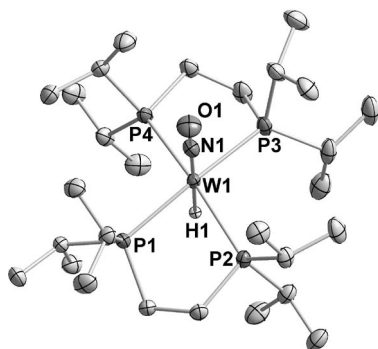


Figure 3. ORTEP drawing of complex [W(dippe)₂(NO)H] (**2a**). Displacement ellipsoids are drawn at the 50% probability level. All hydrogen atoms except H1 have been omitted for clarity. Selected bond lengths [Å] and angles [°]: W1–N1 1.807(2), W1–H1 1.89(3), W1–P3 2.4645(6), W1–P1 2.4691(6), W1–P4 2.4893(6), W1–P2 2.5074(6), H1–W1–N1 177.5(9), P1–W1–N1 92.85(6).

Notably, the transformation of **1a** into **2a** can be carried out in a stepwise procedure with the isolation of intermediates or in a one-pot procedure, which leads to enhanced overall yields.

Molybdenum hydride **2b**, analogous to **2a**, was obtained by the reaction of **1b** with LiBH₄ in Et₃N as solvent at 70 °C. Under these conditions the hydride **2b** was the only product. The LiBH₄ adduct of **2b** is considered to be less tight than **2c** and would therefore be expected to undergo facile cleavage in the presence of NEt₃. Application of excess of LiBH₄ apparently did not lead to noticeable adduct formation (see below), rather it led to a considerable increase in the yield of **2b**, which was presumably effected by a shift of the Cl/hydride exchange equilibrium towards the hydride site. To assure the lower Lewis basicity of **2b** in comparison with **2a**, **2b** was treated in a unique experiment with excess LiBH₄ using Et₂O as a non-coordinating solvent.^[24,25] New ν(NO) bands at lower wavenumbers were not observed, even after stirring the reaction mixture for about 12 h; only starting materials were isolated. The ³¹P{¹H} NMR spectrum of **2b** exhibits a sharp signal at δ = 85.8 ppm, which proves the presence of chemically equivalent phosphorus ligands. In addition to the expected multiplets attributed to dippe ligands, the ¹H NMR spectrum displays a quintet due to the hydride ligand at –3.80 ppm (²J_{PH} = 24.8 Hz). In the region of 2000–1400 cm^{–1}, the IR spectrum of **2b** reveals two strong bands at 1670 (Mo–H) and 1500 cm^{–1} (NO). Based on these spectroscopic data, **2b** was assigned a *trans* structure similar to that of **2a**.

Reaction of [M(dippe)₂(NO)H] (M = W, Mo) with [H(Et₂O)₂][BAR^F₄] [Ar^F = 3,5-(CF₃)₂C₆H₃]

The counter-ion [BAR^F₄][–] is classified as non-coordinating^[28,29] allowing in many cases the observation of dihydrogen complexes upon protonation of transition-metal hydrides.^[30] A weakly coordinating ligand such as dihydrogen cannot be replaced by the [BAR^F₄][–] anion, which is an even weaker electron donor. If dihydrogen ligands are weakly bound, as in **3b**, they might be released as H₂ leaving a vacant site behind. In a formal ligand substitution process the H₂ ligand could then be replaced by other small molecules. The tungsten hydride **2a** indeed reacted with [H(Et₂O)₂][BAR^F₄] to form presumably first the dihydrogen complex **3a**, which then underwent oxidative addition to give the seven-coordinated pentagonal bipyramidal dihydride [W(dippe)₂(NO)H₂][BAR^F₄] (**5a**). Complex **5a** was isolated in good yield as a colourless powder. The ³¹P{¹H} NMR spectrum exhibits three triplets with an integration ratio 1:2:1 at δ = 66.8, 59.5 and 25.2 ppm attributed to three chemically different types of phosphorus atoms: one phosphorus position is equatorial, one is axial and the two remaining phosphorus positions are chemically equivalent and equatorial. In addition to the signals of the dippe ligand, the ¹H NMR spectrum of **5a** reveals a multiplet due to the hydride protons. In the ¹H{³¹P} spectrum the singlet at δ = 1.76 ppm was attributed to the chemically equivalent hydride atoms. The IR spectrum of **5a** reveals a band at 1613 cm^{–1} attributed to a ν(NO) stretching vibration. No bands could be assigned to W–H vibrations, which are presumably of too low intensity.

The structure of **5a** was confirmed by an X-ray diffraction study (Figure 4). Complex **5a** crystallized in the centrosymmetric space group P2₁/c. The molecular structure of **5** shows the spectroscopically derived pseudopentagonal bipyramid. The coordination geometry is even distorted from an ideal C_s symmetry with the planes of the two chelating ligands P3–W–P4 and P1–W–P2 at 80.53(3)°. The P1–W–N1 angle of the equatorial/axial chelate is 160.84(8)°, which demonstrates, together with the long W–P1 bond length of 2.6849(8) Å, that P1 is only weakly bound to the tungsten centre presumably due to the strong *trans* influence^[18,21] of the NO group and thus high lability of the axial P1 is expected. Temperature-dependent ³¹P{¹H} NMR studies showed that the structure of **5a** remained static up to 100 °C as the spectra did not reveal any significant change upon heating. In addition, substitution with coordinating solvents such as THF or acetone apparently did not occur to any significant extent. The two hydride ligands were located in a Fourier difference map and were fully refined. The average W–H distance of **5a** is quite short [1.64(4) Å], not perturbed by any *trans* influence as in **2a** in which the W1–H1 distance was found to be 0.25 Å longer.

The formally 16e[–] complex **4b** was prepared similarly to compound **5a** by the reaction of the hydride **2b** with [H(Et₂O)₂][BAR^F₄] presumably with the dihydrogen complex **3b** as a short-lived intermediate. Complex **4b** was isolated as a green powder. The ³¹P{¹H} NMR spectrum

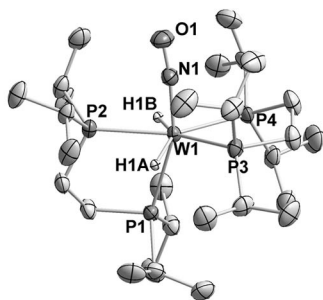


Figure 4. ORTEP drawing of $[\text{W}(\text{dippe})_2(\text{H})_2(\text{NO})][\text{BAr}^{\text{F}}_4]$ (**5a**). Displacement ellipsoids are drawn at the 50% probability level. Only the main residue (without the counter-ion) and selected hydrogen atoms are shown. Selected bond lengths [Å] and angles [°]: W1–H1A 1.62(4), W1–H1B 1.66(4), W1–N1 1.79(3), W1–P2 2.4810(7), W1–P4 2.5363(7), W1–P3 2.5496(7), W1–P1 2.6849(8), N1–W1–P1 160.83(8), N1–W1–P2 82.69(8), P3–W1–P4 78.43(2).

shows a singlet at $\delta = 72.0$ ppm, which indicates chemical equivalence of the four phosphorus atoms. The ^1H NMR spectrum of **4b** displays several multiplets in the region of $\delta = 2.55$ – 0.50 ppm assigned to resonances of the dippe ligands. No special resonance was observed for an agostic hydrogen, which was detected in the X-ray diffraction study of **4b** (see below). The agostic hydrogen is anticipated to undergo rapid exchange with the other H_{Me} atoms of the isopropyl groups.^[31] The fast exchange is also indicated by variable-temperature $^{31}\text{P}\{^1\text{H}\}$ NMR spectra, which show only a single resonance in the temperature range of 193–298 K. The IR spectrum of **4b** displays a $\nu(\text{NO})$ band at 1591 cm^{-1} .

The ORTEP representation of the molecular structure of **4b** is presented in Figure 5. Compound **4b** adopts a square pyramidal geometry in which four phosphorus atoms form the square base of the pyramid. Note that the Mo1–P3 bond length is shorter [2.473(1) Å] than the other three M–P distances, presumably because this P atom bears the substituent with the agostic hydrogen atom.^[32,33] Recently a DFT energy-partitioning scheme for agostic bonds was published^[34,35] from which it became evident that several geometric distortions contribute to the total energy of agostic binding. For comparison, the $\text{Mo}\cdots\text{H}-\text{C}$ distance in **4b** is 2.45 Å, which is considerably shorter than the related distance in $[\text{Mo}(\text{CO})(\text{Ph}_2\text{PCH}_2\text{CH}_2\text{Ph}_2)_2]$ (2.98 Å)^[32,33] but longer than of the value of 2.20 Å reported for the $[\text{Mo}(\text{CO})(i\text{Bu}_2\text{PCH}_2\text{CH}_2i\text{Bu}_2)_2]$ complex.^[36]

Apparently, the weakly agostic $\text{Mo}\cdots\text{H}-\text{C}$ interaction can be readily displaced by donor solvent molecules that are suited to entering the sterically congested coordination sphere. Based on NMR spectroscopic evidence, THF, for example, does enter the “hole”. However, acetone leads to significant broadening of the singlet observed at room temperature. At 40 °C a sharp singlet is observed. At –40 °C this signal splits into two sharp singlets at $\delta = 61.5$ and 60.0 ppm. The $^{31}\text{P}\{^1\text{H}\}$ NMR spectra of **4b** in various THF/acetone mixtures revealed the dependence of the sig-

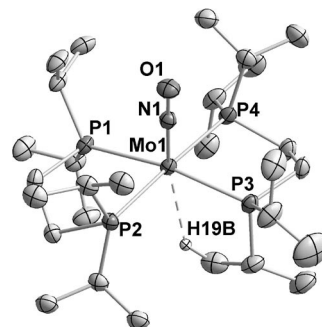


Figure 5. ORTEP drawing of $[\text{Mo}(\text{dippe})_2(\text{NO})][\text{BAr}^{\text{F}}_4]$ (**4b**). Only the main residue is shown without the counter-ion and selected hydrogen atoms. Selected bond lengths [Å] and angles [°]: Mo1–N1 1.767(3), Mo1–H19B 2.4524(3), Mo1–P3 2.473(1), Mo1–P4 2.5189(10), Mo1–P2 2.5231(10), Mo1–P1 2.5368(9), N1–Mo1–P1 96.98(9).

nal integration on the acetone concentration. This observation points to an equilibrium operating at room temperature with fast dynamics on the NMR timescale (Scheme 1).

Reaction of $[\text{M}(\text{dippe})_2(\text{NO})\text{H}]$ ($\text{M} = \text{W}, \text{Mo}$) with $[\text{H}(\text{Et}_2\text{O})][\text{BF}_4]$

The tungsten hydride **2a** reacted with $[\text{H}(\text{Et}_2\text{O})][\text{BF}_4]$ acid to form **6a** structurally related to **5a**. Complex **6a** was isolated as a colourless powder. The $^{31}\text{P}\{^1\text{H}\}$ NMR spectrum of **6a** exhibits three triplets with an integration ratio 1:2:1 at $\delta = 69.2$, 61.9 and 27.3 ppm, which indicates three chemically different phosphorus atoms. In the $^1\text{H}\{^{31}\text{P}\}$ NMR spectra a singlet attributed to the hydride atoms can be found at $\delta = 1.76$ ppm. A single-crystal X-ray diffraction investigation fully confirmed the structure of **6a** (for experimental details see the Supporting Information).

The reaction of **2b** and $[\text{H}(\text{Et}_2\text{O})][\text{BF}_4]$ was carried out in Et_2O at room temperature and was completed within minutes. After addition of the acid the red $[\text{Mo}(\text{dippe})_2(\text{NO})(\text{FBF}_3)]$ complex **6b** started to precipitate. In accord with the general observation that the kinetic sites of protonation of hydride complexes are the hydride ligands,^[29,41] we assume the initial formation of the dihydrogen complex **3b**, which apparently is unstable and decays on substitution of the H_2 ligand by the BF_4^- anion to form **6b** (Scheme 1). In the $^{31}\text{P}\{^1\text{H}\}$ NMR spectrum of **6b** a singlet was observed at $\delta = 64.5$ ppm, which reveals that the square of the phosphorus ligands of **2b** is retained. The ^{19}F NMR spectrum shows two singlets at $\delta = -157.8$ and -157.9 ppm with an integration ratio of 1:3. The non-equivalence of the fluorine atoms can be attributed to strong counter-ion coordination and suppressed coordination dynamics of the BF_4^- anion that normally proceeds by hopping between the fluorine substituents.

An X-ray diffraction study of **6b** corroborated the coordination of BF_4^- . An ORTEP drawing of the crystal structure of **6b** is given in Figure 6. Complex **6b** crystallizes in the centrosymmetric space group $P\bar{1}$. The molybdenum

atom lies at a centre of inversion with a positional disorder between the *trans* NO and BF₄[−] groups. The average Mo–P bond length is 2.535(1) Å, which is similar to the corresponding distances in **1b**. In comparison with the W–F bonds of analogous structures, the Mo1–F4 bond length of 2.265(6) Å in **6b** is slightly longer than the corresponding bond in [W(PMe₃)(CO)₃(NO)(BF₄)] [2.169(11) Å]^[37] or [W(H)(CO)₃(PCy₃)₂(BF₄)] [2.15(2) Å].^[38] Nevertheless, the B1–F4 bond length of 1.487(11) Å is significantly longer than the other B–F bond lengths that are in the range 1.36–1.38(1) Å, which indicates a strong interaction between the counter-ion and the metal centre. This could explain the failure to substitute the counter-ion on pressurizing a THF solution of **6b** even with 3 bar of hydrogen gas.

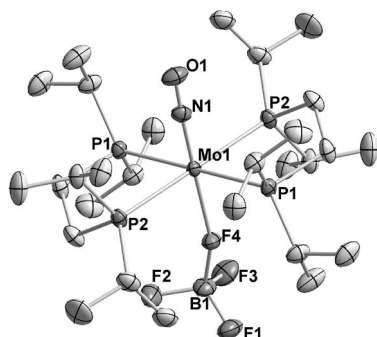


Figure 6. ORTEP drawing of [Mo(dippe)₂(NO)(FBF₃)] (**6b**). Displacement ellipsoids are drawn at the 50% probability level. All hydrogen atoms have been omitted for clarity. Selected bond lengths [Å] and angles [°]: Mo1–N1 1.770(8), Mo1–F4 2.265(6), Mo1–P1 2.5549(8), Mo1–P2 2.5197(6), B1–F1 1.360(9), B1–F2 1.373(9), B1–F3 1.377(10), B1–F4 1.487(11), Mo1–F4–B1 161.6(6), F4–Mo1–N1 177.3(5).

Equilibrium Reaction of [Mo(dippe)₂(NO)][BAR^F₄] with Hydrogen Gas

After pressurising an NMR tube containing a THF solution of **4b** with 1.8 bar of H₂ gas the colour immediately changed from green to yellow. The ³¹P{¹H} NMR spectrum shows a set of three triplets at δ = 89.5, 76.1 and 42.4 ppm with an integration ratio of 1:2:1 assigned to [Mo(dippe)₂(H)₂(NO)][BAR^F₄] (**5b**) with three non-equivalent types of phosphorus atoms. In addition, the ¹H NMR spectrum of **5b** shows at room temperature a characteristic multiplet at δ = 0.32 ppm, which becomes a singlet in the noise-decoupled ¹H{³¹P} NMR spectrum. A comparison with the NMR spectroscopic data of **5a** led to the conclusion that **4b** can react with hydrogen gas to form **5b** presumably via **3b** as intermediate (Scheme 1).

The ratio of **5b** and **4b** depends on the H₂ pressure (Figure 7), which emphasizes the equilibrium character of the interaction between **4b** and H₂. The linear regression allows the calculation of an equilibrium constant amounting to 2.6 ± 0.1 bar^{−1} at 25 °C.

Compound **5b** can be spectroscopically traced at H₂ pressures of approximately 0.2 bar. Lower H₂ pressures caused considerable broadening of the singlet of **4b** in the ³¹P{¹H}

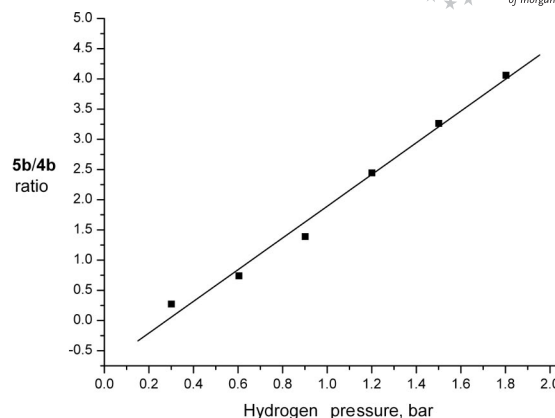


Figure 7. Integration ratio of the **5b/4b** signals versus hydrogen pressure.

NMR spectrum. We believe this observation can be interpreted in terms of a slowing of the H₂ equilibrium and that low H₂ pressures lead to a preference of the **4b/3b** equilibrium with signal averaging of both species similar in rate on the NMR timescale (Scheme 1). In contrast to **5a**, neither the dihydride **5b** nor the dihydrogen complex **3b** could be isolated from solution due to their instability in the absence of H₂.

Based on a comparison with the related species [Mo(CO)(R₂PCH₂CH₂PR₂)₂] (R = Ar, Et, *i*Bu) obtained by Kubas et al.^[13] it can be concluded that the “*trans* ligand” located *trans* to the weakly coordinated H₂ ligand has a great influence on the position of the H₂/dihydride equilibrium. It was demonstrated earlier that the donating ability of the chelating phosphane plays a major role. For instance, all complexes with R = Ar with lower donating abilities showed no tendency to form dihydride complexes. In the cases of R = Et and *i*Bu the dihydride complexes could be isolated in pure form. It is remarkable that all the H₂ complexes of the [Mo(CO)(R₂PCH₂CH₂PR₂)₂] series with CO as a *trans* ligand interact strongly with H₂, whereas **4b** loses the interaction with H₂ instantaneously once the H₂ concentration falls below a certain limit. The *trans* NO exerts a stronger *trans* influence than CO, which labilizes the π-acceptor H₂ ligand through π-acceptor competition. A labilized H₂ ligand could, however, bring about enhanced reactivity.

Catalytic Hydrogenation of [D₆]Acetone

Ionic hydrogenation of unsaturated compounds requires the addition of H⁺ from an acid and H[−] from a hydride source.^[8,39] The traditional mechanism for ketone hydrogenation involves coordination of the ketone to the metal followed by insertion of the ketone into a metal–hydrogen bond.^[1] In the molybdenum or tungsten cases ketone insertion occurs mostly very smoothly, but the formed alcoholate complexes were often shown to be very stable.^[18,21,22,40] Only a few examples of catalytic ionic hydrogenation reactions of ketones^[10,11] or imines^[40] with molybdenum or tungsten catalysts have been reported previously.

The reaction between the molybdenum hydride complex **2b** with $[\text{H}(\text{Et}_2\text{O})_2][\text{BAr}^{\text{F}}_4]$ in deuteriated acetone led to a singlet resonance at $\delta = 3.90$ ppm, which was attributed to the partially deuteriated 2-propanol $(\text{CD}_3)_2\text{CHOH}$.^[41] By comparing the integration of the alcohol and the $\text{BAr}^{\text{F}}_4^-$ aryl signals we can conclude that the amount of alcohol formed was the same as the amount of acid added. However, when the mixture was pressurized with 2 bar of H_2 and heated at 60°C it led to an increased alcohol signal, which was quantified by integration of this signal with reference to the aryl signals of the counter-ion. This observation points towards catalytic behaviour and we therefore studied the reaction of **4b** dissolved in $[\text{D}_6]$ acetone and pressurized with 2 bar of H_2 . The formation of the partially deuteriated 2-propanol was quantitatively pursued by ^1H NMR spectroscopy. The catalytic performance can be judged from the plot of turnover number (TON) versus time (Figure 8).

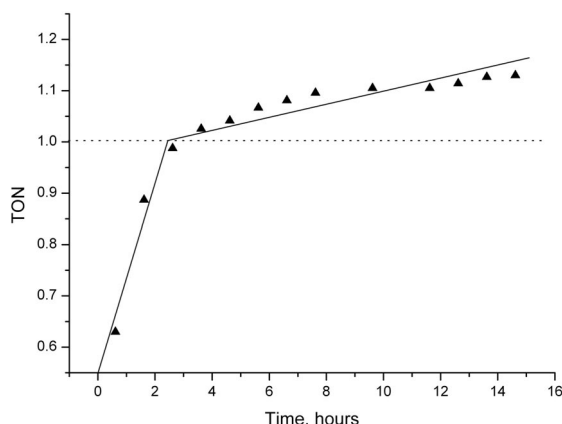


Figure 8. The catalytic activity of complex **6** in acetone hydrogenation at 60°C and 2 bar of H_2 . The linear approximation was carried out to demonstrate the jump in the reaction rate.

There is an initial steep increase in the TON with a limit at a turnover of 1, reached within 3 h. After this time the rate of 2-propanol formation was lower. This observation can be explained by a blocking effect of the molybdenum centre by the 2-propanol molecule coordinating more strongly to the metal centre than acetone. The reaction was completed within 4 d and showed a TON of 7. Ionic hydrogenation reactions with other molybdenum complexes reported in the literature^[10,42,43] revealed comparable activities. Most of the catalytic experiments showed TONs of around 1 in 1 d.

Other substrates (acetophenone, benzophenone, propionaldehyde, pivaldehyde) were also tested in hydrogenation reactions using **4b** as catalyst. Variation of the conditions in these reactions, such as different pressures of H_2 and solvents, including neat media, did not reveal the formation of the corresponding alcohol. We suppose that the bulky dippe ligands shield and additionally protect the molybdenum centre.

Conclusions

LiBH_4 as hydride donor and an appropriate amine to complex the lithium have been shown to be a suitable combination for preparing the hydride complexes **2a** and **2b** starting from the corresponding chlorides. The tungsten hydride **2a** reacted with the acid $[\text{H}(\text{Et}_2\text{O})_2][\text{BAr}^{\text{F}}_4]$ to form the seven-coordinate dihydride complex **5a** that is stable at various temperatures. The analogous molybdenum complex **5b** was found to be unstable and could be detected only in solution under H_2 . It loses H_2 at room temperature to form the $16e^-$ complex **4b** with a weak agostic interaction. In the presence of the BF_4^- anion the H_2 ligand in **3b** was substituted to form **6b**. In contrast, the BF_4^- and $\text{BAr}^{\text{F}}_4^-$ counterions were able to stabilize the seven-coordinate tungsten dihydride cation in the form of **5a** and **6a**. Complex **4b** was found to catalyse acetone hydrogenation with the formation of 2-propanol. Attempts to hydrogenate other ketonic substrates were not successful presumably because the steric congestion exerted by the dippe ligands was too great.

Experimental Section

General: Reagent-grade benzene, toluene, pentane, diethyl ether and tetrahydrofuran were dried and distilled from sodium benzophenone ketyl prior to use. Acetone and CH_2Cl_2 were dried with CaH_2 and then distilled. Literature procedures were used to prepare the following compounds: 1,2-bis(diisopropylphosphanyl)ethane (dippe),^[44] $[\text{MCl}_3(\text{CH}_3\text{CN})_2]$ ($\text{M} = \text{Mo}, \text{W}$)^[45] and $[\text{H}(\text{Et}_2\text{O})][\text{BAr}^{\text{F}}_4]$.^[28] Other reagents were purchased and used without further purification. All the manipulations were carried out under nitrogen using Schlenk techniques or in a dry glovebox. IR spectra were obtained with a Bio-Rad FTS-45 instrument. NMR spectra were measured with a Varian Mercury 200 spectrometer at 81.0 MHz for $^{31}\text{P}\{^1\text{H}\}$, with a Bruker DRX 500 spectrometer at 500.2 MHz for ^1H , 202.5 MHz for $^{31}\text{P}\{^1\text{H}\}$ and 125.8 MHz for $^{13}\text{C}\{^1\text{H}\}$ and with a Bruker DRX 400 spectrometer at 400.1 MHz for ^1H , 162.0 MHz for $^{31}\text{P}\{^1\text{H}\}$ and 100.6 MHz for $^{13}\text{C}\{^1\text{H}\}$. Chemical shifts for ^1H and $^{13}\text{C}\{^1\text{H}\}$ are given in ppm relative to TMS (SiMe_4) and for $^{31}\text{P}\{^1\text{H}\}$ NMR relative to 98% H_3PO_4 as an external reference. Elemental analyses were performed with a Leco CHN(S)-932 instrument.

[M(dippe)₂(NO)(Cl)] (1a, 1b): $[\text{MCl}_3(\text{CH}_3\text{CN})_2]$ ($\text{M} = \text{Mo}, \text{W}$; 1.0 mmol) was dissolved in THF (20 mL). The dippe ligand (650 mg , 2.5 mmol , 2.5 equiv.) in THF (15 mL) was added to the stirring solution. The reaction mixture was stirred for 12 h at the room temperature. Then 1% sodium amalgam (13.9 g ; 6.0 mmol of Na) was added to the reaction mixture and the reaction mixture was stirred for 12 h. The colour of the reaction mixture turned bright yellow. A precipitate formed and was decanted from the amalgam. The solvent was removed under low pressure. The residue was extracted with CH_2Cl_2 until the extract became colourless. After removing the solvent the residue was washed with hexane ($3 \times 10\text{ mL}$) and dried in vacuo.

1a: Yield 658 mg , 85% . ^1H NMR (400.1 MHz , CD_2Cl_2 , 25°C): $\delta = 2.62$ [m, 4 H, $\text{PCH}(\text{CH}_3)_2$], 2.49 [m, 4 H, $\text{PCH}(\text{CH}_3)_2$], 1.63 (m, 8 H, $\text{PCH}_2\text{CH}_2\text{P}$), 1.24 (m, 24 H, CH_3), 1.14 (m, 24 H, CH_3) ppm. $^{31}\text{P}\{^1\text{H}\}$ NMR (162.0 MHz , CD_2Cl_2 , 25°C): $\delta = 44.1$ [s, $^1J_{\text{PW}}$ (d, satellites) = 276.2 Hz] ppm. $^{13}\text{C}\{^1\text{H}\}$ NMR (100.6 MHz , CD_2Cl_2 ,

25 °C): δ = 29.6 (m, $\text{PCH}_2\text{CH}_2\text{P}$), 25.9 [m, $\text{PCH}_2(\text{CH}_3)_2$], 20.6 [s, $\text{PCH}_2(\text{CH}_3)_2$], 20.1 [s, $\text{PCH}_2(\text{CH}_3)_2$], 19.8 [s, $\text{PCH}_2(\text{CH}_3)_2$], 19.7 [s, $\text{PCH}_2(\text{CH}_3)_2$] ppm. IR (ATR): $\tilde{\nu}$ = 1516 (NO) cm^{-1} . $\text{C}_{28}\text{H}_{64}\text{ClMoNOP}_4\text{W}$ (774.0): calcd. C 43.45, H 8.33, N 1.81; found C 43.9, H 9.01, N 1.78.

1b: Yield 522 mg, 80%. ^1H NMR (400.1 MHz, CD_2Cl_2 , 25 °C): δ = 2.64 [m, 4 H, $\text{PCH}(\text{CH}_3)_2$], 2.47 [m, 4 H, $\text{PCH}(\text{CH}_3)_2$], 1.76 (m, 8 H, $\text{PCH}_2\text{CH}_2\text{P}$), 1.32 [m, 24 H, $\text{PCH}(\text{CH}_3)_2$], 1.23 [m, 24 H, $\text{PCH}(\text{CH}_3)_2$] ppm. $^{31}\text{P}\{^1\text{H}\}$ NMR (162.0 MHz, CD_2Cl_2 , 25 °C): δ = 59.9 (s) ppm. $^{13}\text{C}\{^1\text{H}\}$ NMR (100.6 MHz, CD_2Cl_2 , 25 °C): δ = 28.5 [s, $\text{PCH}_2(\text{CH}_3)_2$], 25.6 [s, $\text{PCH}_2(\text{CH}_3)_2$], 20.5 [s, $\text{PCH}_2(\text{CH}_3)_2$], 20.1 [s, $\text{PCH}_2(\text{CH}_3)_2$], 19.9 [s, $\text{PCH}_2(\text{CH}_3)_2$], 19.8 [s, $\text{PCH}_2(\text{CH}_3)_2$], 17.8 (m, $\text{PCH}_2\text{CH}_2\text{P}$) ppm. IR (ATR): $\tilde{\nu}$ = 1528 (NO) cm^{-1} . $\text{C}_{28}\text{H}_{64}\text{ClMoNOP}_4$ (686.1): calcd. C 49.02, H 9.40, N 2.04; found C 49.24, H 9.58, N 1.96.

[W(dippe)₂(Cl)(NO \cdots LiBH₄)] (1c): Et₃N (25 mL) was added to a mixture of [W(dippe)₂(NO)Cl] (**1a**; 470 mg, 0.6 mmol) and LiBH₄ (73 mg, 3.4 mmol, 5 equiv.). The reaction mixture was stirred for 10 h at 40 °C. Then Et₃N was evaporated under low pressure and the residue was extracted with toluene. The toluene solution was concentrated and cooled to –30 °C. The supernatant was decanted and the residue washed with cooled hexane (2 \times 5 mL) and dried in vacuo to afford **1c** as a yellow powder. Yield 260 mg, 53%. ^1H NMR (400.1 MHz, C_6D_6 , 25 °C): δ = 2.85 [m, 4 H, $\text{PCH}(\text{CH}_3)_2$], 2.61 [m, 4 H, $\text{PCH}(\text{CH}_3)_2$], 1.58 (m, 8 H, $\text{PCH}_2\text{CH}_2\text{P}$), 1.40–1.05 (m, 48 H, CH_3), 0.20 (q, $^1J_{\text{B,H}}$ = 82.0 Hz, LiBH₄) ppm. $^{31}\text{P}\{^1\text{H}\}$ NMR (162.0 MHz, C_6D_6 , 25 °C): δ = 62.9 [s, $^1J_{\text{P,W}}$ (d, satellites) = 280.1 Hz] ppm. $^{13}\text{C}\{^1\text{H}\}$ NMR (100.6 MHz, C_6D_6 , 25 °C): δ = 29.6 [s, $\text{PCH}_2(\text{CH}_3)_2$], 26.8 [s, $\text{PCH}_2(\text{CH}_3)_2$], 21.0 [s, $\text{PCH}_2(\text{CH}_3)_2$], 20.6 [s, $\text{PCH}_2(\text{CH}_3)_2$], 20.2 [s, $\text{PCH}_2(\text{CH}_3)_2$], 19.7 [s, $\text{PCH}_2(\text{CH}_3)_2$], 18.4 (m, $\text{PCH}_2\text{CH}_2\text{P}$) ppm. IR (ATR): $\tilde{\nu}$ = 1489 (NO) cm^{-1} . $\text{C}_{28}\text{H}_{68}\text{BClLiNOP}_4\text{W}$ (795.8): calcd. C 42.26, H 8.61, N 1.76; found C 42.59, H 8.76, N 1.89.

[W(dippe)₂(H)(NO \cdots LiBH₄)] (2c): Et₃N (20 mL) was added to a mixture of [W(dippe)₂(NO)Cl] (**1a**; 470 g, 0.61 mmol) and LiBH₄ (73 mg, 3.4 mmol, 5 equiv.). The suspension was stirred at 70 °C for 15 h until no trace of starting material was observed (ca. 15 h, monitoring with ^{31}P NMR). Then Et₃N was removed under low pressure and the residue was extracted with toluene. The precipitate was filtered off. After removing toluene the residue was washed with hexane (3 \times 5 mL) and dried in vacuo. Yield 362 mg, 78%. ^1H NMR (400.1 MHz, C_6D_6 , 25 °C): δ = 2.24 [m, 4 H, $\text{PCH}(\text{CH}_3)_2$], 1.98 [m, 4 H, $\text{PCH}(\text{CH}_3)_2$], 1.23 (m, 32 H, CH_3 and $\text{PCH}_2\text{CH}_2\text{P}$), 1.01 (m, 12 H, CH_3), 0.87 (m, 12 H, CH_3), 0.15 (q, $^1J_{\text{B,H}}$ = 82.0 Hz, 4 H, LiBH₄), –2.91 (m, $^2J_{\text{P,H}}$ = 26.3 Hz, 1 H, W–H) ppm. $^{31}\text{P}\{^1\text{H}\}$ NMR (162.0 MHz, C_6D_6 , 25 °C): δ = 63.8 [s, $^1J_{\text{P,W}}$ (d, satellites) = 274.3 Hz] ppm. $^{13}\text{C}\{^1\text{H}\}$ NMR (100.6 MHz, C_6D_6 , 25 °C): δ = 28.4 [s, $\text{PCH}_2(\text{CH}_3)_2$], 25.7 [s, $\text{PCH}_2(\text{CH}_3)_2$], 20.5 [s, $\text{PCH}_2(\text{CH}_3)_2$], 20.3 [s, $\text{PCH}_2(\text{CH}_3)_2$], 19.8 [s, $\text{PCH}_2(\text{CH}_3)_2$], 19.1 [s, $\text{PCH}_2(\text{CH}_3)_2$], 17.6 (m, $\text{PCH}_2\text{CH}_2\text{P}$) ppm. IR (ATR): $\tilde{\nu}$ = 1672 (W–H) 1459 (NO) cm^{-1} . $\text{C}_{28}\text{H}_{69}\text{BLiNOP}_4\text{W}$ (761.3): calcd. C 44.17, H 9.13, N 1.84; found C 43.94, H 9.03, N 1.94.

[W(dippe)₂(NO)H] (2a): Et₃N (30 mL) was added to a mixture of [W(dippe)₂(NO)Cl] (**1a**; 774 mg, 1.0 mmol) and LiBH₄ (110 mg, 5.0 mmol, 5 equiv.). The suspension was stirred at 70 °C for 15 h until no trace of starting material was observed (ca. 15 h, monitoring with ^{31}P NMR). Then Et₃N was removed under low pressure and the residue was extracted with toluene. $\text{NH}_2\text{CH}_2\text{CH}_2\text{NH}_2$ (2 mL) was added to the toluene solution to remove LiBH₄ coordinated to the NO group. The precipitate was filtered off. The residue, after removing toluene under low pressure, was washed with hexane (3 \times 5 mL) and dried in vacuo. Yield 510 mg, 69%. ^1H NMR

(400.1, C_6D_6 , 25 °C): δ = 2.47 (m, 4 H, $\text{PCH}_2\text{CH}_2\text{P}$), 2.10 [m, 4 H, $\text{PCH}(\text{CH}_3)_2$], 1.36 [m, 24 H, $\text{PCH}(\text{CH}_3)_2$], 1.15 [m, 12 H, $\text{PCH}(\text{CH}_3)_2$], 1.04 [m, 12 H, $\text{PCH}(\text{CH}_3)_2$], –3.38 (m, $^2J_{\text{P,H}}$ = 24.8 Hz, 1 H, W–H) ppm. $^{31}\text{P}\{^1\text{H}\}$ NMR (162.0 MHz, C_6D_6 , 25 °C): δ = 64.5 [s, $^1J_{\text{P,W}}$ (d, satellites) = 279.7 Hz] ppm. $^{13}\text{C}\{^1\text{H}\}$ NMR (160.5 MHz, C_6D_6 , 25 °C): δ = 32.0 [m, $\text{PCH}_2(\text{CH}_3)_2$], 30.0 [m, $\text{PCH}_2(\text{CH}_3)_2$], 23.8 (m, $\text{PCH}_2\text{CH}_2\text{P}$), 21.2 [s, $\text{PCH}_2(\text{CH}_3)_2$], 20.4 [s, $\text{PCH}_2(\text{CH}_3)_2$], 20.3 [s, $\text{PCH}_2(\text{CH}_3)_2$], 18.5 [s, $\text{PCH}_2(\text{CH}_3)_2$] ppm. IR (ATR): $\tilde{\nu}$ = 1670 (W–H) 1456 (NO) cm^{-1} . $\text{C}_{28}\text{H}_{65}\text{NOP}_4\text{W}$ (739.6): calcd. C 45.47, H 8.86, N 1.89; found C 45.66, H 8.81, N 2.00.

[Mo(dippe)₂(NO)H] (2b): Et₃N (15 mL) was added to a mixture of [Mo(dippe)₂(NO)Cl] (**1b**; 275 mg, 0.4 mmol) and LiBH₄ (28 mg, 2.0 mmol, 5 equiv.). The suspension was stirred at 70 °C until no trace of starting material was observed (ca. 15 h, monitoring with ^{31}P NMR). Then Et₃N was removed under low pressure and the residue was extracted with toluene. The toluene fractions were combined and the solvent was removed in vacuo. The substance remaining after the evaporation of toluene was washed with hexane (3 \times 3 mL) and dried in vacuo. Yield 180 mg, 69%. ^1H NMR (200 MHz, C_6D_6 , 25 °C): δ = 2.52 (m, 8 H, $\text{PCH}_2\text{CH}_2\text{P}$), 2.23 [m, 8 H, $\text{PCH}(\text{CH}_3)_2$], 1.57–1.32 (m, 48 H, CH_3), –3.80 (m, $^1J_{\text{H,W}}$ = 28.3 Hz, 1 H, Mo–H) ppm. $^{31}\text{P}\{^1\text{H}\}$ NMR (80 MHz, C_6D_6 , 25 °C): δ = 85.8 (s) ppm. $^{13}\text{C}\{^1\text{H}\}$ NMR (160.5 MHz, C_6D_6 , 25 °C): δ = 31.2 [m, $\text{PCH}_2(\text{CH}_3)_2$], 28.9 [m, $\text{PCH}_2(\text{CH}_3)_2$], 21.2 (m, $\text{PCH}_2\text{CH}_2\text{P}$), 21.0 [s, $\text{PCH}_2(\text{CH}_3)_2$], 20.2 [s, $\text{PCH}_2(\text{CH}_3)_2$], 20.1 [s, $\text{PCH}_2(\text{CH}_3)_2$], 18.5 [s, $\text{PCH}_2(\text{CH}_3)_2$] ppm. IR (ATR): $\tilde{\nu}$ = 1601 (W–H) 1500 (NO) cm^{-1} . $\text{C}_{28}\text{H}_{65}\text{MoNOP}_4$ (651.7): calcd. C 51.61, H 10.05, N 2.15; found C 51.72, H 10.00, N 2.14.

[Mo(dippe)₂(NO)][BAR^F₄] (4b): THF (5 mL) was added to a mixture of [Mo(dippe)₂(NO)H] (**2b**; 50.0 mg, 0.077 mmol) and [H(Et₂O)]-[BAR^F₄] (77.8 mg, 0.077 mmol). After the evolution of hydrogen gas had stopped (few minutes) the solvent was removed in vacuo. The green residue was washed with pentane (3 \times 5 mL). Yield 107.3 mg, 92%. ^1H NMR (500.2 MHz, [D₈]THF, 25 °C): δ = 7.79 (s, 8 H, *o*-Ph), 7.57 (s, 4 H, *p*-Ph), 2.64 [m, 4 H, $\text{PCH}(\text{CH}_3)_2$], 2.45 [m, 4 H, $\text{PCH}(\text{CH}_3)_2$], 2.08 (s, 8 H, $\text{PCH}_2\text{CH}_2\text{P}$), 1.40–1.20 (m, 36 H, CH_3), 0.60 (m, 12 H, CH_3) ppm. $^{31}\text{P}\{^1\text{H}\}$ NMR (202.5 MHz, [D₈]THF, 25 °C): δ = 73.6 (s) ppm. $^{13}\text{C}\{^1\text{H}\}$ NMR (100.6 MHz, [D₈]THF, 25 °C): δ = 163.0 (C_{quat} , $^1J_{\text{B,C}}$ = 50.1 Hz, *i*-BAR^F₄), 135.8 (s, *o*-BAR^F₄), 130.1 (m, *m*-BAR^F₄), 125.5 (C_{quat} , $^1J_{\text{C,F}}$ = 273.1 Hz, CF₃), 118.4 (s, *p*-BAR^F₄), 28.6 [m, $\text{PCH}_2(\text{CH}_3)_2$], 19.9 [s, $\text{PCH}_2(\text{CH}_3)_2$], 19.4 [s, $\text{PCH}_2(\text{CH}_3)_2$], 19.1 [s, $\text{PCH}_2(\text{CH}_3)_2$], 18.9 (t, $^1J_{\text{C,P}}$ = 7.2 Hz, $\text{PCH}_2\text{CH}_2\text{P}$) ppm. $^{19}\text{F}\{^1\text{H}\}$ NMR (376.5 MHz, [D₈]THF, 25 °C): δ = –65.43 (s, CF₃) ppm. IR (ATR): $\tilde{\nu}$ = 1591 (NO) cm^{-1} . $\text{C}_{60}\text{H}_{76}\text{BF}_4\text{MoNOP}_4$ (1513.9): calcd. C 47.60, H 5.06, N 0.93; found C 47.62, H 5.10, N 0.97.

[W(dippe)(H)₂(dippe)(NO)][BAR^F₄] (5a): Et₂O (1.0 mL) was added to a mixture of [W(NO)(dippe)₂H] (**2a**; 17.1 mg, 0.023 mmol) and [H(Et₂O)]-[BAR^F₄] (23.4 mg, 0.023 mmol). A white precipitate formed immediately. The precipitate was filtered off, washed with Et₂O (3 \times 1 mL) and dried in vacuo. Yield 25.3 mg, 68%. $^1\text{H}\{^{31}\text{P}\}$ NMR (500.2 MHz, [D₈]THF, 25 °C): δ = 7.80 (s, 8 H, *o*-BAR^F), 7.59 (s, 4 H, *p*-BAR^F), 2.67 [m, 2 H, $\text{PCH}(\text{CH}_3)_2$], 2.59 [m, 2 H, $\text{PCH}(\text{CH}_3)_2$], 2.32 (m, 4 H, $\text{PCH}_2\text{CH}_2\text{P}$), 2.22 [m, 2 H, $\text{PCH}(\text{CH}_3)_2$], 2.15 (t, 2 H, $\text{PCH}_2\text{CH}_2\text{P}$), 1.99 (t, 2 H, $\text{PCH}_2\text{CH}_2\text{P}$), 1.89 [m, 2 H, $\text{PCH}(\text{CH}_3)_2$], 1.76 (s, 2 H, W–H₂), 1.50–1.43 (m, 6 H, CH_3), 1.41 (d, $^1J_{\text{H,H}}$ = 65.2 Hz, 6 H, CH_3), 1.37 (d, $^1J_{\text{H,H}}$ = 65.3 Hz, 6 H, CH_3), 1.33 (d, $^1J_{\text{H,H}}$ = 65.2 Hz, 6 H, CH_3), 1.31 (d, $^1J_{\text{H,H}}$ = 65.3 Hz, 6 H, CH_3), 1.16 (d, $^1J_{\text{H,H}}$ = 65.2 Hz, 6 H, CH_3), 1.12 (d, $^1J_{\text{H,H}}$ = 65.2 Hz, 6 H, CH_3) ppm. $^{31}\text{P}\{^1\text{H}\}$ NMR (202.5 MHz, [D₈]THF, 25 °C): δ = 69.3 [dt, $^2J_{\text{P,P}}$ = 5.5, $^2J_{\text{P,P}}$ = 17.7,

$^1J_{W,P}(d, \text{satellites}) = 144.0 \text{ Hz}$, $61.9 \text{ [dd, } ^2J_{P,P} = 23.7, ^2J_{P,P} = 17.7, ^1J_{W,P}(d, \text{satellites}) = 158.0 \text{ Hz}]$, $27.6 \text{ [dt, } ^2J_{P,P} = 23.7, ^2J_{P,P} = 5.5, ^1J_{W,P}(d, \text{satellites}) = 96.0 \text{ Hz}]$ ppm. $^{13}\text{C}\{^1\text{H}\}$ NMR (160.5 MHz, $[\text{D}_8]\text{THF}$, 25°C): $\delta = 163.0$ (C_{quat} , $^1J_{B,C} = 50.5 \text{ Hz}$, $i\text{-BAR}^F_4$), 135.6 (s, $o\text{-BAR}^F_4$), 130.1 (m, $m\text{-BAR}^F_4$), 125.5 (C_{quat} , $^1J_{C,F} = 273.1 \text{ Hz}$, CF_3), 118.4 (s, $p\text{-BAR}^F_4$), 29.8 [s, $\text{PCH}_2(\text{CH}_3)_2$], 29.7 [s, $\text{PCH}_2(\text{CH}_3)_2$], 29.5 [s, $\text{PCH}_2(\text{CH}_3)_2$], 29.4 [s, $\text{PCH}_2(\text{CH}_3)_2$], 29.3 [s, $\text{PCH}_2(\text{CH}_3)_2$], 29.2 [s, $\text{PCH}_2(\text{CH}_3)_2$], 26.5 [s, $\text{PCH}_2(\text{CH}_3)_2$], 26.3 [s, $\text{PCH}_2(\text{CH}_3)_2$], 24.7 (m, PCH_2CH_3), 23.2 (m, PCH_2CH_3), 20.5 [s, $\text{PCH}_2(\text{CH}_3)_2$], 20.4 [s, $\text{PCH}_2(\text{CH}_3)_2$], 20.3 [s, $\text{PCH}_2(\text{CH}_3)_2$], 20.2 [s, $\text{PCH}_2(\text{CH}_3)_2$], 19.6 [s, $\text{PCH}_2(\text{CH}_3)_2$], 19.5 [s, $\text{PCH}_2(\text{CH}_3)_2$], 19.2 [s, $\text{PCH}_2(\text{CH}_3)_2$], 18.6 [s, $\text{PCH}_2(\text{CH}_3)_2$] ppm. $^{19}\text{F}\{^1\text{H}\}$ NMR (376.5 MHz, $[\text{D}_8]\text{THF}$, 25°C): $\delta = -64.5$ (s, CF_3) ppm. IR (ATR): $\tilde{\nu} = 1613$ (NO), 1466 (W–H) cm^{-1} . $\text{C}_{60}\text{H}_{78}\text{BF}_{24}\text{NOP}_4\text{W}$ (1603.8): calcd. C 44.93, H 4.90, N 0.87; found C 44.99, H 4.86, N 0.89.

[W(dippe)(H)₂(dippe)(NO)][BF₄] (6a): A 57% solution of $\text{HBF}_4 \cdot \text{Et}_2\text{O}$ (ca. 7 μL) was added dropwise to a solution of $[\text{W}(\text{NO})(\text{dippe})_2\text{H}]$ (**2a**; 25.0 mg, 0.034 mmol) in Et_2O (3 mL). A white precipitate formed immediately. The precipitate was filtered off, washed with Et_2O ($3 \times 1 \text{ mL}$) and dried in vacuo. Yield 18.7 mg, 67%. $^1\text{H}\{^{31}\text{P}\}$ NMR (500.2 MHz, $[\text{D}_8]\text{THF}$, 25°C): $\delta = 2.65$ [m, 2 H, $\text{PCH}(\text{CH}_3)_2$], 2.59 [m, 2 H, $\text{PCH}(\text{CH}_3)_2$], 2.43 (m, 4 H, $\text{PCH}_2\text{CH}_2\text{P}$), 2.31 [m, 2 H, $\text{PCH}(\text{CH}_3)_2$], 2.24 (m, 2 H, $\text{PCH}_2\text{CH}_2\text{P}$), 2.20 (m, 2 H, $\text{PCH}_2\text{CH}_2\text{P}$), 2.02 [m, 2 H, $\text{PCH}(\text{CH}_3)_2$], 1.91 [m, $\text{PCH}(\text{CH}_3)_2$], 1.76 [s, 2 H, W–(H)₂], 1.48 – 1.43 (m, 6 H, CH_3), 1.39 – 1.32 (m, 12 H, CH_3), 1.18 – 1.13 (m, 6 H, CH_3) ppm. $^{31}\text{P}\{^1\text{H}\}$ NMR (202.5 MHz, $[\text{D}_8]\text{THF}$, 25°C): $\delta = 69.2$ [dt, $^2J_{P,P} = 5.8, ^2J_{P,P} = 17.7, ^1J_{W,P}(d, \text{satellites}) = 144.5 \text{ Hz}]$, 61.9 [dd, $^2J_{P,P} = 23.1, ^2J_{P,P} = 17.7, ^1J_{W,P}(d, \text{satellites}) = 160.6 \text{ Hz}]$, 27.3 [dt, $^2J_{P,P} = 23.1, ^2J_{P,P} = 5.8, ^1J_{W,P}(d, \text{satellites}) = 99.8 \text{ Hz}]$ ppm. $^{13}\text{C}\{^1\text{H}\}$ NMR (160.5 MHz, $[\text{D}_8]\text{THF}$, 25°C): $\delta = 29.4$ [m, $\text{PCH}_2(\text{CH}_3)_2$], 26.3 [d, $^1J_{C,P} = 13.1 \text{ Hz}$, $\text{PCH}_2(\text{CH}_3)_2$], 24.7 (t, $^1J_{C,P} = 18.7 \text{ Hz}$), 23.5 (dd, $^1J_{C,P} = 26.3 \text{ Hz}$, $\text{PCH}_2\text{CH}_2\text{P}$), 23.0 (dd, $^1J_{C,P} = 22.9 \text{ Hz}$, $\text{PCH}_2\text{CH}_2\text{P}$), 20.6 (s, CH_3), 20.5 (s, CH_3), 20.3 (s, CH_3), 20.0 (s, CH_3), 19.6 (s, CH_3), 19.6 (s, CH_3), 19.3 (d, $^2J_{C,P} = 1.3 \text{ Hz}$, CH_3), 18.6 (d, $^2J_{C,P} = 1.7 \text{ Hz}$, CH_3) ppm. $^{19}\text{F}\{^1\text{H}\}$ NMR (376.5 MHz, $[\text{D}_8]\text{THF}$, 25°C): $\delta = -155.3$ (s, CF_3) ppm. IR (ATR): $\tilde{\nu} = 1584$ (NO), 1462 (W–H) cm^{-1} . $\text{C}_{28}\text{H}_{66}\text{BF}_4\text{NOP}_4\text{W}$ (827.4): calcd. C 40.65, H 8.04, N 1.69; found C 40.82, H 7.97, N 1.60.

[Mo(dippe)₂(NO)][BF₄] (6b): A 57% diethyl ether solution of $[\text{H}(\text{Et}_2\text{O})][\text{BF}_4]$ was added dropwise to a solution of $[\text{Mo}(\text{NO})(\text{dippe})_2\text{H}]$ (**2b**; 56.0 mg, 0.086 mmol) in Et_2O (5 mL) until the evolution of H_2 gas had stopped (ca. 15 μL). Then the reaction mixture was stirred for 2 h. The ether solution was decanted from the red precipitate formed and then the precipitate was extracted with diethyl ether until the solution became colourless. The combined organic fractions were concentrated in vacuo to a volume of 10 mL and cooled to -30°C . The precipitate formed was filtered, washed with cooled diethyl ether and dried in vacuo. Yield 46.4 mg, 73%. $^1\text{H}\{^{31}\text{P}\}$ NMR (500.2 MHz, $[\text{D}_8]\text{THF}$, 25°C): $\delta = 2.59$ [m, 4 H, $\text{PCH}(\text{CH}_3)_2$], 2.42 [m, 4 H, $\text{PCH}(\text{CH}_3)_2$], 1.96 (m, 4 H, $\text{PCH}_2\text{CH}_2\text{P}$), 1.83 (m, 4 H, $\text{PCH}_2\text{CH}_2\text{P}$), 1.37 (d, $^1J_{H,H} = 7.1 \text{ Hz}$, 12 H, CH_3), 1.35 (d, $^1J_{H,H} = 7.1 \text{ Hz}$, 12 H, CH_3), 1.22 (d, $^1J_{H,H} = 7.0 \text{ Hz}$, 12 H, CH_3), 1.20 (d, $^1J_{H,H} = 7.1 \text{ Hz}$, 12 H, CH_3) ppm. $^{31}\text{P}\{^1\text{H}\}$ NMR (202.5 MHz, $[\text{D}_8]\text{THF}$, 25°C): $\delta = 64.5$ (s) ppm. $^{13}\text{C}\{^1\text{H}\}$ NMR (160.5 MHz, $[\text{D}_8]\text{THF}$, 25°C): $\delta = 29.2$ [m, $\text{PCH}_2(\text{CH}_3)_2$], 24.8 [m, $\text{PCH}_2(\text{CH}_3)_2$], 20.8 [s, $\text{PCH}_2(\text{CH}_3)_2$], 20.2 [s, $\text{PCH}_2(\text{CH}_3)_2$], 20.0 [s, $\text{PCH}_2(\text{CH}_3)_2$], 19.7 [s, $\text{PCH}_2(\text{CH}_3)_2$], 17.7 (m, $\text{PCH}_2\text{CH}_2\text{P}$) ppm. $^{19}\text{F}\{^1\text{H}\}$ NMR (376.5 MHz, $[\text{D}_8]\text{THF}$, 25°C): $\delta = -156.8$ (s, FBF_3), 156.9 (s, FBF_3) ppm. $\text{C}_{28}\text{H}_{64}\text{BF}_4\text{MoNOP}_4$ (737.5): calcd. C 45.60, H 8.75, N 1.90; found C 45.47, H 8.68, N 1.98.

Reaction of $[\text{Mo}(\text{dippe})_2(\text{NO})][\text{BAR}^F_4]$ (4b**) with H_2 :** $[\text{Mo}(\text{NO})(\text{dippe})_2][\text{BAR}^F_4]$ (**4b**; 15.0 mg) was placed in a Young NMR tube. Then $[\text{D}_8]\text{THF}$ (0.7 mL) was added. The NMR tube was filled with 1.8 bar of H_2 gas. After shaking the NMR tube the colour of the solution changed from green to yellow. The estimated conversion is 80% (according to $^{31}\text{P}\{^1\text{H}\}$ NMR). $^1\text{H}\{^{31}\text{P}\}$ NMR (500.2 MHz, $[\text{D}_8]\text{THF}$, 25°C): $\delta = 7.80$ (s, 8 H, $o\text{-BAR}^F$), 7.59 (s, 4 H, $p\text{-BAR}^F$), 2.63 [m, 2 H, $\text{PCH}(\text{CH}_3)_2$], 2.57 [m, 4 H, $\text{PCH}(\text{CH}_3)_2$], 2.28 (m, 4 H, $\text{PCH}_2\text{CH}_2\text{P}$), 2.19 [m, 2 H, $\text{PCH}(\text{CH}_3)_2$], 2.11 (m, 2 H, $\text{PCH}_2\text{CH}_2\text{P}$), 1.88 (m, 2 H, $\text{PCH}_2\text{CH}_2\text{P}$), 1.49 – 1.29 (m, 36 H, CH_3), 1.15 – 1.09 (m, 36 H, CH_3), 0.32 [s, 2 H, Mo–(H)₂] ppm. $^{31}\text{P}\{^1\text{H}\}$ NMR (202.5 MHz, $[\text{D}_8]\text{THF}$, 25°C): $\delta = 87.5$ (t, $^2J_{P,P} = 22.4 \text{ Hz}$), 73.7 (t, $^2J_{P,P} = 22.4 \text{ Hz}$), 39.9 (t, $^2J_{P,P} = 24.0 \text{ Hz}$) ppm. $^{13}\text{C}\{^1\text{H}\}$ NMR (100.6 MHz, $[\text{D}_8]\text{THF}$, 25°C): $\delta = 163.0$ (C_{quat} , $^1J_{B,C} = 50.3 \text{ Hz}$, $i\text{-BAR}^F_4$), 135.8 (s, $o\text{-BAR}^F_4$), 130.1 (m, $m\text{-BAR}^F_4$), 125.5 (C_{quat} , $^1J_{C,F} = 273.1 \text{ Hz}$, CF_3), 118.4 (s, $p\text{-BAR}^F_4$), 29.9 [d, $^1J_{C,P} = 26.2 \text{ Hz}$, $\text{PCH}(\text{CH}_3)_2$], 29.2 [t, $^1J_{C,P} = 11.9 \text{ Hz}$, $\text{PCH}(\text{CH}_3)_2$], 28.8 [t, $^1J_{C,P} = 8.3 \text{ Hz}$, $\text{PCH}(\text{CH}_3)_2$], 26.1 [d, $^1J_{C,P} = 10.9 \text{ Hz}$, $\text{PCH}(\text{CH}_3)_2$], 24.0 (t, $^1J_{C,P} = 17.9 \text{ Hz}$, $\text{PCH}_2\text{CH}_2\text{P}$), 22.7 (dd, $^1J_{C,P} = 9.5 \text{ Hz}$, $\text{PCH}_2\text{CH}_2\text{P}$), 21.3 (dd, $^1J_{C,P} = 8.3 \text{ Hz}$, $\text{PCH}_2\text{CH}_2\text{P}$), 20.5 [s, $\text{PCH}_2(\text{CH}_3)_2$], 20.3 [s, $\text{PCH}_2(\text{CH}_3)_2$], 20.1 [s, $\text{PCH}_2(\text{CH}_3)_2$], 20.0 [s, $\text{PCH}_2(\text{CH}_3)_2$], 19.6 [s, $\text{PCH}_2(\text{CH}_3)_2$], 19.5 [s, $\text{PCH}_2(\text{CH}_3)_2$], 19.2 [s, $\text{PCH}_2(\text{CH}_3)_2$], 18.6 [s, $\text{PCH}_2(\text{CH}_3)_2$] ppm.

Catalytic Hydrogenation of $[\text{D}_6]\text{Acetone}$: $[\text{Mo}(\text{dippe})_2(\text{NO})][\text{BAR}^F_4]$ (13.7 mg, 0.009 mmol) was placed in a Young NMR tube. $[\text{D}_6]\text{acetone}$ (0.6 mL) was added. The mixture was pressurized with 2.0 bar of hydrogen gas and heated at 60°C . The reaction progress was monitored by ^1H NMR spectroscopy recording spectra every hour. The singlet resonance of the BAR^F_4 counter-ion at $\delta = 7.66$ ppm was taken as a reference signal to calculate the rate of formation of the isopropyl alcohol.

X-ray Diffraction Studies of **1a–c, **2a**, **2c**, **4b**, **5a**, **6a** and **6b**:** Relevant details regarding the structure refinements are given in Tables S1 and S2 of the Supporting Information and selected geometrical parameters are included in the captions of the corresponding figures. Intensity data were collected at 183(2) K with a Stoe IPDS diffractometer (Imaging Plate Detector System with graphite-monochromated Mo- K_α radiation, $\lambda = 0.71073 \text{ \AA}$)^[46] for **1a** and **1c** and an Oxford Xcalibur diffractometer (4-circle kappa platform, Ruby CCD detector, and a single wavelength Enhance X-ray source with Mo- K_α radiation, $\lambda = 0.71073 \text{ \AA}$)^[47] for the other crystals. The selected suitable single-crystals were mounted using polybutene oil on the top of a glass fibre fixed on a goniometer head and immediately transferred to the diffractometer. The crystal structures were solved with SHELXS-97^[48] using direct methods. The structure refinements were performed by full-matrix least-squares methods on F^2 with SHELXL-97.^[48] The program PLATON^[49] was used to check the results of the X-ray analyses. All hydrogen atoms were placed at ideal positions and refined with fixed isotropic displacement parameters using a riding model.

CCDC-767893 (for **1a**), -767894 (for **1b**), -767895 (for **1c**), -767896 (for **2a**), -767897 (for **2c**), -767898 (for **4b**), -767899 (for **5a**), -767900 (for **6a**), and -767901 (for **6b**) contain the supplementary crystallographic data for this paper. These data can be obtained free of charge from The Cambridge Crystallographic Data Centre via www.ccdc.cam.ac.uk/data_request/cif.

Supporting Information (see also the footnote on the first page of this article): Crystallographic data for compounds **1a–c**, **2a**, **2c**, **4b**, **5a**, **6a** and **6b**, ORTEP drawings of **1b**, **2c** and **6a**, experimental and refinement details of the X-ray diffraction studies of **1a–c**, **2a**, **2c**, **4b**, **5a**, **6a** and **6b**.

Acknowledgments

We thank the University of Zürich and the Swiss National Science Foundation for financial support.

- [1] P. A. Chaloner, M. A. Esteruelas, F. Jos, L. A. Oro, *Homogeneous Hydrogenation*, Kluwer Academic Publishers, Dordrecht, **1994**.
- [2] R. M. Bullock, *Chem. Eur. J.* **2004**, *10*, 2366–2374.
- [3] H. Berke, *Chem. Phys. Chem.* **2010**, in press.
- [4] T.-Y. Cheng, B. S. Brunschwig, M. R. Bullock, *J. Am. Chem. Soc.* **1998**, *120*, 13121–13137.
- [5] T. Y. Cheng, R. M. Bullock, *J. Am. Chem. Soc.* **1999**, *121*, 3150–3155.
- [6] T. Y. Cheng, R. M. Bullock, *Organometallics* **2002**, *21*, 2325–2331.
- [7] R. M. Bullock, J. S. Song, *J. Am. Chem. Soc.* **1994**, *116*, 8602–8612.
- [8] L. Luan, J. S. Song, R. M. Bullock, *J. Org. Chem.* **1995**, *60*, 7170–7176.
- [9] J. S. Song, D. J. Szalda, R. M. Bullock, C. J. C. Lawrie, M. A. Rodkin, J. R. Norton, *Angew. Chem. Int. Ed. Engl.* **1992**, *31*, 1233–1235.
- [10] M. R. Bullock, M. H. Voges, *J. Am. Chem. Soc.* **2000**, *122*, 12594–12595.
- [11] M. H. Voges, R. M. Bullock, *J. Chem. Soc., Dalton Trans.* **2002**, 759–770.
- [12] G. J. Kubas, *J. Organomet. Chem.* **2001**, *635*, 37–68.
- [13] G. J. Kubas, R. R. Ryan, C. J. Unkefer, *J. Am. Chem. Soc.* **1987**, *109*, 8113–8115.
- [14] G. J. Kubas, C. J. Burns, J. Eckert, S. W. Johnson, A. C. Larson, P. J. Vergamini, C. J. Unkefer, G. R. K. Khalsa, S. A. Jackson, O. Eisenstein, *J. Am. Chem. Soc.* **1993**, *115*, 569–581.
- [15] G. J. Kubas, R. R. Ryan, D. A. Wroblewski, *J. Am. Chem. Soc.* **1986**, *108*, 1339–1341.
- [16] B. F. M. Kimmich, P. J. Fagan, E. Hauptman, W. J. Marshall, R. M. Bullock, *Organometallics* **2005**, *24*, 6220–6229.
- [17] B. F. M. Kimmich, P. J. Fagan, E. Hauptman, R. M. Bullock, *Chem. Commun.* **2004**, 1014–1015.
- [18] Z. Chen, H. W. Schmalle, T. Fox, H. Berke, *Dalton Trans.* **2005**, 580–587.
- [19] N. Avramovic, O. Blacque, H. Berke, *Acta Crystallogr., Sect. E: Struct. Rep. Online* **2008**, *64*, m242.
- [20] F. A. Cotton, R. Llusar, *Acta Crystallogr., Sect. C: Cryst. Struct. Commun.* **1988**, *44*, 952–955.
- [21] L. Fupei, H. W. Schmalle, T. Fox, H. Berke, *Organometallics* **2003**, *22*, 3382–3393.
- [22] J. Cugny, H. W. Schmalle, T. Fox, O. Blacque, M. Alfonso, H. Berke, *Eur. J. Inorg. Chem.* **2006**, 540–552.
- [23] E. F. van der Eide, W. E. Piers, M. Parvez, R. McDonald, *Inorg. Chem.* **2007**, *46*, 14–21.
- [24] L. Fupei, H. W. Schmalle, H. Berke, *J. Organomet. Chem.* **2006**, *691*, 5655–5663.
- [25] L. Fupei, H. W. Schmalle, H. Berke, *Eur. J. Inorg. Chem.* **2006**, 5081–5088.
- [26] H. H. Giese, T. Haberer, J. Knizek, H. Nöth, M. Warchhold, *Eur. J. Inorg. Chem.* **2001**, 1195–1205.
- [27] F. Furno, T. Fox, H. W. Schmalle, H. Berke, *Organometallics* **2000**, *19*, 3620–3630.
- [28] M. Brookhart, B. Grant, A. F. Volpe, *Organometallics* **1992**, *11*, 3920–3922.
- [29] P. J. Alaimo, B. A. Arndtsen, R. G. Bergman, *J. Am. Chem. Soc.* **1997**, *119*, 5269–5270.
- [30] G. J. Kubas, *Metal Dihydrogen and Bond Complexes: Structure, Theory and Reactivity*, Kluwer Academic/Plenum Publishers, New York, **2001**.
- [31] M. Brookhart, M. L. H. Green, *J. Organomet. Chem.* **1983**, *250*, 395–408.
- [32] M. Sato, T. Tatsumi, T. Kodama, M. Hidai, T. Uchida, Y. Uchida, *J. Am. Chem. Soc.* **1978**, *100*, 4447–4452.
- [33] X. L. Luo, G. J. Kubas, C. J. Burns, J. Eckert, *Inorg. Chem.* **1994**, *33*, 5219–5229.
- [34] M. P. Mitoraj, A. Michalak, T. Ziegler, *Organometallics* **2009**, *28*, 3727–3733.
- [35] D. A. Pantazis, J. E. McGrady, M. Besora, F. Maseras, M. Etienne, *Organometallics* **2008**, *27*, 1128–1134.
- [36] X. L. Luo, G. J. Kubas, C. J. Burns, R. Butcher, J. C. Bryan, *Inorg. Chem.* **1995**, *34*, 6538–6545.
- [37] R. V. Honeychuck, W. H. Hersh, *Inorg. Chem.* **1989**, *28*, 2869–2886.
- [38] L. S. Vandersluys, K. A. Kubatmartin, G. J. Kubas, K. G. Caulton, *Inorg. Chem.* **1991**, *30*, 306–310.
- [39] D. N. Kursanov, Z. N. Parnes, N. M. Loim, *Synthesis* **1974**, 633–651.
- [40] Y. Zhao, H. W. Schmalle, T. Fox, O. Blacque, H. Berke, *Dalton Trans.* **2005**, 73–85.
- [41] H. E. Gottlieb, V. Kotlyar, A. Nudelman, *J. Org. Chem.* **1997**, *62*, 7512–7515.
- [42] M. H. Voges, M. R. Bullock, *J. Chem. Soc., Dalton Trans.* **2002**, 759–770.
- [43] F. Wu, V. K. Dioumaev, D. J. Szalda, J. Hanson, R. M. Bullock, *Organometallics* **2007**, *26*, 5079–5090.
- [44] R. J. Burt, J. Chatt, W. Hussain, G. J. Leigh, *J. Organomet. Chem.* **1979**, *182*, 203–206.
- [45] L. Bencze, J. Kohan, *Inorg. Chim. Acta* **1982**, *65*, L17–L19.
- [46] STOE & Cie, GmbH, Darmstadt, Germany, **1999**.
- [47] Xcalibur CCD System, Oxford Diffraction Ltd., Abingdon, England, **2007**.
- [48] G. M. Sheldrick, *Acta Crystallogr., Sect. A* **2008**, *64*, 112–122.
- [49] A. L. Spek, *J. Appl. Crystallogr.* **2003**, *36*, 7–13.

Received: March 16, 2010

Published Online: June 11, 2010

Acentric Polymeric Chains in Radical Cation Salts of Tetrathiafulvalene Derivatives with the *p*-Carboxybenzenesulfonate Anion

Youssef Lakhdar,^[a] Abdelkrim El-Ghayoury,^[a] Leokadiya Zorina,^[a,b] Nicolas Mercier,^[a] Magali Allain,^[a] Cécile Mézière,^[a] Pascale Auban-Senzier,^[c] Patrick Batail,^[a] and Michel Giffard*^[a]

Keywords: Tetrathiafulvalenes / Conducting materials / Mixed-valent compounds / Noncentrosymmetry / Self-assembly

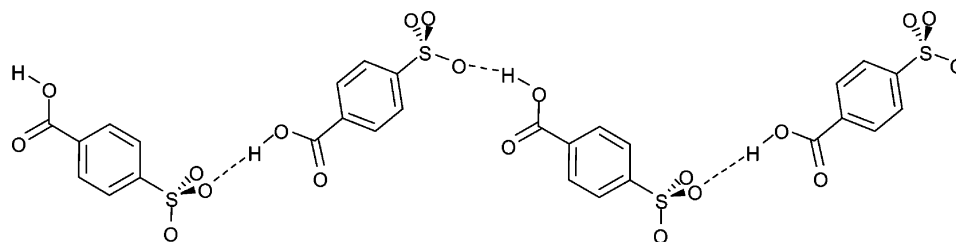
The noncentrosymmetric *p*-carboxybenzenesulfonate anion afforded, in electro-oxidation experiments with bis(ethylenedithio)tetrathiafulvalene (BEDT-TTF), the low-gap semiconductor (room-temperature conductivity: 18 Scm⁻¹) mixed-valency salt BEDT-TTF₂[O₃S-C₆H₄-CO₂H], which is noncentrosymmetric due to head-to-tail arrangement of the

anions, whereas EDT-TTF-CONHMe (EDT-TTF = ethylenedithiotetrathiafulvalene) afforded the fully oxidized centrosymmetric salt [EDT-TTF-CONHMe⁺][HO₂C-C₆H₄-SO₃⁻] in which the driving force for the crystal packing is the existence of strong hydrogen-bonding interactions between the anions and the amido groups of the cations.

Introduction

Tetrathiafulvalenium salts of organic carboxylates (RCO₂⁻) are rather scarce;^[1–3] examples of such salts with organic sulfonate anions (RSO₃⁻) are somewhat more numerous and, noticeably, include the superconductor (BEDT-TTF)₂[SF₅CH₂CF₂SO₃] [BEDT-TTF = bis(ethylenedithio)tetrathiafulvalene].^[1,4] Of particular interest is β-(BEDT-TTF)₂[(*E*)-HO₂C-CH=CH-CO₂], where self-complementary hydrogenfumarate anions derived from the symmetrical dicarboxylic acid (*E*)-HO₂C-CH=CH-CO₂H (fumaric acid) actually self-assemble into H-bonded infinite chain motifs.^[2]

The primary incentive behind the work reported here is to explore how charged organic–organic interfaces respond when engaging an amphoteric anion issued from the monodeprotonation of an *asymmetric* organic diacid like *para*-carboxybenzenesulfonate, [HO₂C-C₆H₄-SO₃⁻]. Here, it is expected that self-complementary monoanionic forms would express, at the macroscopic scale of the crystal, the noncentrosymmetric character of a self-assembled hydrogen-bonded polymer (Scheme 1), hence providing an opportunity to evaluate the influence of this dissymmetry on the structural and physical properties of the macroscopic objects.



Scheme 1.

[a] Institut des Sciences et Technologies Moléculaires, Université d'Angers, UMR CNRS 6200 MOLTECH ANJOU, 2 Bd Lavoisier, 49045 Angers, France
Fax: +33-2-41735405
E-mail: michel.giffard@univ-angers.fr

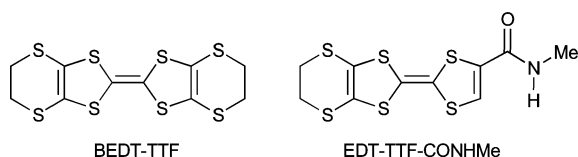
[b] Institute of Solid State Physics, Russian Academy of Sciences, Chernogolovka, 142432 MD, Russia

[c] Laboratoire de Physique des Solides, UMR CNRS 8502, Université Paris-Sud, Bat. 510, 91405 Orsay, France

Supporting information for this article is available on the WWW under <http://dx.doi.org/10.1002/ejic.200900876>.

Another complementary point of interest is to promote situations where transverse hydrogen-bond interactions would occur by using amido group functionalized tetrathiafulvalenes (TTFs) liable to compete in the stabilization of hydrogen-bonded interfaces, a situation where electrostatics are expected to dominate and actually enhance the directionality and stabilization of hydrogen-bond interactions.^[5,6] Here, we report the electro-oxidation of both bis(ethylenedithio)tetrathiafulvalene (BEDT-TTF or ET) and the amido-substituted donor EDT-TTF-CONHMe (EDT-

TTF = thylenedithiotetrathiafulvalene) (Scheme 2) in the presence of the dissymmetrical anion $[\text{HO}_2\text{C}-\text{C}_6\text{H}_4-\text{SO}_3^-]$ (*para*-carboxybenzenesulfonate); two salts of respective formulation $[\text{BEDT-TTF}]_2[\text{HO}_2\text{C}-\text{C}_6\text{H}_4-\text{SO}_3]$ and $[\text{EDT-TTF}][\text{HO}_2\text{C}-\text{C}_6\text{H}_4-\text{SO}_3]$ were obtained.



Scheme 2.

Results and Discussion

The crystal structure of $[\text{BEDT-TTF}]_2[\text{O}_3\text{S}-\text{C}_6\text{H}_4-\text{CO}_2\text{H}]$ was determined at 298 and 150 K. We did not observe any phase transition upon cooling, and the two structures are essentially identical apart from the expected reduction of the cell parameters at low temperature. Thus, we present in this article the results of the room-temperature study; the numerical values observed at 150 K are only mentioned when they can bring pertinent additional information; however, full crystallographic data, both at 293 and 150 K, are available (see Experimental Section).

$[\text{BEDT-TTF}]_2[\text{O}_3\text{S}-\text{C}_6\text{H}_4-\text{CO}_2\text{H}]$ crystallizes in the noncentrosymmetric monoclinic space group Cc with two donor molecules, labeled A and B in Figure 1, and one *p*-carboxybenzenesulfonate anion in the asymmetric unit. By comparing (at 298 K) the lengths of the central carbon-carbon bond [1.378(8) Å in molecule A, 1.359(8) Å in molecule B] to those of the same bond in model compounds such as neutral BEDT-TTF^[7]: 1.319 Å, α -[BEDT-TTF]₂[PF₆]^[8] where the charge of one donor molecule is +1/2: 1.365 Å and $[\text{BEDT-TTF}]_2[\text{Mo}_6\text{O}_{19}]$ ^[9] where this charge is +1: 1.388 Å, it can be seen that the total charge of +1 necessary to balance the charge of the $[\text{HO}_2\text{C}-\text{C}_6\text{H}_4-\text{SO}_3^-]$ anion is shared between molecules A and B, both of them thus carrying a fractional charge. It is truly difficult to be more precise concerning the charge repartition between A and B: the above figures issued from the room-temperature crystal structure seem to indicate that A is more oxidized than B, but in the 150 K structure, normally expected to be more

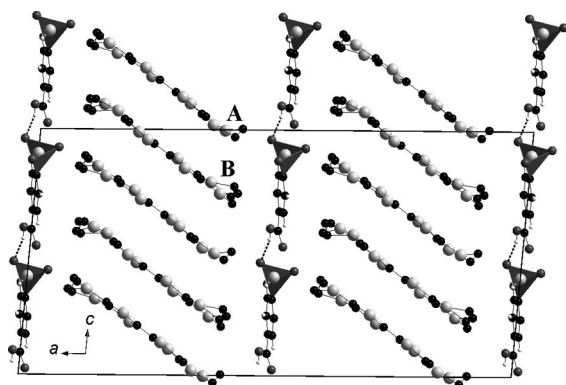


Figure 1. Crystal structure of $[\text{BEDT-TTF}]_2[\text{O}_3\text{S}-\text{C}_6\text{H}_4-\text{CO}_2\text{H}]$ viewed along the *b* axis.

accurate, the observed lengths of the central carbon-carbon bond become almost equal [1.368(7) Å in molecule A, 1.370(7) Å in molecule B], which is in favor of a quasiequal sharing of the positive charge between A and B.

The structure consists of a succession along the *a* axis of slabs of BEDT-TTF cations and of anionic sheets (Figure 1). Within the latter (Figure 2), ribbons of head-to-tail, self-complementary $[\text{O}_3\text{S}-\text{C}_6\text{H}_4-\text{CO}_2\text{H}]^-$ anions are held together by a strong $\text{OH}\cdots\text{O}$ hydrogen bond ($\text{H}\cdots\text{O}$ 1.84 Å and $\text{O}\cdots\text{O}$ 2.56 Å). Thus, it is likely that the overall non-centrosymmetry of the material originates in this head-to-tail disposition of the anions. The slabs of ethylenedithiotetrathiafulvalene molecule adopt δ -type packing^[10] characterized by the occurrence of twisted overlaps between donors; thus, $[\text{BEDT-TTF}]_2[\text{O}_3\text{S}-\text{C}_6\text{H}_4-\text{CO}_2\text{H}]$ is, together with δ -[EDT-TTF-CONMe₂]₂Br,^[11] another rare example of noncentrosymmetric δ -phase.

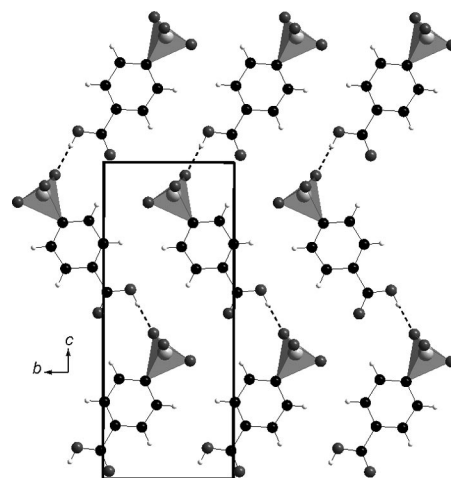


Figure 2. 1D polymeric anionic network in $[\text{BEDT-TTF}]_2[\text{O}_3\text{S}-\text{C}_6\text{H}_4-\text{CO}_2\text{H}]$.

A point of interest is the relative conformation of the terminal ethylene group ($-\text{CH}_2-\text{CH}_2-$) in the BEDT-TTF units.^[12,13] It is known that they can adopt either a centrosymmetric eclipsed conformation (in this case the concerned BEDT-TTF unit possesses an idealized C_{2h} symmetry) or a noncentrosymmetric staggered conformation (idealized D_2 symmetry for BEDT-TTF), but very often, conformational disorder between these two possible positions is observed. Here, as shown in Figure 1, only one out of the two ethylene groups of type A BEDT-TTF molecules is disordered, whereas both ethylene groups of type B molecules are disordered. This implies that one set of two crystallographically independent BEDT-TTF units (A+B) is noncentrosymmetric. This indicates that, although the origin of the noncentrosymmetry of the overall crystal lies, as stressed above, in the relative disposition of anions, it confers appreciable dissymmetry to the cation layer itself. It is also noteworthy that this situation was not modified upon cooling: the same patterns of disorder are also observed in the 150 K structure of $[\text{BEDT-TTF}]_2[\text{O}_3\text{S}-\text{C}_6\text{H}_4-\text{CO}_2\text{H}]$.

Transfer integrals between the BEDT-TTF units in the δ planes of donors have been calculated by using extended

Hückel theory (EHT); seven types of geometrically different interactions appear (Figure 3), and the corresponding energetic values are rather high and of approximately comparable magnitude, as reported in Table 1 together with the associated sulfur–sulfur contact distances.

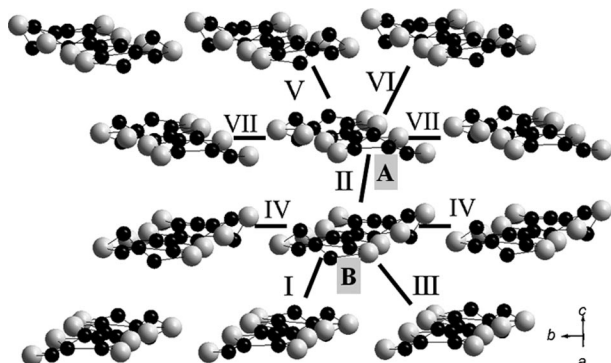


Figure 3. View of the cationic network of [BEDT-TTF]₂[O₃S-C₆H₄-CO₂H] showing the different intermolecular interactions.

Table 1. Calculated interaction energies and S...S distances in [BEDT-TTF]₂[O₃S-C₆H₄-CO₂H].

Interaction	$\beta_{\text{HO-HO}}$ [eV]	S...S contacts <3.75 Å
I	0.2234	3.71(2), 3.74(2), 3.75(2)
II	0.2607	3.690(23)
III	0.2960	3.60(1); 3.67(1)
IV	0.1363	3.51(2), 3.51(1), 3.50(2)
V	0.2229	3.75(2), 3.71(2), 3.74(2)
VI	0.2607	3.67(1), 3.60(1)
VII	0.1363	3.49(1), 3.61(2), 3.64(2), 3.43(1)

Finally, note that, apart from these sulfur contacts between cations and from the above-mentioned strong hydrogen bonds between anions, hydrogen bonds are identified between the terminal ethylene bridges (–CH₂–CH₂–) of the cations and either the oxygen of the sulfonate groups (–SO₃[–]) of the anions [$d(\text{CH}\cdots\text{O}) = 2.47(1)$ Å and $2.49(1)$ Å] or the oxygen atom of the carboxylic groups [$d(\text{CH}\cdots\text{O}) = 2.49(1)$ Å]. Such interactions are considered to be important for the control of the crystal packing and the physical properties of BEDT-TTF derived materials.^[6,13]

The electrical resistivity of a single crystal of BEDT-TTF₂[O₃S-C₆H₄-CO₂H] was measured between 300 and 80 K; a rather high room-temperature conductivity (18 Scm^{–1}) was observed, whereas the temperature dependence of the resistivity (Figure 4) denotes a semiconducting behavior with a low activation energy (0.03 eV) between 185 and 300 K. In addition, the magnetic susceptibility of this salt, measured by SQUID experiments, was found to be temperature independent between ca. 50 and 300 K with a constant value of 6×10^{-4} emu mol^{–1}, in agreement with the low activation energy deduced from resistivity data. The inset of Figure 4 shows a fit of the data between 185 and 300 K to a law of the type $\rho = \rho_0 \exp(E_a/kT)$.

We shall now turn towards the amido group containing salt [EDT-TTF-CONHMe][O₃S-C₆H₄-CO₂H]. This compound was found to crystallize in the centrosymmetric triclinic *P* $\bar{1}$ group. The asymmetric unit consists of one EDT-

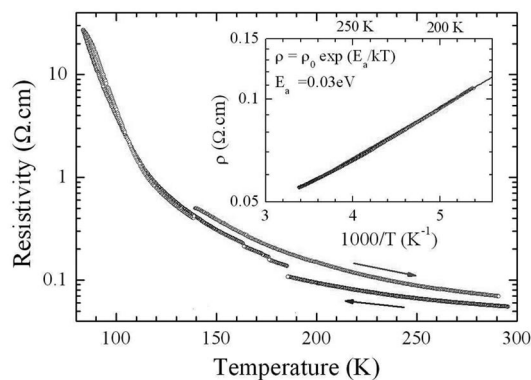


Figure 4. Temperature dependence of the resistivity of [BEDT-TTF]₂[O₃S-C₆H₄-CO₂H] in the 80–300 K range showing cooling and warming curves.

TTF-CONHMe donor and one *p*-carboxybenzenesulfonate anion; thus, it follows from the charge balance that each donor unit is fully oxidized in agreement with the formulation [EDT-TTF-CONHMe]⁺[O₃S-C₆H₄-CO₂H][–]. This is confirmed by the length of the central C=C bond (1.41 Å), which is characteristic of a fully oxidized donor. The structure arrangement of this salt cannot be classified in one of α , β , δ , etc. structural types usually encountered for TTF salts, as it does not consist of separated cationic and anionic salts. Instead, it may be described as composed of mixed sheets; each of these sheets contains dimers of cations and dimers of anions (Figure 5), these two kinds of dimers being centrosymmetric.

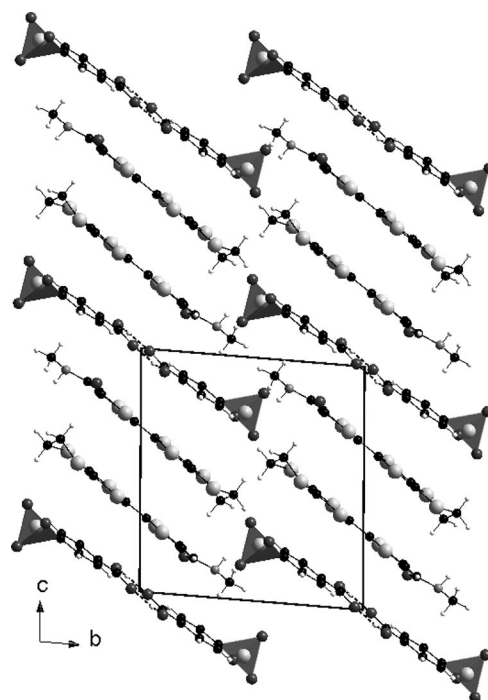


Figure 5. Crystal structure of (EDT-TTF-CONHMe)(O₃S-C₆H₄-CO₂H) viewed along the *a* axis.

The driving force that determines this arrangement seems to be a strong interaction between the amido group -CONHMe of the cation, acting as hydrogen-bond donors, and the sulfonate group -SO_3^- of the anion, acting as hydrogen-bond acceptor through one of its oxygen atoms and thus forming a cyclic motif called $R_2^1(7)$ in the Etter's classification of hydrogen-bonds motifs^[14] (Figure 6). Thus, in difference of what occurs in $\text{BEDT-TTF}_2[\text{O}_3\text{S-C}_6\text{H}_4\text{-CO}_2\text{H}]$, these sulfonate groups are no longer disposable to bind to the carboxy groups $\text{-CO}_2\text{H}$ and, as a consequence, the anions prefer to associate in pairs, linking together thanks to these $\text{-CO}_2\text{H}$ groups which adopt a head-to-head arrangement (Figure 6) and thus form an 8-links $R_2^2(8)$ pattern^[14] frequently encountered in the structural chemistry of carboxylic acids.^[15] It is this head-to-head arrangement of the anions that can be considered to be at the basis of the overall centrosymmetric character of $[\text{EDT-TTF-CONHMe}][\text{O}_3\text{S-C}_6\text{H}_4\text{-CO}_2\text{H}]$; this is in striking contrast with the noncentrosymmetric $\text{BEDT-TTF}_2[\text{O}_3\text{S-C}_6\text{H}_4\text{-CO}_2\text{H}]$ in which, as pointed out above, the anions form head-to-tail chains.

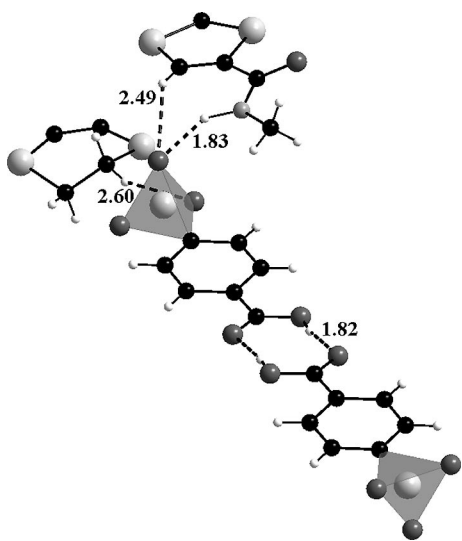


Figure 6. Part of the structure of $(\text{EDT-TTF-CONHMe})(\text{O}_3\text{S-C}_6\text{H}_4\text{-CO}_2\text{H})$ showing both the cation/anion interface and a head-to-head dimer of anions.

EHT calculations of the transfer integrals between the donor units disclose three types of geometrically different interactions I: $\beta_{\text{HOMO}\cdots\text{HOMO}} = 0.31$ eV, II: 0.10 eV, and III: 0.14 eV, among which the intradimer interaction I is by far the most important (Figure 7).

In addition to the strong cation–anion hydrogen bonds mentioned above, which are specifically due to the presence of an amido group in the donor EDT-TTF-CONHMe , weak contacts [$d(\text{CH}\cdots\text{O}) = 2.60(3)$ and $2.58(2)$ Å] involving the terminal ethylene bridge ($\text{-CH}_2\text{-CH}_2\text{-}$) of the donors and the second oxygen of the sulfonate groups are also present.

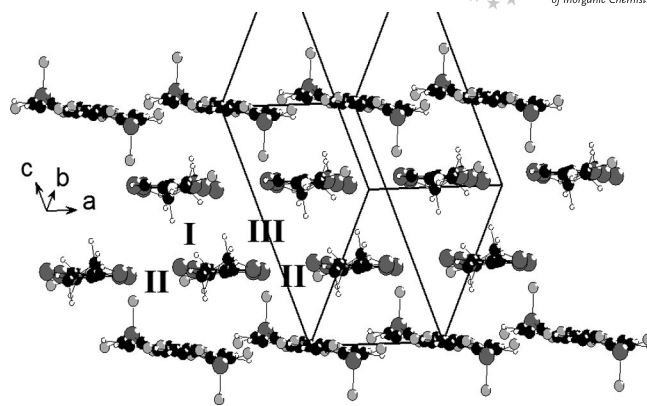


Figure 7. Part of the structure of $(\text{EDT-TTF-CONHMe})(\text{O}_3\text{S-C}_6\text{H}_4\text{-CO}_2\text{H})$ showing a ribbon of donors, running along the a axis and separated by anions, and the different kinds of intermolecular interactions.

Conclusions

To conclude, the use of the dissymmetrical anion $\text{O}_3\text{S-C}_6\text{H}_4\text{-CO}_2\text{H}$ in electrocrystallization experiments with TTF derivatives allowed us to obtain two salts, one of which possesses a noncentrosymmetric overall crystal structure. The obtainment of such noncentrosymmetric cation radicals salts is of interest, especially with respect to their physical properties, and the possibility of coexistence, to some extent, of dielectric and conducting or semiconducting properties^[16] deserves further investigation.

In this context, it is important to predict, as far as possible, in which circumstances such noncentrosymmetric materials can be obtained. The few examples reported here seem to indicate that the use of dissymmetrical anions is a good way to reach such a goal, as they should normally adopt a head-to-tail arrangement, which in turn will induce an overall noncentrosymmetric crystal structure. However, as seen in the case of $[\text{EDT-TTF-CONHMe}][\text{O}_3\text{S-C}_6\text{H}_4\text{-CO}_2\text{H}]$, this natural tendency to head-to-tail arrangement of anions may be overwhelmed if competition with stronger types of interactions is possible. In that sense, it may be difficult to conciliate noncentrosymmetry with strong cation–anion anchoring, at least, in this particular family of materials.

Experimental Section

BEDT-TTF and EDT-TTF-CONHMe were prepared as published previously.^[17] $[\text{18-crown-6}]$ and $\text{KO}_3\text{SC}_6\text{H}_4\text{CO}_2\text{H}$ were purchased from Acros and Avocado, respectively. Both salts were prepared at room temperature by galvanostatic oxidation (1 μA) of a dichloromethane/methanol (90:10, 12 mL) solution of the donor molecule on a platinum wire electrode in the presence of potassium p -carboxybenzenesulfonate and $[\text{18-crown-6}]$, using a conventional U-shaped cell. Typical amounts of reactants and reaction times for the preparation of $(\text{BEDT-TTF})_2[\text{O}_3\text{S-C}_6\text{H}_4\text{-CO}_2\text{H}]$: BEDT-TTF 10 mg, $[\text{18-crown-6}]$ 130 mg, $\text{KO}_3\text{SC}_6\text{H}_4\text{CO}_2\text{H}$ 100 mg, 10 d. For the preparation of $[\text{EDT-TTF-CONHMe}][\text{O}_3\text{S-C}_6\text{H}_4\text{-CO}_2\text{H}]$: EDT-TTF-CONHMe 5 mg, $[\text{18-crown-6}]$ 60 mg, $\text{KO}_3\text{SC}_6\text{H}_4\text{CO}_2\text{H}$ 50 mg, 21 d.

X-ray data collection was carried out with a Bruker KappaCCD diffractometer, graphite-monochromated, Mo- K_{α} radiation ($\lambda = 0.71073 \text{ \AA}$). The structures were solved by direct methods, and refined by full-matrix least-squares routines against F^2 by using the SHELXL97 package. Hydrogen atoms were treated with a riding model. All non-hydrogen atoms (except ethylene disordered carbon atoms) in $(\text{BEDT-TTF})_2[\text{O}_3\text{S-C}_6\text{H}_4\text{-CO}_2\text{H}]$, and sulfur atoms in $[\text{EDT-TTF-CONHMe}][\text{O}_3\text{S-C}_6\text{H}_4\text{-CO}_2\text{H}]$ were refined anisotropically. In $(\text{BEDT-TTF})_2[\text{O}_3\text{S-C}_6\text{H}_4\text{-CO}_2\text{H}]$, carbon atoms of three out of the four ethylene of the two independent BEDT-TTF molecules are disordered over two positions, each with an approximately half occupation rate. A summary of crystallographic data for both structures is given in Table 2.

CCDC-746032 {for $[\text{EDT-TTF-CONHMe}][\text{O}_3\text{S-C}_6\text{H}_4\text{-CO}_2\text{H}]$ }, -746033 {for $(\text{BEDT-TTF})_2[\text{O}_3\text{S-C}_6\text{H}_4\text{-CO}_2\text{H}]$ }, and -770423 {for

Table 2. Room-temperature crystallographic data for $[\text{BEDT-TTF}]_2[\text{O}_3\text{S-C}_6\text{H}_4\text{-CO}_2\text{H}]$ and $[\text{EDT-TTF-CONHMe}][\text{O}_3\text{S-C}_6\text{H}_4\text{-CO}_2\text{H}]$.

	$[\text{BEDT-TTF}]_2[\text{O}_3\text{S-C}_6\text{H}_4\text{-CO}_2\text{H}]$	$[\text{EDT-TTF-CONHMe}][\text{O}_3\text{S-C}_6\text{H}_4\text{-CO}_2\text{H}]$
Formula	$\text{C}_{27}\text{H}_{21}\text{O}_5\text{S}_{17}$	$\text{C}_{17}\text{H}_{14}\text{NO}_6\text{S}_7$
M_r	970.46	552.71
System	monoclinic	triclinic
Space group	Cc	$P\bar{1}$
a [\AA]	32.890(5)	6.8294(15)
b [\AA]	6.7462(8)	11.973(3)
c [\AA]	16.393(2)	13.054(3)
α [$^\circ$]	90	94.12(3)
β [$^\circ$]	94.88(1)	96.53(3)
γ [$^\circ$]	90	91.25(3)
V [\AA^3]	3624(1)	1057.2(4)
Z	4	2
T [K]	298	293
$\mu(\text{Mo-}K_{\alpha})$ [mm^{-1}]	1.052	0.784
Measured reflns	36969	10237
Unique reflns [$R(\text{int})$]	10241 (0.060)	3794 (0.19)
Refined parameters	440	160
GOF [F^2]	1.036	0.80
$R_1(F)$ [$I > 2\sigma(I)$]	0.051	0.077
$wR_2(F^2)$ all data	0.102	0.213

$(\text{BEDT-TTF})_2[\text{O}_3\text{S-C}_6\text{H}_4\text{-CO}_2\text{H}]$ contain the supplementary crystallographic data for this paper. These data can be obtained free of charge from The Cambridge Crystallographic Data Centre via www.ccdc.cam.ac.uk/data_request/cif.

The resistivity measurements were performed on $\text{BEDT-TTF}_2[\text{O}_3\text{S-C}_6\text{H}_4\text{-CO}_2\text{H}]$ single crystals, along the b crystallographic axis (longer dimension of the crystals), with gold contacts evaporated on the samples, by a conventional four-probe method: low frequency (40–70 Hz) and low intensity (1 to 0.1 μA) ac current was applied on outer contacts and voltage on inner contacts was detected by a lock-in amplifier. The magnetic susceptibility of BEDT-

$\text{TTF}_2[\text{O}_3\text{S-C}_6\text{H}_4\text{-CO}_2\text{H}]$ was measured from 80 to 300 K, using a SQUID magnetometer.

Supporting Information (see footnote on the first page of this article): Characteristic bond lengths in $[\text{BEDT-TTF}]_2[\text{O}_3\text{S-C}_6\text{H}_4\text{-CO}_2\text{H}]$ at 298 K and 150 K.

Acknowledgments

This work was supported by the Centre National de la Recherche Scientifique (CNRS, France). We thank Dr. Marc Fourmigué (Rennes, France) for magnetic measurements and EHT calculations.

- [1] U. Geiser, J. A. Schlueter, *Chem. Rev.* **2004**, *104*, 5203.
- [2] M. Giffard, N. Mercier, A. Riou, G. Mabon, P. Molinié, T. P. Nguyen, *J. Mater. Chem.* **1999**, *9*, 851.
- [3] N. Mercier, M. Giffard, G. Pilet, M. Allain, P. Hudhomme, G. Mabon, E. Levillain, A. Gorgues, A. Riou, *Chem. Commun.* **2001**, 2722.
- [4] U. Geiser, J. A. Schlueter, H. H. Wang, A. M. Kini, J. M. Williams, P. P. Sche, H. I. Zakowicz, M. L. Vanzile, J. D. Dudek, P. G. Nixon, R. W. Winter, G. L. Gard, J. Ren, M. H. Whangbo, *J. Am. Chem. Soc.* **1996**, *118*, 9996.
- [5] a) K. Heuzé, M. Fourmigué, P. Batail, E. Canadell, P. Auban-Senzier, *Chem. Eur. J.* **1999**, *5*, 2971; b) T. Devic, PhD Thesis, Université d'Angers, **2003**.
- [6] M. Fourmigué, P. Batail, *Chem. Rev.* **2004**, *104*, 5379.
- [7] H. Kobayashi, A. Kobayashi, Y. Sasaki, G. Saito, H. Inokuchi, *Bull. Chem. Soc. Jpn.* **1986**, *59*, 301.
- [8] H. Kobayashi, R. Kato, T. Mori, A. Kobayashi, Y. Sasaki, G. Saito, T. Enoki, H. Inokuchi, *Mol. Cryst. Liq. Cryst.* **1984**, *107*, 33.
- [9] S. Triki, L. Ouahab, D. Grandjean, J. M. Fabre, *Acta Crystallogr., Sect. C* **1991**, *47*, 645.
- [10] T. Mori, *Bull. Chem. Soc. Jpn.* **1999**, *72*, 2011.
- [11] L. Zorina, S. Simonov, C. Mézière, E. Canadell, S. Suh, S. E. Brown, P. Foury-Leylekian, P. Fertey, J. P. Pouget, P. Batail, *J. Mater. Chem.* **2009**, *19*, 6980.
- [12] J. M. Williams, J. R. Ferraro, R. J. Thorn, K. D. Carlson, U. Geiser, H. H. Wang, A. M. Kini, M.-H. Whangbo in *Organic Superconductors (Including Fullerenes)*, Synthesis Structure, Properties and Theory, Prentice Hall, Englewood Cliff, **1992**, pp. 66–67.
- [13] a) M. H. Whangbo, J. M. Williams, A. J. Schulz, T. J. Emge, M. A. Beno, *J. Am. Chem. Soc.* **1987**, *109*, 90; b) H. Yamochi, T. Komatsu, N. Matsukawa, G. Saito, T. Mori, M. Kusumoki, K. I. Sakaguchi, *J. Am. Chem. Soc.* **1993**, *115*, 11319.
- [14] M. Etter, *Acc. Chem. Res.* **1990**, *23*, 120.
- [15] a) L. Leiserowitz, *Acta Crystallogr. Sect. B* **1976**, *32*, 775; b) W. Bi, N. Mercier, *Chem. Commun.* **2008**, 5743.
- [16] T. Akutagawa, S. Takeda, T. Hasegawa, T. Nakamura, *J. Am. Chem. Soc.* **2004**, *126*, 291.
- [17] a) H. Mueller, Y. Ueba, *Synthesis* **1993**, *9*, 853; b) K. Heuzé, M. Fourmigué, P. Batail, *J. Mater. Chem.* **1999**, *9*, 2373.

Received: September 3, 2009
Published Online: June 15, 2010

Strong Circularly Polarized Luminescence from Highly Emissive Terbium Complexes in Aqueous Solution

Amanda P. S. Samuel,^[a] Jamie L. Lunkley,^[b] Gilles Muller,^[b] and Kenneth N. Raymond^{*[a]}

Keywords: Lanthanides / Terbium / Luminescence / Circularly polarized luminescence (CPL) / Chirality

Two luminescent terbium(III) complexes have been prepared from chiral ligands containing 2-hydroxyisophthalamide (IAM) antenna chromophores and their non-polarized and circularly-polarized luminescence properties have been studied. These tetradentate ligands, which form 2:1 ligand/Tb^{III} complexes, utilize diaminocyclohexane (cyLI) and diphenylethylenediamine (dpenLI) backbones, which we reasoned would impart conformational rigidity and result in Tb^{III} complexes that display both large luminescence quantum yield (Φ) values and strong circularly polarized luminescence (CPL) activities. Both Tb^{III} complexes are highly emissive, with Φ values of 0.32 (dpenLI-Tb) and 0.60 (cyLI-Tb). Lumi-

nescence lifetime measurements in H₂O and D₂O indicate that while cyLI-Tb exists as a single species in solution, dpenLI-Tb exists as two species: a monohydrate complex with one H₂O molecule directly bound to the Tb^{III} ion and a complex with no water molecules in the inner coordination sphere. Both cyLI-Tb and dpenLI-Tb display increased CPL activity compared to previously reported Tb^{III} complexes made with chiral IAM ligands. The CPL measurements also provide additional confirmation of the presence of a single emissive species in solution in the case of cyLI-Tb, and multiple emissive species in the case of dpenLI-Tb.

Introduction

Circularly polarized luminescence (CPL), the emission analog of circular dichroism (CD), combines the sensitivity of luminescence techniques with the specificity of chiroptical spectroscopy.^[1–7] The luminescence of lanthanide complexes is especially sensitive to changes in coordination geometry and molecular environment, and as such, CPL-active lanthanide complexes are excellent candidates for luminescent probes that can report on their chiral surroundings.^[8] To maximize the sensitivity of a luminescent lanthanide-based chiroptical probe the complex should possess both a large luminescence quantum yield and strong CPL activity. Additionally, solubility and stability of the Ln^{III} complex in aqueous solution is very important for practical applications. Such systems, however, remain elusive; often complexes are optimized in respect to either emission intensity or CPL activity, though not both (see below). A system that combines a large luminescence quantum yield with strong CPL activity in aqueous solution would represent a significant advance in the field of Ln^{III}-based CPL.

We have previously shown that Tb^{III} complexes of 2-hydroxyisophthalamide (IAM)-based ligands are exceptionally bright, displaying some of the highest luminescence quantum yield (Φ) values of Ln^{III} complexes in aqueous

solution reported to date ($\Phi \approx 0.60$).^[9] While chiral IAM ligands afford CPL-active Tb^{III} complexes that retain the brightness of the parent achiral forms, their CPL activity is relatively modest. CPL activity is commonly reported as the luminescence dissymmetry factor, g_{lum} , defined as $g_{\text{lum}} = 2(I_L - I_R)/(I_L + I_R)$, where I_L and I_R are the intensities of left- and right-polarized emission respectively. Among chiral Tb^{III}-IAM complexes with large Φ values, $|g_{\text{lum}}|$ values ≤ 0.078 are observed.^[10,11] As a strategy to increase CPL activity we designed chiral IAM ligands that are more rigid than the previously reported tetrapodal octadentate ligands since CPL activity had been shown to increase with the conformational rigidity of the complex.^[12,13] These ligands, cyLI-IAM and dpenLI-IAM (Figure 1), utilize diaminocyclohexane and diphenylethylenediamine backbones respectively. Tetradentate IAM ligands of this type form 2:1 ligand/Ln^{III} (ML₂) complexes,^[14] analogous to the previously reported octadentate ligands that form 1:1 ligand/Ln^{III} complexes. Tetradentate ligands offer the advantage of be-

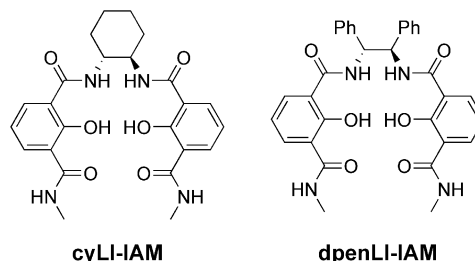


Figure 1. Chemical structures of cyLI- and dpenLI-IAM ligands.

[a] Department of Chemistry, University of California Berkeley, CA 94720-1460, USA
Fax: +1-510-486-5283
E-mail: Raymond@socrates.berkeley.edu

[b] Department of Chemistry, San José State University San José, CA 95192-0101

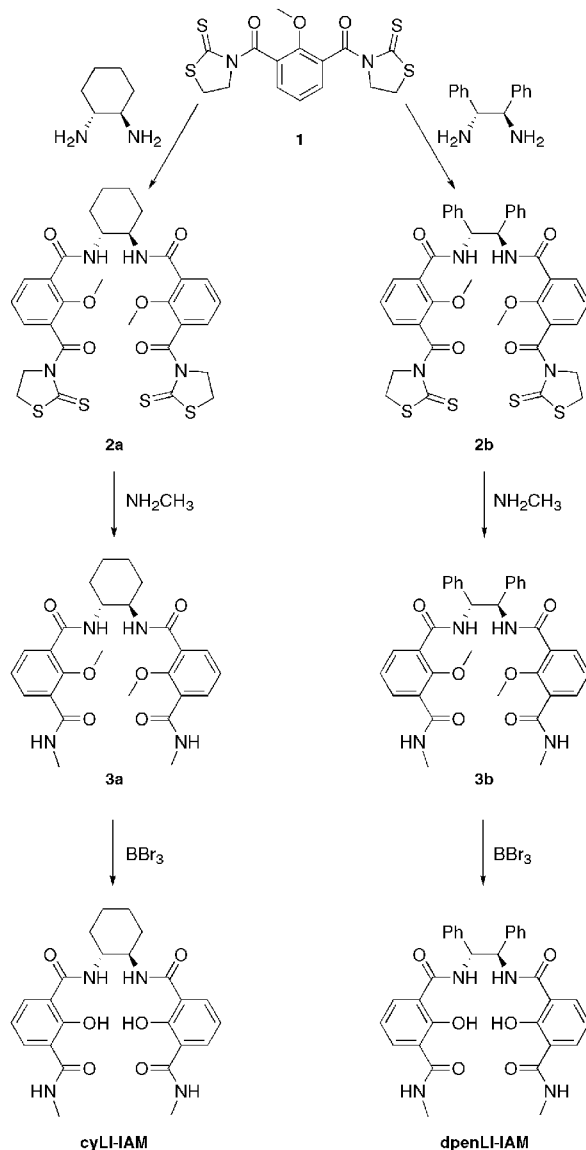
ing more readily synthesized than higher denticity ligands and consequently by utilizing tetradentate ligands we are able to easily investigate how small structural changes in the ligand scaffolds influence the photophysical behavior of the resulting Tb^{III} complexes. Herein we report the syntheses of cyLI- and dpenLI-IAM and their Tb^{III} complexes along with their absorption and luminescence properties in the presence of both circularly-polarized and non-polarized light.

Results and Discussion

CyLI- and dpenLI-IAM were synthesized following the procedure shown in Scheme 1. By starting with the dithiazolidine precursor **1**^[15] one is able to substitute both ends of the molecule with two distinct amines. Dilute solutions of (1*R*,2*R*)-(+)-1,2-diphenylethylenediamine and (1*R*,2*R*)-(+)-

1,2-diaminocyclohexane were each added to **1** over 36 h to produce the mono-substituted species, **2a** and **2b**, respectively. These two species were each then combined with methylamine to yield **3a** and **3b**. The methyl-protected ligands were then both deprotected using BBr₃ to yield the final ligands. The Tb^{III} ML₂ complexes (here referred to as cyLI-Tb and dpenLI-Tb) used for the spectroscopic measurements were prepared in situ by combining 1 equiv. of TbCl₃ (in 1 M HCl) with 2 equiv. of ligand (in a basic aqueous solution) in 0.1 M Tris buffered H₂O (pH = 7.4). The complexes were characterized using mass spectrometry (ES⁺) in addition to the optical techniques that are described in the upcoming sections. The ability to rely on these optical techniques is especially valuable in the study of Tb^{III}-IAM complexes since ¹H NMR spectroscopy is problematic because of signal broadening caused by the paramagnetic Tb^{III} center.^[16]

The absorption spectra of cyLI-Tb and dpenLI-Tb display broad transitions similar to those previously observed for Tb-IAM complexes in aqueous solution, which are attributed to π - π^* transitions in the IAM chromophore (Figure 2, a).^[9,17] As with other Tb-IAM complexes, the broad absorption bands of cyLI-Tb and dpenLI-Tb allow for excitation with wavelengths up to ca. 390 nm, which is more favorable for practical biological applications compared to many other high quantum yield Tb^{III} complexes that require more damaging higher energy excitation wavelengths.^[18,19] Additionally, both cyLI-Tb and dpenLI-Tb show CD activity as expected (Figure 2, b). The CD spectra show strong Cotton effects^[20] for both complexes between 300–380 nm.



Scheme 1. Syntheses of cyLI- and dpenLI-IAM ligands.

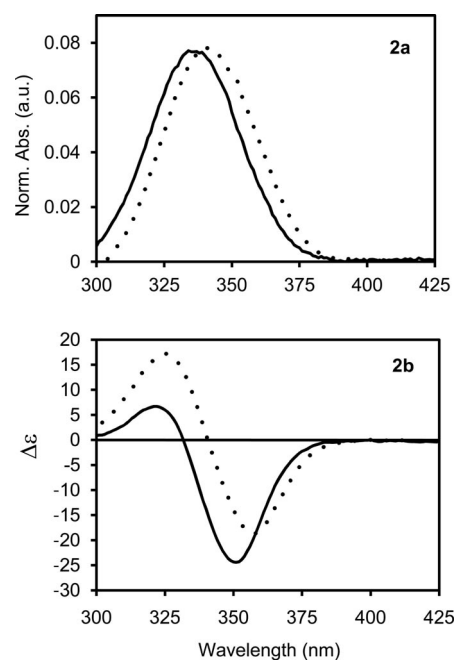


Figure 2. Absorption spectra (**2a**) and CD spectra (**2b**) of cyLI-Tb (solid) and dpenLI-Tb (dashed) in aqueous solution [$C = 10^{-5}$ M, 0.1 M Tris (pH = 7.4)] at 298 K.

To determine the efficiency of Tb^{III} sensitization, the emission behavior of cyLI-Tb and dpenLI-Tb was investigated. A summary of the luminescence quantum yield and lifetime values is given in Table 1. The luminescence spectra display the characteristic bands corresponding to transitions from the ⁵D₄ electronic level to the ⁷F_{*J*} (*J* = 0–6) manifold of Tb^{III} (Figure 3). The two complexes show slight differences in the relative intensities and fine structures of the peaks, which points to variation in the coordination environments experienced by the Tb^{III} ions in each complex.^[21] This difference in coordination environment is supported by the luminescence quantum yield (Φ) values for the two complexes: cyLI-Tb has a quantum yield of 0.60, while dpenLI-Tb has a quantum yield of 0.32. The cyLI-Tb value is consistent with the high quantum yield values observed for Tb^{III} complexes with octadentate IAM ligands.^[9,11,17]

Table 1. Photophysical properties of the Tb^{III} complexes [10^{−5} M (Tris buffer, pH 7.4, λ_{ex} = 340 nm)].

Complex	QY (Φ)	τ (r.t.), ms		<i>q</i> ^[a]	τ (77 K), ms ^[b]	
		H ₂ O	D ₂ O		H ₂ O	D ₂ O
cyLI-Tb	0.60	1.66	1.84	0	1.77	2.05
dpenLI-Tb	0.32	1.51	1.68	0	1.89	2.21
		(84%)	(88%)		(37%)	(37%)
		0.550	1.68	1	1.89	2.21
		(16%)	(12%)		(63%)	(63%)

[a] Calculated from r.t. values using $q = 5 \times (1/\tau_{\text{H}_2\text{O}} - 1/\tau_{\text{D}_2\text{O}} - 0.06)$.^[21] [b] Contained 10% (v/v) glycerol.

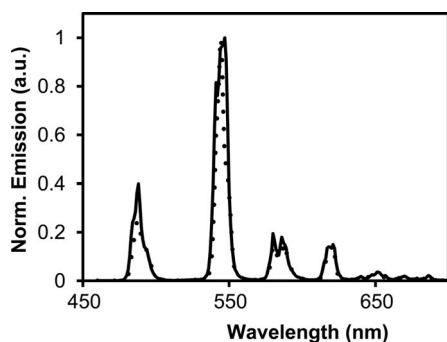


Figure 3. Luminescence spectra of cyLI-Tb (solid) and dpenLI-Tb (dashed) in aqueous solution (0.1 M Tris, pH = 7.4) at 298 K normalized to the intensity of the *J* = 5 peak.

To further investigate this difference in emission intensity the luminescence lifetimes were measured both in H₂O and D₂O at room temperature (r.t.) and at 77 K (Table 1). Mono-exponential lifetime decays are exhibited by cyLI-Tb, while dpenLI-Tb exhibits bi-exponential decays, indicating that for the former, only one luminescent species is present in solution, while for the latter, two luminescent species are present. The number of bound water molecules (*q*) was estimated for each of the complexes based on the lifetimes measured at room temperature using the formula developed by Beeby et al.,^[22] and *q* values of zero were ob-

tained for cyLI-Tb and for one of the two dpenLI-Tb species. The other dpenLI-Tb species, however, has approximately one water molecule in the inner coordination sphere, which quenches Tb^{III} emission and contributes to the low luminescence quantum yield observed for dpenLI-Tb. The overall quantum yield for dpenLI-Tb is the weighted sum of the quantum yields of the *q* = 0 and *q* = 1 species. Since the latter experiences quenching due to bound water, it has a lower quantum yield than a *q* = 0 species.

The CPL spectra of cyLI-Tb and dpenLI-Tb are plotted in Figure 4 for the magnetic dipole allowed ⁵D₄ → ⁷F₅ transition. The *g*_{lum} values are summarized in Table 2. The CPL signals provide additional confirmation that stable chiral species are present in solution. Both spectra display several peaks corresponding to crystal-field splitting; the difference in sign, shape and magnitude of the CPL signal are consistent with the fact that the two systems do not exhibit the same crystal field structure in solution. The CPL signal exhibited by cyLI-Tb is similar whether via direct excitation of the Tb^{III} ion (λ_{ex} = 488 nm) or indirect excitation via the ligand absorption bands (λ_{ex} = 341 nm), which indicates that the same species in solution is responsible for the CPL activity detected. Additionally, the *g*_{lum} values obtained for this complex are the same upon excitation with right-, left-, and plane-polarized light, which is consistent with the presence of only one species in solution;^[23] had the solution contained a mixture of diastereomers, the CPL signal would have been dependent on the polarization of the excitation beam.^[24] In contrast, the *g*_{lum} values obtained for dpenLI-Tb are dependent on the polarization of the excitation beam and on whether direct or indirect excitation is used, which indicates that more than one species in solution is responsible for the CPL signal detected. These results support the lifetime data, which indicate the presence of two emitting species in solution that differ in hydration number and therefore also coordination environment.

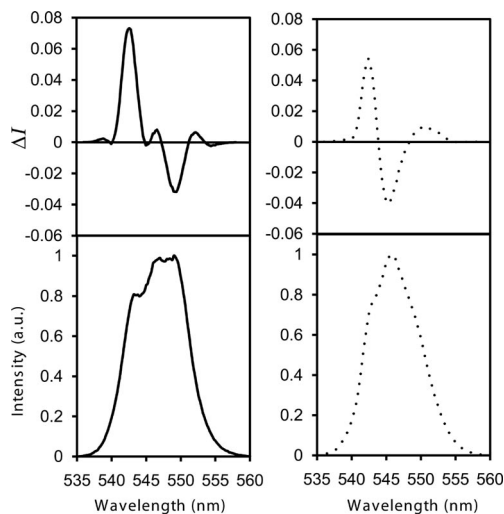


Figure 4. CPL (top) and total luminescence spectra (bottom) for the ⁵D₄ → ⁷F₅ transition for cyLI-Tb (solid) and dpenLI-Tb (dashed) in aqueous solution.

Table 2. Summary of CPL data for cyLI-Tb and dpenLI-Tb.

Complex	λ_{ex}	Transition	λ [nm]	g_{lum}
cyLI-Tb	341 nm	$^5\text{D}_4 \rightarrow ^7\text{F}_5$	542.0	+0.20
			548.6	−0.063
dpenLI-Tb	343 nm	$^5\text{D}_4 \rightarrow ^7\text{F}_5$	542.4	+0.16
			545.4	−0.082
			551.0	+0.043

Conclusions

Tetradentate IAM ligands yield highly luminescent Tb^{III} complexes with large g_{lum} values in aqueous solution at physiologically relevant pH, which may be attributed to the increased rigidity of the ligand frameworks. Varying the chiral amine that serves as the ligand backbone was found to impact solvent access to the Tb^{III} center, which was determined through luminescence lifetime, luminescence quantum yield and CPL measurements. The CyLI-Tb complex is particularly interesting, since it has an extremely high quantum yield, a g_{lum} value over twofold larger than the largest observed for a comparably emissive Tb-IAM complex, and consists of a single emitting species in solution.

Experimental Section

General Methods: All chemicals were obtained from commercial suppliers and used without further purification. ¹H and ¹³C NMR spectra, elemental analyses, and mass spectra were obtained at the corresponding analytical facility in the College of Chemistry, University of California, Berkeley.

2a: (2-Methoxy-1,3-phenylene)bis[(2-thioxothiazolidin-3-yl)methanone]^[15] (**1**) (5.0 g, 12.5 mmol) was dissolved in 10 mL of CH₂Cl₂. A 250 mL solution of (1*R*,2*R*)-(+)-1,2-diaminocyclohexane (0.128 g, 1.1 mmol) in a 95:5 CH₂Cl₂/MeOH solution was cannulated into the solution of **1** over 36 h. The solvents were then removed under vacuum and the reaction mixture was dissolved in CH₂Cl₂ and washed with 1 M NaOH. The product was purified by silica gel chromatography (2% MeOH/98% CH₂Cl₂); yield 0.620 g (84%). ¹H NMR (400 MHz, CDCl₃): δ = 1.35 (m, 4 H, CH₂), 1.74 (m, 2 H, CHH), 2.15 (m, 2 H, CHH), 3.35 (m, 4 H, NCH₂CH₂S), 3.76 (s, 6 H, OCH₃), 3.98 (m, 2 H, CH₂CHN), 4.55 (m, 4 H, NCH₂CH₂S), 7.07 (t, J = 8 Hz, 2 H, ArH), 7.30 (dd, J = 5, 2 Hz, 2 H, ArH), 7.60 (d, J = 8 Hz, 2 H, NH), 7.89 (dd, J = 8, 2 Hz, 2 H, ArH) ppm. ¹³C NMR (100 MHz, CDCl₃): δ = 24.8, 29.2, 32.6, 53.4, 55.7, 63.1, 124.1, 127.1, 129.1, 132.1, 134.0, 155.7, 165.0, 167.4, 201.3 ppm. MS (FAB+): m/z = 673 [MH⁺].

2b: Compound **1**^[15] (7.96 g, 20.0 mmol) was dissolved in 10 mL of CH₂Cl₂. A 250 mL solution of (1*R*,2*R*)-(+)-1,2-diphenylethylenediamine (0.425 g, 2.0 mmol) in a 95:5 CH₂Cl₂/MeOH solution was cannulated into the solution of **1** over 36 h. The solvents were then removed under vacuum and the reaction mixture was dissolved in CH₂Cl₂ and washed with 1 M NaOH. The product was purified by silica gel chromatography (15% EtOAc/85% CH₂Cl₂); yield 0.470 g (30%). ¹H NMR (400 MHz, CDCl₃): δ = 3.30 (m, 4 H, NCH₂CH₂S), 3.86 (s, 6 H, OCH₃), 4.52 (m, 4 H, NCH₂CH₂S) 5.50 (m, 2 H, CHNH), 6.95 (t, J = 8 Hz, 2 H, ArH), 7.16 (m, 10 H, ArH), 7.85 (dd, J = 8, 2 Hz, 2 H, ArH), 7.89 (dd, J = 8, 2 Hz, 2 H, ArH), 8.80 (q, J = 5 Hz, 2 H, NHCH₃), 9.21 (m, 2 H, NH)

ppm. ¹³C NMR (100 MHz, [D₆]DMSO): δ = 29.7, 53.6, 57.5, 64.2, 118.7, 120.2, 126.9, 128.3, 131.5, 136.6, 142.4, 158.6, 167.2, 175.6, 201.8 ppm. MS (FAB+): m/z = 771 [MH⁺].

3a (Representative Procedure): To a solution of **2a** (0.60 g, 0.89 mmol) in 15 mL of CH₂Cl₂ was added 1.0 mL of methylamine (40% aq. soln.). The reaction mixture was stirred at room temperature for 6 h and was then washed with 1 M NaOH. The resulting off-white residue was applied to a silica column and the product was eluted with 4% MeOH/96% CH₂Cl₂; yield 0.402 g (91%). ¹H NMR (400 MHz, [D₆]DMSO): δ = 1.30 (m, 2 H, CHH), 1.44 (m, 2 H, CHH), 1.71 (m, 2 H, CHH), 1.94 (m, 2 H, CHH), 2.76 (d, J = 5 Hz, 6 H, NHCH₃), 3.70 (s, 6 H, OCH₃), 3.89 (m, 2 H, CH₂CHNH), 7.17 (t, J = 8 Hz, 2 H, ArH), 7.53 (m, 4 H, ArH), 8.21 (m, 4 H, NH) ppm. ¹³C NMR (100 MHz, [D₆]DMSO): δ = 24.4, 26.2, 31.7, 52.3, 62.4, 123.4, 130.2, 130.4, 131.0, 131.1, 154.8, 165.4, 166.1 ppm. MS (FAB+): m/z = 497 [MH⁺].

3b: ¹H NMR (400 MHz, [D₆]DMSO): δ = 2.81 (d, J = 4 Hz, 6 H, NHCH₃), 3.80 (s, 6 H, OCH₃), 5.51 (m, 2 H, CHNH), 6.95 (t, J = 8 Hz, 2 H, ArH), 7.16 (m, 10 H, ArH), 7.85 (dd, J = 8, 2 Hz, 2 H, ArH), 7.89 (dd, J = 8, 2 Hz, 2 H, ArH), 8.80 (q, J = 5 Hz, 2 H, NHCH₃), 9.21 (m, 2 H, NH) ppm. ¹³C NMR (100 MHz, [D₆]DMSO): δ = 26.0, 57.5, 64.2, 116.7, 118.1, 120.4, 126.8, 127.3, 127.5, 130.5, 132.4, 138.6, 159.2, 165.6, 168.3 ppm. MS (FAB+): m/z = 595 [MH⁺].

cyLI-IAM (Representative Procedure): A suspension of **3a** (0.325 g, 0.66 mmol) in 30 mL of CH₂Cl₂ was cooled to −78 °C and 1.0 mL (10.6 mmol) of BBr₃ was added. The reaction mixture was warmed to room temperature and stirred for 48 h. The volatiles were removed under vacuum and a few milliliters of 1 M HCl were added, causing the product to precipitate out of solution. The product was recrystallized from hot H₂O; yield 0.229 g (74%). ¹H NMR (400 MHz, [D₆]DMSO): δ = 1.31 (m, 2 H, CHH), 1.48 (m, 2 H, CHH), 1.73 (m, 2 H, CHH), 1.98 (m, 2 H, CHH), 2.81 (d, J = 4 Hz, 6 H, NHCH₃), 3.94 (m, 2 H, CH₂CHNH), 6.93 (t, J = 8 Hz, 2 H, ArH), 7.91 (t, J = 9 Hz, 4 H, ArH), 8.61 (m, 2 H, CH₂CHNH), 8.69 (m, 2 H, NHCH₃), 14.71 (s, 2 H, OH) ppm. ¹³C NMR (100 MHz, [D₆]DMSO): δ = 24.4, 26.1, 31.5, 52.4, 117.9, 118.0, 118.7, 132.2, 132.7, 159.3, 166.6, 167.7 ppm. MS (FAB+): m/z = 469 [MH⁺]. Anal. calcd. (found) for C₂₄H₂₈N₄O₆·0.5H₂O: C, 60.36 (60.15); H, 6.12 (6.06); N, 11.73 (11.42).

cyLI-Tb: [C₄₈H₅₂N₈O₁₂Tb][−], MS (ES[−]): m/z = 1091.2 [M[−]].

dpenLI-IAM: ¹H NMR (400 MHz, [D₆]DMSO): δ = 2.83 (d, J = 4 Hz, 6 H, NHCH₃), 5.60 (m, 2 H, CHNH), 6.97 (t, J = 8 Hz, 2 H, ArH), 7.20 (m, 10 H, ArH), 7.88 (dd, J = 8, 2 Hz, 2 H, ArH), 7.96 (dd, J = 8, 2 Hz, 2 H, ArH), 8.86 (q, J = 5 Hz, 2 H, NHCH₃), 9.25 (m, 2 H, NH), 14.67 (s, 2 H, OH) ppm. ¹³C NMR (100 MHz, [D₆]DMSO): δ = 26.1, 57.5, 116.9, 118.2, 119.9, 127.2, 127.6, 128.0, 131.5, 133.4, 139.6, 159.3, 165.8, 168.6 ppm. MS (FAB+): m/z = 567 [MH⁺]. Anal. calcd. (found) for C₃₂H₃₀N₄O₆·0.5H₂O·MeOH: C, 65.66 (65.46); H, 5.18 (5.35); N, 9.28 (9.48).

dpenLI-Tb: [C₆₄H₅₆N₈O₁₂Tb][−], MS (ES[−]): m/z = 1287.3 [M[−]].

UV/Vis Absorption, Circular Dichroism, Emission, and Circularly Polarized Luminescence Spectra. General Methods: Absorption spectra were recorded on a Cary 300 UV/Vis spectrophotometer using a 1-cm quartz cell. Emission spectra were recorded on a FluoroLog-3 (JobinYvon) fluorimeter using a 1-cm Supracil quartz luminescence cell (room-temperature measurements). The Tb^{III} complexes (10 mM) were prepared in situ in 0.1 M Tris-buffered H₂O (pH 7.4). The complexes were characterized using mass spectrometry (ES[−]). Quantum yields were determined by the optically dilute method^[25] using the following equation:

$$Q_x/Q_r = [A_r(\lambda_r)/A_x(\lambda_x)][I(I_r)/I(I_x)][n_x^2/n_r^2][D_x/D_r]$$

where A is the absorbance at the excitation wavelength (λ), I is the intensity of the excitation light at the same wavelength, n is the refractive index and D is the integrated intensity. Quinine sulfate in 1.0 N sulfuric acid was used as the reference ($Q_r = 0.546$).^[26] Circularly polarized luminescence and total luminescence spectra were recorded on an instrument according to literature procedures,^[23,24,27] operating in a differential photon-counting mode. CPL measurements were performed at 295 K in H₂O (0.1 M Tris, pH = 7.4) with analyte concentrations of 10^{-4} to 10^{-5} M.

Acknowledgments

This research is supported by the Director of the U. S. Department of Energy at LBNL, Office of Science, Office of Basic Energy Sciences, and the Division of Chemical Sciences, Geosciences, and Biosciences (Contract No. DE-AC02-05CH11231. G. M. thanks the National Institute of Health, Minority Biomedical Research Support (1 SC3 GM089589-01) and the Henry Dreyfus Teacher-Scholar Award for financial support.

- [1] H. G. Brittain, in: *Lanthanide Probes in Life, Chemical and Earth Sciences: Theory and Practice*, 3rd ed. (Eds.: J.-C. G. Bünzli, G. R. Choppin), Elsevier, Amsterdam, **1989**.
- [2] F. S. Richardson, J. P. Riehl, *Chem. Rev.* **1977**, *77*, 772–792.
- [3] J. P. Riehl, F. S. Richardson, *Chem. Rev.* **1986**, *86*, 1–16.
- [4] J. P. Riehl, F. S. Richardson, *Methods Enzymol.* **1993**, *226*, 539–553.
- [5] H. G. Brittain, *Appl. Spectrosc. Rev.* **2007**, *35*, 175–201.
- [6] H. P. J. M. Dekkers, in: *Circular Dichroism* (Eds.: N. Berova, K. Nakanishi, R. W. Woody), Wiley-VCH, Weinheim, **2000**.
- [7] J. P. Riehl, G. Muller, in: *Handbook on the Physics and Chemistry of Rare Earths*, vol. 43 (Eds.: K. A. Gschneider, J.-C. G. Bünzli, V. K. Pecharsky), North-Holland Publishing Company, Amsterdam, **2005**, p. 289.
- [8] G. Muller, *Dalton Trans.* **2009**, 9692–9707.
- [9] S. Petoud, S. M. Cohen, J.-C. Bünzli, K. Raymond, *J. Am. Chem. Soc.* **2003**, *125*, 13324–13325.
- [10] S. Petoud, G. Muller, E. G. Moore, J. Xu, J. Sokolnicki, J. P. Riehl, U. N. Le, S. M. Cohen, K. N. Raymond, *J. Am. Chem. Soc.* **2007**, *129*, 77–83.
- [11] M. Seitz, E. G. Moore, A. J. Ingram, G. Muller, K. N. Raymond, *J. Am. Chem. Soc.* **2007**, *129*, 15468–15470.
- [12] R. S. Dickins, J. A. K. Howard, C. W. Lehmann, J. M. Moloney, D. Parker, R. D. Peacock, *Angew. Chem. Int. Ed. Engl.* **1997**, *36*, 521–523.
- [13] J. L. Lunkley, D. Shirotni, K. Yamanari, S. Kaizaki, G. Muller, *J. Am. Chem. Soc.* **2008**, *130*, 13814–13815.
- [14] A. P. S. Samuel, J. Xu, K. N. Raymond, *Inorg. Chem.* **2009**, *48*, 687–698.
- [15] S. M. Cohen, B. O'Sullivan, K. N. Raymond, *Inorg. Chem.* **2000**, *39*, 4339–4346.
- [16] Attempts to characterize IAM-Tb^{III} complexes using ¹H NMR spectroscopy yielded spectra with no distinct resonances that could be assigned unambiguously to IAM protons and thus these results were uninformative.
- [17] A. P. S. Samuel, E. G. Moore, M. Melchior, J. Xu, K. N. Raymond, *Inorg. Chem.* **2007**, *46*, 7535–7544.
- [18] H. Takalo, V.-M. Mikkala, L. Meriö, J.-C. Rodríguez-Ubis, R. Seadno, O. Juanes, E. Brunet, *Helv. Chim. Acta* **1997**, *80*, 372–387.
- [19] M. Xiao, P. R. Selvin, *J. Am. Chem. Soc.* **2001**, *123*, 7067–7073.
- [20] G. Snatzke, in: *Circular Dichroism*, 2nd ed. (Eds.: N. Berova, K. Nakanishi, R. W. Woody), Wiley-VCH, New York, **2000**.
- [21] J.-C. G. Bünzli, in: *Lanthanide Probes in Life, Chemical and Earth Sciences: Theory and Practice* (Eds.: J.-C. G. Bünzli, G. R. Choppin), Elsevier, Amsterdam, **1989**.
- [22] A. Beeby, I. M. Clarkson, R. S. Dickins, S. Faulkner, D. Parker, L. Royle, A. S. d. Sousa, J. A. G. Williams, M. Woods, *J. Chem. Soc. Perkin Trans. 2* **1999**, 493–503.
- [23] K. Do, F. C. Muller, G. Muller, *J. Phys. Chem. A* **2008**, *112*, 6789–6793.
- [24] M. Seitz, D. King, A. J. Ingram, E. G. Moore, G. Muller, K. N. Raymond, *Inorg. Chem.* **2009**, *48*, 8469–8479.
- [25] G. A. Crosby, J. N. Demas, *J. Phys. Chem.* **1971**, *75*, 991–1024.
- [26] S. R. Meech, D. Philips, *J. Photochem.* **1983**, *23*, 193–217.
- [27] S. D. Bonsall, M. Houcheime, D. A. Straus, G. Muller, *Chem. Commun.* **2007**, *35*, 3673–6378.

Received: March 17, 2010
Published Online: June 2, 2010

In₂O₃ Nanofibers and Nanoribbons: Preparation by Electrospinning and Their Formaldehyde Gas-Sensing Properties

Zhipeng Li,^[a] Yingju Fan,^[b] and Jinhua Zhan*^[a]

Keywords: Indium oxide / Formaldehyde / Nanostructures / Electrospinning / Sensors

In₂O₃ nanofibers and nanoribbons were prepared by electrospinning combined with a poly(vinyl pyrrolidone)-assisted sol–gel technique. By tuning the experimental parameters, the morphological transformation of In₂O₃ from nanofibers to nanoribbons was achieved. It was found that both the rapid evaporation of solvent and the concentration of the precursor played important roles in the formation process of In₂O₃ nanoribbons. The average diameter of the In₂O₃ nanofibers is 180 nm. The nanoribbons have an average width of 1 μm

and a thickness of about 150 nm. The lengths of both can reach millimeters. The average grain size consisting of nanofibers and nanoribbons is 18.6 and 11.2 nm, respectively. The gas-sensing properties of In₂O₃ nanofibers and nanoribbons toward formaldehyde vapor were investigated. Interestingly, the gas sensor fabricated with In₂O₃ nanoribbons exhibited a higher and faster response at a relatively lower operating temperature than that fabricated with nanofibers.

Introduction

Recently, the controllable synthesis of one-dimensional (1D) nanomaterials, including nanotubes, nanowires, nanofibers, and nanobelts, has attracted considerable attention due to the fact that the physical and chemical properties of nanomaterials are greatly affected by their reduced dimensionality and size.^[1] 1D nanostructures with prominent characteristics have been extensively applied for use as chemical sensors.^[2] It has been noted that 1D nanomaterials could greatly reduce the interfacial areas between the active sensing region of the nanofibers and the underlying substrates.^[3] The fibers with large surface areas can facilitate fast mass transfer of the gas molecules around the interaction region, thereby improving the rate for charge carriers to traverse the barriers induced by molecular recognition along the fibers.^[4] Additionally, the conductivity of the oxide materials is expected to be promoted in the continuous 1D nanostructure, therefore affecting the sensing temperature.^[5] These advantages may make the 1D nanostructure an excellent candidate in the application of chemical sensors.

In₂O₃, an important n-type semiconductor with a band gap of approximately 3.55–3.75 eV, has been widely used in

solar cells,^[6] transparent conductors,^[7] and gas sensors for the detection of NO₂,^[8] HCHO,^[9] NH₃,^[10] H₂S,^[11,12] and CO.^[13] Up to now, In₂O₃ nanostructures with various morphologies, such as nanowires,^[14] nanofibers,^[15] nanotubes,^[16] nanorods and nanocubes,^[17,18] quasi-monodisperse nanocrystals,^[19] hollow spheres,^[20] and needlelike nanostructures,^[21] have been synthesized through different routes including thermal evaporation,^[14] a hot-injection technique,^[19] a hydrothermal reaction,^[20] a solvothermal reaction,^[15] sonochemistry,^[21] and so forth.

Electrospinning is a facile method for fabricating ultrathin nanofibers that involves the use of a high voltage to charge the surface of a polymer solution droplet that rests on a sharp conduction tip. When the strength of the electric field surpasses a threshold value, the surface tension of the polymer solution could be overcome by the electrostatic forces to cause the ejection of a thin jet from the tip. The subsequently stretched jet could result in the formation of continuous, ultrathin fibers, owing to the bending instability. Besides polymers, this technique has been extended to the synthesis of inorganic ceramic materials such as TiO₂,^[22] In₂O₃,^[23] SnO₂,^[24] WO₃,^[5] ZnO,^[25] and Co₃O₄.^[26] Furthermore, electrospinning has proven to be a highly successful technique for controlling the synthesis of 1D nanostructures including nanofibers,^[27] nanotubes,^[28] nanoribbons,^[29,30] and others novel structures.^[31] In this paper, an electrospinning technique combined with a poly(vinyl pyrrolidone) (PVP)-assisted sol–gel technique was utilized to realize the controllable synthesis of In₂O₃ nanofibers and nanoribbons by tuning experimental parameters. The gas-sensing properties of as-prepared nanomaterials toward formaldehyde vapor were investigated.

[a] Key Laboratory of Colloid & Interface Chemistry, Department of Chemistry, Shandong University, Ministry of Education, Jinan 250100, P. R. China
Fax: +86-0531-8836-6280
E-mail: jhzhzhan@sdu.edu.cn

[b] School of Chemistry and Chemical Engineering, Jinan University, Jinan 250020, P. R. China

Results and Discussion

The detailed experimental parameters and corresponding product morphologies during electrospinning preparation are summarized in Table 1. Figure 1 shows the scanning electron microscopy (SEM) images of the gel-like precursors that were obtained by tuning the experimental parameters. As is shown in part a of Figure 1, for a precursor with a lower concentration and a lower amount of ethanol solvent, the as-spun products were nanofibers (sample 1) with diameters of around 300 nm. From Figure 1 (b) we can see that the as-spun products were mixed with nanofibers and nanoribbons (sample 2) by increasing the ratio of ethanol to water and keeping the concentration of precursor unchanged. Figure 1 (c) gives the SEM image of nanoribbon precursors (sample 3) that have widths of about 2 μm and thicknesses of around 300 nm, which suggests that complete nanoribbon structures could only be obtained by increasing the concentration of the inorganic salts and PVP to a certain extent.

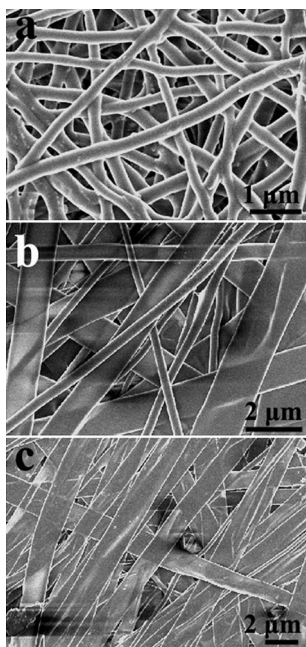


Figure 1. SEM images of In(NO₃)₃/PVP precursors: (a) sample 1; (b) sample 2; and (c) sample 3.

Thermogravimetric (TG) and differential scanning calorimetric (DSC) curves of the as-spun precursors (sample 1 and sample 3) are displayed in Figure 2. It is clear from the TG curves that all the volatiles (H₂O, ethanol, etc.), organic component (PVP), and NO₃[−] groups were removed completely below 510 °C in the two samples, which resulted in a metal oxide phase. The first minor weight loss

before 185 °C in parts a and b of Figure 2 corresponds to the removal of the free solvent in the precursors. The significant weight loss of approximately 68.1 % (dominant exothermic DSC peak at 337 °C) in Figure 2 (a) and 63.3 % (dominant exothermic DSC peak at 209 °C) in Figure 2 (b) between 185 and 510 °C was attributed to the complete decomposition of In(NO₃)₃ and the degradation of PVP, which involves both intra- and intermolecular transfer reactions.^[32] The exothermic peaks at 503 °C in Figure 2 (a) and at 488 °C (b) were the result of the oxidation of carbon and carbon monoxide released by the decomposition of PVP.^[30]

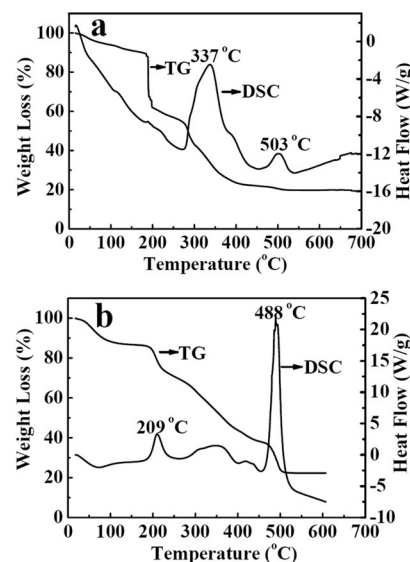


Figure 2. TG-DSC curves of the as-spun In(NO₃)₃/PVP precursors: (a) nanofibers (sample 1) and (b) nanoribbons (sample 3).

The XRD patterns of products calcined at 550 °C are shown in parts a and b of Figure 3 corresponding to the body-centered cubic structure of In₂O₃ [JCPDS 65-3170, space group: *Ia*3 (206)]. No phases corresponding to impurities are detected in either pattern.

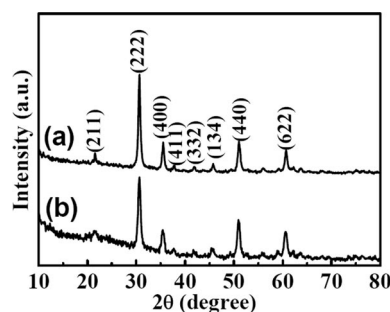


Figure 3. XRD patterns of (a) In₂O₃ nanofibers; (b) In₂O₃ nanoribbons.

Table 1. Detailed experimental parameters and corresponding results of In₂O₃ morphologies.

Sample	In(NO ₃) ₃ ·4.5H ₂ O [g]	PVP [g]	Solvent	Morphology
1	0.5	0.5	5 mL H ₂ O + 8 mL ethanol	fibers
2	0.5	0.5	3 mL H ₂ O + 10 mL ethanol	fibers + ribbons
3	1	1	3 mL H ₂ O + 10 mL ethanol	ribbons

Figure 4 shows the SEM images of the In_2O_3 products calcined at 550 °C. Compared with the gel precursor counterparts, it is clearly shown that the average diameters of the nanofibers and the nanoribbons decreased due to the removal of PVP from the precursors. After calcination, the fiber and ribbon texture were well maintained. Parts a and b of Figure 4 show that the In_2O_3 nanofibers are relatively uniform with diameters of 150–200 nm. The high-resolution SEM image of an individual In_2O_3 nanofiber (the inset in Figure 4, b) clearly demonstrates that the surfaces of the nanofibers are slightly rough, which reveals that the nanofibers are composed of small nanoparticles. Figure 4 (c and d) show the images of the products of sample 2. Both nanofibers and nanoribbons are clearly found in this product. Figure 4 (e and f) shows the SEM images of In_2O_3 nanoribbons. Figure 4 (f) shows the cross section of a single nanoribbon, in which the flat structure and relatively smooth surface of a nanoribbon with a width of 1 μm and a thickness of 150 nm is observed.

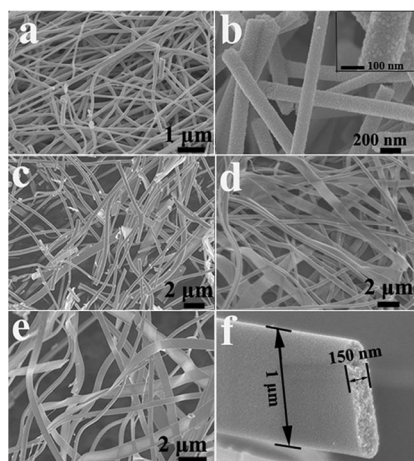


Figure 4. SEM images of In_2O_3 products calcined at 550 °C: (a) and (b) sample 1; (c) and (d) sample 2; (e) and (f) sample 3. The inset in (b) shows the high-resolution SEM image of an individual In_2O_3 nanofiber.

Further detailed microstructural analyses of individual nanofibers and nanoribbons were carried out by using transmission electron microscopy (TEM) and electron diffraction (ED). Figure 5 (a–d) shows TEM images of an individual In_2O_3 nanofiber and nanoribbon after calcination, which indicates that the nanofibers and nanoribbons were formed through the agglomeration of small In_2O_3 nanoparticles. The selected-area electron-diffraction (SAED) patterns of the In_2O_3 nanofibers and nanoribbons are shown in the insets a and c of Figure 5. All diffraction rings on the patterns could be attributed to cubic In_2O_3 , suggesting a polycrystalline nature. Size distributions of the nanofibers and nanoribbons are shown in Figure 5 (e and f) and suggest that the domain size is 16–20 and 10–13 nm, respectively.

Up to now, several kinds of metal oxide nanoribbons prepared by electrospinning, such as BaTiO_3 ^[29] and MFe_2O_4 ($\text{M} = \text{Co}, \text{Ni}$)^[30] have been reported. Li and co-

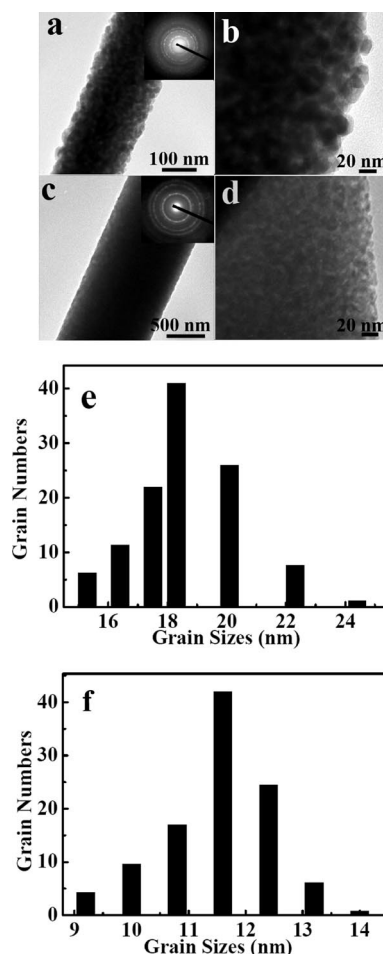


Figure 5. TEM images of an individual In_2O_3 (a) and (b) nanofiber; (c) and (d) nanoribbon; and (e) and (f) size distributions of the nanofibers and nanoribbons.

workers have demonstrated that flat ribbons with a mesoporous structure could be fabricated by increasing the concentration of the sol–gel precursor and feeding rate in a low-humidity electrospinning environment.^[33] However, the formation mechanism for ribbon-like structures is still controversial. For example, Meng et al. reported that ribbon-like structures made up of two parallel fibers may result from the incomplete spitting of the charged jet during the electrospinning.^[30] As can be seen from the experimental results in Figures 1 and 4, both the solvent and the concentration of the precursor have a significant effect on the formation process of nanoribbon structures. As is well known, the spinning mechanism is rather complicated. It has been demonstrated that the bending instability associated with the electrified jet may cause thinning of the jet during electrospinning, though splaying of the electrified jet might also happen.^[34,35] If the concentration of the sol–gel precursor is sufficiently high, rapid gelation on the surface of the electrospun jet at an earlier stage leads to the formation of an elastic skin, while the core is still solution. Once elastic behavior overcomes viscous behavior, the electrospun fiber can buckle into a flattened ribbon by anisotropic shrinkage.^[36] The result of sample 2 seems to confirm the above

viewpoint that rapid gelation on the surface of the electrospun jet is more likely to result in the formation of ribbon-like structures because the rapid evaporation of solvent can accelerate the gelation on the surface of the charged jet. Therefore, both the ribbon-like precursors in Figure 1 (c) and the cross section of a single nanoribbon after calcination in Figure 4 (f) show the flat structure and very smooth surface, which indicates that the ribbon-like structures were not the result of incomplete splitting of the charged jet, but rather the result of rapid gelation on the surface of the electrospun jet and the buckling of the skin associated with the bending instability.

Chemical contaminants contained in construction materials have become an important factor of indoor air pollution. These compounds are strongly associated with sick building syndrome (SBS). HCHO, a colorless, strong-smelling compound, is particularly considered as a major cause of SBS as a result of its extensive use in homes as an adhesive resin in pressed wood products.^[37] Therefore, two gas sensors fabricated using In₂O₃ nanofibers and nanoribbons have been produced, and both show high sensitivity to formaldehyde at different temperature stages.

Figure 6 shows the schematic diagram of the sensor system. The as-prepared In₂O₃ powder of nanofibers and nanoribbons with the same weight (0.05 g) was mixed with water to form a paste, and then uniformly coated onto the ceramic tube on which two platinum wires had been installed at each end. After the solvent was evaporated, the electrospun nanofibers and nanoribbons formed a thin film on the ceramic tube. As is shown in Figure 6, the 1D morphologies of the nanofiber and nanoribbon films on the ceramic tube remained. A Ni-Cr heating wire was inserted into the tube. The sensing element was aged at 300 °C for three days to improve its stability and repeatability, and the gas sensor was fabricated. The operating temperature can be controlled by adjusting the heating voltage (V_H). In the test process, a load resistor was serialized and a working voltage (V_W) at 5 V was applied to this system. By monitoring the load resistor voltage (V_O), the response of the sensor in air or in a test gas can be measured. The resistance or conductance of the sensor can be calculated from Ohm's law. The sensor response was defined as the ratio R_a/R_g , in which R_a and R_g are the resistance of the sensor in atmospheric air and in HCHO/air mixed gas, respectively. The response and recovery times were defined as the time to reach 90% of the total resistance change in the adsorption and desorption process. The measurement was processed by a static process. A given amount of the test gas was injected into a glass chamber and mixed with air. When the response reached a constant value, the sensor was taken out to recover in air.

It is well known that the operating temperature highly influences the response of a semiconductor gas sensor. To determine the optimum operating temperature, the response of the as-fabricated gas sensors toward 100 ppm formaldehyde in air was tested as a function of operating temperature, as shown in Figure 7. It is clear that the response of both gas sensors varied with operating temperature. Inter-

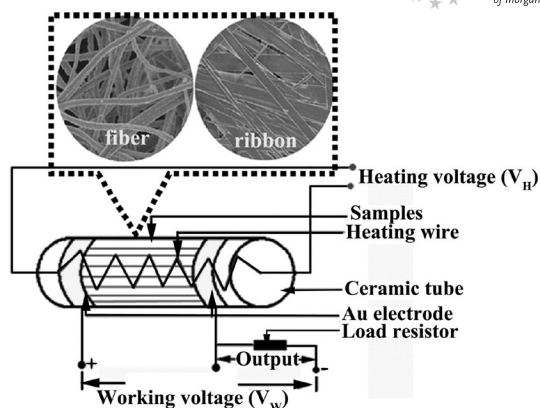


Figure 6. Schematic illustration of the sensor system.

estingly, the gas sensor fabricated using In₂O₃ nanoribbons displayed a higher and faster response than the sensor based on nanofibers. For the sensor of nanofibers, the response to formaldehyde first increased with temperature, up to 340 °C, and then decreased. The maximum response obtained was 3.113, at 340 °C. For the sensor fabricated with nanoribbons, the maximum response obtained was 4.214 at 300 °C. Therefore, an optimal operating temperature of 300 °C was chosen to further examine the characteristics of the gas sensor fabricated with In₂O₃ nanoribbons. Response and recovery times are also important parameters in a gas sensor. The two sensors immediately responded when 100 ppm formaldehyde was introduced. The response and recovery times of the as-fabricated In₂O₃ sensors were 18 and 17 s for nanofibers, and 16 and 15 s for nanoribbons, respectively.

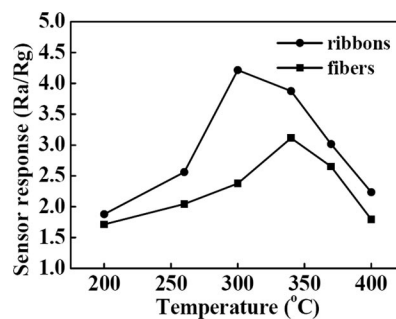


Figure 7. Sensor response versus operating temperature of In₂O₃ nanofiber and nanoribbon sensors toward 100 ppm HCHO.

The difference in the response and recovery times between the two samples is believed to be due to the size-dependent gas-sensing property. On the one hand, according to the size-dependence theory of gas-sensing properties, the response is a function of nanoparticle size in the 10–20 nm range. As the size becomes small, the concentration and energy position of absorption sites in the band gap of the semiconductor are affected significantly. The response of the gas sensor will increase with the decreasing size of the particle.^[38] On the other hand, small particles can result in a large surface area, meaning that more indium atoms on the surface of nanoribbons can participate in the sensing

reaction.^[39] Together, these factors result in the gas sensor fabricated with In_2O_3 nanoribbons (average grain size of 11.2 nm) representing higher sensing and a faster response and recovery time than that of a sensor fabricated with nanofibers, which have an average grain size of 18.6 nm.

Figure 8 shows the representative dynamic gas response of the In_2O_3 nanoribbons toward toxic HCHO with a concentration range from 50 to 250 ppm at the operating temperature of 300 °C. First, five cycles were successively recorded, corresponding to five different HCHO concentrations ranging from 50 to 250 ppm. The conductance underwent a drastic rise upon the injection of HCHO and dropped to its initial value after the sensor was exposed to air. When HCHO with 100 ppm concentration was re-injected into the glass chamber, the response had little change, indicating the good reversibility and repeatability of the In_2O_3 nanoribbon sensor. When the HCHO concentration was in the range of 50–250 ppm, the logarithm of the sensor response showed good linearity with the logarithm of the HCHO concentration (Figure 9), which is in good agreement with the theory of power laws for semiconductor sensors.^[40] According to the model developed by Moseley and Crocker,^[41] the resistance of an n-type semiconductor in the presence of reductive gases will decrease. Most semiconducting-oxide gas sensors operate on the basis of modification of the electrical properties of an active element, brought about by the absorption of an analyte to the surface of the sensor. When the sensor is exposed to reductive HCHO at a high temperature, HCHO reacts with the oxy-

gen species on the surface, resulting in a decrease in the O^{2-} ion concentration. This effect eventually increases the conductivity of the In_2O_3 nanoribbons. From the response curve, the conductance of the sensor increases clearly with respect to the baseline at each HCHO concentration, which is in accord with the above theory. These experimental results suggest that the sensor may be able to meet practical application demands for the detection of HCHO at several concentrations.

Conclusion

In summary, In_2O_3 nanofibers and nanoribbons were prepared by electrospinning combined with PVP-assisted sol-gel technology. By tuning the experimental parameters, the morphological transformation of In_2O_3 from nanofibers to nanoribbons was achieved. In_2O_3 nanofibers were prepared at a lower concentration of the sol-gel precursor, whereas higher concentration resulted in the formation of complete nanoribbon structures. It was found that the formation mechanism of the ribbon-like structures can be ascribed to rapid gelation on the surface of the electrospun jet followed by buckling of the skin associated with bending instability. The gas sensor based on the In_2O_3 nanoribbons exhibits a higher and faster sensor response to formaldehyde vapor than that based on nanofibers at a relatively lower operating temperature owing to the size-dependent property.

Experimental Section

Preparation: In a typical experiment for preparing the electrospinning solution, $\text{In}(\text{NO}_3)_3 \cdot 4.5\text{H}_2\text{O}$ (0.5 g) was dissolved in a mixed solvent containing H_2O (5.0 mL) and absolute ethanol (8.0 mL) under magnetic stirring. To this solution, PVP (0.5 g, $M_r = 1300000$) was added, and a transparent electrospinnable sol was formed after 12 h of stirring. The as-prepared solution was viscous and was transferred into a hypodermic syringe with 10 mL capacity. The positive terminal of a variable high-voltage power supply was connected to the needle tip of the syringe, while the other was connected to a stainless steel collector. The applied voltage was 20 kV, and the distance between the needle tip and the collector was kept at 20 cm. The as-spun gel fibers were first dried overnight at 60 °C then calcined in air at 550 °C for 4 h. The heating rate was set at 1 °C min⁻¹ during the elevation process from room temperature to 550 °C.

To investigate the formation mechanism of the ribbon-like structure during the electrospinning process, a series of experiments were carried out. Detailed experimental parameters and the corresponding results are summarized in Table 1.

Characterization: TG analysis and DSC measurements were carried out on an American TA SDT Q600 simultaneous thermogravimetric analyzer under air in the temperature range from 40 to 700 °C with a heating rate of 10 °C min⁻¹. The XRD patterns were obtained using a Bruker D8 advanced X-ray diffractometer equipped with graphite-monochromatized $\text{Cu-K}\alpha$ radiation ($\lambda = 1.5418 \text{ \AA}$). The SEM images were obtained with a JEOL JSM-6700F field emission scanning electron microscope. The high-resolution TEM images and SAED patterns were recorded on a JEOL 2100 trans-

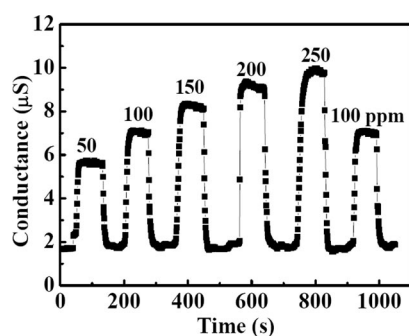


Figure 8. Response curve of the In_2O_3 nanoribbons gas sensor toward HCHO with increasing concentration, at an operating temperature of 300 °C.

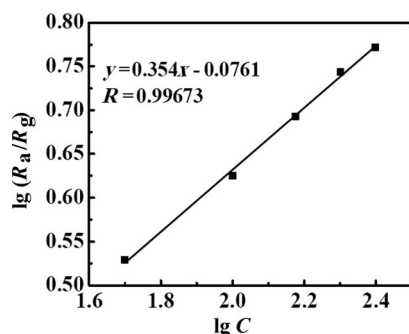


Figure 9. Variation of the response of the In_2O_3 nanoribbons sensor with HCHO concentration.

mission electron microscope with an acceleration voltage of 200 kV. The HCHO gas-sensing properties were measured with a China HW-30A gas-sensitivity instrument.

Acknowledgments

We thank the helpful discussion with Professor Yitai Qian and financial support from the National Natural Science Fund of China (NSFC 50972083), the Key Project of the Chinese Ministry of Education (no. 109098), National Basic Research Program of China (973 Program 2005CB623601, 2007CB936602), and Independent Innovation Foundation of Shandong University (IIFSDU-2009JQ011).

- [1] Y. N. Xia, P. D. Yang, Y. G. Sun, Y. Y. Wu, B. Mayers, B. Gates, Y. D. Yin, F. Kim, Y. Q. Yan, *Adv. Mater.* **2003**, *15*, 353–389.
- [2] I. D. Kim, A. Rothschild, B. H. Lee, D. Y. Kim, S. M. Jo, H. L. Tuller, *Nano Lett.* **2006**, *6*, 2009–2013.
- [3] Z. Y. Li, H. N. Zhang, W. Zheng, W. Wang, H. M. Huang, C. Wang, A. G. MacDiarmid, Y. Wei, *J. Am. Chem. Soc.* **2008**, *130*, 5036–5037.
- [4] A. Kolmakov, M. Moskovits, *Annu. Rev. Mater. Res.* **2004**, *34*, 151–180.
- [5] G. Wang, Y. Ji, X. Huang, X. Yang, P. I. Gouma, M. Dudley, *J. Phys. Chem. B* **2006**, *110*, 23777–23782.
- [6] R. Katoh, A. Furube, T. Yoshihara, K. Hara, G. Fujihashi, S. Takano, S. Murata, H. Arakawa, M. Tachiya, *J. Phys. Chem. B* **2004**, *108*, 4818–4822.
- [7] H. Kim, J. S. Horwitz, G. P. Kushto, S. B. Qadri, Z. H. Kafafi, D. B. Chrisey, *Appl. Phys. Lett.* **2001**, *78*, 1050–1052.
- [8] P. Xu, Z. Cheng, Q. Pan, J. Xu, Q. Xiang, W. Yu, Y. Chu, *Sens. Actuators B: Chem.* **2008**, *130*, 802–808.
- [9] T. Chen, Q. J. Liu, Z. L. Zhou, Y. D. Wang, *Sens. Actuators B: Chem.* **2008**, *131*, 301–305.
- [10] N. Du, H. Zhang, B. D. Chen, X. Y. Ma, Z. H. Liu, J. B. Wu, D. R. Yang, *Adv. Mater.* **2007**, *19*, 1641–1645.
- [11] M. Kaur, N. Jain, K. Sharma, S. Bhattacharya, M. Roy, A. K. Tyagi, S. K. Gupta, J. V. Yakhmi, *Sens. Actuators B: Chem.* **2008**, *133*, 456–461.
- [12] J. Xu, X. Wang, J. Shen, *Sens. Actuators B: Chem.* **2006**, *115*, 642–646.
- [13] K. I. Choi, H. R. Kim, J. H. Lee, *Sens. Actuators B: Chem.* **2009**, *138*, 497–503.
- [14] C. Li, D. H. Zhang, S. Han, X. L. Liu, T. Tang, C. W. Zhou, *Adv. Mater.* **2003**, *15*, 143–146.
- [15] D. B. Yu, S. H. Yu, S. Y. Zhang, J. Zuo, D. B. Wang, Y. T. Qian, *Adv. Funct. Mater.* **2003**, *13*, 497–501.
- [16] Y. P. Fang, X. G. Wen, S. H. Yang, *Angew. Chem. Int. Ed.* **2006**, *45*, 4655–4658.
- [17] Z. Zhuang, Q. Peng, J. Liu, X. Wang, Y. Li, *Inorg. Chem.* **2007**, *46*, 5179–5187.
- [18] Q. Tang, W. Zhou, W. Zhang, S. Ou, K. Jiang, W. Yu, Y. Qian, *Cryst. Growth Des.* **2005**, *5*, 147–150.
- [19] Q. Liu, W. Lu, A. Ma, J. Tang, J. Lin, J. Fang, *J. Am. Chem. Soc.* **2005**, *127*, 5276–5277.
- [20] B. X. Li, Y. Xie, M. Jing, G. X. Rong, Y. C. Tang, G. Z. Zhang, *Langmuir* **2006**, *22*, 9380–9385.
- [21] S. Avivi, Y. Mastai, A. Gedanken, *Chem. Mater.* **2000**, *12*, 1229–1233.
- [22] D. Li, Y. Xia, *Nano Lett.* **2004**, *4*, 933–938.
- [23] W. Zheng, X. F. Lu, W. Wang, Z. Y. Li, H. N. Zhang, Y. Wang, Z. J. Wang, C. Wang, *Sens. Actuators B: Chem.* **2009**, *142*, 61–65.
- [24] Q. Qi, T. Zhang, L. Liu, X. Zheng, *Sens. Actuators B: Chem.* **2009**, *137*, 471–475.
- [25] X. H. Yang, C. L. Shao, H. Y. Guan, X. L. Li, H. Gong, *Inorg. Chem. Commun.* **2004**, *7*, 176–178.
- [26] N. A. M. Barakat, M. S. Khil, F. A. Sheikh, H. Y. Kim, *J. Phys. Chem. C* **2008**, *112*, 12225–12233.
- [27] D. Li, T. Herricks, Y. N. Xia, *Appl. Phys. Lett.* **2003**, *83*, 4586–4588.
- [28] S. H. Zhan, D. R. Chen, X. L. Jiao, C. H. Tao, *J. Phys. Chem. B* **2006**, *110*, 11199–11204.
- [29] J. T. McCann, J. I. L. Chen, D. Li, Z. G. Ye, Y. Xia, *Chem. Phys. Lett.* **2006**, *424*, 162–166.
- [30] Z. Wang, X. Liu, M. Lv, P. Chai, Y. Liu, J. Meng, *J. Phys. Chem. B* **2008**, *112*, 11292–11297.
- [31] Z. Liu, D. D. Sun, P. Guo, J. O. Leckie, *Nano Lett.* **2007**, *7*, 1081–1085.
- [32] S. J. Azhari, M. A. Diab, *Polym. Degrad. Stab.* **1998**, *60*, 253–256.
- [33] D. Li, J. T. McCann, Y. N. Xia, *J. Am. Ceram. Soc.* **2006**, *89*, 1861–1869.
- [34] Y. M. Shin, M. M. Hohman, M. P. Brenner, G. C. Rutledge, *Polymer* **2001**, *42*, 09955–09967.
- [35] A. L. Yarin, S. Koombhongse, D. H. Reneker, *J. Appl. Phys.* **2001**, *90*, 4836–4846.
- [36] N. Tsapis, E. R. Dufresne, S. S. Sinha, C. S. Riera, J. W. Hutchinson, L. Mahadevan, D. A. Weitz, *Phys. Rev. Lett.* **2005**, *94*, 018302.
- [37] W. J. Kim, N. Terada, T. Nomura, R. Takahashi, S. D. Lee, J. H. Park, A. Konno, *Clin. Exp. Allergy* **2002**, *32*, 287–295.
- [38] M. K. Kennedy, F. E. Kruis, H. Fissan, B. R. Mehta, S. Stapert, G. Dumpich, *J. Appl. Phys.* **2003**, *93*, 551–560.
- [39] C. Wu, P. Yin, X. Zhu, C. OuYang, Y. Xie, *J. Phys. Chem. B* **2006**, *110*, 17806–17812.
- [40] N. Yamazoe, K. Shimanoe, *Sens. Actuators B: Chem.* **2008**, *128*, 566–573.
- [41] P. T. Moseley, A. J. Crocker, *Sensor Materials*, Institute of Physics Publishing, Philadelphia (USA), **1996**.

Received: March 18, 2010

Published Online: June 11, 2010

Mesoporous CeO₂ Hollow Spheres Prepared by Ostwald Ripening and Their Environmental Applications

Zhijie Yang,^[a] Jingjing Wei,^[a] Hongxiao Yang,^[a] Ling Liu,^[a] Hui Liang,^[a] and Yanzhao Yang*^[a]

Keywords: Hydrothermal synthesis / Template-free synthesis / Water treatment / Heterogeneous catalysis / Adsorption

CeO₂ hollow spheres (250–350 nm in diameter), with mesoporous shells of approximately 50 nm, were synthesized by a one-pot, template-free hydrothermal method. X-ray diffraction (XRD), X-ray photoelectron spectroscopy (XPS), transmission electron microscopy (TEM), scanning electron microscopy (SEM), high resolution transmission electron microscopy (HRTEM), and nitrogen adsorption–desorption measurements were used to characterize the products. The for-

mation of these hollow spheres involves the aggregation of the initial nanoparticles followed by solid evacuation driven by an Ostwald ripening process. The mesoporous CeO₂ hollow spheres showed an excellent adsorption capacity for organic pollutants (Congo red) from waste water (about 84 mg Congo red per g CeO₂). Furthermore, relative to commercial CeO₂ powders, the CeO₂ hollow spheres exhibited a higher catalytic activity towards CO oxidation.

Introduction

There is a growing interest in the fabrication of nanostructures with desirable morphologies and properties.^[1–4] Among the various morphologies of nanostructures, hollow spheres are drawing interest not only for their great importance in basic research, but also for their broad range of applications in areas such as catalysis, drug delivery, gas storage, and so forth.^[5–7] For example, Lou et al. have reported a high initial reversible charge capacity of 1140 mAh/g, and improved cycling performance for hollow SnO₂ nanospheres.^[5] Hollow TiO₂ nanospheres have been reported to exhibit high activities for photocatalytic degradation of organic pollutants.^[6] Porous hollow silica nanoparticles have been employed as a carrier to study the controlled release behavior of a model drug.^[7] Furthermore, hollow spheres with mesoporous shells have received considerable attention because of their novel properties and possible applications. For example, porous hollow metal oxides possess high surface areas, low production costs, and regeneration capacities through combusting the adsorbed species. They may provide new options for the removal of organic pollutants from waste water.^[8,9]

Cerium oxide is one of the most reactive rare-earth metal oxides, which has been widely employed in applications

such as catalysis,^[10,11] UV blocking,^[12] fuel cells,^[13] adsorbing pollutants,^[14] and polishing materials.^[15] To date, a variety of CeO₂ nanostructures such as octahedra,^[16] cubes,^[17] spheres,^[15,18] wires,^[19] rods,^[20] and flowers^[14a] have been fabricated. Recently, CeO₂ hollow structures have been synthesized through a variety of methods.^[21] Zhou et al. reported a facile synthesis of large-cavity CeO₂ nanotubes by etching Ce(OH)₃ nanotubes/nanorods with H₂O₂.^[21a] Li's group has synthesized CeO₂–ZrO₂ nanocages through use of the Kirkendall effect.^[21b] Suib's group reported the controlled synthesis of self-assembled CeO₂ hollow spheres through the tuning of redox potentials.^[21c] Very recently, Chen et al. fabricated CeO₂ hollow nanocubes by the oriented attachment of CeO₂ nanoparticles followed by Ostwald ripening under solvothermal conditions.^[21d] However, CeO₂ hollow spheres with mesoporous shells have not yet been reported. Moreover, both previous studies on the fabrication of ceria nanotubes and the synthesis of CeO₂ hollow nanocubes need multistep processing. Herein, we report a facile one-pot, template-free route to fabricate CeO₂ hollow spheres with mesoporous shells by hydrothermal treatment. The products were characterized by XRD, XPS, TEM, SEM, HRTEM, and nitrogen adsorption–desorption measurements. A hollowing mechanism is proposed based on the results of these detailed experiments. It is believed that the facile and economical synthesis route reported here will provide an opportunity for the large-scale production of CeO₂ hollow spheres. Furthermore, the applications of the mesoporous CeO₂ hollow spheres as an adsorbent of organic pollutants and as catalysts were explored.

[a] Key Laboratory for Special Functional Aggregate Materials of Education Ministry, School of Chemistry and Chemical Engineering, Shandong University, Jinan 250100, P. R. China
Fax: +86-531-88564464
E-mail: yzhyang@sdu.edu.cn

Supporting information for this article is available on the WWW under <http://dx.doi.org/10.1002/ejic.201000030>.

Results and Discussion

Normally, upon heating to certain temperature, urea will decompose to release CO₃²⁻ and OH⁻ anions slowly. Previous studies have revealed that Ce(OH)CO₃ is the sole product of the reaction of Ce³⁺ with urea under hydrothermal conditions.^[22] In the process described herein Ce³⁺ is oxidized to form Ce⁴⁺ in the presence of H₂O₂.^[21c,23] Therefore, CeO₂ is formed through forced hydrolysis of Ce⁴⁺ at an elevated temperature in the presence of urea. Figure 1 shows a typical XRD pattern of the as-synthesized products from a hydrothermally treated solution of CeCl₃, H₂O₂, urea, and deionized water at 180 °C for 10 h. All of the peaks in this pattern can be indexed as the face-centered cubic pure phase of ceria (JCPDS No. 34-0394). Peaks arising from impurities are not observed, indicating the high purity of the final products. Figure 2 depicts XPS spectra of the CeO₂ hollow spheres. Peaks of Ce 3d, O 1s, and C 1s can be identified from the survey spectrum shown in Figure 2a. In Figure 2b, we observe several Ce 3d binding energy (BE) peaks, such as those at 883.7, 889.6, 899.6 and 918.3 eV, for the hollow spheres that are consistent with a previous report on Ce⁴⁺.^[24] The peaks labeled 883.7 and 889.6 are assigned to Ce 3d⁹4f⁰Lⁿ⁻² and Ce 3d⁹4f¹Lⁿ⁻¹ states respectively. The peaks labeled 899.6 and 918.3 eV are attributed to the Ce 3d⁹4f⁰Lⁿ and final state of Ce^{IV} 3d_{5/2} and Ce^{IV} 3d_{3/2}, respectively. Based on this analysis, the main valence of cerium in the hollow spheres is +4.^[14a]

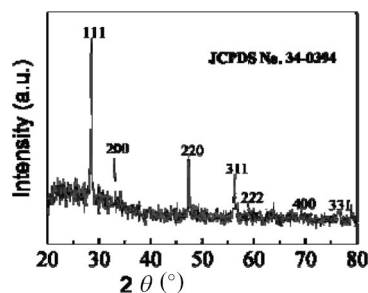


Figure 1. XRD pattern of the as-prepared CeO₂ hollow spheres.

The morphology and structure of the products obtained were investigated by SEM and TEM as shown in Figure 3. The low-magnification SEM image (Figure 3a) of the product obtained at 180 °C after 10 h shows that the sample consists of many spheres, with an average diameter of about 300 nm, along with a few broken spheres. The magnified SEM image shown in Figure 3b shows the detailed morphology of the product obtained, and indicates that the shells of the hollow spheres are composed of numerous nanocrystals with an average size of 15 nm, and shell thickness of about 50 nm. The hollow structure was further investigated by TEM as shown in Figure 3c, and the intense contrast between the black margins and the bright centers of the particles confirms the existence of hollow structures in the resulting spheres, which is consistent with the SEM observation. Figure 3d gives the typical HRTEM image of a single particle, further confirming that the shells of the hollow spheres are constructed by smaller nanocrystals.

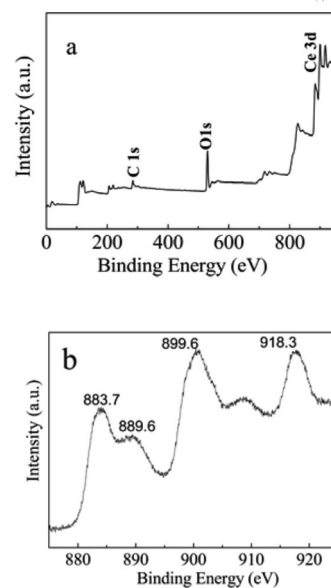


Figure 2. XPS survey spectrum (a) and Ce 3d spectrum (b) of the CeO₂ hollow spheres.

Figure 3e shows a HRTEM image of CeO₂ hollow nanostructures obtained from the area marked with a white pane shown in Figure 3d. Visible lattice fringes are observed in the HRTEM image with a d-spacing of about 0.27 nm, corresponding to the {200} plane of the cubic CeO₂ structure.

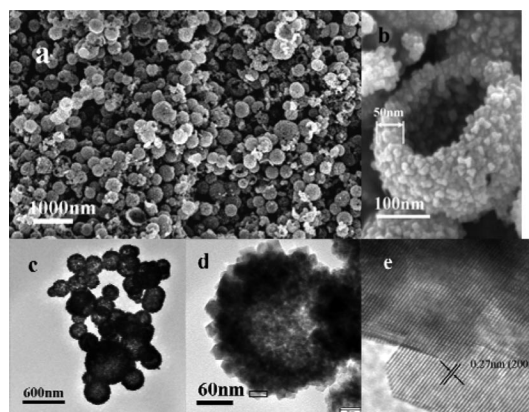


Figure 3. SEM images (a and b), TEM image (c), and HRTEM images (d and e) of typical CeO₂ hollow spheres.

The N₂ adsorption–desorption isotherm (at 77 K) was employed to determine the pore size distribution of the porous CeO₂ material. The results of the measurements are depicted in Figure 4 and show a hysteresis loop in the relative pressure range of 0.4–1.0, which suggests that the CeO₂ sample is a mesoporous material.^[25] The corresponding pore size distribution curve calculated from the desorption branch by the Barrett–Joyner–Halenda (BJH) method displays a pore size distribution from 3 to 10 nm, centered at approximately 5 nm. The calculated pore volume is 0.23 cm³/g, and the specific surface area is 85.4 m²/g by the Brunauer–Emmett–Teller (BET) method.

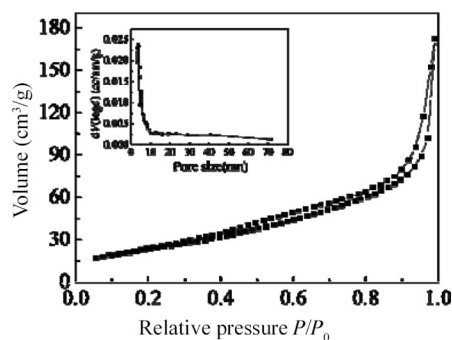


Figure 4. N_2 adsorption-desorption isotherm of the as-prepared CeO_2 hollow spheres; inset is the corresponding BJH pore size distribution curve.

To further investigate the formation process of mesoporous CeO_2 spheres with hollow interiors, the samples obtained after different reaction times were studied in detail by TEM (Figure 5) and XRD (Figure 6) analysis. It is clear that the sample obtained after 40 min of hydrothermal treatment contains a large amount of solid spheres with a mean diameter of 300 nm (Figure 5a). When the reaction time was prolonged to 60 min, a homogeneous core-shell structure is formed, which can be observed by the difference in contrast between the center and edge in Figure 5b. Further increasing the reaction time to 2 h, causes these cores to shrink to form a sphere-in-sphere structure, which can be observed in Figure 5c. The inner nanospheres disappeared completely after 6 h of hydrothermal treatment and a hollow interior is created (Figure 5d). It is worth noting that this process did not cause any obvious change in size, which is similar to a previous report on TiO_2 .^[26a] Our XRD investigations in Figure 6 reveal that poor crystalline CeO_2 with a peak indexed to (111) can be observed at the beginning. No peaks could be assigned to $Ce(OH)CO_3$, which demonstrates the pure phase of CeO_2 . When the reaction time was 1 h, all the peaks in XRD pattern can be indexed to the face-centered cubic pure phase of CeO_2 . Furthermore, the samples obtained display a gradual increase of crystallinity with reaction time.

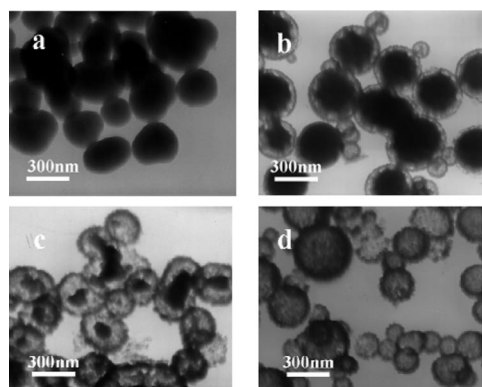


Figure 5. TEM images of the particles obtained at 180 °C at different reaction times: (a) 40 min; (b) 60 min; (c) 2 h; (d) 6 h.

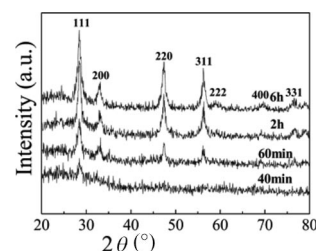


Figure 6. XRD patterns of the samples obtained at different reaction times.

It is clear that the growth process for the formation of the mesoporous CeO_2 hollow spheres is neither surfactant-assisted nor template-directed, because neither surfactants nor templates were used in the reaction system. Based on the link between the time dependence of the morphology and the crystallinity, it is believed that Ostwald ripening is a plausible mechanism for these transformations.^[26] The process of the formation of the hollow structures is illustrated in Scheme 1. In the initial stage, poorly crystallized CeO_2 nanoparticles are produced and aggregate together to form solid spheres driven by the minimization of the total energy in the system. A hollowing effect starts at a particular region underneath the immediate surface layer, observed for those samples with longer reaction times, which could be attributed to the existence of intrinsic density variations inside the solid spheres. The smaller interior crystallites that have a higher solubility will dissolve while the ones located in the outermost surface of the aggregates would serve as the new starting sites for the crystal growth. Therefore, the solid spheres are divided into two discrete regions to form a core-shell structure. The void space between the outer shell and the inner core will be enlarged, and the core region will reduced with a longer ripening treatment. In the final stage, the inner core is completely consumed through “solid-solution-solid” mass transportation. Furthermore, the crystallinity of the product increases gradually with the increase in reaction time, which also confirms that the Ostwald ripening process should be the main driving force for the construction of the hollow interiors. Similar phenomena are also observed in the formation of ZnS , and the $Co(OH)_2$ core-shell structure.^[26b,26c] It is worth noting here that the core evacuation stage proposed here is much shorter than that reported in previous studies on ZnS .^[26b]



Scheme 1. Illustration of the proposed mechanism of formation of the CeO_2 hollow spheres by Ostwald ripening.

Generally, metal oxide nanostructures can be used as adsorbents for the removal of organic pollutants from waste water by adsorption and subsequent catalytic combustion at relatively low temperatures.^[8,9,27] Compared with activated carbon, metal oxide nanostructure systems will be

more promising due to the relative ease of regeneration and recycling. Herein, we give an example of the potential application of the as-obtained mesoporous CeO₂ hollow spheres as an adsorbent in waste water treatment for the first time. Congo red is an example of an anionic secondary diazo dye that is difficult to degrade photocatalytically due to its large and complicated molecular structure. UV/Vis absorption spectroscopy was used to record the adsorption behavior of the solution after treatment (Figure 7a). The characteristic absorption of Congo red at 498 nm was chosen as the parameter that was monitored. When 20 mg of CeO₂ hollow spheres was added to 40 mL of Congo red solution with an initial concentration of 50 mg/L, the CeO₂ hollow spheres removed about 84% of the Congo red at room temperature without any additives as shown by curve I in Figure 7b. This is a removal capacity of 84 mg Congo red per g CeO₂. In a previous report, the removal capacity of a MnO₂ hierarchical hollow nanostructure is 60 mg per g MnO₂.^[27a] In comparison, commercial CeO₂ powders were used to remove Congo red from waste water (curve III in Figure 7b), and their saturation adsorption capacity was found to be 15 mg Congo red per g CeO₂, which is a much lower efficiency for removing Congo red. Furthermore, the mesoporous CeO₂ hollow spheres containing Congo red were regenerated by catalytic combustion at 400 °C in air for 2 h, and the regenerated CeO₂ material had almost the same adsorption performance as shown by curve II in Figure 7b. In addition, after calcination, the shapes of the adsorbents were nearly unchanged (Figure S1). Due to its high surface area, large adsorption capacity, and recyclability, the mesoporous CeO₂ hollow spheres could be an ideal candidate for waste water treatment.

In addition, CO removal is of fundamental significance in air purification because of the increasing emission of toxic auto exhaust gases. Among the various reducible oxides, ceria is of importance in three-way catalysis owing to its oxygen storage capacity associated with the ability to undergo a facile conversion between Ce^{III} and Ce^{IV}.^[10,11,28] Herein, to demonstrate the potential application of the mesoporous CeO₂ hollow spheres in CO removal, we studied the catalytic activity of the as-obtained products towards CO oxidation using a continuous-flow, fixed-bed microreactor. Figure 8 shows the activity curves of the as-prepared CeO₂ hollow spheres along with that of commercial CeO₂ for comparison. It is clear that the CeO₂ hollow spheres show a much higher conversion at the same temperature. For example, at 295 °C, the CO conversion of hollow spheres is 43%, which is much higher than that of commercial CeO₂ (5%). The clear contrast of the catalytic activity between CeO₂ hollow spheres and commercial powders can be attributed to the difference in surface areas. The BET specific surface area of commercial CeO₂ is only 8.5 m²/g, which is much lower than that of CeO₂ hollow spheres (85.4 m²/g). Previous reports revealed that the catalytic process is mainly related to the adsorption and desorption of gas molecules on the surface of the catalyst.^[28] In the course of the reaction, Ce^{IV} is reduced by CO, and an oxygen vacancy is created. Molecular oxygen then reacts

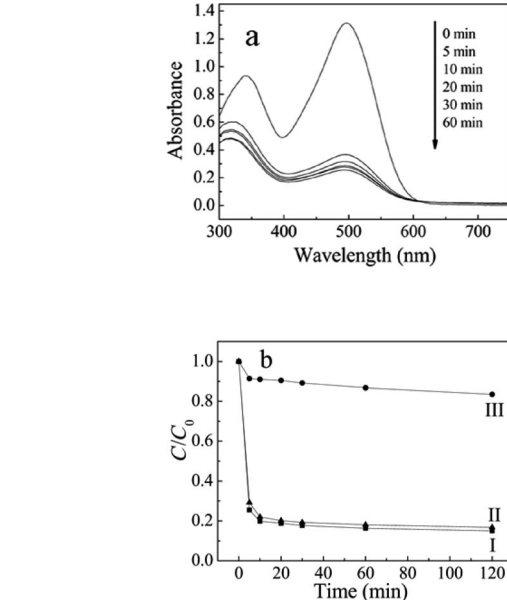


Figure 7. (a) UV/Vis absorption spectra of Congo red solutions after treatment with CeO₂ hollow spheres at different time intervals; (b) adsorption rate of Congo red on newly prepared CeO₂ hollow spheres (curve I), secondary (curve II), and commercial CeO₂ powders (curve III).

with the surface to regenerate a surface oxygen atom. Highly reactive atomic oxygen is formed due to the dissociation of molecular oxygen at the vacancy site. Finally, CO reacts with the highly reactive atomic oxygen to form CO₂. For CO oxidation, CO reacts with the catalyst surface, forming an oxygen vacancy, which is then replenished by gas-phase oxygen thereby completing the cycle by the formation and desorption of CO₂. In this case, the hollow spheres with mesoporous shells would be more easily attacked by CO molecules than commercial powders in the initial stage due to its hollow nature and porous shell. As a result, they exhibited a higher catalytic activity. After the catalysis, the hollow structure of the catalyst is nearly unchanged (Figure S2), which demonstrates that the catalyst can be recycled.

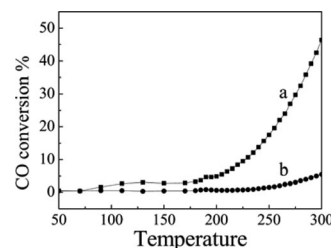


Figure 8. CO conversion rate in the presence of the as-obtained CeO₂ spheres (a), and commercial CeO₂ powders (b).

Conclusions

In summary, we have presented a simple one-step, template-free route for the synthesis of CeO₂ hollow spheres

with mesoporous shells. Based on the shape evolution of the time-dependent samples, it is believed that Ostwald ripening occurs and is the main driving force for the core evacuation of the solid aggregates during the hollowing process. Water treatment experiments indicated that the ceria hollow spheres prepared exhibited excellent removal capacity. Furthermore, the CeO₂ hollow spheres show better catalytic performance on CO oxidation than commercial CeO₂, possibly due to its large surface area. In prospect, this work will not only contribute to the development of template-free synthetic strategy for the fabrication of other hollow metal oxides, but also points towards promising applications of CeO₂ hollow spheres in water treatment and catalysis.

Experimental Section

Preparation of Mesoporous CeO₂ Hollow Spheres: H₂O₂ was used as a freshly standardized 30% (w/w) aqueous solution, and other reagents were of analytical grade, used without further purification. In a typical experiment, CeCl₃·7H₂O (0.099 g) and CO(NH₂)₂ (0.12 g) were dissolved in deionized water (19 mL) with vigorous magnetic stirring. H₂O₂ (0.2 mL) was then added to the solution, and stirring was continued for 30 min. The yellow solution was transferred into a Teflon-lined autoclave of 25 mL capacity and heated for 10 h at 180 °C. After the autoclave was cooled to room temperature naturally, light yellow products were collected and washed four times with deionized water. Finally, the product was washed with absolute ethanol and dried in an electric oven for 12 h at 80 °C.

Characterization: The phase purity of the product was examined by using a Rigaku D/Max 2200PC diffractometer with a graphite monochromator and Cu-K_α radiation ($\lambda = 0.15418$ nm). X-ray photoelectron spectra (XPS) were measured by using a PHI 5300 X-ray photoelectron spectrometer with Al-K_α radiation. The binding energy reference was taken at 284.7 eV for the C1s peak. The morphology and structure of the products were characterized by using a transmission electron microscope (TEM, JEM 100-CX II) with an accelerating voltage of 80 kV, a field-emission scanning electron microscope (FE-SEM, Hitachi, S4800), and a high-resolution transmission electron microscope (HRTEM, JEM-2100) with an accelerating voltage of 200 kV. N₂ adsorption-desorption isotherms were measured with a QuadraSorb SI apparatus at 77 K. The surface areas were calculated by the Brunauer-Emmett-Teller (BET) method, and the pore-size distribution was calculated from the desorption branch by using the Barrett-Joyner-Halenda (BJH) theory. UV/Vis absorption spectra were obtained with a UV/Vis spectrometer (Hitachi, U-4100).

Adsorption of Congo Red: The CeO₂ sample (30 mg) was dispersed in Congo red aqueous solution (40.0 mL, 50.0 mg/L) with stirring. At several time intervals, small amounts of the dispersion were centrifuged to separate the solid particles, and the Congo red concentration was analyzed by UV/Vis absorption spectroscopy.

Measurement of Catalytic Activity: The catalytic activity of the as-obtained sample was evaluated with a continuous-flow, fixed-bed microreactor operating under atmospheric pressure. In a typical experiment, catalyst particles (50 mg) were placed in the reactor. The reactant gases (1% CO, 10% O₂, and 89% N₂) were passed through the reactor at a rate of 30 mL/min. The composition of the gas exiting the reactor was analyzed with an online infrared gas

analyzer (Gasboard-3121, China Wuhan Cubic Co.), which simultaneously detects CO and CO₂ at a sensitivity of 10 ppm. The results were further confirmed with a Shimadzu gas chromatograph (GC-14C).

Supporting Information (see footnote on the first page of this article): TEM and SEM images of the hollow spheres after calcination at 400 °C for 2 h and after the catalytic measurement.

Acknowledgments

This work was supported by the Natural Science Foundation of China (Grant no. 20876089) and Key Technologies R&D Programme of China (Grant no. 2007BAD87B05). The authors would like to thank Prof. Yi Ding for the catalytic measurements.

- [1] S. Park, J. H. Lim, S. W. Chung, C. A. Mirkin, *Science* **2004**, 303, 348–351.
- [2] X. Wang, J. Zhuang, Q. Peng, Y. D. Li, *Nature* **2005**, 437, 121–124.
- [3] J. Goldberger, R. R. He, Y. F. Zhang, S. Lee, H. Q. Yan, H. J. Choi, P. D. Yang, *Nature* **2003**, 422, 599–602.
- [4] Y. G. Sun, Y. N. Xia, *Science* **2002**, 298, 2176–2179.
- [5] X. W. Lou, Y. Wang, C. Yuan, J. Y. Lee, L. A. Archer, *Adv. Mater.* **2006**, 18, 2325–2329.
- [6] a) X. X. Li, Y. J. Xiong, Z. Q. Li, Y. Xie, *Inorg. Chem.* **2006**, 45, 3493–3495; b) X. B. Cao, L. Gu, W. J. Gao, W. C. Wang, S. F. Wu, *Adv. Funct. Mater.* **2006**, 16, 896–902; c) Z. Y. Liu, D. D. Sun, P. Guo, J. O. Leckie, *Chem. Eur. J.* **2007**, 13, 1851–1855.
- [7] a) M. Darbandi, R. Thomann, T. Nann, *Chem. Mater.* **2007**, 19, 1700–1703; b) J. Zhou, W. Wu, D. Caruntu, M. H. Yu, A. Martin, J. F. Chen, C. J. O'Connor, W. L. Zhou, *J. Phys. Chem. C* **2007**, 111, 17473–17477.
- [8] Y. Y. Xu, D. R. Chen, X. L. Jiao, K. Y. Xue, *J. Phys. Chem. C* **2007**, 111, 16284–16289.
- [9] S. W. Cao, Y. J. Zhu, *J. Phys. Chem. C* **2008**, 112, 6253–6257.
- [10] A. Trovarelli, *Catal. Rev. Sci. Eng.* **1996**, 38, 439–520.
- [11] P. G. Harrison, I. K. Ball, W. Azelee, W. Daniel, D. Goldfarb, *Chem. Mater.* **2000**, 12, 3715–3725.
- [12] S. Tsunekawa, T. Fukuda, *J. Appl. Phys.* **2000**, 87, 1318–1321.
- [13] a) S. Park, J. M. Vohs, R. J. Gorte, *Nature* **2000**, 404, 265–267; b) Z. Zhan, S. A. Barnett, *Science* **2005**, 308, 844–847.
- [14] a) L. S. Zhong, J. Q. Hu, A. M. Cao, Q. Liu, W. G. Song, L. J. Wan, *Chem. Mater.* **2007**, 19, 1648–1655; b) X. J. Peng, Z. K. Luan, J. Ding, Z. H. Di, Y. H. Li, B. H. Tian, *Mater. Lett.* **2005**, 59, 399–403; c) Z. C. Di, J. Ding, X. J. Peng, Y. H. Li, Z. K. Luan, J. Liang, *Chemosphere* **2006**, 62, 861–865.
- [15] X. D. Feng, D. C. Sayle, Z. L. Wang, M. S. Paras, B. Santora, A. C. Sutorik, T. X. T. Sayle, Y. Yang, Y. Ding, X. D. Wang, Y. S. Her, *Science* **2006**, 312, 1504–1508.
- [16] a) Z. L. Wang, X. D. Feng, *J. Phys. Chem. B* **2003**, 107, 13563–13566; b) F. Zhang, Q. Jin, S.-W. Chan, *J. Appl. Phys.* **2004**, 95, 4319–4326; c) S. V. N. T. Kuchibhatla, A. S. Karakoti, S. Seal, *Nanotechnology* **2007**, 18, 075303–075307.
- [17] a) S. W. Yang, L. Gao, *J. Am. Chem. Soc.* **2006**, 128, 9330–9331; b) Z. Q. Yang, K. B. Zhou, X. W. Liu, Q. Tian, D. Y. Lu, S. Yang, *Nanotechnology* **2007**, 18, 185606; c) Z. J. Yang, Y. Z. Yang, H. Liang, L. Liu, *Mater. Lett.* **2009**, 63, 1774–1777.
- [18] F. Zhou, X. M. Zhao, H. Xu, C. G. Yuan, *J. Phys. Chem. C* **2007**, 111, 1651–1657.
- [19] B. Tang, L. H. Zhuo, J. C. Ge, G. L. Wang, Z. Q. Shi, J. Y. Niu, *Chem. Commun.* **2005**, 3565–3567.
- [20] a) S. C. Kuiry, S. D. Patil, S. Deshpande, S. Seal, *J. Phys. Chem. B* **2005**, 109, 6936–6939; b) C. Ho, J. C. Yu, T. Kwong, A. C. Mak, S. Lai, *Chem. Mater.* **2005**, 17, 4514–4522; c) C. Sun, H. Li, H. Zhang, Z. X. Wang, L. Q. Chen, *Nanotechnology* **2005**, 16, 1454–1463.

- [21] a) K. B. Zhou, Z. Q. Yang, S. Yang, *Chem. Mater.* **2007**, *19*, 1215–1222; b) X. Liang, X. Wang, Y. Zhuang, B. Xu, S. M. Kuang, Y. D. Li, *J. Am. Chem. Soc.* **2008**, *130*, 2736–2737; c) C.-H. Chen, S. F. Abbas, A. Morey, S. Sithambaram, L.-P. Xu, H. F. Garces, W. A. Hines, S. L. Suib, *Adv. Mater.* **2008**, *20*, 1205–1209; d) G. Z. Chen, C. X. Xu, X. Y. Song, S. L. Xu, Y. Ding, S. X. Sun, *Cryst. Growth Des.* **2008**, *8*, 4449–4453; e) G. Z. Chen, C. X. Xu, X. Y. Song, W. Zhao, Y. Ding, S. X. Sun, *Inorg. Chem.* **2008**, *47*, 723–728; f) M. M. Titirici, M. Antonietti, A. Thomas, *Chem. Mater.* **2006**, *18*, 3808–3812; g) Z. Y. Guo, F. F. Jian, F. L. Du, *Scripta Mater.* **2009**, *61*, 48–51.
- [22] a) Z. Y. Guo, F. L. Du, G. C. Li, Z. L. Cui, *Inorg. Chem.* **2006**, *45*, 4167–4169; b) S. F. Chen, S. H. Yu, L. Ren, W. T. Yao, H. Colfen, *Chem. Eur. J.* **2004**, *10*, 3050–3058.
- [23] a) D. Boro, N. J. Stephen, *J. Eur. Ceram. Soc.* **1999**, *19*, 1925–1934; b) F. H. Scholes, A. E. Hughes, S. G. Hardin, P. Lynch, P. R. Miller, *Chem. Mater.* **2007**, *19*, 2321–2328.
- [24] F. Zhang, P. Wang, J. Koberstein, S. Khalid, S. W. Chan, *Surf. Sci.* **2004**, *563*, 74–78.
- [25] J. C. Groen, L. A. A. Peffer, J. Pérez-Ramírez, *Microporous Mesoporous Mater.* **2003**, *60*, 1–17.
- [26] a) H. G. Yang, H. C. Zeng, *J. Phys. Chem. B* **2004**, *108*, 3492–3495; b) B. Liu, H. C. Zeng, *Small* **2005**, *1*, 566–571; c) R. Qiao, X. L. Zhang, R. Qiu, J. C. Kim, Y. S. Kang, *Chem. Eur. J.* **2009**, *15*, 1886–1892.
- [27] a) J. B. Fei, Y. Cui, X. Y. Yan, W. Qi, Y. Yang, K. W. Wang, Q. He, J. B. Li, *Adv. Mater.* **2008**, *20*, 452–456; b) C. C. Yu, X. P. Dong, L. M. Guo, J. T. Li, F. Qin, L. X. Zhang, J. L. Shi, D. S. Yan, *J. Phys. Chem. C* **2008**, *112*, 13378–13382.
- [28] K. B. Zhou, X. Wang, X. M. Sun, Q. Peng, Y. D. Li, *J. Catal.* **2005**, *229*, 206–212.

Received: January 13, 2010
Published Online: May 31, 2010

Chromium(III) Complexes with Chelating Anilido–Imine Ligands: Synthesis, Structures, and Catalytic Properties for Ethylene Polymerization

Tieqi Xu,^{*[a]} Haiyan An,^[a] Wei Gao,^[b] and Ying Mu^{*[b]}

Keywords: Chromium / Polymerization / Homogeneous catalysis / Ligand effects

A series of novel chromium complexes that bear anilido–imine ligands, $[\{ortho\text{-}C_6H_4(NAr')(CH=NAr'')\}CrCl_2(thf)_2]$ [$Ar' = Ar'' = C_6H_5$ (**1**); $Ar' = Ar'' = p\text{-}MeC_6H_4$ (**2**); $Ar' = Ar'' = 2,6\text{-}Me_2C_6H_3$ (**3**); $Ar' = 2,6\text{-}iPr_2C_6H_3$, $Ar'' = 2,6\text{-}Me_2C_6H_3$ (**4**); $Ar' = Ar'' = 2,6\text{-}iPr_2C_6H_3$ (**5**)], have been synthesized and characterized by elemental analysis, IR spectroscopy, and

ESI-MS. The molecular structures of complexes **1** and **2** have been confirmed by single-crystal X-ray diffraction analysis. When activated with methylaluminoxane (MAO), these complexes exhibit reasonable to good catalytic activity for ethylene polymerization and produce polyethylene with moderate molecular weights.

Introduction

The chromium-based heterogeneous Phillips catalyst (CrO_3/SiO_2)^[1] and the Union Carbide Unipol catalyst (Cp_2Cr/SiO_2 ; Cp = cyclopentadienyl)^[2] play an important role in the global production of polyolefins. However, as heterogeneous catalysts they have not proven amenable to intimate study on account of the relatively ill-defined nature of these catalysts with respect to coordination environment and oxidation state.^[3] Consequently, there is a great need to develop well-defined homogeneous chromium-based catalysts that can offer the potential for understanding the modus operandi of heterogeneous chromium catalysts.^[3d] Over the past decades, significant advances have been made in the synthesis of homogeneous metallocene chromium catalysts that contain cyclopentadienyl ligands as a model system for the Union Carbide Unipol family.^[4,5] However, only a few nonmetallocene chromium complexes for modeling the Phillips catalyst have been reported. Recently, chromium complexes with bidentate β -diketiminate ligands for modeling the Phillips catalyst have received attention because these ligands approximate the hard coordination environment of the silica surface and the N-substituents allow for steric protection of the active site. Theopold and co-workers first used the mononuclear β -diketiminate chromium complexes for ethylene polymerization^[6] and found a reasonable candidate for the active surface species of the heterogeneous Phillips catalyst.^[7] Subsequently, Gibson et al. reported chromium complexes with similar ligands for

ethylene polymerization.^[3d,8] But these β -diketiminate ligands are not easily modified and the corresponding chromium catalysts show only moderate activity for ethylene polymerization. The bidentate salicylaldiminate chelate ligands possess easily modified features and have been applied in olefin polymerization chemistry. Gibson et al. reported mononuclear salicylaldiminate chromium complexes, which showed good catalytic activity and can tune catalytic activity and molecular weight by easily modified ligands.^[9]

Taking these into account, our current research interest is to choose the anilido–imine ligands that combine the steric effect of the β -diketiminate ligand framework and the more easily modified features of the salicylaldiminate ligand framework to construct chromium metal catalysts for modeling the Phillips catalyst. To date, only a few complexes based on anilido–imine ligands are known. The successful examples include the yttrium(III),^[10] nickel(II),^[11] and nickel(I)^[12] complexes that the groups of Piers, Wu, and Jin, respectively, synthesized with these ligands. Recently, we have also addressed some anilido–imine aluminum complexes.^[13] Herein we report the first chromium(III) complexes based on anilido–imine ligands (Scheme 1) and explore their catalytic activity for ethylene homopolymerization. These complexes exhibit much higher catalytic activity and more easily modified features than analogue β -diketiminate chromium complexes.^[6a,7]

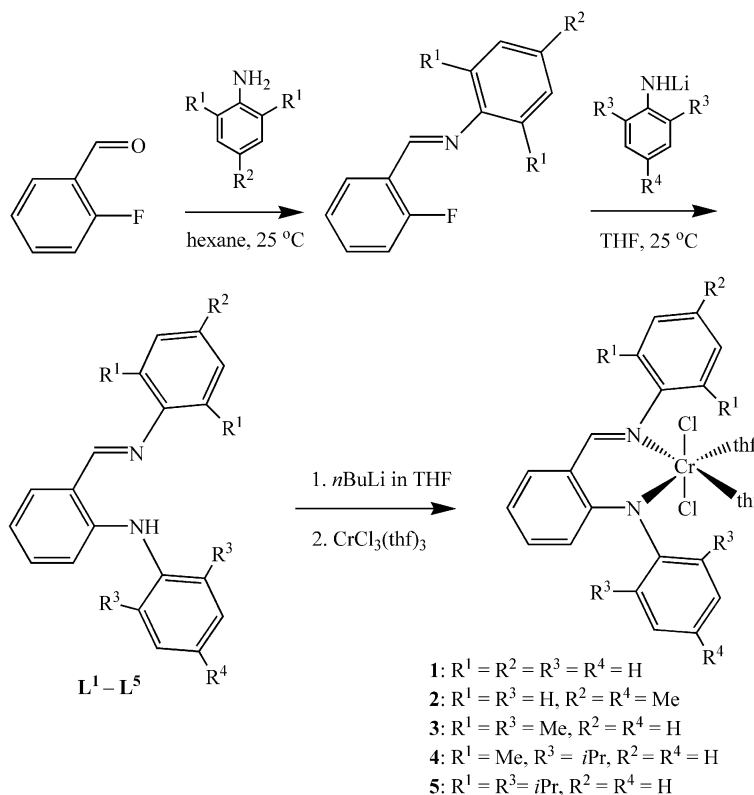
Results and Discussion

Synthesis of Chromium Complexes

The syntheses of five chromium complexes as catalytic precursors are shown in Scheme 1. The free ligands **L**¹–**L**⁵ were prepared according to the literature procedure.^[10–12] It was noteworthy that the steric bulkiness of the ligands

[a] Department of Chemistry, Dalian University of Technology, Dalian 116023, P. R. China
E-mail: tqxu@dlut.edu.cn

[b] State Key Laboratory of Supramolecular Structure and Materials, School of Chemistry, Jilin University, Changchun 130012, P. R. China
E-mail: ymu@jlu.edu.cn



Scheme 1. Synthesis of chromium complexes 1–5.

could be easily adjusted by changing various arylamines. These five ligands were characterized by 1H NMR and IR spectroscopy. The infrared absorption bands of the imine $C=N$ stretch occur in the region $1621\text{--}1624\text{ cm}^{-1}$. After the anilido–imine ligands were treated with $nBuLi$ in THF, $[CrCl_3(thf)_3]$ (0.95 equiv.) was added to give a dark brown solution. The chromium(III) complexes 1–5 were obtained as brown crystals in high yields by recrystallization from a solution of CH_2Cl_2/n -hexane. The complexes were well characterized by ESI-MS and IR spectroscopy as well as elemental analysis. The IR spectra of these complexes show absorption bands of the imine $C=N$ at $1606\text{--}1608\text{ cm}^{-1}$, which are clearly blueshifted in comparison with the free ligands.

Crystal Structures

Crystals of complexes 1 and 2 for single-crystal X-ray diffraction analysis were grown from a solution of CH_2Cl_2/n -hexane at room temperature or $0\text{ }^\circ\text{C}$. The ORTEP drawings of the molecular structures of complexes 1 and 2 are shown in Figure 1 and Figure 2, respectively. Selected bond lengths and bond angles for complexes 1 and 2 are depicted in Table 1. Single-crystal X-ray analysis reveals that complexes 1 and 2 adopt an octahedral geometry with the metal center chelated by the bidentate ligand by means of the amido and imine nitrogen atoms. The $Cr\text{--}N$ (amido) distances [$1.990(2)\text{ \AA}$ for 1 and $1.985(4)\text{ \AA}$ for 2] are much shorter than the $Cr\text{--}N$ (imine) distances [$2.033(2)\text{ \AA}$ for 1 and $2.024(4)\text{ \AA}$ for 2], because the anionic amido nitrogen

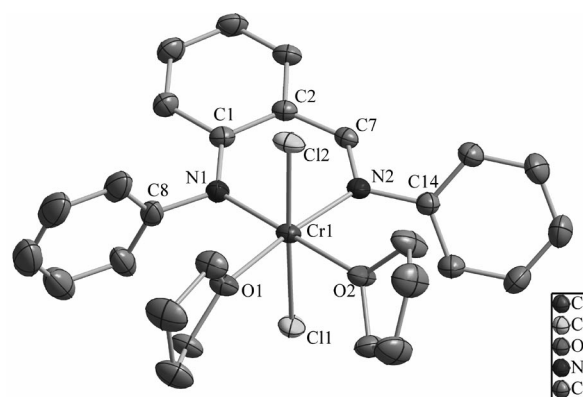


Figure 1. Structure of complex 1 (thermal ellipsoids are drawn at the 30% probability level).

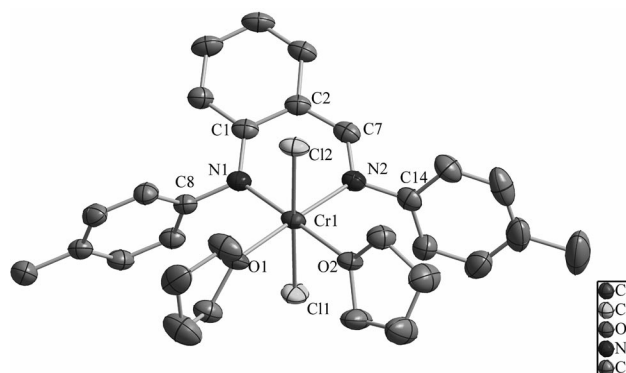


Figure 2. Structure of complex 2 (thermal ellipsoids are drawn at the 30% probability level).

can also donate π electrons to the chromium, whereas the neutral imine nitrogen has no available lone pair for π donation. The Cr–N (imine) distances are close to the values [2.032(6), 2.033(5) Å] previously reported for $[\{\text{N}(\text{Ph})\text{C}(\text{Me})_2\text{CH}\}_2\text{CrCl}_2(\text{thf})_2]$,^[6a] but shorter than those values [2.073(4) Å] of $[(2-\{\text{CH}=\text{N}(2,6\text{-}i\text{Pr}_2\text{C}_6\text{H}_3)\}-\text{C}_4\text{H}_3\text{N})_2\text{-CrMe}]^{[3d]}$ and [2.098(3) Å] of $[\text{Cr}\{\text{3,5-}(t\text{Bu})_2\text{-2-(O)-C}_6\text{H}_2\text{CH}_2\text{NH}(2,6\text{-Me}_2\text{C}_6\text{H}_3)\}(\eta^1\text{-NCCCH}_3)_2\text{Cl}_2]$.^[9a] The N–Cr–N angles ($90.83(10)^\circ$ for **1** and $89.38(17)^\circ$ for **2**) in these complexes are less than that [$91.7(2)^\circ$] of a similar complex $[(\{\text{N}(\text{Ph})\text{C}(\text{Me})_2\text{CH}\}_2\text{CrCl}_2(\text{thf})_2)]$, whereas they are larger than those in the five-membered chelating ring [$80.9(2)^\circ$] of $[\text{Cr}\{\text{3,5-}(t\text{Bu})_2\text{-2-(O)-C}_6\text{H}_2\text{CH}_2\text{NH}(2,6\text{-Me}_2\text{C}_6\text{H}_3)\}(\eta^1\text{-NCCCH}_3)_2\text{Cl}_2]$. The values of four Cr–Cl bond lengths are close to each other and close to those observed in some reported chromium complexes ligated by β -diketiminato,^[6] imino–pyrrolide,^[3d] salicylaldiminato,^[9] and cyclopentadienyl.^[4] In these two complexes, the six-membered chelating ring is nearly planar, with the chromium atom lying 0.1336 and 0.2260 Å out of the plane, respectively. The dihedral angles between the six-membered chelating ring and aromatic ring attached to the amido nitrogen atom are 90.9 and 91.7° , and the dihedral angles between the six-membered chelating ring and aromatic ring attached to the imine nitrogen atom are 56.3 and 61.5° , respectively. The imino C=N bonds in these complexes retain their double-bond character, being 1.301(3) and 1.306(6) Å for complexes **1** and **2**, respectively.

Table 1. Selected bond lengths [Å] and angles [$^\circ$] for complexes **1** and **2**.

Complex 1			
Cr1–N1	1.990(2)	Cr1–N2	2.033(2)
Cr1–O1	2.117(2)	Cr1–O2	2.122(2)
Cr1–Cl1	2.3338(12)	Cr1–Cl2	2.3138(12)
N1–C1	1.358(3)	C14–N2	1.444(3)
N1–C8	1.431(4)	C7–N2	1.301(3)
N1–Cr1–N2	90.83(10)	N1–Cr1–O1	95.43(9)
N2–Cr1–O1	173.74(8)	N1–Cr1–O2	176.77(8)
N2–Cr1–O2	91.26(9)	O1–Cr1–O2	82.50(9)
N1–Cr1–Cl2	89.55(7)	N2–Cr1–Cl2	88.67(7)
O1–Cr1–Cl2	91.57(6)	O2–Cr1–Cl2	88.04(6)
N1–Cr1–Cl1	92.57(7)	N2–Cr1–Cl1	90.69(7)
O1–Cr1–Cl1	88.84(6)	O2–Cr1–Cl1	89.87(6)
Cl2–Cr1–Cl1	177.80(3)		
Complex 2			
Cr1–N1	1.985(4)	Cr1–N2	2.024(4)
Cr1–O1	2.093(3)	Cr1–O2	2.126(3)
Cr1–Cl1	2.3229(17)	Cr1–Cl2	2.3233(17)
N1–C1	1.367(6)	C14–N2	1.437(7)
N1–C8	1.438(6)	C7–N2	1.306(6)
N1–Cr1–N2	89.38(17)	N1–Cr1–O1	95.07(15)
N2–Cr1–O1	174.92(16)	N1–Cr1–O2	178.21(15)
N2–Cr1–O2	92.09(15)	O1–Cr1–O2	83.42(13)
N1–Cr1–Cl2	90.22(13)	N2–Cr1–Cl2	86.97(12)
O1–Cr1–Cl2	90.54(10)	O2–Cr1–Cl2	88.83(10)
N1–Cr1–Cl1	91.25(13)	N2–Cr1–Cl1	92.38(12)
O1–Cr1–Cl1	89.99(11)	O2–Cr1–Cl1	89.72(10)
Cl2–Cr1–Cl1	178.39(7)		

Ethylene Polymerization Studies

The experimental results of ethylene polymerization with complexes **1–5** as precatalysts are summarized in Table 2. Upon activation with methylaluminoxane (MAO), complexes **1–5** show good catalytic activity [up to 1.37×10^6 g PE(molCr)^{−1}h^{−1}] for ethylene polymerization, producing polyethylene with moderate molecular weight. The influences of the Al/Cr molar ratio and reaction temperature on ethylene reactivity were studied with a **3**/MAO system. Increasing the Al/Cr molar ratio from 300 to 500 greatly enhanced its productivity of ethylene polymerization (Table 2, entries 3 and 4). However, further increasing the Al/Cr molar ratio to 1000 resulted in a lower activity of ethylene polymerization (Table 2, entry 5). Elevation of the reaction temperature from 20 to 60 °C resulted in a sharp decrease of polymerization activity, which can be explained as catalyst decomposition and lower ethylene solubility at higher temperature (Table 2, entries 4, 6, and 7). In view of these observations, further experiments were performed at an Al/Cr molar ratio of 500 and at 20 °C. The order of catalyst activity for ethylene polymerization under similar conditions (Table 2, entries 1, 2, 4, 8, and 9) is **3** > **4** > **5** > **2** > **1**, which implies that the ligand environment, with regards to their substituents on the aryl ring linked to the imino–N atom and amido–N atom, has a significant influence on the catalytic behavior of chromium complexes on ethylene reactivity. Increasing the size of *ortho* substituents from R¹ = R³ = H to R¹ = R³ = Me greatly enhanced ethylene polymerization activity (Table 2, entries 1, 2, and 4). The higher catalytic activity is believed to arise from improved cation–anion separation in the active species as well as increased protection of active species. However, further increasing the size of *ortho* substituents to R¹ = R³ = *i*Pr resulted in lower catalytic activities (Table 2, entry 9). This might be explained by the fact that bulkier substituents slow down ethylene coordination and hinder chain propagation. Complex **1**, which bears *para*-methyl substituents on the ligands, exhibited greater activity than the unsubstituted complex **2**. It indicates that the remote electron-donating electronic effect also increased activity for polymerization. ¹³C NMR spectroscopic analysis of the typical polymer

Table 2. Results of ethylene polymerization using precatalysts **1–5**.^[a]

	Cat.	Al/Cr	T [°C]	Yield [g]	Activity ^[b] × 10 ^{−6}	M _n ^[c] × 10 ^{−5}
1	1	500	20	trace	–	–
2	2	500	20	0.08	0.02	1.56
3	3	300	20	5.12	1.02	1.54
4	3	500	20	6.87	1.37	1.38
5	3	1000	20	3.96	0.79	0.67
6	3	500	40	3.45	0.69	0.96
7	3	500	60	2.66	0.53	0.89
8	4	500	20	1.68	0.34	1.06
9	5	500	20	1.45	0.29	0.61

[a] Polymerization conditions: 60 mL toluene, 10 μmol catalyst, 5 bar ethylene pressure, 30 min. [b] g of PE(molCr)^{−1}h^{−1}. [c] Measured in decahydronaphthalene at 135 °C.

sample (Table 2, entry 5) reveals that the polyethylene contains long-chain branches; the degree of branching is 5 branches per 1000 C atoms. The molecular weight distribution (M_w/M_n) of this polymer sample was 23.8, which was measured by gel permeation chromatography at 150 °C.

Conclusion

Five new anilido–imine chromium complexes have been synthesized and characterized. They displayed high catalytic activity up to 1.37×10^6 g PE (mol Cr) $^{-1}$ h $^{-1}$ for ethylene polymerization upon treatment with MAO. The catalytic activity of these complexes and the molecular weight of the produced polyethylenes can be tuned in a broad range by changing the substituents on the aryl ring linked to the imino-N atom and amido-N atom. These new catalysts represent a remarkable addition to the limited list of nonmetallocene-type chromium ethylene polymerization catalysts.

Experimental Section

General: Reactions with organometallic reagents were carried out under a nitrogen atmosphere (ultrahigh purity) using standard Schlenk techniques or in an inert atmosphere glove box. Solvents were dried by means of the appropriate drying agent, distilled, degassed, and stored over molecular sieves (4 Å). Polymerization-grade ethylene was further purified by passage through columns of molecular sieves (3 Å) and MnO. MAO and *n*BuLi were purchased from Aldrich. $[\text{CrCl}_3(\text{thf})_3]$ ^[14] was prepared according to literature procedures. Elemental analyses were performed with a Vario EL microanalyzer. Mass spectra were measured with a Micromass Q-TOF mass spectrometer instrument using electrospray ionization (ESI). IR spectra were recorded with a Nicolet NEXUS FTIR spectrometer.

[*ortho*-C₆H₄N(C₆H₅)(CH=NC₆H₅)]CrCl₂(thf)₂ (1): Under nitrogen, a solution of *ortho*-C₆H₄NLi(C₆H₅)(CH=NC₆H₅) was prepared at –78 °C by the addition of *n*BuLi (2.55 mmol) to *ortho*-C₆H₄NH(C₆H₅)(CH=NC₆H₅) (0.68 g, 2.50 mmol) in THF (10 mL). The solution was warmed to room temperature and stirred for 2 h and then was added dropwise to $[\text{CrCl}_3(\text{thf})_3]$ (0.94 g, 2.50 mmol) in THF (20 mL). The resulting mixture was warmed to room temperature and stirred for 15 h, during which time the color changed from purple to brown. The solvents were removed under vacuum, and the residue was extracted with CH₂Cl₂ (20 mL) and filtered. The filtrate was concentrated to 5 mL and mixed with hexane (50 mL). Cooling to room temperature afforded brown crystals of complex **1** after several days (1.10 g, 2.05 mmol, 82%). IR (KBr): $\tilde{\nu}$ = 3059 (m), 2976 (m), 2876 (m), 1609 (s), 1586 (s), 1527 (m), 1487 (w), (m), 1465 (m), 1438 (m), 1392 (m), 1334 (m), 1267 (w), 1204 (w), 1180 (m), 1163 (m), 1129 (w), 1043 (m), 1028 (w), 937 (w), 859 (m), 697 (s) cm $^{-1}$. ESI-MS: m/z = 393.1 $[\text{M} - 2\text{THF}]^+$, 358.2 $[\text{M} - 2\text{THF} - \text{Cl}]^+$. C₂₇H₃₁Cl₂CrN₂O₂ (538.45): calcd. C 60.23, H 5.80, N 5.20; found C 59.98, H 5.71, N 5.24.

[*ortho*-C₆H₄N(C₆H₄Me-*p*)(CH=NC₆H₄Me-*p*)]CrCl₂(thf)₂ (2): Complex **2** was synthesized in the same way as described above for the synthesis of **1** with *ortho*-C₆H₄NH(C₆H₄Me-*p*)(CH=NC₆H₄Me-*p*) (0.75 g, 2.50 mmol) as starting material. Pure **2** (1.07 g, 1.90 mmol, 76%) was obtained as brown crystals. IR (KBr): $\tilde{\nu}$ = 3020 (m), 2975 (m), 2872 (m), 1611 (s), 1587 (s), 1526

(m), 1503 (s), 1466 (w), 1465 (m), 1439 (s), 1389 (m), 1337 (m), 1266 (w), 1225 (w), 1208 (m), 1181 (m), 1163 (m), 1129 (m), 1042 (m), 1020 (m), 926 (w), 882 (m), 820 (w), 796 (w), 746 (m) cm $^{-1}$. ESI-MS: m/z = 421.2 $[\text{M} - 2\text{THF}]^+$, 386.2 $[\text{M} - 2\text{THF} - \text{Cl}]^+$. C₂₇H₃₁Cl₂CrN₂O₂ (566.50): calcd. C 61.48, H 6.23, N 4.94; found C 60.99, H 6.24, N 4.85.

[*ortho*-C₆H₄N(C₆H₄Me₂-2,6)(CH=NC₆H₄Me₂-2,6)]CrCl₂(thf)₂ (3): Complex **3** was synthesized in the same way as described above for the synthesis of **1** with *ortho*-C₆H₄NH(C₆H₄Me₂-2,6)(CH=NC₆H₄Me₂-2,6) (0.82 g, 2.50 mmol) as starting material. Pure **3** (1.13 g, 1.90 mmol, 76%) was obtained as brown crystals. IR (KBr): $\tilde{\nu}$ = 3018 (m), 2975 (m), 2870 (m), 1607 (s), 1581 (s), 1523 (m), 1464 (m), 1435 (w), 1381 (m), 1327 (m), 1262 (w), 1215 (m), 1160 (s), 1129 (m), 1095 (m), 1049 (m), 969 (m), 871 (w), 768 (m), 747 (m) cm $^{-1}$. ESI-MS: m/z = 449.2 $[\text{M} - 2\text{THF}]^+$, 414.2 $[\text{M} - 2\text{THF} - \text{Cl}]^+$. C₃₁H₃₉Cl₂CrN₂O₂ (594.56): calcd. C 62.62, H 6.61, N 4.71; found C 62.94, H 6.49, N 4.74.

[*ortho*-C₆H₄N(C₆H₄iPr₂-2,6)(CH=NC₆H₄Me₂-2,6)]CrCl₂(thf)₂ (4): Complex **4** was synthesized in the same way as described above for the synthesis of **1** with *ortho*-C₆H₄NH(C₆H₄iPr₂-2,6)(CH=NC₆H₄Me₂-2,6) (0.96 g, 2.50 mmol) as starting material. Pure **4** (1.01 g, 1.55 mmol, 62%) was obtained as brown crystals. IR (KBr): $\tilde{\nu}$ = 3023 (m), 2972 (m), 2870 (m), 1608 (s), 1582 (s), 1522 (m), 1465 (m), 1432 (m), 1382 (m), 1320 (m), 1262 (w), 1210 (m), 1160 (s), 1129 (m), 1095 (m), 1049 (m), 969 (m), 873 (w), 796 (m), 745 (m) cm $^{-1}$. ESI-MS: m/z = 505.2 $[\text{M} - 2\text{THF}]^+$, 470.3 $[\text{M} - 2\text{THF} - \text{Cl}]^+$. C₃₅H₄₇Cl₂CrN₂O₂ (650.66): calcd. C 64.61, H 7.28, N 4.31; found C 64.38, H 7.23, N 4.40.

[*ortho*-C₆H₄N(C₆H₄iPr₂-2,6)(CH=NC₆H₄iPr₂-2,6)]CrCl₂(thf)₂ (5): Complex **5** was synthesized in the same way as described above for the synthesis of **1** with *ortho*-C₆H₄NH(C₆H₄iPr₂-2,6)(CH=NC₆H₄iPr₂-2,6) (1.10 g, 2.50 mmol) as starting material. Pure **5** (0.90 g, 1.27 mmol, 51%) was obtained as brown crystals. IR (KBr): $\tilde{\nu}$ = 3057 (m), 2970 (s), 2867 (m), 1608 (s), 1581 (s), 1523 (m), 1464 (w), (m), 1432 (m), 1383 (m), 1360 (m), 1319 (m), 1236 (w), 1204 (w), 1158 (s), 1093 (m), 1043 (m), 929 (w), 868 (w), 795 (m), 745 (m) cm $^{-1}$. ESI-MS: m/z = 561.3 $[\text{M} - 2\text{THF}]^+$, 526.4 $[\text{M} - 2\text{THF} - \text{Cl}]^+$. C₃₉H₅₅Cl₂CrN₂O₂ (706.77): calcd. C 66.28, H 7.84, N 3.96; found C 65.99, H 7.67, N 3.96.

Crystal Structure Determination: Single crystals of complexes **1** and **2** were obtained from a solution of CH₂Cl₂/*n*-hexane. Diffraction data were collected at 293 K with a Bruker SMART-CCD diffractometer using graphite-monochromated Mo-*K* α radiation (λ = 0.71073 Å). Details of the crystal data, data collections, and structure refinements are summarized in Table 3. The structures were solved by direct methods^[15] and refined by full-matrix least-squares on F^2 . All non-hydrogen atoms were refined anisotropically, and the hydrogen atoms were included in idealized position. All calculations were performed with the SHELXTL^[16] crystallographic software packages.

CCDC-764274 (for **1**) and -764275 (for **2**) contain the supplementary crystallographic data for this paper. These data can be obtained free of charge from The Cambridge Crystallographic Data Centre via www.ccdc.cam.ac.uk/data_request/cif.

General Procedure of Polymerization Reactions: A dry 200 mL steel autoclave was charged with a solution of MAO in toluene (60 mL), thermostatted at the desired temperature, and saturated with ethylene (1.0 bar). The system was maintained by continuously stirring for 30 min, and then the polymerization reaction was started by injection of the chromium catalyst solution (3 mM). The vessel was repressurized to the necessary pressure with ethylene immediately

Table 3. Crystal data and structural refinement details for complexes **1** and **2**.

	1	2
Formula	C ₂₇ H ₃₁ Cl ₂ CrN ₂ O ₂	C ₂₉ H ₃₅ Cl ₂ CrN ₂ O ₂
Molecular weight	538.44	566.49
Crystal system	triclinic	monoclinic
Space group	<i>P</i> $\bar{1}$	<i>P</i> 2 ₁ / <i>c</i>
<i>a</i> [Å]	8.125(4)	13.478(4)
<i>b</i> [Å]	12.036(8)	8.746(3)
<i>c</i> [Å]	13.618(7)	25.916(9)
α [°]	80.27(2)	90
β [°]	82.357(18)	113.552(18)
γ [°]	82.76(2)	90
<i>V</i> [Å ³]	1293.6(12)	2800.5(16)
<i>Z</i>	2	4
<i>D</i> _{calcd.} [g cm ⁻³]	1.382	1.344
<i>F</i> (000)	562	1188
Absorption coeff. [mm ⁻¹]	0.676	0.628
Collection range [°]	3.02 ≤ θ ≤ 27.48	3.05 ≤ θ ≤ 25.00
Independent reflections	5889	4930
<i>R</i> _{int}	0.0254	0.1281
Data / restraints / parameters	5889 / 18 / 307	4930 / 12 / 327
<i>R</i> ₁ (<i>I</i> > 2 σ)	0.0473	0.0638
<i>wR</i> ₂ (<i>I</i> > 2 σ)	0.1246	0.1273
Goodness of fit	1.092	1.003
Largest difference peak	0.778	0.293
Largest hole [e Å ⁻³]	-0.343	-0.390

and the pressure was maintained by a continuous feed of the monomer. After 30 min, the polymerization was quenched by injecting acidified methanol [HCl (3 M)/methanol, 1:1]. The mixture was stirred and the polymer was collected by filtration, washed with water, methanol, and dried in vacuo.

Acknowledgments

This work was supported by the National Natural Science Foundation of China (grant 20804006) and Specialized Research Fund for the Doctoral Program of Higher Education (grant 200801411015).

- [1] a) J. P. Hogan, *J. Polym. Sci. Polym. Chem. Ed.* **1970**, *8*, 2637–2652; b) M. P. McDaniel, *Adv. Catal.* **1985**, *33*, 47–98.
- [2] a) F. J. Karol, G. L. Karapinka, C. Wu, A. W. R. Dow, N. Johnson, W. L. Carrick, *J. Polym. Sci. Polym. Chem. Ed.* **1972**, *10*, 2621–2628; b) G. L. Karapinka, US 3709853, **1973**.
- [3] a) K. H. Theopold, *Eur. J. Inorg. Chem.* **1998**, 15–24; b) M. P. McDaniel, *Adv. Catal.* **1985**, *33*, 47–54; c) J. A. N. Ajjou, S. L. Scott, V. Paquel, *J. Am. Chem. Soc.* **1998**, *120*, 415–416; d) V. C. Gibson, P. J. Maddox, C. Newton, C. Redshaw, G. A. Solan, A. J. P. White, D. J. Williams, *Chem. Commun.* **1998**, 1651–1652.
- [4] a) S. Randall, P. G. Jones, M. Tamm, *Organometallics* **2008**, *27*, 3232–3239; b) A. Dohring, J. Gohre, P. W. Jolly, B. Kruger, J. Rust, G. P. J. Verhovnik, *Organometallics* **2000**, *19*, 388–402; c) M. Enders, P. Fernandez, G. Ludwig, H. Pritzkow, *Organometallics* **2001**, *20*, 5005–5007; d) J. S. Rogers, G. C. Bazan, *Chem. Commun.* **2000**, 1209–1210; e) M. H. Voges, C. Romming, M. Tilset, *Organometallics* **1999**, *18*, 529–533; f) U. Peucker, W. Heitz, *Macromol. Chem. Phys.* **2001**, *202*, 1289–1297.
- [5] a) B. J. Thomas, K. H. Theopold, *J. Am. Chem. Soc.* **1988**, *110*, 5902–5903; b) B. J. Thomas, S. K. Noh, G. K. Schulte, S. C. Sendlinger, K. H. Theopold, *J. Am. Chem. Soc.* **1991**, *113*, 893–902; c) O. Heinemann, P. W. Jolly, C. Kruger, G. P. J. Verhovnik, *J. Organomet. Chem.* **1998**, *553*, 477–479; d) G. Mani, F. P. Gabbaï, *Angew. Chem. Int. Ed.* **2004**, *43*, 2263–2266; e) Y. Huang, W. Yu, G. Jin, *Organometallics* **2007**, *26*, 4598–4603; f) Y. Huang, W. Yu, G. Jin, *Dalton Trans.* **2009**, 767–769; g) T. Xu, Y. Mu, W. Gao, J. Ni, L. Ye, Y. Tao, *J. Am. Chem. Soc.* **2007**, *129*, 2236–2237.
- [6] a) W. K. Kim, M. J. Fevola, L. M. Liable-Sands, A. L. Rheingold, K. H. Theopold, *Organometallics* **1998**, *17*, 4541–4543; b) L. A. MacAdams, W. K. Kim, L. M. Liable-Sands, I. A. Guzei, A. L. Rheingold, K. H. Theopold, *Organometallics* **2002**, *21*, 952–960.
- [7] L. A. MacAdams, G. P. Buffone, C. D. Incarvito, A. L. Rheingold, K. H. Theopold, *J. Am. Chem. Soc.* **2005**, *127*, 1082–1083.
- [8] V. C. Gibson, C. Newton, C. Redshaw, G. A. Solan, A. J. P. White, D. J. Williams, *Eur. J. Inorg. Chem.* **2001**, 1895–1903.
- [9] a) V. C. Gibson, C. Newton, C. Redshaw, G. A. Solan, A. J. P. White, *J. Chem. Soc., Dalton Trans.* **1999**, 827–829; b) D. J. Jones, V. C. Gibson, S. Green, P. J. Maddox, *Chem. Commun.* **2002**, 1038–1039; c) V. C. Gibson, S. Mastroianni, C. Newton, C. Redshaw, G. A. Solan, A. J. P. White, D. J. Williams, *J. Chem. Soc., Dalton Trans.* **2000**, 1969–1971.
- [10] P. G. Hayes, G. C. Welch, D. J. H. Emslie, C. L. Noack, W. E. Piers, M. Parvez, *Organometallics* **2003**, *22*, 1577–1579.
- [11] H. Y. Gao, W. J. Guo, F. Bao, G. Q. Gui, J. K. Zhang, F. M. Zhu, Q. Wu, *Organometallics* **2004**, *23*, 6273–6280.
- [12] H. Y. Wang, X. Meng, G. X. Jin, *Dalton Trans.* **2006**, 2579–2585.
- [13] X. M. Liu, W. Gao, Y. Mu, G. H. Li, L. Ye, H. Xia, Y. Ren, S. H. Feng, *Organometallics* **2005**, *24*, 1614–1619.
- [14] J. Shamir, *Inorg. Chim. Acta* **1989**, *156*, 163–164.
- [15] *SHELXTL*, PC Siemens Analytical X-ray Instruments, Madison, WI, **1993**.
- [16] G. M. Sheldrick, *SHELXTL Structure Determination Programs*, version 5.0, PC, Siemens Analytical Systems, Madison, WI, **1994**.

Received: February 6, 2010
Published Online: June 2, 2010

The Adaptable Coordination Chemistry of 6-Chloro-2-(quinolin-2-yl)-2,4-dihydro-1*H*-benzo[*d*][1,3]oxazine Towards Zinc(II) and Mercury(II)

G. Attilio Ardizzoia,^[a] Stefano Brenna,^{*,[a]} and Bruno Therrien^[b]

Keywords: Polydentate ligands / Coordination modes / N ligands / N,O ligands / Zinc / Mercury

The coordination chemistry of 6-chloro-2-(quinolin-2-yl)-2,4-dihydro-1*H*-benzo[*d*][1,3]oxazine (LH₂) towards zinc and mercury has been explored. The ligand exhibits high versatility and provides different environments to the metal centre as a function of its diverse coordination modes. In one of the isolated and characterized complexes, [Zn(L^{OH})Cl₂], the zinc

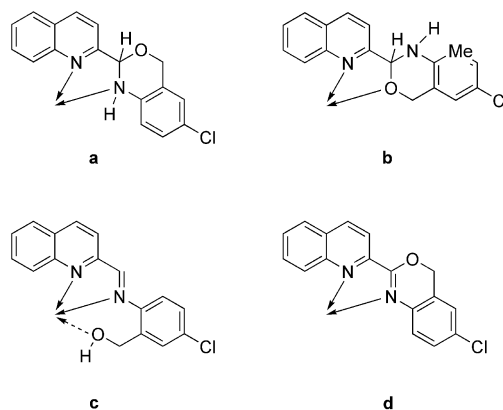
centre is found pentacoordinated with the ligand present in an iminic “open” structure. The oxidized form, which contains the 4*H*-benzo[*d*][1,3]oxazine part (L), is also encountered in [Zn(L)Cl₂], whereas the crystal structure of the trinuclear compound [Hg₃(LH₂)₂Cl₆] shows the ligand LH₂ in its original arrangement.

Introduction

Heteropolydentate ligands represent an important tool that allows for the design of suitable coordination compounds.^[1] Among others, 1,3-oxazine-based polydentate ligands have been demonstrated to be very useful. They showed high versatility together with remarkable properties when coordinated to transition metals, and their catalytic efficiency was usually proven to be higher when compared to the more extensively used 1,3-oxazolines. Singh et al. reported on vanadium and manganese complexes that contained bidentate *N,O*-oxazine ligands,^[2] whereas the catalytic activity of palladium complexes with bidentate *N,P*-oxazine ligands has also been documented.^[3] Moreover, the crystal structure of a zinc(II) complex that contains the same *N,P*-oxazine species has been described.^[4] Commonly, strong donation from the metal centre to the π* orbitals of the oxazine ring has been invoked to justify these uncommon performances.^[5]

This prompted us to investigate the coordination behaviour of the polydentate ligand 6-chloro-2-(quinolin-2-yl)-2,4-dihydro-1*H*-benzo[*d*][1,3]oxazine (LH₂). This ligand could in principle reveal a broad range of coordination modes, thereby providing the metal centre with a variety of coordination environments (e.g., *N,N*; *N,N,O*; *N,O*; see Scheme 1). We previously explored the coordination chemistry of species LH₂ towards copper(I) and copper(II) centres.^[6] There, two different coordination modes were encountered, namely, an *N,NH* coordination by use of the

quinolinic sp² nitrogen and the sp³ nitrogen of the dihydrooxazine moiety, and a *N,N* coordination in which both the donor atoms were sp² nitrogen. Herein, we continue the investigation and report a study on the coordination chemistry of LH₂ towards zinc and mercury. In the course of this study, LH₂ displayed a further iminic “open” structure, with an *N,N,O* coordination to the zinc centre, thus resulting in a pentacoordinate species.



Scheme 1. Potential coordination modes of ligand LH₂ (a: *N,NH*; b: *N,O*; c: open *N,N* or *N,N,O*; d: oxidized *N,N*).

The reactivity of this complex in the presence of bases, together with an X-ray structure determination of the synthesized complexes, are presented. Finally, a parallel survey on mercury(II) complexes allowed for the isolation and characterization of a trinuclear Hg^{II} compound.

Results and Discussion

The reaction at room temperature of LH₂ with ZnCl₂ (1:1) in methanol or acetonitrile results in the formation of a yellow solid. The infrared spectrum of the solid shows an

[a] Dipartimento di Scienze Chimiche e Ambientali, Università dell'Insubria, via Valleggio 11, 22100 Como, Italy
Fax: +39-031-2386119
E-mail: stefano.brenna@uninsubria.it

[b] Service Analytique Facultaire, Université de Neuchâtel, Case Postale 158, 2009, Neuchâtel, Switzerland

Supporting information for this article is available on the WWW under <http://dx.doi.org/10.1002/ejic.201000175>.

intense, large stretching band at 3319 cm^{-1} , firstly attributed to the N–H vibration. The very low solubility of this complex allowed NMR spectroscopic investigation only in $[\text{D}_6]\text{DMSO}$: The ^1H NMR spectrum exhibits the typical roof pattern (quartet centred at $\delta = 4.98\text{ ppm}$) of the CH_2O moiety as observed in the free ligand LH_2 , together with a doublet at $\delta = 5.78\text{ ppm}$ ($^3J = 2.92\text{ Hz}$) assigned to the CH fragment. Consequently, according to elemental analysis and spectroscopic data, the compound was initially formulated as $[\text{Zn}(\text{LH}_2)\text{Cl}_2]$, with the ligand LH_2 coordinated in the $N,N\text{H}$ mode (Scheme 1, a) and the metal was assumed to be tetrahedral. Unexpectedly, the structure determination by means of X-ray single-crystal diffraction revealed a pentacoordination to the metal centre with the ligand present in the iminic (open) form (Scheme 1, c). The molecular structure of **1** with the corresponding atom labelling scheme is given in Figure 1 together with selected bond lengths and angles.

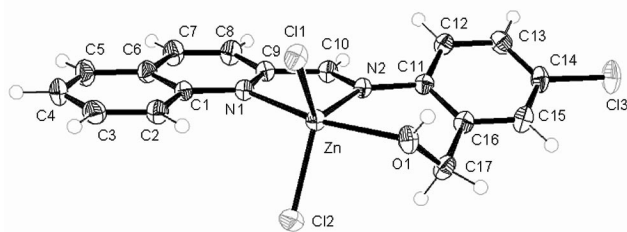


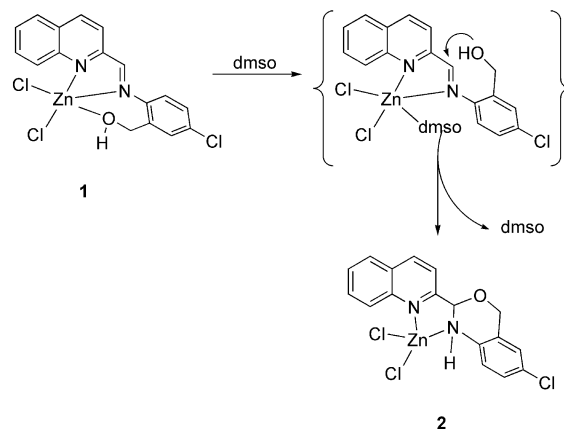
Figure 1. ORTEP drawing of **1** at 50% probability level ellipsoids. Selected bond lengths [Å] and angles [°]: Zn–N1 2.170(2), Zn–N2 2.148(2), Zn–Cl1 2.2742(10), Zn–Cl2 2.2418(11), Zn–O1 2.171(2), N1–C1 1.368(3), N1–C9 1.331(3), N2–C10 1.276(3), N2–C11 1.437(3), O1–C17 1.432(3); N1–Zn–N2 77.80(7), N1–Zn–O1 160.85(6), N2–Zn–O1 83.06(7), Cl1–Zn–Cl2 119.51(3), Cl1–Zn–N2 122.08(6), Cl2–Zn–N2 118.12(6).

The LH_2 molecule behaves in this case as an N,N,O -tridentate ligand and coordinates to the zinc centre by means of the two nitrogen atoms [Zn–N distances being 2.170(2) and 2.148(2) Å] and the oxygen of the pendant CH_2OH group [Zn–O distance: 2.171(2) Å]. Pentacoordination of zinc is not unusual and occurs especially in some structural motifs of enzymes active sites; however, to date only a few cases have been reported in the Cambridge Structural Database for compounds with a ZnCl_2 attached to two nitrogen atoms and an OH function.^[7] In compound **1**, the Addison parameter^[8] presents a value of $\tau = 0.65$, thereby suggesting that the real coordination polyhedron is about halfway between a square pyramidal and a trigonal bipyramidal geometry, with a little preference for the latter. Two neighbouring molecules form in the solid state a weak hydrogen-bonded dimer (see the Supporting Information). The Cl1–O hydrogen-bond lengths are 3.079(2) Å with O–H···Cl1 angles of $159(3)^\circ$; the total distance between the two Zn atoms is 6.149(3) Å.

Herein, such a coordination mode can be rationalized if one considers the ring opening of LH_2 , which is responsible for the formation of its new iminic arrangement (indicated hereafter for brevity as L^{OH}) in a process analogous to one already encountered for some pyridinyloxazolidine li-

gands.^[9] Most probably, the presence of a rather acidic ion (due to the relatively small size) like zinc drives the ligand opening to the formation of a Zn–OH bond. The resulting complex is then better described as $[\text{Zn}(\text{L}^{\text{OH}})\text{Cl}_2]$ (**1**). The adsorption at 3319 cm^{-1} in the infrared spectrum of **1**, firstly attributed to the N–H stretching of coordinated LH_2 , is most correctly assigned to the O–H group.

To justify the ^1H NMR spectroscopic data discussed above, in which the presence of the ligand in the original closed form LH_2 is revealed, one should assume the occurrence of a process in which dimethylsulfoxide is involved (Scheme 2).



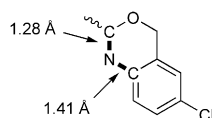
Scheme 2. Probable **1**→**2** interconversion mechanism mediated by DMSO.

Most likely, dissolving $[\text{Zn}(\text{L}^{\text{OH}})\text{Cl}_2]$ (**1**) in $[\text{D}_6]\text{DMSO}$ caused the breaking of the Zn–OH bond through the coordination of a DMSO molecule to the zinc centre, thus generating a zinc complex that contains the ligand coordinated in the iminic form with a free pendant CH_2OH arm. The latter immediately underwent ring closing and converted into the most stable closed form of LH_2 coordinated in the $N,N\text{H}$ mode. This species was effectively detected during the NMR spectroscopic investigation, as evidenced by the AB system assigned to the CH_2O moiety.

Conversely, the reaction of ZnCl_2 with LH_2 in the presence of a base (Et_3N) results in the formation of a pale yellow solid. The infrared spectrum shows a broad adsorption at about 3420 cm^{-1} , whereas in the ^1H NMR spectroscopy conducted in $(\text{CD}_3)_2\text{CO}$ an AB system attributed to the CH_2O moiety [centred at $\delta = 4.98\text{ ppm}$ ($J_{\text{AB}} = 14.9\text{ Hz}$)] is observed, and the CH proton appears as a doublet centred at $\delta = 5.77\text{ ppm}$, the multiplicity of which originates from the coupling with the N–H proton ($^2J = 2.8\text{ Hz}$). The coordination to the zinc centre clearly forces the ligand in a sort of “blocked position”, thus preventing the rotation along the C–C bond between the quinoline and the oxazine moieties. Furthermore, after treatment with D_2O and the consequent disappearance of the N–H coupling, the doublet becomes a singlet. On the basis of these observations, the yellow compound is formulated as $[\text{Zn}(\text{LH}_2)\text{Cl}_2]$ (**2**).^[10] Coloured zinc complexes (bearing colourless ligands) are quite rare, due the impossibility of

d-d transitions in a closed-shell ion such as zinc(II). However, a few examples are present in the literature, such as for the mixed-ligand complexes of phenanthroline or bipyridyl and 8-hydroxyquinoline or derivatives of 8-amino-2-methylquinoline.^[11–13] As in our case, the yellow colour can be explained by assuming charge transfer from the metal to a low-energy empty molecular orbital of the ligand. On the contrary, the yellow colour of **1** can be likely attributed to π - π^* transitions within the coordinated iminic ligand (L^{OH}).

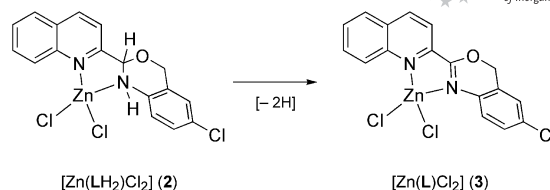
In species **2**, the ligand LH_2 is coordinated in an N,NH fashion (i.e., in the same mode found in solutions of **1** in DMSO). It is worth noting that the same species **2** can also be isolated by treatment of the pentacoordinate species **1** with Et_3N in methanol or acetonitrile. Reasonably, the role of Et_3N in this reaction is the same as for DMSO as discussed above (i.e., blocking a coordination site on the zinc), thus hampering the coordination of the OH group and hence forcing the ligand closure. To support this assumption, the reaction was conducted by employing *N*-cyclohexyl-*N*-ethylcyclohexanamine instead of Et_3N . Because of the higher steric hindrance, $(C_6H_{11})_2NC_2H_5$ behaves essentially as a noncoordinating amine. Indeed, complex **1** (IR evidence) is quantitatively formed. The strict similarity among the 1H NMR spectra of **2** and **1** (in DMSO) seems to suggest the leaving of coordinated DMSO from the intermediate species in Scheme 2 and the existence, also in DMSO (or in the presence of Et_3N), of the tetracoordinate species **2**. However, the presence in solution of penta- (or hexa-)coordinated zinc(II) species that bear ancillary DMSO (or Et_3N) ligands cannot in principle be excluded. Unfortunately, all attempts to grow single crystals of **2** failed, but in one of the several efforts, we isolated a crop of yellow crystals that were subjected to X-ray analysis. The molecular structure disclosed a marked difference between the two C–N distances in the oxazine portion of the ligand (see Scheme 3).



Scheme 3. Significant differences in C–N distances in the structurally characterized complex.

In fact, although the C–N distance of 1.412(3) Å agreed with a single C–N bond, the second C–N distance [1.281(3) Å] is significantly shorter and therefore is attributed to a double C=N bond. This could be rationalized by considering an oxidative dehydrogenation of the 2,4-dihydro-1*H*-benzo[d][1,3]oxazine portion of ligand LH_2 to the corresponding 4*H*-benzo[d][1,3]oxazine derivative **L**, thus leading to complex $[Zn(L)Cl_2]$ (**3**) (Scheme 4).

To confirm this finding, the direct synthesis of **3** was performed. First, ligand LH_2 was oxidized with $KMnO_4$ to form **L** following a procedure previously reported for dihydroisoquinolines.^[14] Subsequently, species **L** was reacted with $ZnCl_2$ in a 1:1 molar ratio in methanol. From the re-



Scheme 4. Dehydrogenation of 2,4-dihydro-1*H*-benzo[d][1,3]oxazine to 4*H*-benzo[d][1,3]oxazine coordinated to a zinc(II) centre.

sulting suspension a yellow solid was isolated, formulated as $[Zn(L)Cl_2]$ (**3**) on the basis of analytical and spectroscopic data. In particular, the 1H NMR spectroscopic investigation ($[D_6]DMSO$) revealed the presence of a singlet centred at $\delta = 5.56$ ppm (CH_2) together with the set of quinoline protons, whereas the ^{13}C NMR spectrum showed a resonance at $\delta = 65.9$ ppm attributed to the endocyclic CH_2 fragment and a resonance at $\delta = 150.08$ ppm assigned to the C=N carbon. Eventually, the molecular structure of complex **3** was confirmed by single-crystal diffraction analysis and the structural information was in total agreement with those previously acquired. An ORTEP^[15] drawing of **3** including the atom labelling scheme is given in Figure 2 together with selected bond lengths and angles.

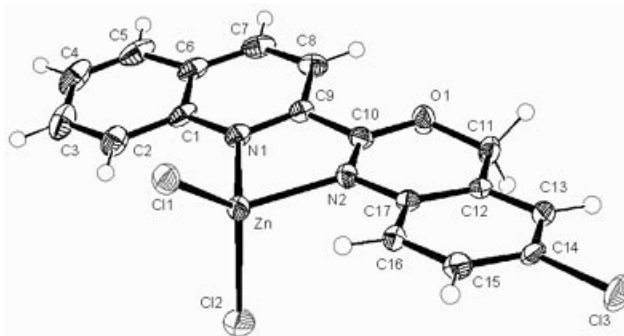


Figure 2. ORTEP drawing of **3** at 50% probability level ellipsoids. Selected bond lengths [Å] and angles [°]: Zn–Cl1 2.1911(7), Zn–Cl2 2.2162(8), Zn–N1 2.082(2), Zn–N2 2.050(2), N1–C1 1.367(3), N1–C9 1.324(3), N2–C10 1.281(3), N2–C17 1.412(3); N1–Zn–N2 80.18(8), Cl1–Zn–Cl2 118.43(3), Cl1–Zn–N1 116.26(6), Cl1–Zn–N2 118.10(6), Cl2–Zn–N1 111.97(6), Cl2–Zn–N2 105.56(6).

The molecular structure of **3** shows the zinc atom to be in a slightly distorted tetrahedral geometry. The geometrical parameters around the zinc atom are comparable to those found in analogous complexes $[Zn(C_{10}H_8N_2)Cl_2]$ ^[16] and $[Zn(C_{20}H_{20}N_2)Cl_2]$.^[17] Despite coordination of the imine nitrogen atom to the metal centre, the imine function preserves its C=N double bond character with a C–N distance of 1.281(3) Å. In the crystal packing of **3**, the molecules of **3** form a network through π -stacking interactions between parallel aromatic rings of adjacent complexes. Different types of π - π stacking interactions are involved in the multimeric system, the strongest being a face-to-face arrangement between quinoline moieties (see the Supporting Information). The centroid–centroid distances are 3.574 Å.

Oxidative dehydrogenation is rare for a ligand coordinated to a nonredox metal like zinc, and to the best of our

knowledge only a single example of such a reaction has been reported to date.^[18] Therefore, we decided to better examine the dehydrogenation process, already encountered by us with copper(II) complexes that bear the same ligand.^[6] In that case, the process involved the concomitant reduction of the two copper centres of the starting dimer $[\text{Cu}^{\text{II}}(\text{LH}_2)\text{Cl}_2]_2$, thus giving $[\text{Cu}^{\text{I}}(\text{L})\text{Cl}]$ and $[\text{Cu}^{\text{I}}(\text{LH}_2)\text{Cl}]$ as a mixture of products. Here, due to the presence of two chlorido ligands bound to the zinc centre, the reduction of the metal is obviously excluded. Therefore, the only possibility to justify the oxidation of ligand LH_2 into L is a reaction that requires molecular oxygen as oxidant. The synthesis of **3** from **1** and Et_3N was then performed under a constant stream of oxygen. As expected, it was not possible to isolate **2**, and all the spectroscopic data of the product are in total agreement with those of complex **3**.

Finally, we could reasonably assume that some adventitious oxygen was present during the slow growth of single crystals of **2**. As mentioned above, any subsequent attempt to grow single crystals of **2** failed, thus preventing the possibility of an additional comparison of the zinc complexes. However, crystallographic evidence of the *N,NH*-coordination mode (Scheme 1, **a**) of LH_2 was obtained conducting the reaction between LH_2 and HgCl_2 .

The choice turned to mercury because of its marked different hard–soft properties with respect to zinc. The first alternative to zinc within Group 12 was represented by cadmium. Nevertheless, its use was excluded as a consequence of its toxicity (which reduces its attractiveness) and especially because, relative to zinc, its hard–soft character does not differ as markedly as it would be with mercury. In fact, due to its longer radius, Hg^{2+} has a lower charge density with respect to Zn^{2+} , thus showing a softer acidic character (absolute hardness^[19] (eV): Zn^{2+} 10.8, Cd^{2+} 10.3, Hg^{2+} 7.7). The consequent less oxyphilic inclination could prevent ligand opening into the L^{OH} species.

The reaction was originally performed using a 1:1 molar ratio between HgCl_2 and LH_2 , with the aim of obtaining the $[\text{Hg}(\text{LH}_2)\text{Cl}_2]$ derivative. Instead, quite unexpectedly, the trinuclear compound $[\text{Hg}_3(\text{LH}_2)_2\text{Cl}_6]$, (**4**) is obtained in

quantitative yields. Its infrared spectrum shows a stretching frequency at 3210 cm^{-1} assigned to the N–H group, the presence of which is afterwards corroborated by a broad resonance at $\delta = 6.33\text{ ppm}$ in the ^1H NMR spectrum in $(\text{CD}_3)_2\text{CO}$. The characteristic aliphatic signals of ligand LH_2 appear as a singlet at $\delta = 5.92\text{ ppm}$ (CH) and as an AB system (CH_2O) centred at $\delta = 5.11\text{ ppm}$. The ^{13}C NMR confirms the incidence of the closed form of the ligand coordinating in the *N,NH*-bidentate mode (Scheme 1, **a**; see also the Exp. Section).

This feature, together with the trinuclear nature of compound **4**, was eventually confirmed by crystallographic analysis: In the complex, ligand LH_2 is coordinated to the terminal tetrahedral mercury centres, whereas the central mercury atom is surrounded by four chloride anions in a square-planar geometry. Square-planar coordination geometries for Hg^{II} is rare, but have been observed previously.^[20] The crystal structure of **4** is presented in Figure 3 together with selected bond lengths and angles.

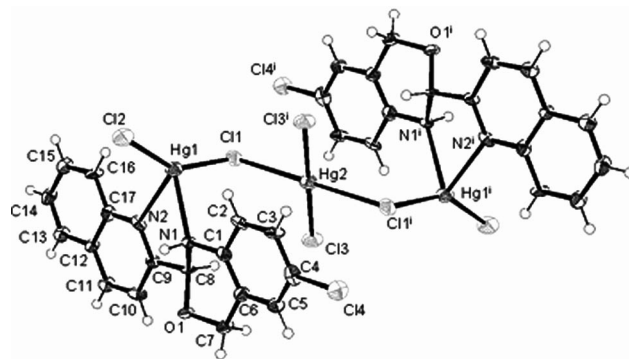


Figure 3. ORTEP drawing of **4** at 50% probability level ellipsoids. Selected bond lengths [Å] and angles [°]: Hg1–N1 2.514(10), Hg1–N2 2.426(8), Hg1–Cl1 2.352(3), Hg1–Cl2 2.324(3), Hg2–Cl1 3.114(3), Hg2–Cl3 2.283(3), N1–C1 1.458(14), N1–C8 1.448(11), N2–C9 1.324(15), N2–C17 1.365(14); Cl1–Hg1–Cl2 145.17(12), Cl1–Hg1–N1 100.6(2), Cl1–Hg1–N2 102.7(2), Cl2–Hg1–N1 106.9(2), Cl2–Hg1–N2 107.2(2), N1–Hg1–N2 68.0(3), Hg1–Cl1–Hg2 103.32 (11), Cl1–Hg2–Cl3 84.85(10) (*i*: $-x$, $2 - y$, $2 - z$).

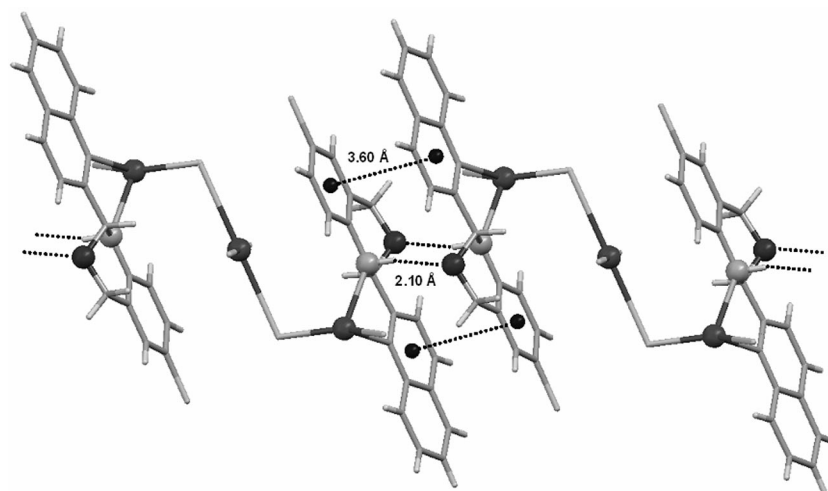


Figure 4. Main interactions in the crystal packing of **4**.

In the crystal packing of **4**, slipped-parallel π -stacking interactions are observed between adjacent complexes, which involve the chlorophenyl and pyridyl rings of the LH_2 ligands: The centroid-centroid distance being 3.60 Å. The distance observed between the π - π interacting systems is in accordance with the theoretical value calculated for this stacking mode.^[21] Moreover, the N-H function of LH_2 forms a strong hydrogen bond with a neighbouring oxygen atom: The N...O distance is 3.00(1) Å with an N-H...O angle of 167.9°. These interactions are summarized in Figure 4.

Conclusion

In summary, we investigated the coordination chemistry of 6-chloro-2-(quinolin-2-yl)-2,4-dihydro-1*H*-benzo[d][1,3]-oxazine (LH_2) towards zinc(II) and mercury(II). In the course of this study, the ligand revealed a broad range of coordination modes, thus providing the metal centre with a variety of coordination environments. Indeed, it was possible to isolate and fully characterize $[\text{Zn}(\text{L}^{\text{OH}})\text{Cl}_2]$ (**1**), in which the *N,N,O* arrangement of the ligand provided a pentacoordination to the zinc centre. This open form of LH_2 underwent a ring-closing reaction of the oxazine moiety in the presence of Et_3N or a coordinating solvent such as DMSO. Furthermore, it could take part to an oxidative dehydrogenation process induced by molecular oxygen, thereby generating the oxidized form of LH_2 (**L**). This latter was unequivocally identified by means of X-ray analysis in the complex $[\text{Zn}(\text{L})\text{Cl}_2]$ (**3**), whereas the synthesis and characterization of the trinuclear compound $[\text{Hg}_3(\text{LH}_2)_2\text{Cl}_6]$ (**4**) confirmed the *N,NH*-coordination mode of the nonoxidized closed species LH_2 .

Experimental Section

Materials and Measurements: All reactions were carried out under purified nitrogen using standard Schlenk techniques. The solvents were dried and distilled according to standard procedures prior to use. ZnCl_2 and HgCl_2 , 2-quinolinecarbaldehyde, 2-amino-5-chlorobenzyl alcohol, triethylamine and *N*-cyclohexyl-*N*-ethylcyclohexanamine (Aldrich) were used as purchased. Ligand LH_2 was prepared according to a well-established procedure.^[6] Infrared spectra were recorded with a Shimadzu Prestige 21 FTIR instrument, NMR spectra were acquired with a Bruker 400 Avance instrument and elemental analyses were obtained with a Perkin-Elmer CHN Analyser 2400 Series II instrument.

$[\text{Zn}(\text{L}^{\text{OH}})\text{Cl}_2]$ (1**):** Ligand LH_2 (330 mg, 1.11 mmol) was added to a solution of ZnCl_2 (150 mg, 1.10 mmol) in methanol or acetonitrile (10 mL), and the resulting yellow suspension was stirred for 2 h at room temperature. Then the solid was filtered, washed with diethyl ether and dried under vacuum; yield 371 mg (78%). IR (nujol): $\tilde{\nu} = 3119 \text{ cm}^{-1}$. ^1H NMR (400 MHz, $[\text{D}_6]\text{DMSO}$, 25 °C): NMR spectroscopic features were identical to those obtained in $(\text{CD}_3)_2\text{CO}$ for complex **2** (see text for explanation). $\text{C}_{17}\text{H}_{13}\text{Cl}_3\text{N}_2\text{OZn}$ (433.07): calcd. C 47.15, H 3.03, N 6.47; found C 46.89, H 2.94, N 6.36. Single crystals suitable for X-ray analysis were obtained by slowly cooling a hot saturated solution of **1** in ethanol to room temperature.

$[\text{Zn}(\text{LH}_2)\text{Cl}_2]$ (2**):** Ligand LH_2 (330 mg, 1.11 mmol) was added to a solution of ZnCl_2 (150 mg, 1.10 mmol) in methanol (10 mL), and the yellow suspension stirred for 2 h at room temperature. Then Et_3N was added (160 μL , 1.15 mmol) and the suspension was stirred for a further 2 h. The solid was filtered, washed with diethyl ether and dried in vacuo; yield 410 mg (86%). IR (nujol): $\tilde{\nu} = 3421$ (br.) cm^{-1} . ^1H NMR [400 MHz, $(\text{CD}_3)_2\text{CO}$, 25 °C]: $\delta = 4.98$ [d, $^2J_{\text{H,H}} = 14.8 \text{ Hz}$, 1 H, H_a part of an AB system $-\text{CH}_2\text{O}$], 5.21 (d, $^2J_{\text{H,H}} = 14.8 \text{ Hz}$, 1 H, H_b part of an AB system $-\text{CH}_2\text{O}$), 5.85 (d, $^2J_{\text{H,H}} = 3.6 \text{ Hz}$, 1 H, C-H), 6.32 (br. s, 1 H, N-H), 6.91 (d, $^3J_{\text{H,H}} = 8.5 \text{ Hz}$, 1 H), 7.07 (s, 1 H), 7.10 (dd, $^3J_{\text{H,H}} = 8.5 \text{ Hz}$, $^4J_{\text{H,H}} = 2.3 \text{ Hz}$, 1 H), 7.66 (t, $^3J_{\text{H,H}} = 7.0 \text{ Hz}$, 1 H), 7.81 (d, $^3J_{\text{H,H}} = 8.5 \text{ Hz}$, 1 H), 8.02 (d, $^3J_{\text{H,H}} = 7.8 \text{ Hz}$, 1 H), 8.09 (d, $^3J_{\text{H,H}} = 8.8 \text{ Hz}$, 1 H), 8.46 (d, $^3J_{\text{H,H}} = 8.5 \text{ Hz}$, 1 H), 8.76 (m, $^3J_{\text{H,H}} = 6.1 \text{ Hz}$, $^4J_{\text{H,H}} = 1.7 \text{ Hz}$, 1 H) ppm. ^{13}C NMR [100 MHz, $(\text{CD}_3)_2\text{CO}$, 25 °C]: $\delta = 68.2$ (CH_2O), 84.7 (CH), 119.1, 119.9, 123.5, 124.3, 125.1, 127.2, 127.8, 128.1, 128.7, 129.6, 130.1, 137.9, 140.0, 147.5, 156.8 ppm. $\text{C}_{17}\text{H}_{13}\text{Cl}_3\text{N}_2\text{OZn}$ (433.07): calcd. C 47.15, H 3.03, N 6.47; found C 47.43, H 2.99, N 6.71.

Synthesis of Ligand L: Solid KMnO_4 (267 mg, 1.69 mmol) and [18]crown-6 (45 mg, 0.170 mmol) were added to a solution of ligand LH_2 (500 mg, 1.68 mmol) in CH_2Cl_2 (20 mL). The suspension was stirred at room temperature for 12 h, then it was filtered through Celite to remove MnO_2 . The filtrate was washed with H_2O ($2 \times 20 \text{ mL}$), the organic phase was dried with Na_2SO_4 , filtered and the solvents evaporated to dryness. The residue was repeatedly washed with diethyl ether to give a light-yellow solid; yield 323 mg (65%). ^1H NMR (400 MHz, CDCl_3 , 25 °C): $\delta = 5.55$ (s, 2 H, $-\text{CH}_2\text{O}$), 7.06 (s, 1 H), 7.27 (s, 1 H), 7.31 (s, 1 H), 7.62 (t, $^3J_{\text{H,H}} = 7.2 \text{ Hz}$, 1 H), 7.77 (t, $^3J_{\text{H,H}} = 6.9 \text{ Hz}$, 1 H), 7.87 (d, $^3J_{\text{H,H}} = 8.1 \text{ Hz}$, 1 H), 8.26 (d, $^3J_{\text{H,H}} = 8.4 \text{ Hz}$, 1 H), 8.31 (d, $^3J_{\text{H,H}} = 8.5 \text{ Hz}$, 1 H), 8.41 (d, $^3J_{\text{H,H}} = 8.4 \text{ Hz}$, 1 H) ppm. ^{13}C NMR (100 MHz, CDCl_3 , 25 °C): $\delta = 66.5$ (CH_2O), 120.5, 123.9, 124.0, 126.7, 127.5, 127.9, 128.9, 129.1, 129.9, 130.4, 132.6, 136.6, 137.7, 147.6, 150.1, 156.5 ppm. $\text{C}_{17}\text{H}_{11}\text{ClN}_2\text{O}$ (294.74): calcd. C 69.28, H 3.76, N 9.50; found C 69.51, H 3.98, N 9.33.

$[\text{Zn}(\text{L})\text{Cl}_2]$ (3**):** Ligand **L** (325 mg, 1.10 mmol) was added to a solution of ZnCl_2 (150 mg, 1.10 mmol) in methanol (10 mL). The resulting yellow suspension was stirred at room temperature for 2 h, then it was filtered and the solid was dried under vacuum; yield 337 mg (71%). ^1H NMR (400 MHz, $[\text{D}_6]\text{DMSO}$, 25 °C): $\delta = 5.56$ (s, 2 H, $-\text{CH}_2\text{O}$), 7.29 (d, $^3J_{\text{H,H}} = 8.3 \text{ Hz}$, 1 H), 7.32 (d, $^3J_{\text{H,H}} = 2.3 \text{ Hz}$, 1 H), 7.40 (dd, $^3J_{\text{H,H}} = 8.3 \text{ Hz}$, $^4J_{\text{H,H}} = 2.4 \text{ Hz}$, 1 H), 7.71 (dt, $^3J_{\text{H,H}} = 7.5 \text{ Hz}$, $^4J_{\text{H,H}} = 1.2 \text{ Hz}$, 1 H), 7.85 (dt, $^3J_{\text{H,H}} = 7.7 \text{ Hz}$, $^4J_{\text{H,H}} = 1.5 \text{ Hz}$, 1 H), 8.07 (dd, $^3J_{\text{H,H}} = 7.9 \text{ Hz}$, $^4J_{\text{H,H}} = 1.0 \text{ Hz}$, 1 H), 8.14 (d, $^3J_{\text{H,H}} = 8.4 \text{ Hz}$, 1 H), 8.33 (d, $^3J_{\text{H,H}} = 8.6 \text{ Hz}$, 1 H), 8.51 (d, $^3J_{\text{H,H}} = 8.6 \text{ Hz}$, 1 H) ppm. ^{13}C NMR (100 MHz, $[\text{D}_6]\text{DMSO}$, 25 °C): $\delta = 65.9$ (CH_2O), 120.7, 125.0, 125.5, 126.6, 128.4, 128.6, 128.9, 129.3, 130.0, 130.8, 131.7, 137.4, 138.1, 147.4, 150.1, 157.2 ppm. $\text{C}_{17}\text{H}_{11}\text{Cl}_3\text{N}_2\text{OZn}$ (431.03): calcd. C 47.37, H 2.57, N 6.50; found C 47.72, H 2.39, N 6.31. Single crystals suitable for X-ray analysis were obtained by slow diffusion of diethyl ether into a saturated solution of **3** in DMF.

$[\text{Hg}_3(\text{LH}_2)_2\text{Cl}_6]$ (4**):** Ligand LH_2 (330 mg, 1.11 mmol) was added to a solution of HgCl_2 (300 mg, 1.10 mmol) in methanol (10 mL). The suspension was stirred at room temperature for 2 h and was filtered. The yellow solid was then washed with diethyl ether and dried in vacuo; yield 423 mg (82%). ^1H NMR [400 MHz, $(\text{CD}_3)_2\text{CO}$, 25 °C]: $\delta = 5.00$ (d, $^2J_{\text{H,H}} = 14.8 \text{ Hz}$, 1 H, H_a part of an AB system $-\text{CH}_2\text{O}$), 5.22 (d, $^2J_{\text{H,H}} = 14.9 \text{ Hz}$, 1 H, H_b part of an AB system $-\text{CH}_2\text{O}$), 5.92 (s, 1 H, C-H), 6.33 (br. s, 1 H, N-H), 6.91 (d, $^3J_{\text{H,H}} = 8.5 \text{ Hz}$, 1 H), 7.07 (s, 1 H), 7.14 (dd, $^3J_{\text{H,H}} =$

Table 1. Crystallographic and structure-refinement parameters for complexes **1**, **3** and **4**.

	1	3	4
Chemical formula	C ₁₇ H ₁₃ Cl ₃ N ₂ OZn	C ₁₇ H ₁₁ Cl ₃ N ₂ OZn	C ₃₄ H ₂₆ Cl ₈ Hg ₃ N ₄ O ₂
Formula weight	433.01	431.00	1407.96
Crystal system	triclinic	monoclinic	triclinic
Space group	<i>P</i> $\bar{1}$ (no. 2)	<i>P</i> 2 ₁ / <i>n</i> (no. 14)	<i>P</i> $\bar{1}$ (no. 2)
Crystal colour and shape	yellow block	yellow block	yellow block
Crystal size	0.19 × 0.17 × 0.12	0.21 × 0.20 × 0.16	0.15 × 0.14 × 0.13
<i>a</i> [Å]	8.542(2)	12.9244(10)	9.4605(15)
<i>b</i> [Å]	8.571(2)	8.3419(7)	10.1435(16)
<i>c</i> [Å]	12.231(4)	15.1907(12)	11.2617(19)
<i>a</i> [°]	98.55(4)		67.339(18)
<i>β</i> [°]	101.41(4)	92.688(9)	71.352(18)
<i>γ</i> [°]	98.24(3)		78.669(18)
<i>V</i> [Å ³]	854.1(4)	1636.0(2)	941.6(3)
<i>Z</i>	2	4	1
<i>T</i> [K]	173(2)	173(2)	173(2)
<i>D</i> _{calcd.} [g cm ⁻³]	1.684	1.750	2.483
<i>μ</i> [mm ⁻¹]	1.913	1.997	12.805
Scan range [°]	2.44 < <i>θ</i> < 26.00	2.02 < <i>θ</i> < 26.06	2.04 < <i>θ</i> < 26.17
Unique reflections	3119	3176	3481
Reflections used [<i>I</i> > 2σ(<i>I</i>)]	2555	2261	2474
<i>R</i> _{int}	0.0305	0.0521	0.0727
Final <i>R</i> indices [<i>I</i> > 2σ(<i>I</i>)] ^[a]	0.0259, <i>wR</i> ₂ 0.0634	0.0280, <i>wR</i> ₂ 0.0583	0.0472, <i>wR</i> ₂ 0.1141
<i>R</i> indices (all data)	0.0352, <i>wR</i> ₂ 0.0661	0.0505, <i>wR</i> ₂ 0.0552	0.0681, <i>wR</i> ₂ 0.1263
Goodness of fit	0.960	0.870	0.913
Max., min. Δρ [e Å ⁻³]	0.591, -0.464	0.533, -0.461	2.905, -4.522

[a] Structures were refined on F_o^2 : $wR_2 = [\sum \{w(F_o^2 - F_c^2)^2\} / \sum w(F_c^2)^2]^{1/2}$, in which $w^{-1} = [\Sigma(F_o^2) + (aP)^2 + bP]$ and $P = [\max(F_o^2, 0) + 2F_c^2]/3$.

8.5 Hz, $^4J_{\text{H,H}} = 2.4$ Hz, 1 H), 7.68 (dt, $^3J_{\text{H,H}} = 7.5$ Hz, $^4J_{\text{H,H}} = 1.2$ Hz, 1 H), 7.84 (dd, $^3J_{\text{H,H}} = 8.6$ Hz, $^4J_{\text{H,H}} = 1.4$ Hz, 1 H), 7.86 (d, $^3J_{\text{H,H}} = 8.5$ Hz, 1 H), 8.04 (dd, $^3J_{\text{H,H}} = 8.1$ Hz, $^4J_{\text{H,H}} = 1.3$ Hz, 1 H), 8.16 (d, $^3J_{\text{H,H}} = 8.4$ Hz, 1 H), 8.50 (d, $^3J_{\text{H,H}} = 8.3$ Hz, 1 H) ppm. ^{13}C NMR [100 MHz, (CD₃)₂CO, 25 °C]: $\delta = 67.3$ (CH₂O), 84.5 (CH), 117.1, 119.5, 121.2, 122.6, 125.0, 127.3, 127.5, 128.2, 128.6, 129.2, 130.3, 137.4, 141.8, 146.7, 158.0 ppm. C₃₄H₂₆Cl₈Hg₃N₄O₂ (1408.00): calcd. C 29.00, H 1.86, N 3.98; found C 29.12, H 2.04, N 3.81.

X-ray Crystallography: Crystals of complexes **1**, **3** and **4** were mounted on a Stoe Image Plate Diffraction system equipped with a ϕ circle goniometer, using Mo-*K*_α graphite-monochromated radiation ($\lambda = 0.71073$ Å) with ϕ range of 0 to 200°. The structures were solved by direct methods using the program SHELXS-97, whereas refinement and all further calculations were carried out using SHELXL-97.^[22] The H atoms were located on a Fourier difference map or included in calculated positions and treated as riding atoms using the SHELXL default parameters. The non-H atoms were refined anisotropically using weighted full-matrix least-squares on F^2 . In **4**, the residual electron densities greater than 1 e Å⁻³ are all located at less than 1 Å from the mercury atoms. Crystallographic details are summarized in Table 1. Figures 1, 2 and 3 were drawn with ORTEP-32.^[15]

CCDC-765623 (for **1**), -765624 (for **3**) and -765625 (for **4**) contain the supplementary crystallographic data for this paper. These data can be obtained free of charge from The Cambridge Crystallographic Data Centre via www.ccdc.cam.ac.uk/data_request/cif.

Supporting Information (see also the footnote on the first page of this article): Hydrogen-bonded dimer of solid **1** (Figure S1) and π - π stacking interactions in complex **3** (Figure S2).

- [1] D. Aguilà, E. Escribano, S. Speed, D. Talancón, L. Yermán, S. Alvarez, *Dalton Trans.* **2009**, 6610–6625, and references cited therein.
- [2] K. Kandasamy, H. B. Singh, R. J. Butcher, J. P. Jasinski, *Inorg. Chem.* **2004**, *43*, 5704–5713.
- [3] P. A. Evans, T. A. Brandt, *Tetrahedron Lett.* **1996**, *37*, 9143–9146.
- [4] S. M. Lait, M. Parvez, B. A. Keay, *Tetrahedron: Asymmetry* **2004**, *15*, 155–158.
- [5] R. F. Khairutdinov, K. Giertz, J. K. Hurst, E. N. Voloshina, N. A. Voloshin, V. I. Minkin, *J. Am. Chem. Soc.* **1998**, *120*, 12707–12713.
- [6] G. A. Ardizzoia, S. Brenna, F. Castelli, S. Galli, N. Masciocchi, *Inorg. Chim. Acta* **2010**, *363*, 324–329.
- [7] a) X.-X. Sun, C.-M. Qi, S.-L. Ma, H.-B. Huang, W.-X. Zhu, Y.-C. Liu, *Inorg. Chem. Commun.* **2006**, *9*, 911–914; b) A. Višnjevac, L. Tušek-Boži, M. Majerić-Elenkov, Z. Hameršak, H. Kooijman, E. De Clercq, B. Kojić-Prodic, *Polyhedron* **2002**, *21*, 2167–2177; c) J. K. Nag, P. K. Santra, C. Sinha, F.-L. Liao, T.-H. Lu, *Polyhedron* **2001**, *20*, 2253–2259.
- [8] A. W. Addison, T. N. Rao, J. Reedijk, J. van Rijn, G. C. Verschoor, *J. Chem. Soc., Dalton Trans.* **1984**, 1349–1356.
- [9] S. A. Cardile, M. C. Jennings, N. D. Jones, *Dalton Trans.* **2006**, 4672–4678.
- [10] Ligand LH₂ in the form shown in Scheme 1(a) has a stereogenic centre in position 2 of the oxazine moiety. However, no attention was dedicated to a deeper understanding of any aspect related to chirality. Consequently, ligand LH₂ and the resulting complex **2** were always obtained as a racemic mixture.
- [11] K. H. Reddy, Y. Lingappa, *J. Chem. Sci.* **1993**, *105*, 87–94.
- [12] A. Furuhashi, H. Yokota, *Bull. Chem. Soc. Jpn.* **1979**, *52*, 3753–3754.
- [13] X. L. Liu, Q. Y. Cheng, X. Yang, Z. W. Miao, W. Liu, F. M. Miao, *Chin. Chem. Lett.* **2001**, *12*, 563–564.

- [14] A. T. Soldatenkov, A. V. Temesgen, N. M. Kolyadina, *Chem. Heterocycl. Compd.* **2004**, 40, 537–560.
- [15] L. J. Farrugia, *J. Appl. Crystallogr.* **1997**, 30, 565.
- [16] M. A. Khan, D. G. Tuck, *Acta Crystallogr., Sect. C* **1984**, 40, 60–62.
- [17] H.-L. Cai, B. Liu, Z.-D. Lin, *Acta Crystallogr., Sect. E* **2008**, 64, m1597.
- [18] P. de Hoog, L. Durán Pachón, P. Gamez, M. Lutz, A. L. Spek, J. Reedijk, *Dalton Trans.* **2004**, 2614–2615.
- [19] R. G. Parr, R. G. Pearson, *J. Am. Chem. Soc.* **1983**, 105, 7512–7516.
- [20] R. Haid, R. Gutmann, G. Czermak, C. Langes, W. Oberhauser, H. Kopacka, K.-H. Ongania, P. Bruggeller, *Inorg. Chem. Commun.* **2003**, 6, 61–67.
- [21] S. Tsuzuki, K. Honda, T. Uchimura, M. Mikami, K. Tanabe, *J. Am. Chem. Soc.* **2004**, 124, 104–112.
- [22] G. M. Sheldrick, *Acta Crystallogr., Sect. A* **2008**, 64, 112–122.

Received: February 12, 2010
Published Online: June 2, 2010

Better Performance of Monodentate *P*-Stereogenic Phosphanes Compared to Bidentate Analogues in Pd-Catalyzed Asymmetric Allylic Alkylations

Arnald Grabulosa,^[a] Guillermo Muller,^{*[a]} Rosa Ceder,^[a] and Miguel Ángel Maestro^[b]

Keywords: Palladium / Allylic compounds / Asymmetric catalysis / Nucleophilic substitution

The cationic allylpalladium complexes **3a–3f**, **4a**, **4e**, **5e** of type $[\text{Pd}(\eta^3\text{-2-Me-C}_3\text{H}_4)\text{P}_2]\text{PF}_6$ were synthesized using a group of monodentate *P*-stereogenic phosphanes, P=PPhRR' (**a–f**) and diphosphanes $(\text{PhRPCCH}_2)_2$ (**1a**, **1e**) or $\text{PhRPCCH}_2\text{Si(Me)}_2\text{CH}_2\text{PPhR}$ (**2e**). The analogous cationic complexes with the disubstituted allyl group ($\eta^3\text{-1,3-Ph}_2\text{-C}_3\text{H}_3$) and monodentate phosphanes were not isolated as stable solids; only $[\text{PdCl}(\eta^3\text{-1,3-Ph}_2\text{-C}_3\text{H}_3)\text{P}]$ (**6a**, **6d**) were obtained. Palladium allyl complexes were screened as precatalysts in the allylic substitution of *rac*-3-acetoxy-1,3-diphenyl-1-propene (**I**) and (*E*)-3-acetoxy-1-phenyl-1-propene (**III**) with dimethyl malonate as the nucleophile. The various catalytic precursors showed a wide range of activity and selectivity. The bimonodentate phosphane complexes **3** are more active

than the bidentate analogues. With regard to the regioselectivity, precursors containing monodentate phosphanes favour the formation of the linear product in the allylic substitution of cinnamyl acetate (**III**) compared with those containing bidentate phosphanes. With substrate **I**, compounds with the diphosphanes **1a** and **1e**, containing a five-membered chelate ring, gave low enantioselectivities (less than 10 % *ee*), but those with the diphosphane **2e**, forming a six-membered chelate ring or with two monodentate phosphanes, afforded products with moderate enantioselectivity under standard conditions (*ee* up to 74 %). The results show that the performance of precursors containing monodentate phosphanes was superior to those containing bidentate ligands in both activity and selectivity.

Introduction

Palladium-catalyzed asymmetric allylic substitution has been thoroughly investigated in recent years. A large number of ligands containing mainly phosphorus-, nitrogen- or sulfur-coordinating atoms have been prepared and tested in catalysis.^[1,2] In particular, the use of *P*-stereogenic phosphanes has been widely studied, initially with limited success, like those obtained with (*R,R*)-DIPAMP.^[3] Today, however, several *P*-stereogenic monodentate or bidentate phosphanes produce good results in the benchmark allylic alkylation of 1,3-diphenylallyl acetate (see examples in Table 1 and in ref.^[2]).

The reaction is characterized by a well-established generic catalytic cycle involving an oxidative addition step followed by a nucleophilic attack on an allylpalladium(II) intermediate. It is normally assumed that the resting state of the process is the allylpalladium intermediate but recent findings have improved our understanding of the reaction. These include the observation of allyl-bridged dinuclear

palladium(I) complexes formed by the interaction of the Pd^0 and allyl- Pd^{II} species of the standard catalytic cycle,^[4] careful kinetic studies of the ion-pair implications when different stabilizing anions are present,^[5] observations of the chloride effect in both systems, the consequences of strong regioretention in the allylic substitution^[6] and the non-equivalence of the catalytic precursors prepared using mixtures of $[\text{PdCl}(\mu\text{-Cl})(\text{allyl})]_2$ plus ligand or ionic $[\text{Pd}(\text{allyl})(\text{ligand})_2]\text{X}$ compounds.^[7] Impressive turnover numbers have been obtained using chiral diphosphite ligands in the allylic alkylation and amination of *rac*-1,3-diphenyl-3-acetoxyprop-1-ene,^[8a] and the origin of enantioselectivities has been explored using a library of phosphite-phosphoramidite ligands.^[8b] Furthermore, the cationic nature of the palladium allyl intermediates allowed the use of mass spectrometric screening (ESI-MS) to evaluate the enantioselectivity of a chiral catalyst or to measure the discrimination power of several chiral ligands in a single experiment.^[9] Other metals have also been used successfully in allylic substitution reactions: for example, high regioselectivity and enantioselectivity have been obtained with Ir complexes containing a single phosphoramidite ligand.^[10]

The effect of monodentate phosphanes on the regioselectivity and enantioselectivity of symmetric and asymmetric allylic substrates has been studied in some detail. For example, some monodentate phosphoramidites show over 90 % *ee* in the allylic alkylation of 1,3-diphenylallyl acetate.^[19] In the regioselectivity for asymmetric substrates like (*E*)-3-

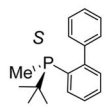
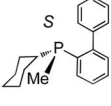
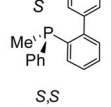
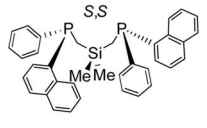
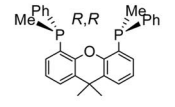
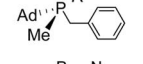
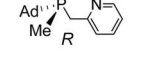
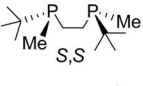
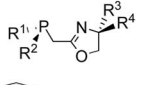
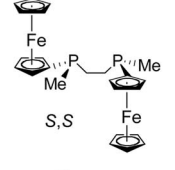
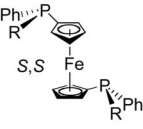
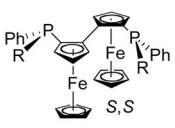
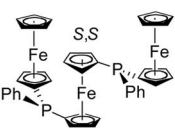
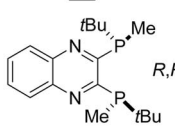
[a] Departament de Química Inorgànica, Universitat de Barcelona, Martí i Franquès 1–11, 08028 Barcelona, Spain
Fax: +34-934907725

E-mail: guillermo.muller@qi.ub.es

[b] Área de Química Orgánica, Departamento de Química Fundamental, Faculdade de Ciências, Campus da Zapateira, Universidade da Coruña, 15071 A Coruña, Spain

Supporting information for this article is available on the WWW under <http://dx.doi.org/10.1002/ejic.201000308>.

Table 1. Asymmetric allylic alkylation of *rac*-3-acetoxy-1,3-diphenyl-1-propene with dimethyl malonate catalyzed by Pd/*P*-stereogenic phosphane complexes.^[a]

Entry	Ligand	<i>t</i> (h)	Conv. (%)	<i>ee</i> (%)
1 ref. 11		15	> 99	81 (–) ^[b]
2 ref. 11		105	> 99	96 (–) ^[b]
3 ref. 11		17	> 99	0 (–)
4 ref. 12		4	> 99	27 (<i>R</i>)
5 ref. 13		6	96	85 (<i>R</i>)
6 ref. 14		2.5	91	74 (<i>R</i>)
7 ref. 14		0.1	93	44 (<i>R</i>)
8 ref. 14		16	96	88 (<i>S</i>)
9 ref. 14		16	99	96 (<i>S</i>)
10 ref. 15		1	99	95 (<i>S</i>)
11 ref. 16		2–48	82	77 (<i>R</i>)
12 ref. 17		2–48	87	88 (<i>R</i>)
13 ref. 17		2–48	84	81 (<i>R</i>)
14 ref. 18		1	85	92 (<i>R</i>)

[a] Reaction conditions were not the same for all the entries. The results shown are the best reported for each ligand. [b] Absolute configuration not reported.

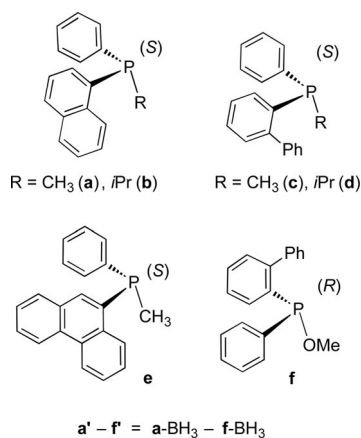
acetoxy-1-phenyl-1-propene (cinnamyl acetate), the linear product of substitution is usually favoured. However, if PCy₃ is used the stereochemistry of the starting allylic acetate is retained (“memory effect”).^[20] This effect is also observed when MOP is used.^[21] With monodentate diamidophosphites^[22] or 9-PBN^[23] the *ee* obtained in the benchmark reaction can be 97%. When it is possible to compare the results of palladium catalysts stabilized by a bidentate or two monodentate phosphanes containing the same substituents, the rate observed is usually faster in the systems that contain monodentate ligands, whereas the selectivity is similar in both cases.^[14] When the palladium/monodentate phosphane ratio is reduced to 1:1 the enantioselectivity of the reaction severely decreases.^[14,24] In this reaction the 3,5-dialkylphenyl effect has also been observed, which increases the *ee* in the alkylation of cyclohexenyl acetate by 20%.^[25]

In this study we have applied cationic palladium complexes containing two monodentate or a bidentate *P*-stereogenic phosphane as catalytic precursors in the allylic substitution reaction of *rac*-3-acetoxy-1,3-diphenyl-1-propene (**I**) and (*E*)-3-acetoxy-1-phenyl-1-propene (**III**) with dimethyl malonate as the nucleophile. From the results of activity and selectivity it has been possible to compare the performance of catalytic systems containing monodentate phosphanes with those containing bidentate phosphanes with analogous substituents at the phosphorus atoms.

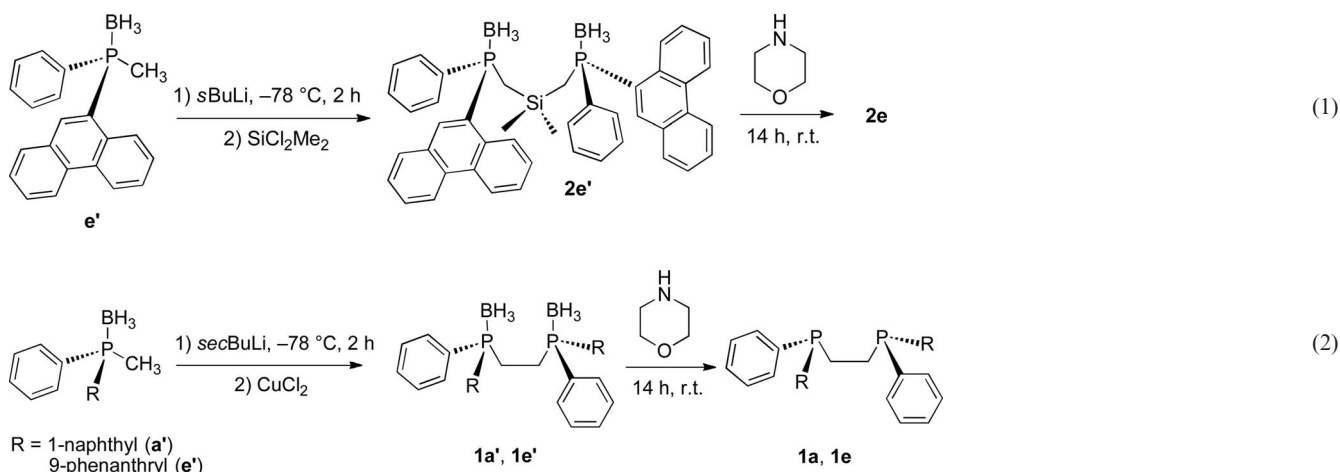
Results and Discussion

Ligand Synthesis

Monodentate *P*-stereogenic phosphanes **a–f** have already been described (Scheme 1).^[26] From borane-protected methylphosphanes **a'**, **c'** and **e'** diphosphanes were prepared by the activation of a methyl proton by *sec*-BuLi, followed by a coupling reaction using CuCl₂, or directly with SiCl₂Me₂. Both methods have been described elsewhere.^[27–30]



Scheme 1. Monodentate phosphanes **a–f**, the corresponding borane-protected phosphanes are indicated with primes.



Cu^{II}-promoted oxidative coupling is widely used [Equation (1)]. Careful adjustment of the excess of the alkyllithium compound is needed to ensure that mixtures of the desired diphosphane and the starting monophosphane are not obtained. The preparation of **1a'** and **1e'** was successful, but we were unable to obtain the pure diphosphane containing the *o*-biphenyl group, possibly because this group is more sterically demanding. Several signals between -27 and $+35$ ppm were observed in the $^{31}\text{P}\{^1\text{H}\}$ NMR spectrum of the reaction mixture from **c'**, indicating the decomposition of the phosphane.

By the methodology depicted in Equation (2) the diphosphanes containing 1-naphthyl (**2a**) and 9-phenanthryl (**2e**) groups were obtained in excellent yields. Phosphanes **1a** and **2a** have already been reported by Mezzetti and coworkers.^[29,30]

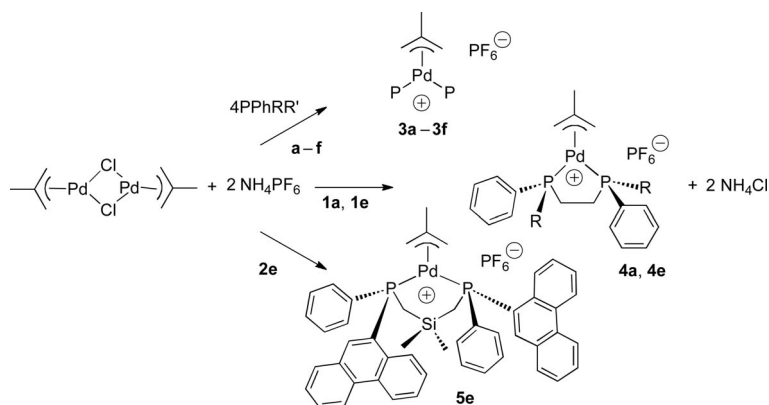
The mixtures can be purified by column chromatography. Starting from monodentate phosphanes of the *S*-absolute configuration, the diphosphanes **1** and **2** are expected to retain the same configuration (*S,S*) as reported for analogous ligands. The diastereomeric ratio of around 98:2 was improved by a single recrystallization. The crystal structure of allyl complex **3e** (vide infra) confirms the configuration of the stereogenic phosphorus atoms proposed for **1e**.

Preparation of Allyl Palladium Complexes

Reaction of $[\text{Pd}(\eta^3\text{-2-Me-C}_3\text{H}_4)(\mu\text{-Cl})_2]$ with the appropriate amount of ligand (**a-f**, **1a**, **1e** and **2e**) in the presence of an excess of ammonium hexafluorophosphate afforded ionic allylic palladium complexes of the general formula $[\text{Pd}(\eta^3\text{-2-Me-C}_3\text{H}_4)(\text{P}_2)]\text{PF}_6$ (see **3a-3f**, **4a**, **4e**, **5e** in Scheme 2). The yields were in the range 40–60%. These compounds are soluble in coordinating solvents (acetonitrile, acetone, DMF), but only scarcely soluble in noncoordinating solvents such as toluene, chloroform or dichloromethane. Complexes **3c**, **3d** and **3f** containing phosphanes with the 2-biphenyl substituent decomposed in solution, precluding the acquisition of their ^{13}C NMR spectra.

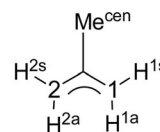
All these complexes were fully characterized by the usual techniques (see Exp. Section). From IR spectroscopy data, the most interesting absorption is the C–C stretch of the allylic moiety: for these complexes, one signal of medium intensity is observed in the range $1440\text{--}1420\text{ cm}^{-1}$. As expected, the intense $\nu(\text{P-F})$ vibration band is present at $750 \pm 5\text{ cm}^{-1}$.

Since all the allylic complexes contain two stereogenic phosphorus atoms with the same absolute configuration, the PdP_2 fragment displays C_2 symmetry. Accordingly, only



Scheme 2.

one isomer is expected to appear in solution, as was confirmed by ^{31}P NMR spectroscopy. However, because the C_2 symmetry is lost in the presence of the allyl ligand, two coupled signals are observed in all compounds showing a second-order effect.^[31a] Interestingly, one of the doublets shows a considerable broadening, enhanced in nonpolar solvents, as was also reported by Filipuzzi et al.^[31b] (see Supporting Information). This broadening is more pronounced in the complexes of the more crowded phosphanes, in accordance with the different lability of each ligand. ^1H NMR spectroscopic data were acquired in CDCl_3 or $[\text{D}_6]$ -acetone at room temperature. The spectra revealed a single stereoisomer, showing different chemical shifts for the two halves of the symmetric allyl group ($H_{\text{anti}} \neq H_{\text{anti}}'$; $H_{\text{syn}} \neq H_{\text{syn}}'$). The signals of the *anti* protons appeared as doublets because of the coupling with the phosphorus atom in the *trans* position. Table 2 and Table 3 list relevant ^{31}P NMR and ^1H NMR spectroscopic data. ^{13}C NMR spectra show the same pattern: the terminal allylic atoms appear as doublets because of the coupling with the phosphorus atom in the *trans* position, and only complex **4a** shows coupling with both the *trans*- and *cis*-phosphorus atoms (see Supporting Information). The maximum differences between the chemical shifts of the terminal allylic carbon atoms are less than 3 ppm. Other effects of the allyl fragment include the nonequivalence of the two methyl groups in the silyl linker of the bridge in **5e**, and the nonequivalence of the pair of protons of each methylene bridge in the other di-phosphanes.



Some ^1H 2D NOESY experiments were performed at room temperature to examine the nuclear Overhauser effects between different protons and proton-exchange processes. The most relevant NOE interactions were observed between the *syn* and *anti* protons of each terminal allyl carbon, and also between the *syn* protons and the central methyl-allyl group. No contacts were found between the phosphanes and the allylic protons. Furthermore, no off-diagonal exchange signals were observed and therefore no interconversion between the allyl protons was detected under the conditions of measurement.

When ^{13}C NMR spectra of **3c**, **3d** and **3f** containing the phosphanes with the 2-biphenyl substituent were recorded an unexpected number of low intensity signals appeared. Proton spectra showed the decomposition of the initial complex after a few hours, suggesting the decoordination of one phosphane. This process would be favoured with the more sterically demanding phosphanes and is supported by the different pattern of the ^{31}P signals of the two phosphanes in several ionic complexes of type **3**.

Acceptable crystals for X-ray determination were obtained for complex **4e**. The data obtained for the organometallic cation were sufficient to establish the atom connectivity although disordered CH_2Cl_2 and toluene molecules are

Table 2. ^{31}P NMR and selected ^1H NMR spectroscopic data^[a] (δ in ppm, J [Hz]) for complexes $[\text{Pd}(\eta^3\text{-(2-Me-C}_3\text{H}_4))\text{P}_2]\text{PF}_6$.

Complex	$\delta^{31}\text{P}$	P-CH _n	P-X-CH ₃	allyl CH ₃	<i>syn</i>	<i>anti</i>
3a	-0.4	1.74	—	1.65	3.53	3.65
	(d, 38.4)	(d, 8.0)	—		(s, br.)	(d, 10.0)
	2.2	1.97	—		3.74	3.34
3b	(d, 38.4)	(d, 8.0)			(s, br.)	(d, 9.6)
	21.3	1.20 –	0.24, 0.47	1.89	3.96	3.60
	(d, 32.4)	1.72 (m)	(d, 14.8), (d, 14.8)		(s, br.)	(d, 9.6)
	24.2		0.59, 0.67		4.43	3.48
	(d, 32.9)		(dd, 14.0, 6.8), (dd, 14.4, 6.4)		(s, br.)	(d, 9.2)
3c ^[b]	10.5	0.98	—	1.95	3.54	3.14
	(d, 39.5)	(d, 7.8)	—		(s, br.)	(d, 9.2)
	12.4	1.33	—		3.75	3.00
3d ^[c]	(d, 39.5)	(d, 7.7)			(s, br.)	(d, 9.1)
	39.4	1.26 –	0.61 –	2.20	4.13	3.60
	(d, 31.0)	1.68 (m)	0.91 (m)		(s, br.)	(d, 9.5)
	40.0				4.42	3.36
3e	(d, 31.0)				(s, br.)	(d, 8.8)
	0.5	1.80	—	1.81	3.76	3.78
	(d, 37.8)	(d, 8.0)	—		(s, br.)	(d, 10.0)
	3.7	2.09	—		3.92	3.47
3f ^[d]	(d, 37.8)	(d, 7.6)			(s, br.)	(d, 9.6)
	120.7	—	3.11	1.61	3.71	1.96
	(d, 53.9)		(d, 10.4)		(s, br.)	(d, 8.8)
	124.7	—	3.21		3.85	2.38
	(d, 53.9)		(d, 10.0)		(s, br.)	(d, 8.8)

[a] CDCl_3 , 298 K, ^{31}P NMR and ^1H NMR spectra measured at 101.2 and 400.1 MHz, respectively. [b] ^1H NMR spectra measured in CD_3COCD_3 and at 250.1 MHz. [c] ^1H NMR spectra measured at 250.1 MHz. [d] ^1H NMR spectra measured at 500.1 MHz.

Table 3. ^{31}P NMR and selected ^1H NMR spectroscopic data^[a] (δ in ppm, J [Hz]) for complexes $[\text{Pd}(\eta^3\text{-}(2\text{-Me-C}_3\text{H}_4))(\text{P-P})]\text{PF}_6$.

Complex	$\delta^{31}\text{P}$	$\text{P-CH}_2\text{-}$	-Si-CH_3	allyl CH_3	H_{syn}	H_{anti}
4a	44.2	2.38–2.59	–	1.71	4.11	3.27
	(d, 29.7)	(m, 2 H)			(s, br.)	(d, 10.4)
	45.6	3.14–3.30			4.54	2.95
4e	(d, 29.7)	(m, 2 H)			(s, br.)	(d, 10.0)
	44.7	2.40–2.70	–	1.69	4.11	3.31
	(d, 29.8)	(m, 2 H)			(s, br.)	(d, 9.6)
5g^[b]	45.4	3.18–3.33			4.52	3.03
	(d, 29.98)	(m, 2 H)			(s, br.)	(d, 10.0)
	12.2	2.36–2.44	–0.56	1.78	3.63	3.46
	(d, 47.9)	(m)			(t, br., 4.0)	(d, 10.4)
	13.4		–0.48		3.79	3.23
	(d, 47.6)				(t, br., 4.0)	(d, 10.0)

[a] CDCl_3 , 298 K, ^{31}P NMR and ^1H NMR spectra recorded at 101.2 and 400.1 MHz, respectively. [b] Measured in CD_3COCD_3 .

included in the crystal. The ORTEP representation of the cation is given in Figure 1. Table 4 contains selected bond lengths and angles. Pd–P and Pd–C allylic bond lengths were in good agreement with other π -allylic Pd^{II} complexes containing either two monodentate or one bidentate phosphane and the 2-Me-allyl fragment reported in the literature.^[32]

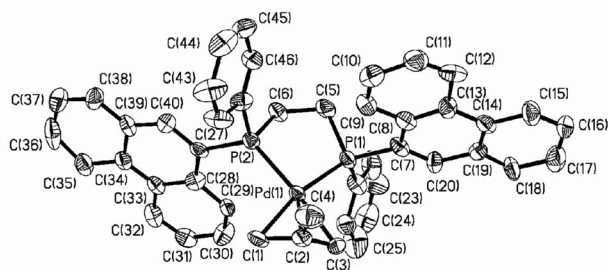


Figure 1. ORTEP view of the molecular structure of **4e**. Hydrogen atoms, solvents and hexafluorophosphate anion have been omitted for clarity.

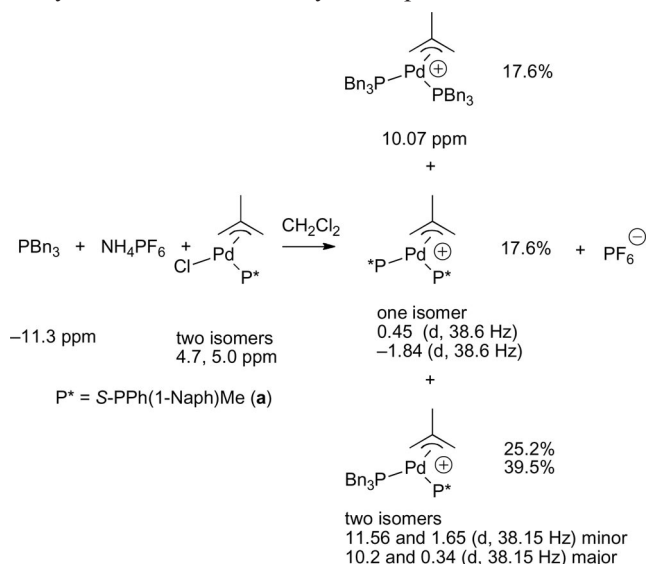
Table 4. Selected bond lengths [Å] and angles [°] for complex **4e**.

Pd(1)–C(3)	2.135(9)		
Pd(1)–C(1)	2.158(10)	C(3)–Pd(1)–C(1)	67.8(4)
Pd(1)–C(2)	2.178(9)	P(1)–Pd(1)–P(2)	87.11(9)
Pd(1)–P(1)	2.285(2)	C(1)–C(2)–C(3)	115.6(9)
Pd(1)–P(2)	2.297(2)		
P(1)–C(5)	1.826(10)		
P(2)–C(6)	1.817(10)		
C(1)–C(2)	1.402(14)		
C(2)–C(3)	1.425(13)		
C(2)–C(4)	1.436(16)		
C(5)–C(6)	1.575(15)		

Combination of Phosphanes

Heterocombinations of monodentate chiral phosphonites with achiral phosphites or phosphanes^[33] and chiral phosphoramidites with achiral phosphanes^[34] improved the conversion and enantioselectivity in the Rh-catalyzed hydrogenation reactions compared to the systems formed by homocombination of two chiral ligands. This strategy has been further extended.^[35] The relative amounts of the com-

plexes present in solution was investigated in one case^[33] and the ratio between the two homocombinations and the heterocombination observed was 1:1:16. We have checked the combination of the chiral phosphane **a** and tribenzylphosphane in detail, and the result is shown in Scheme 3. All the possible combinations of cationic complexes were observed by ^{31}P NMR spectroscopy. The two isomers of the complex corresponding to the heterocombination of ligands accounted for 65% of the mixture. The precipitate from toluene solutions mainly contained the achiral ligand homocombination and the heterocombination. Finally, by pentane precipitation we separated the chiral ligand homocombination, which was only slightly contaminated by the other complexes. The amount of the precursor containing the heterocombination of ligands was too small to be used in catalysis and no further essays were performed.

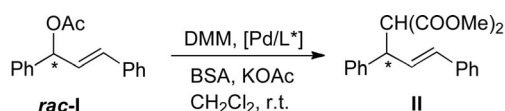


Scheme 3. Relative amounts of homo-/heterocombination of palladium allyl complexes type **3** with a 1:1 ratio of PBn_3 and **a** phosphanes.

Palladium-Catalyzed Asymmetric Allylic Alkylation of *rac*-3-Acetoxy-1,3-diphenyl-1-propene (*rac*-I)

Palladium complexes **3**, **4** and **5** were tested as precatalysts in the allylic alkylation of *rac*-I, the model substrate

for the allylic substitution processes. This group of complexes was suitable for the comparison of the importance of the metallacycle size and the consequences of the monodentate or bidentate nature of the ligands (electronically analogous) and their influence on the activity and selectivity of the process. The fragment PdP_2 displays C_2 symmetry in all complexes.



Complexes of type **3** with two monodentate phosphanes showed higher activity than those we observed with dithioethers or bis(oxazolines), and similar activity to that reported for phosphane-oxazolines^[37] or phosphane-phosphoramidite ligands^[38] (entries 1–6, Table 5). Complexes **4** and **5** containing bidentate phosphanes showed lower rates of reaction, which is consistent with the findings of Imamoto^[14] and Mezzetti.^[12] Complex **3e**, which contains two monodentate phosphanes, showed a higher selectivity than **4e** or **5e**, which have the same group of substituents at the phosphorus atom. Complexes **4** containing a five-membered metallic cycle gave almost racemic mixtures of the substitution products, as reported by Bosnich,^[3] who used bis aryl-substituted phosphanes. The results showed a clear dependence of the enantioselectivity on the phosphorus substitution in the MePhPR series. The enantiomeric excesses follow the trend: 2-biphenyl < 1-naphthyl < 9-phenanthryl (entries 1, 3 and 5, respectively). The increase of steric hindrance of the sp^3 arm is more sensitive. When the methyl group (entry 3 phosphane **S-c**) was substituted by a methoxy (entry 6 phosphane **R-f**) or an isopropyl group (entry 4 phosphane **S-d**) the *ee* improved but the di-

rection of the asymmetric induction was inverted for the more hindered isopropylphosphanes (entries 1 vs. 2 and 3 vs. 4). The origin of this inversion must be produced in the very crowded allyl intermediate that could not be isolated since the crystal structures of the phosphane–boranes **c** and **d** do not show any remarkable differences.^[26] For this reason the neutral allylic complex $[\text{PdCl}(\eta^3\text{-2-Me-C}_3\text{H}_4)(\text{f})]$ was tested as a precursor in the reaction (entries 7 and 8). It showed a lower but still remarkable *ee* and an initially lower rate of reaction, as expected for the less favoured initial nucleophilic attack on a neutral intermediate. The reorganization of the neutral complex $[\text{PdCl}(\eta^3\text{-2-Me-C}_3\text{H}_4)(\text{f})]$ affording cationic species that may be suitable as catalytic precursors can be considered.^[39] Similar results have been reported when the ratio Pd/L is reduced to 1:1, with a severe decrease of the *ee*.^[24]

Preparation of $\eta^3\text{-1,3-Diphenylallyl}$ Palladium Complexes

The synthesis of palladium $\eta^3\text{-1,3-diphenylallyl}$ bisphosphane intermediates were attempted by reaction among the palladium dimer, monodentate phosphane and NH_4PF_6 .^[40] Only neutral $[\text{PdCl}(\eta^3\text{-1,3-diphenylallyl})(\text{P})]$ complexes were obtained. The use of an excess of phosphane and AgPF_6 did not afford any stable species. Possibly, the more sterically demanding 1,3-diphenylallyl group hinders the stabilization of the desired ionic compounds. The neutral complexes were fully characterized by the usual techniques.

^1H NMR signals from the CDCl_3 solution of complex **6a** at room temperature showed broad, poorly defined signals. Therefore, spectra were recorded at temperatures ranging from 25 to -40°C (see Supporting Information). In contrast, the spectrum of compound **6d** is well defined at room temperature.

1D and 2D NMR spectroscopic data indicate that the number of isomers observed in these solutions are limited to those with the phenyl groups of the allyl ligand in *syn*-positions.^[40,41] So, two isomers were observed in complexes **6a** and **6d** in the relative proportions shown in Table 6 [Equation (3)]. ^{31}P NMR spectra of both complexes show two signals, which is consistent with the presence of the two isomers. Discrimination between them increases with the size of the phosphane (**6d** > **6a**), but it is similar to that observed in the analogous $[\text{PdCl}(\eta^3\text{-2-Me-C}_3\text{H}_4)(\text{P})]$ complexes.^[26] NOESY spectra showed dynamic exchange between the groups of hydrogen atoms. In particular, the exchange between *anti*-allylic protons of the two isomers indicates that the allyl pseudorotation is the main operating mechanism of exchange.^[42]

A set of signals is observed for each isomer. The central allylic hydrogen appears as a triplet at a lower field than the terminal allylic hydrogen atoms. In addition, the *anti*-allylic hydrogen atom located on the carbon atom *trans* to the phosphorus atom appears (coupled with the central hydrogen and phosphorus atoms) at lower fields than those in the *cis* position (which are only coupled to the central hydrogen atom). This is also observed for similar compounds.^[14]

Table 5. Results of asymmetric allylic alkylation of *rac*-3-acetoxy-1,3-diphenyl-1-propene (**I**) with dimethyl malonate catalyzed by type **3**, **4** and **5** complexes.^[a]

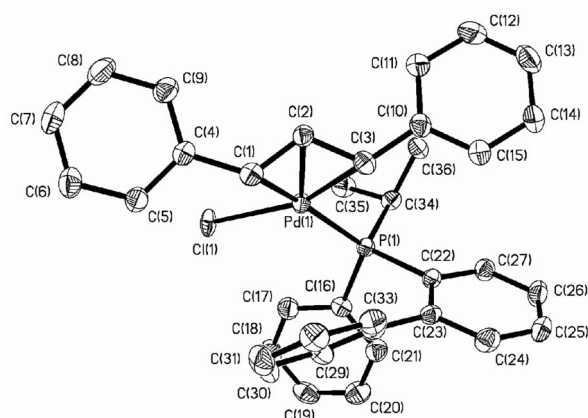
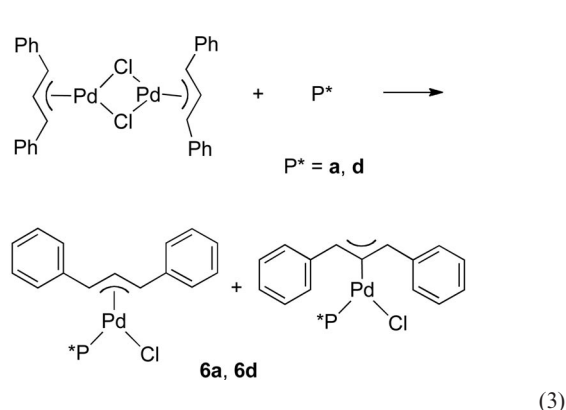
Entry	Complex	<i>t</i> [h]	Conversion [%] ^[b]	<i>ee</i> [%] ^[c]
1	3a	1	>99.0	28 (<i>R</i>)
2	3b	1	92.6	45 (<i>S</i>)
3	3c	1	89.5	8 (<i>R</i>)
4	3d	1	87.5	14 (<i>S</i>)
5	3e	1	>99.0	68 (<i>R</i>)
6	3f	1	>99.0	74 (<i>S</i>)
7	$[\text{PdCl}(\text{allyl})(\text{f})]$	1	<2.0	– (–)
8	$[\text{PdCl}(\text{allyl})(\text{f})]$	24	>99.0	60 (<i>S</i>)
9	4a	1	2.0	– (–)
10	4a	24	>99.0	5 (<i>S</i>)
11	4e	1	4.1	– (–)
12	4e	24	>99.0	8 (<i>R</i>)
13	5a ^[d]	4	99	27 (<i>R</i>)
14	5e	1	12.3	58 (<i>R</i>)
15	5e	24	>99.0	60 (<i>R</i>)

[a] Catalytic conditions: 0.02 mmol of [Pd], complex **3**, **4** or **5**, 1 mmol of *rac*-1,3-diphenyl-2-propenyl acetate, 3 mmol of dimethyl malonate, 3 mmol of BSA and a catalytic amount of KOAc in 4 mL of CH_2Cl_2 . [b] Conversion percentage based on the substrate. [c] Enantiomeric excesses determined by HPLC with a Chiralcel-OD column. Absolute configuration, in parentheses, determined by optical rotation: ref.^[36] [d] Ref.^[12]

Table 6. ^{31}P NMR and selected allyl ^1H NMR and ^{13}C NMR spectroscopic data^[a] (δ in ppm, J [Hz]) for complexes $[\text{PdCl}(\eta^3\text{-1,3-Ph}_2\text{C}_3\text{H}_3)(\text{P})]$ **6a** and **6d**.

Complex	^{31}P NMR δ	^1H NMR <i>anti-tP</i>	^1H NMR <i>anti-cP</i>	^1H NMR <i>central</i>	^{13}C NMR <i>anti-tP</i>	^{13}C NMR <i>anti-cP</i>	^{13}C NMR <i>central</i>
6a							
(253 K)							
major							
1.2	7.8	5.44 (dd, 13.5, 10)	4.08 (d, 11)	6.19 (ps-t, 11.5)	97.7 (d, 25.2)	58.6 (s)	109.1 (s)
minor							
1	7.7	5.49 (dd, 13.5, 10)	3.97 (d, 11.5)	−6.34 (ov.)	96.7 (d, 25.2)	59.2 (s)	108.4 (s)
6d							
(298 K)							
major							
1.4	33.6	4.75 (ps-t, 10.5)	3.88 (d, 11)	6.21 (ps-t, 12)	98.1 (d, 24.4)	80.0 (s)	106.8 (s)
minor							
1	31.4	4.88 (ps-t, 10.5)	3.57 (d, 11)	6.13 (ps-t, 12)	96.2 (d, 25.2)	80.3 (s)	107.4 (s)

[a] CDCl_3 , ^{31}P NMR, ^1H NMR and ^{13}C NMR spectra measured at 101.2, 500 and 100.6 MHz, respectively; ps-t: pseudo triplet, ov.: overlapped.

Figure 2. ORTEP view of the molecular structure of **6d**. Hydrogen atoms have been omitted for clarity.

^{13}C chemical shifts for the allylic carbon atoms show that the central atom resonates at a lower field than the terminal ones and that the carbon atom located at a position *trans* to phosphorus is less shielded than the *cis* atom, and is coupled to the phosphorus atom. Compared with the analogous $[\text{PdCl}(\eta^3\text{-2-Me-C}_3\text{H}_4)(\text{P})]$ complexes,^[26] the carbon atoms *trans* to phosphorus are about 10 ppm more deshielded in the diphenylallyl complexes. Complex **6d** shows a large shift to lower fields in the allylic carbon atom *cis* to phosphorus, possibly as a result of the proximity of the *o*-phenyl group of the phosphane, as reflected in the crystal structure (see below).

Suitable crystals for X-ray diffraction measurements were obtained from dichloromethane solutions of **6d** by slow diffusion of hexane at 4 °C (Figure 2).

The crystal structure shows only the diastereoisomer with *R* configuration at the palladium centre with the substituted allyl ligand in *syn,syn* geometry. The palladium atom shows a distorted square-planar coordination, bonded to one chlorine ligand, one phosphorus ligand and the three allylic carbon atoms (Table 7). The position of the

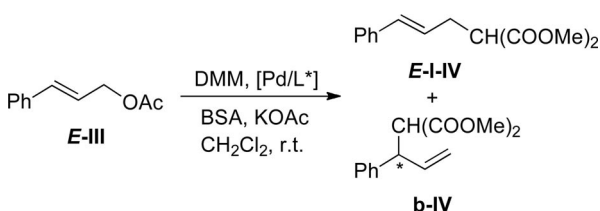
allylic ligand with respect to the plane defined by the palladium, chlorine and phosphorus atoms is heavily distorted: C(3) lies -0.021 Å away from the plane, while C(1) is at 0.577 Å, probably because of the disposition of the biphenyl substituent of the coordinated phosphane. This distortion is similar to those observed in the $[\text{Pd}(\eta^3\text{-1,3-Ph}_2\text{C}_3\text{H}_3)(\text{PPh}_3)_2]^+$ cation.^[43] However, in the crystal structure of the analogous $[\text{PdCl}(\eta^3\text{-2-Me-C}_3\text{H}_4)(\text{P}(i\text{Pr})(o\text{-Ph}_2)\text{-Ph})]$ complex,^[26] the allyl moiety (C1 and C3) remains in the plane defined by the same three atoms. These features suggest that the steric hindrance of the $\text{P}(i\text{Pr})(o\text{-Ph}_2)\text{Ph}$ phosphane blocks the formation of the $[\text{Pd}(\eta^3\text{-1,3-Ph}_2\text{C}_3\text{H}_3)_2]^+$ cation. The difference between the two Pd–C bond lengths, *trans* to the P and *trans* to the Cl atom (2.253 vs. 2.194 Å), indicates a major *trans* influence of the phosphane ligand, and consequently a different double bond character of the C(1)–C(2) and C(2)–C(3) allylic bonds (see Table 7).

Table 7. Selected bond lengths [Å] and bond angles [°] for **6d**.

Pd(1)–Cl(1)	2.4202(10)	Cl(1)–Pd(1)–P(1)	103.22(4)
Pd(1)–P(1)	2.3308(11)	C(1)–Pd(1)–C(3)	66.41(15)
Pd(1)–C(1)	2.253(4)	C(2)–Pd(1)–P(1)	138.24(11)
Pd(1)–C(2)	2.180(4)	C(2)–Pd(1)–Cl(1)	117.43(11)
Pd(1)–C(3)	2.194(4)	C(1)–C(2)–C(3)	119.7(4)
C(1)–C(2)	1.387(6)		
C(2)–C(3)	1.429(6)		

Palladium-Catalyzed Asymmetric Allylic Alkylation of (*E*)-3-Acetoxy-1-phenyl-1-propene (**III**)

In order to compare the regioselectivity of the allylic alkylation reaction catalyzed by these palladium complexes, the substrate (*E*)-3-acetoxy-1-phenyl-1-propene (**III**) was used (Table 8). The reaction for this substrate was faster than for **I** and total conversion was achieved in less than one hour. The main difference was that for **III** a similar activity was observed with catalytic precursors containing bidentate phosphanes (4 and 5, entries 14–16) and those stabilized by monodentate phosphanes (3, entries 1–6). A short induction time for the activation of the catalytic precursor is necessary (entries 1 and 2, 7 and 8 or 9 and 10) as indicated by the colour change from pale yellow to orange. A similar induction time was observed when the catalytic precursor was prepared in a ratio Pd/ligand: 1:1 (entries 7 and 8). Furthermore, the initially inactive neutral allylic complex [PdCl(η³-2-Me-C₃H₄)(a)] achieved complete conversion in 45 min (entries 9 and 10). Only the neutral complex, which contained the most hindered phosphane (**d**), showed limited activity (entries 12 and 13).



All precursors favoured the formation of the linear product, but the amount of branched compound **b-IV** obtained with type-4 precursors (entries 14 and 15) was larger than the amount obtained with types 3 or 5 (Table 8). The bite angle of bidentate ligands strongly affects the regioselectivity. Van Leeuwen et al. studied the palladium-catalyzed allylic alkylation of 2-hexenyl acetate, and showed that the increase in the bite angle of the diphosphanes leads to the increase in the proportion of the linear isomer.^[44] When the phosphane substituents are analogous, the pure steric interaction of the diphosphane and the allyl fragment determines the outcome.^[44] Our results with complexes **4** and **5** follow the same trend. The selectivity observed with compounds **3**, which contain two monodentate phosphanes, can be explained in the same way, bearing in mind that the coordination of two bulky monodentate phosphanes will produce large P–Pd–P angles. For example the angles for palladium allyl bis(triphenylphosphane) complexes are

Table 8. Results obtained in the allylic alkylation of (*E*)-3-acetoxy-1-phenyl-1-propene (**III**) with dimethyl malonate catalyzed by type **3**, **4** and **5** complexes.^[a]

Entry	Complex	<i>t</i> [min]	Conv. [%] ^[b]	Branched/linear ^[c]
1	3a	10	6.2	— ^[e]
2	3a	20	>99.0	1:15
3	3b	60	>99.0	1:>20
4	3c	60	>99.0	1:15
5	3e	60	>99.0	1:16
6	3f	60	>99.0	1:>20
7 ^[d]	[PdCl(allyl)(a)]	30	37.2	1:17
8 ^[d]	[PdCl(allyl)(a)]	45	>99.0	1:16
9	[PdCl(allyl)(a)]	30	4.0	— ^[e]
10	[PdCl(allyl)(a)]	45	>99.0	1:18
11	[PdCl(allyl)(b)]	60	>99.0	1:>20
12	[PdCl(allyl)(d)]	60	<2.0	— ^[e]
13	[PdCl(allyl)(d)]	150	10.0	— ^[e]
14	4a	60	86.2	1:9
15	4e	60	>99.0	1:8
16	5e	60	85.1	1:13

[a] Reaction conditions: 0.02 mmol of palladium complex, 1 mmol of cinnamyl acetate, 3 mmol BSA and a catalytic amount of KOAc in 4 mL of CH₂Cl₂. [b] Conversion percentage based on the substrate, determined by GC. [c] Branched/linear ratio of isomers obtained by GC. [d] Palladium precursor obtained by reaction of the [PdCl(allyl)(phosphane)] complex with AgBF₄ in the presence of cinnamyl acetate. [e] The small conversion observed precludes the formulation of a confident ratio of isomers.

100.0%.^[43,45] The low amounts of branched product obtained precluded the measurement of enantiomeric excesses. A similar range of selectivity was observed when bulky monodentate phosphoramidites were used.^[19]

When the cationic precursor species were obtained from [PdCl(η³-2-Me-C₃H₄), **a**], where the ratio Pd/P was 1:1, the reaction was slower (entries 1, 2, 7, 8) but the regioselectivity was similar. The use of the neutral complexes (Pd/P = 1:1) as precursors led to the same regioselectivity as that observed for the cationic complexes **3** (Pd/P = 1:2).

Conclusions

In summary, we have obtained a group of cationic palladium compounds **3**, **4** and **5** containing *P*-stereogenic monodentate and bidentate phosphanes that have two different aryl substituents at each phosphorus atom. The different labilities of the two coordinated phosphorus atoms were dependent on the size of the substituents, as is clearly demonstrated by comparing the ³¹P NMR spectra of the complexes in which a methyl group was substituted by an isopropyl group or in the sequence **3a**, **3c**, **3e** (see Supporting Information).

All the cationic complexes were tested in Pd-catalyzed allylic substitution reactions. The alkylation of 3-acetoxy-1-phenyl-1-propene showed that the monodentate ligands favour the formation of the linear product. When alkylation was tested with *rac*-3-acetoxy-1,3-diphenyl-1 propene some noteworthy results were obtained. Complexes **3** containing two monodentate phosphanes were more active than **4** and **5**.

With regard to the asymmetric induction, the enantioselectivity with catalysts **3** increases with the size of the substituents of the phosphane, achieving the best result of 74% *ee* with the phosphinite ligand **f**. The sequence of *ee* observed was as follows: P(2-biphenyl)PhMe (**3c**, 8%), P(2-biphenyl)Ph(*i*Pr) (**3d**, 14%), P(2-biphenyl)Ph(OMe) (**3f**, 74%), P(2-biphenyl)(*t*Bu)Me (81%)^[11] and P(2-biphenyl)CyMe (96%).^[11] This sequence illustrates the diversity and subtlety of factors determining the discrimination ability of apparently similar ligands. The lack of enantioselectivity observed for bidentate ligands with an ethylene bridge (**1a** and **1e**) is similar to the results reported for DI-PAMP,^[3] all of which contain two different aryl substituents. However, with the same bridge but with methyl and *tert*-butyl substituents, 88% *ee* has been obtained,^[14] and with a completely planar bridge, 92% *ee* has been reported.^[18] In both cases bisalkylaryl-monodentate or bidentate phosphanes gave the best selectivities. Bidentate ligands with three atoms in the bridge (**2**) showed a similar discrimination ability to that obtained with monodentate phosphanes.

The results of this study confirm that *P*-stereogenic monodentate phosphanes show higher activity and an analogous or better discrimination ability than bidentate phosphanes in the catalytic asymmetric allylic substitution reaction.

Experimental Section

General Data: All compounds were prepared under a purified nitrogen atmosphere using standard Schlenk and vacuum-line techniques. The solvents were purified by standard procedures and distilled under nitrogen. [Pd(η^3 -2-Me-C₃H₄)(μ -Cl)]₂ and [Pd(η^3 -1,3-Ph₂-C₃H₃)(μ -Cl)]₂ were prepared as described previously.^[40,46] The routine ¹H, ¹³C and ³¹P NMR spectra were recorded with a Varian XL-500 or Mer-400 MHz (¹H NMR, standard SiMe₄), Varian Gemini (¹³C NMR, 50.3 MHz, standard SiMe₄) and Bruker DRX-250 (³¹P NMR, 101.2 MHz) spectrometer in CDCl₃ unless otherwise specified. Chemical shifts were reported downfield from standards. The two-dimensional experiments were carried out with a Bruker DMX-500 or a Varian XL-500 instrument. IR spectra were recorded with the following spectrometers: FTIR Nicolet 520, FTIR Nicolet Impact 400, FTIR Avatar 330 and FTIR Nicolet 5700. FAB mass chromatograms were obtained with a Fisons V6-Quattro instrument. The routine GC analyses were performed with a Hewlett–Packard 5890 Series II gas chromatograph (50-m Ultra 2 capillary column 5% phenylmethylsilicone and 95% dimethylsilicone) with a FID detector. The GC–MS analyses were performed with a Hewlett–Packard 5890 Series II gas chromatograph (50-m Ultra 2 capillary column) interfaced to a Hewlett–Packard 5971 mass selective detector. HPLC analyses were carried out with a Waters 717 plus autosampler chromatograph with a Waters 996 multidiode array detector, fitted with a Chiracel OD-H chiral column (25 cm × 0.46 cm). The eluent, in all the determinations, was a mixture of *n*-hexane/*i*PrOH, 95:5. Optical rotations were measured with a Perkin–Elmer 241MC spectropolarimeter at 23 °C. Enantiomeric excesses were determined by GC with a Hewlett–Packard 5890 Series II gas chromatograph (30-m ChiralDEX DM column) with a FID detector. Elemental analyses were carried out by the Serveis Científicotècnics of the Universitat Rovira i Virgili with an Eager 1108 microanalyzer.

Synthesis

(*S,S*)-1,2-Bis[(1-naphthyl)phenylphosphanyl]ethane–Borane(*P*) (*S,S*)-1a'**:** The phosphane–borane (*S*)-**a'** (0.816 g, 3.1 mmol) was dissolved in THF (30 mL) and the solution was cooled to –78 °C. *sec*-butyllithium (2.9 mL of a 1.3 M solution in hexane/cyclohexane, 3.7 mmol) was added by syringe and the mixture was stirred for 2 h. A precooled (–78 °C) suspension of CuCl₂ (1.25 g, 9.2 mmol) in THF (50 mL) was added and the mixture was warmed slowly to room temperature. A HCl solution (1 M, 10 mL) was added and the mixture was extracted with ethyl acetate. The combined organic fractions were washed with a 10% NaOH solution (3 × 10 mL) and eventually with an ammonia solution. The organic fraction was washed with brine and dried with anhydrous sodium sulfate. Filtration and evaporation of the solvent furnished the product as a white foam that could appear contaminated with small amounts of the methylmonophosphane–borane (*S*)-**a'** (<10%). The monosubstituted product was removed by flash chromatography (SiO₂, CH₂Cl₂). Combined yield 0.800 g (99%). ¹H NMR (250.1 MHz, CDCl₃, 298 K): δ = 0.20–2.10 (s, br., 6 H), 2.60 (s, br., 4 H), 7.37–7.98 (m, 24 H, Ar) ppm. ¹³C{¹H} NMR (62.9 MHz, CDCl₃, 298 K): δ = 20.2 (d, *J*_{CP} = 37.5 Hz, CH₂), 125.2–134.8 (m, 1 C, CH, Ar) ppm. ³¹P{¹H} NMR (101.1 MHz, CDCl₃, 298 K): δ = +18.6 (s, br.) ppm.

(*S,S*)-1,2-Bis[(9-phenanthryl)phenylphosphanyl]ethane–Borane(*P*) (1/2**), (*S,S*)-**1e'**:** This diphosphane–borane was obtained by the same method as that used for (*S,S*)-**1a'**. From (*S*)-**e'** (0.942 g, 3 mmol), the desired product was obtained as a white foam that could appear contaminated with the monophosphane–borane (*S*)-**e'** (<15%). Combined yield 0.795 g (79%). ¹H NMR (250.1 MHz, CDCl₃, 298 K): δ = 0.60–2.10 (s, br., 6 H), 2.65 (s, br., 4 H), 7.00–8.88 (m, 28 H, Ar) ppm. ³¹P{¹H} NMR (101.1 MHz, CDCl₃, 298 K): δ = +21.0 (s, br.) ppm.

(*S,S*)-2,2-Dimethyl-1,3-bis[(9-phenanthryl)phenylphosphanyl]-2-sila-propane–Borane(*P*) (1/2**), (*S,S*)-**2e'**:** The phosphane–borane (*S*)-**e'** (0.628 g, 2.0 mmol) was dissolved in THF (5 mL) and cooled to –78 °C. *sec*-Butyllithium (1.70 mL of a 1.3 M solution in hexane/cyclohexane, 2.2 mmol) was added and the solution was stirred for 2 h. Dichlorodimethylsilane (0.129 g, 1 mmol) was quickly added by syringe and the mixture was warmed slowly to room temperature. A HCl solution (1 M, 10 mL) was added and the THF was removed. The aqueous suspension was extracted with dichloromethane (3 × 10 mL) and the combined organic layers were washed with brine and dried with anhydrous sodium sulfate and filtered. Evaporation of the solvent yielded the title compound as a yellowish foam that could appear contaminated with the monophosphane–borane (*S*)-**e'** (<10%). Combined yield 0.650 g (95%). ¹H NMR (250.1 MHz, CDCl₃, 298 K): δ = –0.31 (s, 6 H), 0.20–1.80 (s, br., 6 H), 1.60–2.15 (s, br., 4 H), 7.29–8.75 (m, 28 H, Ar) ppm. ³¹P{¹H} NMR (101.1 MHz, CDCl₃, 298 K): δ = +14.3 (s, br.) ppm.

(*S,S*)-1,2-Bis[(1-naphthyl)phenylphosphane]ethane (*S,S*)-1a**:** The diphosphane–borane (*S,S*)-**1a'** (0.263 g, 0.5 mmol) was dissolved in degassed morpholine (15 mL) and stirred for 14 h at room temperature. The morpholine was removed and the pasty residue was passed through a short column of alumina with toluene as eluent. Evaporation of toluene furnished the free diphosphane as a white pasty solid; yield 0.120 g (48%). ¹H NMR (250.1 MHz, CDCl₃, 298 K): δ = 2.06–2.36 (br., s, 4 H), 7.16–8.48 (m, 24 H, Ar) ppm. ³¹P{¹H} NMR (101.1 MHz, CDCl₃, 298 K): δ = –23.4 (s) ppm.

(*S,S*)-1,2-Bis[(9-phenanthryl)phenylphosphanyl]ethane (*S,S*)-1e**:** This diphosphane–borane was obtained by the same method as that used for (*S,S*)-**1a**. From (*S,S*)-**1e'** (0.795 g, 1.27 mmol), the desired product was obtained as a white pasty solid that could appear con-

taminated with the methylmonophosphane (**S**)-**e** (<10%). Combined yield 0.356 g (47%). ^1H NMR (250.1 MHz, CDCl_3 , 298 K): δ = 2.10–2.78 (br., s, 4 H), 7.16–8.48 (m, 24 H, Ar) ppm. $^{31}\text{P}\{^1\text{H}\}$ NMR (121.5 MHz, CDCl_3 , 298 K): δ = –26.9 (s) ppm.

(*S,S*)-2,2-Dimethyl-1,3-bis[(9-phenanthryl)phenylphosphanyl]-2-silapropane (*S,S*)-2e****: This diphosphane–borane was obtained by the same method as that used for (*S,S*)-**1a**. From (*S,S*)-**2e'** (0.650 g, 0.95 mmol), the free diphosphane was obtained as a viscous oil that could appear contaminated with the monophosphane (**S**)-**e** (<15%). Combined yield 0.234 g (38%). ^1H NMR (250.1 MHz, CDCl_3 , 298 K): δ = –0.05 (s, 6 H), 0.90–0.95 (m, 4 H), 7.20–8.69 (m, 28 H, Ar) ppm. $^{31}\text{P}\{^1\text{H}\}$ NMR (101.1 MHz, CDCl_3 , 298 K): δ = –32.9 (s) ppm.

(η^3 -2-Methylallyl)bis[(*R*)-methyl(1-naphthyl)phenylphosphane]palladium(II) Hexafluorophosphate (3a**)**: The phosphane (**S**)-**a** (0.299 g, 1.19 mmol) was dissolved in CH_2Cl_2 (20 mL). Ammonium hexafluorophosphate (0.278 g, 1.71 mmol) and the palladium dimer $[\text{PdCl}(\mu\text{-Cl})\eta^3\text{-(2-CH}_3\text{-C}_3\text{H}_4)]$ (0.112 g, 0.28 mmol) were added and the yellow solution was stirred for 1 h. Water (20 mL) was added and the resulting mixture was extracted with dichloromethane (3×10 mL). The combined organic fractions were washed with water and dried with sodium sulfate. The solvent was then removed and the resulting yellowish foam was suspended in pentane, filtered and washed with more pentane. The product was finally obtained as a yellow solid; yield 0.310 g (66%). ^1H NMR (400.1 MHz, CDCl_3 , 298 K): δ = 1.65 (s, 3 H), 1.74 (d, J = 8.0 Hz, 3 H), 1.97 (d, J = 8.0 Hz, 3 H), 3.34 (d, J = 9.6 Hz, 1 H), 3.53 (s, 1 H), 3.65 (d, J = 10.0 Hz, 1 H), 3.74 (s, 1 H), 6.96–8.10 (m, 24 H, Ar) ppm. $^{13}\text{C}\{^1\text{H}\}$ NMR (100.0 MHz, CDCl_3 , 298 K): δ = 13.6 (d, J_{CP} = 28.2 Hz, CH_3), 15.0 (d, J_{CP} = 28.2 Hz, CH_3), 23.5 (s, CH_3), 74.3 (d, J_{CP} = 28.2 Hz, CH_2), 76.1 (d, J_{CP} = 29.7 Hz, CH_2), 125.2–138.3 (m, 1 C, CH, Ar) ppm. $^{31}\text{P}\{^1\text{H}\}$ NMR (101.1 MHz, CDCl_3 , 298 K): δ = –0.4 (d, J = 38.4 Hz, 1 P), +2.2 (d, J = 38.4 Hz, 1 P) ppm. $\text{C}_{38}\text{F}_6\text{H}_{37}\text{P}_3\text{Pd}$ (807.03): calcd. C 56.56, H 4.62; found C 57.16, H 5.04.

(η^3 -2-Methylallyl)bis[(*R*)-isopropyl(1-naphthyl)phenylphosphane]palladium(II) Hexafluorophosphate (3b**)**: This complex was obtained by the same method as that used for **3a**. From (**S**)-**b** (0.200 g, 0.72 mmol), ammonium hexafluorophosphate (0.168 g, 1.03 mmol) and the dimer $[\text{PdCl}(\mu\text{-Cl})\eta^3\text{-(2-CH}_3\text{-C}_3\text{H}_4)]$ (0.068 g, 0.17 mmol), the title complex was obtained as a red solid; yield 0.125 g (42%). ^1H NMR (400.1 MHz, CDCl_3 , 298 K): δ = 0.24 (d, J = 14.8 Hz, 3 H, br.), 0.47 (d, J = 14.8 Hz, 3 H, br.), 0.59 (dd, J = 14.0, 6.8 Hz, 3 H), 0.67 (dd, J = 14.4, 6.4 Hz, 3 H), 1.20–1.72 (m, 2 H), 1.89 (s, 3 H), 3.48 (d, J = 9.2 Hz, 1 H), 3.60 (d, J = 9.6 Hz, 1 H) ppm. $^{13}\text{C}\{^1\text{H}\}$ NMR (100.0 MHz, CDCl_3 , 298 K): δ = 18.4 (d, J_{CP} = 3.8 Hz, CH_3), 18.5 (s, CH_3), 19.2 (d, J_{CP} = 6.9 Hz, CH_3), 19.6 (d, J_{CP} = 8.4 Hz, CH_3), 23.1 (s, CH_3), 25.2–25.8 (br., CH), 75.4 (d, J_{CP} = 26.6 Hz, CH_2), 125.4–137.6 (m, 1 C, CH, Ar) ppm. $^{31}\text{P}\{^1\text{H}\}$ NMR (101.1 MHz, CDCl_3 , 298 K): δ = +21.3 (d, J = 32.4 Hz, 1 P), +24.2 (d, J = 32.9 Hz, 1 P) ppm. $\text{C}_{42}\text{F}_6\text{H}_{45}\text{P}_3\text{Pd}$ (863.14): calcd. C 58.45, H 5.26; found C 58.55, H 5.82.

(η^3 -2-Methylallyl)bis[(*R*)-methyl(9-phenanthryl)phenylphosphane]palladium(II) Hexafluorophosphate (3c**)**: This complex was obtained by the same method as that used for **3a**. From the phosphane (**S**)-**e** (0.442 g, 1.47 mmol), ammonium hexafluorophosphate (0.343 g, 2.10 mmol) and the dimer $[\text{PdCl}(\mu\text{-Cl})\eta^3\text{-(2-CH}_3\text{-C}_3\text{H}_4)]$ (0.138 g, 0.35 mmol), the desired compound was obtained as a red solid; yield 0.330 g (52%). ^1H NMR (400.1 MHz, CDCl_3 , 298 K): δ = 1.80 (d, J = 8.0 Hz, 3 H), 1.81 (s, 3 H), 2.09 (d, J = 7.6 Hz, 3 H), 3.47 (d, J = 9.6 Hz, 1 H), 3.76 (s, 1 H), 3.78 (d, J = 10.0 Hz, 1

H) ppm. 3.92 (s, 1 H), 7.01–8.53 (m, 28 H, Ar) ppm. $^{13}\text{C}\{^1\text{H}\}$ NMR (100.0 MHz, CDCl_3 , 298 K): δ = 14.3 (d, J_{CP} = 27.4 Hz, CH_3), 16.1 (d, J_{CP} = 28.2 Hz, CH_3), 23.7 (s, CH_3), 74.2 (d, J_{CP} = 28.9 Hz, CH_2), 76.4 (d, J_{CP} = 29.0 Hz, CH_2), 122.6–138.3 (m, 1 C, CH, Ar) ppm. $^{31}\text{P}\{^1\text{H}\}$ NMR (101.1 MHz, CDCl_3 , 298 K): δ = +0.5 (d, J = 37.9 Hz, 1 P), +3.7 (d, J = 37.7 Hz, 1 P) ppm. $\text{C}_{46}\text{F}_6\text{H}_{41}\text{P}_3\text{Pd}$ (907.15): calcd. C 60.90, H 4.56; found C 60.13, H 5.33.

(η^3 -2-Methylallyl)bis[(*R*)-(2-biphenyl)methylphenylphosphane]palladium(II) Hexafluorophosphate (3c**)**: This complex was obtained by the same method as that used for **3a**. From the phosphane (**S**)-**c** (0.539 g, 1.95 mmol), ammonium hexafluorophosphate (0.454 g, 2.79 mmol) and the dimer $[\text{PdCl}(\mu\text{-Cl})\eta^3\text{-(2-CH}_3\text{-C}_3\text{H}_4)]$ (0.183 g, 0.46 mmol), the product was obtained as a red solid; yield 0.485 g (62%). ^1H NMR (250.1 MHz, CDCl_3 , 298 K): δ = 0.98 (d, J = 7.8 Hz, 3 H), 1.33 (d, J = 7.7 Hz, 3 H), 1.95 (s, 3 H), 3.00 (d, J = 9.1 Hz, 1 H), 3.14 (d, J = 9.2 Hz, 1 H), 3.54 (s, 1 H), 3.75 (s, 1 H), 6.86–8.17 (m, 28 H, Ar) ppm. $^{31}\text{P}\{^1\text{H}\}$ NMR (101.1 MHz, CD_3COCD_3 , 298 K): δ = +10.5 (d, J = 39.5 Hz, 1 P), +12.4 (d, J = 39.5 Hz, 1 P) ppm. $\text{C}_{42}\text{F}_6\text{H}_{41}\text{P}_3\text{Pd}$ (859.11): calcd. C 58.72, H 4.81; found C 59.27, H 4.98 H.

(η^3 -2-Methylallyl)bis[(*R*)-(2-biphenyl)isopropylphenylphosphane]palladium(II) Hexafluorophosphate (3d**)**: This complex was obtained by the same method as that used for **3a**. From the phosphane (**S**)-**d** (0.140 g, 0.46 mmol), ammonium hexafluorophosphate (0.0937 g, 0.57 mmol) and the dimer $[\text{PdCl}(\mu\text{-Cl})\eta^3\text{-(2-CH}_3\text{-C}_3\text{H}_4)]$ (0.0442 g, 0.11 mmol), the title product was isolated as a yellow solid; yield 0.100 g (50%). ^1H NMR (250.1 MHz, CDCl_3 , 298 K): δ = 0.61–0.91 (m, 12 H), 1.26–1.68 (m, 2 H), 2.20 (s, 3 H), 3.36 (d, J = 8.8 Hz, 1 H), 3.60 (d, J = 9.5 Hz, 1 H), 4.13 (s, 1 H), 4.42 (s, 1 H), 6.79–7.48 (m, 28 H, Ar) ppm. $^{31}\text{P}\{^1\text{H}\}$ NMR (101.1 MHz, CD_3COCD_3 , 298 K): δ = +39.4 (d, J = 31.0 Hz, 1 P), +40.0 (d, J = 31.0 Hz, 1 P) ppm. $\text{C}_{46}\text{F}_6\text{H}_{49}\text{P}_3\text{Pd}$ (915.21): calcd. C 60.37, H 5.40; found C 60.77, H 5.94.

(η^3 -2-Methylallyl)bis[(*S*)-(2-biphenyl)methoxyphenylphosphane]palladium(II) Hexafluorophosphate (3f**)**: This complex was obtained by the same method as that used for **3a**. From the phosphinite (**R**)-**f** (0.265 g, 0.99 mmol), ammonium hexafluorophosphate (0.231 g, 1.42 mmol) and the dimer $[\text{PdCl}(\mu\text{-Cl})\eta^3\text{-(2-CH}_3\text{-C}_3\text{H}_4)]$ (0.093 g, 0.24 mmol), the desired complex was obtained as a red solid; yield 0.233 g (58%). ^1H NMR (500.1 MHz, CDCl_3 , 298 K): δ = 1.61 (s, 3 H), 1.96 (d, J = 8.8 Hz, 1 H), 2.38 (d, J = 8.8 Hz, 1 H), 3.11 (d, J = 10.4 Hz, 3 H), 3.21 (d, J = 10.0 Hz, 3 H), 3.71 (s, 1 H), 3.84–3.86 (m, 1 H), 6.81–7.62 (m, 28 H, Ar) ppm. $^{31}\text{P}\{^1\text{H}\}$ NMR (101.1 MHz, CDCl_3 , 298 K): δ = +120.7 (d, J = 53.9 Hz, 1 P), +124.7 (d, J = 53.9 Hz, 1 P) ppm. $\text{C}_{38}\text{F}_6\text{H}_{37}\text{O}_2\text{P}_3\text{Pd}$ (839.03): calcd. C 54.40, H 4.44; found C 57.00, H 5.19.

(η^3 -2-Methylallyl){(*R,R*)-1,2-bis[(1-naphthyl)phenylphosphanyl]ethane}palladium(II) Hexafluorophosphate (4a**)**: The phosphane **1a** (0.110 g, 0.22 mmol) was dissolved in CH_2Cl_2 (10 mL). Ammonium hexafluorophosphate (0.059 g, 0.36 mmol) and the dimer $[\text{PdCl}(\mu\text{-Cl})\eta^3\text{-(2-CH}_3\text{-C}_3\text{H}_4)]$ (0.047 g, 0.12 mmol) were added and the mixture was stirred for 1 h. Water (10 mL) was added and the mixture was extracted with dichloromethane (3×10 mL). The combined organic fraction was washed with water and dried with anhydrous sodium sulfate. The solvent was removed and the remaining yellowish foam was recrystallized from toluene/dichloromethane to yield the title product as a white crystalline solid; yield 0.110 g (57%). ^1H NMR (400.1 MHz, CDCl_3 , 298 K): δ = 1.71 (s, 3 H), 2.38–2.59 (m, 2 H), 2.95 (d, J = 10.0 Hz, 1 H), 3.14–3.30 (m, 2 H), 3.27 (d, J = 10.4 Hz, 1 H), 4.11 (s, 1 H), 4.54 (s, 1 H), 6.98–8.00 (m, 26 H, Ar) ppm. $^{13}\text{C}\{^1\text{H}\}$ NMR (100.0 MHz, CDCl_3 ,

298 K): δ = 24.1 (s, CH₃), 26.6 (d, J_{CP} = 12.9 Hz, CH₂), 27.0 (d, J_{CP} = 12.9 Hz, CH₂), 69.8 (dd, J_{CP} = 29.8, 3.8 Hz, CH₂), 70.6 (dd, J_{CP} = 29.0, 3.8 Hz, CH₂), 124.1–138.2 (m, 1 C, CH, Ar) ppm. $^{31}\text{P}\{^1\text{H}\}$ NMR (101.1 MHz, CDCl₃, 298 K): δ = +44.2 (d, J = 29.7 Hz, 1 P), +45.6 (d, J = 29.6 Hz, 1 P) ppm. C₃₇F₆H₃₅P₃Pd (793.01): calcd. C 56.04, H 4.45; found C 58.28, H 5.08.

(η^3 -2-Methylallyl){(*R,R*)-1,2-bis[(9-phenanthryl)phenylphosphanyl]ethane}palladium(II) Hexafluorophosphate (4e**):** This complex was obtained by the same method as that used for **4a**. From the diphosphane (**S,S**)-**1e** (0.271 g, 0.45 mmol), ammonium hexafluorophosphate (0.147 g, 0.90 mmol) and the dimer [PdCl(μ -Cl) η^3 -(2-CH₃-C₃H₄)] (0.087 g, 0.23 mmol), the desired product was obtained as a pale yellow solid; yield 0.222 g (55%). ^1H NMR (400.1 MHz, CDCl₃, 298 K): δ = 1.69 (s, 3 H), 2.40–2.70 (m, 2 H), 3.03 (d, J = 10.0 Hz, 1 H), 3.18–3.33 (m, 2 H), 3.31 (d, J = 9.6 Hz, 1 H), 4.11 (s, 1 H), 4.52 (s, 1 H), 7.06–8.71 (m, 28 H, Ar) ppm. $^{13}\text{C}\{^1\text{H}\}$ NMR (100.0 MHz, CDCl₃, 298 K): δ = 24.2 (s, CH₃), 26.6 (d, J_{CP} = 13.7 Hz, CH₂), 27.0 (d, J_{CP} = 13.7 Hz, CH₂), 70.2 (d, J_{CP} = 28.9 Hz, CH₂), 71.0 (d, J_{CP} = 29.8 Hz, CH₂), 122.7–138.3 (m, 1 C, CH, Ar) ppm. $^{31}\text{P}\{^1\text{H}\}$ NMR (121.5 MHz, CDCl₃, 298 K): δ = +44.7 (d, J = 29.8 Hz, 1 P), +45.4 (d, J = 29.8 Hz, 1 P) ppm. C₄₆F₆H₃₉P₃Pd (905.13): calcd. C 61.04, H 4.34; found C 62.96, H 4.51.

Crystal Structure Determination of 4e: Colourless crystals, suitable to perform X-ray diffraction studies, were obtained by slow diffusion of toluene over a solution of the complex in dichloromethane at 4 °C. C₅₀H₄₄ClF₆P₃Pd (1/2 toluene, 1/2 CH₂Cl₂) M_r = 993.69 g mol^{−1}, orthorhombic, a = 19.9089(11) Å, b = 19.9089(11) Å, c = 66.178(5) Å, U = 22716(2) Å³, T = 298(2) K, space group R_{32n} , Z = 18, 38579 reflections measured, 11451 unique (R_{int} = 0.1321), which were used in all calculations. The final $wR(F2)$ was 0.2402 (all data).

CCDC-753099 contains the supplementary crystallographic data for **4e**. These data can be obtained free of charge from The Cambridge Crystallographic Data Centre via www.ccdc.cam.ac.uk/data_request/cif.

(η^3 -2-Methylallyl){(*R,R*)-2,2-dimethyl-1,3-bis[(9-phenanthryl)phenyl]-2-silapropene}palladium(II) Hexafluorophosphate (5e**):** This complex was obtained by the same method as that used for **4a**. From the diphosphane (**S,S**)-**2e** (0.200 g, 0.30 mmol), ammonium hexafluorophosphate (0.196 g, 1.20 mmol) and the dimer [PdCl(μ -Cl) η^3 -(2-CH₃-C₃H₄)] (0.059 g, 0.15 mmol), the title complex was isolated as a white solid; yield 0.104 g (36%). ^1H NMR (400.1 MHz, CD₃COCD₃, 298 K): δ = −0.56 (s, 3 H), −0.48 (s, 3 H), 1.78 (s, 3 H), 2.36–2.55 (m, 4 H), 3.23 (d, 1 H, J = 10.0 Hz), 3.46 (d, 1 H, J = 10.4 Hz), 3.63 (t, 1 H, J = 4.0 Hz), 3.79 (t, 1 H, J = 4.0 Hz), 7.13–9.05 (m, 28 H, Ar) ppm. $^{13}\text{C}\{^1\text{H}\}$ NMR (100.0 MHz, CD₃COCD₃, 298 K): δ = −0.3 (s, CH₃), −0.2 (s, CH₃), 11.0–11.3 (m, 2CH₂), 23.5 (s, CH₃), 74.0 (d, J_{CP} = 32.7 Hz, CH₂), 76.6 (d, J_{CP} = 31.2 Hz, CH₂), 123.6–139.9 (m, 1 C, CH, Ar) ppm. $^{31}\text{P}\{^1\text{H}\}$ NMR (101.1 MHz, CD₃COCD₃, 298 K): δ = +12.2 (d, J = 47.9 Hz, 1 P), +13.4 (d, J = 47.6 Hz, 1 P) ppm. C₄₈F₆H₄₅P₃PdSi (963.29): calcd. C 59.85, H 4.71; found C 60.05, H 4.35.

Chloro(η^3 -1,3-diphenylallyl){(*R*)-methyl(1-naphthyl)phenylphosphane}palladium(II) (6a**):** The phosphane (**S**)-**a** (0.140 g, 0.56 mmol) was dissolved in CH₂Cl₂ (10 mL). The dimer [PdCl(μ -Cl)(η^3 -1,3-diphenylallyl)]₂ (0.181 g, 0.27 mmol) was added and the mixture was stirred for 1 h. The solvent was removed and the remaining yellowish foam was washed several times with pentane. Finally the yellow powder obtained was filtered and dried under vacuum; yield 0.150 g (46%). ^1H NMR (500.1 MHz, CDCl₃, 253 K): δ = P–CH₃ major 1.8 (d, 3 H, J = 9.0 Hz), minor 2.1 (d, 3 H, J = 9.0 Hz) ppm.

Allyl system: see discussion. $^{13}\text{C}\{^1\text{H}\}$ NMR (100.0 MHz, CDCl₃, 298 K): δ = 13.8 (s, CH₃), 14.1 (s, CH₃), 72.0 (s, CH₃), 96.6 (d, J_{CP} = 25.4 Hz, CH), 97.7 (d, J_{CP} = 25.4 Hz, CH), 108.4 (s, CH), 109.1 (s, CH), 124.8–138.1 (m, 1 C, CH, Ar) ppm. $^{31}\text{P}\{^1\text{H}\}$ NMR (101.1 MHz, CDCl₃, 298 K): δ = 3.4 (b) ppm. $^{31}\text{P}\{^1\text{H}\}$ NMR (11.1 MHz, CDCl₃, 253 K): δ = 7.7 (45%), 7.8 (55%) ppm. C₃₂ClH₂₈PPd (585.41): calcd. C 65.66, H 4.82; found C 65.90, H 5.30.

Chloro(η^3 -1,3-diphenylallyl){(*R*)-(2-biphenyl)isopropylphenylphosphane}palladium(II) (6d**):** This complex was obtained by the same method as that used for **6a**. From the phosphane (**S**)-**d** (0.215 g, 0.706 mmol) and the dimer [PdCl(μ -Cl)(η^3 -1,3-diphenylallyl)]₂ (0.235 g, 0.350 mmol), the desired product was obtained as a pale orange solid; yield 0.320 g (71%). IR: $\tilde{\nu}$ = 3056 ν (C–H), 3030 ν (C–H), 2984 ν (C–H), 2964 ν (C–H), 2928 ν (C–H), 1548, 1490, 1463, 1434, 1385, 1183, 1091, 761, 752, 738, 709, 697, 690, 649, 508 cm^{−1}. ^1H NMR (500.1 MHz, CDCl₃, 298 K): δ = P–CH–(CH₃)₂ major 1.48 (m), minor 2.55 (m), P–CH–(CH₃)₂ major 0.65, 0.88 (dd, J = 13, 7 Hz), minor 0.90, 1.1 (dd, J = 18.5, 7 Hz, 3 H) ppm. Allyl system: see discussion. $^{13}\text{C}\{^1\text{H}\}$ NMR (100.0 MHz, CDCl₃, 298 K): δ = 19.0 (d, J_{CP} = 43.5 Hz, CH₃), 19.5 (d, J_{CP} = 37.4 Hz, CH₃), 21.2 (d, J_{CP} = 6.1 Hz, CH₃), 21.6 (d, J_{CP} = 9.2 Hz, CH₃), 25.1 (d, J_{CP} = 20.6 Hz, CH), 27.1 (d, J_{CP} = 21.4 Hz, CH), 71.8 (s, CH), 72.3 (d, J_{CP} = 5.4 Hz, CH), 96.2 (d, J_{CP} = 25.2 Hz, CH), 98.1 (d, J_{CP} = 24.4 Hz, CH), 106.8 (d, J_{CP} = 4.6 Hz, CH), 107.4 (s, CH), 126.2–147.1 (C, CH, Ar) ppm. $^{31}\text{P}\{^1\text{H}\}$ NMR (11.1 MHz, CDCl₃, 298 K): δ = 31.4 (43%), 33.6 (57%) ppm. C₃₆ClH₃₄PPd (639.50): calcd. C 67.62, H 5.36; found C 67.05, H 5.90.

Crystal Structure Determination for 6d: Orange crystals, suitable to perform X-ray diffraction studies, were obtained by slow diffusion of hexane over a solution of the complex in dichloromethane at 4 °C. C₃₆H₃₄ClPPd, M_r = 947.66 g mol^{−1}, orthorhombic, a = 12.991(3) Å, b = 13.684(3) Å, c = 16.864(3) Å, U = 2997.7(10) Å³, T = 173 K, space group $P2_12_12_1$ (no. 19), Z = 4, 17564 reflections measured, 6129 unique (R_{int} = 0.0208), which were used in all calculations. The final $wR(F2)$ was 0.1062 (all data).

CCDC-753100 contains the supplementary crystallographic data for **6d**. These data can be obtained free of charge from The Cambridge Crystallographic Data Centre via www.ccdc.cam.ac.uk/data_request/cif.

Supporting Information (see also the footnote on the first page of this article): Selected ^{13}C NMR spectroscopic data of complexes **3**, **4** and **5**. Crystal data and structure refinement for **4e** and **6d**. ^1H NMR spectra of **6a** in CDCl₃ at different temperatures. $^{31}\text{P}\{^1\text{H}\}$ NMR spectra for selected palladium complexes.

Acknowledgments

The authors thanks the Ministerio de Educación y Ciencia (MEC) (CTQ2007-61058/BQU) for financial support of this work.

- [1] a) B. M. Trost, D. L. Van Vranken, *Chem. Rev.* **1996**, 96, 395–422; b) B. M. Trost, M. L. Crawley, *Chem. Rev.* **2003**, 103, 2921–2943.
- [2] Z. Lu, S. Ma, *Angew. Chem. Int. Ed.* **2008**, 47, 258–297.
- [3] P. R. Auburn, P. B. Mackenzie, B. Bosnich, *J. Am. Chem. Soc.* **1985**, 107, 2033–2046.
- [4] C. Markert, M. Neuburger, K. Kulicke, M. Meuwly, A. Pfaltz, *Angew. Chem. Int. Ed.* **2007**, 46, 5892–5895.
- [5] L. A. Evans, N. Fey, J. N. Harvey, D. Hose, G. C. Lloyd-Jones, P. Murray, A. G. Orpen, R. Osborne, G. J. J. Owen-Smith, M. Purdie, *J. Am. Chem. Soc.* **2009**, 131, 14471–14473.

- [6] a) P. Fristrup, T. Jensen, J. Hoppe, P. O. Norrby, *Chem. Eur. J.* **2006**, *12*, 5352–5360; b) C. Amatore, A. A. Bahsoun, A. Jutand, L. Mensah, G. Meyer, L. Ricard, *Organometallics* **2005**, *24*, 1569–1577.
- [7] a) C. Amatore, A. Jutand, M. A. M'Barki, G. Meyer, L. Mottier, *Eur. J. Inorg. Chem.* **2001**, 873–880; b) T. Cantat, E. Génin, C. Giroud, G. Meyer, A. Jutand, *J. Organomet. Chem.* **2003**, *687*, 365–376.
- [8] a) A. B. Castillo, I. Favier, E. Teuma, S. Castellón, C. Godard, A. Aghmiz, C. Claver, M. Gómez, *Chem. Commun.* **2008**, 6197–6199; b) E. Raluy, O. Pàmies, M. Diéguez, *Adv. Synth. Catal.* **2009**, *351*, 1648–1670.
- [9] a) C. A. Müller, A. Pfaltz, *Angew. Chem. Int. Ed.* **2008**, *47*, 3363–3366; b) C. Markert, P. Rösel, A. Pfaltz, *J. Am. Chem. Soc.* **2008**, *130*, 3234–3235.
- [10] a) S. Spiess, C. Welter, G. Franck, J. P. Taquet, G. Helmchen, *Angew. Chem. Int. Ed.* **2008**, *47*, 7652–7655; b) S. T. Madrahimov, D. Markovic, J. F. Hartwig, *J. Am. Chem. Soc.* **2009**, *131*, 7228–7229.
- [11] H. Tsuruta, T. Imamoto, *Synlett* **2001**, 999–1002.
- [12] R. M. Stoop, A. Mezzetti, *Organometallics* **1998**, *17*, 668–675.
- [13] Y. Hamada, F. Matsuruta, M. Oku, K. Hatano, T. Shiori, *Tetrahedron Lett.* **1997**, *38*, 8961–8964.
- [14] H. Danjo, M. Higuchi, M. Yada, T. Imamoto, *Tetrahedron Lett.* **2004**, *45*, 603–606.
- [15] N. Oohara, K. Katagiri, T. Imamoto, *Tetrahedron: Asymmetry* **2003**, *14*, 2171–2175.
- [16] U. Nettekoven, M. Widhalm, P. C. J. Kamer, P. W. N. M. van Leeuwen, *Tetrahedron: Asymmetry* **1997**, *8*, 3185–3188.
- [17] U. Nettekoven, M. Widhalm, H. Kalchhauser, P. C. J. Kamer, P. W. N. M. van Leeuwen, M. Lutz, A. L. Spek, *J. Org. Chem.* **2001**, *66*, 759–770.
- [18] T. Imamoto, M. Nishimura, A. Koide, K. Yoshida, *J. Org. Chem.* **2007**, *72*, 7413–7416.
- [19] M. D. K. Boele, P. C. J. Kamer, M. Lutz, A. L. Spek, J. G. de Vries, P. W. N. M. Leeuwen, G. P. F. van Strijdonck, *Chem. Eur. J.* **2004**, *10*, 6232–6246.
- [20] A. J. Blacker, M. L. Clarke, M. S. Loft, J. M. J. Williams, *Org. Lett.* **1999**, *1*, 1969–1971.
- [21] T. Hayashi, M. Kawatsura, Y. Uozumi, *J. Am. Chem. Soc.* **1998**, *120*, 1681–1687.
- [22] V. N. Tsarev, S. E. Lyubimov, A. A. Shiryaev, S. V. Zhiglov, O. G. Bondarev, V. A. Davankov, A. A. Kabro, S. K. Moiseev, V. N. Kalinin, K. N. Gavrilov, *Eur. J. Inorg. Chem.* **2004**, 2214–2222.
- [23] Y. Hamada, N. Seto, H. Ohmori, K. Hatano, *Tetrahedron Lett.* **1996**, *37*, 7565–7568.
- [24] Y. Y. Yan, T. V. RajanBabu, *Org. Lett.* **2000**, *2*, 199–202.
- [25] P. Dotta, P. G. A. Kumar, P. S. Pregosin, A. Albinati, S. Rizzato, *Organometallics* **2004**, *23*, 2295–2304.
- [26] A. Grabulosa, G. Muller, J. I. Ordinas, A. Mezzetti, M. Á. Maestro, M. Font-Bardía, X. Solans, *Organometallics* **2005**, *24*, 4961–4973.
- [27] S. Jugé, M. Stephan, J. A. Laffitte, J. P. Genet, *Tetrahedron Lett.* **1990**, *31*, 6357–6360.
- [28] T. Imamoto, J. Watanabe, Y. Wada, H. Masuda, H. Yamada, H. Tsuruta, S. Matsukawa, K. Yamaguchi, *J. Am. Chem. Soc.* **1998**, *120*, 1635–1636.
- [29] R. M. Stoop, C. Bauer, P. Setz, M. Wörle, T. Y. H. Wong, A. Mezzetti, *Organometallics* **1999**, *18*, 5691–5700.
- [30] R. M. Stoop, A. Mezzetti, F. Spindler, *Organometallics* **1998**, *17*, 668–675.
- [31] P. Dotta, P. G. A. Kumar, P. S. Pregosin, A. Albinati, *Helv. Chim. Acta* **2004**, *87*, 272–278.
- [32] a) E. Cesarotti, M. Grassi, L. Prati, F. Demartin, *J. Organomet. Chem.* **1989**, *370*, 407–419; b) F. Ozawa, T. Son, S. Ebina, K. Osakada, A. Yamamoto, *Organometallics* **1992**, *11*, 171–176; c) J. Cermak, S. D. Perera, B. L. Shaw, M. Thornton-Pett, *Inorg. Chim. Acta* **1996**, *244*, 115–120; d) M. Lejeune, C. Jeunesse, D. Matt, N. Kyritsakas, R. Welter, J.-P. Kintzinger, *J. Chem. Soc., Dalton Trans.* **2002**, 1642–1650.
- [33] M. T. Reetz, X. Li, *Angew. Chem. Int. Ed.* **2005**, *44*, 2959–2962.
- [34] R. Hoen, J. A. F. Boogers, H. Bernsmann, A. J. Minnaard, A. Meetsma, T. D. Tiemersma-Wegman, A. H. M. de Vries, J. G. de Vries, B. L. Feringa, *Angew. Chem. Int. Ed.* **2005**, *44*, 4209–4212.
- [35] a) M. T. Reetz, O. Bondarev, *Angew. Chem. Int. Ed.* **2007**, *46*, 4523–4526; b) M. T. Reetz, M. Surowiec, *Heterocycles* **2006**, *67*, 567–574.
- [36] U. Leutenegger, G. Umbricht, C. Fahrni, P. V. Matt, A. Pfaltz, *Tetrahedron* **1992**, *48*, 2143–2156.
- [37] P. von Matt, A. Pfaltz, *Angew. Chem. Int. Ed. Engl.* **1994**, *32*, 566–568.
- [38] J. Wassenaar, S. van Zutphen, G. Mora, P. Le Floch, M. A. Siegler, A. L. Spek, J. N. H. Reek, *Organometallics* **2009**, *28*, 2724–2734.
- [39] a) E. Szurómi, H. Shen, B. L. Gooddall, R. F. Jordan, *Organometallics* **2008**, *27*, 402–409; b) R. M. Ceder, C. García, A. Grabulosa, F. Karićin, G. Muller, M. Rocamora, M. Font-Bardía, X. Solans, *J. Organomet. Chem.* **2007**, *692*, 4005–4019.
- [40] P. von Matt, G. C. Lloyd-Jones, A. B. E. Minidis, A. Pfaltz, L. Macko, M. Neuburger, M. Zehnder, H. Rüegger, P. S. Pregosin, *Helv. Chim. Acta* **1995**, *78*, 265–284.
- [41] O. Hoarau, H. Aiet-Haddou, J.-C. Daran, D. Cramailere, G. G. A. Balavoine, *Organometallics* **1999**, *18*, 4718–4723.
- [42] Sometimes it is possible to observe this exchange by NMR spectroscopy as in: M. A. Pericàs, C. Puigjaner, A. Riera, A. Vidal-Ferran, M. Gómez, F. Jiménez, G. Muller, M. Rocamora, *Chem. Eur. J.* **2002**, *8*, 4164–4178; or it is not observed as in: D. Franco, M. Gómez, F. Jiménez, G. Muller, M. Rocamora, M. A. Maestro, J. Mahía, *Organometallics* **2004**, *23*, 3197–3209.
- [43] C. Amatore, A. A. Bahsoun, A. Jutand, L. Mensah, G. Meyer, L. Ricard, *Organometallics* **2005**, *24*, 1569–1577.
- [44] M. Kranenburg, P. C. J. Kamer, P. W. N. M. van Leeuwen, *Eur. J. Inorg. Chem.* **1998**, 25–27, and references cited therein.
- [45] a) M. W. Baize, P. W. Blosser, V. Plantevin, D. G. Schimpff, J. C. Gallucci, A. Wojcicki, *Organometallics* **1996**, *15*, 164–173; b) S. Ogoshi, K. Tsutsumi, H. Kurosawa, *J. Organomet. Chem.* **1995**, *493*, C19–C21.
- [46] W. T. Dent, R. Long, A. J. Wilkinson, *J. Chem. Soc.* **1964**, 1585–1588.

Received: March 17, 2010
Published Online: June 2, 2010